Water Science and Technology Library

Ramakar Jha · Vijay P. Singh ·
Vivekanand Singh · L. B. Roy ·
Roshni Thendiyath *Editors*

River and Coastal Engineering

Hydraulics, Water Resources and Coastal Engineering

Springer

Water Science and Technology Library

Volume 117

The aim of the *Water Science and Technology Library* is to provide a forum for dissemination of the state-of-the-art of topics of current interest in the area of water science and technology. This is accomplished through publication of reference books and monographs, authored or edited. Occasionally also proceedings volumes are accepted for publication in the series. *Water Science and Technology Library* encompasses a wide range of topics dealing with science as well as socio-economic aspects of water, environment, and ecology. Both the water quantity and quality issues are relevant and are embraced by *Water Science and Technology Library*. The emphasis may be on either the scientific content, or techniques of solution, or both. There is increasing emphasis these days on processes and *Water Science and Technology Library* is committed to promoting this emphasis by publishing books emphasizing scientific discussions of physical, chemical, and/or biological aspects of water resources. Likewise, current or emerging solution techniques receive high priority. Interdisciplinary coverage is encouraged. Case studies contributing to our knowledge of water science and technology are also embraced by the series. Innovative ideas and novel techniques are of particular interest.

Comments or suggestions for future volumes are welcomed.

Vijay P. Singh, Department of Biological and Agricultural Engineering & Zachry Department of Civil and Environment Engineering, Texas A&M University, USA
Email: vsingh@tamu.edu

All contributions to an edited volume should undergo standard peer review to ensure high scientific quality, while monographs should also be reviewed by at least two experts in the field.

Manuscripts that have undergone successful review should then be prepared according to the Publisher's guidelines manuscripts: https://www.springer.com/gp/authors-editors/book-authors-editors/book-manuscript-guidelines

Ramakar Jha · Vijay P. Singh · Vivekanand Singh ·
L. B. Roy · Roshni Thendiyath
Editors

River and Coastal Engineering

Hydraulics, Water Resources and Coastal Engineering

Springer

Editors
Ramakar Jha
Department of Civil Engineering
National Institute of Technology Patna
Patna, India

Vivekanand Singh
Department of Civil Engineering
National Institute of Technology Patna
Patna, Bihar, India

Roshni Thendiyath
Department of Civil Engineering
National Institute of Technology Patna
Patna, India

Vijay P. Singh
Department of Biological and Agricultural Engineering
Zachry Department of Civil and Environmental Engineering
Texas A&M University
College Station, TX, USA

L. B. Roy
Department of Civil Engineering
National Institute of Technology Patna
Patna, India

ISSN 0921-092X ISSN 1872-4663 (electronic)
Water Science and Technology Library
ISBN 978-3-031-05056-5 ISBN 978-3-031-05057-2 (eBook)
https://doi.org/10.1007/978-3-031-05057-2

This Springer imprint is published by the registered company Springer Nature Switzerland AG
The registered company address is: Gewerbestrasse 11, 6330 Cham, Switzerland

Preface

The book is unique in nature by covering the coastal engineering and river engineering aspects related to the engineering solutions with case studies. The Shoreline oscillations are the response of natural endeavors such as wind, wave and storm which are termed as short term or temporary modification. Shore line changes are the phenomenon of permanent modification to a coast induced by natural calamities such as Tsunami, sea level rise and by human intervention such as the improper implication of structures like the groin, detached breakwaters, seawalls and coastal related activities such as dredging and beach nourishment. A suite of meso-scale and submeso-scale processes effect the ocean shoreline properties, such as the mixed layer depth, *sea surface temperature* (SST) and *sea surface salinity* (SSS), which shape the weather and climate conditions by balancing the exchange of mass, momentum, energy and heat between the atmosphere and the ocean. Carrying out conventional bathymetry survey for inter-tidal zones is a tedious and time-consuming process. This demands to use of the remote sensing for such regions. However, remote sensing of intertidal zones has the issues of water clarity and turbidity, which contributes error in mapping the bottom topography.

In the book, the depth values of the inter-tidal zones have been extracted using two methods such as band ratio and tide co-ordinated shoreline method. Moreover, cases studies are done for the assessment of shoreline position, rate of sediment movement, short-term shoreline oscillation and volumetric changes using a most reliable and accepted system of data acquisition and manipulation.

Fisheries sector is another powerful income and employment generator as it stimulates growth of a number of subsidiary industries and is a source of cheap and nutritious food and foreign exchange earner as well. The mathematical models has been used to simulate wave conditions in Mangrol harbours and ports. Moreover, in the Sagarmala project, it is envisaged to develop small tourist cum fishing harbours along the coast. In view of this, a feasibility to develop a small harbour in the open sea near Korlai is studied using mathematical modelling.

Coastal erosion is one of the significant issues throughout the globe. Coastal areas are more prone and vulnerable against the natural and anthropogenic changes that take place along the coast. A lot of developmental activities along the coast are being

ubiquitous nowadays, which has a direct or indirect impact on the coastal areas. In the book, the effect of developmental activities on the coast has been studied, and proper measures were made to reduce the impact. Coastal stretches from Ennore creek to Pulicat of Tiruvallur district were considered using DSAS to identify the causes and hotspots of erosion.

In India, 45% of its 7500 km coastline is disintegrated. Infrastructural development like harbour, hinders the ideal sand sediment stream, additionally embankments and groins deter the long shore drift. Such constructions, which are beneficial for infrastructural growth, create problems to nature and part of society lying within those regions. Construction of a seawall seems a beneficial option for addressing the excessive unwanted erosion. For the design and construction of a seawall with increased sustainability, preliminary investigation on structures response to the attacked wave is essential. Such studies have been conducted experimentally, analytically and using numerical tools using commercial packages for wave-structure interaction (WSI) studies are compared. Solvers based on Navier–Stokes equation, volume of fluid (VOF), nonlinear shallow water equations and finite element method (FEM) are compared using literature.

As the ocean covers 70% of earth surface, it has a very significant role in providing the clean energy in the form of tidal energy, tidal currents, wave energy, temperature gradient and salinity gradient which are sufficient enough to meet the global energy demand. The book presents an overview in respect of current state of research and development in the field of tidal energy as this form of renewable energy is considered as most advanced one.

River engineering is another important area of research, which is being extensively used for water resource projects affected by the amount and concentration of sediment transported, heavy precipitation and human interventions including hydropower projects. In this regard, studies related to various aspects have been discussed in the book with some cases studies of Ganga, Mahanada, Tapi and other Himalayan rivers. For the analysis, different numerical and analytical models in support with remote sensing and GIS have been used. Some of the models are generalized reduced gradient technique, magnitude frequency analysis (MFA), computational fluid dynamic (CFD) program-based Flow3D, Mann–Kendall trend test, river hydraulic model and MATLAB/SIMULINK.

Patna, India — Ramakar Jha
College Station, TX, USA — Vijay P. Singh

Acknowledgements

The editors are grateful to Prof. P. K. Jain, Director, NIT Patna, for his constructive support and encouragement for completing the book. They also thank reviewers for reviewing the papers included in the book.

This book would not have been possible without the support of Indian Society for Hydraulics, CWPRS Pune, and sponsors who supported the annual conference. This book constitutes a portion of the proceedings of conference.

The editors thank all the experts who delivered Keynote address, all the participants, faculties, staff and the students who contributed to the completion of the book. Some of the students are Kamakshi Singh, Saba Khurshid and Ratnesh Kumar.

Finally, the editors acknowledge all those who helped with bringing the book to fruition, especially the authors of all the papers.

Contents

About the Editors

Ramakar Jha is a chair professor at the Department of Civil Engineering and has 30 years of experience in the field of hydrology and water resources engineering. Dr. Jha is presently working as Chair Professor in the Department of Civil Engineering, National Institute of Technology (NIT) Patna-India, which is a Premier Institute in India under the Ministry of Human Resource Development, Government of India. Dr. Jha has served at various levels from Scientist-B to Scientist-E1 at National Institute of Hydrology (NIH), Roorkee, India, and as Professor in the Department of Civil Engineering, NIT Rourkela. He has worked and working as Country Co-ordinator of UNESCO-GWADI and Principal Investigator for many International (EU-FP7, DAAD, ADB, AUS-Aid) and National research and consultancy projects (ISRO, DST, MoWR, MHRD). Moreover, he served as Chair for many administrative positions and received a couple of international and national awards for research papers. Presently, he is working as Dr. Rajendra Prasad Chair for Water resources under the Ministry of Water Resources, Government of India, in the Department of Civil Engineering, NIT Patna, Bihar.

Vijay P. Singh is University Distinguished Professor, Regents Professor, and Caroline and William N. Lehrer Distinguished Chair in Water Engineering at Texas A&M University. He received his B.S., M.S., Ph.D. and D.Sc. degrees in engineering. He is a registered professional engineer, a registered professional hydrologist and an honorary diplomate of ASCE-AAWRE. He is a distinguished member of ASCE, a distinguished fellow of AGGS, and an honorary member of AWRA, and a fellow of EWRI-ASCE, IAH, ISAE, IWRS and IASWC. He has published extensively in the areas of hydrology, irrigation engineering, hydraulics, groundwater, water quality and water resources (more than 1320 journal articles; 31 textbooks; 75 edited reference books; 110 book chapters; and 315 conference papers). He has received more than 95 national and international awards, including three honorary doctorates. He is a member of 11 international science/engineering academies. He has served as President of the American Institute of Hydrology (AIH), Chair of Watershed Council of American Society of Civil Engineers, and is currently President of American Academy of Water Resources Engineers. He has served/serves as editor-in-chief of

three journals and two book series and serves on editorial boards of more than 25 journals and three book series. His Google Scholar citations include: 65120; h-index: 113, and I10-index: 993.

Vivekanand Singh is a professor at the Department of Civil Engineering and has 28 years of experience in the field of river hydraulics, groundwater and water resources engineering. Dr. Singh has published research papers in international journals including ASCE Journal. He has done national projects and consultancy during his work at NIT Patna. Prior to this, Dr. Singh was Scientist at National Institute of Hydrology Roorkee. He organized several summer courses, conferences and workshops. He has been working as Editor in some Indian Journals.

L. B. Roy is a professor at the Department of Civil Engineering and has 33 years of experience in the field of water resources engineering as well as geotechnical engineering. Dr. Roy has been serving the Water Resources Engineering Department for long time and carried out various field based research activities for different river systems of the region with special emphasis to floods. Dr. Roy has been involved in many research projects and published several research papers in peer reviewed journals. He has been working for intellectual property rights (IPR) and received awards for various activities.

Roshni Thendiyath is an assistant professor at the Department of Civil Engineering and has nine years of experience in the field of water resources engineering. Dr. Roshni earned her Ph.D. in Civil Engineering at the University of Pisa, Italy. After obtaining Ph.D., Dr Roshni had joined National Institute of Technology Calicut, India, as an ad-hoc faculty and later joined National Institute of Technology Patna as an assistant professor. She has supervised 2 Ph.D., more than 30 Master theses. Furthermore, she has been awarded DST-SERB project for the topic Two Phase Flows and Water Quality in Rivers, funded by the Department of Science and Technology, MHRD India. Results obtained from her research have been published nearly 30 papers in international journals and more than 15 papers in international conferences and three book chapters. Dr. Roshni is active in a variety of professional bodies and she has organized numerous workshops and conferences in her academic career.

Establishing Sediment Rating Curves Using Optimization Technique

Mohammad Zakwan and Zeenat Ara

1 Introduction

Deposition of sediment transported by a river is an important aspect of water resource engineering. Water resource projects is affected by the amount and concentration of sediment transported by a river as it results in reduction of reservoir capacity (Zakwan et al. 2017a; Ara and Zakwan 2018; Pandey et al. 2020). Therefore, quantification of sediment volume is required for estimation of design life of reservoirs and river training (Nagy et al. 2002; Muzzammil et al. 2018; Zakwan et al. 2018).

In the past, several attempts were made to correlate the sediment load and different flow properties such as discharge, velocity, precipitation and friction factor. Investigating uncertainties related to sediment transport curves, it has been found that accuracy of estimated sediment concentrations is largely dependent on the method used for fitting the sediment-rating curve. Therefore, the fundamental challenge in estimating sediment load is to select an appropriate curve fitting method and to determine the accuracy with which that technique fits the observed data. Ferguson (1986) pointed out that linear regression of logarithmic transformed sediment rating curve introduces a bias in the estimates of sediment load which may lead to underestimation of sediment load by as much as 50%. Asselman (2000) developed sediment rating curves using linear regression with and without a correction factors and concluded that they underestimate sediment loads. Demissie et al. (2004) too suggested nonlinear regression as better approach to estimate sediment load rather than linear regression which underestimates sediment load as observed by them for several streams in Illinois. Therefore, several researchers have turned towards the machine learning and non-linear optimization techniques to estimate sediment load.

Jain (2001) utilized the Artificial Neural Network (ANN) approach to establish the stage discharge-sediment relationship. Nagy et al. (2002) used ANN to model

M. Zakwan · Z. Ara (✉)
Civil Engineering Department, MANUU, Hyderabad 500032, India
e-mail: zeenatiitd@rediffmail.com

R. Jha et al. (eds.), *River and Coastal Engineering*, Water Science and Technology Library 117, https://doi.org/10.1007/978-3-031-05057-2_1

sediment concentration with various inputs and demonstrated that ANN models are more reliable than the conventional models. Most commonly used neural network, multi-layer perceptron (MLP), was used by Kisi (2004) for more accurate estimation of suspended sediment concentration as compared to multiple linear regression. Sakai et al. (2005) applied multi-objective optimization technique to model suspended sediment concentration curves. Crowder et al. (2007) used nonlinear optimization technique for developing sediment rating curves for several gauging sites. They suggested that regression technique that would yield best rating curve would depend on the shape and variability of sediment–discharge relationship, the amount of data used for calibrating the equation and the time frame over which sediment load is to be estimated. Lohani et al. (2007) proposed the concept of developing integrated stage–discharge–sediment relationship using fuzzy logic. Following a similar approach, Jain (2008) tested the capabilities of compound neural networks by developing the integrated stage discharge sediment rating curves. Based on coefficient of correlation and sum of square of error statistics Jain (2008) concluded that CNN consisting of two network can model the rating curve more accurately than single artificial neural network. Aytek and Kisi (2008) developed sediment rating curves using Genetic programming (GP) and demonstrated the superiority of GP over traditional rating curves. Cobaner et al. (2009) estimated the suspended sediment concentration using adaptive neuro-fuzzy approach with discharge, rainfall and sediment data of different periods as an input. Comparing the results of multi-layer perceptron (MLP), generalized regression neural networks (GRNN), the radial basis neural networks (RBNN) and sediment rating curves (SRC) with the adaptive neuro-fuzzy approach they reported neuro-fuzzy approach estimates the sediment concentration more accurately. Reddy and Ghimire (2009) demonstrated the superiority of Model Tree M5 over simple sediment rating curve, multi-linear regression and Gene Expression Programming. Kumar et al. (2012) compared ANN with back propagation and Levenberg-Merquardt algorithms, radial basis function, Fuzzy Logic, and decision tree algorithms M5 and REPTree to model sediment concentration and reported model tree M5 as the better approach among them to model sediment rating curves. It has also been reported that Genetic Algorithm (GA) is more reliable approach than model tress (MT) in developing rating curves as demonstrated by Ghimire and Reddy (2010) in case of discharge rating curves. Recently, Zakwan et al. (2017a, b b) demonstrated that GRG technique is as efficient as GA in case of discharge rating curve. In this regard, the present paper employs GRG technique to establish the sediment rating curves for two sites.

2 Materials and Method

In the present study daily sediment discharge data of two sites in USA has been used. The first data set correspond to a period of January 1, 1969–December 31, 1972 for Missouri river at Hermann, Missouri (site number: 6934500). Second data set correspond to a period of October 1, 1997–January 31, 2002 for Mississippi

Table 1 Statistical parameters of Sediment-discharge data

Data	Station	Quantity	Mean (μ)	Coefficient of variance	Max	Min
Calibration	Hermann	Discharge (m^3/s)	2551	0.59	9995	467
		SSL (ton/d)	245,039	1.45	2,010,000	3120
	Grafton	Discharge (m^3/s)	3303	0.65	10,081	830
		SSL (ton/d)	66,617	1.16	43,300	5080
Validation	Hermann	Discharge (m^3/s)	2133	0.42	6286	572
		SSL (ton/d)	169,027	0.99	94,900	9330
	Grafton	Discharge (m^3/s)	3873	0.70	10,363	977
		SSL (ton/d)	38,016	1.03	197,000	4590

river below Grafton, Illinois (site number: 5587455). These data sets are available on USGS website[1]. The salient features of the data set are reported in Table 1.

Continuous measurement of sediment load is very costly and impractical especially in large rivers, therefore, in majority of the rivers, sediment loads are generally estimated by indirect means of developing a relation between discharge and sediment load (Zakwan et al. 2021). This relationship is generally expressed as:

$$S = a(Q)^b \tag{1}$$

where S = SSL in ton/day; Q = discharge in m^3/s; a and b are regression coefficients.

Conventionally, the regression coefficients are estimated by using the linear regression method involving logarithm transformation of Eq. (1), but such transformation introduces a bias in the estimates as pointed out earlier therefore, the present paper presents the use of nonlinear optimization techniques to estimate these regression coefficients.

In the present study daily sediment discharge data sets of two sites i.e. Hermann site on Missouri river and Grafton site on Mississippi river was used. From these data sets 75% of the data set was randomly used for the calibration and 25% was used for validation. In the calibration period SSL discharge data was utilised to establish the sediment rating curve using conventional method (RM) and GRG technique. To obtain the optimal relation between SSL and discharge, sum of square of deviation between calculated SSL and estimated SSL was set to minimization defined as

$$\text{Min SSE} = \sum_{i=1}^{N} [X_i - Y_i]^2 \tag{2}$$

where X_i is calculated SSL; Y_i is predicted SSL. The details of optimization tools used in the present study are as follows.

[1] (cida.usgs.gov/sediment)

3 GRG Technique

GRG technique is a non-linear optimization code developed by L. S. Lasdon, A. D. Waren, A. Jain and M. Ratner in FORTRAN language (1978). Lasdon et al. (1978) modified the earlier work of Abadie and Carpentier (1969) on GRG technique. GRG technique integrates the function of graphical user interface (GUI), algebraic modelling languages like AMPL or GAMS and optimizers of linear, non-linear and integer programs. It is nonlinear extended version of simplex method. GRG technique involves either of the two techniques viz. Quasi-Newton method or Conjugate Gradient method for determination of the search direction (Zakwan 2017).

Jewell (2001) demonstrated the application of TK solver in handling the hydraulic design problems. Karahan (2009) proposed the use of GRG technique, to estimate the parameters of linear form of Muskingum flood routing equation. Barati (2013) demonstrated the superiority of excel solvers over Immune clonal selection algorithm (ICSA) and Genetic algorithm (GA) in estimating the outflow using nonlinear Muskingum flood routing equation. Stage discharge relationship was established by using GRG technique by Muzzammil et al. (2015) and Muzzammil et al. (2018). Zakwan et al. (2016) used GRG technique for estimating parameters of infiltration models. Zakwan and Muzzammil (2016) applied GRG technique for estimating the parameters of nonlinear Muskingum model.

4 Results and Discussion

In the present study daily sediment discharge data of two sites was used. From these data sets 75% of the data sets were used for the calibration and 25% were used for testing. In the calibration period SSL discharge data was utilised to establish the sediment rating curve using conventional regression analysis. Further, the relationship between SSL and discharge was also established using GRG nonlinear optimization techniques.

The parameters of sediment rating equation as obtained by regression and nonlinear optimization method for the two sites under consideration have been reported in Table 2. Kumar et al. (2012) reported model tree M5 as the better approach

Table 2 Sediment rating curve parameters

Station	Method	a	b
Hermann	RM	0.0043	2.226
	GRG	0.176	1.785
Grafton	RM	0.0337	1.751
	GRG	0.841	1.386

among them to model sediment rating curves. Ghimire and Reddy (2010) demonstrated that Genetic Algorithm (GA) is more reliable approach than model tress (MT) in developing discharge rating curves. Spreadsheet based approach (GRG technique) has been found as efficient as GA, however, the simplicity of GRG technique is an advantage over GA.

The SSL estimated by regression method and non-linear optimization were compared based on following criteria.

$$\text{Root mean square (RMSE)} = \sqrt{\frac{\sum_{i=1}^{n}(X_i - Y_i)^2}{N}} \tag{3}$$

$$\text{Correelation coefficient} = \frac{N\left(\sum XY\right) - (\sum Y)(\sum X)}{\sqrt{(N(\sum(Y^2) - \left(\sum Y\right)^2)(N\left(\sum X^2\right) - \left(\sum X\right)^2)}} \tag{4}$$

$$\text{Nash coefficient} = \left[1 - \frac{\sum_{i=1}^{N}(X_i - Y_i)^2}{\sum_{i=1}^{N}\left(X_i - \overline{X}\right)^2}\right] \tag{5}$$

where X_i is calculated SSL corresponding to any discharge; Y_i is predicted SSL corresponding to any discharge.

The results of comparative analysis are reported in Tables 3 and 4, which demonstrate that the application nonlinear optimization techniques result in lower root mean square error, values of Nash efficiency and correlation coefficient closer to unity as compared to those obtain by regression analysis for both calibration and validation in either case. Therefore, it may be inferred that sediment discharge rating estimated by using nonlinear optimization techniques are more reliable (Fig. 1).

Table 3 Performance indices during calibration

Station	Method	RMSE	Nash coefficient	Correlation coefficient
Hermann	RM	169,315	0.77	0.90
	GRG	137,704	0.85	0.99
Grafton	RM	43,000	0.68	0.83
	GRG	41,003	0.82	0.99

Table 4 Performance indices during validation

Station	Method	RMSE	Nash coefficient	Correlation coefficient
Hermann	RM	82,692	0.76	0.89
	GRG	71,191	0.83	0.99
Grafton	RM	95,555	0.75	0.85
	GRG	86,948	0.80	0.99

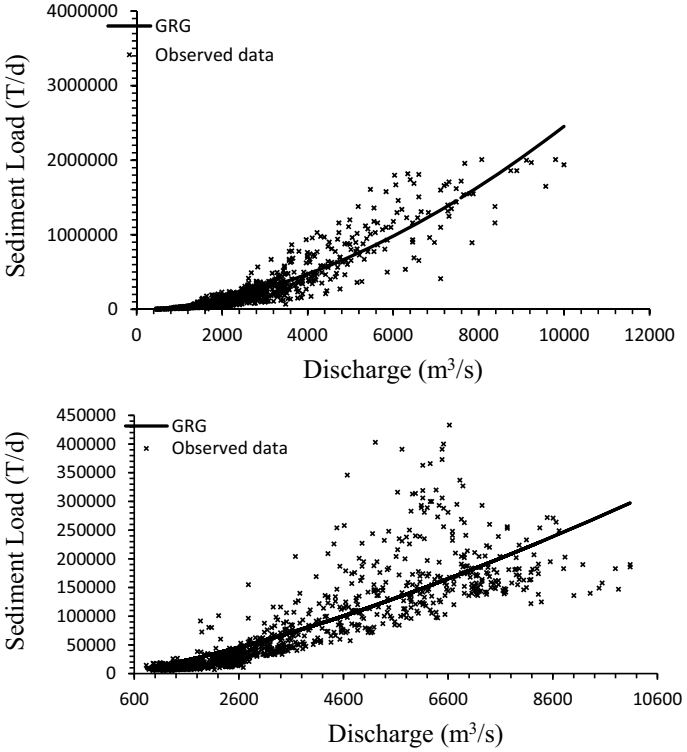

Fig. 1 Sediment load curve for Hermann and Grafton gauging sites

5 Conclusion

The sediment rating curves were established using conventional regression method and nonlinear optimization method for the two different sites. The performance of both the methods was assessed using different fitness criteria's. It has been found that nonlinear optimization approach is more reliable than the regression analysis for estimating the sediment rating parameters. Results also demonstrate that GRG technique is a powerful, simple and promising tool for nonlinear optimization. Even without utilising complicated programming techniques they can be used as an efficient optimization tool in the field of water resource engineering. Unlike most of the soft computing techniques application of GRG technique does not obscure theoretical background of the problem therefore, it can be helpful in teaching various problems involving optimization.

References

Abadie J, Carpentier J (1969) Generalization of the Wolfe reduced gradient method to the case of nonlinear constraints. Optimization. Academic Press, New York, p 37–47

Ara Z, Zakwan M (2018) Reservoir sedimentation analysis: a case study. In: Proceedings national conference on water, environment & society (NCWES-2018). Hyderabad, India p 286–292

Asselman NEM (2000) Fitting and interpretation of sediment rating curves. J Hydrol 234:228–248

Aytek A, Kisi O (2008) A genetic programming approach to suspended sediment modelling. J Hydrol 351:288–298

Barati R (2013) Application of excel solver for parameter estimation of the nonlinear Muskingum models. KSCE J Civ Engg 17(5):1139–1148

Cobaner M, Unal B, Kisi O (2009) Suspended sediment concentration estimation by an adaptive neuro-fuzzy and neural network approaches using hydro-meteorological data. J Hydrol 367(1–2):52–61

Crowder DW, Demissie M, Markus M (2007) The accuracy of sediment loads when log-transformation produces nonlinear sediment load—discharge relationships. p 250–268. https://doi.org/10.1016/j.jhydrol.2006.12.024

Demissie M, Xia R, Keefer L, Bhowmik N (2004) The sediment budget of the Illinois river. Illinois State Water Survey, Contract Report 2004–13. Champaign, IL

Ferguson RI (1986) River loads underestimated by rating curves. Water Resour Res 22(1):74–76

Ghimire BNS, Reddy MJ (2010) Development of stage-discharge rating curve in river using genetic algorithms and model tree. Int Workshop Adv Stat Hydrol. Taormina, Italy

Jain SK (2001) Development of integrated sediment rating curves using ANNs. J Hydrol Engg 13(3):124–213

Jain SK (2008) Development of integrated discharge and sediment rating relation using a compound neural network. J Hydrol Eng 13(3):124–131

Jewell TK (2001) Teaching hydraulic design using equation solvers. J Hydrol Engg 0733–9429/127(12):1013–1021

Karahan H (2009) Predicting Muskingum flood routing parameters using spreadsheet. Wiley Periodicals Inc., p 280–286

Kisi O (2004) Multi-Layer perceptrons with Levenberg-Marquardt training algorithm for suspended sediment concentration prediction and estimation. Hydrol Sci J 49(6):1025–1040

Kumar ARS, Ojha CSP, Goyal MK, Singh RD, Swamee PK (2012) Modelling of suspended sediment concentration at Kasol in India using ANN, fuzzy logic, and decision tree algorithms:394–404. https://doi.org/10.1061/(ASCE)HE.1943-5584.0000445

Lasdon LS, Waren AD, Jain A, Ratner M (1978) Design and testing of a generalized reduced gradient code for nonlinear programming. ACM Trans Math Softw 4(1):34–50

Lohani AK, Goel NK, Bhatia KKS (2007) Deriving stage discharge-sediment concentration relationships using Fuzzy logic. Hydrol Sci J 52(4):793–807

Muzzammil M, Alam J, Zakwan M (2015) An optimization technique for estimation of rating curve parameters. Nat Symp Hydrol 234–240

Muzzammil M, Alam J, Zakwan M (2018) A spreadsheet approach for prediction of rating curve parameters. In: Singh V, Yadav S, Yadava R (eds) Hydrologic modeling. water science and technology library, vol 81. Springer, Singapore

Pandey M, Zakwan M, Khan MA, Bhave S (2020) Development of scour around a circular pier and its modelling using genetic algorithm. Water Supply 20(8):3358–3367

Nagy HM, Watanabe K, Hirano M (2002) Prediction of sediment load concentration in rivers using artificial neural networks. J Hydrol Eng 128(6):588–595

Reddy MJ, Ghimire BNS (2009) Use of Model tree and Gene expression programming to predict the suspended sediment load in rivers. J Intell Syst 18(3):211–227

Sakai K, Osawa K, Yoshinaga A (2005) Development of suspended sediment concentration (SSC) analysis model and its application with multi-objective optimization. Paddy Water Environ 3:201–209

USGS website, cida.usgs.gov/sediment
Zakwan M, Muzzammil M (2016) Optimization approach for hydrologic channel routing. Water Energ Int 59(3):66–69
Zakwan M, Muzzammil M, Alam J (2016) Application of spreadsheet to estimate infiltration parameters. Perspect Sci 8:702–704
Zakwan M (2017) Assessment of dimensionless form of Kostiakov model. Aquademia Water Environ Technol 1(1):01
Zakwan M, Muzzammil M, Alam J (2017a) Application of data driven techniques in discharge rating curve-an overview. Aquademia 1(1):02
Zakwan M, Muzzammil M, Alam J (2017b) Developing stage-discharge relations using optimization techniques. Aquademia Water Environ Technol 1(2):05
Zakwan M, Ahmad Z, Sharief SMV (2018) Magnitude-frequency analysis for suspended sediment transport in Ganga river. J Hydrol Engg https://doi.org/10.1061/(ASCE)HE.1943-5584.0001671
Zakwan M, Pham QB, Zhu S (2021) Effective discharge computation in the lower Drava River. Hydrol Sci J:1–12

A Study on Some Characteristics of an Alluvial Channel for Varying Flows

Mayuraksha Bardhan

1 Introduction

The object of the present study is to gather some qualitative knowledge on some characteristics of alluvial channels when their patterns undergo a continuous change to straight or meandering or combination of both due to the interaction of a particular bed material and two different discharges flowing on these channels for a definite period of time to obtain them into regime conditions. An attempt has also been made here to find the effect of inclusion of a river training structure on those regime channels.

2 Literature Study

Chatterjee (1987) discussed about movable bed hydraulic model for studying morphological problems and various constraints in obtaining reliable results from those studies. Ghosh (1987) discussed about effect of meandering and fluming on alluvial channels. Ghosh and Bose (1989) made a study on some characteristics of an alluvial channel. Langbein and Leopold (1966) made extensive studies on the fluvial processes in rivers by using prototype data and physical model. The effect of meandering and width of the alluvial channel on the friction factors and sediment transport capacity had been investigated by Onishi, Jain and Kennedy (1976). Emmett, Leopold and Myrick (1983) made extensive study on some characteristics of fluvial processes. The effect of overall deformation of beds of curved alluvial channels on flow characteristics in a smooth rigid-bed meandering channel had been

M. Bardhan (✉)
River Research Institute, P.O.-Haringhata, R.R.I, Nadia, West Bengal 741246, India
e-mail: mayur.bardhan@gmail.com

R. Jha et al. (eds.), *River and Coastal Engineering*, Water Science and Technology Library 117, https://doi.org/10.1007/978-3-031-05057-2_2

studied by Yen (1970). In spite of the above studies about the fluvial processes in rivers, many short comings still remain in understanding the processes.

3 Experimental Set-Up

Experiments were conducted during the year 1997. An experimental alluvial channel of 300 ft (91.44 m) in length with a trapezoidal cross section of 4 inch (10 cm) in depth, 4 inch (10 cm) bed width and side slope 2: 1 (as shown in Fig. 1) was laid on a sand tray of 300 ft (91.44 m) in length and 30 ft (9.144 m) in width.

The initial slope of the channel was introduced as 0.003 and the size of the bed material was taken as $D_{50} = 0.332$ mm. At the entrance of the channel, an initial curvature was introduced to accelerate the meandering process of the channel. At first, under this condition, a steady flow of discharge 0.003 cumecs (Q1) was circulated through the experimental straight channel for a period of 150 h when a regime channel was obtained on the basis of observation of the steadiness of channel slope and channel morphology, taken at every 50 h interval. It was noticed that only three successive meanders of about same length had developed up to a distance of 120 ft (36.576 m) along the longitudinal direction of the channel. The rest portion of the channel remained straight.

At this stage, a river training structure (like barrage) was introduced at a section of 56 ft (17.069 m) from the entrance of the channel. The opening of waterway downstream of the barrage was allowed at 30% and thus a horizontal fluming of the order of about 70% was introduced on the regime channel. Under this condition and with the same discharge, the flume was again allowed to run for a period of 150 h until a regime channel was again supposed to have attained. The experiment

Fig. 1 View of the experimental alluvial channel

was repeated in the same process with another discharge of 0.007 cumecs (Q2). The regime channel thus formed is supposed to have composed of two major reaches, meandering reach with or without a structure and straight reach with or without a structure.

4 Analysis of Data

The data obtained from the experimental channel under two varying discharges (Q1 & Q2) are analyzed and presented here.

4.1 Fluvial View

The net changes in the cross sectional flow areas for two different discharges Q1 & Q2 along the longitudinal direction of the channel are shown graphically in Fig. 2.

The curve showing separately the net change in cross sectional area- scour or filling between two flows have also been presented in the upper portion of the same figure. Here the scour is assumed when the flow area for Q2 is greater than that for Q1 and filling is assumed when the flow area for Q2 is smaller than that for Q1. It is clear that in the meandering reach flow areas for each discharge varies remarkable in the same pattern and there also exists a considerable scour through out the reach. However, in

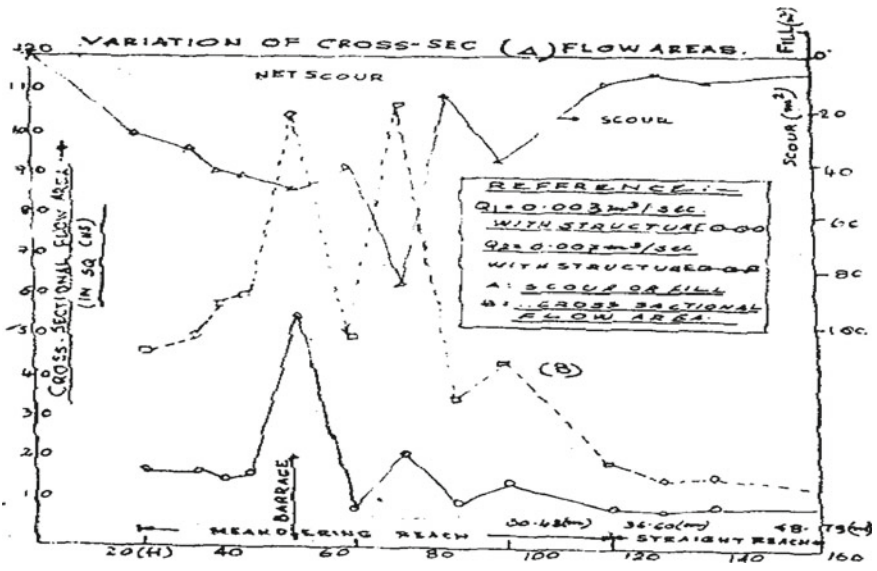

Fig. 2 Changes in cross sectional flow areas for two different discharges

the straight reach, the variation of flow areas for each discharge is not so perceptible though throughout most part of this reach, there is scouring process to some extent. It can be stated from this figure that in the meandering reach, considerable scour is always associated with the increase of discharge and no systematic correlation between scour and increase or decrease of flow areas can be obtained.

Figure 3 presents the elevation of deepest points of the channel in longitudinal direction. Here the deepest point alternatively rises or falls for each discharge but it is always higher in the discharge Q2 than that in the discharge Q1 in both the reaches. Figure 4 shows the elevation of mean depth of the channel. Here also same phenomenon is noticed. Hence from Figs. 2, 3 and 4, it can be stated that any considerable scour which occurs has got no correlation with the elevation of deepest point or mean depths of the channel.

Figures 5 and 6 represent the profiles of total bed width (W) and water surface width (B) of the channels for two different discharges Q1 and Q2 respectively. It appears from these figures that both total bed width and water surface width increase considerably with the increase of discharge in the meandering reach of the channel and this phenomenon is more in case of total width of the channel.

In the straight reach, both total width and water surface width increase due to increase of discharge but this is significantly smaller than that observed in the meandering reach. From these facts, it can be inferred that the considerable scour that always occurs with increase of discharge in the meandering reach may be associated

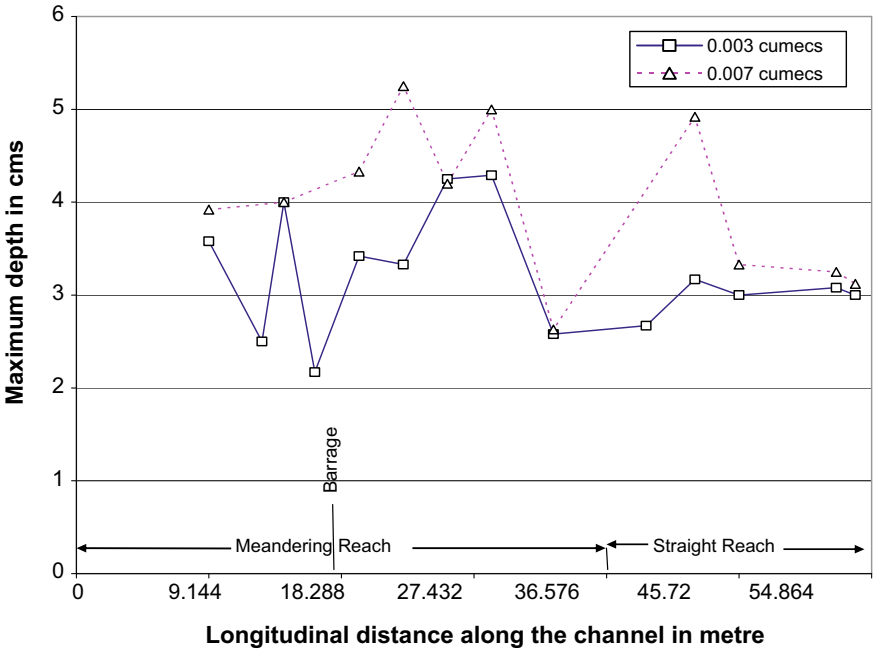

Fig. 3 Maximum depth along channel after 150 h of model run

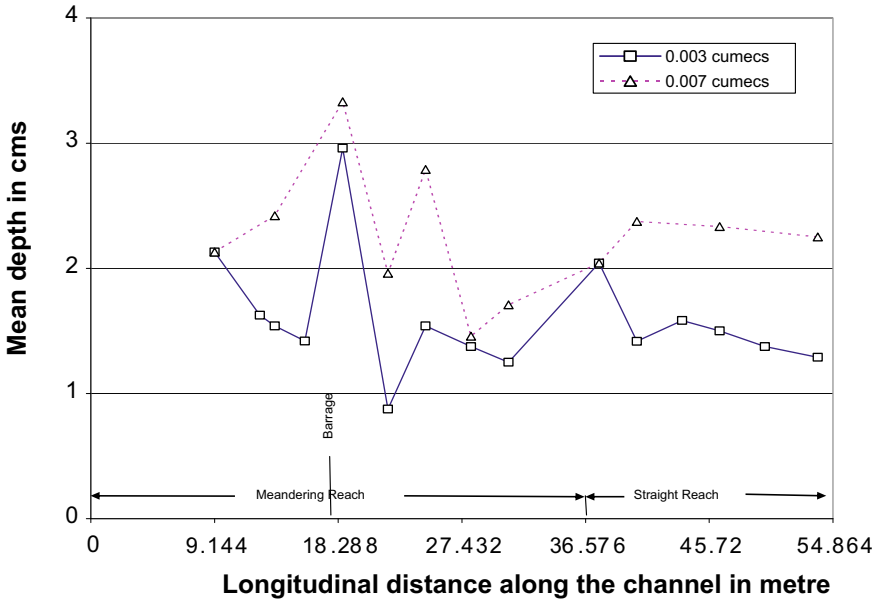

Fig. 4 Mean depth along channel after 150 h of model run with structure (barrage)

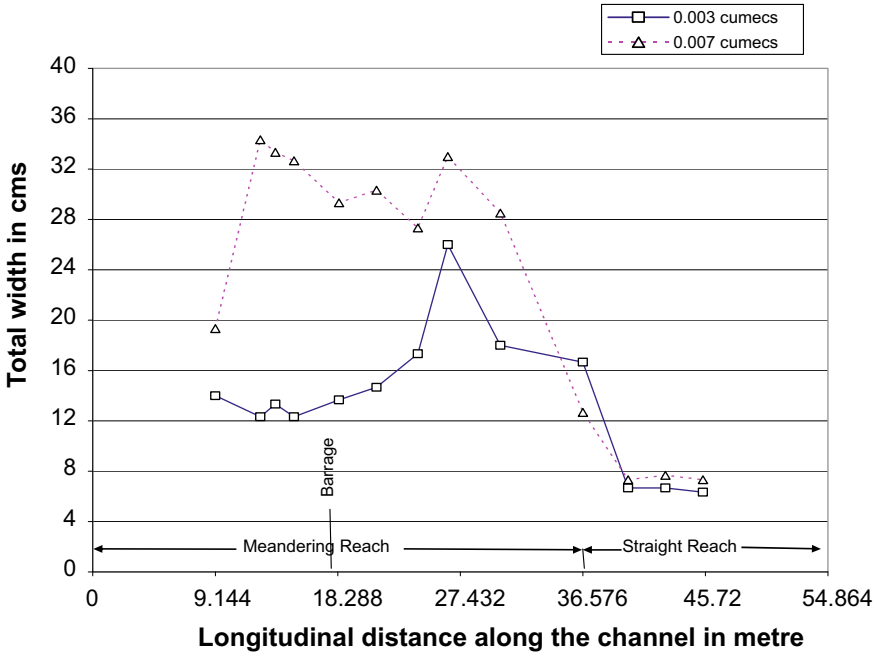

Fig. 5 Variation of bank width along the channel at different discharges (with barrage)

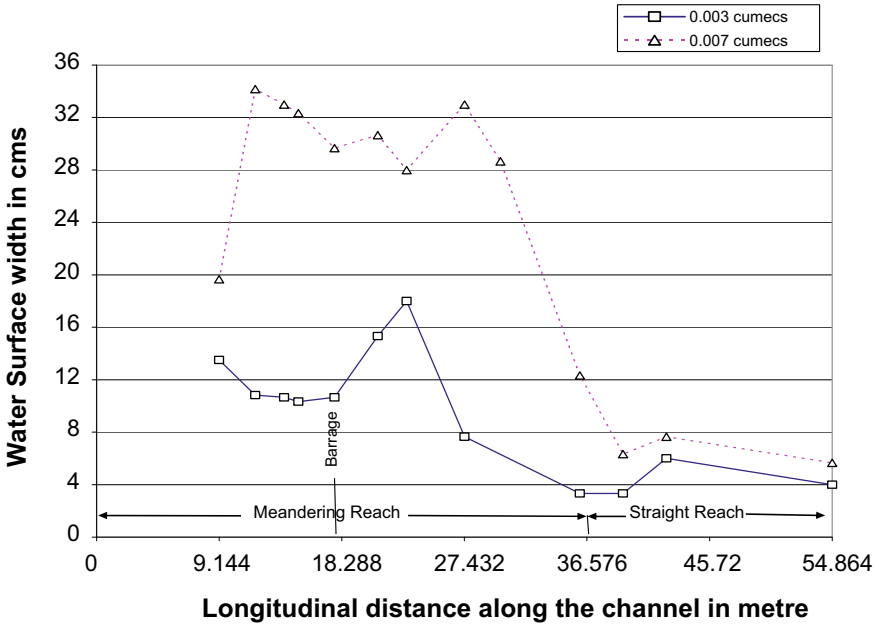

Fig. 6 Variation of water surface width along the channel (with barrage)

with the increase in total width or water surface width and as such there may exist a good correlation between scour and total width or water surface width in this reach. The absolute magnitude of flow area and total surface width as shown in Fig. 2 may not reveal the real effect of flow phenomenon, the relative increase in flow areas and total surface width for two flows would describe more accurately the effect that happens. The upper and lower part in the Fig. 7 represents respectively the relative changes in the flow areas and the total surface width (W) for two flows. It appears from these curves that with the change of total surface width, the cross-sectional flow areas also change and in the upstream of the barrage, the variation in total width (W) is wide and higher than variation in cross- section but at the downstream of the barrage, it is reverse.

4.2 Analytical View

For alluvial channels undergoing changes, the total rate of energy expenditure or power expenditure of a channel reach at an instant is defined as:

$$P = \int_{\gamma}^{m} Q\,S\,X\,dx \tag{1}$$

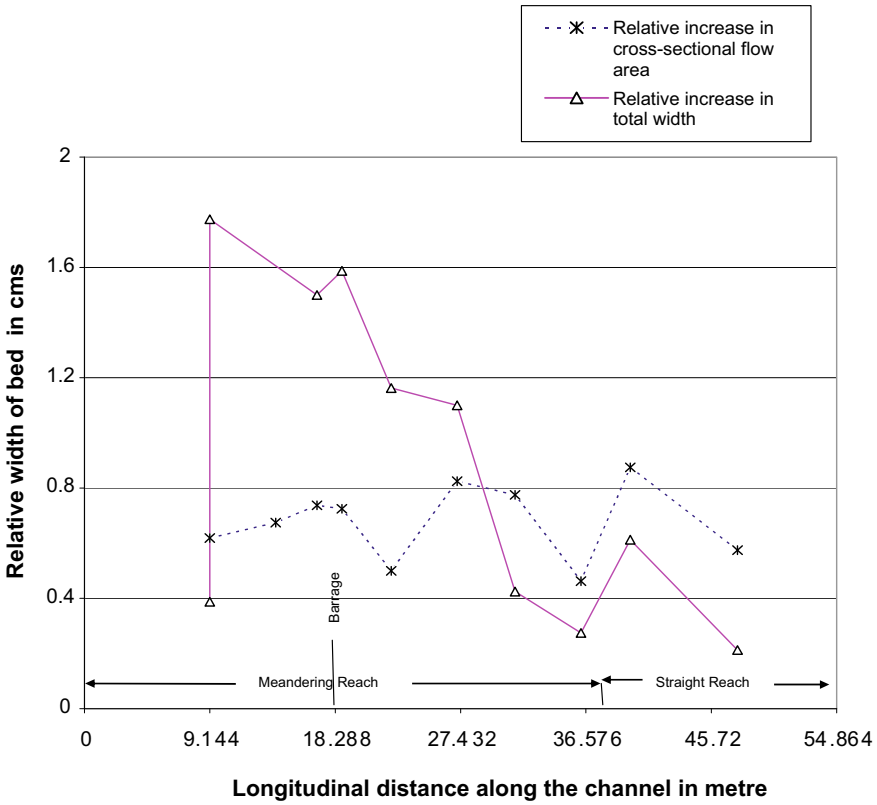

Fig. 7 Relative increase in total bed width and cross-sectional flow area

where P is total stream power of a reach in energy / time, γ is specific weight of water, m is length of the reach, Q is discharge, X is distance along flow direction and S is energy gradient. Any changes in the pattern of these channels reflect the changes of resistance to flow or in power expenditure.

The curves in Fig. 8 reflect the power expenditure of two regime channels obtained for two flows Q1 and Q2. It appears from these curves that in the meandering reach, power expenditure increases slowly and in the straight reach, it is almost uniform.

Again from Figs. 2, 3, 4, 5, 6 and 7, it appears that any change in the channel morphology is associated with the increase of channel surface width or total width which is usually accompanied by a variation in flow resistance or power expenditure. Then it can be inferred that any adjustment of the channel morphology for becoming a regime channel is closely related to the change in power expenditure. Figures 9, 10, 11 and 12 depict the sequential changes in the cross-sectional profiles.

The curves in Figs. 9 and 10 represent the sequential variation of two cross-sections under two different discharges Q1 & Q2 at 10.97 m and 14.02 m upstream of the barrage in the meandering reach. It appears from both the figures that water

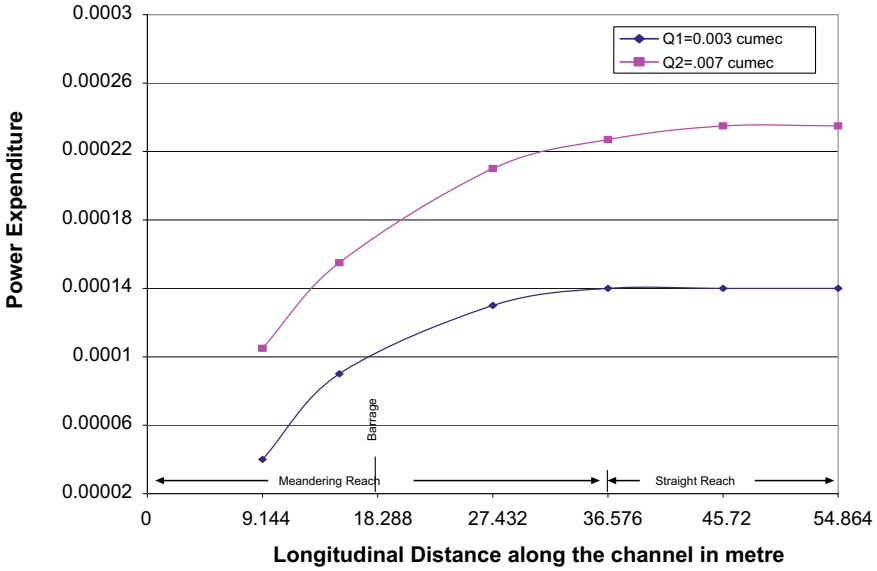

Fig. 8 Power expenditure along the channel for two different flow conditions

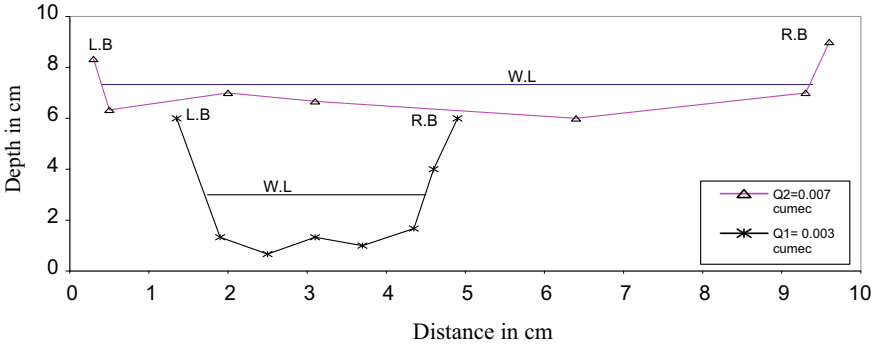

Fig. 9 Changes in cross-section of the channel at 10.97 m u/s of barrage in meandering reach

surface or total bed width increased and the bed is elevated. Figure 11 represents the same at 27.43 m downstream of the barrage in the meandering reach of the channel and the same phenomenon is observed here also. Figure 12 represents the sequential variation of cross-section 44.2 m downstream of the barrage in the straight reach. Here it is observed that bed of the channel is depressed and the water surface or total bed width increases.

From all Figs. 9, 10, 11 and 12, it can be said that with increase in discharge, water surface or total bed width of an alluvial channel increases and is accompanied by increase in boundary resistance or power expenditure.

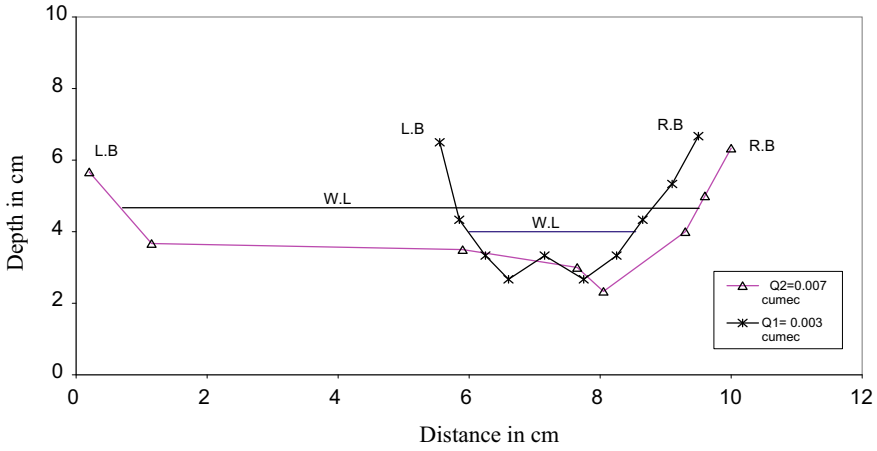

Fig. 10 Changes in cross-section of the channel at 14.02 m u/s of barrage in meandering reach

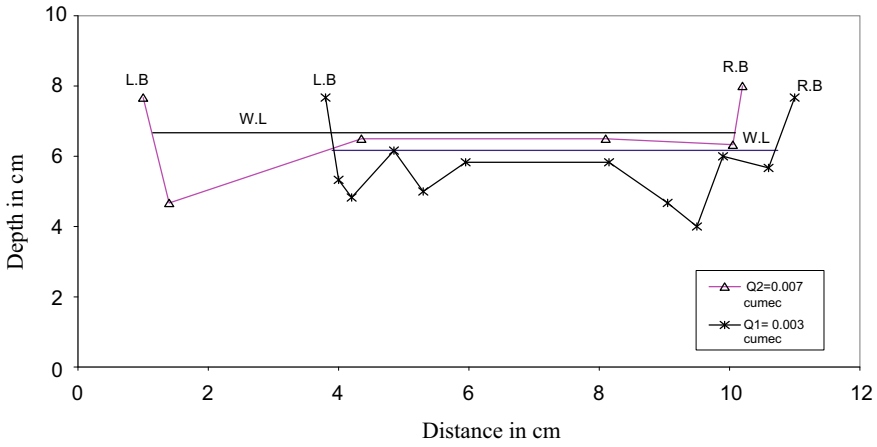

Fig. 11 Changes in cross-section of the channel at 27.43 m d/s of barrage in meandering reach

5 Conclusions

From the analysis of the experimental data, it may be concluded that in the meandering reach of an alluvial regime channel, any change in cross-sectional flow area is associated with the increase of water surface width or total bed width which is again accompanied by the increase in boundary resistance or power expenditure. As such, there may be a good correlation between scour and increase of water surface or total bed width and hence to power expenditure in the meandering reach of an alluvial regime channel. But it may not exist in the straight reach of the same channel.

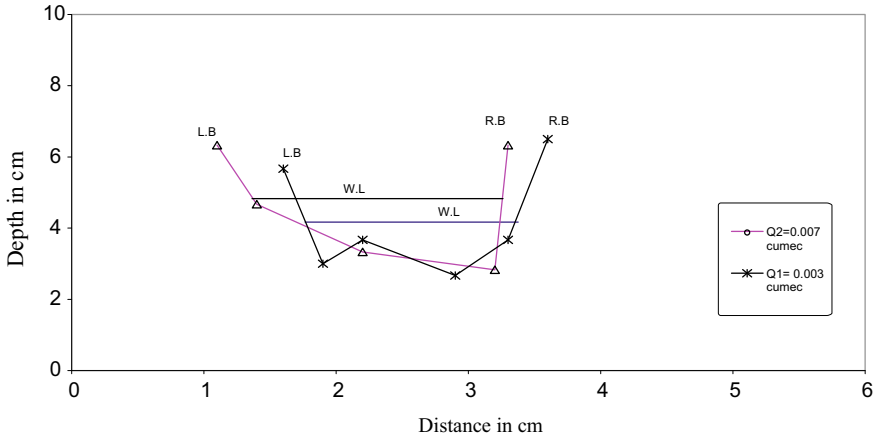

Fig. 12 Changes in cross-section of the channel at 44.2 m d/s of barrage in meandering reach

Acknowledgements This study is a part of the research work sponsored by the Central Board of Irrigation and Power, New Delhi under the project titled "Changes in river regime due to engineering structure and river regulation works".

References

Chatterjee SN (1987) Movable bed hydraulic model for studying morphological problems and their limitations. J River Res Inst West Bengal River Behav Control XIX:18–29, 1987–88

Ghosh SK (1987) Effect of meandering and fluming on some of the characteristics of an alluvial channel. J River Res Inst West Bengal River Behav Control XIX:30–39, 1987–88

Ghosh SK, Bose SK (1989 Jul) A study on some characteristics of an alluvial channel. In: Proceedings of 53rd R&D Session of C.B.I & P. New Delhi. pp 25–28

Langbein WB, Leopold LB (1966) River meanders- theory of minimum variance"-physiographic and hydraulic studies of rivers. Geological survey professional paper 422-H. United States Government Printing Office

Onishi Y, Jain SC, Kennedy JF (1976 Jul) Effects of meandering in alluvial streams. J Hydraulics Div ASCE 102(HY 7):899–917

Emmett WW, Leopold LB, Myrick RM (1983) Some characteristics of fluvial processes in rivers. In: Proceedings of 2nd international symposium on river sedimentation. Nanjing, China. pp 730–756, 11–16 Oct 1989

Yen C (1970 Jan) Bed topography effect on flow in a meander. J Hydraulics Div, ASCE 96(HY 1):57–73

Model Study for Determination of Efficiency of a Typical Silt Ejector

Mayuraksha Bardhan

1 Introduction

Normally Silt Excluder is used for exclusion of silt. But it was not feasible for Teesta Barrage under prevailing field condition. As such, Silt Ejector was preferred and it was first of its kind in West Bengal. To control the quantity of silt, a silt ejector was proposed to be constructed in the Teesta Mahananda Link Canal. The design discharge of the canal upstream and downstream of the Silt Ejector was 438.91 cumecs and 382.28 cumecs respectively and the discharge through the Silt-Ejector was 56.63 cumecs. The discharge passing through the Silt Ejector was to fall on the main river downstream of the barrage. It was proposed by the authorities to carry out hydraulic model experiments to study the hydraulic performance of the Silt Ejector. The problem was referred to River Research Institute, West Bengal for model study. The model study was performed and necessary report was submitted. After detailed study, it can be said that the above report is still valid today with some modifications.

2 Related Work

Ahmad and Kaliq (1960) and Bhavan (1980) discussed different sediment exclusion methods and devices at the intake of canals. It was established by various experiments that an off take from a straight channel would draw greater proportion in its water than its due share depending on the discharge extraction ratio and the angle of twist. The excluders were tested for full supply discharge in power tunnel and the river discharge equal to 100,000 cusecs. It was envisaged that an excluder of ejector type or vortex excluder would be efficient for exclusion of coarse silt from power tunnel. King

M. Bardhan (✉)
River Research Institute, P.O.- Haringhata, R.R.I, Nadia, West Bengal 741246, India
e-mail: mayur.bardhan@gmail.com

R. Jha et al. (eds.), *River and Coastal Engineering*, Water Science and Technology Library 117, https://doi.org/10.1007/978-3-031-05057-2_3

(1933) reported that silt carrying capacity of fluid at any point depended on difference in velocity of filaments of flow just above and below the point. A small obstruction over the bed throws up the silt which fall backs and is thrown up again. This motion of silt particle is terms as siltation and depends on the bed roughness, velocity and particle size. Raju and Kothyari (2004) explained the design principles of two kinds of sediment withdrawal methods namely settling basins and vortex chambers. They accomplished that the vortex chamber with high efficiency as compared to settling basin would require small flushing discharge. The negative aspect of vortex chamber is that it is suitable for small channels only.

3 Justification for Hydraulic Model Study

There are many unknown factors in the design of silt ejector such as the capacity of the silting basin in the approach channel, layout of the sub-tunnels and main tunnels, flushing velocity for the particular characteristics of the sediment to be ejected, and flow pattern of the bottom layers of the discharge, etc. As such it is essential that the layout based on the theoretical design be checked by model studies to ascertain the efficiency of the silt ejector.

4 Hydraulic Model

The model was constructed inside the Indoor Hydraulics Laboratory and the model was constructed on the basis of design drawings. A geometrically similar model of scale 1:36 was constructed. The model incorporated about 500 m long stretch of the Link Canal, the reach covered a length of about 400 m upstream and about 100 m downstream of the Silt Ejector. Due to shortage of space, the Escape Channel was reproduced for a length of about 30 m only. The water was supplied to the model through a re-circulating water supply system. The required discharge was measured over a rectangular sharp crested weir and fed into the canal through a stilling basin. Silt traps were provided on the downstream of the canal and also at the downstream ends of the Escape Channel. Four nos. of gauges (shown in Figs. 1 and 2) were provided at 360 m upstream (G_1), 75 m upstream (G_2), 22 m downstream (G_3) and 100 m downstream (G_4) of the proposed Silt Ejector. One gauge G_5 was provided at a place about 12 m from the start of the Escape Channel, about 22 m from the exit of the Silt ejector tunnel. In the model, the Silt Ejector structure was made of thin Perspex sheets.

Fig. 1 Photograph of silt ejector model

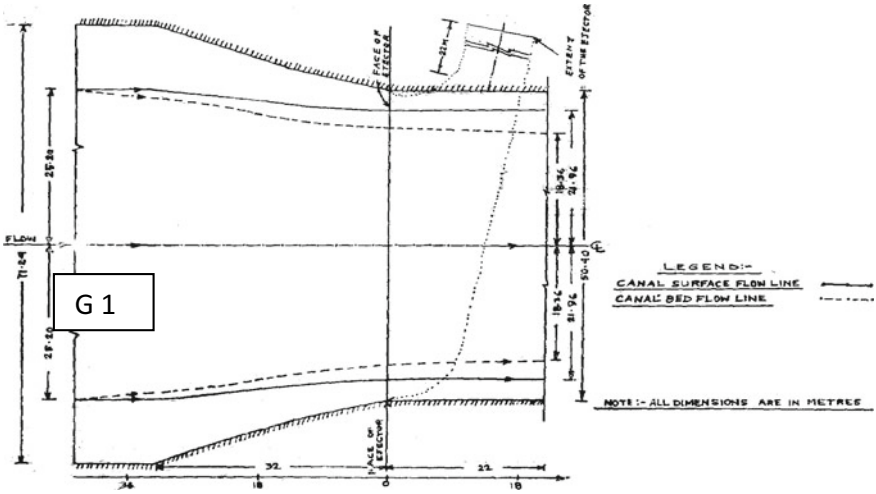

Fig. 2 Canal surface and bed flow-lines for canal discharge 438.91 cumecs

5 Observations

A discharge equivalent to 438.91 cumecs was passed through the model. The downstream canal gauge G_4 was maintained at the design value of 115.588 m with the help of the downstream control gate. The gauge G_5 of the Escape Channel was maintained at the design value of 112.174 m by controlling the downstream gate of the Escape Channel. Gauge readings of G_1, G_2 and G_3 were observed. Model gauge readings were 113.808, 113.698 and 113.643 m whereas the computed gauge readings from the design data supplied were 113.731, 113.631 and 113.610 m respectively. Both surface flow lines and bed flow lines of the canal were taken from about 45 m

Table 1 Velocity distribution in the canal at 324 m upstream of the Silt Ejector with design discharge 438.91 cumecs

Velocity in m/s	Vertical numbers from Left to Right (vide Fig. 3)					Average velocity in m/s
	1	2	3	4	5	
Bed velocity	1.681	1.879	1.879	1.879	1.879	1.839
Velocity at 0.6 depth	2.059	2.224	2.143	1.783	2.143	2.07
Surface velocity	2.377	2.521	2.45	1.971	2.45	2.354
Mean velocity						2.088

Table 2 Velocity distribution in the canal at 80 m downstream of the Silt Ejector with design discharge 438.91 cumecs

Velocity in m/s	Vertical numbers from Left to Right (vide Fig. 4)					Average velocity in m/s
	1	2	3	4	5	
Bed velocity	1.681	1.681	1.681	1.681	1.681	1.681
Velocity at 0.6 depth	1.879	1.971	1.879	1.879	1.879	1.897
Surface velocity	2.224	2.224	2.224	2.143	2.143	2.192
Mean velocity						1.923

upstream of Silt Ejector to 22 m downstream of the sub-tunnel entrance. These are presented in Fig. 2. No undesirable flow features were noticed at the entry of the Silt Ejector. No eddies or vortices were observed. The flow was tranquil and smooth in all cases. Velocity observations were taken at 324 m upstream point near G_1, near the upstream face of the Silt Ejector, 80 m downstream point of the Silt Ejector near G_4. The velocities are presented in Tables 1, 2 and 3. The average velocity of the whole section near G_1 comes to about 2.088 m/s whereas the design value is 2.013 m/s.

The verticals of velocity observations are presented in Fig. 3 and Fig. 4. Plan of a typical Silt Ejector is shown in Fig. 5.

5.1 Escape Discharge

The discharge passing through the Silt Ejector into the Escape channel was measured volumetrically and they reasonably agreed with the design discharge. The measured model discharge corresponds to about 61.71 cumecs as against the design discharge of 56.63 cumecs. In order to measure the discharges passing through the individual tunnels separately, water was allowed to flow through each tunnel closing the other three tunnels at the end. Due to this closure, there was a rise of water level in the main canal model. However it indicates that with a particular canal water level, the discharge through each of the tunnels was reasonably the same.

Table 3 Observation of velocities at the upstream face of the Silt Ejector Sub-tunnels with design discharge of 438.91 cumecs in the canal upstream of the Silt Ejector (velocities were observed at 3.6 m upstream of the face of the Silt Ejector)

Velocity in m/s	Sub-tunnel numbers (from Left to Right)												Average velocity in m/s
	1	2	3	4	5	6	7	8	9	10	11	12	
Bed velocity	1.57	1.46	1.57	1.46	1.33	1.33	1.46	1.33	1.33	1.33	1.46	1.46	1.424
Velocity at 0.6 depth	1.78	1.78	1.78	1.68	1.68	1.78	1.88	1.78	1.68	1.78	1.68	1.78	1.755
Surface velocity	1.97	1.97	1.97	1.97	1.88	1.97	1.97	1.97	1.88	1.88	1.88	1.97	1.94
Mean velocity													1.706

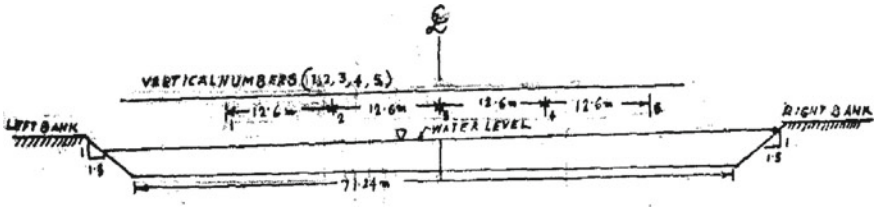

Fig. 3 Canal cross-section at 324 m upstream of Silt Ejector

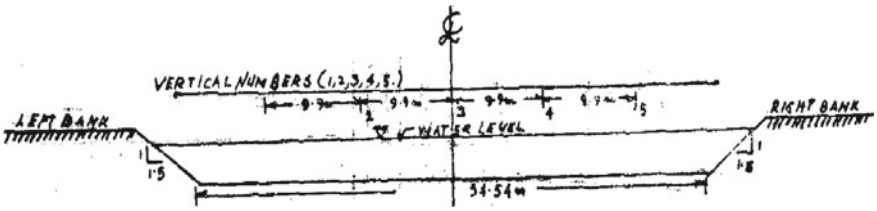

Fig. 4 Canal cross-section at 80 m downstream of the Silt Ejector

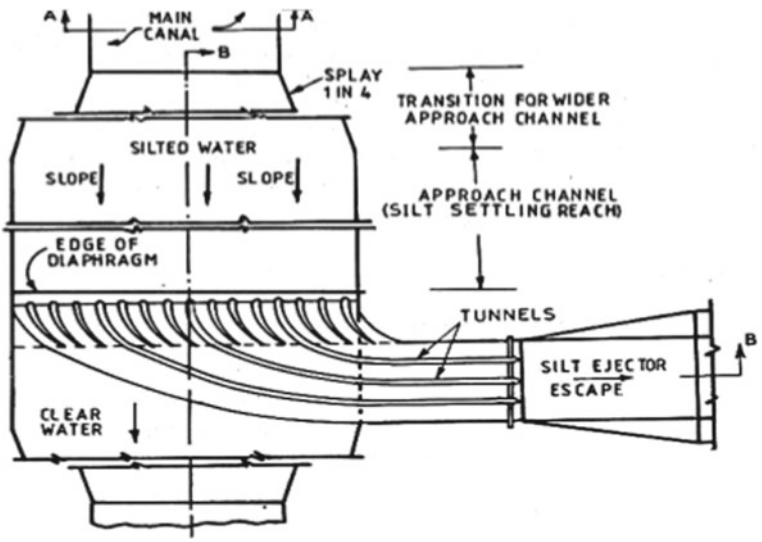

Fig. 5 Plan of a Silt Ejector *Source* Google search

5.2 Silt Movement

The bed load transport was simulated in the model by injection of mustard seeds. Mustard seeds were injected at a section 380 m upstream of the Silt Ejector. The entire quantity of the mustard seeds passed through the Silt Ejector into the Escape

Channel. The same experiments were repeated with plastic balls which rolled along the bed and the same result was observed. The mechanism of suspended sediment transport and deposition was not included in the present study.

6 Model Run with Discharges Lower Than Design Discharge

Considering the fact that for a part of the year, the canal may have to run with discharges lower than the design discharge, it would be of interest to know the discharge passing through the Silt Ejector and the indication of bed load movement. The model was run with discharges 70, 50 and 30% of the design discharge (438.91 cumecs) which were discharges of 307.24 cumecs, 219.46 cumecs and 131.67 cumecs respectively. The velocities observed at 324 m upstream and 80 m downstream of the Silt Ejector at 0.6 depths are presented in Tables 4 and 5.

The velocities observed at the face of the sub-tunnels are presented in Tables 6, 7 and 8. The discharges passing through the Silt Ejector tunnels for discharges 70, 50

Table 4 Velocity at 0.6 depth in the canal at 324 m upstream of the Silt Ejector with different canal discharges

Discharge in cumecs	Vertical numbers from Left to Right (vide Fig. 3)					Average velocity in m/s
	1	2	3	4	5	
307.24 (70% of design discharge)	1.97	2.057	2.057	2.057	1.97	2.022
219.46 (50% of design discharge)	1.878	1.878	1.97	1.97	1.878	1.915
131.67 (30% of design discharge)	1.97	1.878	1.782	1.782	1.571	1.797

Table 5 Velocity at 0.6 depth in the canal at 80 m downstream of the Silt Ejector with different canal discharges

Discharge in cumecs	Vertical numbers from Left to Right (vide Fig. 4)					Average velocity in m/s
	1	2	3	4	5	
307.24 (70% of design discharge)	1.878	2.057	2.057	1.97	1.878	1.968
219.46 (50% of design discharge)	1.878	1.878	1.782	1.782	1.571	1.778
131.67 (30% of design discharge)	1.571	1.571	1.571	1.571	1.571	1.571

Table 6 Velocities at the upstream face of the Silt Ejector Sub-tunnels with discharge 307.24 cumecs (70% of design discharge) in the canal upstream of the Silt Ejector (velocities were observed at 3.6 m upstream of the face of the Silt Ejector).

Velocity in m/s	Sub-tunnel numbers (from Left to Right)												Average velocity in m/s
	1	2	3	4	5	6	7	8	9	10	11	12	
Bed velocity	1.03	1.03	1.03	1.03	1.03	1.03	1.03	1.11	1.11	1.33	1.33	1.33	1.12
Velocity at 0.6 depth	1.78	1.78	1.78	1.68	1.68	1.78	1.88	1.78	1.68	1.78	1.68	1.78	1.76
Surface velocity	1.97	1.97	1.97	1.97	1.88	1.97	1.97	1.97	1.88	1.88	1.88	1.97	1.94
Mean velocity													1.61

Table 7 Velocities at the upstream face of the Silt Ejector Sub-tunnels with discharge 219.48 cumecs (50% of design discharge) in the canal upstream of the Silt Ejector (velocities were observed at 3.6 m upstream of the face of the Silt Ejector).

Velocity in m/s	Sub-tunnel numbers (from Left to Right)												Average velocity in m/s
	1	2	3	4	5	6	7	8	9	10	11	12	
Bed velocity	1.19	1.03	1.11	1.03	1.03	1.03	1.03	0.94	0.94	0.94	0.94	1.03	1.02
Velocity at 0.6 depth	1.19	1.19	1.19	1.19	1.19	1.19	1.19	1.11	1.11	1.11	1.11	1.11	1.16
Surface velocity	1.33	1.33	1.33	1.26	1.33	1.33	1.26	1.26	1.26	1.26	1.26	1.26	1.29
Mean velocity													1.16

Table 8 Velocities at the upstream face of the Silt Ejector Sub-tunnels with discharge 131.67 cumecs (30% of design discharge) in the canal upstream of the Silt Ejector (velocities were observed at 3.6 m upstream of the face of the Silt Ejector).

Velocity in m/s	Sub-tunnel numbers (from Left to Right)												Average velocity in m/s
	1	2	3	4	5	6	7	8	9	10	11	12	
Bed velocity	1.11	1.03	1.03	1.03	1.03	1.03	1.03	0.94	0.94	0.94	0.94	0.94	1.00
Velocity at 0.6 depth	1.19	1.19	1.19	1.19	1.19	1.19	1.11	1.03	1.11	1.11	1.19	1.11	1.15
Surface velocity	1.19	1.26	1.26	1.33	1.33	1.26	1.19	1.19	1.19	1.26	1.26	1.19	1.24
Mean velocity													1.13

and 30% of the design discharge were about 46.24 cumecs, 33.94 cumecs and 18.54 cumecs respectively.

Mustard seeds were injected as bed materials and in all cases except very low discharge of the order of 30% of the design discharge, entire quantity of the injected materials passed out of the Silt Ejector Sub-tunnels. In case of 30% design discharge, the injected materials were observed to get accumulated in front of the Silt Ejector sub-tunnels. Even if they were pushed inside the sub-tunnels, they were not easily moving out. This phenomenon may be attributed to low average bed velocity in front of the sub-tunnels. The flow was smooth in all cases.

7 Discussion

It was seen that the water surface slope in the canal was fairly reproduced in the model. The discharge passing through the tunnels reasonably agreed with the design discharge of 56.63 cumecs. Experiments with mustard seeds and plastic balls as bed load showed that ejection by the Silt Ejector is satisfactory in all cases except for very low discharge of the order of 30% of the design discharge. No undesirable flow features were observed at the entry of the Ejector.

8 Conclusions

The following conclusions are drawn from the present study.

i. Efficiency of the Silt Ejector is satisfactory in all the cases except for very low discharge of the order of 30% of design discharge. The efficiency of the Silt Ejector is calculated for bed load primarily. It will also be indicative for suspended load.
ii. The difference in water level in the canal upstream of the Silt Ejector and the outfall channel at the exit of the ejector tunnel should be sufficient to extract the desired sediment. A working head of about 1 m is generally considered satisfactory for the purpose.
iii. The quantum of discharge to be run through sediment ejector and frequency of its operation would vary in different periods of the year depending on the sediment load carried in the canal and this may be achieved by operating regulating gates as and when required. It would be desirable to operate the gates fully open or fully closed.
iv. A velocity of 8 ft/s to 10 ft/s through the tunnel is adequate to move sand size sediments.
v. An escape discharge equal to 10–20% of the full supply discharge of the canal downstream of the ejector will be sufficient for removal of silt load. The

escape channel is given a steeper slope so that the silt is discharged back to the river through the shortest route.

vi. The height of tunnel should be 20–25% of the design depth of water in canal.

vii. Normally a minimum head of at least 2.5 ft is required to operate the Silt Ejector.

viii. During the period when sediment ejector is not required to function, it is desirable to operate the regulation gates occasionally for short periods to flush the tunnels consistent with the economy in water requirements for irrigation. Otherwise, the tunnels are likely to get choked and may require manual clearance which may be possible only during closure of the canal.

ix. At times during the normal operation of the sediment ejector, the approach channel and/or tunnels or both may require flushing. This may be done by running the tunnels in rotation to achieve higher velocities.

References

Ahmad M, Khaliq (1960) A sediment exclusion methods and devices at the intake of canals. Punjab Engineering Congress

Bhavan M (1980) Criteria for hydraulic design of Sediment Ejector for irrigation and power channels-giudelines. Bureau of Indian Standards, vol IS-6004

King H (1933) Silt exclusion from distributaries, P-169. In: Punjab Engineering Congress, vol 12, pp 263–298

Raju KGR, Kothyari UC (2004) Sediment management in hydro-electric project. Yichang, China

Comparative Review on Model Selection for Hydrological Studies

Mudesir Nesru and M. K. Nagaraj

1 Introduction

The use of models in hydrological studies has become a vital means for better grasping knowledge about the natural phenomenon happening at the water-shed scale. The models are principally utilized for knowing numerous hydrologic processes and envisaging system behaviour. The better model provide results close to real value by using optimal parameters and least model complexity (Devi et al. 2015). Every model have its own unique features. Now days, for applications in hydrological modeling and water resources lessons various types of computer-based hydrological models have been developed across the globe (Dhami and Pandey 2013). These models ranging from those that deal with simple empirical relationship which contains various kinds of models that have a certain degree of physicality to stochastic and to more recent numerically complex physically based distributed models (Borah et al. 2003; Dhami and Pandey 2013).

With the growing in demand of usage with the increase in demand of usage, potential applications and extensive characteristics of the models, it is becoming the challenging task for the probable model users to pick out a best-acceptable model for the given problem (Dhami and Pandey 2013). In addition, the continuous modifications of the current models, innovative models are also accessible each year. Therefore, updated, reliable and comprehensive evaluations of hydrological models are a nonstop need for the practitioners. A model can be evaluated by comparing the model outputs or abilities to another model or some other anticipated/specific response. In

M. Nesru (✉) · M. K. Nagaraj
Department of Applied Mechanics and Hydraulics, National Institute of Technology Karnataka, Surathkal, Mangalore 575025, India
e-mail: marude03@yahoo.com

M. Nesru
Department of Hydraulic and Water Resource Engineering, Wolaita Sodo University, P.O. Box138, Wolaita Sodo, Ethiopia

R. Jha et al. (eds.), *River and Coastal Engineering*, Water Science and Technology Library 117, https://doi.org/10.1007/978-3-031-05057-2_4

the past, many different attempts have been initiated to evaluate the inter-comparison of hydrological models (World Meteorological Organization 1975; 1992; Borah et al. 2003; Migliaccio and Srivastava 2007; Golmohammadi et al. 2014).

Generally, Hydrological models are tools that combine our know-how of the hydrologic systems to simulate hydrologic processes in the real world. These models comprises portions of the hydrologic cycle which is characterized by the set of mathematical equations (Singh and Woolhiser 2002) and they're primarily founded on a set of mathematical equations which govern extraordinarily complicated natural phenomena. This equations abstract mathematical forms and attempt to convert the physical laws.

2 Types of Models

Moreover, hydrologic models could be very complicated and depend on physically based flow equation using a model domain called distributed (Abbott et al. 1986) or semi-distributed (Reggiani and Rientjes 2005) approach. The two main sets of well-known hydrological models are deterministic/process-based and stochastic models.

2.1 Process-Based/Deterministic Models

These models represent the observed physical processes. They use physical variables which are functions of both space and time and are quantifiable (Devi et al. 2015). Moreover, for their calibration they do not require wide-ranging meteorological and hydrologic data but the assessment of huge quantity of variables depicting the state features of the area are needed (Abbott et al. 1986). If all parameters are considered to be free from random-variation, that means, the model is non-probabilistic distribution, then the model is called a deterministic model. Mostly, these models contain representations of evapotranspiration, groundwater flow, and surface run-off but they can be much more complicated. For a single set of input values these model will give the same result.

2.2 Stochastic Models

These models are rely on data and using statistical and numerical ideas to interrelate a certain input value with the model output. Unlike to deterministic models, these models generates different output values for a single set of inputs (Devi et al. 2015). The aim of these model is to symbolize one or more time-series significant properties of statistical data instead of probabilistic to emphasize the time dependence of the

hydrologic parameters associated to the model. Some of the common techniques used are regressions, transfer-functions, neural-networks and system evaluation (Devi et al. 2015).

3 Descriptions of Some Hydrological Models

3.1 Soil and Water Assessment Tool (SWAT) Model

It is a complex physically-based, time-series, conceptual, distributed watershed-scale, long-term hydrologic model envisioned to envisage land-use impact trends on sediment, hydrology and pollutant conveyance in large, complex in ungauged basins (Arnold et al. 1998; Dhami and Pandey 2013). It is effective in performing long term simulations to large ungauged water-basin in which the water-basin is split into several sub-basins which further are broken down into specific land use or soil classes, usually known as the Hydrologic Response Unit (HRU) (Islam 2011). The model is derivative of numerous predecessors (Davie 2004). These are:

- SWRRB (Simulator for Water Resources in Rural Basins):-which gives the principal watershed hydrology of the area of interest.
- CREAMS (Chemicals, Run-off and Erosion from Agricultural Management Systems): used in minerals and solute conveyance.
- GLEAMS (Ground-water Loading Effects on Agricultural Management Systems): used in understanding subsurface water quality components.
- EPIC (Erosion Productivity Impact Calculator): used in understanding the relationship between erosion, sediment transportation and nutrient losses or gains.

The physical processes take in to account in SWAT model are evapotranspiration, infiltration, interception, percolation, rainfall, subsurface-runoff, and surface-runoff (Islam 2011). Numerous process descriptions exist for all the basic hydrologic processes that could be studied. The SWAT model is known for its complexity and requires vast data; however, only limited data could be effectively met (Islam 2011).

3.2 System Hydrologique European (MIKE-SHE) Model

This is a deterministic, spatially-distributed process-based model which have the ability to simulating all basic processes in the land levels of the hydrological cycle (DHI 2007; Dhami and Pandey 2013; Golmohammadi et al. 2014). These processes can be expressed at a multitude points of spatial dissemination and difficulty based on accessibility of site data, goal of the modeling and selections outlined by the modeler (Butts et al. 2004; Dhami and Pandey 2013). This system has no limits on the extent of the water-basin rather it requires sub-dividing the water-basin into

adjacent polygons using site information that includes land-use, type of soil and rainfall. The MIKE-SHE system models hydrologic elements such as the surface water flow, saturated and unsaturated groundwater flow, evapotranspiration, open channel flow, and flows between surface and subsurface water. This system also simulates sediment, mineral and chemical transport as variables to water quality in the study area. It is also capable of modeling water uses and handling encompassing irrigation systems, pump-wells and several water-barrier structures (Golmohammadi et al. 2014). However, the required quantity of input data that simulates the model is too much, and it is, therefore, hardly to find out a water-basin with full needed data to run the model as a well measured and accessible (Dhami and Pandey 2013).

3.3 Hydrologiska Byråns Vattenbalansavdelning (HBV) Model

It is part of semi distributed model which requires less input data and produces better simulation results, which means that in addition to a number of sub-basins the entire basin are able to split into different vegetation zones and elevations (Bergstroem 1976; Devi et al. 2015; Xu et al. 2016). It requires a daily and monthly data of air temperature, precipitation and evapotranspiration. Currently several versions of models are available in different countries of the world and these are used for different climatic situations. To simulate snowmelt and snow accumulation a degree day technique is used. Actual evaporation, runoff, and groundwater recharge are modelled as functions of definite storage of water. The latest type of HBV model is called HBV-light, which uses a period of comfortable temperature, wherein physical variables gets suitable values per parameter and meteorological data (Devi et al. 2015; Xu et al. 2016).

3.4 Topography Based Hydrological Model (TOPMODEL)

It is part of semi-distributed model which utilizes benefits of topographic data associated with run-off generation (Devi et al. 2015). Utilizing gridded elevation data for the entire basin, it can also be used in different sub-basins. Additionally it helps in the estimation of the hydrological behaviour of the water-basin. The important factors taken into consideration on this system are the basin physical and soil water transmissivity factor (Islam 2011). This model is founded up the concept of topographic index (Beven and Kirkby 1979, Islam 2011). The major goal of this model is to calculate the depth of ground water table or local storage deficit at any point for every time step. The value of ground water table depth is a function of $\ln(a/\tan\beta)$ (called topographic index), where a, and $\tan\beta$ respectively are drained area per unit-contour length at a point and surface gradient at that point. The index is used as a

measure of hydrologic resemblance in the points by assuming all locations with identical topographic index values respond in a similar way to the hydrologic processes. The output of the model is only for representative indices values when the index is depending on topography of the basin (Islam 2011). TOPMODEL is based on three sets of assumptions that includes downward transmissivity, the dynamics and hydraulic gradient of saturated zone (Islam 2011). Depending on the infiltration excess technique for calculating runoff value it uses (Beven, 1984) method known as exponential Green-Ampt method, and is recommended to minimize the number of parameters for the input data. The result the model is in the form of simulated hydrographs or area maps (Devi et al. 2015).

3.5 Agricultural Policy Environmental Extender (APEX) Model

It is a flexible dynamic system have the ability to modeling impacts of land-use and management for entire ranches and small water basins (Gassman & Williams 2009; Golmohammadi et al. 2014). It is basically a multi-field version but can also be implemented for single sites in addition to whole ranch or water-basin that is further split down on the basis of site's soil type, land-scape locations or sub-watersheds. It can be used for modeling the effects of numerous mineral/nutrient managing approaches, cultivation processes, soil–water conservation skills, alternative farming habits, and other similar action on run-off, sediment losses, nutrient, and other contaminant indicators based on short-term to long-term continuous simulation (Gassman and Williams 2009). APEX is also a good choice in innovative land administration approaches such as buffer-strip effects on pollutant leakages from up-slope farms, rigorous grazing situations, vegetated grassed channels, and dung application or surface impoundments. Additionally it is one of the rare current models that have the ability to modeling flow and contaminant conveyance routing at the field-scale as stated by (Gassman and Williams 2009).

3.6 Annualized Agricultural Non-point Source (AnnAGNPS) Model

It is a basin-scale, batch-process model developed to support the assessment of prolonged hydrological and water quality data to agronomic activities (Bingner & Theurer 2005; Parajuli et al. 2010; Dhami & Pandey 2013; Luo et al. 2015). This model combines the up-to-date developments of data management in Geographic Information Systems (GIS) with physical description of water-basins, creating simulation prospects for un-gauged sites with inadequate data which hinders the role of model that depends on the input parameters calibration (Dhami & Pandey 2013;

Luo et al. 2015). In this model, the analysed water-basin is split into several similar (based on soil types, land-uses and land-management scenarios) cells or sub-basins to numerically evaluate run-off and sediments, as well as nutrients and pesticides loadings (Hua et al. 2012; Luo et al. 2015).

3.7 Gridded Surface Subsurface Hydrologic Analysis (GSSHA) Model

It is part of distributed physical-based, water-basin simulation used for of modeling of hydrological components, hydraulic parameters, sediments/mineral carriage in arid and wet regions (Downer and Ogden 2004). It splits the water-basin into cells; and these cells are used to routing flows and solutes in a cascading fashion (Dhami and Pandey 2013). GSSHA computes mass-balancing results of partial differential equations (PDEs) and carefully link hydrological elements to guarantee an over-all mass-balance and accurate response. Spatial heterogeneity is considered by dividing the water-basin into cells embracing an even finite-difference grids. The processes are computed for every grid-cell, secondly the results from the specific grid-cells are combined to give water-basin response.

3.8 Distributed Hydrology Vegetation Soil (DHVSM) Model

It is part of physical-based distributed parameter model which offers a jointed re-presentation of water-shed processes at the spatial-scale marked by DEM data (Wigmosta et al. 2002). It models most elements of the hydrologic cycle, at grid points through the entire water-basin (Davie 2004).

3.9 Patuxent landscape Model (PLM)

It is explicit multi-scale, process-based model intended to work as a tool in an organized study of interactions between biological and physical dynamics of the water-basin, conditioned on socio-economic characteristics in the sit (Costanza et al. 2002; Davie 2004). This model works on a grid-cell network (known as general ecosystem model-GEM) functioning at each grid-cell. The GEM is analysing flux-balances in each grid-cell and transferring-mass between cells. The GEM is made of three modules: Hydrology (rainfall, evapotranspiration, infiltration and percolation) ; Nutrients (Nitrogen and Phosphorus input and output with cycling) and Plants (biomass-accumulation). Within each grid-cell the hydrologic components, nutrients

and plant conditions are modelled within a daily time-step and then a distinct routine analyses the fluxes between cells.

3.10 Hydrological Predictions for the Environment (HYPE) Model

It is part of semi-distributed physical-process based, conceptual hydrologic model developed to simulate different multi-basin regions (small-scale and large-scale), encompassing wide variations in geomorphology, soil types, land uses and topography (Lindström et al. 2010; Dhami & Pandey 2013). HYPE links land-scape components and hydrologic sections sideways the flow path with mineral turn-over and conveyance. The parameters of this model are associated with soil type, land use (Dhami & Pandey 2013).

3.11 Hydrologic Modelling System (HEC-HMS)

It is developed for both continuous and event based hydrological modeling. It provides several different options to the users for modelling various components of hydrologic cycle. Initially it was designed to model the run-off process of dendritic-catchments patterns but lately was modified to address wide ranges of problems comprising of huge river-basins, water supply systems, flood-hydrographs, and small catchment run-off (USACE-HEC 2010; Dhami & Pandey 2013).

3.12 Precipitation Runoff Modeling System (PRMS) Model

It is part of modular-designed physical-based, distributed water-basin simulation designed to assess the effects of rainfall, several combinations of land-use and climate on basin-hydrology, stream-flow, and sediment yield (Markstrom et al. 2008; Dhami and Pandey 2013). Each elements of the hydrological cycle are described in terms of recognized empirical relationships or physical-laws which have some physical explanation based on quantifiable water-basin features (Dhami and Pandey 2013).

3.13 Water and Energy Transfer Between Soil, Plants and Atmosphere (Wet Spa) Model

It is part of distributed hydrologic, grid based model for envisaging the transfer of water and energy among plants, atmosphere and soil in the water basin (Wang et al. 1997; De Smedt et al. 2000; Dhami and Pandey 2013). The water-basin is discretized into several grid-cells and each of these grid-cell is further split into different land cover (e.g. vegetation cover and bare-soil), for which the equations of energy and water balance are maintained (Liu and Smedt 2009; Dhami and Pandey 2013). This model combines daily meteorological time series data, land-use and soil maps, and topography to forecast spatial dissemination of hydrologic variables and discharge hydrographs in the water-basin (Rwetabula et al. 2007; Dhami and Pandey 2013).

3.14 Variable Infiltration Capacity (VIC) Model

It is part of grid based semi-distributed hydrologic model and is utilizes the equations both water balance and energy. The main inputs data are rainfall, wind velocity and daily temperature (minimum and maximum values). Within each model grid it allows lots of land cover types. The surface run-off is generated by Dunne-flow called excess runoff infiltration and Hortonian-flow called excess runoff saturation (Devi et al. 2015). By considering precipitation and heterogeneity of soil the model simulates excess runoff saturation.

4 Conclusion

In this review fourteen newly developed or frequently updated hydrological models namely: AnnAGNPS, APEX, DHVSM, GSSHA, HBV, HEC-HMS, HYPE, MIKE-SHE, PLM, PRMS, SWAT, TOPMODEL, VIC and Wet Spa have been designated for the model comparison purpose. The criteria used for the assessment of hydrological models are based on the simulation, governing equation and data availability of the model. Each models have their own advantages and dis advantages. Their performance are depends on where and why we are using. For instance: **APEX** is a flexible dynamic system capable of modeling impacts of land-use and management for entire ranches and small water basins; **GSSHA** is a physical-based, distributed, water-basin simulation used for of modeling of hydrological components, hydraulic parameters, sediments/mineral carriage in arid and wet regions; **HBV** model is part of semi distributed model that requires less data input and produces better simulation results; **HYPE** model is used to simulate different multi-basin regions (small-scale and large-scale), encompassing wide variations in geomorphology, soil types, land

uses and topography; **MIKE-SHE** is a deterministic, spatially-distributed process-based model which have the ability to simulating all basic processes in the land levels of the hydrological cycle; **PRMS** is designed to assess the effects of rainfall, several combinations of land-use and climate on basin-hydrology, stream-flow, and sediment yield; **SWAT** is effective in performing long term simulations to large ungauged water-basin; and considering precipitation and soil heterogeneity **VIC** simulates excess runoff saturation. Before selecting a model for future use the above criteria must be always addressed.

References

Abbott MB, Bathurst JC, Cunge JA, O'Connell PE, Rasmussen J (1986) An introduction to the European hydrological system—systeme hydrologique Europeen, "SHE", 1: history and philosophy of a physically-based, distributed modelling system. J Hydrol 87(1–2):45–59

Arnold JG, Srinivasan R, Muttiah RS, Williams JR (1998) Large area hydrologic modeling and assessment part i: model development. J Am Water Resour Assoc 34(1):73–89

Bergstroem S (1976 Jan) Development and application of a conceptual runoff model for Scandinavian catchment 153

Beven K (1984) Infiltration into a class of vertically non-uniform soils. Hydrol Sci J 29(4):425–434

Beven KJ, Kirkby MJ (1979) A physically based, variable contributing area model of basin hydrology. Hydrol Sci Bull 24(1):43–69

Beven KJ, Kirkby MJ, Schofield N, Tagg AF (1984) Testing a physically-based flood forcasting model (TOPMODEL) for three U. K. catchments. J Hydrol 69:119–143

Bingner RL, Theurer FD (2005) AnnAGNPS technical processes, 110 pp

Borah DK, Bera M, Shaw S (2003) Water, sediment, nutrient, and pesticide measurements in an agricultural watershed in Illinois during storm events. Trans ASAE 46(3):657–674

Butts MB, Payne JT, Kristensen M, Madsen H (2004) An evaluation of the impact of model structure on hydrological modelling uncertainty for streamflow simulation. J Hydrol 298(1–4):242–266

Costanza R, Voinov A, Boumans R, Maxwell T, Villa F, Wainger L, Voinov H (2002) Integrated ecological economic modeling of the Patuxent River watershed, Maryland. Ecol Monogr 72(2):203–231

Davie T (2004) Review of different hydrological modelling frameworks for usage in the Motueka integrated catchment management programme of research, pp 1–22

De Smedt F, Liu Y, Gebremeskel S (2000) Hydrologic modeling on a catchment scale using GIS and remote sensed land use information. Risk analysis II, WIT Press, pp 295–304

Devi GK, Ganasri BP, Dwarakish GS (2015) A review on hydrological models. Int Conf Water Resour Coast Ocean Eng (ICWRCOE'15), 4(Icwrcoe), pp 1001–1007

Dhami BS, Pandey A (2013) Comparative review of recently developed hydrologic models. J Indian Water Resour Soc 33:34–42

DHI (2007) MIKE SHE user manual voume 1: user guide. Dan Hydraul Inst, Denmark (1), 420

Downer CW, Ogden FL (2004) GSSHA: model to simulate diverse stream flow producing processes. J Hydrol Eng 9(3):161–174

Gassman P, Williams J (2009) The agricultural policy environmental extender (APEX) model: an emerging tool for landscape and watershed environmental analyses. Cent Agric Rural Dev (49):109

Golmohammadi G, Prasher S, Madani A, Rudra R (2014) Evaluating three hydrological distributed watershed models: MIKE-SHE, APEX, SWAT. Hydrol 1(1):20–39

Hua L, He X, Yuan Y, Nan H (2012) Assessment of runoff and sediment yields using the AnnAGNPS model in a three-gorge watershed of China. Int J Environ Res Public Health 9(5):1887–1907

Islam Z (2011) A review on physically based hydrologic modeling 46 pp
Lindström G, Pers C, Rosberg J, Stromqvist J, Arheimer B (2010) Development and testing of the HYPE (hydrological predictions for the environment) water quality model for different spatial scales. Hydrol Res 41(3–4):295–319
Liu YB, Smedt F De (2009 Mar) WetSpa extension, a GIS-based hydrologic model for flood prediction and watershed management documentation and user manual. Manage:1–126
Luo C, Li Z, Li H, Chen X (2015) Evaluation of the annAGNPS model for predicting runoff and nutrient export in a typical small watershed in the hilly region of Taihu lake. Int J Environ Res Public Health 12(9):10955–10973
Markstrom SL, Niswonger RG, Regan RS, Prudic DE, Barlow PM (2008) GSFLOW—coupled ground-water and surface-water flow model based on the integration of the precipitation-runoff modeling system (PRMS) and the modular ground-water flow model (MODFLOW-2005). US Geol Surv Tech Methods 6-D1:240
Migliaccio KW, Srivastava P (2007) Hydrologic components of watershed-scale models. Am Soc Agric Biol Eng 50(5):1695–1703
Parajuli PB, Nelson NO, Frees LD, Mankin KR (2010) Comparison of AnnAGNPS and SWAT model simulation results in USDA-CEAP agricultural watersheds in south-central Kansas. Wiley Inter Sci 2274(15):2267–2274
Reggiani P, Rientjes THM (2005) Flux parameterization in the representative elementary watershed approach: application to a natural basin. Water Resour Res 41(4):1–18
Rwetabula J, Smedt FD, Rebhun M (2007) Prediction of runoff and discharge in the Simiyu River (tributary of Lake Victoria, Tanzania) using the WetSpa model. Hydrol Earth Sys Sci Discuss 4:881–908
Singh VP, Woolhiser DA (2002) Mathematical modeling of watershed hydrology. J Hydrol Eng 7(4):270–292
USACE-HEC (2010 Aug) Hydrologic modeling system HEC-HMS v3.5. User's manual, US army crops of engineers. Hydrol Eng Cent, 318
Wang ZM, Batelaan O, De Smedt F (1997) A distributed model for water and energy transfer between soils, plants and atmosphere (WetSpa). Phys Chem Earth 21(3):189–193
Wigmosta M, Nijssen B, Storck P (2002) The distributed hydrology soil vegetation model. Math Models Small Watershed Hydrol Appl:7–42
World Meteorological Organization (1975) Intercomparison of conceptual models used in operational hydrological forecasting. Operational Hydrology Report No. 7, Geneva, Switzerland, 172 pp
World Meteorological Organization (1992) Simulated real-time intercomparison of hydrological models. Operational Hydrology Report No. 38, Geneva, Switzerland
Xu M, Han H, Kang S (2016 Oct). Modeling glacier mass balance and runoff in the Koxkar river basin on the south slope of the tianshan mts. During 1959 to 2009, China, 1–22

An Automatic Integrated Tool for Deriving Morphometric Parameters

Vinit Lambey and A. D. Prasad

1 Introduction

Analysis of drainage basin is an important reference for any hydrological studies as it offers the data which is concerned with the quantitative explanation of the drainage system, which is an important stage in the process of basin characterization (Strahler, 1964). Horton (1945), Strahler (1952, 1957), Leopold and Miller (1956) and Krishnamurthy et al. (1996) have used conventional methods of studying the drainage characteristics of many rivers around the world. Measurements of linear features, areal aspects, gradient of channel network and contributing ground slopes of the drainage basin comes under morphometric analysis. (Nautiyal 1994). Geoinformatics plays a significant role in study of morphometry in designing, and development of hydraulic structures. Advanced methods like remote sensing helps in identification of drainage networks in a basin. However, to perform the analysis it requires step by step process without any flaw. Various sources are available for deriving the morphometric parameters. The available tools make the processing tedious job which involves various sources. It gives strain to system and also increases chances of human error. To overcome this task, an integrated tool has been developed in ArcGIS model builder which is a proprietary software to identify the drainage networks with the help of Digital Elevation Model (DEM) which is an input parameter for basin delineation and other supporting data for morphometric analysis.

The main objective of this study is to develop a tool for deriving morphometric parameters such as Slope, Hill shade, Aspect, Compound Topographic Index, Drainage Density, Shape Factor, Form Factor, Elongation ratio, Circulatory Ratio, length area relationship, lemniscate, fitness ratio and wandering ratio. The developed tool was tested over the Jonk river sub basin and it was observed that the model derived data are reliable for further morphometric investigation.

V. Lambey · A. D. Prasad (✉)
Department of Civil Engineering, National Institute of Technology Raipur, Raipur, India
e-mail: adprasadiit@gmail.com

R. Jha et al. (eds.), *River and Coastal Engineering*, Water Science and Technology Library 117, https://doi.org/10.1007/978-3-031-05057-2_5

2 Methodology

The morphometric analysis of the Jonk basin is carried out using integrated tool developed in ArcGIS environment. The main remote sensing data used in the study is Advanced Spaceborne Thermal Emission and Reflection Radiometer (ASTER) Digital Elevation Model (DEM) of 30 m spatial resolution. DEM was converted from geographic coordinate system to projected coordinate system (UTM, datum: WGS84). Calculation of parameters like stream length, area of the watershed and stream order generation has been done using integrated tool. The proposed methodology is given in Fig. 1.

2.1 Integrated Tool

For this study, a GIS based tool has been developed on the basis of methodology adopted by Magesh and Chandrasekar (2014). The model input parameters are DEM, watershed outlet shape file and number of cells to define stream are user defined. Also, the location path for the resultant output parameters has to be given by the user. Figure 2 shows morphometry model developed in ArcGIS model builder.

Projected DEM is the first and the primary input to the model. Fill tool is used to process the DEM which eliminates the gaps that has occurred during process of DEM formation. The output of the filled DEM is input to flow direction tool. This tool calculates the direction in which water will flow out of the pixel. It follows the eight direction (D8) rule which was coined by Fairfield and Leymarie P (1991). The output of flow direction acts as an input to flow accumulation tool. By applying the condition of numbers of cell required for stream development, streams have been developed and segmented. This output data is input to stream order tool which

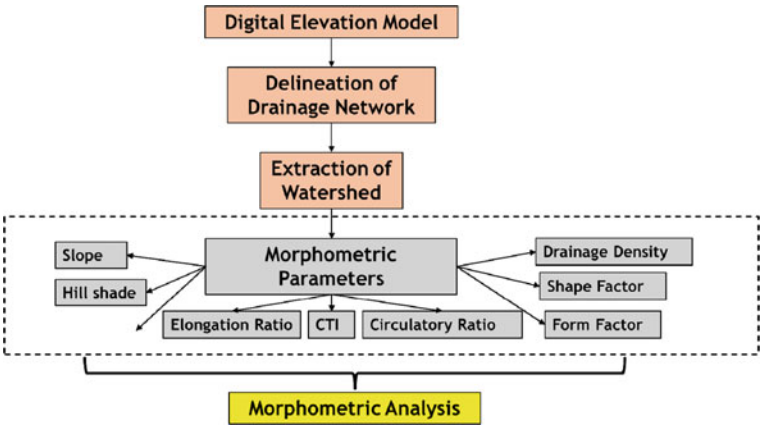

Fig. 1 Proposed methodology

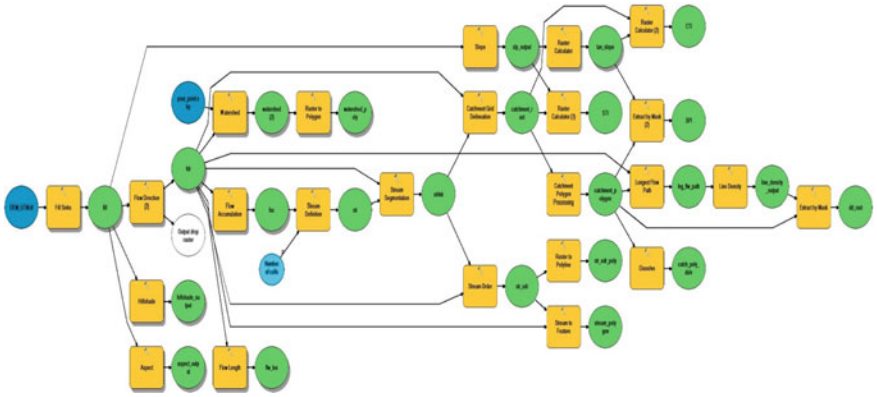

Fig. 2 Morphometric model using ArcGIS model builder

follows Strahler's method. The resultant data obtained from this process is converted to polylines (vector file). Line density tool is applied to the resultant stream network shape file to create drainage density raster. Field geometry option in the attribute table have been used to calculate stream length of each stream order. Figure 3 shows the Graphical User Interface (GUI) for the model.

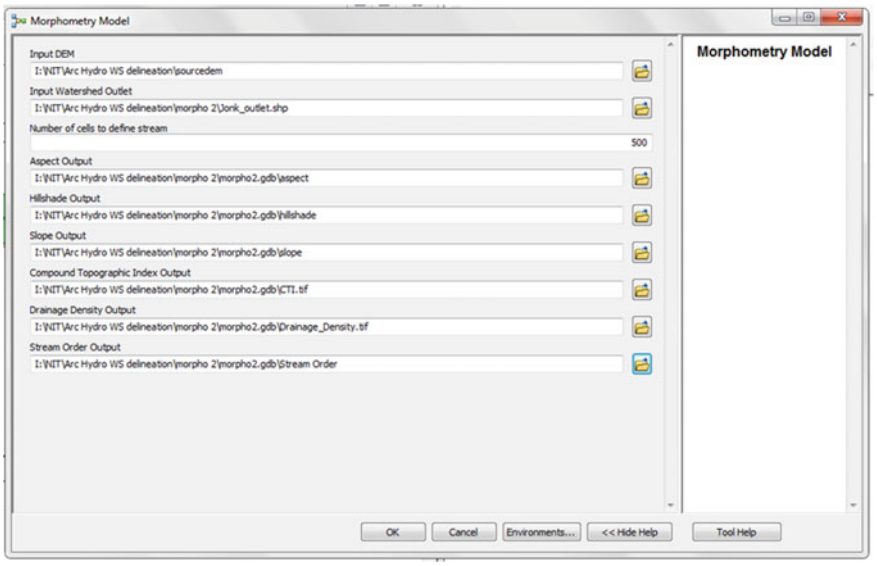

Fig. 3 GUI of morphometry model

3 Study Area

The Jonk watershed is selected as study area which lies between geographic latitude 20° 28′ and 21° 44′ N and longitudes 82° 20′ and 83° 00′ E. The river Jonk originates from Nuapada district of Orissa at an elevation of 700 m from MSL. It merges with Seorinarayan in Chhattisgarh, upstream of Hirakud Dam after travelling the distance of 182 km having a drainage area of 3424 km^2. The climatic condition of the area is dominated by hot summer except during southwestern monsoon. The watershed receives about 90% of the rainfall during monsoon which is active from middle of June to the end of the September. Normal maximum temperature is 43 °C and minimum temperature is 10 °C (CWC). Geologically, the watershed consists of gneiss rock formation. The sub-basin comprises of alluvial formation of various thickness. Figure 4 shows the study area.

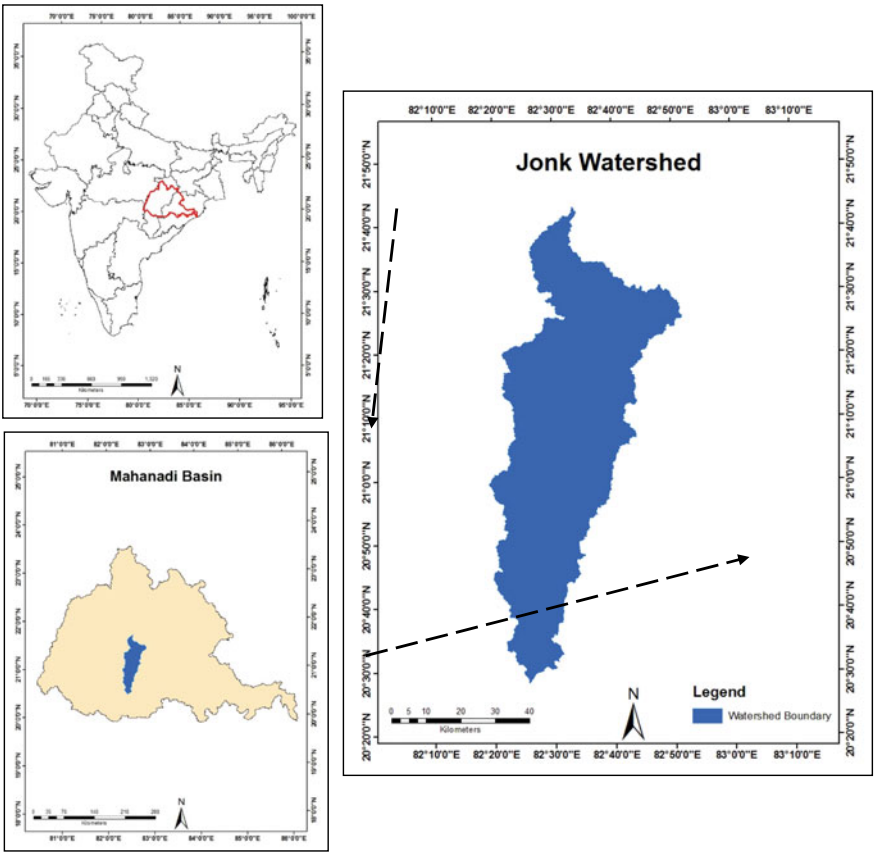

Fig. 4 Study area

4 Results and Discussion

The output from the integrated model affirms that the Jonk sub-basin have dendritic drainage pattern and is a sixth order basin. The slope varies from 0 to 58°. The aspect output shows that the study area is governed by the west-facing slope and the elevation ranges from 217 to 867 m. Figures 5, 6, 7 and 8 shows the raster map

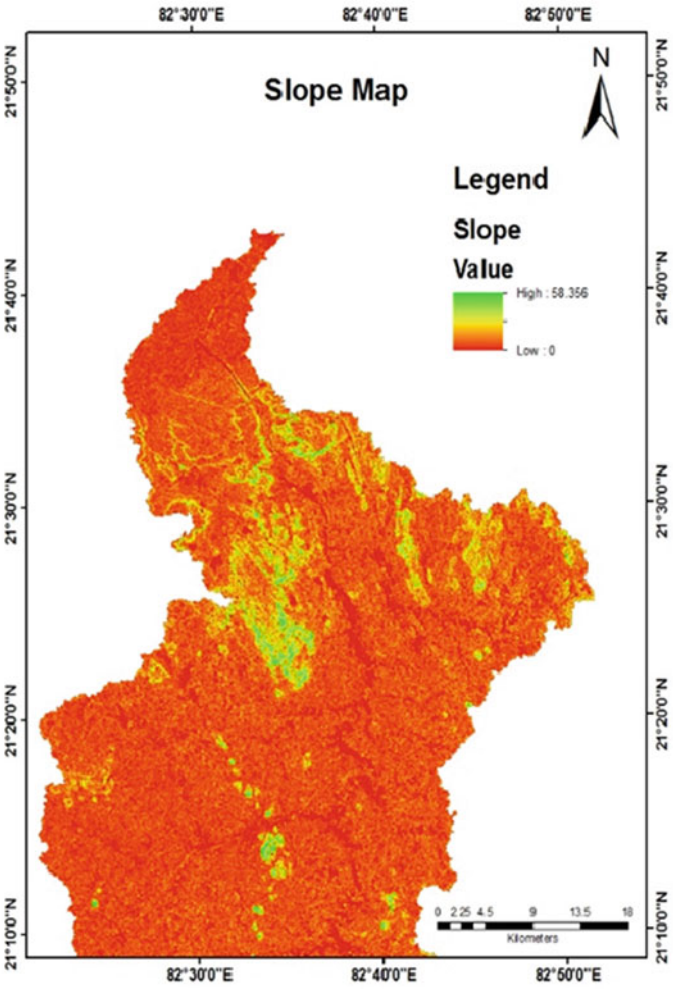

Fig. 5 Slope map

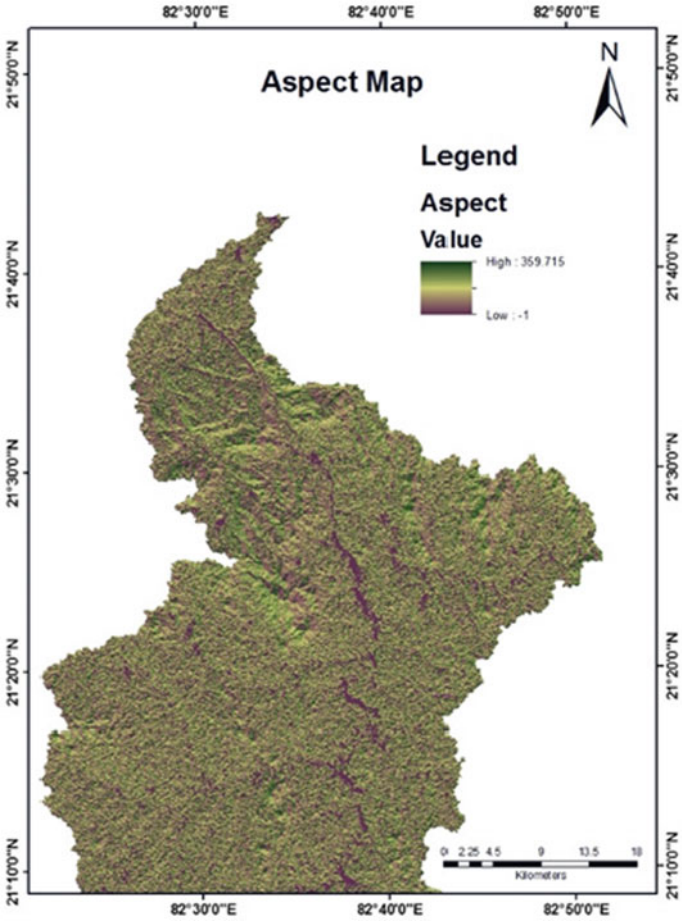

Fig. 6 Aspect map

generated for slope, aspect and hill shade and stream order from the developed tool respectively.

Drainage density (Dd)

As per Horton (1945), drainage density is the stream length per unit area in area of basin or watershed. It is defined as the ratio of total stream segment length of all order within a basin to the basin area, which is expressed in terms of km/km^2 and is expressed as shown in Eq. (1). The drainage density indicates that how closed are the streams spaced from each other. Higher density of 2.29 km/km^2 is identified from results of model developed. Figure 9 shows the drainage density map obtained from morphometry tool.

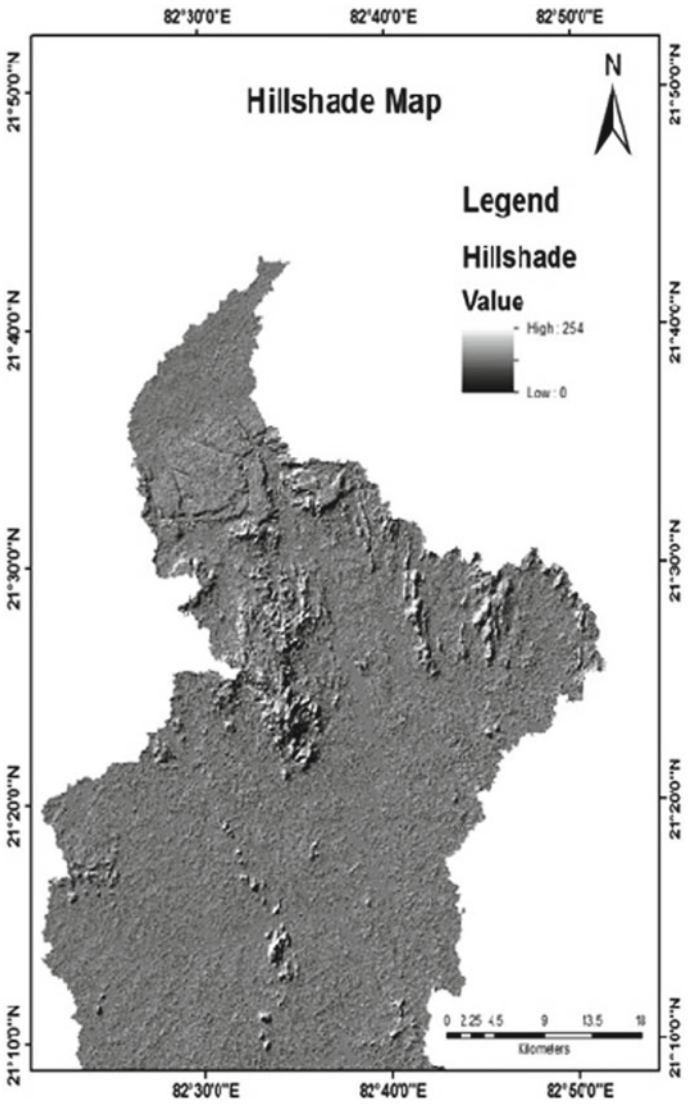

Fig. 7 Hillshade map

$$\mathrm{Dd} = \frac{Ls}{\mathrm{A}} \tag{1}$$

where, Ls is the total length of stream and A is the area of watershed in Sq. km.

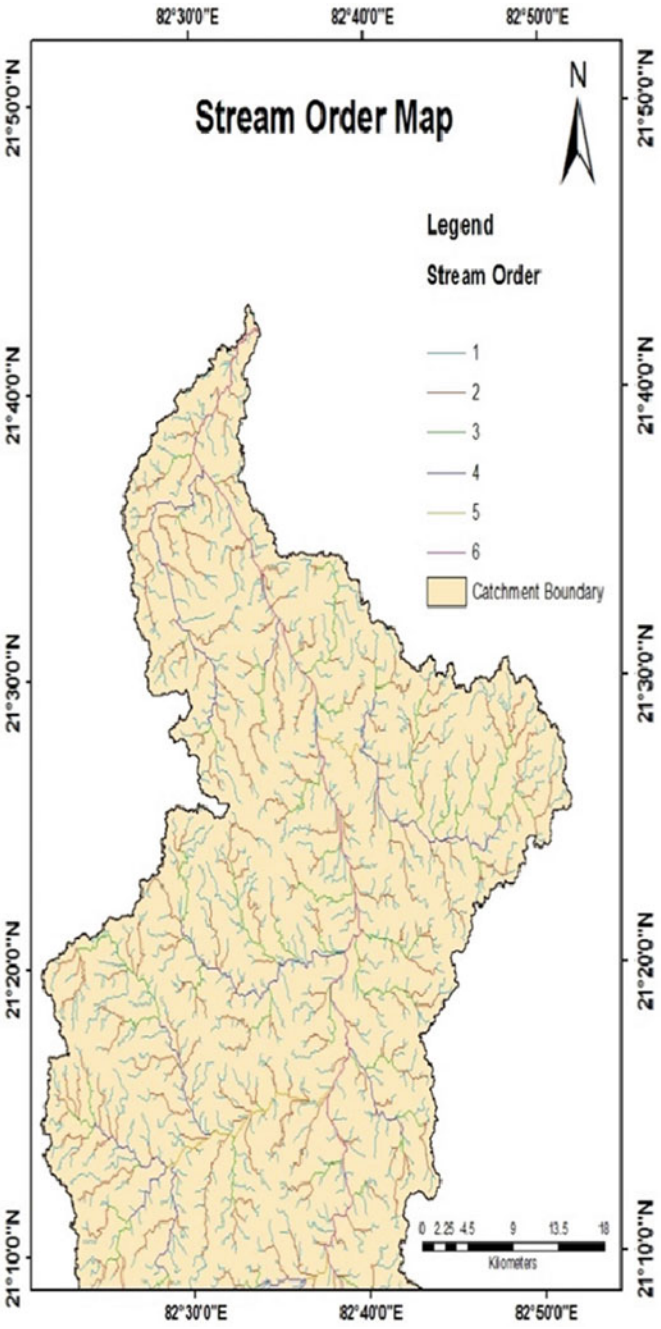

Fig. 8 Stream order map

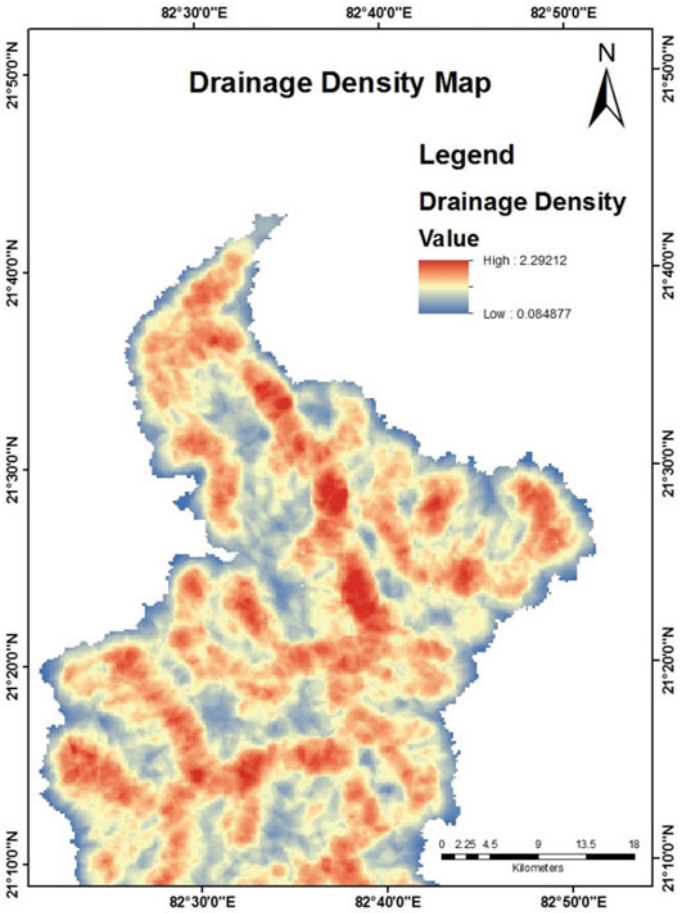

Fig. 9 Drainage density map

Compound Topographic Index (CTI)

Compound Topographic Index is commonly used to quantify topographic control on hydrological processes (Sorenson et al. 2006). Compound Topographic Index (CTI) is also called Topographic Moisture Index or Wetness Index. It is defined as a ratio between the slope and catchment area and is expressed as:

$$\mathrm{CTI} = ln\left(\frac{A}{\tan\beta}\right) \tag{2}$$

where, A is the area of watershed and β is the slope angle.

The CTI value obtained from model is 26.61. Figure 10 represents the CTI map.

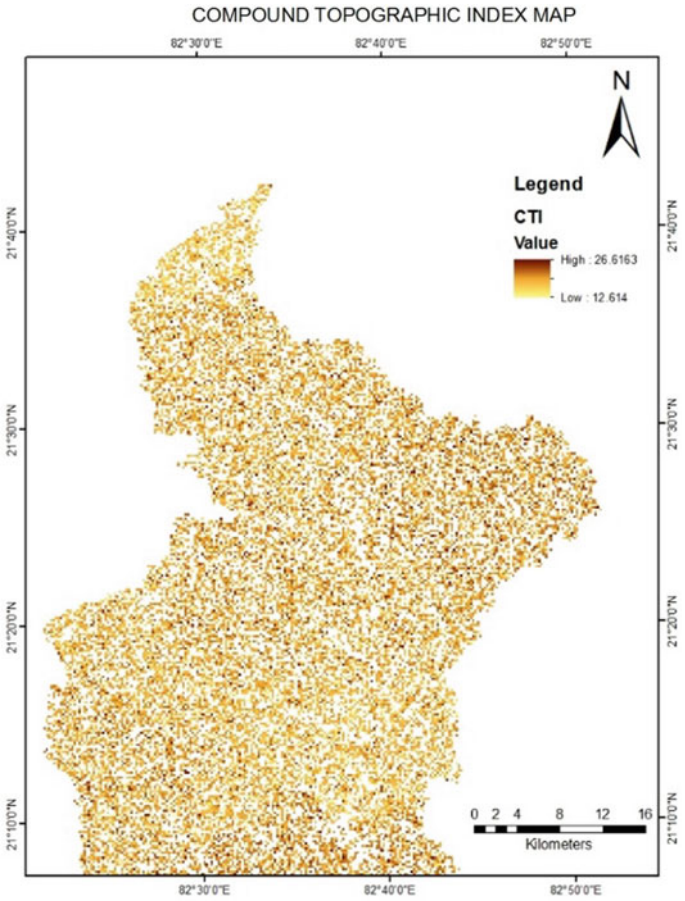

Fig. 10 CTI map

Elongation ratio (R_e)

Schumm (1956) defined the elongation ratio as the ratio of diameter of a circle of the same area as the basin to the maximum basin length. This ratio runs between 0.6 and 1.0 over a wide variety of climatic and geologic types. The varying slopes of watershed can be classified with the help of the index of elongation ratio, i.e., circular (0.9–0.10), oval (0.8–0.9), less elongated (0.7–0.8), elongated (0.5–0.7), and more elongated (<0.5) (Strahler, 1952). Elongation ratio is computed as:

$$\mathrm{Re} = \frac{2}{L_b} \times \sqrt{\frac{\mathrm{A}}{\pi}} \tag{3}$$

where, L_b is the length of basin in km and A is the area of watershed sq. km.

The computed value from integrated model is found to be 0.486 which shows steep slope and high relief.

Lemniscate's (k)
Lemniscate's value computes the slope of the basin Chorley et al. (1957). A basin is circular when k = 1, and becomes more elongate as k increases. It is computed as shown below in Eq. (4).

$$k = \frac{L_b^2}{4A} \tag{4}$$

In present study, Jonk watershed is found to be more elongated as the value obtained from integrated tool is 1.346.

Form factor (F_f)
Horton (1932) defined the form factor as the ratio of basin area to square of the basin length. The smaller the form factor value, more elongated will be the watershed. Equation (5) shows the formula for form factor.

$$F_f = \frac{A}{L_b^2} \tag{5}$$

Form factor (F_f) of Jonk watershed is 0.018 that gives the high elongated shape.

Circularity ratio (R_c)
As per Strahler (1964) and Miller (1953), circularity ratio is the ratio of watershed area to the area of a circle having the same perimeter as the watershed as shown in Eq. (6), and it is pretentious by the lithological character of the watershed. Miller (1953) has described the basin of the circularity ratios that range 0.40–0.50, which indicates strongly elongated and highly permeable homogenous geologic materials.

$$R_c = 12.57 * \left(\frac{A}{P^2}\right) \tag{6}$$

The circularity ratio of the Jonk basin i.e. 0.088 which indicates that the watershed is elongated in shape and is highly permeable.

The morphometric parameters of Jonk river sub basin have been studied, and the results obtained from model is represented in Table 1.

Table1 Model output

S. No	Parameters	Model output
1	Drainage density (km/km^2)	2.292
2	Compound topographic index	26.616
3	Elongation ratio	0.486
4	Circularity ratio	0.088
5	Form factor	0.0185
6	Shape factor	5.405
7	Length area relationship	185.193
8	Lemniscate	1.346
9	Fitness ratio	0.282
10	Wandering ratio	1.450

5 Conclusions

Remote sensing and GIS techniques are much helpful in understanding the the terrain characteristics of the basin. They have been proved to be a proficient tool for morphometric assessment. Automatic extraction of morphometric parameters derived from developed integrated tool using ArcGIS have demonstrated its efficiency for sub basin analysis. It has reduced the chances of human error and also strain acting on the system used for performing analysis. This tool is reliable for any basin analysis as the data produced from it is accurate. ASTER-DEM data of 30 m resolution have been used for detailed analysis using GIS. This paper very well defines the quantitative morphometric parameters of Jonk sub basin. The stream order of Jonk River sub basin varies from 1 to 6 and average drainage density of the basin is moderate. The elongation ratio of the basin indicates the elongated shape of the basin. Hence, the integrated tool may be considered as a time-saving techniques for basin analysis in the future and can be effectively use for morphometric analysis.

References

Chorley RJ, Malm DE, Pogorzelski HA (1957) A new standard for estimating drainage basin shape. Am J Sci 255(2):138–141

Fairfield J, Leymarie P (1991) Drainage networks from grid digital elevation models. Water Resour Res 30(6):1681–1692

Horton RE (1932) Drainage-basin characteristics. Trans Am Geophys Union 13(1):350–361

Horton RE (1945) Erosional development of streams and their drainage basins: hydrophysical approach to quantitative morphology. Geol Soc Am Bull 56:275–370

Krishnamurthy J, Srinivas G, Jayaram V, Chandrasekar MG (1996) Influence of rock types and structures in the development of drainage networks in typical hardrock terrain. ITC Journal 3(4):252–259

Leopold LB, Miller JP (1956) Ephermeral streams: hydraulic factors and their relation to the drainage network. U.S Geol Surv Prof Pap 282-A:38

Magesh NS, Chandrasekar N (2014) GIS model-based morphometric evaluation of Tamiraparani sub-basin, Tirunelveli district, Tamil Nadu, India. Arab J Geosci 7:131–141

Miller VC (1953) Quantitative geomorphic study of drainage basin characteristics in the clinch mountain area, Virginia and Tennessee. Technical report (Columbia University. Department of Geology); no 3

Nautiyal MD (1994) Morphometric analysis of drainage basin using aerial photographs: a case study of Khairkuli basin, District Dehradun, U.P. J. Indian Soc Remote Sens 22(4):251–261

Schumm SA (1956) Evolution of drainage systems and slopes in badlands at Perth Amboy, New Jersey. Geol Soc Am Bull 67(5):597–646

Sørensen R, Zinko U, Seibert J (2006) On the calculation of the topographic wetness index: evaluation of different methods based on field observations. Hydrol Earth Syst Sci Discuss Eur Geosci Union 10(1):101–112

Strahler AN (1952) Dynamics basis of geomorphology. Bull Geol Soc Am 63:923–938

Strahler AN (1957) Quantitative analysis of watershed geomorphology. Trans Am Geophys Union 38:913–920

Strahler AN (1964) Quantative geomorphology of drainage basins and channel networks. In: Chow VT (ed) Hand book of Applied Hydrology. McGraw Hill Book Company, New York

Flood Frequency Analysis in Seonath and Hasdeo River Basins

Mani Kant Verma and Mukesh Kumar Verma

1 Introduction

Analysis of Extreme events holds paramount importance in the hydrologic and hydraulic design of any water resource project (s). Flood Frequency Analysis (FFA) of the river basin is necessary because they leave an impact on the Hydrologic systems. The goal of FFA is to estimate flood quantiles (Q_T) for different return periods. Statistical estimation of quantiles for extreme events depends solely on length and accuracy of time series data. There arise certain situations where the observation data on the site is lesser than the return period. To overcome data scarcity Regional Flood Frequency Analysis (RFFA) technique is adopted which help in estimation of design flood (Jingyi and Hall 2004). Regionalization helps in identifying the homogenous regions and then transfers data from neighboring sites which fall under same homogenous regions. There are wide ranges of approach for delineating homogeneous regions; such as linkage analysis, spatial correlation analysis, Principal Component Analysis (PCA), cluster analysis and L-moments in association with cluster analysis (Ngongondo et al. 2011). Some researchers have also compared flood frequency results of individual stations and region, and they have suggested that regional analysis improves the quantile estimation (Kumar et al. 2003; Lim and Lye 2003; Macdonald et al. 2006). Apart from parametric distributions researchers (Adamowski 1989; Lall et al. 1993) have suggested application of non-parametric frequency distribution for frequency analysis. Kernel estimation (Moon and Lall 1994), Spline estimation (Haktanir 1991) and Local polynomial estimation (Locfit) (Loader 2006) are some of the most applied non-parametric methods in frequency

M. K. Verma (✉)
Department of Civil Engineering, National Institute of Technology Raipur, Raipur, Chhattisgarh, India
e-mail: manikverma.ce@nitrr.ac.in

M. K. Verma
CSVTU Bhilai, Durg, Chhattisgarh, India

R. Jha et al. (eds.), *River and Coastal Engineering*, Water Science and Technology Library 117, https://doi.org/10.1007/978-3-031-05057-2_6

analysis. The locfit method is applied in flood frequency analysis which is simple and based on site data only (Apipattanavis et al. 2010). The locfit approach shows a better result than modified K- nearest neighborhood method (Şarlak 2012). The locfit method is simple and based on site data only.

This work focuses on RFFA and At Site Frequency Analysis (ASFA) i.e., flood frequency studies of Seonath and Hasdeo river basins in Chhattisgarh state through regionalization approach. In the study area, there are some guage locations where data scarcity problem was there. Further, this study also compares different cluster variables used for regionalization along with the comparison of flood quantiles estimated by RFFA and ASFA techniques. Previous studies on Sheonath river basin were carried out using L-moments approach which forms the cluster variables for delineating homogeneous regions. Past studies (Jingyi and Hall 2004; Ngongondo et al. 2011; Kumar et al. 2003; Lim and Lye 2003) of FFA on individual stations suggest that results are improved in quantile estimates through regional analysis. In this study, Regionalization was only based on annual flood series data. Objectives of the current study are, (1) To perform RFFA and at-site frequency analysis (ASFA) for Seonath and Hasdeo River basins; (2) To compare different cluster variables adopted for regionalisation; (3) To compare flood quantiles estimated by RFFA and ASFA.

2 Study Area and Data Availability

Basins considered for this study are, Hasdeo and Seonath river basins which are sub-basins of Mahanadi river basin. The Seonath River that originates near Panabaras village in Rajnandhgaon District has a transverse length of 380 km up to its confluence with the Mahanadi River. The basin area of Seonath basin is 30,560 sq. Km. Tandula, Kharun, Arpa, Hamp, Agar and Maniyari Rivers are the main tributaries of the Seonath River. The Hasdeo River that originates near kaimur about 10 km from Sonhat in Surguja district has a transverse length of 333 km up to its confluence with the Mahanadi River. The basin area of Hasdeo basin is 9856 sq. Km. The major tributary of Hasdeo River is Gej River. Figure 1 shows the location of the study area and the geographic distribution of the Gauge- Discharge stations used in this study. The climatic condition of regions under consideration is similar. These regions receive rainfall through southwest monsoon from the third week of June to the second week of October and post monsoon season starts from the second half of October and continue until the end of November. Winter season of the region is from December to February. Hot season of the region is from March to May. Mean annual rainfall of these regions ranges from 666 to 1487 mm.

Water Resources Department of Chhattisgarh, Indian Meteorological Department, and Central Water Commission are public organizations that collect hydrological and meteorological time series data. There are 20 Gauge- Discharge stations located in this basin. Among these stations, 17 Gauge- Discharge stations have record length

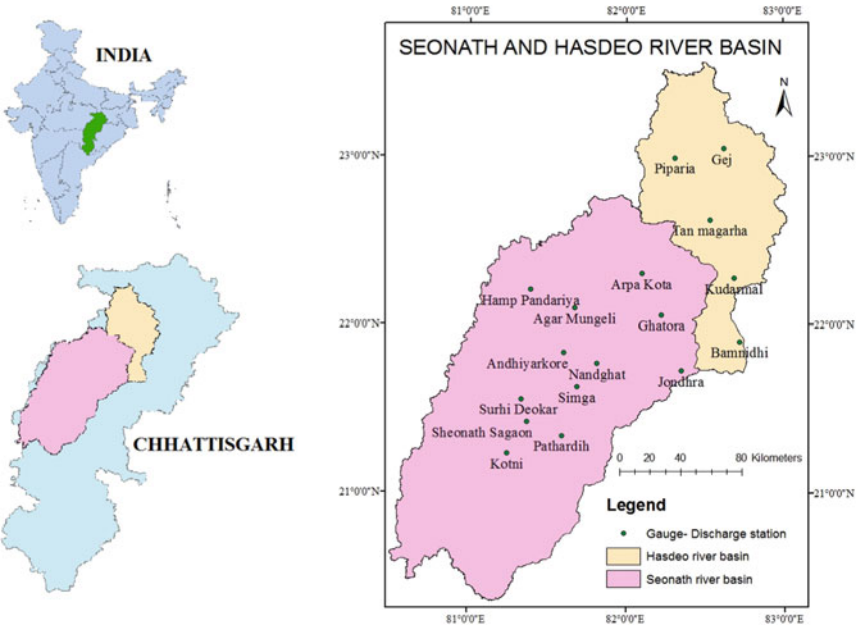

Fig. 1 Location map of the study area

more than or equal to 10 years are taken for further analysis. Stations that fulfil the criteria are shown in Table 1. Digital Elevation Model (DEM) of 30 m resolution from ASTER is used in this study for obtaining catchment characters (http://gdem.ersdac.jspacesystems.or.jp).

3 Methodology

This section explains RFFA and ASFA procedure applied. Initial data screening procedures for independence, randomness, and consistency of the at-site mean annual peak flood are firstly presented. A summary of RFFA using the L-moments approach and ASFA using Locfit are presented. In this study, Annual Maximum Series (AMS) was chosen for frequency analysis mainly to preserve the number of stations and available record length of data. Ward's hierarchical unsupervised technique was applied to identify homogeneous regions. This clustering technique was chosen due to its superiority over average linkage cluster analysis (Rao 2004). L-moments approach (Hosking and Wallis 2005) and index-flood method (Dalrymple 1960) were used for RFFA. L-moments and Locfit (Loader 2006) approach were adopted for ASFA.

Table 1 Station name, Station location, Record length, Catchment area and Annual mean peak discharge (Q_{MEAN})

Station name	Latitude (North)	Longitude (East)	Record length in years	Area (sq. Km)	Annual mean Peak Dischage (cumec)
Agar Mungeli	22.10	81.67	13	716.63	113.45
Andhiyaroki	21.83	81.61	32	2222.26	290.66
Arpakota	22.3	82.1	14	1622.45	283.99
Bamnidhi	21.9	82.72	40	9754.9	3195.65
Gej	23.05	82.62	13	527.39	397.75
Ghatora	22.06	82.22	31	2929.45	655.92
Hamp Pandaria	22.21	81.4	13	552.29	119.38
Jondhra	21.73	82.35	31	29,439.2	5025.98
Khudarmal	22.28	82.68	12	9064.95	2817.9
Kotni	21.24	81.25	32	6894.73	2052.5
Nanghat	21.77	81.81	11	19,784.2	4924.67
Pathardih	21.34	81.6	23	2475.16	1019.32
Piparia	22.99	82.31	13	491.59	355.82
Seonath Sagoan	21.42	81.37	11	9290.47	1184.09
Simga	21.63	81.69	32	16,610.7	4431.05
Surkhi Deokar	21.56	81.34	11	1049.79	179.54
Tan Mahagarh	22.62	82.53	13	641.15	145.46

3.1 Analysis of Hydrological Data

Hydrological data that is to be statistically analyzed for frequency analysis should be independent, random and consistent (Mkhandi et al. 2000). The basic assumption in this analysis is that all peak magnitudes in annual maximum series are independent in a statistical sense. If the peak magnitudes are dependent then the data of extreme events may bias results of frequency analysis. In this study, serial correlation coefficient (SCC) was employed to verify the dependency (Box and Jenkins 1976). Test for randomness was performed to identify whether there is any recognized pattern. If the data is non-random, it shows that process that generates the event is following a trend. The data series should be random for any flood frequency analysis. Runs test (Bradley 1968) was performed for this purpose. Consistency test was performed to identify that the behavior of mechanism that generates a part of time series data is consistent with other segments of the time series data. For this purpose, Standard Normal Homogeneity (SNH) Test (Alexandersson, 1997) was performed using XLSTAT plug in a package for MS- Excel. A 5% significance level was taken in

these data screening tests. Topographical characteristics of each Gauge- Discharge stations were extracted from DEM using software ArcGIS.

3.2 Delineation of Homogeneous Regions

Delineation of hydrologic homogenous regions is performed based on (1) AMS flood data and (2) Geographic characters. To delineate homogeneous region based on AMS flood data, L-moment ratios are used. L-moments are linear functions of Probability Weighted Moments (PWMs) (Hosking and Wallis 2005). L-moment ratios such as L-covariance and L-skewness are helpful in delineating the homogeneous regions. Clusters are identified in the scatter plot between L- moment ratios. Clusters identified are considered as homogeneous regions. To delineate homogeneous region based on site characteristics, Ward cluster analysis is performed for different combinations of characteristics of Gauge-discharge stations. Physiographical characteristics extracted for cluster analysis from DEM are catchment area, the average slope of catchment, longest flow path of catchment and elevation range; mean annual rainfall is the only meteorological attribute included in the analysis. The geographic location attributes Latitude and Longitude are included to identify regions that are geographically contiguous (Rao 2004). Among different combinations of characteristics, the combination that has minimum heterogeneous station is finally selected.

3.3 Discordancy Measure

Discordancy test is performed to identify whether the station in the homogeneous cluster belongs to the cluster are not. To identify those sites that are incongruous with the group a measure of discordancy is required, Discordancy is measured in terms of L-Moments and Discordancy for a site 'i' is given in Eq. 1:

$$Di = \frac{1}{3} N(ui - \overline{u})^T A^{-1}(ui - \overline{u}) \tag{1}$$

where N denotes the number of sites, ui is a vector of L-Moment ratios, and $\overline{u}$ is the group average, given in Eq. 2:

$$\overline{u} = N^{-1} \sum_{i=1}^{N} ui \tag{2}$$

A is defined as the matrix of sums of squares and cross-products, given by Eq. 3:

$$A = \sum_{i=1}^{N} (ui - \overline{u})(ui - \overline{u})^T \tag{3}$$

Thus, Discordancy measure, D_i is a key characteristic in identifying the discordant site. It measures the distance of each station to its corresponding region. If Di is large, then the site i is declared as discordant i.e., here larger value implies that Di should be greater than 3 for a site to be declared as discordant but this is not satisfactory for small regions. $D_i \leq (N-1)/3$ can be accepted for a region having station number less than 10. Computation details for the calculation of D_i are given by Hosking and Wallis (Hosking and Wallis 1993).

3.4 Heterogeneity Test

Heterogeneity test gives us a measure of the Degree of Heterogeneity in a group of sites to determine whether the sites might be treated as homogenous. In this test Heterogeneity measures, H are computed using L-moments. The Heterogeneity measure is given in Eq. 4:

$$Hn = \frac{Vn - \mu v}{\sigma v} \tag{4}$$

where Hn (n = 1,2,3) is the Heterogeneity Measure, Vn is the weighted standard deviation of the at site sample L-CV (L Covariance), μv and σv are the mean and standard deviation of N_{sim} values of V.

The region is regarded as 'acceptably homogeneous' according to given test if $Hn < 1$, 'possibly heterogeneous' if $1 \leq Hn < 2$, and 'definitely heterogeneous' if $Hn \geq 2$. Computation statistics for the calculation of Hn are given by Hosking and Wallis (Hosking and Wallis 2005).

3.5 Selection of Parametric Distribution

Three parameter candidate distributions selected for fitting annual maximum time series data are Generalized Logistic (GLO), Generalized Extreme Value (GEV), Generalized Normal (GNO), Generalized Pareto (GPA) and Pearson type III (PE3). The goodness of fit test is employed to find whether the probability distribution selected fits the data or not within the preferred significant level. The distribution selected to be fit if goodness of fit measure, $\left|Z^{DIST}\right|$ is sufficiently closer to zero and the distribution selected is unfit if $\left|Z^{DIST}\right| > 1.64$ (for 10% significance). The statistics suggested for the goodness of fit test are given by Hosking and Wallis (Hosking

and Wallis 2005). The station that does not follow any one of above distribution is subjected to Anderson–Darling test and the parametric distribution is selected.

3.6 Locfit Approach

In this study, locally weighted polynomial model (locfit) is applied to each station. Parametric techniques cannot capture non-linearity of the data hence non-parametric approaches are used and this study adopts a Non-Parametric approach which is Locally Weighted Polynomial Model (Locfit), to perform ASFA. The Locfit approach is considered owing to its simplicity and ease of implementation. Here the estimate at any point is obtained by fitting a polynomial to a small number of its neighbors. The model is represented in Eq. 5:

$$Y_t = g(X_t) + e_t \tag{5}$$

where $g(X_t)$ is the local polynomial function and e_t is the residual. The function g can be linear or non-linear and the errors e_t are assumed to be normally distributed with zero mean and standard deviation σ_e. X_t is probability plotting position of a ranked annual maximum data and Y_t is the ranked annual maximum data. The brief methodology is given by Loader (2006) and the description follows:

1. The Residuals (e_t) from the fit are saved,
2. A neighborhood is defined around X_t. The number of neighbors is taken as $K = \sqrt{n}$, n is the total sample data points.
3. The neighbors are weighted as per their distance to X_t using the weight function Wi as,

$$Wi = \frac{\frac{1}{i}}{\sum_{i=1}^{k} \frac{1}{i}} \tag{6}$$

4. For the neighbors captured in the neighborhood, a polynomial of order p is fitted which can be linear or non-linear, then the fitted polynomial is used to estimate the value $Ynew$.
5. Once dependent variable is determined from the local polynomial, normal random variate with a zero mean and standard deviation, σ_e of error term of K nearest neighbors are then added to the mean estimate Yt thus obtaining one of the ensemble members.
6. Steps 1 to 6 is repeated at all points where the estimates are required.

3.7 RFFA for Un-Gauged Catchments

Regional formula developed for annual mean peak discharge Q_{MEAN} is multiplied to scaled flood quantiles estimated by index flood method. Multiple regression approach is employed to develop regional formula for homogeneous regions. The parameters selected for framing regional formula of Q_{MEAN} are mean annual precipitation (P) in the catchment, area of catchment the (A) and average slope (S) of the catchment.

3.8 Flood Quantiles Estimation and Comparison

In RFFA, flood quantiles of the best frequency distribution were derived for each region using the index flood method (Dalrymple 1960). At- site flood quantiles are estimated using L-moments and Locfit. In this study, lmomRFA package (http://cran.r-project.org/web/packages/lmomRFA/index.html) and locfit package (http://cran.r-project.org/web/packages/locfit/index.html) in R Software (R Development Core Team 2008) were used for scaled quantile (Q_T/Q_{MEAN}) estimations.

Mean absolute error (MAE) was determined for at-site and regional quantile estimates obtained by various methods to measure variation in regional quantile estimates with individual quantile estimates and to identify a better method to estimate flood quantiles.

4 Results and Discussions

4.1 Data Quality Check

Data quality analysis was performed for AMS flood data of all Gauge-discharge stations. Among all stations, Agar Mungeli was the only station that that did not pass SNH Test. This station was excluded from further analysis. Results are shown in Table 2.

4.2 Regionalisation

L-moments were computed for AMS flood data and from the scatter plot between L_{SK} and L_{CV} shown in Fig. 2, it was observed that two stations Gej and Hamp Pandaria do not belong to any of the homogeneous regions. Homogeneous regions (R1, R2, and R3) grouped by visual interpretation were justified by cluster analysis and discordancy measure. Two stations were removed from further analysis.

Table 2 Basic statistics of AMS flood data for Gauge-Discharge stations

Gauge-Discharge station name	Test for Independence	Test for Randomness	Test for Homogeinity
	SCC Test	Runs Test	SNH Test
	P < 0.5	P > 0.05	P > 0.05
Agar Mungeli	0.49	0.06	**0.0266**
Andhiyarkori	0.35	0.26	0.34
Arpa Kota	0.34	0.53	0.539
Bamnidhi	0.43	0.09	0.194
Gej Ganipur	0.06	0.88	0.28
Ghatora	0.43	0.5	0.21
Hamp Pandaria	0.49	0.1	0.125
Jondhra	0.49	0.34	0.673
Khodharmal	0.21	0.89	0.07
Kotni	0.49	0.56	0.933
Pathardhi	0.43	0.26	0.91
Piparia	0.44	0.1	0.11
Seonath Sagaon	0.4	0.5	0.06
Simga	0.48	0.16	0.58
Surki Deokar	0.49	0.22	0.14
Tan Mahagar	0.46	0.24	0.79

*Bold value mean statistically significant at 0.05 level (less than critical value (P) of 0.05)

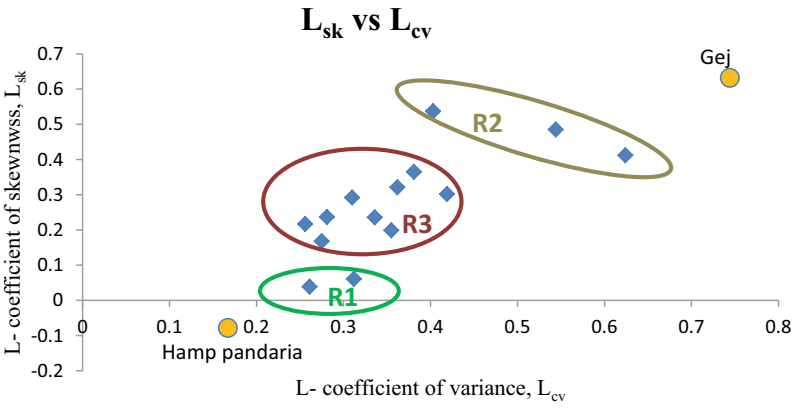

Fig. 2 Scatter plot between L_{SK} and L_{CV} (R1, R2 and R3 are visually interpreted homogeneous regions)

Table 3 Results of homogeneity and Goodness of fit test

Homogeneous region	Homogeneity measure			Goodness of fit distance for candidate distributions, Z^{DIST}				
	H1	H2	H3	GLO	GEV	GNO	PE3	GPA
R 1	-0.23	-1.08	-0.25	1.77	1.01	1.14	1.13	**-0.44**
R 2	0.79	-0.45	-1.06	0.56	0.44	**0.05**	-0.06	-0.08
R 3	0.65	-0.81	-0.71	1.3	0.34	**-0.22**	-1.21	-2.16

*Bold values denote the lowest $|Z^{DIST}|$ value, which indicates the best distribution the region follows

4.2.1 Based on AMS Flood Data

Homogeneous regions were delineated based on L-moment ratios of AMS flood data. Three homogeneous regions were delineated and discordancy measure of stations in the region, homogeneity measure of regions and goodness of fit of frequency distribution were determined for each region. Region 1 (R1) includes Arpa Kota and Piparia, Region 2 (R2) includes Pathardih, Seonath Sagoan and Surkhi Deokar and Region 3 (R3) includes rest of the stations. The results of homogeneity and Goodness of fit test are given in Table 3.

4.2.2 Based on Site Characters

Homogeneous regions were delineated based on site (Gauge-discharge station) characters using Ward cluster analysis. Cluster variables considered for analysis are an area of the catchment (A), the length of the catchment (L), the average slope of the catchment (S), mean annual precipitation (P), an elevation range of catchment (H), latitude (lat) and longitude (long). Catchment characters are shown in Table 4. Ward cluster analysis is performed for different combinations of cluster variables. Clusters that discord minimum number of stations are selected. Three homogeneous regions clustered based on cluster variables combination of ALSPH discarded only one station (Pathardih, since $D_i > 3$). Region 1 (R1) includes Andhiyarokhi, Kotni, Seonath Sagoan, Surkhi Deokar and Piparia, Region 2 (R2) includes Arpa Kota, Tan Mahagarh, Khudarmal, Ghatora, and Bamnidhi. Region 3 (R3) includes rest of the stations. Homogeneity measure and goodness of fit of frequency distribution are determined for each delineated homogeneous region. Results are shown in Table 5.

4.3 Parameter Estimation and Regional Formula

Three parameters (Shape (ξ), location (α) and scale (k)) of selected frequency distribution are estimated using L-moment Probability Weighted Moments. The regional formula is formulated for mean discharge for each homogeneous region delineated

Table 4 Station name and respective catchment characteristics

Station name	A (sq.Km)	S (%)	L (Km)	P (mm)	H (m)	lat (North)	Long (East)
Andhiyaroki	2222.26	12.27	143.71	856.13	755	21.83	81.61
Arpa Kota	1622.45	15.17	107.09	1102.19	912	22.3	82.1
Bamnidhi	9754.9	12.6	325.37	1550.22	937	21.9	82.72
Gej Ganipur	527.39	9.63	51.83	1486.86	259	23.05	82.62
Ghatora	2929.45	12.91	150.31	1134.48	928	22.06	82.22
Hamp Pandaria	552.29	15.99	60.95	722.7	657	22.21	81.4
Jondhra	29,439.2	10.22	386.49	1030.28	1013	21.73	82.35
Khudarmal	9064.95	13.23	276.03	1362.19	937	22.28	82.68
Kotni	6894.73	9.7	161.56	1042.22	547	21.24	81.25
Nanghat	19,784.2	9.96	307.27	987.01	832	21.77	81.81
Pathardih	2475.16	9.2	143.89	1112.08	299	21.34	81.6
Piparia	491.59	10.16	50.62	1198.43	285	22.99	82.31
Seonath Sagoan	9290.47	9.99	194.23	1007.57	598	21.42	81.37
Simga	16,610.7	9.76	269.14	998.33	673	21.63	81.69
Surkhi Deokar	1049.79	12.04	98.91	856.17	570	21.56	81.34
Tan Mahagar	641.15	15.91	69.46	1308.45	636	22.62	82.53

Table 5 Results of Homogeneity and Goodness of fit test

Homogeneous Region	Homogeneity measure			Goodness of fit distance for candidate distributions, Z^{DIST}				
	H1	H2	H3	GLO	GEV	GNO	PE3	GPA
R 1	0.82	0.59	0.22	**0.03**	-0.45	-0.79	-1.38	-1.74
R 2	0.52	0.27	0.52	1.33	0.7	**0.3**	-0.39	-0.98
R 3	0.36	-1.09	-0.69	0.96	0.3	**0.06**	-0.38	-1.29

*Bold values denote the lowest $|Z^{DIST}|$ value, which indicates the best distribution the region follows

by both methods. Three parameters considered for multiple regression analysis are an area of the catchment (A), mean annual precipitation (P) and the average slope of the catchment (S). Results are shown in Table 6.

4.4 At-site Frequency Analysis

Here, frequency analysis was performed for each station based on AMS flood data of that station only.

Table 6 Regional parameter estimates for selected distributions and regional formula for Q_{MEAN}

Regionalisation method	Region	Selected distribution	Parameter estimated			Regional formula for Q_{MEAN}
			ξ	α	K	
Based on AMS flood data	R 1	GPA	0.193	1.459	0.808	$10^{10.57} A^{3.15} P^{-5.99}$
	R 2	GNO	0.585	0.644	-0.995	$10^{6.44} A^{0.42} S^{-5.08}$
	R 3	GNO	0.838	0.536	-0.558	$10^{-5.44} A^{0.86} S^{-2.37} P^{2.59}$
Based on site characters	R 1	GLO	0.832	0.323	-0.287	$10^{4.26} A^{0.50} S^{-4.78} P^{0.57}$
	R 2	GNO	0.825	0.567	-0.569	$10^{-5.11} A^{1.01} S^{-1.18} P^{1.88}$
	R 3	GNO	0.881	0.475	-0.473	$10^{-4.27} A^{-0.64} S^{10.75}$

4.4.1 Parametric Approach

Individual Station Frequency Distribution (ISFD) for each station was selected by the goodness of fit test. Parameters of corresponding distribution were estimated by Probability Weighted Moments. All stations (except Nanghat) follow any of the five (GLO, GEV, GPA, GNO & PE3) distributions. Based on Anderson–Darling test performed by Stat Assist software it is found that Nanghat station follows Log Logistic (2 parameters) distribution (LL2P). Results are shown in Table 7.

Table 7 Lowest Goodness of fit distance for candidate distributions for each station and parameter estimates for the selected distribution

Station name	Lowest Goodness of fit distance for candidate distributions	Selected distribution function	Parameters estimated		
	Z^{DIST}		ξ	α	k
Andhiyaroki	-0.24	GLO	0.818	0.304	-0.321
Arpa kota	0.6	GPA	0.138	1.525	0.768
Bamnidhi	0.09	GPA	0.13	0.933	0.073
Ghatora	-0.67	GLO	0.786	0.303	-0.365
Jondhra	-0.68	GLO	0.911	0.237	-0.217
Khudarmal	0.61	GPA	0.334	0.949	0.425
Kotni	0.04	PE3	1	0.658	1.203
Nanghat	**1.74**	**LL2P**	0	3.053	0.836
Pathardih	-0.07	PE3	1	1.324	2.486
Piparia	-0.07	PE3	1	0.463	0.239
Seonath Sagoan	-0.25	GLO	0.691	0.237	-0.537
Simga	0.14	GNO	0.86	0.539	-0.49
Surkhi Deokar	-0.02	GNO	0.573	0.604	-1.056
Tan mahagar	-0.31	GLO	0.857	0.268	-0.292

*Bold value denotes statistically significant at 0.1 level ($|Z^{DIST}| > 1.64$)

Table 8 Flood quantile estimates of Locfit approach

Station name	Flood quantiles (Locfit approach)			
	Return period, T in years			
	50	100	500	1000
Andhiyaroki	956.7	1022.99	1317.48	1376.38
Arpa kota	587.93	614.64	716.15	765.02
Bamnidhi	12,202.9	13,848.7	18,556.7	19,148.4
Ghatora	2552.2	3157.03	4333.01	4507.78
Jondhra	12,357.5	13,081.4	14,477.8	14,655
Khudarmal	5185.77	8096.43	10,965.7	15,236.9
Kotni	5232.21	5284.05	5383.49	5430.19
Nanghat	12,234	25,235.3	80,417.9	91,834.6
Pathardih	2431.97	4430.79	11,277.8	20,034.1
Piparia	2638.72	5852.95	21,420.7	41,200
Seonath Sagoan	7969.71	19,935.9	83,420	96,684.8
Simga	11,251.7	11,325	11,535.3	11,575.5
Surkhi Deokar	665.47	820.79	975.51	1025
Tan Mahagarh	475.97	808.11	2265.3	3994.29

4.4.2 Locfit Approach

Flood quantiles were predicted using the Locfit algorithm, which provides values of the locally fitted polynomial function.

4.5 Comparative Analyses of Flood Quantiles

Mean Absolute Error (MAE) was computed for flood quantiles estimated by different regional and at-site flood frequency analysis. MAE of quantiles estimated based on AMS flood data, site characters and Locfit regarding quantiles of at-site parametric quantile estimates.

Observations from MAE based on at- site parametric estimation is,

i. Flood quantiles of regionalization based on AMS flood data have lowest MAE among all other methods. Record length did not have much impact on quantile estimation.
ii. Flood quantiles based on locfit method have highest MAE among all other methods which prove 'k' is insufficient (especially for lower record length). In this study k=$\sqrt{n}$ is chosen for analysis. Record length has much impact in this quantile estimation.

Table 9 MAE statistics based on at-site parametric approach

Station name	Record length in years (N)	Based on at-site parametric approach					
		Region based on AMS flood data		Region based on site characters		Locfit	
		100 year return period	1000 year return period	100 year return period	1000 year return period	100 year return period	1000 year return period
Bamnidhi	40	0.11	0.09	0.08	0.07	0.03	0.03
Andhiyaroki	32	0.06	0.14	0.01	0.03	0.13	0.2
Kotni	32	0.05	0.1	0.11	0.28	0.14	0.28
Simga	32	0.03	0.05	0.06	0.08	0.14	0.22
Ghatora	31	0.1	0.2	0.08	0.17	0.08	0.19
Jondhra	31	0.17	0.17	0.06	0.06	0.06	0.07
Pathardih	23	0.08	0.15	-	-	0.45	0.46
Arpa Kota	14	0.04	0.04	0.33	0.64	0.03	0.08
Piparia	13	0.05	0.09	0.37	0.74	1.91	10.1
Tan Mahagarh	13	0.04	0.08	0.08	0.09	0.16	0.75
Khudarmal	12	0.23	0.44	0.27	0.5	0.1	0.31
Nanghat	11	0.05	0.11	0.1	0.19	0.16	0.51
Seonath Sagoan	11	0.25	0.22	0.16	0.26	0.58	1.6
Surkhi Deokar	11	0.02	0.03	0.31	0.36	0.14	0.28
Average MAE		0.09	0.14	0.16	0.27	0.29	1.08
Average MAE (N $\geq$ 30 years)		0.09	0.13	0.07	0.12	0.10	0.17
Average MAE (N < 30 years)		0.10	0.15	0.23	0.40	0.44	1.76

iii. In all cases, MAE is lesser for stations with a record more than 30 years than stations with a record less than 30 years. This shows that both parametric and non-parametric approach estimates reliably with higher station record.

iv. MAE with flood quantiles of regionalization based on site characters is higher. This shows that geophysical homogeneity does not mean hydrological homogeneity.

v. MAE of 100-year return period is lesser than MAE of the 1000-year return period. This shows that quantile estimates of all methods vary in higher return periods.

5 Conclusion

For flood frequency analysis based on L-moments and Index, flood approaches in Seonath and Hasdeo river basins, regionalisation based on AMS flood data may be suggested. It shows a better result than regionalisation based on site characters and non-parametric Locfit approach. Homogeneous regions follow GNO and GPA distributions. In Locfit approach, assumption $k=\sqrt{n}$ is not appropriate for stations with poor record length (less than 30 years). Therefore, alternative mathematical function should be formulated for 'k'. Regression formula developed for each homogeneous region can be applied for quantile estimation of ungauged catchments. Application of other RFFA and ASFA are suggested for future studies in these river basins.

Acknowledgements Authors thank Water Resources Department of Chhattisgarh, Indian Meteorological Department and Central Water Commission for providing data for this study. Authors are also thankful to NIT Raipur for providing all the support for carrying out this work.

References

Adamowski K (1989) A Monte Carlo comparison of parametric and nonparametric estimation of flood frequencies. J Hydrol 108:295–308

Apipattanavis S, Rajagopalan B, Lall U (2010) Local polynomial–based flood frequency estimator for mixed population. J Hydrol Eng 15(9):680–691

Box GE, Jenkins, GM (1976) Time series analysis: forecasting and control, revised ed. Holden-Day

Bradley JV (1968) Distribution-free statistical tests

Dalrymple T Flood-frequency analyses, manual of hydrology: Part 3 (No. 1543-A), USGPO

Haktanir T (1991) Statistical modeling of annual maximum flows in Turkish rivers. Hydrol Sci J 36(4):367–389

Hosking JRM, Wallis JR (2005) Regional frequency analysis: an approach based on L-moments, Cambridge University Press

Hosking JRM, Wallis JR (1993) Some statistics useful in regional frequency analysis. Water Resour Res 29(2):271–281

Jingyi, Z, Hall MJ (2004) Regional flood frequency analysis for the Gan-Ming River basin in China. J Hydrol 296(1):98–117

Kumar R, Chatterjee C, Panigrihy N, Patwary BC, Singh RD (2003) Development of regional flood formulae using L-moments for gauged and ungauged catchments of North Brahmaputra river system. J Inst Eng India Civ Eng Div 84(mai):57–63

Lall U, Moon YI, Bosworth K (1993) Kernel flood frequency estimators: bandwidth selection and kernel choice. Water Resour Res 29(4):1003–1015

Lim YH, Lye LM (2003) Regional flood estimation for ungauged basins in Sarawak, Malaysia. Hydrol Sci J 48(1):79–94

Loader C (2006) Local regression, and likelihood, Springer Science & Business Media

Macdonald N, Werritty A, Black AR, McEwen LJ (2006) Historical and pooled flood frequency analysis for the River Tay at Perth, Scotland. Area 38(1):34–46

Mkhandi SH, Kachroo RK, Gunasekara TAG (2000) Flood frequency analysis of southern Africa: II. Identification of regional distributions. Hydrol Sci J 45(3):449–464

Moon YI, Lall U (1994) Kernel quantile function estimator for flood frequency analysis. Water Resour Res 30(11):3095–3103

Ngongondo CS, Xu CY, Tallaksen LM, Alemaw B, Chirwa T (2011) Regional frequency analysis of rainfall extremes in Southern Malawi using the index rainfall and L-moments approaches. Stoch Env Res Risk Assess 25(7):939–955

Rao A (2004) Regionalization of Indiana watersheds for flood flow predictions phase I: studies in regionalization of Indiana watersheds. Joint Transp Res Program 180

Şarlak N (2012) Flood frequency estimator with nonparametric approaches in Turkey. Fresen Environ Bull 21(5):1083–1089

Assessment of Plan Form Development Due to Erosion and Deposition of Soil

Snigdhadip Ghosh and Vijay Kumar Dwivedi

1 Introduction

Soil erosion is a natural process, that is occurring over geological time and it can occur either by water or wind (Borah et al. 1982). More significant is the erosion that is related to accelerated erosion (Misri et al. 1984). In such a situation, the natural rate of erosion gets significantly increased due to human activities such as changes in management and land cover. Accelerated erosion due to flowing water is a complex process (Morvan et al. 2002). Therefore, it is necessary to develop an indicator that helps to quantify the factor causing erosion due to flowing water. In this project we have used Acoustic Doppler velocimeter to measure the erosion and sedimentation characteristics of soil in mobile river bed (Ghosh et al. 2018; Kostaschuk et al. 2005).

2 Inferences

Most of the previous works were case studies based on land loss data of previous decades of different landforms, different countries under different climates (Wu et al. 2000). None of the studies cited in the literature review concludes how to avoid or prevent land losses from an island in a natural stream.

GIS data were used to monitor land losses due to river flow (Biron et al. 1998; Rennie et al. 2002; Shields and Rigby 2005), but methodologies have not been put

S. Ghosh
Water Resource Engineering Laboratory, National Institute of Technology Durgapur, Durgapur, West Bengal, India

V. K. Dwivedi (✉)
Department of Civil Engineering, National Institute of Technology Durgapur, Durgapur, West Bengal, India
e-mail: vkdwivedi10725@yahoo.co.in

R. Jha et al. (eds.), *River and Coastal Engineering*, Water Science and Technology Library 117, https://doi.org/10.1007/978-3-031-05057-2_7

forward to determine the cause of erosion around and downstream of an island in a stream and predict the plan form due to resultant flow.

3 Objectives

Based on the inferences, it was decided to first understand the flow field around an island in a natural stream and downstream of the island.

I. Estimation of soil erosion and deposition around an island in a natural stream.
II. Estimation and prediction of changes in plan form development around the island and downstream of the island.

4 Methodology

4.1 Details of the Experimental Set up

The experiments were conducted in the experimental setup created at National Institute of Technology, Durgapur. The setup consists of a flume 20 m long, 4 m wide and 10 m deep. The flume has a cemented bottom and glass wall on both side with a grid of 5 × 5 cm up to a height of 50 cm from the bottom of the flume to measure the bed profile. Experiments were done at several slopes of bed in the flume. The discharge in the flume was provided by an upstream reservoir feed by two 10″ mild steel pipes. There were two pumps of 7.5 HP each to supply water to the MS pipe from the underground reservoir. The water supply into flume was regulated with the help of a valve provided in the inlet pipe coming from reservoir. There was an escape channel to drain the water from flume to reservoir which was 41.2 m long, 1 m wide and 0.6 m deep. The water level and discharge through the flume was controlled by a motor operated sluice gate at the tailed end of the flume. The schematic diagram of the setup is shown Fig. 1.

Directional current (DCM) and acoustic Doppler Velocity (ADV) meters were used for the field measurements of velocity and turbulence (Biron et al. 1998; Kostaschuk et al. 2005) in the region around the island in the channel as well as in the interface region between the main channel and flood plain. The values of local shear velocity and roughness length for the reach under study was calculated and analyzed using measured velocity data (Biron et al. 1998; Rennie et al. 2002) to provide a scientific pattern of plan form development. Measurements were carried out through different steps, such as measurement of Discharge by Electronic Flow Meter, discharge measurement using V Notch, the measurement for the velocity distribution with the help of ADV (Yorke and Oberg 2002), the value of the dry

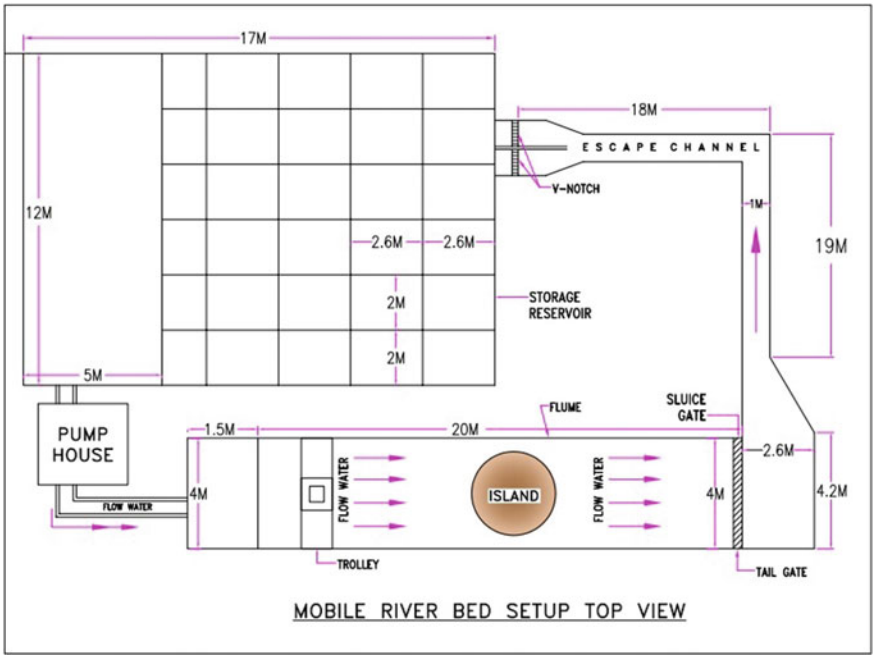

Fig. 1 Schematic diagram of mobile river bed setup

density computed by using the observed value of bulk density and antecedent moisture content. The void ratio was derived from the computed value of the dry density of the sediments (Figs. 2 and 3).

5 Experiment Method

After spreading the desired sediment in the flume, the bed surface was smoothened with the help of a wooden template by moving it from upstream to downstream. A hemispherical island of the same bed material was created in the middle of the flume. The water was then allowed to enter into the flume first at very low discharge. Velocity vectors at different spatial locations were measured with the help of the ADV. Bed load measurements were taken at regular intervals. Suspended load samples were taken at the beginning of the flow when the flow gets stabilized. Water surface profile (depth of water surface below the datum) as well as bed surface profile (depth of bed surface below the datum) reading was taken at regular intervals along with transverse and longitudinal intervals along the flume. These water and bed surface profiles were measured at a regular time interval. The velocity vectors were noted around the island and throughout the flood plain downstream of the island, as well

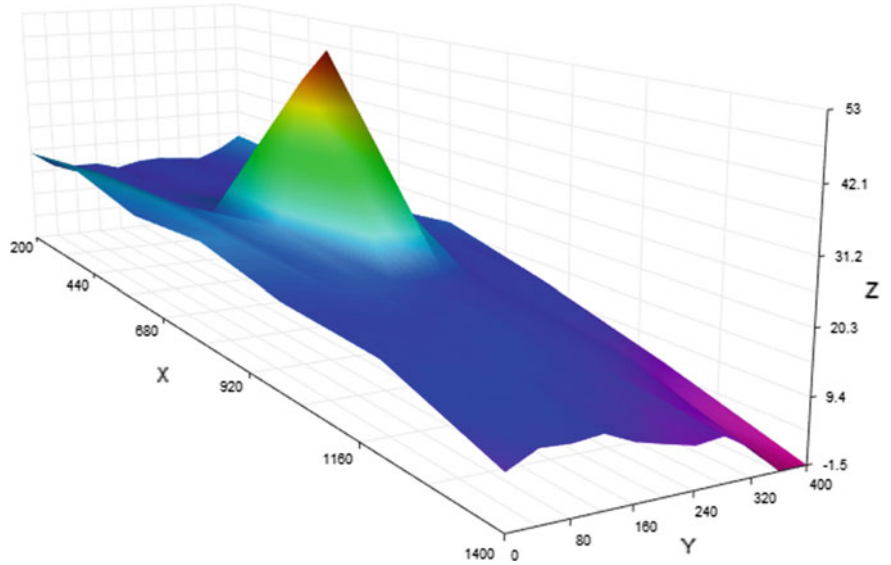

Fig. 2 Plan form development on 12.01.2018

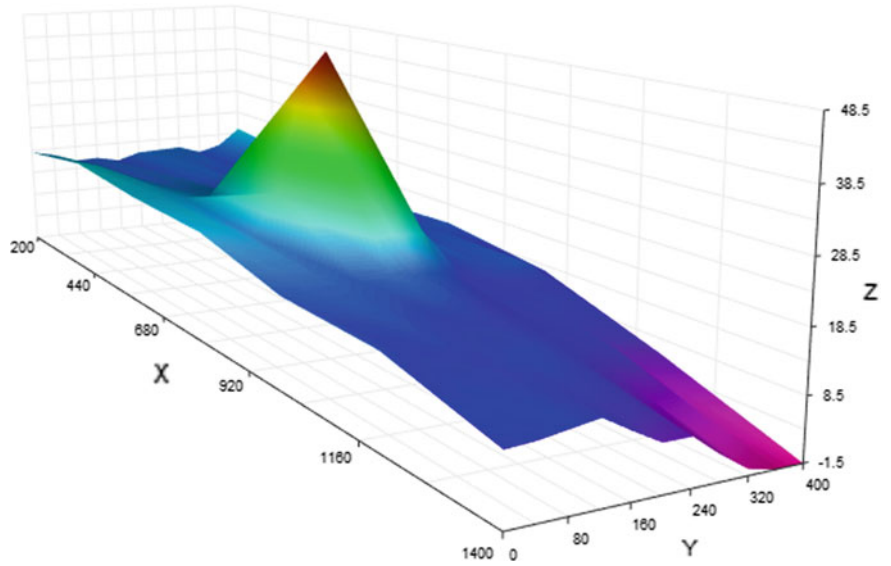

Fig. 3 Plan form development on 13.01.2018

as the three directional bed profiles around the island and downstream of the island (Figs. 4, 5 and 6).

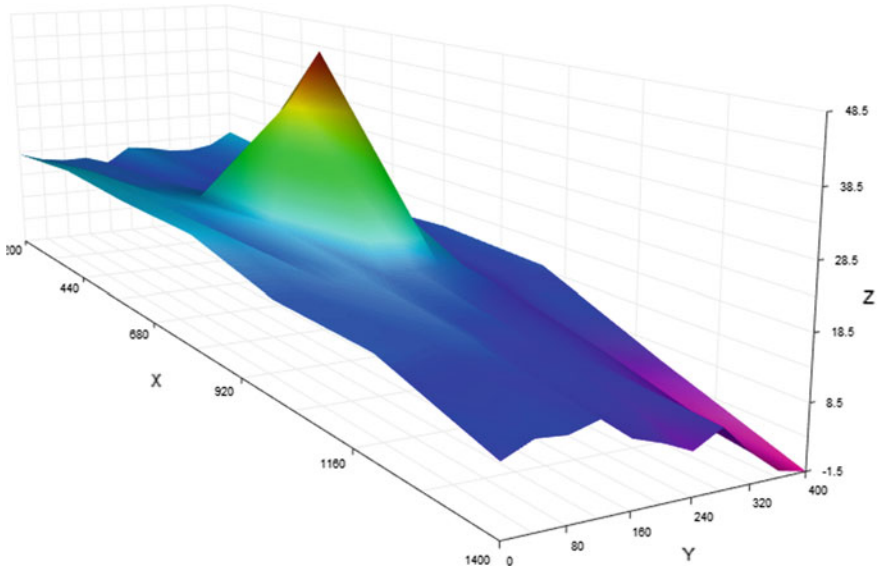

Fig. 4 Plan form development on 14.01.2018

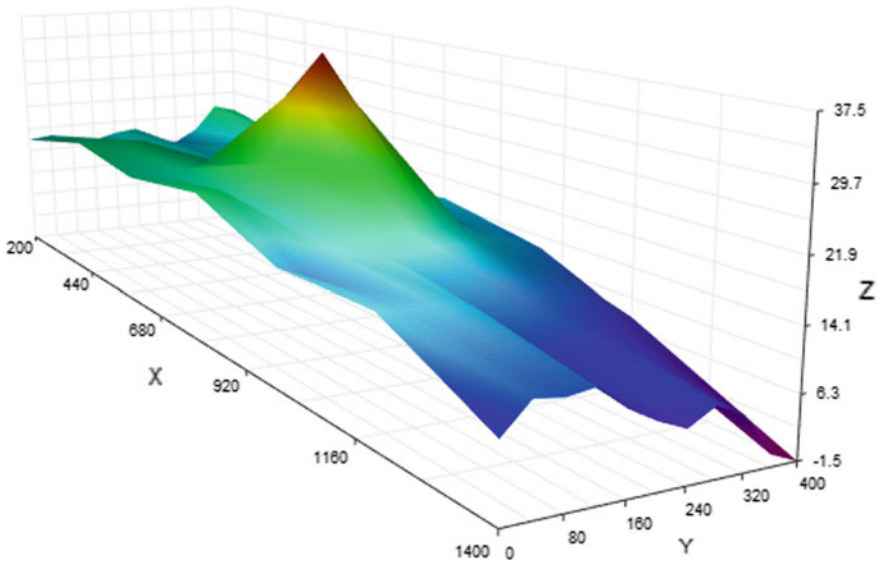

Fig. 5 Plan form development on 18.01.2018

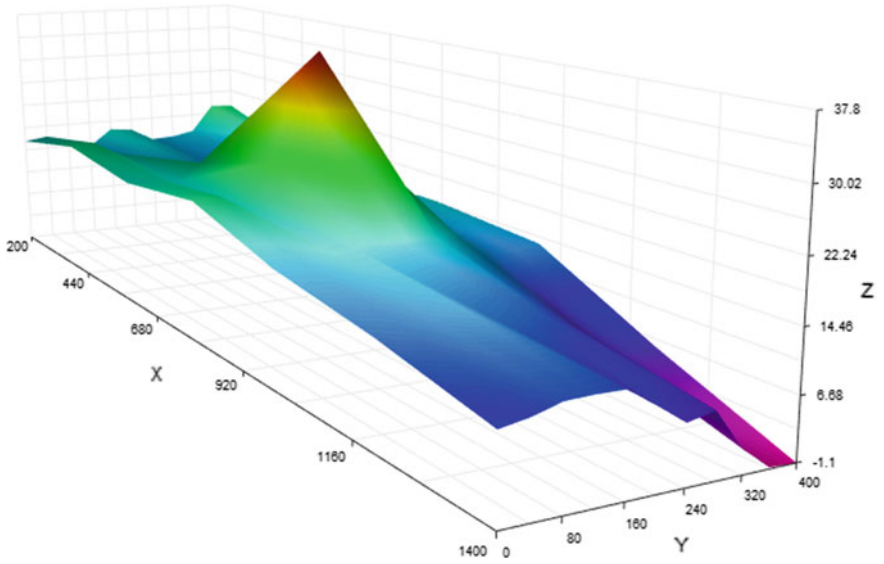

Fig. 6 Plan form development on 19.01.2018

6 Data Collected and Analysis

7 Graphical Representation

8 Summary and Conclusion

- The experimental setup runs continuously by gradually varied flow (Table 1).
- Right bank of island get more erosion than left side, and eroded soil particles were deposited in the left side of flume bank after velocity contraction.
- Materials of Island were clay soil as per the results of determination of physical properties.
- Accuracy of data of velocity profile depends on sound to noise ratio.
- The difference in inlet discharge and outlet discharge in escape channel caused by groundwater contribution and flume leakage.
- Some amount of eroded soil has deposited in around the island as well as downstream of the island and some amount of eroded soil has deposited in escape channel from where the eroded soil has been removed for smooth running of the set up regularly.
- Diameter of the island was 2/10 of the width of flume, and then it was placed

Table 1 Values of X, Y, Z of the river bed

Date	X (cm)	Y (cm)	12.01.18 Z (cm)	13.01.18 Z (cm)	14.01.18 Z (cm)	18.01.18 Z (cm)	19.01.18 Z (cm)
Station (1)	215	0	20	19.5	19.5	17.5	17.5
	215	40	17.5	18.5	18	18	18
	215	80	17	16.8	17.4	16.7	16.5
	215	120	17	17	17.5	16.5	15.7
	215	160	15.5	16	16	17.5	18.4
	215	200	16.7	17.4	19	18	18
	215	240	17	17.6	18.5	15.5	16
	215	280	16.5	17.8	17.5	15	16.2
	215	320	16	16.3	17.2	17	16.9
	215	360	18	17.5	18	21	21.2
	215	400	21	21	20.6	20	21
Station (2)	430	0	22	22	21	21	20.2
	430	40	21.2	21	20.5	20	20.5
	430	80	18	18.8	18	20.5	18.5
	430	120	16	16.6	17	20	15.9
	430	160	16.2	17.5	17	16.5	15.8
	430	200	16	16.5	16	17.5	16.3
	430	240	16.5	17.2	16.5	16.5	15.5
	430	280	16	16	15	17.5	14.7
	430	320	15.5	15.5	16	16	15.8
	430	360	16	16.3	16.5	16	14.5
	430	400	19.5	19.2	18.5	17.5	17
Station (3)	645	0	18.5	20.5	20.2	19	18.5
	645	40	21	20.4	20	19	19
	645	80	19.5	19.5	19.6	19.5	18
	645	120	16.2	19	19.5	20	20.5
	645	160	19	19.2	19	19.5	20.5
	645	200	17	17.5	17.5	18.5	18.3
	645	240	15	15.5	15.2	17	15.6
	645	280	13	13.5	14	13.5	14.5
	645	320	13.5	13	13	13.5	13
	645	360	13	13	13	13	12.7
	645	400	15.5	15.5	15	14	15.5
Station (4)	860	0	20	20	20.2	21	20.2
	860	40	20.2	20.2	20.2	21	20.5

(continued)

Table 1 (continued)

Date	X (cm)	Y (cm)	12.01.18 Z (cm)	13.01.18 Z (cm)	14.01.18 Z (cm)	18.01.18 Z (cm)	19.01.18 Z (cm)
	860	80	18.5	18.4	17	17.5	18.4
	860	120	21	25.5	20.5	24	24.5
	860	160	49	44.8	42.5	34.5	36.3
	860	200	54.5	50	50	39	39.3
	860	240	34	31.5	30	33	28
	860	280	20.3	19.2	19	20	18.8
	860	320	16	16.5	15.6	16.5	16.8
	860	360	17	16.5	15.5	16.5	17.6
	860	400	18	16.4	16.4	16.5	16
Station (5)	1075	0	16.5	16	16.2	16	16.2
	1075	40	16.5	16.5	16.3	14.5	16.3
	1075	80	17	16.5	17.5	17	17.3
	1075	120	17.5	16	18.4	18	17.2
	1075	160	17.3	17	17.3	18.5	16.9
	1075	200	16.5	16.4	18	18	16.8
	1075	240	16.5	16.2	17.5	18.2	17.5
	1075	280	16	13.5	17	17.5	16.6
	1075	320	14	15.4	14.5	16	14.8
	1075	360	15.5	16.5	14.5	15.5	14.5
	1075	400	13	14	15.7	14	15
Station (6)	1290	0	15.7	15.5	16	16.5	14
	1290	40	14.5	14.2	15.7	16	14.3
	1290	80	15.2	15	15.5	16	15.2
	1290	120	15	14.2	16.3	16	15.6
	1290	160	13.5	13.5	14.5	13.5	14
	1290	200	13.5	13.6	14.7	13.5	13.6
	1290	240	11.8	12	12	12.7	12.9
	1290	280	10.5	10.5	10.5	12	11.3
	1290	320	11	10.4	10	11.5	8.4
	1290	360	8	7	6	11	7.4
	1290	400	7	7.5	7.5	7.5	7.2
Station (7)	1505	0	9	11	10.5	9.5	11
	1505	40	11.5	11.3	12.6	13	11.6
	1505	80	11.2	12	12.2	12.5	12.6
	1505	120	11.7	12.7	13.5	13	12.7

(continued)

Table 1 (continued)

Date	X (cm)	Y (cm)	12.01.18 Z (cm)	13.01.18 Z (cm)	14.01.18 Z (cm)	18.01.18 Z (cm)	19.01.18 Z (cm)
	1505	160	9.5	10	10	10	12.6
	1505	200	8.2	7.5	8.5	8	10.2
	1505	240	7	7.5	6.5	6.5	7.7
	1505	280	7.5	4	9	8.5	8.4
	1505	320	4.5	1	4.5	6.7	3.4
	1505	360	0	0	1	1.5	0.6
	1505	400	0	0	0	0	0.4

in the middle of flume. Surprisingly it was observed that there was segregation in flow turbulence and soil materials gate segregated before contraction point of island.

- Variation in Sediment load transport was the main reason for changes in plan form development for different types of soil.

References

Biron PM, Lane SN, Roy AG, Bradbrook KF, Richards KS (1998) Sensitivity of bed shear stress estimated from the vertical velocity profiles: the problem of sampling resolution. Earth Surf Proc Land 23:133–139

Borah DK, Alonso CV, Prasad SN (1982) Routing of graded sediments in streams: formulations. J Hydraul Eng 10812:1486–1503

Ghosh S, Das S, Dwivedi VK (2018) Study of soil erosion and deposition around an island in a natural stream. In: Singh V, Yadav S, Yadava R (eds) Hydrologic modeling. Water science and technology library, vol 81. Springer, Singapore

Kostaschuk R, Best J, Villard P, Peakall J, Franklin M (2005) Measuring flow velocity and sediment transport with an acoustic Doppler current profiler. Geomorphology 68:25–37

Misri RL, Ranga Raju KG, Garde RJ (1984) Bed load transport of coarse nonuniform sediments. J Hydraul Eng 1103:312–328

Morvan H, Pender G, Wright NG, Ervine DA (2002) Three dimensional hydrodynamics of meandering compound flows. Proc ASCE J Hydraul Eng 128(7):674–682

Rennie CD, Millar RG, Church MA (2002) Measurement of bed load velocity using an acoustic Doppler current profiler. J Hydraul Eng 128:473–483

Shields FD, Rigby JR (2005) River habitat quality from river velocities measured using acoustic Doppler current profiler. Environ Manage 36:565–575

Wu W, Wang SY, Jia Y (2000) Nonuniform sediment transport in alluvial rivers. J Hydraul Eng 386:427–434

Yorke TH, Oberg KA (2002) Measuring river velocity and discharge with acoustic Doppler profilers. Flow Meas Instrum 13:191–195

Assessment and Application of the Morphometric Attributes of the Bharathapuzha River Basin, India Using Geographical Information System

Jisha John, N. R. Chithra, and Santosh G. Thampi

1 Introduction

In molding the topographical surface of a catchment, the slope of the basin and the orientation of the drainage networks play a vital role. The present state of the topographical characteristics of a drainage basin can be explained as a function of certain variables such as lithology, land use, altitude, and the structural components within the catchment. The technique for the quantitative assessment of the topographical characteristics of a drainage basin is known as morphometric analysis. It measures the size and form properties of the catchment area either in terms of linear scale measurements or dimensionless numbers (Strahler 1957). Analyzing the morphometric characteristics of the drainage basins by geospatial technique became more popular in hydrologic science in light of the increase in intensities of extreme hydrological events worldwide. The morphometric factors are a composition of the topography of the landforms in the drainage basin and the form and extent of the drainage network within it (Horton 1932). The determination of the morphological attributes of a drainage basin is necessary to formulate the sustainable developmental policies of water resources in the basin. Conventional methods have used for the measurement of morphological parameters before the emergence of geospatial techniques. The morphometric analysis performed in the Western Ghats by traditional methods has been reported from Jacob & Narayanaswami (1954) onwards. But by these conventional methods could not generate the actual drainage network

J. John (✉) · N. R. Chithra · S. G. Thampi
Department of Civil Engineering, NIT Calicut, Kozhikode, Kerala, India
e-mail: jisha_p150076ce@nitc.ac.in

N. R. Chithra
e-mail: chithranr@nitc.ac.in

S. G. Thampi
e-mail: santosh@nitc.ac.in

R. Jha et al. (eds.), *River and Coastal Engineering*, Water Science and Technology Library 117, https://doi.org/10.1007/978-3-031-05057-2_8

due to systematic, random and spurious errors (Chorley et al. 1957). With the emergence of advanced geospatial technologies, a combination of remote sensing and Geographical Information System (GIS), assessing the morphological parameters of a watershed having a complex topographical nature has become more efficient and accurate.

The geospatial techniques use geospatial algorithms to derive the terrain parameters from Digital Elevation Model (DEM). To date, numerous studies using geospatial techniques have been reported on the determination of morphological attributes of catchments by using different data sets and different resolutions (Ahmed et al. 2010; Bhatt and Ahmed 2014; Dikpal et al. 2017; Genchi et al. 2016; Jones and Vaughan 2010; Kaliraj et al. 2015; Kumar and Chaudhary 2016; Magesh et al. 2012, 2013; Markose et al. 2014; Samal et al. 2015; Singh et al. 2013; Sreedevi et al. 2013; Thomas and Prasannakumar 2015). In all these studies, the watershed is chosen as the ideal natural unit for assessing the landforms because they operate as closed systems and hence the collection, processing, organization and interpretation of data can be accomplished more effectively (Singh 1989). The morphological features of each watershed will be unique, and it will vary from micro-watershed to the regional river basin and depend on the complex nature of the topography. The estimation of morphometric parameters in a quantitative manner help to compare the basin characteristics and describe certain hydrological processes (Strahler 1957). Cartosat-1 DEM is a promising data source for the morphometric analysis at the Indian sub-continent as they show a clear demarcation of the catchment ridge line and natural flow patterns compared with other DEMs (summary report, India CartoDEM 2011). It must be noted that most of the river basin morphometric studies have used SRTM, ASTER or other DEMs without considering the topographical characteristics of the catchment area (Kumar and Chaudhary 2016; Magesh et al. 2012, 2013). Another drawback of the previous studies has been observed that without defining a threshold contributing area, the drainage networks were delineated and physical characteristics were determined (Ahmed et al. 2010; Bhatt and Ahmed 2014; Kaliraj et al. 2015; Magesh et al. 2012, 2013; Markose et al. 2014; Singh et al. 2013; Sreedevi et al. 2013). The results obtained through the evaluation of morphometric characteristics has been used as an input for the assessment of watershed management, soil erosion, sediment yield, environmental assessment, installation of rainwater harvesting structures, hydropower system, flood/drought estimation and management and identification of groundwater potential (Magesh et al. 2013; Rai et al. 2012).

The primary objective of this study is to extract the drainage network of the Bharathapuzha River basin (BRB) with a defined threshold drainage area and to obtain the morphometric features of the basin thematically and quantitatively from a 1-arc second resolution Cartosat DEM. Also, the linear, aerial and relief morphometric aspects were quantified by using the mathematical equations put forwarded by Horton (1932), Horton(1945), Miller (1953) and Schumm (1956). Then by integrating certain morphometric attributes, the status of groundwater potential in the basin was mapped. The peak discharge and time of concentration of the basin were

also estimated from the derived morphometric attributes. These are important components in BRB since it lacks proper number of gauging stations for accurate flood forecasting system due to the complex nature of the drainage basin.

2 Study Area

The Bharathapuzha is the second-longest west-flowing river and largest river basin in the state of Kerala, India. It lies between 10° 26′ N to 11° 13′ N latitudes and 75° 53′ E to 77° 13′ E longitudes (Fig. 1). It is an interstate river, and two-thirds of the drainage area is within Kerala (71%), and the remaining is in Tamil Nadu. The river originates from the Annamalai hills in the Western Ghats, in the east part of the basin, at an altitude of about 2250 m above the mean sea level. It flows through Coimbatore and Tiruppur districts in Tamil Nadu and continues through Malappuram, Palakkad, and Thrissur districts in Kerala before finally meeting the Arabian Sea. The areal extent of the catchment surface drainage is about 6153.78 km^2. The four main tributaries—Gayathripuzha, Chitturpuzha, Kalpathipuzha and Tuthapuzha comprises the Bharathapuzha drainage system. The physiographical nature of the basin consists of highland, midland, lowland, and coastal plains, and most of the highland regions are covered with forest. The watershed area comes under the tropical climatic zone, and the average annual rainfall in highland areas varies between 2000 and 2800 mm; it

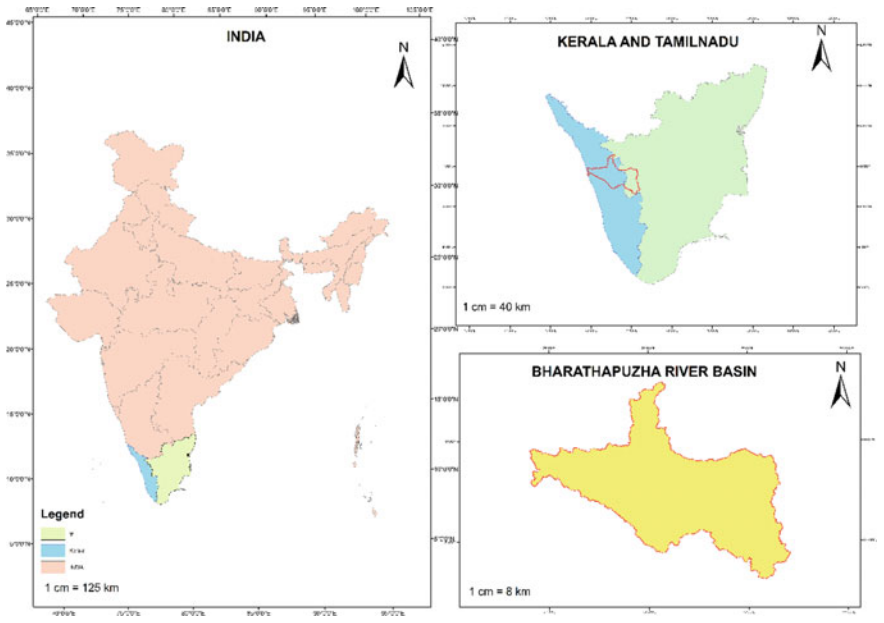

Fig. 1 Location map of the Bharathapuzha River basin

is about 3000 mm in coastal regions (WRIS). The basin receives most of the rainfall from the southwest monsoon (June–September). The normal maximum temperature in the basin is 32.3 °C during the dry season and a minimum of 23.3 °C in the wet season. Geologically the area contains Archean crystalline formation, tertiary formation, sub-recent and recent riverine alluvium (CGWB, 2007). In the last couple of decades, certain anomalies in the climatic conditions have been observed in the drainage basin. From 1980 onwards, the watershed is under rapid urbanization processes (Raj and Azeez 2010).

3 Methodology

In this study, the terrain and the morphometric characteristics of the BRB were assessed by using the Cartosat-1 DEM data. The BRB was delineated from the DEM data by using a GIS software package. The thematic layers useful for explaining the terrain and the morphometric characteristics of the basin were derived from the DEM data as subsequent layers. Most of the thematic layers such as slope, aspect, flow direction, flow accumulation and stream network were derived from the DEM as a function of local neighbours (Moore et al. 1991). The morphometric characteristics of the basin were categorized into linear, areal, relief aspect and shape parameters.

For delineating the watershed from the one arc-second resolution DEM, the following steps were adopted. The Cartosat-1 tiles are of uniform size, and one arc second tile composed of 3601 rows and 3601 columns (MacMillan and Shary 2008). The entire BRB is spread over different Cartosat-1 files with one arc-second resolution. So, to create a coherent DEM for the basin, these tiles were mosaicked with the mosaicking function in the GIS platform. It was followed by filling the sinks—to remove unusual features present in the mosaicked DEM. The output flow direction of each grid cell was determined. Then the spatial extent of the contributing planar area was identified using the flow accumulation function. By assigning a defined threshold value depend on topographical nature (Maidment and Morehouse 2002), the streams were extracted from the DEM, and the watershed boundary was determined. From the output obtained, specific geomorphometric parameters (Table 1) of the basin were calculated.

Using the derived morphometric attributes, the peak discharge and time of concentration of the basin were estimated with the help of mathematical equations. Then by utilizing the slope and drainage density map, the low, medium, and high groundwater potential zones in the basin were identified by overlay operation. Even though the occurrence of groundwater is influenced by certain parameters such as land use, hydraulic conductivity, porosity, etc., slope and drainage density are the basic components in determining the water storage potential in an area.

Table 1 Computation of morphometric parameters

Sl. No	Morphometric parameter	Formulae	
1	Bifurcation ratio (R_b)	$R_b = N_u/N_{u+1}$	Horton (1945)
2	Mean stream length (ML_u)	$ML_u = {}^{L_u}/_{N_u}$	Horton (1945)
3	Stream length ratio (R_L)	$R_L = {}^{ML_u}/_{ML_{u-1}}$	Horton (1945)
4	Drainage density (D_d)	$D_d = {}^{\sum L_u}/_{A_u}$	Horton (1932)
5	Drainage texture (R_t)	$R_{t=}{}^{\sum N_u}/_{P}$	Horton (1945)
6	Stream frequency (F_s)	$F_{s=}{}^{\sum N_u}/_{A_u}$	Horton (1932)
7	Infiltration number (I_f)	$I_f = D_d * F_s$	Zavoianu (2011)
8	Form factor (R_f)	$R_f = {}^{A_u}/_{L_m^2}$	Horton (1932)
9	Circularity ratio (R_c)	$R_c = {}^{A_u}/_{A_c}$	Miller (1953)
10	Elongation ratio (R_e)	$R_e = 1.129\sqrt{A}/L$	Schumm (1956)
11	Length of overland flow (L_g)	$L_{g=}{}^{1}/_{2D_d}$	Horton (1945)
12	Constant of channel maintenance (l_f)	$l_f = {}^{1}/_{D_d}$	Schumm (1956)
13	Compactness coefficient (m)	$m = 0.282P/\sqrt{A}$	Luchisheva (1950)
14	Ruggedness number (R_n)	$R_n = R*D_d$	Strahler (1957)
15	Lemniscate ratio (R_L)	$R_L = P/Pm$	Chorley et al. (1957)
16	Degree of elongation (R_a)	$R_a = {}^{\sqrt{A_u}}/_{L}$	(Zavoianu 2011)

Where, N_u: Number of u^{th} order stream, L_u: Length of uth order stream, A_u: Area of the drainage basin, Pm: Perimeter of the basin, L_m: Maximum length of the basin, A_c: Area of the circle whose circumference is equal to the basin perimeter, R: Basin relief, P: Lemniscate perimeter.

4 Data Analysis and Discussion

4.1 Primary Morphometric Attributes

The topographical characteristics of the drainage basin, which can be directly derived from digital elevation data, were classified as primary morphometric attributes. These characteristics can be mapped and quantified for further applications.

Drainage basin area (A_u)

The drainage basin area is one of the fundamental parameters and is derived directly from the DEM layer. It is the extent to which surface flow emanating from each point in the study area can flow to a common point of water bodies such as a lake or ocean. The BRB has a geographical surface area of 6153.78 km^2 (Fig. 2) that extends over sub-humid and semi-arid regions. The drainage basin extracted from SRTM DEM having 90 m resolution shows the area of BRB as 5988.56 km^2

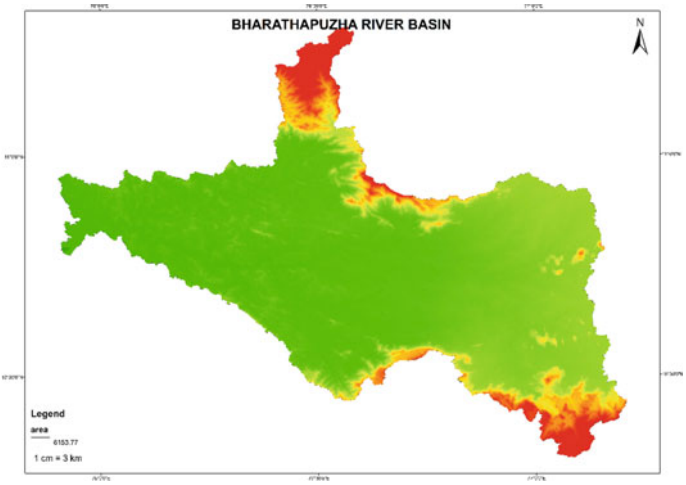

Fig. 2 Area of the Bharathapuzha River basin

(Magesh et al. 2013). As per the statistics of the Water Resources Information System of India (http://www.indiawris.gov.in), and Kerala Water Atlas by Centre for Water Resources Development and Management, the total drainage area of the basin is recorded as 6186 km^2. As the first-order streams in this region have a good chance of growth, the basin will be elongated in shape (Sharma 1987).

Slope

It is an important geometric parameter of the land surface and reflects the topography and the orientation of a watershed. The slope is a measure of the maximal rate of elevation change. Slope values help in better understanding the time of concentration, soil erosion and deposition, soil and nutrient losses, soil wetness, hillslope stability and many others (Singh 1996). In ArcGIS, it is analyzed by forming a filter with 3 × 3 cell around the centre cell in the DEM data. Then the maximum change in elevation within the 3 × 3 cell identifies the steepest downhill descent from the cell (ESRI, 2014). The slope can express in degree or percentage rise. In degree measurement, the slope value varies between 0 and 90, and in percentage, it varies from zero to infinity. For a flat surface, the slope should be zero percent. From the obtained slope map of the BRB, it is observed that the slope of the basin varies between zero to 342.879 percentage; the steeper slopes in the basin appear as red shades in Fig. 3. The physical properties of the steeper slope areas consist of shallow soils with low infiltration capacity and low soil moisture content.

Aspect

Aspect indicates the downslope direction of the maximum rate of change in value from each cell to its neighbors (Gökçekus et al. 2011), that is, the direction to which the watershed faces. It is measured in degrees and ranges from zero to 360°. The

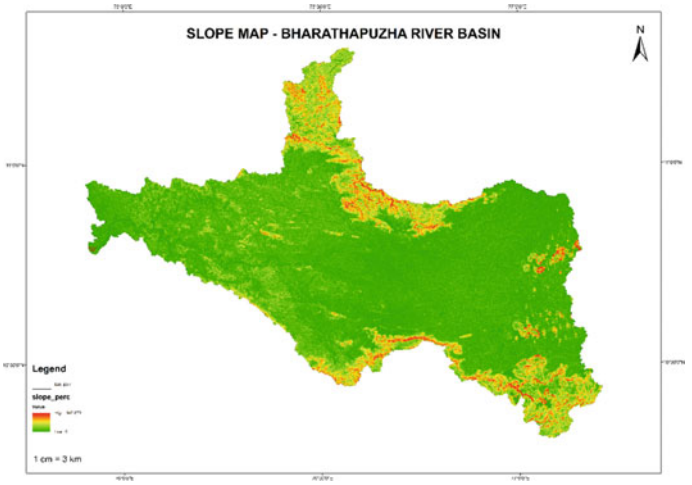

Fig. 3 Slope map of the Bharathapuzha River basin

values can only be multiples of 45° and are read in the clockwise direction from the north. Aspect indicates the flow line direction, and it is the basis for flow direction algorithms. The aspect map of the BRB (Fig. 4) shows that it is a west-facing catchment area. Determination of the aspect helps to analyze the solar illumination at a location, the diversity of life at that place, runoff analysis, snowmelt, precipitation pattern, etc. Usually, shaded relief maps are generated as a combination of slope and aspect of a region.

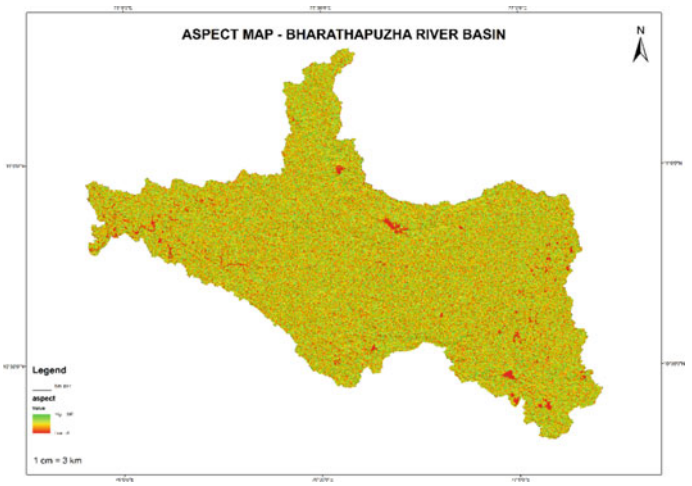

Fig. 4 Aspect map of the Bharathapuzha River basin

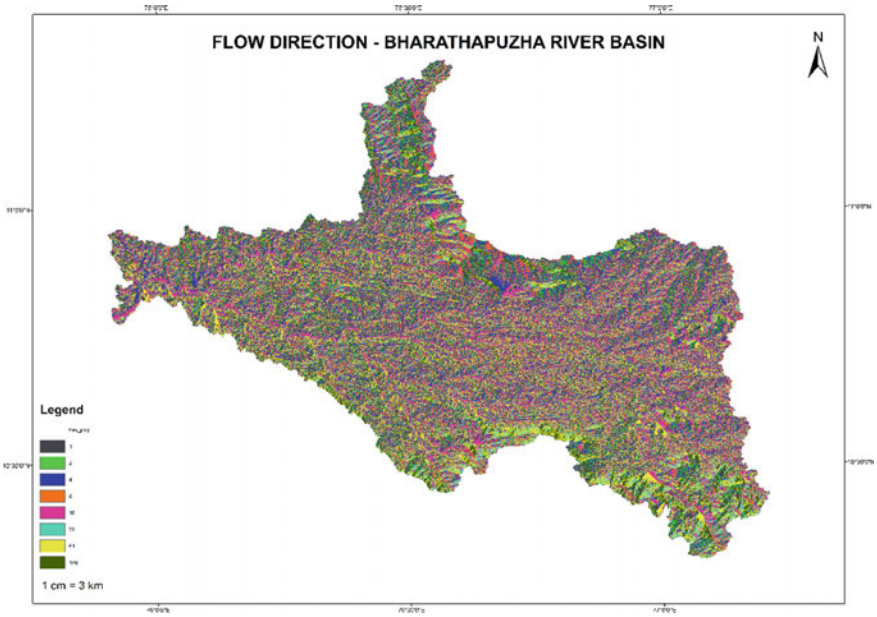

Fig. 5 Flow direction map of the Bharathapuzha River basin

Flow direction of the basin

The flow direction determines the ultimate destination of the water flowing across the drainage basin under the influence of gravity. The flow direction map is generated by the nature of the landform, and it shows the direction of the flow of water from a particular cell. The GIS platform using D_8 the algorithm to generate the flow direction map of the basin from the raster format DEM. The grid cells with blue color shade along the margin of the basin show the flow direction of the basin (Fig. 5).

Flow accumulation of the basin

The accumulation value was obtained by the number of upstream cells flowing into a particular cell based on the landscape/ topography. The cells corresponding to lower elevation will have higher flow accumulation values. The flow accumulation map of the basin was generated from the flow direction map of the basin, and it shows the area required to generate sufficient runoff in the stream channels (Mujumdar and Kumar 2012). Figure 6 shows the flow accumulation map of the study area. This map helps to identify the areas of concentrated flow and the stream channels.

Stream network

It shows the orientation of streams on the land surface in the catchment area. In a National elevation dataset, the threshold land surface draining to the streams is considered as 4.5 km^2 (Maidment and Morehouse 2002). So the stream network in the basin was extracted by the specified threshold area. The obtained stream network

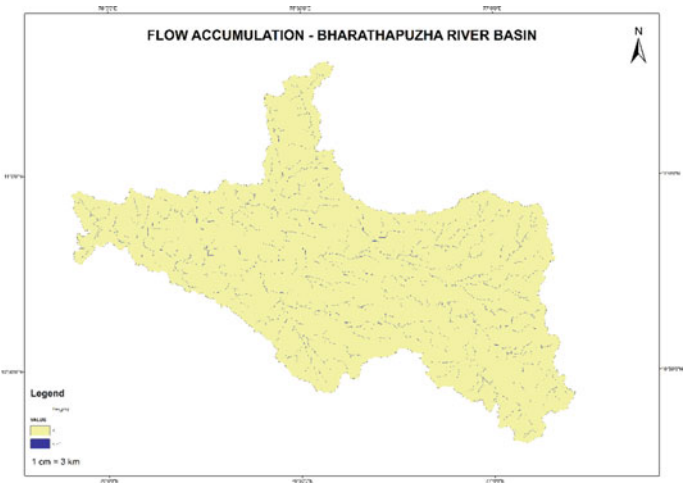

Fig. 6 Flow accumulation map of the Bharathapuzha River basin

map is a function of flow direction and flow accumulation maps. From Fig. 7, it is observed that the catchment contains a denser stream network.

Flow length of the basin

It is the distance from any point in the watershed to the watershed outlet. In the GIS platform, the flow length from a pixel is determined by calculating the accumulated distances from the center to center of each pixel along the flow path from the selected pixel up to the outlet pixel (Dixon et al. 2015). The flow length of the basin was used

Fig. 7 Stream network of the Bharathapuzha River basin

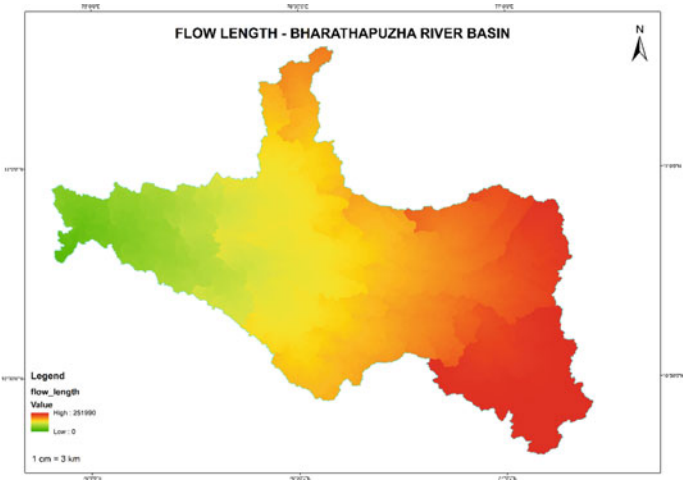

Fig. 8 Flow length of the Bharathapuzha River basin

as the primary parameter for determining the time of concentration. The flow length of the BRB is shown in Fig. 8. The maximum flow length in the basin is 226.791 km.

5 Secondary Morphometric Attributes

The topographical features of the catchment area derived by using the primary morphometric attributes are categorized as secondary morphometric attributes. Mathematical expressions can quantify these features.

5.1 Linear Aspects of the Drainage Basin

In the quantitative analysis of a drainage basin, the linear elements are concerned with the linear characteristics of the stream channels in the catchment. The linear features help to explain the influence of physiographic and geologic constraints in molding the drainage channels in the basin (Jaganathan 2015). Morphometric parameters such as stream order (U), stream number (N_u), stream length (L_u), bifurcation ratio (R_b), mean length of streams (ML_u), and stream length ratio (R_L) were analyzed. To study the linear aspects of the drainage basin, the methods suggested by Horton (1945), Miller (1953) and Strahler (1957) were used. The Strahler system—a modified form of Horton's method was used to assign the stream order. This method was adopted because of its simplicity.

Table 2 Stream numbers in the Bharathapuzha River basin

Stream order	I	II	III	IV	V
Number of stream segments	293	57	14	5	1

Stream order (U)

The highest order stream in a basin is the prefix in naming that basin. The analysis of the network shows that the BRB is a fifth-order basin. In the current study, stream ordering has been carried out by one of the most widely used methods put forward by Strahler (1957). Stream ordering is the ranking of the relative sizes of the creek within a watershed, based on the nature of its tributaries (Lee 2005). Identifying the streams and the stream order is the preliminary step in the extraction of the catchment area. First-order streams are those that have no tributaries, and those dominated by the overland flow of water, and they have no reliable upstream flow. The streams which receive only the first-order tributaries are the second order, and the branches which receive only the first order and second-order tributaries are designated as the third order, and so on. Manual identification of stream orders is much more challenging because stream order will vary with map scale, so it will affect all higher-order designations (Allan and Castillo 2007).

Stream number (N_u)

Stream number indicates the total number of stream segments of a particular order. The number of stream segments goes on decreasing as the stream order increases in a geometric manner. The number of streams in each order is presented in Table 2. If the stream density is more, the area will have high moisture content and low runoff than when the stream density is low. It is observed that totally the basin has 370 stream segments.

Stream length (L_u)

The law proposed by Horton (1945) was used to calculate the stream length of the basin. The length of the streams in a catchment is mainly influenced by the topographical condition of the area and the underlying geological structure (Kaliraj et al. 2015). Table 3 shows the summary statistics about the length of streams of different orders. It can be observed that the length of first-order stream segments is higher than the remaining orders in the hierarchy.

Bifurcation ratio (R_b)

Horton (1945) defined bifurcation ratio as the ratio between the number of streams of a given order (N_u) to the number of streams of the next higher-order (N_{u+1}) (Schumm 1956). It can be considered as an index of relief and dissection (Sharma

Table 3 Length of streams in the Bharathapuzha River basin

Stream order	I	II	III	IV	V
Stream length (km)	1082.68	543.82	303.57	221.69	119.03

Table 4 Bifurcation ratio of the Bharathapuzha River basin

R_{C_i}	I/II	II/III	III/IV	IV/V
N_u/N_{u+1}	5.14	4.07	2.8	5

1987). This dimensionless parameter can be used to define the catchment response. The highest bifurcation ratio is for humid regions because of the greater degree of dissection of drainage networks in this region. The R_b values in the basin are presented in Table 4. The mean bifurcation ratio for the study area is 4.79. The topographical area with uniform surficial materials not affected by structural disturbances will show a low bifurcation ratio. This index can also be used to measure drainage efficiency (Rai et al. 2012). If the basin has homogenous geology, this value will be between 3 and 5 (Babar 2005).

Mean stream length (ML_u)

According to Horton's law (1945), mean stream length is the ratio of the length of the streams of a particular order (L_u) to the number of streams of the same order (N_u). Always the mean stream length of the first-order stream will be higher than that of other stream orders. The mean stream length of the BRB is 6.135 km.

Stream length ratio (R_L)

Horton (1945) explained this index as the ratio of the mean length of a stream of a given order (ML_u) to the average length of the next lower order stream (ML_{u-1}) in the basin. The R_L Value of the basin is 2.45. This ratio can be used as an index for evaluating the permeability of the soil media in the basin. Recharge of groundwater in the basin will be a function of the nature of soil media. The high stream length ratio indicates that the watershed consists of soil media having high soil permeability.

5.2 Aerial Aspects of the Drainage Basin

Schumm's system (1956) was adopted for the estimation of the aerial aspects. The aerial aspect consists of morphometric parameters such as basin area (A_U), drainage density (D_d), drainage texture (R_t), stream frequency (F_s), form factor (R_f), shape factor (R), circularity ratio (R_c), elongation ratio (R_e), the length of overland flow (L_g), constant of channel maintenance, and compactness coefficient. Parameters such as form factor, circularity ratio and elongation ratio are used to determine the shape of the watershed. The shape of the watershed has a predominant role in determining the discharge from the catchment area.

Drainage density (D_d)

It is one of the most important parameters which determines the runoff potential of a drainage basin. It was introduced by Horton (1932). The drainage density of a river network is the ratio of the total length of the drainage courses ($\sum L_u$) to the catchment drainage area (A_u). This parameter is useful in drainage system design,

spatial prediction of drainage basin processes, and interpreting temporal changes in the drainage network. Drainage density is mainly affected by soil type, the permeability of the ground and land use. The drainage density of the BRB is 0.369 km/km^2. The runoff volume carried by each stream will be less in a watershed having a higher drainage density value. High drainage density also reduces sediment yield from a basin. Low stream order watersheds mostly show low drainage density values. Highly permeable soil surface shows drainage density values less than 1km/km^2.

Drainage texture (R_t)

It is defined by Horton (1945) as the total number of stream segments per unit perimeter. This index represents the spacing between the streams in a basin (Smith 1950). Drainage density is a significant factor influencing drainage texture. Fine drainage texture will appear in high drainage density areas, and low drainage density areas will have coarse drainage texture. So, these parameters can be used as an indicator of the determination of soil erosion. The value estimated for the BRB is 0.56. According to Smith's classification (1950), the catchment has a very coarse drainage texture based on drainage density.

Stream frequency (F_s)

Stream frequency is the ratio of the number of streams of all orders to the total area of the basin (Horton 1932). It is a modified form of stream segment density due to the modification of Horton's classification system by Strahler. Usually, the stream frequency values are positively correlated with the drainage density of the basin. F_s for the BRB is 0.06/km^2. Rainfall and topographical conditions are the two main constraints that influence the stream frequency within a basin. The stream frequency value reflects the geological properties of the surficial materials in the watershed.

Form factor (R_f) *and shape factor* (R)

The form factor is used to describe the nature and shape of the drainage basin. Horton (1932) introduced form factor as the ratio of the area of the drainage basin (A_u) to the square of the maximum length of the basin (L_m). The form factor value converges to zero as the shape of the catchment gets elongated, and the structural disturbance increases. Higher form factor values up to one represent catchments having uniform lithology and circular shaped watersheds. The form factor for the study area is 0.3391. The inverse of the form factor is the shape factor. The shape factor of the BRB is 2.94. For elongated drainage basins, the shape factor will be high.

Circularity ratio (R_c)

It is a dimensionless parameter introduced by Miller (1953) to identify the form of the drainage basin. This index depends on the area and perimeter of the drainage basin. This parameter is defined as the ratio of the area of the catchment (A_u) to the area of a circle (A_c) whose circumference is equal to the basin perimeter. The maximum value of the circularity ratio of a basin is unity. If the R_c value is unity, then the shape of the basin will be circular. If the basin has a rectangular shape, then the R_c value decreases to 0.785; it continues to decrease as the length of the basin increases. The R_c value of the BRB is 0.18; so, it can be concluded that it is an

elongated watershed with homogeneous geologic material having high permeability (Horton 1945).

Elongation ratio (R_e)

Schumm (1956) introduced this index to characterize the basin shape. It is the ratio of the diameter of a circle having the same area as that of the basin to the maximum basin length measured parallel to the axis of the mainstream (L) (Schumm 1956). It can be calculated as 1.129 times the ratio of the square root of the area of the basin (A_u) to the length of the basin (L). The least value of elongation ratio of a basin is 0.2; it will be in the case of the most elongated watershed. For a square-shaped watershed, the elongation ratio value is up to 1.128, and for a circular basin, the value will be 1.275. For the BRB, the elongation ratio value obtained is 0.65, and this shows that it is elongated in nature.

Length of overland flow (L_g)

It is the primary constraint affecting the hydrologic and physiographic evolution of a catchment area (Horton 1945). It depicts the average distance traveled by the surface runoff before it reaches stream channels. It is observed that in most of the cases, the length of overland flow would be half the average distance between the stream channels, and hence it is approximately equal to half the reciprocal of the drainage density (Chorley 1969). This factor is inversely related to the average slope of the basin (Ansari et al. 2012). For the study area, the calculated length of overland flow is 1.355. That means, in the catchment area, rainwater travels about 1.355 km before joining the stream channels. It is an important parameter in the determination of flood intensity from the basin.

Constant of channel maintenance (l_f)

Schumm (1956) defined the constant of channel maintenance as the surface area required to maintain a foot of the channel. For the study area, the constant of channel maintenance value is 2.71 square kilometer.

Compactness coefficient (m)

Luchisheva (1950) described the drainage basin shape by introducing this factor. It is a ratio of the actual basin perimeter to the perimeter of a circle of equal area. If the drainage basin shape is a perfect circle m value will be unity, and it will increase up to 1.128 for a square and very elongated watersheds it exceeds 3. The compactness coefficient of the BRB is 2.36, so it is an elongated watershed.

5.3 Shape Parameters

Some other shape parameters were also calculated. These are explained below.

Lemniscate ratio (R_L)

Chorley (1975) introduced the lemniscate ratio to show the resemblance of the shape of the drainage basin with that of the lemniscate curves; it helps to determine the

slope of the basin. This index is the ratio of the lemniscate parameter P corresponding to the length and the area of the basin to the actual perimeter of the basin Pm. To determine the lemniscate shape of the basin, the rotundity coefficient (p) should be obtained.

$$Rotunditycoefficient,\ p = {}^{L^2\pi}/_{4A}$$

The perimeter P of the ideal lemniscate curve constitutes a complete elliptical integral $E(k)$, that can be obtained from the tables of mathematical functions (Jahnke and Emde 1945). The value of K can be obtained as

$$k = \sqrt{p^2 - 1}/p$$

By using this, the lemniscate perimeter can be calculated as $P = 2LE(k)$. Then the lemniscate ratio of the basin can be obtained by $R_L = P/Pm$. For a circular shaped basin, the R_L value will be unity; it decreases to 0.897 for a square-shaped basin, and the value increases up to 0.978 for very elongated watersheds. For the study area, the lemniscate ratio was obtained as 0.93. According to Chorley et al. (1975), for a basin whose $L = 20B$ the R_L value will be 0.959. So, it can be stated that the BRB is elongated in shape (whose length is approximately 20 times the breadth).

Degree of elongation (R_a)

It is an index introduced by Diaconu and Lăzărescu in 1965 (Zavoianu 2011) used to define the shape of the watershed. This index can be calculated by considering different dimensions of the watershed, such as length, the average width and the area of the basin. In this study, the degree of elongation (R_a) is considered as the ratio of the square root of the area (A_u) to the length of the basin. For a perfectly circular shaped drainage basin, R_a value will be 1.130, and it decreases to unity for a square-shaped basin; in the case of very elongated basins with length 40 times of the width, R_a value will be 0.156. For the BRB, the R_a value is obtained as 0.582. It shows that it is an elongated basin with a length approximately 20 times that of the breadth.

5.4 Relief Aspects

The relief aspect analysis of the watershed was carried out by the methods suggested by Horton (1945). In this, the hydrogeological characteristics of the watershed were analyzed by using the three-dimensional features of the catchment area. Critical relief parameters such as maximum basin relief (R), channel gradient, relief ratio (R_r), ruggedness number (R_n) etc., were estimated for the study area.

Maximum basin relief (R)

The maximum relief within a basin is the elevation difference between the highest and lowest points. It is calculated by measuring the elevation difference between the highest point in the perimeter to the basin outlet. For the BRB, it is 2625 m. The high R value indicates higher runoff due to the steepness of the basin.

Relief ratio (R_r)

It is the ratio of the total watershed relief to the overall basin length (Schumm 1956). R_r value increases with a decrease in the drainage area and the size of the watershed (Gottschalk 1964). This index depends on the overall steepness of the basin and so it can be used as an indicator of sediment delivery from the basin. Sediment yield from a basin is highly correlated with Rr. For BRB, the Rr is measured as 0.011. This simple morphometric index reflects differences in active tectonism, bedrock geology, geomorphic process, climate effects etc. A low R_r value indicates that the basin consists of a resistant geological structure and a relatively low degree of slope (Mahadevaswamy et al. 2011).

Ruggedness number (R_n)

It is an important dimensionless attribute, and it was introduced by Melton in 1957 (Zavoianu 2011) and Strahler (1958). It is the product of basin relief (R) in meter and drainage density (D_d) in km^{-1}. Ruggedness number increases directly with increases in basin relief and relative relief of the area. The catchment area receiving high precipitation with high basin relief, steep and long slopes, and less resistant rocks will have extremely high R_n values. For the BRB, the ruggedness number obtained is 968.625. It indicates the structural complexity and high erodibility of the basin.

6 Applications of the Obtained Morphometric Attributes

In this study, the obtained morphometric attributes were used to estimate the time of concentration and peak discharge of the basin and to map the potential groundwater zones.

Infiltration number (I_f)

It is the product of the drainage density (D_d) to the stream frequency of the basin (F_s) (Zavoianu 2011). It is an important parameter in the determination of surface runoff from the catchment. For BRB, the I_f value of the BRB is 0.022. A low value of infiltration number indicates that in the basin, infiltration is more and runoff generated from the basin is low (Ansari et al. 2012). So, the underlying rock structure will be more permeable.

Time of concentration

Time of concentration (t_c) indicates the response of the drainage basin from precipitation events regarding time duration. This parameter shows the time taken by the

water to flow from the hydraulically most remote point in a basin to the basin outlet (Haan et al. 1994). It is an important parameter for the prediction of flood and in the assessment of flood risk. The time of concentration of the BRB was obtained as 37.04 h from the Kirpich equation (1940).

$$t_c = 0.01947 L^{0.77} S^{-0.385}$$

where L is the maximum flow length and S is the slope of the basin. The high value of time of concentration justifies the elongated nature of the river basin.

Flood peak discharge

It is the rate of maximum surface runoff from the drainage basin for a given rainfall event (Singh et al. 2013). The peak discharge of the BRB was determined by using an empirical method Şen (2018). This parameter can be mainly used for the design of hydraulic structures. The peak discharge from the basin is a function of the basin area and the nature of the topography.

$$Q_p = 60 C_3 \sqrt{A}$$

where C_3 is a parameter with a value of 0.7 for mountainous areas. For the BRB, the peak discharge that can be generated from the basin is estimated as 3294.73 cumecs. The maximum volume of runoff from the basin during 1982–2011 was measured as 3079 cumecs (CWC 2015). The estimated quantity shows the maximum runoff volume that can be generated from the basin without any human intervention. So, it is useful for spatial planning of the basin by considering the extreme events that may occur in future due to climate change.

Groundwater potential zones

About 30% of fresh water is stored as groundwater (USGS) and most used by humans due to quality and accessibility. The identification of groundwater potential zones and their planning and management is a challenge in drought-prone areas. In this catchment area, multinational companies operating by groundwater are more, especially in Palakkad district than in other Kerala districts. Hence the groundwater level has been declining at an alarming rate, and some parts of the catchment were declined as drought-affected during 2002–2004 itself by Central Groundwater Board (Chand 2013). In this study, the groundwater potential zones in the BRB, such as—high to low, were identified by coupling geomorphometric attributes. The obtained groundwater potential map (Fig. 9) of the basin shows that a major part of the catchment area has medium groundwater potential. The map depicts the low groundwater potential zones, and hence these locations may be considered for the installation of rainwater harvesting structures or artificial recharging structures such as contour bunds, percolation tanks, dug wells, trenches or recharge pits to increase the groundwater potential.

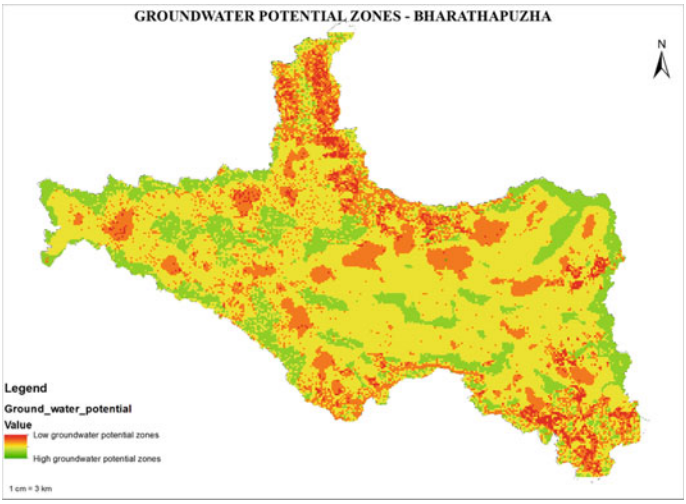

Fig. 9 Groundwater potential zones of the Bharathapuzha River basin

7 Conclusions

This study shows that the extraction of drainage network and catchment area from a national DEM using the geospatial technique can produce more accurate results than conventional methods. Though the GIS platform can automatically delineate the drainage network, incorporating a defined threshold area resulted in the drainage network matching the natural pattern well.

- BRB is a 5th order elongated basin whose length is approximately 20 times that of breadth.
- The watershed is facing the western direction, so under the influence of gravity, the water from the basin is flowing in the same direction.
- The peak discharge from the basin is estimated as 2353.38m^3/s and the time of concentration as 37.04 h. These parameters can be considered for spatial planning since the basin lacks the proper number of gauging stations, and the probability of occurrence of extreme events due to climate change may increase in future.
- The obtained bifurcation and circularity ratios show that the river basin consists of uniform surficial materials and are not affected by structural disturbance.
- The stream length ratio and drainage density show that the catchment area has a highly permeable soil surface, and the infiltration number shows that the infiltration rate is more and hence the runoff generated from the basin may be low.
- The linear aspects of the drainage basin show that the basin is in the mature stage of geographic development.

- The generated groundwater potential map can be used to formulate proper sustainable water management policies and identify artificial recharge zones in the catchment area.

From the morphometric analysis, it was able to understand the hydrological regimes of the BRB. Even though Magesh et al. (2013) carried out morphometric analysis for the basin using SRTM DEM with 90 m resolution, more accurate results were obtained in this study by using Cartosat DEM. The study demonstrates the efficiency of national DEM in generating more accurate results in a mountainous watershed.

References

Ahmed S, Chandrashekarappa K, Raj S, Nischitha V, Kavitha G (2010) Evaluation of morphometric parameters derived from ASTER and SRTM DEM—a study on Bandihole sub-watershed Basin in Karnataka. Journal of the Indian Society of Remote Sensing 38(2):227–238

Allan, J. D., & Castillo, M. M. (2007). "Stream ecology: structure and function of running waters": Springer Science & Business Media.

Ansari ZR, Rao L, Yusuf A (2012) GIS based morphometric analysis of Yamuna drainage network in parts of Fatehabad area of Agra district, Uttar Pradesh. J Geol Soc India 79(5):505–514

Babar, M. (2005). "Hydrogeomorphology: fundamentals, applications and techniques": New India Publishing.

Bhatt S, Ahmed S (2014) Morphometric analysis to determine floods in the Upper Krishna basin using Cartosat DEM. Geocarto Int 29(8):878–894

Chand, A. D. A. (2013). "Ground Water Information booklet of Palakkad district, Kerala state": Government of India, Ministry of water resources, Central ground water board.

Chorley RJ, Malm DE, Pogorzelski HA (1957) A new standard for estimating drainage basin shape. Am J Sci 255(2):138–141

CWC (2015) Integrated hydrological data book (non-classified river basins): hydrological data directorate information systems organisation water planning & projects wing

Dikpal RL, Prasad TR, Satish K (2017) Evaluation of morphometric parameters derived from Cartosat-1 DEM using remote sensing and GIS techniques for Budigere Amanikere watershed, Dakshina Pinakini Basin, Karnataka, India. Appl Water Sci 7(8):4399–4414

Dixon, B., Uddameri, V., & Ray, C. (2015). "GIS and Geocomputation for Water Resource Science and Engineering": John Wiley & Sons.

Genchi SA, Vitale AJ, Perillo GM, Piccolo MC (2016) Geomorphometric assessment of drainage systems in a semi-arid region of Argentina using geospatial tools and multivariate statistics. Earth Sci Inf 9(3):309–324

Gökçekus, H., Türker, U., & LaMoreaux, J. W. (2011). "Survival and Sustainability: Environmental concerns in the 21st Century": Springer Science & Business Media.

Haan, C. T., Barfield, B. J., & Hayes, J. C. (1994). "Design hydrology and sedimentology for small catchments": Elsevier.

Horton RE (1932) Drainage-basin characteristics. EOS Trans Am Geophys Union 13(1):350–361

Horton RE (1945) Erosional development of streams and their drainage basins; hydrophysical approach to quantitative morphology. Geol Soc Am Bull 56(3):275–370

Jacob K, Narayanaswami S (1954) The structural and drainage patterns of the Western Ghats in the vicinity of the Palghat Gap. Paper presented at the Proc. Nat. Inst. Sci, India

Jaganathan, R., Annaidasan, K., Surendran, D., & Balakrishnan, P. (2015). "Morphometric analysis for prioritization of watersheds in the Mullayar River basin, South India" Environmental Management of River Basin Ecosystems (pp. 127–136): Springer.

Jahnke E, Emde F (1945) Tables of functions with formulae and curves
Jones, H. G., & Vaughan, R. A. (2010). "Remote sensing of vegetation: principles, techniques, and applications": Oxford university press.
Kaliraj S, Chandrasekar N, Magesh N (2015) Morphometric analysis of the River Thamirabarani sub-basin in Kanyakumari District, South west coast of Tamil Nadu, India, using remote sensing and GIS. Environmental Earth Sciences 73(11):7375–7401
Kumar S, Chaudhary B (2016) GIS applications in morphometric analysis of Koshalya-Jhajhara watershed in northwestern India. J Geol Soc India 88(5):585–592
Lee, C. C. (2005). "Environmental engineering dictionary": Government Institutes.
Luchisheva AA (1950) Practical hydrology
MacMillan, R., & Shary, P. (2008). "Geomorphometry: concepts, software, applications": Elsevier Science. Chap. Landforms and Landforms elements in geomorphometry.
Magesh N, Jitheshlal K, Chandrasekar N, Jini K (2012) GIS based morphometric evaluation of Chimmini and Mupily watersheds, parts of Western Ghats, Thrissur District, Kerala, India. Earth Sci Inf 5(2):111–121
Magesh N, Jitheshlal K, Chandrasekar N, Jini K (2013) Geographical information system-based morphometric analysis of Bharathapuzha river basin, Kerala, India. Appl Water Sci 3(2):467–477
Mahadevaswamy G, Nagaraju D, Siddalingamurthy S, Nagesh P, Rao K (2011) Morphometric analysis of Nanjangud taluk, Mysore District, Karnataka, India, using GIS Techniques. Int J Geomat Geosci 1(4):721–734
Maidment, D. R., & Morehouse, S. (2002). "Arc Hydro: GIS for water resources" (Vol. 1): ESRI, Inc.
Markose VJ, Dinesh A, Jayappa K (2014) Quantitative analysis of morphometric parameters of Kali River basin, southern India, using bearing azimuth and drainage (bAd) calculator and GIS. Environmental Earth Sciences 72(8):2887–2903
Miller, V. C. (1953). "Quantitative geomorphic study of drainage basin characteristics in the Clinch Mountain area, Virginia and Tennessee". Technical report (Columbia University. Department of Geology); no. 3.
Moore ID, Grayson R, Ladson A (1991) Digital terrain modelling: a review of hydrological, geomorphological, and biological applications. Hydrol Process 5(1):3–30
Mujumdar, P., & Kumar, D. N. (2012). "Floods in a changing climate: hydrologic modeling": Cambridge University Press.
Rai, R. K., Upadhyay, A., Ojha, C. S. P., & Singh, V. P. (2012). "Geomorphology and Geology" The Yamuna River Basin (pp. 107–134): Springer.
Raj PN, Azeez P (2010) Land use and land cover changes in a tropical river basin: a case from Bharathapuzha River basin, southern India. J Geogr Inf Syst 2(04):185
Samal DR, Gedam SS, Nagarajan R (2015) GIS based drainage morphometry and its influence on hydrology in parts of Western Ghats region, Maharashtra, India. Geocarto Int 30(7):755–778
Şen Z (2018) Flood modeling, prediction and mitigation. Springer
Schumm SA (1956) Evolution of drainage systems and slopes in badlands at Perth Amboy, New Jersey. Geol Soc Am Bull 67(5):597–646
Sharma, H. S. (1987). "Tropical geomorphology: a morphogenetic study of Rajasthan": Concept Publishing Company.
Singh A (1989) Review article digital change detection techniques using remotely-sensed data. Int J Remote Sens 10(6):989–1003
Singh P, Thakur JK, Singh U (2013) Morphometric analysis of Morar River Basin, Madhya Pradesh, India, using remote sensing and GIS techniques. Environmental Earth Sciences 68(7):1967–1977
Singh, V. P. (1996). "Kinematic wave modeling in water resources, surface-water hydrology": John Wiley & Sons.
Smith KG (1950) Standards for grading texture of erosional topography. Am J Sci 248(9):655–668
Sreedevi P, Sreekanth P, Khan H, Ahmed S (2013) Drainage morphometry and its influence on hydrology in an semi arid region: using SRTM data and GIS. Environmental Earth Sciences 70(2):839–848

Strahler AN (1957) Quantitative analysis of watershed geomorphology. EOS Trans Am Geophys Union 38(6):913–920
Thomas J, Prasannakumar V (2015) Comparison of basin morphometry derived from topographic maps, ASTER and SRTM DEMs: an example from Kerala, India. Geocarto Int 30(3):346–364
Zavoianu I (2011) Morphometry of drainage basins, vol 20. Elsevier

Integrated Tool for Morphometric Analysis Using QGIS

Indrajeet Sahu, A. D. Prasad, and Ishtiyaq Ahmad

1 Introduction

The advancement of remote sensing technology and geographical information system (GIS) tools have emerged as powerful tool for watershed management. For assessing various topography and morphometric parameters of the drainage basins and watersheds Geographical Information System (GIS) techniques have already been used. GIS techniques along with Remote Sensing data is a fast, precise, and economical way for calculating morphometric analysis (Grohmann et al. 2007).

Morphometry is the measurement and mathematical analysis of the configuration of the earth's surface, shape and dimension of its landforms, Agarwal (1998); Obi Reddy et al. (2002).

Morphometric analysis of a watershed provides a quantitative description of the drainage system which is an important aspect of the characterization of watersheds, Strahler (1964). Evaluation of the morphometric parameters requires preparation of drainage map, measurement of the catchment area and perimeter, length of drainage channels, ordering of the numerous streams, drainage density, circulatory ratio, bifurcation ratio, which helps to understand the nature of drainage basins (Krishnamurthy et al. 1996; Kumar et al. 2000; Obi Reddy et al. 2002).

The objective of this study is to develop an integrated model tool using an open source platform (QGIS) and an attempt has been made to utilize Digital Elevation Model (DEM) and the techniques of QGIS to find out the morphometric parameters, as they provide a feasible environment and a powerful tool for the analysis of spatial information particularly for the extraction of information and the feature identification for better understanding. A DEM of Asan river watershed is taken as an input for model tool and present study provides the results showing parameters of the morphometric model tool.

I. Sahu · A. D. Prasad (✉) · I. Ahmad
Department of Civil Engineering, National Institute of Technology Raipur, Raipur, India
e-mail: adprasadiit@gmail.com

R. Jha et al. (eds.), *River and Coastal Engineering*, Water Science and Technology Library 117, https://doi.org/10.1007/978-3-031-05057-2_9

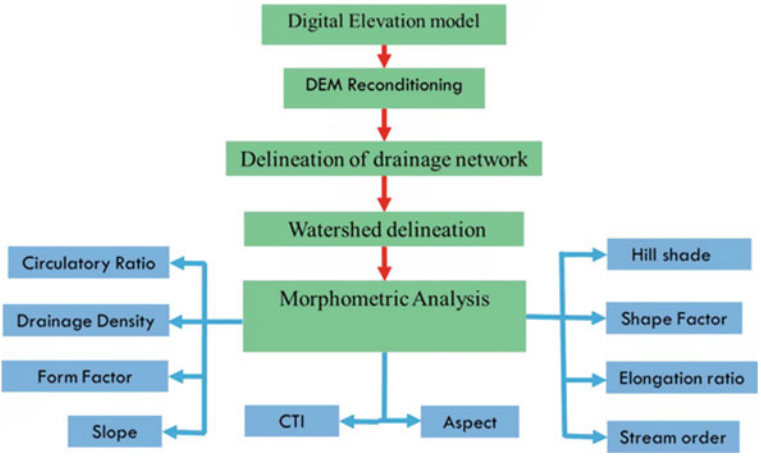

Fig. 1 Workflow of methodology

2 Methodology

The primary task before going for developing model is to know the workflow of how the tools are dependent on each other and understanding the parameter related to each tool is shown in Fig. 1. To assess the morphometric parameters an Advanced Spaceborne Thermal Emission and Reflection Radiometer (ASTER) DEM with 30-m spatial resolution of Asan river watershed is used for the integrated model. Since a DEM file can have inaccuracy which causes creation of sink area in result, DEM reconditioning is essential which produces sink less DEM raster file as output.

After analyzing the workflow and methodology adopted by, Obi Reddy et al., (2002) and Magesh et al. (2013) of Morphometric analysis, an integrated tool has been developed in QGIS an open source platform as shown in Fig. 2. Morphometric analysis of a drainage system involves delineation of all prevailing streams and the drainages have been delineated using 'r.watershed' tool. Along with the different tool set there are some user defined parameter that need to be introduce are the threshold value of the cell for defining streams, shape file of output point for delineating watershed and location of directory where output file is to be saved is entered using a Graphical User Interphase (GUI) shown in Figs. 3 and 4. Separate tools that is aspect, slope, topographic wetness index and channel network are properly linked and raster calculator is opted for calculating the drainage density.

3 Study Area

The Asan River watershed is in Dehradun, Uttarakhand state and is located between latitudes 30° 14′ 14″ N to 30° 29′ 54″ N and longitudes 77° 39′ 42″ E to 78° 05′

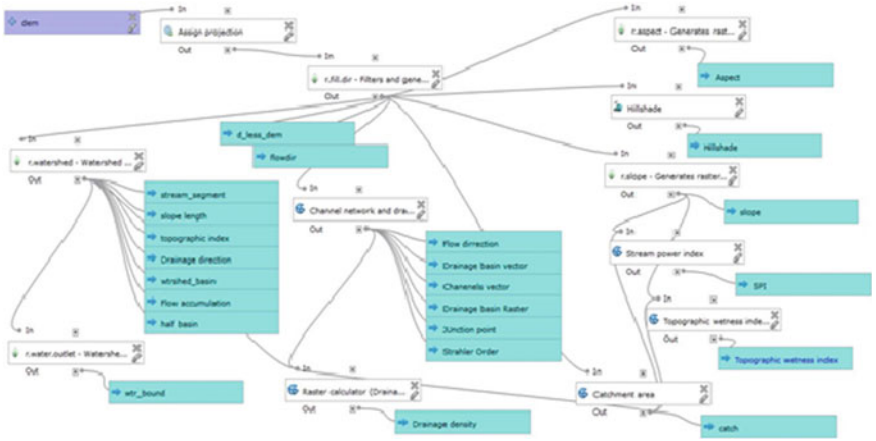

Fig. 2 Integrated morphometric model

Fig. 3 GUI of model

30″ E as shown in Fig. 5. It covers an area of 655 km^2 approximately. Asan River is flowing in central portion of the area from south-west to north-east direction and flow into the Yamuna River. The tributaries of these two rivers made gentle slopping plain on both side of the Asan River. The climate of study area is sub-tropical to temperate on higher elevation (more than 1800 m.). It varies greatly from tropical to severe cold depending upon the altitude of area. The average annual temperature of 21 °C in summers to 5 °C in winters. Rainfall in study area received mostly during the months from June to September, July and August being rainiest among them. The mean annual rainfall in the watershed is around 1917 mm. There are three distinct

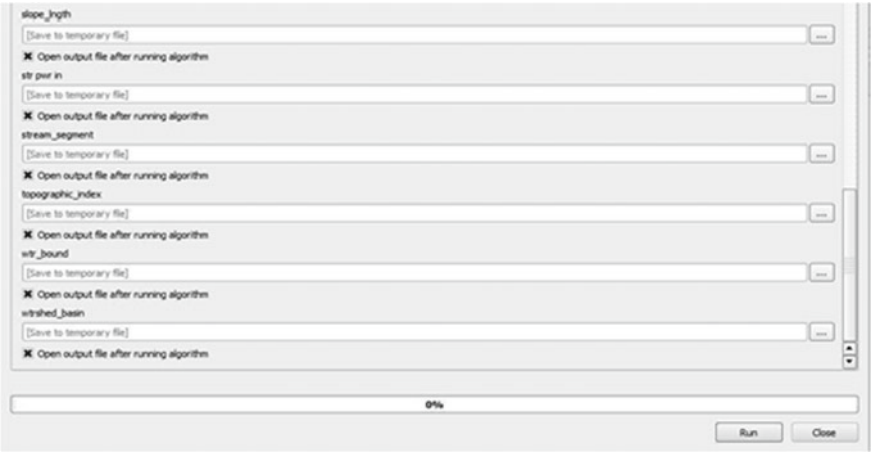

Fig. 4 GUI of model (conti.)

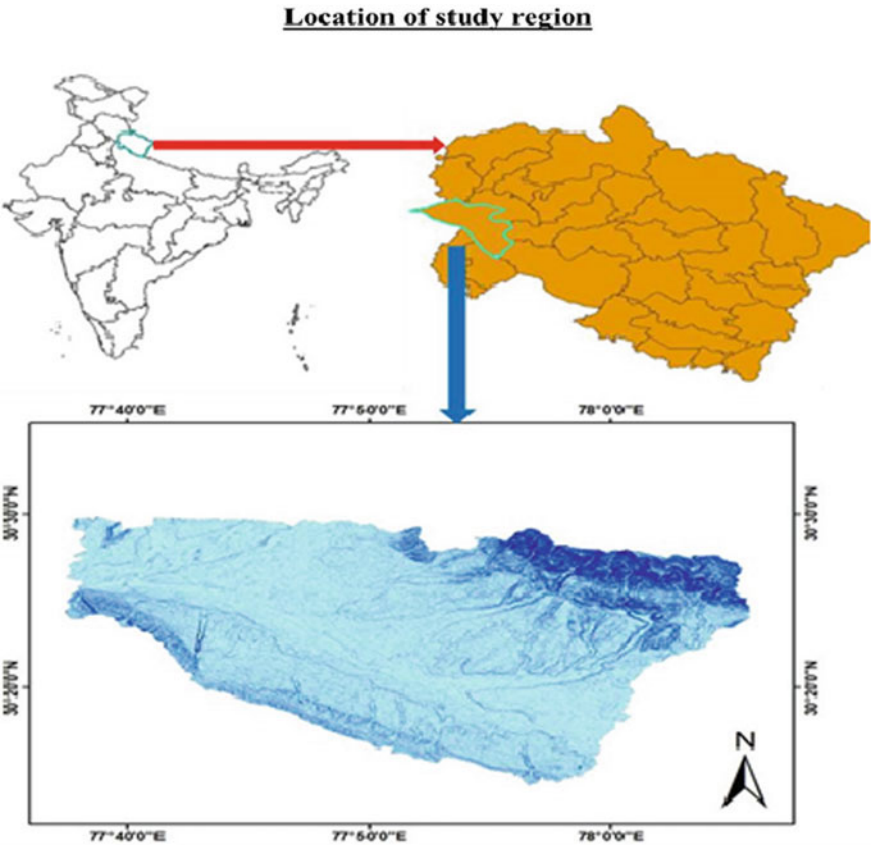

Fig. 5 Location of study area

seasons of Monsoon, winter and summer. The extreme of temperature recorded in the area as 0–42° during winter and summer season respectively.

4 Results Stream Order (U)

The smallest permanent streams are called "first order". Two first order streams meets to form second order; two second order meets to form a third order stream, and so on. Streams with smaller order entering a higher-ordered stream will not change its order number (Strahler 1964). Stream order resulted from the model is in order from 1 to 5 Fig. 6 represent the stream order map.

Stream Length Ratio (RL)
The stream length ratio (RL) is the ratio of mean stream segment length (Lu) of order u, to mean stream segment length (Lu − 1) of the next lower order u − 1. Value of RL is obtained from Eq. 1.

$$RL = Lu/(Lu - 1) \tag{1}$$

Stream length ratio of order 5–4, 4–3, 3–2, and 2–1 obtain from the integrated model are 0.8, 0.32, 0.44, and 0.67 respectively.

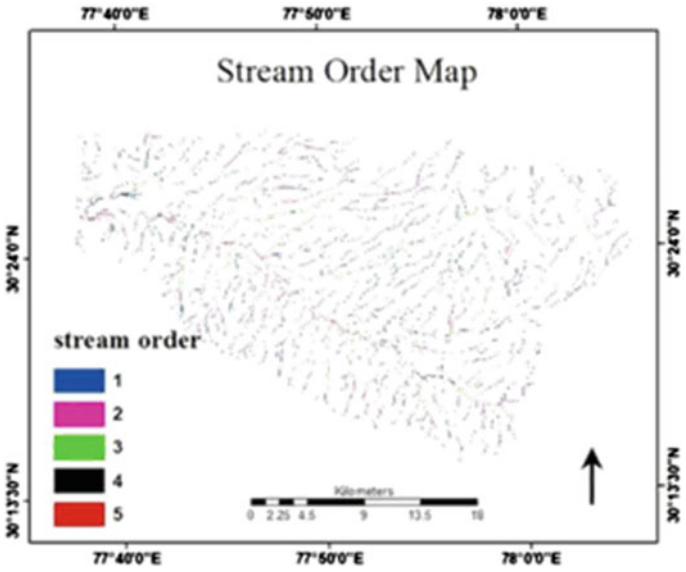

Fig. 6 Stream order map

Bifurcation Ratio

The ratio of the number of streams of any given order to the number in the next lower order bifurcation ratio (Rb) given by Horton (1932). According to Strahler (1964), the ratio of number of streams of a given order (Nu) to the number of segments of the higher order (Nu + 1) is termed as the Rb as in Eq. 2.

$$\mathrm{Rb} = \mathrm{Nu}/\mathrm{Nu} + 1 \tag{2}$$

Bifurcation ratio of 1–2, 2–3, 3–4, and 4–5 are given by model tool are 2.11, 1.69, 3.5, and 1.32 respectively.

Drainage Density

It is the ratio of total stream length to the area of the basin, high Drainage density (Dd) is favored in regions of weak or impermeable subsurface materials, sparse vegetation and mountainous relief whereas low Dd is more expected to happen in regions of highly permeable subsoil material under dense vegetative cover, Nag (1998).

$$\mathrm{Dd} = \mathrm{Lu}/\mathrm{A} \tag{3}$$

where, Lu is the total stream length and A is the area of basin (km^2).

The output from the model is having drainage density of 0.63 shown in Table 1 and Fig. 7 shows the drainage density map with maximum of 3.18 value of Dd.

Elongation Ratio

The ratio between the diameter of the circle having same area as the drainage basin and the maximum basin length is termed as elongation ratio, Schumn (1956). It indicates that the areas with higher Re values have low runoff and high infiltration capacity. The values of elongation ratio generally vary from 0.6 to 1.0 over a wide variety of geologic and climate types and output from model found out be 0.706 which is in range and represent the slightly elongated watershed. Equation 4 is used for obtaining Re value.

Table 1 Morphometric parameters

Morphometric parameters	Formula	References	Output from model
Drainage density (Dd)	$\mathrm{Dd} = \mathrm{Lu}/\mathrm{A}$	Horton (1932)	0.63
Circulatory ratio (Rc)	$\mathrm{Rc} = (4\ \pi\ \mathrm{A})/\mathrm{P}^2$	Miller (1953)	0.487
Elongation ratio (Re)	$\mathrm{Re} = 2/\mathrm{Lb}\ \sqrt{(\mathrm{A}/\pi)}$	Schumm (1956)	0.706
Stream frequency (Fs)	$\mathrm{Fs} = \mathrm{Nu}/\mathrm{A}$	Horton (1932)	2.42
Form factor (Ff)	$\mathrm{Ff} = \mathrm{A}/\mathrm{L}^2$	Horton (1945)	0.41

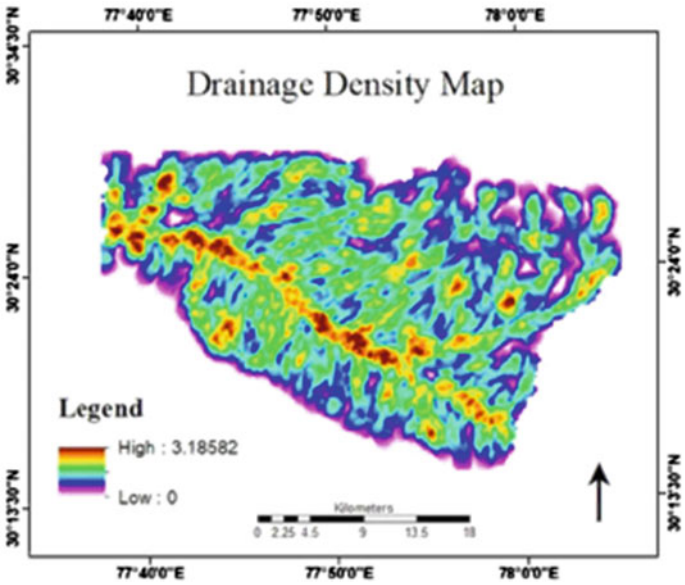

Fig. 7 Drainage density map

$$\mathrm{Re} = 2/\mathrm{Lb}\sqrt{(\mathrm{A}/\pi)} \tag{4}$$

where, Lb is the length of the basin.

Circularity Ratio

Miller (1953) defined circularity ratio as the ratio of the area of the basin to the area of a circle having the same circumference as the perimeter of the basin. Factor affecting the circularity ratio are slope of the watershed, land use/ land cover, length and frequency of streams, and climate, and Table 1 shows the output value of the model and is calculated using Eq. 5.

$$\mathrm{Rc} = (4\pi\ \mathrm{A})/\mathrm{P} \tag{5}$$

where, P = Perimeter of the basin (km).

Figures 8, 9, and 10 show the result parameter of model that is hillshade, slope and aspect map respectively.

Form Factor

The ratio of basin area to the square of the basin length is termed as form factor (Ff) by Horton (1932). The values of Ff would always be less than 0.78 (value for a totally circular basin). Result obtain from the model using Eq. 6 is 0.41 which is within the limit, Smaller the value of Form factor (Ff) more elongated will be the basin.

$$\mathrm{Ff} = \mathrm{A}/\mathrm{L}^2 \tag{6}$$

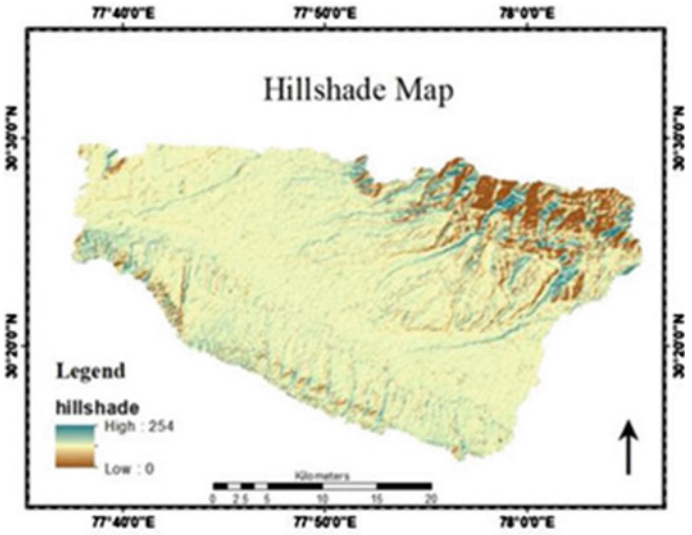

Fig. 8 Hillshade map

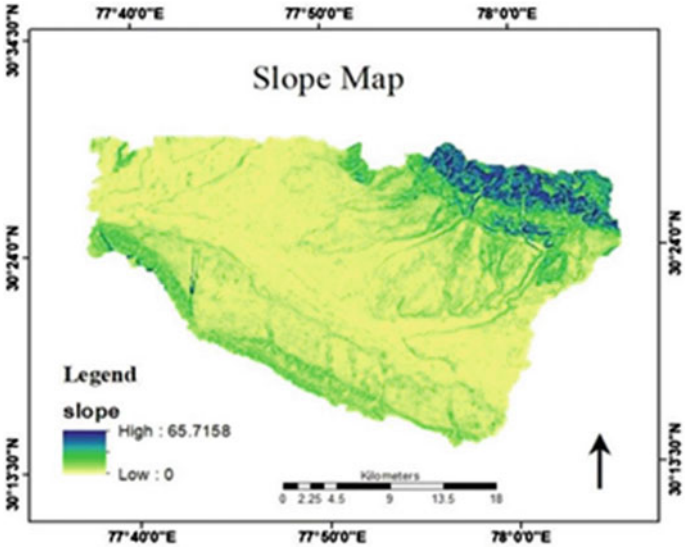

Fig. 9 Slope map

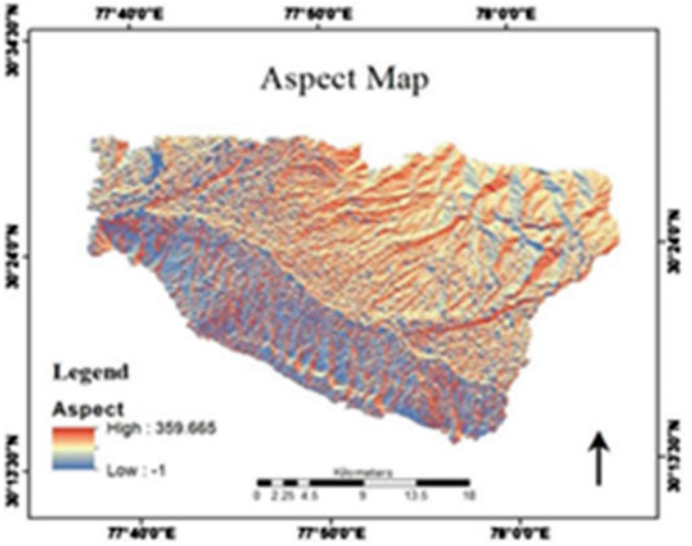

Fig. 10 Aspect map

Compound Topographic Index (CTI)
Compound Topographic Index (CTI) Moore et al. (1991) or Topographic Wetness Index (TWI) transformation can be used to models aspects of hydrologic systems. CTI is strongly correlated with soil moisture. Thus it can provide indirect information on land cover and agricultural potential. Areas with low CTI values represent places with small catchments, and steep slopes or hills and with high CTI values represent places with large catchments, and gentle slopes are depressions or plains. Study area is having maximum 14.72 CTI value shown in Fig. 11.

Stream Power Index (SPI)
Stream power index is used to describe potential flow erosion at the given point of the topographic surface. As catchment area and slope gradient increase, the amount of water contributed by upslope areas and the velocity of water flow increase, hence stream power index and erosion risk increase. Figure 12 represent Stream Power Index map.

5 Conclusion

GIS techniques prove to be a competent tool in morphometric analysis. The quantitative analysis of morphometric parameters which is obtained from the integrated tool developed in QGIS is found to be accurate. Similar studies in combination with high resolution satellite data in different climatic and geological conditions help in better understanding of parameters. Values of elongation ratio, form factor and circularity

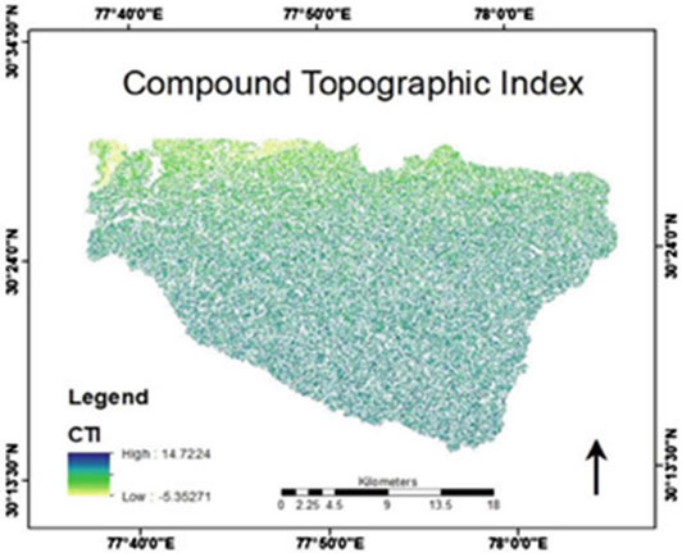

Fig. 11 CTI map

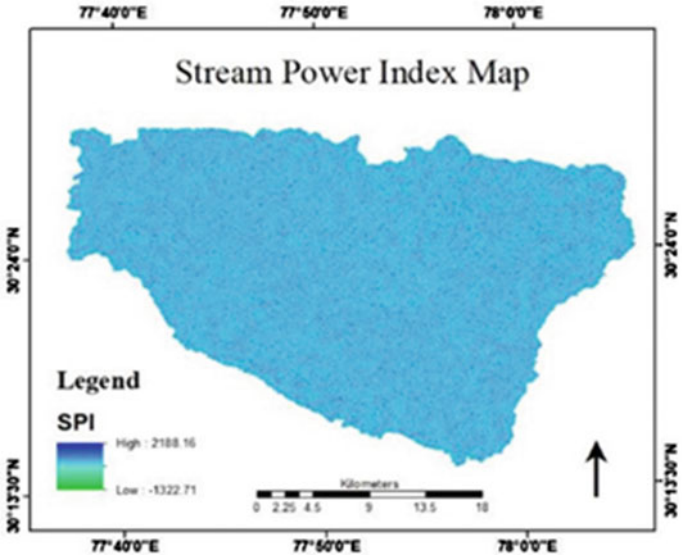

Fig. 12 SPI map

ratio shows that the study area is having elongated basin. Hence the present study exhibits the effectiveness of GIS model tool for morphometric analysis and further used to understand the status of landforms, drainage management and evaluation of groundwater potential conditions for watershed planning and management. When numerous and big data is handle it tends to be tedious and time consuming. The developed automatic integrated tool in GIS environment helps efficiently in reducing the workload and data file of workstation.

References

Agarwal CS (1998) Study of drainage pattern through aerial data in Naugarh area of Varanasi district, U.P. J Ind Soc Remote Sens 26:169–175

Grohmann CH, Riccomini C, Alves FM (2007) SRTM – based morphotectonic analysis of the Pocos de caldas alkaline massif Southeastern Brazil. Comput Geosci 33:10–19

Horton RE (1932) Drainage basin characteristics. Trans Am Geophys Union 13:350–361

Horton RE (1945) Erosional development of streams and their drainage basins; hydro physical approach to quantitative morphology. Geol Soc Am Bull 56:275–370

Krishnamurthy J, Srinivas G, Jayaram V, Chandrasekhar MG (1996) Influence of rock types and influence in development of drainage network in typical hard rock terrain. ITC 3(4):252–259

Kumar R, Kumar S, Lohani AK, Nema RK, Singh RD (2000) Evaluation of geomorphological characteristics of a catchment using GIS. GIs India 9(3):13–17

Magesh NS, Jitheshlal KV, Chandrasekar N, Jini KV (2013) Geographical information system-based morphometric analysis of Bharathapuzha river basin, Kerala, India. Appl Water Sci

Miller VC (1953) A quantitative geomorphic study of drainage basin characteristics in the Clinch Mountain area, Virginia and Tennessee. Project NR 389-402, Technical report 3. Department of Geology, Columbia University, ONR, New York

Moore ID, Grayson RB, Ladson AR (1991) Digital terrain modelling: a review of hydrological, geomorphological and biological applications. Hydrol Process 5:3–30

Nag SK (1998) Morphometric analysis using remote sensing techniques in the Chaka sub-basin, Purulia district, West Bengal. J Indian Soc Rem Sens 26(1):69–76

Obi Reddy GE, Maji AK, Gajbhiye KS (2002) GIS for morphometric analysis of drainage basins. GIS India 4:9–14

Sreedevi PD, Owais S, Khan HH, Ahmed S (2009) J Geol Soc India 73:543–552

Schumn SA (1956) Evolution of drainage systems and slopes in badlands at Perth Amboy, New Jersey. Geol Soc Am Bull 67:597–646

Strahler AN (1964) Quantitative geomorphology of basins and channel networks. In: Chow VT (ed) Hand book of applied hydrology. McGraw-Hill Book Company, New York, Section 4-II.

Short Term and Seasonal Observation on Shoreline Changes from Kanagachettikulam to Veerampattinam of the Puducherry Coastal Region Using GPS Technique

V. Anandabaskaran and G. Vijayakumar

1 Introduction

Coastal areas play a major role for the human being from ancient time for trading, livelihood etc. Due to this phenomena, rapid urbanisation developed on the coastal area and several developmental activities were conceded in order to fulfil the requirements of the settlements which have created a negative impact on the coast and its upland. The developments of the coastal structure are the root cause behind the phenomenal changes of the shoreline such as unremitting beach erosion, seawater intrusion, shoreline modification etc. Salghuna and Baratwaj (2015) state that shoreline is a more dynamic and complex region for all geological features present, as it has mixed results of tidal, Aeolian, tectonic, and sometimes river activity. Ateeth Shetty et al. (2015) states that coastal zone is increasingly under pressure from human activities such as fishing coral, sand mining, sewage disposal, urban expansion and tourism. Harvesting of Mangroves, sand mining are the major negative impact on beach stability, it gives the results of beach erosion and drastic shoreline changes. Dredging, construction of the harbour, mineral exploration, removal of vegetation, gives a major impact on the coastal stretch among the other human activities. Coastal erosion are not a single country problem but a universal one, which mostly causes a sea level rise and increases the number of storms events across the globe. Chentamilselvan et al. (2016) studied the shoreline changes of Puducherry on the Northern side of Puducherry fishing harbour reported that shoreline change that have occurred for the past 23 years due to construction of harbour breakwater on the northern side elsewhere have contributed substantially modification of shoreline. The use of GPS technique and analysing shoreline changes provide a better understanding of beach changes, sediment transport, and storm impact (Robert et al. 1993).

V. Anandabaskaran (✉) · G. Vijayakumar
Department of Civil Engineering, Pondicherry Engineering College, Pondicherry, India
e-mail: anandabaskar@gmail.com; anandabaskar@pec.edu

R. Jha et al. (eds.), *River and Coastal Engineering*, Water Science and Technology Library 117, https://doi.org/10.1007/978-3-031-05057-2_10

2 Scope of the Present Study

The study focus on a better understanding of the short term shoreline changes such as erosion and deposition. The study will be very much useful to identify the impact of hydrological and morphological factors which are responsible for the shoreline modification confronting a coast. An attempt has been made for monitoring short term shoreline change of the Puducherry coast for a period of three years (from 2015 to 2017) and to analyze morphological changes during the study period.

3 Study Area

Puducherry called as a French city of India gaining economic importance due to urbanisation, Industrialisation and Tourism. The coastal zone of Puducherry extends for over 34 km from Kanagachettikulam to Pudukkuppam, from latitude (12.057) and longitude (79.8978) to the latitude of (11.817) to longitude (79.821) with the Bay of Bengal in the East direction. The study area receives three monsoon seasons namely South East, Non Monsoon, and North East Monsoon season. The north east monsoon climate were characterised by heavy rainfall from October to December ranging from 250–350 mm. The Pennaiyaar and Sangaraparani river flowing on south of the Puducherry city and drain into the Bay of Bengal on its eastern side. The unpredictable morphological and shoreline change in this region are many due to human development activities which obstructs the natural movement of longshore sediment transport and beach reclamation.

The selected area as given in Fig. 1 for the study comprises a total length of 16.5 km extending from Kanagachettikulam to Veerampattinam. The entire stretch is divided into three zones Like, River zone, structure zone and stable zone in order to understand the erosion/accretion patterns, shoreline changes and impact of manmade structures. The divided zones of study area and list of structure present on the table are given below.

4 Materials and Methods

GPS surveying technique can be used for monitoring the beaches, to develop a procedure to collect data and analyse the data for coastal application and to evaluate the accuracy of GPS beach surveys. These methods require a minimum manpower equipment, necessary for a successful beach survey. The land based GPS surveying gives more accurate result compared with other surveying techniques. GPS techniques determine the volumetric changes of beaches, monitoring the morphologic and shoreline changes of beaches, before and after the storm for the assessment and establishment of ground truth and compared with aerial reconnaissance work.

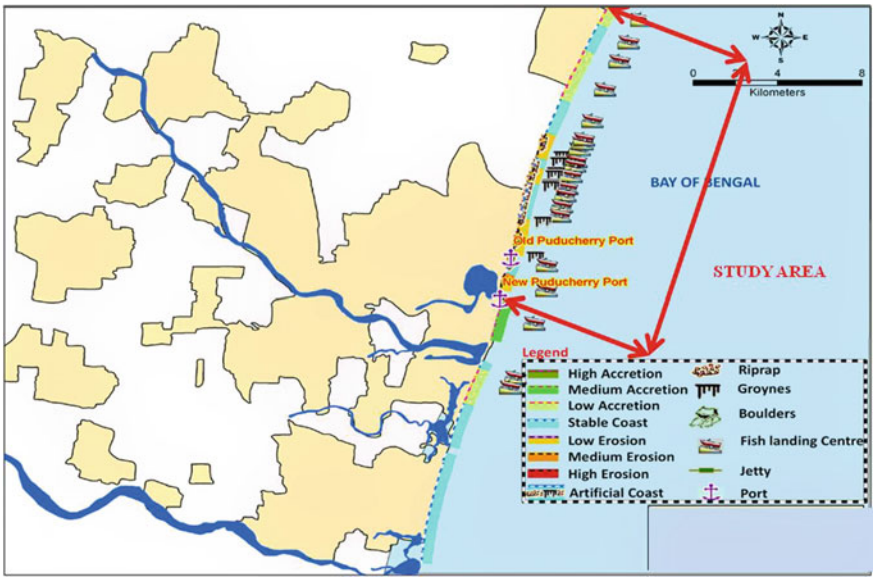

Fig. 1 Study area of Puducherry coasatal region

The conventional survey equipment consisted of a Theodolite and range pole. In order to allow to get greater accuracy of erosion and accretion every 200 m of a stretch, a transect line was driven into the beach of the seaward side.

For the GPS surveys, the Beach profile surveying method as given in Fig. 2 was adopted. A reference or initial point was established using two different stable known points on the landward of the stable sand dunes located approximately 7 m from the

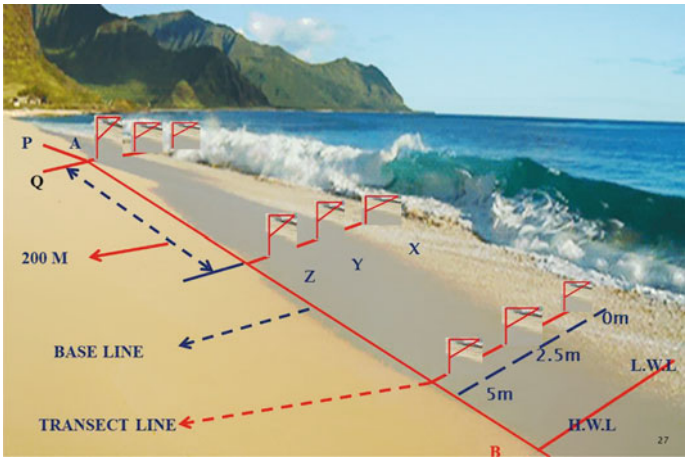

Fig. 2 Methods of collecting data on the coast

low water line. This reference point should consider as the baseline. This initial point should be extended straight upto 1 km using a metric chain of 30 m. A straight line of one km is divided into five 200 m parts. From these five points, a transect line should be extended into the seaward direction. From the low water line to the berm of the transect line should be divided into three points like 0 m from the low water line, 2.5, 5 m. For every 200 m of the full stretch this procedure should be repeated. From 0, 2.5, 5 m of the sand dune the elevation data should be collected using GPS. This procedure was repeated from the entire stretch of the Puducherry for the past three years 2015, 2016, 2017 from Kanagchettikulam to Veerampattinam. Using these data, the Trapezoidal rule should be applied to get an accurate result of shoreline erosion/accretion. The result found that seasonal and short term shoreline changes.

Trapezoidal Rule

$$\text{AREA} = \frac{\left(e_{1+e_n}\right)}{2} + e_2 + e_3 + \cdots) * D$$

$e_{1,}$ e_2—elevation of the section

D—interval between elevation

$$\text{Volume} = (A_1 + A_2) * D$$

where, A1, A2 = area of the section.

5 Results

From the GPS, Beach profile surveying techniques the results for the past three years (2015, 2016, 2017) were analysed in order to identify the short term and seasonal shoreline changes of the Puducherry coastal region extends from Kanagachettikulam to Veerampattinam. For the clear identification of shoreline changes the coastal stretch of the Puducherry was divided into two zones. From Kanagachettikulam to Periyamudaliyarchavady called a normal zone because of stable beach formation and Periyamudaliyarchanvady to Veerampattinam called as structural zone due to the presence of structure like seawall, groin, Breakwater harbour etc.

6 Normal Zone (Kanaga Chettikulam to Periyamudaliyarchavady)

The results obtained for the past three years (2015–2017) of observation on this zone was given in Fig. 3, It was found that from Kangachettikulam to Periyamudaliyarchavady the coast has experienced a major beach formation for nearly 7 km

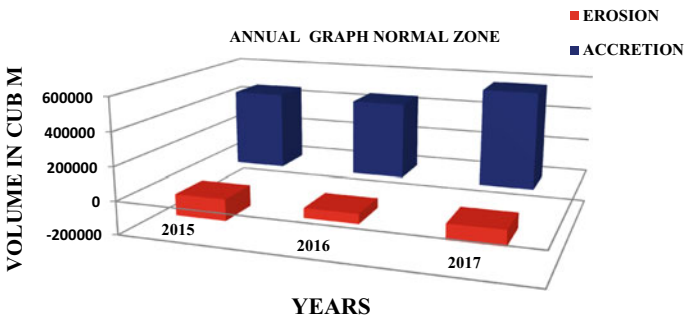

Fig. 3 Year graph for normal zone

due to the wave action and the longitudinal current which was normal and had no interfaced by human induced endeavours. A scanty erosion was found near on china Kalapet region may be due to monsoonal modification. From the overall observation for all the seasons it was found that, the total sediment deposited was found to be around 0.4–0.6 million cubic metre rate of the erosion was found to be around 0.2 million cubic metres. The sediment deposits along the coast were during Southwest monsoon as well as Northeast monsoon. The Major accretion (5,75,000 cubic metre) was observed in the midst of year 2017 in the northern side of Puducherry coast near Kanagachetikulam. The Major erosion (1,26,600 cubic metre) was observed in the year of 2015 due to seasonal changes, climatic condition, velocity of current etc.

7 Results Based on Seasonal Observation

7.1 Accretion

The result based on seasonal variation for the normal zone are given in Fig. 4. The maximum amount of accretion observed was found to be around 7,04,000 cubic meters during the season of Northeast monsoon in the year of 2015 and the minimum amount of accretion observed was found to be around 63,700 cubic meters during the season of Non-monsoon in the year of 2016 during the study period of 2015–2017.

7.2 Erosion

The maximum amount of erosion observed was found to be around 82,000 cubic meters during the season of Northeast monsoon in the year of 2017 and the minimum amount of erosion observed was found to be around −750 cubic meters during the season of non-monsoon in the year of 2016 during the study period of 2015–2017.

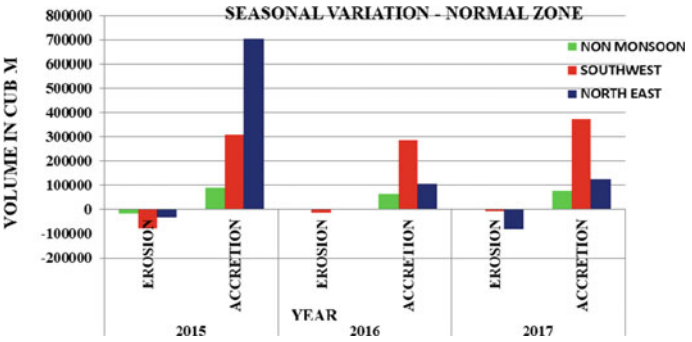

Fig. 4 2015–2017 Various seasonal graph at normal zone

7.3 Structure Zone (Periya Mudaliyarchavady to Veerampattinam)

The results obtained from the structure zone (Periya mudaliyachavady to Veerampattinam) for the assessment period (2015–2017) was given in Fig. 5, it was found that the coast has experienced an accretion of around 0.2–0.3 m^3. The predominant sediment transport along this zone was during Southwest monsoon which transported the sediment towards northern side.

8 Accretion Results

The overall result obtained from the three years on this structure zone was the maximum accretion (309,000 CUB M) obtained from the three years are 2017 due to construction of artificial reef working platform constructed at Puducherry city, sand

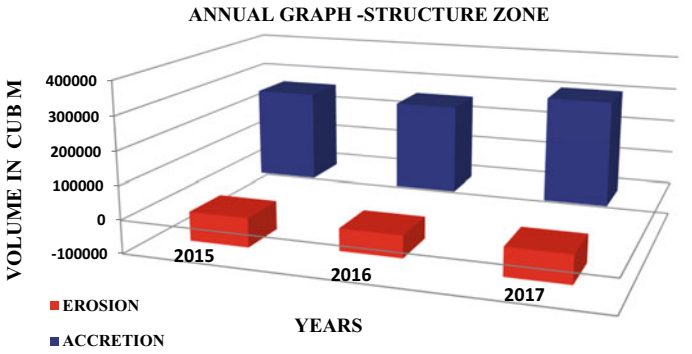

Fig. 5 Year graph for Structure zone

bypassing from Veerampatinam to new pier, the velocity of current disturbed and accreted in the south of the platform zone and eroded in the adjacent area.

9 Erosion Results

The overall the result obtained from the three years on this normal zone was the maximum erosion (87,750 CUB M) obtained from the three years are 2015 due to seasonal variation, climatic condition, velocity of current etc.

10 Results Based on Seasonal Observation

10.1 Accretion

The result based on seasonal variation for the structure zone are given in Fig. 6. The maximum amount of accretion observed was found to be around 2,14,000 cubic meter during the season of South west monsoon in the year of 2017 and the minimum amount of accretion observed was found to be around 31,500 cubic meter during the season of Non-monsoon in the year of 2017 during the study period of 2015–2017.

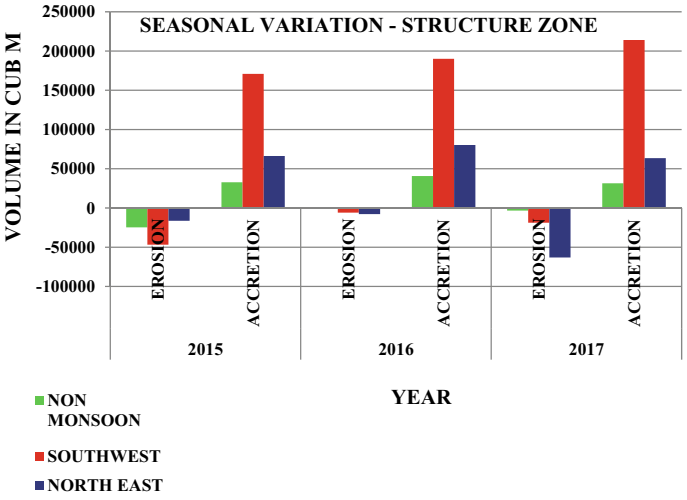

Fig. 6 2015–2017 Various seasonal graphs at structure zone

10.2 Erosion

The maximum amount of erosion observed was found to be around 63,000 cubic meter during the season of North East monsoon in the year of 2017 and the minimum amount of erosion observed was found to be around −1000 cubic meter during the season of Non-monsoon in the year of 2016 during the study period of 2015–2017.

11 Summary and Conclusion

The Study has revealed that during 2015–2017 major erosion/accretion was observed in all the zone of the study area. Construction of seawall on the Puducherry main city has resulted in shifting of the erosion from Puducherry to Thanthriyankuppam which is very adjacent to Puducherry city. The breakwater constructed along the Pondicherry fishing harbour acts as a barrier of littoral drift. The sediment transport are facilitated by the action of progressive waves induced by the longshore current, the sediments are pushed towards the northerly or southerly direction. As per the natural scenario, the predominant sediment movements are towards the North. The propagation of sediment towards northerly direction is obstructed by the human inference such as the construction of breakwaters, groins and seawalls. Analysis of shoreline changes using GPS was found to be very much suitable for the identification of shoreline changes. Shoreline changes study is of critical importance for coastal resource management, environmental protection and sustainable development and planning. A detailed study on shoreline changes caused by human activities should be studied using GPS technique to monitor the expected changes in the future. Further, a study can be made based on real time shoreline changes using real time shoreline data in which shoreline change can be predicted more accurately.

References

Ateeth Shetty, Jayappa KS, Mitra D (2015) Shoreline change analysis of Mangrove coast and Morphometric analysis of Netravathi-Gurupur and Mulky-Pavanje Spits. Elsvier Aqautic Procedia 4:182–189

Chentamilselvan, Kankara RS, Markose VJ, Rajan B, Prabhu K (2016, August) Shoreline change and impacts of coastal protection structures on Puducherry, SE coast of India, Springer. Int Soc Prev Mitig Nat Hazards 83(1):293–308

Robert A, Morton, Leach MP, Cardoz MA (1993) Monitoring beach changes using GPS surveying techniques. J Coastal Res 9(3):702–720

Salghuna NN, Baratwaj A (2015) Shoreline change analysis for northern part of Coromandel coast. Elsvier Aquatic Procedia 4:317–324

A Review of Computational Studies on Indian Coast Considering Climate Change Effects

Upadhyaya K. Sandesh, Subba Rao, and Manu

1 Introduction

The projected global sea level rise is expected to be at a rate of 8–16 mm/year during the years 2081–2100 according to IPCC (2007). Most of Indian landmass has sea level only a few meters high. Population density in coastal India is larger due to the various factors, making it very sensitive for effects of climate change.

Brenkert and Malone (2005) expresses their concern, as India is dependent on agriculture, variation in rainfall widely effects the economy and will create additional pressure on India's ecology and socio-economic system. The eastern coast is prone to tropical cyclone, increasing annual surface air temperature, sea level rise amongst the other effects. The changes in temperature gradient by global warming increases pressure over the earth which in turn changes the wind pattern (Deepthi and Deo 2010). Wind plays an important role in wave generation. Gayathri et al. (2015) mention that Bay of Bengal is prone to high frequency of cyclones and the funneling effect at its head bay region amplifies surge and indentation. Portions of West Bengal is most effected along with Bangladesh and Myanmar. India is one of the most important countries with regard to climate change sources and its impacts (Brenkert and Malone 2005). The changes in monsoon pattern are the highlights of the studies done on climate change. Heat waves, cold waves, cyclones, floods, draughts and monsoons are some of the important weather events observed in India (Dash et al. 2007). Effects on Indian climatology due to climate change are discussed below.

U. K. Sandesh (✉)
Department of Civil Engineering, Manipal Institute of Technology, Manipal Academy of Higher Education, Manipal, Karnataka 576104, India
e-mail: sandesh.uk@manipal.edu

S. Rao · Manu
Department of Water Resources and Ocean Engineering, National Institute of Technology Karnataka, Surathkal, Srinivasnagar 575025, India

R. Jha et al. (eds.), *River and Coastal Engineering*, Water Science and Technology Library 117, https://doi.org/10.1007/978-3-031-05057-2_11

1.1 Rainfall and Temperature

The western central part of India is expected to have an increase in rainfall and the frequency of extreme rainfall is also expected to increase. The night temperatures are increasing at a faster rate than the day temperatures (Kumar et al. 2006). The measured mean air temperatures from 1948 to 2008 show increasing trend of yearly mean air temperature at all atmospheric layers from surface up to 10 km height (Ganguly 2011).

The study of Dash et al. (2007) focuses on both spatial and temporal aspects of climate changes in various locations of India. India has been divided into seven zones and zone wise studies have been performed. Rainfall has been studied for a period of 1871–2002 and temperatures from 1901 to 2003. Sea surface temperature from 1901 to 2003 is obtained from National Climate Data Center and cyclonic variations were analyzed based on data from India Meteorological Department. The temperature anomalies show increasing trends, amongst which Andra Pradesh and Orissa were affected by heat waves. Sharannya et al. (2018) assessed the climate change effects on Western Ghats of India. Decreasing trend of rainfall of about 2.63 mm based on historical measurements and 8.85 mm based on future scenario was predicted. The rate of increase in temperature of 0.1 °C per decade can be expected in the study area.

1.2 Sea Level Rise and Floods

Indentation and salinization of freshwater are some of the effects expected by rising sea levels along the low lying Indian landmass (Panda 2009). The importance of mapping of inundation in vulnerable coastal areas was given importance in the study by Gayathri et al. (2015).

Over the last two decades the flood risks have increased on the eastern coast of India according to Guhathakurta et al. (2011). Prediction of water levels during flood is important for planning for further flood management and also for insurance database. Hence, studies in this regard was performed by Timbadiya et al. (2015).

1.3 Wind and Wave Climate

Generally, the cyclonic events are more common in Bay of Bengal when compared to Arabian Sea. The cyclone intensity over Arabian Sea is basically linked to the strength of Indian monsoon (Reuter et al. 2013). Wave heights obtained in eastern locations show less increase when compared to western coast of India according to Roshin and Deo (2017) and wave heights are expected to increase from 5 to 58% in different offshore locations along the Indian coast.

Kulkarni et al. (2014) observed that climate change effect on the regional wind, hence a study was done on design and operational wind conditions of two offshore locations on the west coast of India. Another study by Kulkarni et al. (2016) mentions high wind potential days might increase by 5–7% on west coast and 2% along east coast of India. Deepthi and Deo (2010) mentions long term wind speeds significantly increased by 44 and 77% for 100 year return period along Goa and Machilipatnam region respectively due to future climate changes.

In the following sections more emphasis is on research articles related on Indian coast. Availability of data for computational studies, computational tools used and vulnerability of the Indian coast are discussed in detail below.

2 Availability of Data

The accuracy of a prediction model depends entirely on the climate model prepared and the data imputed. Ocean observing system relies on information obtained from in-situ observations and remote sensing satellites. Indian Metrological Department (IMD) is a major data provider which covers areas such as hydrometeorology, cyclone, marine meteorology, environmental monitoring services, seismic monitoring etc. IMD has established about 6000 rain gauge stations all over India which provides daily rainfall data. Earth System Science Organization (ESSO)-Indian National Centre for Ocean Information Services (INCOIS) which is an autonomous body under Ministry of Earth Sciences provides ocean observation, information and advisory services. This data repository helps to provide vital information for Navy, IMD, National Hydrographic Office, Ports and harbours, fishing communities, research institutions and academia. Indian Institute of Tropical Meteorology (IITM), Pune provides map of homogeneous temperature for regions of India.

2.1 In-Situ Measured Data

Initially, historical data was obtained from ship observations which is confined to calm weather season and along particular routes only. Nowadays, in-situ measurements recorded with the help of different instruments are considered reliable. Location specific measured data of ocean parameters are sparse. Compared to the Atlantic and Pacific region, Indian Ocean region has limited in-situ observations (Thomas and Dwarakish 2015; Patra and Bhaskaran 2016). As there are number of potential areas for development along Indian coast and offshore, good quality wave measurements through wave buoys is very much essential (Kumar et al. 2012). Figure 1 shows argo floats (yellow vertical lines), drifting buoys (grey spheres), moored buoys (red balloon), Expendable Bathythermograph (XBT), current meter arrays, research vessels, tide gauges (green triangles), wave rider buoys (yellow sphere), tsunami deep ocean buoys (blocks), coastal radars and gliders which are some of the devices

Fig. 1 Instruments along Indian coast providing in-situ measurements. *Source* http://www.incois.gov.in/geoportal/OON/index.html

providing in-situ measurements. Most of these give real time measurements which can be used for research (Table 1). There is a possibility of data gaps as buoys might have to be taken out for maintenance or buoys might even get displaced during a storm event (Aboobacker et al. 2009). Hence, measured data are widely used as a reliable measure for validation of results obtained.

Table 1 Platforms along Indian coast providing in-situ measurements (Rao 2014)

Platforms	Parameter	Number of platforms	Years of availability
Argo profiling floats	Temperature and salinity profile	1971 floats	2002—Till data
Moored buoy	Met-Ocean	63	1997—Till data
Drifting buoy	Surface	300	1991—Till data
Ship based Automatic Weather Station (AWS)	Met-Ocean	11	2009—Till data
XBT/XCTD	Temperature profile	4391 profiles	1990—July 2014
Tidal gauge	Sea level	26	2010—till date
Wave rider Buoy	Wave parameters	10	2007—till date
Coastal ocean monitoring and predicting system	Biological, zoological, chemical	88 stations	1987—2012

2.2 Satellite Measurements

Satellite systems works based on algorithms which converts electromagnetic radiations into geophysical variables (Venkatesan et al. 2016). As a result of large galaxy of satellites along with the remote sensing techniques and sensors like scatterometer and altimeter, it is possible to understand basin-scale variability of wind and waves (Patra and Bhaskaran 2016). Satellite missions like ERS/ENVISAT/SAR/ASAR data and Near-Infrared (NIR) satellite images have been used in studies regarding oil spill event. Real time data can be obtained from NOAA, MODIS and OCEANSAT-2 missions (Rao 2014). Historical satellite imageries of shoreline were studied based on GIS tools for the period of 1979–2014 (Rajasree et al. 2016). QuickSCAT scatterometer winds blended with ECMWF model winds was used in a model study by Remya et al. (2012), where wind data was obtained from IFREMER, France.

2.3 Global Climate Models

The studies to assess changes in the climate at any given geographic location can be performed using global climate models. Global climate models contain downscaled data of future variables at larger spatial grids. These are earth models which is a mathematical representation of the physical processes that happens in the atmosphere, ocean, land surface and cryosphere as mentioned in fifth assessment report of IPCC (IPCC AR5 2014). Data assimilation technique is used to initialize numerical forecast model which is obtained by the combination of meteorological observations of variables like atmosphere pressure and temperature.

There are two types of models widely used for climate change studies former one being General Circulation Models (GCMs) latter one being Regional Climate Models (RCMs). Ocean atmospheric models help us to understand the planetary scale features but as it has a coarser resolution (about 300 km) it fails to give realistic nature of the topography. Hence, regional models are used to dynamically down scale the global model by superimposing the specific detail of a region (Kumar et al. 2006). These RCM data can be obtained from agencies like Coordinated Regional Downscaling Experiment (CORDEX), Providing Regional Climates for Impact Studies (PRECIS).

There are several climate model simulations performed to study the changes in pressure, temperature and wind at a region (Reistad 2001). The global climate data inputs in the form of GCM data developed from different agencies like European Centre for Medium-range Weather Forecasts (ECMWF), Coupled Model Intercomparison Project (CMIP), National Centers for Environmental Prediction (NCEP) under National Oceanic and Atmospheric Administration (NOAA), Climate Forecast System Reanalysis (CFSR) etc. These datasets are highly regarded in the scientific community as they provide reasonably good estimates which are closer to the observed measurements (Alexandru and Sushama 2015; Umesh et al. 2017). In a numerical model based analysis by Umesh et al. (2017), NCEP blend wind data

produced accurate results for both calm and storm conditions. For the study by Radhika et al. (2013) wind data was taken from NCEP/NCAR reanalyzed data and was used for downscaled model of the study region. Roshin and Deo (2017) used Coordinated Regional Climate Downscaling Experiment (CORDEX) as wind data input. The study was on 39 offshore stations at 50 km from Indian coast at a water depth ranging from 20 to 2000 m.

2.4 Climate Change Scenarios

Representative Concentration Pathways (RCPs) are scenarios which help in predicting trajectories of the future climate, majorly as a consequence of anthropogenic activities. The amount of greenhouse gases, aerosols and land use are the key variables contributing to climate change which will be accounted by RCPs. RCP 2.6, RCP 4.5, RCP 6 and RCP 8.5 are four RCP scenarios used in climate modelling and research which is also been adopted by IPCC AR5 (2014). RCP 4.5 denotes a concentration pathway which may results in a radiative forcing of 4.5 W/m^2 in the year 2100. Scenarios has to be carefully selected for futuristic prediction based on human behavior, greenhouse gases and aerosol concentration of that region. RCP 2.6 and RCP 6 are some of popular scenarios used for climate predictions IPCC (2007).

3 Methods and Computational Tools Used in Climatology

Earlier, in-situ measurements were the preferred inputs for climatology. Later with advancements in numerical modelling and computational techniques, betterment in terms of precision in climate studies was achieved whose outputs were closer to measured data.

3.1 Numerical Modelling

Numerical modelling has become an essential and popular tool in coastal planning. Numerical modelling involves various stages like data formulation, model preparation, validation and analysis. Transformation of wind generated waves and swells in offshore region can be simulated by solving energy and mass balance equations (Pentapati et al. 2015). This has resulted in development of third generation models. Numerical modelling tools popularly used for coastal studies are MIKE, SWAN, Wave Modelling (WAM), WaveWatch III (WWIII) and CFD (Aboobacker et al. 2009 Patra and Bhaskaran 2016 and Umesh et al. 2017). Some of the published research work using these numerical tools are discussed below:

3.1.1 MIKE 21 by DHI

MIKE 21 is a computer programed tool for 2 dimensional wave modeling, developed by Danish Hydraulic Institute, Denmark (DHI 2015). It is one of the popular tools used worldwide to simulate climate change effects. Versatility of this tool helps in modelling coastal zones, physical, chemical and biological processes. Regions with extensive detail can be represented by small elements and areas with lesser detail can be large elements during meshing. MIKE tool has a wide range of modules for specific problem solution (MIKE 2011). One such module MIKE 21 SW does modelling based on unstructured meshing. Bathymetry can be generated based on Mike 21 tool C-MAP along with digitized National Hydrographical Office (NHO) charts. For better prediction model parameters like roughness, breaking and white capping can be considered (Roshin and Deo 2017). Patra et al. (2015) studied offshore characteristics of Bay of Bengal region and justified wind wave model's accuracy over empirical equations.

3.1.2 SWAN

SWAN (Simulating WAves Nearshore) is a third generation tool for wave modelling. SWAN model results were in close proximity to the observed data except for extreme events which occurred on a forecasting study at coastal Puducherry by Sandhya et al. (2014). SWAN accurately predicts wave period below 10 s.

The results of Hoque et al. (2017) depicts that at shallow water region, SWAN gave good wave height predictions and MIKE 21 estimated wave period better. In deep water, both models gave closer values and their variation with recorded storm events were compared. Moeini and Shahidi (2007) performed a comparison study based on hindcasting using different computing tools, they conclude that numerical method in SWAN is superior to MIKE 21 SW for significant wave height estimation and MIKE 21 outperforms SWAM during the peak wave period estimation. These differences were because of the wind input parameterization using various formulation techniques.

3.2 Artificial Neural Network

Artificial Neural Network (ANN) has found its application for solving coastal engineering problems as well. A downscaled model was conveniently modelled using ANN and wind data was used for training ANN model (Radhika et al. 2013). There was alternate computation done using ANN along with numerical modelling to study the future changes due to climate change on shoreline shifts at a straight and continuous coast. Numerical modelling indicated an erosion rate to be −2.21 m/year and ANN predicted it as −1.66 m/year (Rajasree et al. 2016).

3.3 Analysis Based on Long-Term Probability Distributions

An understanding of long-term variation in climate is a necessity when an engineer has to design an offshore or a coastal structure. Long-term analysis is a traditional design criteria performed based on statistical analysis of existing data or probability based methods. Kumar and Deo (2004) mention that the long-term distributions like Generalized Pareto Distribution (GPD), Generalized Extreme Value (GEV), Gumbel distribution and Weibull distributions can be used to obtain design wave height for different return period using short-term measurements. These variations inclusive of climate change effect should be taken into account when the structure is to be designed.

4 Computational Studies Along Indian Coast

According to IPCC's fourth assessment report IPCC (2007), vulnerability is defined as the degree to which a system is susceptible to, and unable to cope with adverse effects of climate change, including climate variability and extremes. Brenkert and Malone (2005) studied vulnerability of six Indian states to climate change effects when compared to global values. Orissa and Tamil Nadu showed high sensitivity to sea storm surges. A comparison between Kerala and Maharashtra was performed which revealed Kerala having higher vulnerability index. Authors conclude by their assessment for India that water is one of the sensitive parameters, resulting in sea level rise and storm surges.

Nayak et al. (2013) assessed the effects of distant swells generated from Southern Ocean and its role in modifying the local wind-waves at the coast using numerical modelling technique. Three different models were used, the outer domain was a finite difference coarse grid and numerical experiments were performed using WAM wave prediction model. The results showed the coast was dominant with land breeze of about 55% followed by wind occurrence of about 39% almost parallel to coast. The resultant energy is almost doubled when swell effects are considered for the Kalpakkam region studied. Alexandru and Sushama (2015) compared current climate with expected climate change effects over India using regional climate model. The simulations were based on GCM models (CanESM2 and MPI-ESM-LR) for the period 1950–2100 including future predictions using corresponding to RCP 4.5 for 2006–2100. Temporal and spatial patterns of runoff, 850 HPa winds, sea level pressure, precipitation and soil moisture were studied based on seasonal variations. The authors suggested multiple RCM-GCMs ensembles and various RCP scenarios for better results. The results obtained is expected to contribute to CORDEX project.

Sandhya et al. (2014) contributed to develop a wave forecasting system at Puducherry coast which will help in marine related operations. Two dimensional energy density spectra which is time varying was developed using a tool WWIII this data was used as boundary conditions for SWAN model. SWAN under predicted

the wave height in Dec 2008 which was because of weak wind input. Similarly, the model over predicted Nov 2007 wave heights as 'SIDR' Cyclone hit Bay of Bengal but its effect was least felt in Puducherry coast. Patra and Bhaskaran (2016) studied annual and season variability in wind speeds and significant wave heights for Bay of Bengal region. The study showed spatial distribution of percentage variability of wind speed observed was less for east of head Bay of Bengal when compared to west of the Bay. The authors conclude by correlating Mean Sea Level Pressure to the contrasting trend in wind speed and significant wave height for the east–west direction of coast.

A study on Mumbai High region which has highest number of offshore oil platforms (more than 200) in India was performed. Past and future wave height was estimated by MIKE 21 SW numerical model. The wave heights may increase by 10–20% in this region due to climate change effects (Pentapati et al. 2015). Satyavathi et al. (2016) based on 21 offshore locations along the west coast of India (about 50 km offshore) worked on, re-evaluation of design waves considering climate change effects. The results obtained indicate that as wave height increases wave period also increases except for regions at the southern tip where complex wind wave system between Indian Ocean and Arabian Sea. The significant wave heights might increase from 7 to 45% and wave period by 14–51% along the west coast of India. Sandesh et al. (2020) performed long-term analysis on the waves off Mangaluru coast using MIKE21 SW numerical model. Based on the hindcasting study driven by ERA-Interim wind dataset they found an increase of 2.6, 5.44 and 6.42% in the design significant wave height for return periods 10, 50 and 100 years respectively.

The significant wave heights were estimated on three different locations along Indian coast considering climate change effect for a return period of 100 years. The two locations were offshore from coasts of Chennai and Goa and the third location at shallow region of Mangalore coast. Weibull distribution was adopted to arrive at wave heights with 100 year return periods. The results reveal an increase of about 8–42% in offshore of Bay of Bengal location. An increase of 27–44% at offshore of Arabian Sea and at near shore region of Arabian Sea it was about 22–32% (Radhika et al. 2013). The study on the shore line changes of Udupi, located at south west coast of India was based on two methods, former based on satellite imageries and the latter using numerical shoreline model. The study was performed for past period and future predictions of 35 years. They concluded based on the satellites imageries that the coast is subjected to continuous erosion with an average rate of −1.46 m/year and the significant wave height may increase at a rate of 0.042 m/year (Rajasree et al. 2016).

5 Summary

Data discontinuity, uncertainties in in-situ measurements has made General Circulation Models as a preferred method to study climate change effects. Further, GCM

studies have proved to be an effective method as the results obtained can be validated against in-situ measurements. Futuristic climate can be predicted using RCP scenarios as input to the numerical models. Satellite measurements are being instrumental for assessing climate variability, if there is an unavailability of in-situ measurement. The performance of numerical model purely depends on the quality of input data, spatial resolution, initial and boundary conditions. Hence, bathymetry data plays a vital role in the output of atmosphere-ocean model. Coupled models or hybrid models have shown promising results which are more realistic. Long-term analysis performed on the dataset which considers climate change effects is providing results closer to reality.

Vulnerable low lying areas has to be identified and a problem specific solution can be obtained by performing computational studies. Policymakers can reinforce their collaborations with research agencies and academic institutions for promoting research on effects of climate change. A collective study incorporating possible variations to climate parameters due to climate change along Indian coast can result in a reliable regional model. This regional model will be useful for developing strategies to effectively combat climate change effects.

References

Aboobacker VM, Vethamony P, Sudheesh K, Rupali SP (2009) Spectral characteristics of the nearshore waves off Paradip, India during monsoon and extreme events. Nat Hazards 49(2):311–323

Alexandru A, Sushama L (2015) Current climate and climate change over India as simulated by the Canadian regional climate model. Clim Dyn 45(3–4):1059–1084

Architesh P (2009) Technical note on assessing vulnerability to climate change in India. Econ Pol Wkly 44(16):105–107

Brenkert AL, Malone EL (2005) Modeling vulnerability and resilience to climate change: a case study of India and Indian states. Clim Change 72(1–2):57–102

Dash SK, Jenamani RK, Kalsi SR, Panda SK (2007) Some evidence of climate change in twentieth-century India. Clim Change 85(3–4):299–321

DHI (2015) MIKE 21 wave modelling: MIKE 21 SW-Spectral waves FM. Short description. DHI, Denmark

Deepthi R, Deo MC (2010) Effect of climate change on design wind at the Indian offshore locations. Ocean Eng 37(11–12):1061–1069

Ganguly ND (2011) Investigating the possible causes of climate change in India with satellite measurements. Int J Remote Sens 32(3):687–700

Gayathri R, Bhaskaran PK, Sen D (2015) Numerical study on storm surge and associated coastal inundation for 2009 AILA cyclone in the head bay of Bengal. Aquatic Procedia (ICWRCOE) 404–411

Guhathakurta P, Sreejith OP, Menon PA (2011) Impact of climate change on extreme rainfall events and flood risk in India. J Earth Syst Sci 120(3):359–373

Hoque MA, Perrie W, Solomon SM (2017) Evaluation of two spectral wave models for wave hindcasting in the Mackenzie Delta. Appl Ocean Res 62:169–180

IPCC (2007) Climate change 2007: synthesis report. Intergovernmental Panel on Climate Change, Core Writing Team IPCC

IPCC (2014) Climate change 2014: synthesis report. Contribution of Working Groups I, II and III to the Fifth Assessment Report of the Intergovernmental Panel on Climate Change. IPCC, Geneva, Switzerland, p 151

Kulkarni S, Deo MC, Ghosh S (2014) Changes in the design and operational wind due to climate change at the Indian offshore sites. Mar Struct 37:33–53

Kulkarni S, Deo MC, Ghosh S (2016) Evaluation of wind extremes and wind potential under changing climate for Indian offshore using ensemble of 10 GCMs. Ocean Coast Manag 121:141–152

Kumar VS, Deo MC (2004) Design wave estimation considering directional distribution of waves. Ocean Eng 31(17–18):2343–2352

Kumar KR, Sahai AK, Kumar KK, Patwardhan SK, Mishra PK, Revadekar JV, Kamala K, Pant GB (2006) High resolution climate change scenarios for India for the 21st century. Curr Sci 90(3):334–345

Kumar VS, Johnson G, Dora GU, Chempalayil SP, Singh J, Pednekar P (2012) Variations in nearshore waves along Karnataka, west coast of India. J Earth Syst Sci 121(2):393–403

Moeini MH, Etemad-Shahidi A (2007) Application of two numerical models for wave hindcasting in Lake Erie. Appl Ocean Res 29(3):137–145

Nayak S, Bhaskaran PK, Venkatesan R, Dasgupta S (2013) Modulation of local wind-waves at Kalpakkam from remote forcing effects of Southern Ocean swells. Ocean Eng 64:23–35

Patra A, Bhaskaran PK (2016) Trends in wind-wave climate over the head Bay of Bengal region. Int J Climatol 36(13):4222–4240

Patra SK, Mohanty PK, Mishra P, Pradhan UK (2015) Estimation and validation of offshore wave characteristics of bay of Bengal cyclones (2008–2009). Aquatic Procedia, (ICWRCOE) 1522–1528

Satyavathi P, Deo MC, Kerkar J, Vethamony P (2016) Reevaluation of design waves off the western Indian coast considering climate change. Mar Technol Soc J 50(1):88–98

Pentapati S, Deo MC, Kerkar J, Vethamony P (2015) Projected impact of climate change on waves at Mumbai High. Proc Inst Civil Eng Maritime Eng 168(1):20–29

Radhika S, Deo MC, Latha G (2013) Evaluation of the wave height used in the design of offshore structures considering the effects of climate change. Proc Inst Mech Eng Part m: J Eng Maritime Environ 227(3):233–242

Rajasree BR, Deo MC, Sheela Nair L (2016) Effect of climate change on shoreline shifts at a straight and continuous coast. Estuarine. Coastal Shelf Sci 183:221–234

Rao EPR (2014) Ocean data and information system. Indian National Centre for Ocean Information Services (INCOIS)

Reistad M (2001) Global warming can result in higher waves. Cicerone 1–6

Remya PG, Kumar R, Basu S, Sarkar A (2012) Wave hindcast experiments in the Indian Ocean using MIKE 21 SW model. J Earth Syst Sci 121(2):385–392

Roshin E, Deo MC (2017) Derivation of design waves along the Indian coastline incorporating climate change. J Mar Sci Technol 22(1):61–70

Reuter M, Piller WE, Harzhauser M, Kroh A (2013) Cyclone trends constrain monsoon variability during late Oligocene sea level highstands (Kachchh Basin, NW India). Climate past 9(5):2101–2115

Sandhya KG, Balakrishnan Nair TM, Bhaskaran PK, Sabique L, Arun N, Jeykumar K (2014) Wave forecasting system for operational use and its validation at coastal Puducherry, east coast of India. Ocean Eng 80:64–72

Sharannya TM, Mudbhatkal A, Mahesha A (2018) Assessing climate change impacts on river hydrology—A case study in the Western Ghats of India. J Earth Syst Sci 127(6):78

Thomas TJ, Dwarakish GS (2015) Numerical wave modelling—A review. Aquatic Procedia 4:443–448

Timbadiya PV, Patel PL, Porey PD (2015) A 1D–2D Coupled hydrodynamic model for river flood prediction in a coastal urban floodplain. J Hydrol Eng 20(2):05014017

Umesh PA, Bhaskaran PK, Sandhya KG, Balakrishnan Nair TM (2017) An assessment on the impact of wind forcing on simulation and validation of wave spectra at coastal Puducherry, east coast of India. Ocean Eng 139(April):14–32

Sandesh UK, Rao S, Manu (2020) Long-term analysis of waves off Mangaluru coast. Ind J Geo-Marine Sci (IJMS) 49(05):717–723

Venkatesan R, Lix JK, Phanindra Reddy A, Arul Muthiah M, Atmanand MA (2016) Two decades of operating the Indian moored buoy network: significance and impact. J Oper Oceanogr 9(1):45–54

Determination of Effective Discharge Responsible for Sediment Transport in Cauvery River Basin

Shobhit Maheshwari and Sagar Rohidas Chavan

1 Introduction

Reservoirs/dams are usually used as a consistent source of water in arid as well as semiarid areas and their sustainability is of huge importance for the society (Araujo et al. 2006). However, various natural and anthropogenic changes in the river basin lead to affect the sediment transport in the stream flow. Excess sediment transport can affect the carrying capacity of channel networks as well as the storage capacity of reservoirs/dams and reduce the availability of water in the reservoirs. In addition, the sediment content in water affects the quality of river water. An important task for most of the hydrologists is to determine the reliable stream flow estimate which causes majority of the sediment transport within river basins/stream channels. Hudson and Mossa (1997) proposed that stream flow magnitude and its frequency can help in calculating the timing and fluctuation of sediment transports from river basins. Marginal changes in stream flow to sediment transport ratio over the channel networks modifies the channel morphology considerably which alters the stream flow event.

Wolman and Miller (1960) presented the concept of effective discharge which can be described as a product of the load of sediment carried by a given stream flow and the frequency of the stream flow. They introduced the concept of magnitude frequency analysis (MFA) to determine effective discharge. The effective discharge is considered as the stream flow which is responsible for transportation of majority of the sediments from a river basin or catchment over a long period of time. In MFA, the stream flow at a location is assumed to follow a continuous probability distribution (e.g., Normal, Lognormal, Exponential, Gamma, Generalized Pareto and Poisson) whereas the sediment transport is described by a power law function between stream flow and sediment rate. Subsequently, a transport effectiveness

S. Maheshwari (✉) · S. R. Chavan
Department of Civil Engineering, Indian Institute of Technology, Ropar, India
e-mail: 2017cez0003@iitrpr.ac.in

R. Jha et al. (eds.), *River and Coastal Engineering*, Water Science and Technology Library 117, https://doi.org/10.1007/978-3-031-05057-2_12

function is constructed by taking product of stream flow distribution with power law function. Finally, the effective discharge can be obtained by maximizing the transport effectiveness function with respect to stream flow. The determination of this effective discharge can help in assessment of stream flow for the consistency of channel networks and reservoirs/dams (Wahl et al. 1995; Hester et al. 2006), water structures construction, ecological refurbishment and environmental augmentation of rivers (Shields et al. 2003). Leopold (1994) advocated that small stream flow events have higher frequency, but these events do not have sufficient capacity to transport higher quantity of sediments. Contrary to this, catastrophic or large stream flow events have enough capacity to transport higher quantities of sediments but have less probability of occurrence. Consequently, the effective discharge is that stream flow which is in-between the small and large stream flows, that are capable of transporting most of the sediment loads on long-term basis (Wolman and Miller 1960; Lenzi et al. 2006; Ma et al. 2010). Many researchers have also suggested that stream flow events of a particular recurrence interval cannot be considered to be characteristic of effective discharge for all rivers because stream flow values are influenced by basin geology, catchment area, hydrologic system and sediment transportation (Ashmore and Day 1988; Nash 1994; Whiting et al. 1999; Phillips 2002; Lenzi et al. 2006). The aim of the present study is to check the validity of various probability distributions to calculate the frequency of stream flow event and provide estimates of effective discharge and recurrence interval based on MFA for stream gauges in Cauvery River basin.

2 Methodology

2.1 Goodness of Fit Test for Stream Flow Data

In this study, the stream flow data corresponding to various gauges in Cauvery basin were assessed to follow different frequency distributions using the Kolmogorov–Smirnov test (KS test) at 1% significance level. It is a nonparametric check of the equality of continuous probability distributions which can be used to compare data samples with a reference continuous probability distribution. Various probability distributions considered in the study are Normal, Lognormal, Exponential, Gamma, Generalized Pareto and Poisson.

2.2 Determination of Effective Discharge Using MFA

MFA involves assumptions about daily stream flow frequency and sediment transport rate. For stream flow, log transformed daily stream flow is assumed to follow continuous normal distribution as shown in Eq. (1).

$$f(Ql) = \frac{1}{\beta\sqrt{2\pi}} e^{-(Ql-\alpha)^2/2\beta^2} \tag{1}$$

where Ql is the log transformed daily stream flow, α and β are the mean and standard deviation of the log transformed stream flow respectively.

On the other hand, the sediment load is assumed to exhibit a power law function of daily stream flow as given by Eq. (2).

$$S = aQ^b \tag{2}$$

where S and Q are sediment load and daily stream flow respectively; a and b are empirically calculated coefficient and exponent.

Based on stream flow frequency and empirically derived sediment load, sediment transport effectiveness (E) is determined as,

$$E = \frac{aQ^b}{\beta\sqrt{2\pi}} e^{-(Ql-\alpha)^2/2\beta^2} \tag{3}$$

By maximizing the effectiveness function with respect to stream flow Q, "effective discharge", Q_e is obtained (Nash 1994).

$$For,\ \frac{dE}{dQ} = 0\ and\ Ql = \ln(Q)$$

$$\frac{d}{dQ}\left[\frac{a}{\beta\sqrt{2\pi}}\left\{Q^b.e^{-(\ln Q-\alpha)^2/2\beta^2}\right\}\right] = 0$$

$$\frac{a}{\beta\sqrt{2\pi}}\left[Q^b.e^{-(\ln Q-\alpha)^2/2\beta^2}.\left\{\frac{-2(\ln Q-\alpha)}{2\beta^2}.\frac{1}{Q}\right\} + e^{-(\ln Q-\alpha)^2/2\beta^2}.bQ^{b-1}\right] = 0$$

$$Q^b.e^{-(\ln Q-\alpha)^2/2\beta^2}.\left\{\frac{-2(\ln Q-\alpha)}{2\beta^2}.\frac{1}{Q}\right\} = -e^{-(\ln Q-\alpha)^2/2\beta^2}.bQ^{b-1}$$

$$\frac{Q_b}{Q^{b-1}.Q}\left\{\frac{(\ln Q-\alpha)}{\beta^2}\right\} = b$$

$$(\ln Q-\alpha) = b\beta^2 \Rightarrow \ln Q = b\beta^2+\alpha$$

$$Q_e = \exp(b\beta^2+\alpha) \tag{4}$$

2.3 Recurrence Interval Prediction

Recurrence interval of effective discharge Q_e is defined as the inverse of probability of stream flow equal or greater than the effective discharge. The predicted recurrence interval T_P of a particular stream flow Q, in years, is given as,

$$T_P = \frac{1/365.25}{1 - \phi\left[\frac{Ql-\alpha}{\beta}\right]}$$

where $\phi[.]$ represents the cumulative distribution function (CDF) of an assumed standard normal variable.

3 Study Area and Data Considered for MFA

The Cauvery River is one of the major rivers of the peninsula (Fig. 1). The River is also the main source for drinking, irrigation and electricity facilities to most part of southern Karnataka specifically Mysore region. Several dams have been built on the River. The Cauvery River originates from Brahmagiri Range of hills in the Western Ghats at an elevation of 1341 m (above MSL) at Talakaveri near Cherangala village of Kodagu District of Karnataka and has catchment area of 81,155 km^2 which is nearly 2.7% of the total geographical area of the country. The basin lies between 10°9′ to 13°30′ N latitudes and 75°27′ to 79°54′ E longitudes. It is circumscribed on the west by the Western Ghats, on the east by the Eastern Ghats and in north by the ranges separating it from Krishna River basin and Pennar River basin. The total length of the river from source to drain is 800 km. It has important tributaries joining from the left are the Arkavati, the Harangi, the Hemavati and the Shimsha. The river drains into the Bay of Bengal. Most of the basin is covered with agricultural land which accounts up to 66.21% of the total area and water bodies also have considerable coverage accounts for 4.09% of the total area (http://www.india-wris.nrsc.gov.in/wrpinfo/index.php?title=Cauvery).

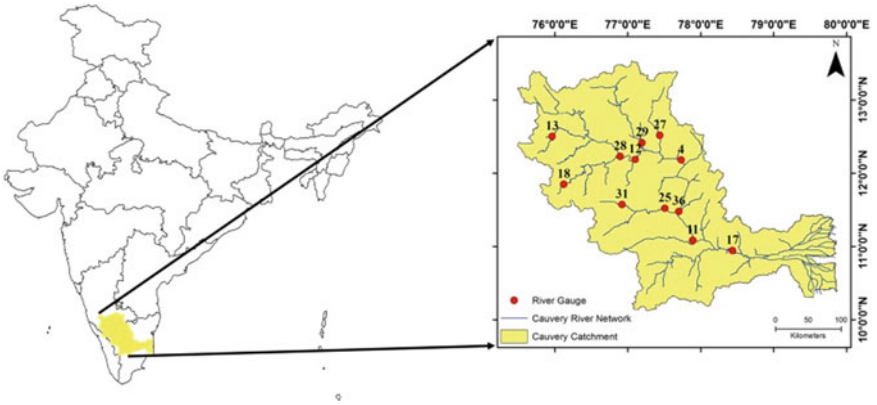

Fig. 1 Locations of the 12 gauges of Cauvery River basin considered in this study (numbers correspond to IDs of the stream gauges)

Gauge-Discharge Data and Sediment Concentration data were obtained from Water Resources Information System (WRIS), Government of India. Sediment load in terms of tons per day was calculated from Sediment Concentration (gram per liter) and Gauge-Discharge (cubic meter per second) using a suitable constant factor (86.4). In order to evade the problem of gaps in the data only years with complete accounts of Gauge-Discharge and sediment concentrations were included in the analysis. Finally, Gauge-Discharge and Sediment Concentrations data of 12 gauges were selected for the study. River basin and Stream flow characteristics are presented in Table 1.

4 Results and Discussions

4.1 KS Test for Fitting Probability Distributions to Daily Stream Flow Data

In this study, KS test at 1% significance level was considered for fitting probability distributions to daily stream flow data at each of the gauges. The distributions considered included Normal, Lognormal, Exponential, Gamma, Generalized Pareto, Poisson, etc. The stream flow at each of the gauges failed to pass the KS test for all distributions. Results are presented in Table 2. However, following the previous literature (Ashmore and Day 1988; Nash 1994; Whiting et al. 1999; Phillips 2002; Lenzi et al. 2006; Sichingabula 1999), the daily stream flow data was assumed to follow Log-normal distribution.

4.2 Stream Flow Distribution and Sediment Transport Analysis

As discussed earlier, Log-transformed stream flow data was considered in this study. Subsequently, that transformed stream flow data of each gauge was fitted with normal probability distribution. Sediment transport rate and the streamflow data was found to exhibit power law as shown in Fig. 2. Loglog plot of discharge and sediment transport rate for each of the 12 gauges was prepared. The plots are found to be fairly linear for all the gauges. The correlation coefficients (R^2) for power function of daily stream flow and sediment transport rate are provided in Table 3.

Table 1 River basin and stream flow characteristics

ID #	River gauge	Elevation (m)	Area (km^2)	Length of record (days)	Mean Q (m^3/s)	α	β	Skew	Kurto-sis
4	'Biligundulu'	255	36,682	13,149	238.5	4.83	1.08	0.43	2.80
11	'Kodumudi'	130	53,233	13,148	275.4	4.89	1.35	−0.33	2.46
12	'Kollegal'	622	21,082	11,689	199.9	4.55	1.16	0.18	3.82
13	'Kudige'	809	1934	6209	89.6	3.18	1.64	0.17	2.75
17	'Musiri'	89	66,243	12,418	260.8	4.44	1.80	−0.29	1.82
18	'Muthankera'	705	1260	13,879	77.4	2.92	2.12	−1.20	6.06
25	'Savandapur'	189	5776	10,958	20.3	2.72	0.77	−1.04	8.36
27	'Tbekuppe'	600	3500	365	6.0	1.72	0.38	0.95	4.50
28	'Tnarasipur'	635	7000	10,957	92.1	3.69	1.26	0.02	3.88
29	'Tkhalli'	580	7890	6209	23.3	1.92	1.94	−1.40	5.94
31	'Thengumarahada'	345	1370	2557	12.3	2.12	0.81	0.11	5.79
36	'Urachikottai'	168	44,100	3652	193.7	1.79	4.52	−0.37	1.25

ID: River Gauge ID according to WRIS
Elevation: Height of a river gauge above MSL (Mean Sea Level)
Area: Total area in river gauge in km^2, including non-contributing areas
Length of record: Number of days for which the continuous data is available for years
Mean Q: Average of daily stream flow in m^3/sec for the length of record
α: Mean of log-transformed daily stream flow.
β: Standard deviation of log-transformed daily stream flow
Skew: Skewness of log-transformed daily stream flow
Kurtosis: Kurtosis of log-transformed daily stream flow

Table 2 KS test for fitting different probability distributions

ID #	River gauge	Normal	Lognormal	Exponential	Gamma	Generalized pareto	Poisson
4	'Biligundulu'	Fail	Fail	Fail	Fail	Fail	Fail
11	'Kodumudi'	Fail	Fail	Fail	Fail	Fail	Fail
12	'Kollegal'	Fail	Fail	Fail	Fail	Fail	Fail
13	'Kudige'	Fail	Fail	Fail	Fail	Fail	Fail
17	'Musiri'	Fail	Fail	Fail	Fail	Fail	Fail
18	'Muthankera'	Fail	Fail	Fail	Fail	Fail	Fail
25	'Savandapur'	Fail	Fail	Fail	Fail	Fail	Fail
27	'Tbekuppe'	Fail	Fail	Fail	Fail	Fail	Fail
28	'Tnarasipur'	Fail	Fail	Fail	Fail	Fail	Fail
29	'Tkhalli'	Fail	Fail	Fail	Fail	Fail	Fail
31	'Thengumarahada'	Fail	Fail	Fail	Fail	Fail	Fail
36	'Urachikottai'	Fail	Fail	Fail	Fail	Fail	Fail

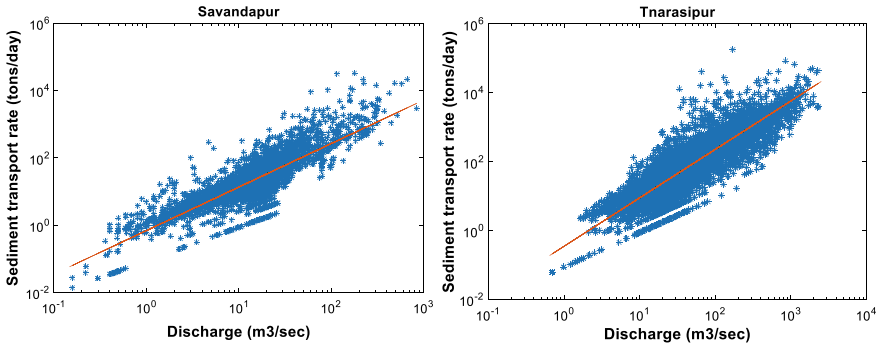

Fig. 2 Power law relationship between sediment transport rate and discharge observed at 2 typical stream gauges

4.3 Effective Discharge and Recurrence Interval Determination

Based on MFA, Effective discharge, $Q_{e,}$ was determined for 12 stream gauges in the Cauvery basin based on effectiveness function at each of the gauges (Fig. 3). In addition, the effective discharge estimates were also computed by finding the peak of transport effectiveness function and designated as Observed Q_e. Finally, recurrence intervals were calculated for Predicted Q_e and Observed Q_e (by ranking the daily stream flows, dividing the rank of Observed Q_e by the length of record in years). They were named as Predicted RI and Observed RI respectively. Results are tabulated in Table 3. Predicted Effective discharges and Observed Effective discharges are found

Table 3 Effective discharge and recurrence intervals determined for 12 stream gauges

River gauge	a	b	R^2	Predicted Q_e (m^3/s)	Predicted RI (years)	Observed Q_e (m^3/s)	Observed RI (years)
'Biligundulu'	0.15	1.53	0.891	739.9	0.055	739.9	0.065
'Kodumudi'	0.32	1.32	0.930	1484.6	0.074	1485.0	0.587
'Kollegal'	0.15	1.44	0.923	657.3	0.057	657.4	0.092
'Kudige'	0.60	1.22	0.983	656.2	0.124	656.0	0.783
'Musiri'	0.19	1.46	0.863	9544.8	0.640	6400.0	34.999
'Muthankera'	0.97	1.30	0.964	6378.4	0.922	2050.0	38.999
'Savandapur'	0.69	1.29	0.957	32.9	0.017	32.9	0.087
'Tbekuppe'	4.87	1.00	1.000	6.4	0.008	6.4	0.019
'Tnarasipur'	0.35	1.41	0.938	379.0	0.073	379.1	0.128
'Tkhalli'	0.51	1.38	0.938	1211.0	0.727	971.2	17.999
'Thengumarahada'	0.74	1.48	0.868	22.0	0.024	22.0	0.038
'Urachikottai'	0.13	1.10	0.988	37,030,426,837.5	8957.526	5854.5	10.999

where a and b are empirically calculated constant coefficient and exponent

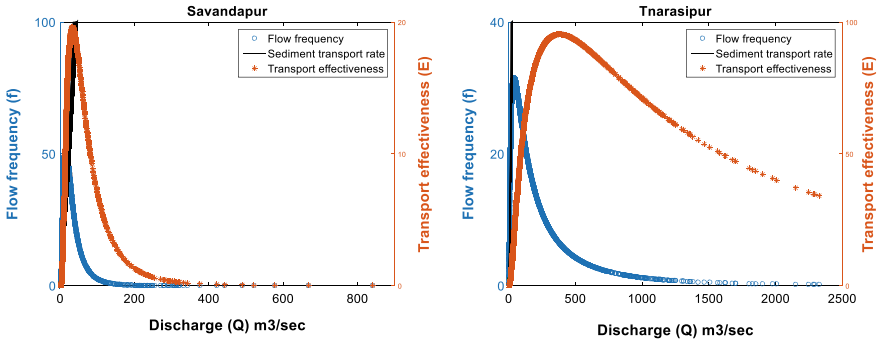

Fig. 3 Transport effectiveness curves of 2 typical stream gauges

to have significant correlation. This implies fit between the observed daily stream flow frequency and the log-transformed normal distribution is good.

4.4 Duration of Effective Discharge

Duration curves for discharge and sediment load show that they are quite similar in shape. The curves indicate that most of the discharges are able to transport sediments through the channels at each gauge, but the magnitude of sediment transport varies with the varying discharges consistently. The steep portion of the duration curve is

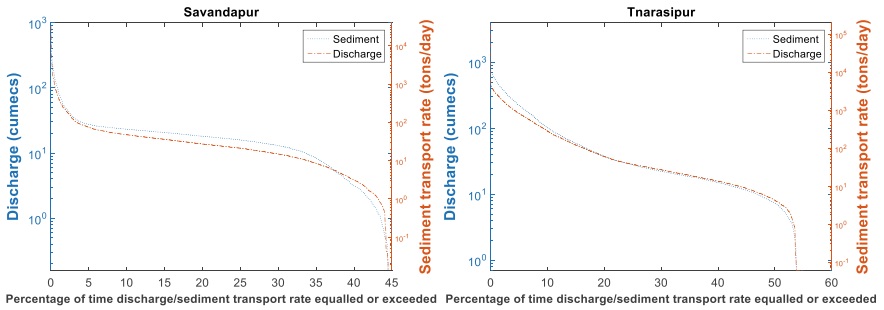

Fig. 4 Discharge and sediment load duration curves of 2 typical stream gauges

the zone of effective sediment transport. Sediment load duration curves show that the extreme low discharges do not have the capacity for sediment transport (Fig. 4).

5 Conclusions

In this paper, effective discharge and recurrence interval based on MFA were determined for 12 stream gauges in Cauvery River basin. The major observations from this study are as follows:

1. None of the (Normal, Lognormal, Exponential, Gamma, Generalized Pareto and Poisson) probability distribution was able to pass the KS test at 1% significance level.
2. Predicted Effective discharges and Observed Effective discharges are found to be in good correlation. This implies fit between the observed daily stream flow frequency and the log-transformed normal distribution is good.
3. The correlation coefficients (R^2) for power function of daily stream flow and sediment transport rate were found to be in the range 0.86 to 0.99. So, the assumption of sediment transport rate is a power function of daily stream flow is also valid.

References

Ashmore PE, Day TJ (1988) Effective discharge for suspended sediment transport in streams of the Saskatchewan River basin. Water Resour Res 24(6):864–870

De Araujo JC, Güntner A, Bronstert A (2006) Loss of reservoir volume by sediment deposition and its impact on water availability in semiarid Brazil. Hydrol Sci J 51(1):157–170

Hester G, Carsell K, Ford D (2006) Benefits of USGS streamgaging program—users and uses of USGS streamflow data. National Hydrologic Warning Council

Hudson PF, Mossa J (1997) Suspended sediment transport effectiveness of three large impounded rivers, US Gulf Coastal Plain. Environ Geol 32(4):263–273

Lenzi MA, Mao L, Comiti F (2006) Effective discharge for sediment transport in a mountain river: computational approaches and geomorphic effectiveness. J Hydrol 326(1–4):257–276
Leopold LB (1994) A view of the river. Harvard University Press
Ma Y, Huang HQ, Xu J, Brierley GJ, Yao Z (2010) Variability of effective discharge for suspended sediment transport in a large semi-arid river basin. J Hydrol 388(3–4):357–369
Nash DB (1994) Effective sediment-transporting discharge from magnitude-frequency analysis. J Geol 102(1):79–95
Phillips JD (2002) Geomorphic impacts of flash flooding in a forested headwater basin. J Hydrol 269(3–4):236–250
Shields FD, Knight SS, Morin N, Blank J (2003) Response of fishes and aquatic habitats to sand-bed stream restoration using large woody debris. Hydrobiologia 494(1–3):251–257
Sichingabula HM (1999) Magnitude-frequency characteristics of effective discharge for suspended sediment transport, Fraser River, British Columbia, Canada. Hydrol Process 13(9):1361–1380
Wahl KL, Thomas WO, Hirsch RM (1995) The stream-gaging program of the US Geological Survey. (No. 1123), US Geological Survey
Whiting PJ, Stamm JF, Moog DB, Orndorff RL (1999) Sediment-transporting flows in headwater streams. Geol Soc Am Bull 111(3):450–466
Wolman MG, Miller JP (1960) Magnitude and frequency of forces in geomorphic processes. J Geol 68(1):54–74

Pervious Concrete as an Effective Urban Flood Management Tool

Preeti Jacob, G. S. Dwarakish, G. O. Sharath, and G. N. Ramesh

1 Introduction

Pervious Concrete is a special type of concrete in which same size aggregates are used to increase the porosity. It is also called as no-fines concrete. It is a mixture of gravel or stone, cement, water and little or no sand which creates an open cell structure that allows water and air to pass through it. Huang et al. (2010) used latex, natural sand and fiber to improve the strength and drainage characteristics of pervious concrete. It is used to allow storm water to infiltrate through the pavement and reduce or eliminate the need for additional control structures, such as retention ponds. It is in fact one of the Best Management Practices (BMPs) recommended by US Environmental Protection Agency (EPA).

1.1 Mix Proportion

The pervious concrete has the same proportion as that of normal concrete but the amount of fine aggregates is reduced to create macro pores which allow the passage of air and water. The cementitious material generally used are Portland cement and pozzolonic cement. Flyash, quarry dust, ground granulated blast furnace slag can be used as additional cementitious materials. It is important to evaluate the critical water cement ratio to prevent flow of cement to lower layers (Nguyen et al. 2014). Admixtures are added to increase workability and setting time of the pervious concrete mix. Rounded aggregates are preferred since they yield higher strength to the concrete.

P. Jacob (✉) · G. O. Sharath · G. N. Ramesh
Department of Civil Engineering, CMRIT, Bangalore 560037, India
e-mail: preeti.j@cmrit.ac.in

G. S. Dwarakish
Department of Applied Mechanics & Hydraulics, NITK Surathkal, Mangaluru 575025, India

R. Jha et al. (eds.), *River and Coastal Engineering*, Water Science and Technology Library 117, https://doi.org/10.1007/978-3-031-05057-2_13

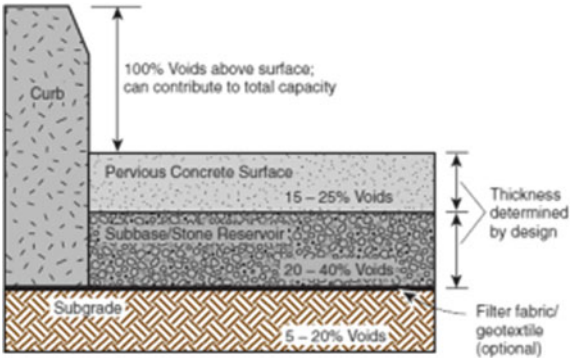

Fig. 1 Layers of pervious concrete pavement

Below the pervious concrete layer, there is a layer of stone aggregates as shown in Fig. 1 which are required for temporary storage of rain water. The depth of the layer depends on the amount of rainfall and the infiltration capacity of the soil.

1.2 Environment Benefits

Pervious concrete pavement systems provide valuable storm water management tool. Welker et al. (2013) conducted tests for evaluating the performance of pervious concrete for pollutant removal. By capturing the first flush of rainfall and allowing it to percolate into the ground, soil chemistry and biology are allowed to treat the polluted water naturally. Furthermore, by collecting rainfall and allowing it to infiltrate, groundwater and aquifer recharge is increased, peak water flow through drainage channels is reduced and flooding is minimized. The light colour of concrete pavements absorbs less heat from solar radiation than darker pavements, and the relatively open pore structure of pervious concrete stores less heat, helping to lower heat island effects in urban areas.

2 Research Significance

The aggregate used in the pervious concrete mix is greater than 6 mm size. The large size of aggregates in pervious concrete mixes causes raveling. It is a process of removal of top surface of aggregates due to weak bonding of aggregates. The materials used in the pervious concrete mix are cement, aggregates ranging between 2.36 and 4.75 mm in size, micro GGBS (Ground Granulated Blast Furnace Slag) as admixture and superplasticizer. The above aggregates are selected to provide a smoother surface and avoid ravelling of aggregates which is a common phenomena in pervious concrete. The smaller aggregates ensures better bonding between the

cement paste and the aggregates. The aggregate cement ratio is ranging from 3 to 4 and the water cement ratio is maintained at 0.3. The mix is not vibrated but it is compacted. The vibration causes the settlement of cement at the bottom creating uneven distribution of cement and also reducing the permeability of concrete. Lin et al. (2016) studied the effect of vehicle vibration on clogging of pervious concrete. The permeability and clogging potential is determined for the mix to study the impact of smaller pore size on the permeability. Though the permeability is reduced, the strength of the concrete increases making it useful for wider applications.

3 Materials and Methodology

3.1 Composition and Mix Design

The composition in pervious concrete mix is designed in such a way that it has an open pore structure. A balance is maintained between voids, strength, paste content and workability (Kia et al. 2017). Generally in this mix, fine aggregate is reduced to create interconnected voids in concrete. The most important requirement is to provide optimum cement paste to bind aggregates without paste drain at the bottom. Xie et al. (2018) established that empirical functions for the mechanical properties of pervious concretes can be maximized by optimizing W/C, SP dosage, and mixture proportion of cementitious materials under the same rheological properties. The materials used in the pervious concrete mix are cement, aggregates ranging between 2.36 and 4.75 mm in size, micro GGBS (Ground Granulated Blast Furnace Slag) as admixture and superplasticizer. The above aggregates are selected to provide a smoother surface and avoid ravelling of aggregates which is a common phenomena in pervious concrete. The aggregate cement ratio is taken from 3, 3.5, 3.7 and 4. The mix is not vibrated but it is compacted. The vibration causes the settlement of cement at the bottom creating uneven distribution of cement and also reducing the permeability of concrete. Admixtures are added to increase the strength of the mix. The constituents of the mix are as follows:

3.1.1 Cement

The cement used is OPC Grade 53 with a compressive strength of 60 MPa is used.

3.1.2 Aggregates

The aggregates used in the mix have a narrow gradation of 2.36–4.75 mm. The narrow gradation is used to increase the number of pores in the concrete and improve permeability. The gradation is the last range of fine aggregate. It is chosen to reduce

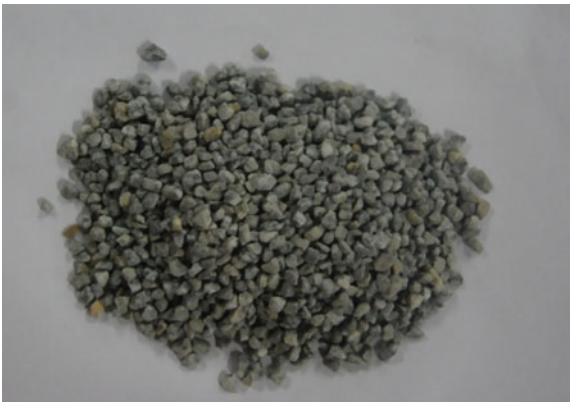

Fig. 2 Aggregate size ranging from 2.36 to 4.75 mm

the effect of ravelling and increase the compressive strength of concrete. Ravelling is a process of chipping off of aggregates on the top surface due to weak bonding. The aggregates are mixed in their natural moisture content to avoid the absorption of excess water during mixing. Rounded aggregates are used to increase the compressive strength (Fig. 2).

3.1.3 Micro GGBS

There are many admixtures added to the pervious concrete mix to improve its mechanical properties. Zhang et al. (2017) used flyash, silica fume, mineral powder, ethylene vinyl acetate, latex and polyethylene fiber to improve the freeze—thaw properties of pervious concrete. GGBS (Ground Granulated Blast-furnace Slag) is a by-product from the blast-furnaces used to make iron. It is a cementitious material which is used widely in conventional concrete. Micro GGBS is ultrafine GGBS where the particle size is in nanometers. It is formed by quenching molten iron slag. The chemical composition depends on the composition of the raw materials in the iron production process. It is greyish-white in colour which has a composition of 40% calcium oxide, 35% silica, 13% alumina and 8% magnesia (Fig. 3).

3.1.4 Mix Design

The mix design for pervious concrete is done based on weigh batching. Haselbach et al. (2015) concluded that screening appears to not impact the hydraulic functionality of pervious concrete made with the local gravel in the Porto Alegre region. Table 1 shows the different proportion of aggregate/cement and water/content for mix design. In some of the specimens, there was paste drain at the bottom due to fluidity of cement paste. Ketcheson and Price (2014) conducted laboratory experiments on pervious concrete slabs to determine the effect of sand application and

Fig. 3 Micro GGBS (Ground granulated blast slag)

Table 1 Mix proportions

Aggregate/cement ratio	Water/cement ratio	Amount of Micro GGBS	Superplasticizer	Status
3	0.3	1/5th of cement weight	5% of water weight	There was max settlement at the bottom. Permeability was almost zero
3.5	0.3	1/5th of cement weight	5% of water weight	Less settlement. Permeability can be calculated
3.7	0.3	1/5th of cement weight	5% of water weight	There was max settlement at the bottom. Permeability was almost zero
3.7	0.3	No GGBS	5% of water weight	Less settlement. Permeability can be calculated
4.0	0.3	1/5th of cement weight	5% of water weight	No settlement

temperature (frozen and thawed conditions) on flow dynamics and salt retention/transport. The pervious concrete mix cannot be vibrated since paste drain occurs resulting in non-uniform spread of porosity and decrease the permeability drastically. The pervious concrete should be casted in controlled compaction environment to attain near uniform permeability across the vertical profile. The below table shows

Fig. 4 Specimen showing cement paste drain at the bottom

the different types of mixes used in the study. For each mix, six cubes for compressive strength and six cylinders for permeability was casted (Fig. 4).

3.2 Sample Preparation

The cement and micro GGBS was mixed well. It was mixed with the aggregates. The superplasticizer was added to the water and the water was poured to the mix in a pan mixer. It was cast in cube of 15 cm side for compressive strength and cylinder of diameter 15 cm and length 15 cm for permeability and clogging test. It was only compacted in three layers. Vibration caused the cement paste to settle down. It was kept for 48 h in the cast and then demoulded and cured in a water tank (Fig. 5).

3.3 Experimental Set up

Fwa et al. (2015) fabricated a constant head test apparatus for permeability and clogging test porous asphalt and pervious concrete and plotted deterioration trends of permeability coefficient k as a function of clogging cycles. The setup allows a test specimen with a 150-mm diameter and thickness varying from 40 to 200 mm to be tested. Their permeability and clogging resistance increased substantially when mixture porosity was increased beyond 20%. A transparent acrylic pipe of diameter 15 cm was fabricated for evaluating the permeability of concrete. The fabrication can be dismantled into three parts: the upper part for maintaining head, the middle part for holding the specimen and the lower part for collecting water. A tap is inserted in the upper portion to maintain constant head. The exfiltrate is collected at the bottom and released through a tap system. The tap can also be used to create a pressured atmosphere beneath the pervious concrete layer which effects the permeability of

Fig. 5. 150 mm × 150 mm × 150 mm specimen for compressive strength

pervious concrete. The three parts are sealed with the help of clay. The pervious concrete specimen is wrapped with transparent plastic to avoid the leakage of water through the sides of the concrete (Fig. 6).

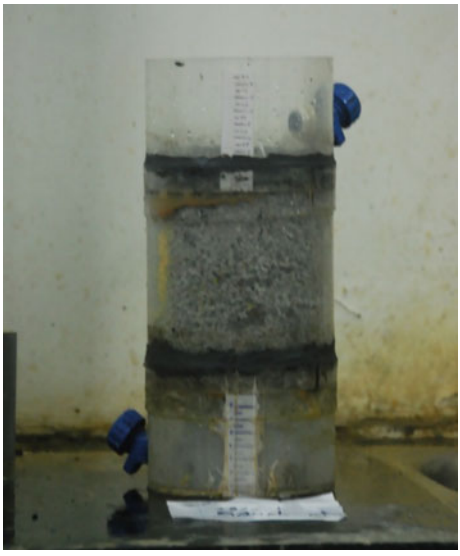

Fig. 6 Fabrication of transparent acrylic for permeability

Fig. 7 Compressive testing of pervious concrete specimen

3.4 Properties of Concrete

3.4.1 Compressive Strength Test

Compression test is the most common test conducted on hardened concrete for finding out the strength of concrete. The IS standard compression test as per IS 516: 2004 (Methods of Tests for Strength of Concrete) is carried out on cubes of size 150 mm × 150 mm × 150 mm. The cast iron moulds are used to prevent distortion of specimen. The test is carried out on 7th, 14th and 28th from the date of curing. The specimens were cured for 48 h as after 24 h, the concrete was not set properly. McCain and Dewoolkar (2010) studied the compressive strength and permeability using falling head method for different water cement ratio (Fig. 7).

3.4.2 Porosity

The porosity or void ratio of the concrete is the amount of voids present in the concrete. It is calculated by the method adopted by Haselbach which is given by the formula (Description 1997).

$$P = \left[1 - \left\{\frac{(W_D - W_S)}{\rho_w * V_T}\right\}\right] * 100.$$

where:

P = porosity, %, W_D = oven dry weight, g, W_S = submerged weight, g, ρ_w = density of water, g/cm^3, V_T = Volume of the specimen

$$V_T = \frac{\pi D_{\text{avg}}^2 \text{H}_{\text{avg}}}{4}$$

The pervious concrete mixes are designed for target porosity. Though there is relationship between porosity and permeability, it can be weakly correlated as interconnected pores change depending on the amount of compaction, size of the aggregates etc.

3.4.3 Permeability Test

Permeability (or hydraulic conductivity) refers to the ease with which water can flow through a concrete. It is the intrinsic property of the porous material to transmit liquid under a hydraulic gradient. The permeability is calculated at saturated conditions. It is found by the principle of constant head or falling head. Both the methods are used for finding permeability for pervious concrete. Since there is no standard method to measure permeability of pervious concrete, a fabricated unit made of transparent acrylic is used to measure the permeability. The principle of constant head permeameter is used. A constant head of 5 cm is maintained for the test. The time taken for one cm rise in the collecting tank is measured to calculate the permeability.

3.4.4 Clogging Test

Since pervious concrete allows the passage of air and water through its surface, there are chances that dust particles, soil from nearby areas or clayey water can clog the pervious concrete matrix. Lee et al. (2015) analysed clogging process as a function of deposited sediments. It is important to understand the clogging potential of pervious concrete to schedule its maintenance cycles. Haselbach (2010) performed clogging cycle tests emulating natural conditions on several cores for kaolin, bentonite and red clay with the suspension concentrations more than 10 g/l simulating extreme rainfall conditions until the sample was non-functional. Clogging causes the decrease of infiltration and permeability over time as particles gets embedded in the concrete matrix. To understand the effect of clogging, it is exposed to six soil condition. The first two samples are clay and sand. For the remaining four, soil samples are collected from four areas in east Bangalore namely K R Puram, Mahadevapura, HAL and Koramagala. A concentration of 10 g/l is prepared by mixing 30 g of soil sample with 3 L of water. It mixed at 40 rpm for 1 min in a motorized mixer, Fig. 8. This solution is passed through the matrix and the same principle of calculating permeability is used. It is repeated for three cycles to evaluate the decrease of permeability. Deo et al. (2010) used fine (0.1–0.84 mm) and coarse (0.84–1.8 mm) grained river sand were used as clogging material.

Fig. 8 Mixing of soil particles for clogging test

4 Results and Discussion

4.1 Compressive Strength

The compressive strength is calculated for 7th, 14th and 28th day for aggregate cement ratio of 3, 3.5, 3.7 and 4 with micro GGBS as admixture. To understand the effect of micro GGBS on the strength of concrete, at aggregate cement ratio of 3.7, the mix is prepared with and without micro GGBS.

4.1.1 Influence of Aggregate/Cement Ratio

Aggregate/ cement ratio is the major influencing factor in determining the variation of permeability (Chandrappa and Biligiri 2016). The compressive strength is calculated using the average of two trials. The graph shows that the maximum compressive strength of 34.6 MPa is achieved at 3.5 aggregate/cement ratio. The mix of aggregate cement ratio of 3 and 3.7 showed cement paste drain at the bottom which has decreased the compressive strength of concrete due to non-uniform distribution of cement paste across the vertical profile. Since there is no vibration, the amount of compaction, the point of compaction and the pressure of compaction plays an important role in determining the compressive strength (Fig. 9).

4.1.2 Influence of Micro GGBS

To understand the effect of micro GGBS on the strength of concrete, a mix was prepared with and without the admixture. The admixture showed more than 100%

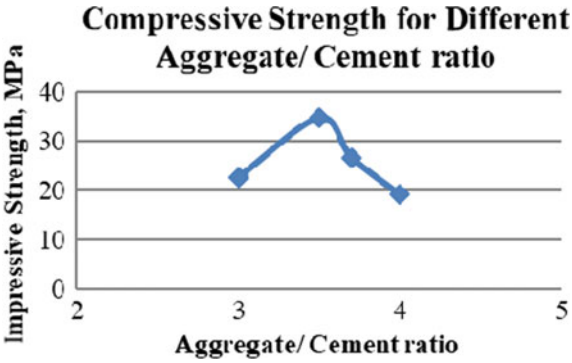

Fig. 9 Comparison of 28 day compressive strength for different aggregate cement ratio

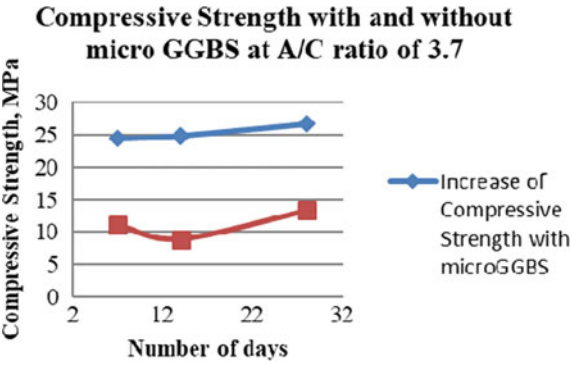

Fig. 10 Influence of microGGBS on the compressive strength of concrete

increase in the strength. Since the amount of micro GGBS is additionally added, the volume of cement—GGBS paste is more for the aggregates to bind together. Since it is a nano particle, GGBS infused pervious concrete has a fine layer of GGBS coating on the surface. Further, experiments can be conducted to calculate the optimum amount of microGGBS to be added as an admixture (Fig. 10).

4.1.3 Rate of Increase of Compressive Strength

The increase of compressive strength varies across different aggregate cement ratio. 63–91% of the strength is achieved within 7 days of curing. The specimen with aggregate cement ratio of 3.7, which had the maximum cement paste drain showed less increase of strength after 7 days. Though the aggregate cement ratio of 3 has a dense concrete matrix, it showed reduced strength due to its non uniformity of cement binder across the vertical profile. 3.5 ratio shows a good strength gain and records the highest compressive strength at 34.6 MPa. The permeability can be improved by adding suitable admixtures (Fig. 11).

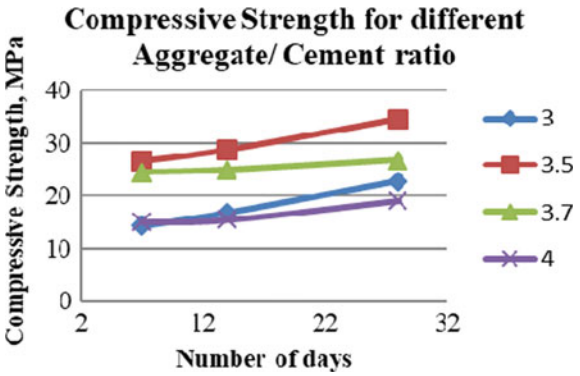

Fig. 11 Rate of increase of compressive strength for 7, 14 and 28 days

4.2 Porosity

Chindaprasirt (2008) concluded that compressive strength in the range of 22–39 MPa is achieved with porosity in the range of 15–25% by maintaining low water cement ratio of 0.2–0.25. Of the average porosity ranged between 13 and 18% with aggregate cement of 4 and 3 recording the maximum and minimum porosity of 18% and 13% respectively.

4.3 Permeability

The permeability was analyzed for aggregate cement ratio of 4 since there was no settlement at the bottom. For the other mixes, the permeability was calculated but not analyzed since there was partial settlement at the bottom (Fig. 12).

The specimens are only compacted in three layers each 15 times. Since it is hand compacted, there is variation in the permeability. The porosity calculated above is the total porosity. It is important to calculate the interconnected pores to have a strong correlation with permeability (Deo et al. 2010). The permeability varies 0.0009–0.003 m/s for the same mix proportion. The range can be reduced with proper control over the compaction methodology.

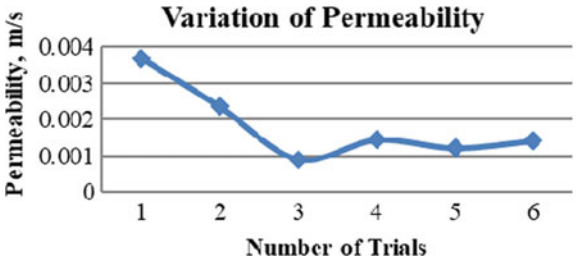

Fig. 12 Variation of permeability for specimens of aggregate cement ratio of 4

4.3.1 Reduction of Permeability Due to Clogging

The six specimens are exposed to six different soil samples as mentioned in Sect. 3.4.4. Walsh et al. (2014) developed a laboratory study to record how sediment accumulation affects the hydraulic conductivity of pervious concrete. D_{50} of the sediments were found out to identify the mean size of the particle. The D_{50} or median size of aggregates is determined by performing sieve analysis on the soil samples (Table 2). For clay, wet sieve analysis is performed since the particles size is less than 0.002 mm. The 0th cycle shows the initial permeability without any soil particles. From the 1st cycle, the specimen is exposed to solution containing the soil particles. The decrease in permeability is almost 50% in specimen exposed to clayey soil. The collected soil samples across four sampling points in East Bangalore show similar trend in decrease of permeability. Cui et al. (2016) measured the electrical conductivity as an indicator of pervious concrete clogging, which is much more convenient. The continuous pore clogging process generally includes three phases, i.e. quick clogging, temporary mitigation of clogging and progressive clogging.

Figure 13 shows the R squared value for the decrease in permeability. The values

Table 2 Median particle size of collected soil

S. No.	Soil type	D_{50} (mm)
1	Sand	0.58
2	Maha	0.388
3	K R Puram	0.389
4	HAL	0.914
5	Kora	0.747

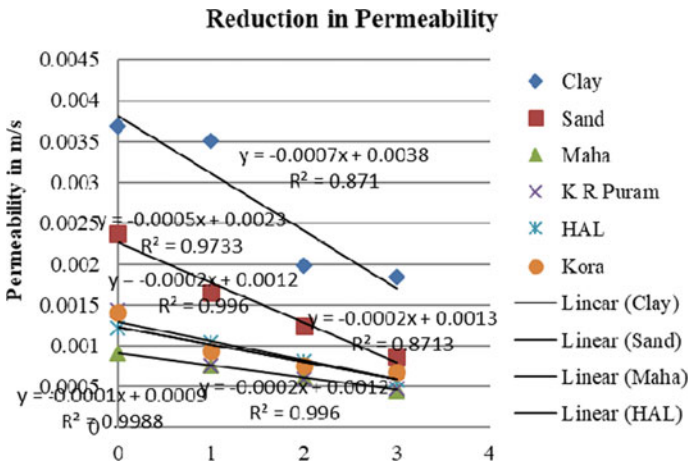

Fig. 13 Goodness of fit for regression model

are greater than 0.8 indicating that it fits the linear regression model with good accuracy.

5 Conclusions

The compressive strength and hydraulic properties are analysed for aggregate cement ratio varying from 3 to 4 maintaining the water cement ratio as 0.3. The use of micro GGBS as admixture is used to improve the strength of pervious concrete. The clogging potential of pervious concrete exposed to different soil conditions were analysed to schedule the maintenance cycles required to increase the life of pervious concrete.

Acknowledgements I thank Prakash Sreenivasan, RMC Readymix (India) A Division of PRISM CEMENT LIMITED for providing us Alccofine—microGGBS for the project work.

References

Chandrappa AK, Biligiri KP (2016) Comprehensive investigation of permeability characteristics of pervious concrete: a hydrodynamic approach. Constr Build Mater 123(July):627–637

Chindaprasirt P (2008) Cement paste characteristics and porous concrete properties. 22:894–901

Cui X, Zhang J, Huang D, Tang W, Wang L, Hou F (2016) Experimental simulation of rapid clogging process of pervious concrete pavement caused by storm water runoff. Int J Pavement Eng 8436(November):1–9

Deo O, Sumanasooriya M, Neithalath N (2010) Permeability reduction in pervious concretes due to clogging: experiments and modeling. J Mater Civ Eng 22(7):741–751

Description M (1997) Technical bulletin. 0(September):0–3

Fwa TF, Lim E, Tan KH (2015) Comparison of permeability and clogging characteristics of porous asphalt and pervious concrete pavement materials. Transp Res Rec J Transp Res Board 2511(2511):72–80

Haselbach L, Dutra VP, Schwetz P, Silva Filho LCP (2015) A pervious concrete mix design based on clogging performance in Rio Grande do Sul Introduction Problem Statement. In: International conference on best practices for concrete pavements, vol 1, pp 1–11

Haselbach LM (2010) Potential for clay clogging of pervious concrete under extreme conditions. J Hydrol Eng 15(1):67–69

Huang B, Wu H, Shu X, Burdette EG (2010) Laboratory evaluation of permeability and strength of polymer-modified pervious concrete. Constr Build Mater 24(5):818–823

Ketcheson S, Price J (2014) Transport and retention of water and salt within pervious concrete pavements subjected to freezing and sand application. J Hydrol…, 19(Marsalek 2003):1–7

Kia A, Wong HS, Cheeseman CR (2017) Clogging in permeable concrete: a review. J Environ Manage 193:221–233

Lee JG, Borst M, Brown RA, Rossman L, Simon MA (2015) Modeling the hydrologic processes of a permeable pavement system. J Hydrol Eng 20(5):04014070

Lin W, Park DG, Ryu SW, Lee BT, Cho YH (2016) Development of permeability test method for porous concrete block pavement materials considering clogging. Constr Build Mater 118:20–26

McCain G, Dewoolkar M (2010) Porous concrete pavements. Transp Res Rec J Transp Res Board 2164:66–75

Nguyen DH, Sebaibi N, Boutouil M, Leleyter L, Baraud F (2014) A modified method for the design of pervious concrete mix. Constr Build Mater 73:271–282

Walsh SP, Rowe A, Ph D, Asce AM, Guo Q, Asce M (2014) Laboratory scale study to quantify the effect of sediment accumulation on the hydraulic conductivity of pervious concrete. J Irrig Drain Eng 140(6):1–7

Welker A, Jenkins J, McCarthy L, Nemirovsky E (2013) Examination of the material found in the pore spaces of two permeable pavements. J Irrig Drain Eng 139(4):278–284

Xie X, Zhang T, Yang Y, Lin Z, Wei J, Yu Q (2018) Maximum paste coating thickness without voids clogging of pervious concrete and its relationship to the rheological properties of cement paste. Constr Build Mater 168:732–746

Zhang J, Ming R, Ma G, Li L, Cui X (2017) Experimental study on the effects of admixtures on freezing-thawing resistance of pervious concrete. In: ICTIM

Numerical Simulation of Wave Conditions for Mangrol Fishing Harbour

Santosh Kori and Prabhat Chandra

1 Introduction

India is surrounded by water on the east, west, and south coasts. The fisheries industry in India is huge. Most importantly, it is the source of livelihood for a large section of economically backward population in coastal regions of India. As demanded by a section of the fishermen society, a fishery harbour at about 1 km to the west of the existing Mangrol fishery harbour was reconnoitered by Fisheries Department of Government of Gujarat. The Mangrol Phase III fishing Harbour is located (latitude 21° 06′ N and longitude 70° 05′ E) (Fig. 1). The near-shore bathymetry at the site is having mild slope and the coastline orientation is 135° N. Mean tidal level is about 1.93 m. The wave conditions during the non monsoon period between October and May sea are relatively calm. During the monsoon period, the waves are very critical. Wave disturbance in the harbour basin plays an important role in functioning of the fishery harbour, hence, the information of waves becomes a very vital parameter for designing and planning of fishery harbour. Initial layout plan of Mangrol fishery harbour phase III had two breakwaters viz. Eastern Breakwater of length 737 m and Western breakwater of length 532 m with south westerly harbour entrance opening of 135 m. The predominant wave directions were SSW, SW, WSW and West near Mangrol fishery harbour. Due to south westerly entrance opening of Mangrol fishery harbour phase III, it was exposed to direct attack of SW waves which resulted in down time for operation of fishing activity about 75 days in a year. To reduce wave disturbance in the harbour basin and also to provide safe navigation and maneuvering near the entrance, necessary modifications were suggested in the proposed harbour layout. This paper presents Mathematical model studies carried to optimize the harbour layout to reduce wave disturbance in the harbour basin and also to provide safe navigation and maneuvering near the entrance.

S. Kori (✉) · P. Chandra
CWPRS, Khadakwasla, Pune 411024, India
e-mail: kori.sk@cwprs.gov.in

R. Jha et al. (eds.), *River and Coastal Engineering*, Water Science and Technology Library 117, https://doi.org/10.1007/978-3-031-05057-2_14

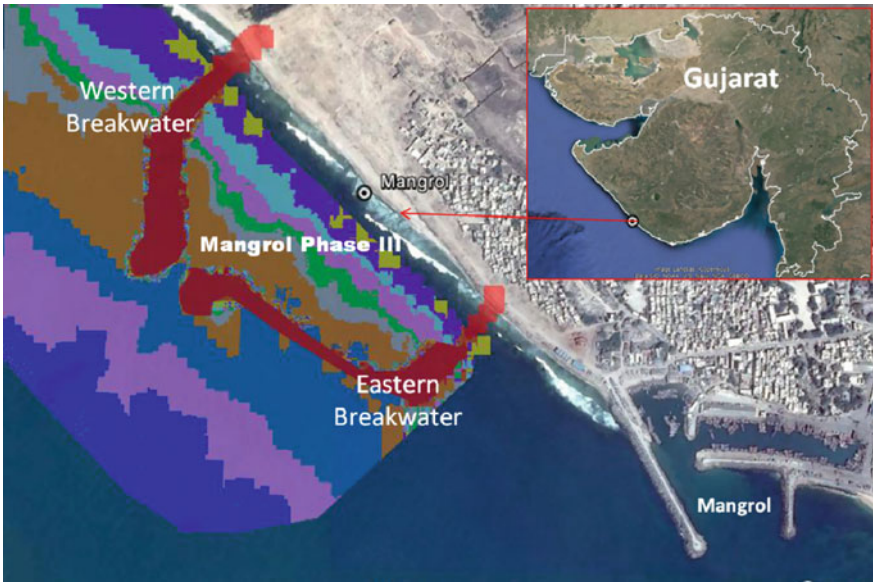

Fig. 1 Location map and initial layout of Mangrol fishing harbor

2 Methodology

In the absence of measured near-shore wave data, offshore wave data reported by India Meteorological Department as observed from ships plying in deep waters off Mangrol were transformed by MIKE 21 (SW) Spectral Wave model to get the near-shore wave climate at the fishing harbour. These were taken as boundary conditions for evaluating wave propagation in the harbour. MIKE21- (BW) Boussinesq Wave was used for assessment of near-shore wave field and wave penetration in the fishing harbour.

3 Wave Transformation

The wave climate near Mangrol was obtained by transforming the offshore wave data of 13 years from 2000 to 2012 year off Mangrol, by India Meteorological Department as observed from ships plying in deep waters, using MIKE 21 SW model. Model area considered for SW model is shown in Fig. 2. Bathymetry in the model region of about 100 km $\times$ 100 km and extending upto 120 m depth contour was schematized with an unstructured triangular mesh. The model was run to obtain near-shore wave climate at the inshore point at (−) 14 m depth contour.

The Offshore wave climate during the entire year indicates that the predominant wave directions in deep water are from SSW to West with the maximum significant

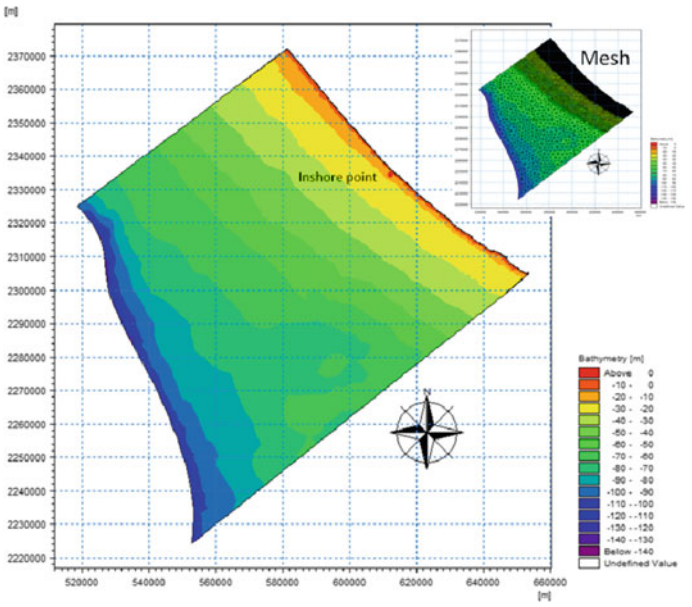

Fig. 2 Bathymetry for wave transformation from offshore to nearshore

wave heights of the order of 4.5 m (Fig. 3). Frequency distribution of near-shore waves for entire year is shown in Fig. 3. The predominant incident wave directions at (−) 14 m depth are SSW, SW, WSW and W.

Significant Wave conditions shown in Table 1 were considered for simulation of wave propagation in the harbour using MIKE21-BW model.

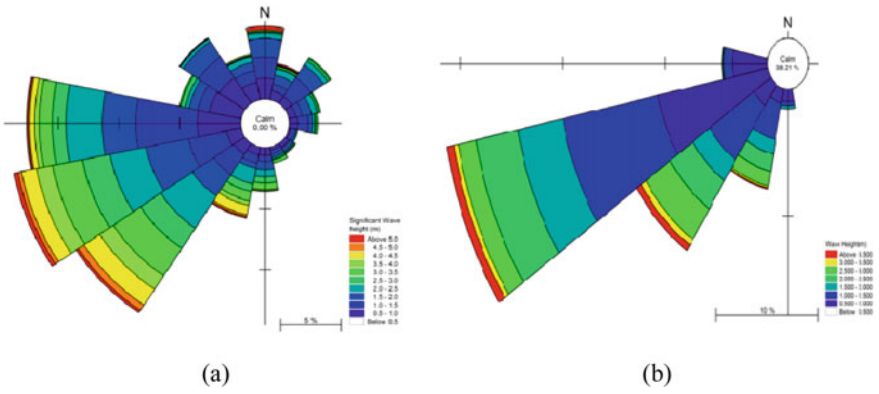

Fig. 3 **a** Offshore wave rose, **b** near shore wave rose

Table 1 A input wave conditions for MIKE-21 BW model

Wave direction (deg. N)	Wave period (s)	Significant wave height (m)
202.5 (SSW)	10	3
225 (SW)	10	3
247.5 (WSW)	10	3
270 (W)	10	2

4 Wave Tranquility

Wave propagation inside the harbour was simulated for the above mentioned incident wave conditions for the harbor layout proposed by government of Gujarat. MIKE21-BW was used for studying the wave disturbance in the harbour (DHI 2014). The model is based on time dependent Boussinesq equations of conservation of mass and momentum obtained by integrating the three-dimensional flow equations without neglecting vertical acceleration. The model simulates the processes of shoaling, refraction, diffraction from breakwater tips and bed friction. It also takes into account partial reflections from the boundaries, piers and breakwaters. The wave tranquility studies were conducted for the initial layout and then to evolve the modified layout as described in succeeding paragraphs.

Initial Layout

The initial layout consisted of two breakwaters; 532 m long north breakwater and 737 m long south breakwater with 135 m (center to center) wide opening at the harbor entrance. The plots of bathymetry and layout are shown in Fig. 4. MIKE 21 BW model was run for four predominant incident wave directions as shown in Table 1. Area of 1.5 km by 1.5 km was discretised with a grid size of 5 m by 5 m. Simulations were carried out for the tidal level at +2.51 m corresponding to MHWS.

Permissible wave height for fishing boats in a harbour is 0.3 m. Maximum significant wave heights observed at different locations in the proposed Mangrol Harbour Basin, obtained from studies with MIKE 21-BW model are given in Table 2. The wave disturbances in the proposed harbour basin are shown in Fig. 5.

It could be seen that wave heights are generally within the permissible tranquility limit of 0.3 m near Outfitting Quay, Wharf and Gravity wall almost for entire year. However landing area in front of the harbour opening is exposed to direct wave attack. Wave heights in these areas are greater than the permissible tranquillity limit of 0.3 m. Therefore, it was required to modify the initial layout to reduce wave disturbance in the harbour basin throughout the year.

Modified Layout

The layout was modified to obtain the adequate wave tranquility in the harbour throughout the year. Also, due consideration was given to obtain the suitable wave conditions near the entrance to avoid the broad side wave attack to ensure safe

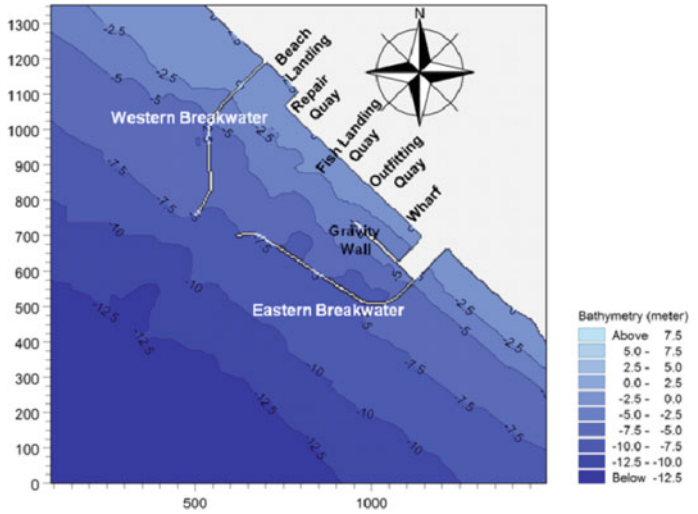

Fig. 4 Bathymetry and proposed layout of Mangrol

Table 2 Wave heights at various locations inside the harbour for initial layout

No.	Incident wave directions/Incident wave height	202.5°N/3.0 m	225°N/3.0 m	247.5°N/3.0 m	270°N/2.0 m
	Locations				
1	Beach landing	0.31	0.6	0.32	0.06
2	Repair quay	0.34	1.2	1.2	0.16
3	Fish landing quay	0.34	1.3	1.6	0.22
4	Outfitting quay	0.26	0.4	0.4	0.23
5	Wharf	0.16	0.16	0.2	0.13
6	Gravity wall	0.28	0.24	0.3	0.31

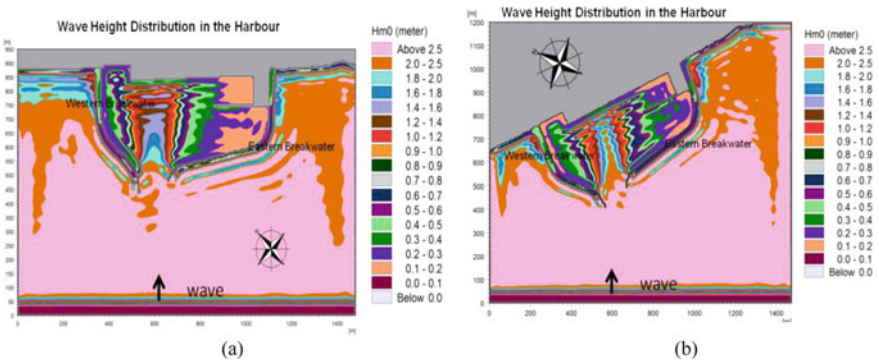

Fig. 5 Wave height distribution for the initial proposal of harbor. **a** For waves from 225°, **b** for Waves From 247.5°

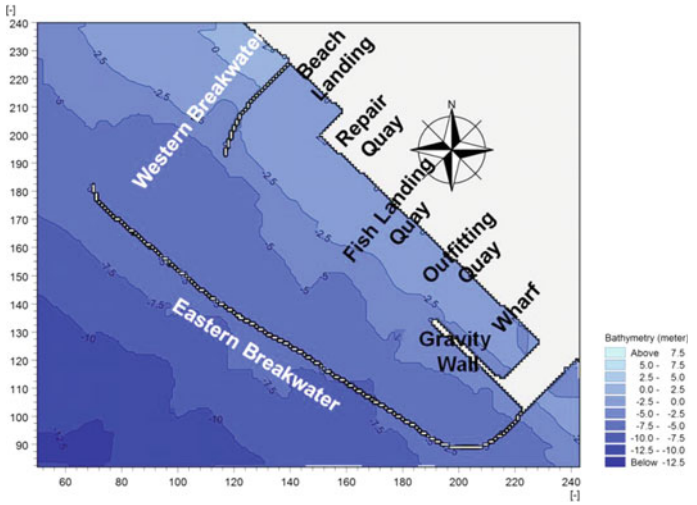

Fig. 6 Modified layout of Mangrol harbour

navigation and maneurving. After studying various alternatives, the modified layout was evolved as shown in Fig. 6.

As per PIANC/IAPH (1997), width of entrance channel should be 5 to 8 times of beam of design ship with additional 1.3 times of beam of ship for cross wind and current conditions or 0.7–1.0 times of LOA of design ship. The modified harbour layout consisted of Eastern Breakwater of length 1110 m and Western breakwater was reduced to the of length 250 m with an increased opening of 240 m. Eastern breakwater length at (−) 6 m depth contour and overlapping will provide shadow zone for the fishing vessels from the attack of broad side high waves while entering into the habour to ensure safe maneuvering. Western breakwater length at (−) 4 m depth contour will provide wider entrance of 240 m which will again help for safe operation of boats. Maximum significant wave heights observed at different locations in the Mangrol Harbour Basin for modified layout are given in Table 3 and wave disturbance in the modified harbour basin are shown in Fig. 7.

5 Conclusions

- In the nearshore region of Mangrol, at (−) 14 m water depth, the predominant wave directions are from SSW, SW, WSW and West directions.
- In the harbour layout suggested by Government of Gujarat, wave heights are generally within the permissible tranquility limit of 0.3 m near Outfitting Quay, Wharf and Gravity wall almost for entire year. However, landing area in front of the harbour opening is exposed to direct wave attack. Wave heights in these areas

Table 3 Wave heights at various locations inside the harbour with modified layout

No.	Incident wave directions/Incident wave height	202.5°N/3.0 m	225°N/3.0 m	247.5°N/3.0 m	270°N/2.0 m
	Locations				
1	Beach landing	0.21	0.23	0.18	0.09
2	Repair quay	0.15	0.24	0.21	0.12
3	Fish landing quay	0.15	0.23	0.38	0.19
4	Outfitting quay	0.11	0.16	0.24	0.16
5	Wharf	0.14	0.18	0.23	0.11
6	Gravity wall	0.12	0.14	0.22	0.23

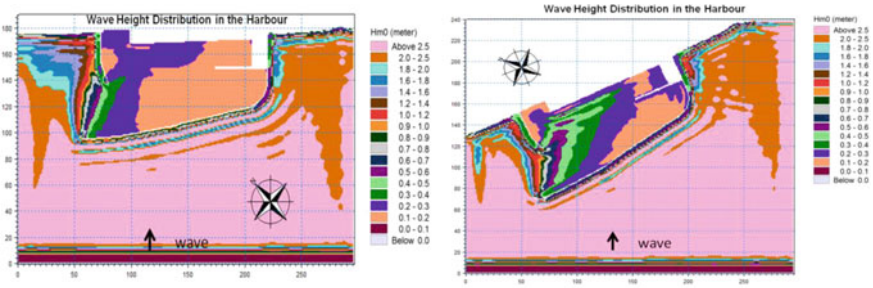

Fig. 7 Wave height distribution in the modified harbor. **a** For waves from 225°, **b** For waves from 247.5°

would be greater than the permissible wave height of 0.3 m for about 75 days in a year.

- To reduce wave disturbance in the harbour basin the harbour layout was modified and about 70% reduction in the wave heights near the exposed berthing area was observed. The modified layout (Eastern breakwater at (−) 6 m depth of length 1110 m and Western breakwater at (−4) m depth of length 250 m with north westerly harbour entrance of 240 m) will provide shadow zone for the fishing vessels from the attack of broad side high waves while entering into the habour and also provide tranquility conditions throughout the year near the berths and for parking of vessels inside the harbour. Due consideration was given to the direction and net quantity of prevailing littoral drift while evolving the harbour entrance.

References

DHI (2014) Boussinesq waves module user guide. In: DHI (ed) Boussinesq waves module user guide. DHI

PIANC/IAPH (1997) Report on approach channels a guide for design. PTC2 report of WG 30 June 1997

Erodibility of Cohesive Sediments Using Jet Erosion Tests

Sarfaraz Ali Ansari

1 Introduction

Determination of the erodibility of cohesive sediments is important for predicting scour below or around hydraulic structures, stream channel degradation, riverbank stability, soil losses from fields, potential landform evolution for mine covers, and the stability of embankments etc. (Allen et al. 1997; Annandale 2006; Arulanandan et al. 1975; ASTM Standard D5852 2000 2007; Beltaos and Rajaratnam 1974; Clark and Wynn 2007; Hanson et al. 1990; Hanson and Cook 1997; Hanson 1993; Mazurek et al. 2001; Mazurek 2010; Shurgar et al. 2007; Thoman and Niezgoda 2008). Erodibility accounts for two parameters: the critical shear stress, τ_c and the erodibility coefficient, k_d. At present, there is no widely accepted, reliable method to estimate these two parameters for cohesive sediments.

Many techniques to determine erodibility of soils have been developed. These are: rotating cylinder apparatus (Moore and Masch 1962), a rotating annular flume (Krishnappan 1993), open-channel flume tests (Hanson 1990a), closed-channel tests such as the Erosion Function Apparatus (Briaud et al. 2001), and vertical impinging jet (Bhasin et al. 1969; Hollick 1976; Hanson 1991; Tolhurst et al. 1999; Hanson and Cook 2004; Ansari 2017, 2018). For reliability, an in-situ technique for determining erodibility is preferable. This is because the sediment is not disturbed by sampling and jet-tests can be conducted easily. Hanson and Cook (2004) have presented analytical procedures for using the jet test for quantitative estimation of both the critical shear stress and erodibility coefficient of a sediment respectively based on the time development of scour hole.

The objective of this paper is to study the variation of coefficient of erodibility with respect to the time in cohesive sediments for some of the data available in literature covering a wide range of pertinent variables.

S. A. Ansari (✉)
Professor, Civil Engineering Department, A.M.U., Aligarh, U.P. 202002, India
e-mail: sarfaraz59.cv@amu.ac.in

R. Jha et al. (eds.), *River and Coastal Engineering*, Water Science and Technology Library 117, https://doi.org/10.1007/978-3-031-05057-2_15

2 Experimental Equipment and Procedure

The experimental work being reported herein is the part of a major experimental programme for study on the influence of cohesion on local scour, details of which are given in Ansari (1999) and Ansari et al. (2002, 2003, 2007 etc.). These experiments were conducted in the Hydraulics Laboratory of Indian Institute of Technology, Roorkee.

2.1 Properties of Clay and Sand Used

A laser particle size analyser was used to obtain the particle size distribution curve for the clay. The clay material was found to have median size, d_{50} size equal to 0.0053 mm and geometrical standard deviation equal to 2.1 while sand had d_{50} size of 0.27 mm and geometrical standard deviation of 1.48. Relative density of sand was 2.65. Other properties of clay materials were: Liquid limit, $W_L = 53\%$, Plastic limit, $W_P = 27\%$, Plasticity index = 26%, Maximum dry density, = 17.4 KN/m^3, Optimum Moisture Content, O.M.C. = 18%, Cohesion, C_u at Optimum Moisture Content = 65.66 KN/m^2, Angle of internal friction = 14° and Relative density = 2.60. As per IS-1498, the clay was classified as *CH* i.e. clay with high compressibility. The differential free swell test was obtained as 28.6% indicating this clay to be moderately expansive as per IS-2911.

The X-ray diffraction (X.R.D.) test was conducted for identification of clay minerals present in clay. The percentage composition of the clay minerals was found to be Kaoline = 10%, Illite = 74.5% and Montmorillonite = 15.5%. In the present investigation, the maximum possible range of antecedent moisture content has been considered so that it may represent various states of cohesive sediments found in natural conditions. The tests were performed at all the possible moisture consistencies of the cohesive sediment ranging from very soft with negligible cohesion (viscous state) to hard soil with a very high value of cohesion viz. 250 KN/m^2. Cohesive sediments were prepared by properly mixing clay material with sand.

2.2 Tank for Experimentation on Jet-Scour

A circular steel tank having diameter 1.25 m and depth l.25, filled with the desired sediment upto a height of −0.65 m was used for experiment on scour due to submerged vertical round jet as shown in Fig. 1. It was ensured that the diameter of the tank was sufficiently large so that it would have no influence on scour process. The impinging jet was produced by a nozzle located at the bottom of a cylindrical pipe of diameter 0.0254 m and of variable length and provided with a suitable constant head arrangement. The nozzle could be located at any desired vertical height above the

Fig. 1 View of experimental setup used for scour studies

prepared sediment bed. Velocity distributions across the jet diameters were observed and found to be symmetric in nature. The jet discharge was measured by using a venturimeter provided in the inlet pipe. Only one nozzle of diameter 12.5 mm was used and two jet velocities of 1.7 m/s and 2.0 m/s were used with jet heights of 0.15 m and 0.20 m respectively.

3 Methods of Analysis

Commonly, the erosion rate of cohesive streambanks is simulated using the excess shear stress equation (Partheniades 1965; Hanson 1990a, 1990b), which is defined as:

$$\frac{dJ}{dt} = k_d \left[\frac{\tau_o J_p^2}{J^2} - \tau_c \right] for J \geq J_p \tag{1}$$

$$\varepsilon_r = k_d(\tau_i - \tau_c)^a \tag{2}$$

where, k_d = the erodibility or detachment coefficient (m^3/N-s), τ_i = average hydraulic boundary shear stress (Pa), τ_c = the critical shear stress (Pa) and a = empirical exponent commonly assumed to be unity (Hanson 1990a, 1990b; Hanson and Cook 2004). And

$$\tau_i = \tau_o \left(\frac{J_p}{J} \right)^2 J_p = C_d d_o, \ \tau_c = \tau_o \left(\frac{J_p}{J_e} \right)^2, \ \tau_o = C_f \rho U_o^2,$$

where, τ_o = the maximum stress due to the jet velocity at the nozzle, J_p = the potential core length, J = the Scour Depth from jet origin, J_i = the initial jet orifice height, C_d = the diffusion constant = 6.3, d_o = the nozzle diameter, C_f = the coefficient of friction = 0.00416, ρ = the fluid density, U_o = the velocity at the jet nozzle, g = the gravity acceleration constant, h = the differential head measurement.

The relationship between the time of scouring measured from the start of a test, t, and the scour depth can be expressed as (Stein et al. 1993; Hanson and Cook 1997, 2004; Mazurek 2010)

$$\mathrm{t} = \mathrm{T_r}\left(0.5\ln\left(\frac{1+\mathrm{j_*}}{1-\mathrm{j_*}}\right) - \mathrm{j_*} - 0.5\ln\left(\frac{1+\mathrm{j_{i*}}}{1-\mathrm{j_{i*}}}\right) - \mathrm{j_{i*}}\right) \tag{3}$$

where Tr is a reference time defined as $Tr = Je/(k_d\,\tau_c)$; Je is the sum of the impingement height J_i and the equilibrium depth of scour at the jet centreline (dse); J_* is the dimensionless scour depth, defined as $J^* = J/Je$; and Ji^* is the initial height of the soil surface expressed in dimensionless form as $Ji^* = J_i/Je$. The general form (Blaisdell et al. 1981) of the equation with an asymptote from which the ultimate depth of scour can be computed with

$$\mathrm{x} = \left[(\mathrm{f} - \mathrm{f_o})^2 - \mathrm{A}^2\right]^{0.5} \tag{4}$$

wherein, $f = \log[J/d_o] - \log[(U_o t)/d_o]$, $f_o = \log(J_e/d_o)$, $x = \log[(U_o t)/d_o]$,

A = the value for the semi-transverse and semi-conjugate axis of the hyperbola, U_o = the velocity of the jet at the origin, t = time of data reading, d_o = orifice diameter.

4 Analysis, Results and Discussions

Figures 2 and 3 and Table 1 were prepared to study the variation of the erodibility coefficient and scour depth with time for cohesive sediments covering a wide range of pertinent variables such as antecedent moisture, plasticity index dry density, clay content etc. In these Figures and Table, it may be noted that there is large variation in the values of k_d with respect to time required for the development of scour hole which ultimately affects the average value of k_d. With the increase in dry density, erodibility coefficient was found to decrease as well as k_d was found to decrease with increase in plasticity index for a given sediment and flow characteristics.

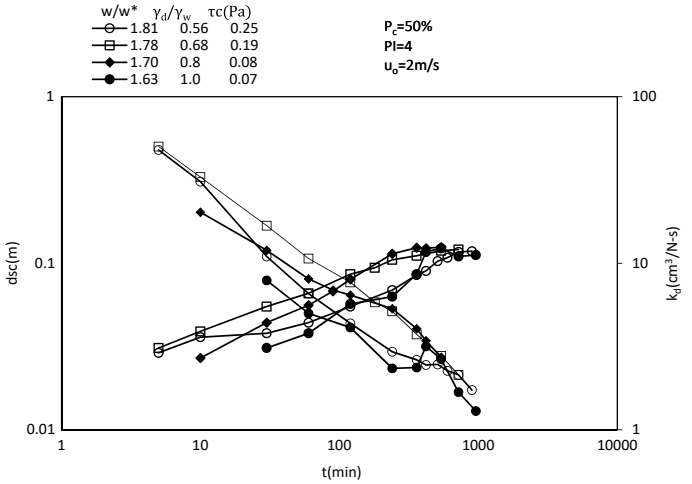

Fig. 2 Variation of erodibility coefficient and scour depth with test duration for the data of (Ansari 1999)

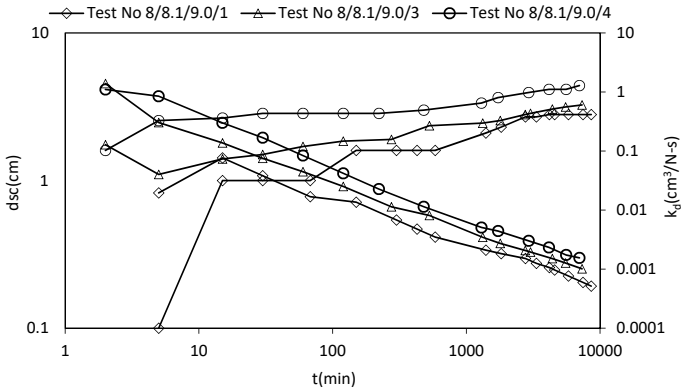

Fig. 3 Variation of erodibility coefficient and scour depth with test duration for the data of (Mazurek 2001)

Table 1 Various parameters considered (Mazurek 2001)

Test No.	Q (l/s)	Sv (kPa)	w_f (%)	w_c (%)	w_p (%)	T (°C)	k_d (cm^3/N-s)	τ_c (Pa)
8/8.1/9.0/1	0.45	20.4	28.0425			16	0.011	29.36
8/8.1/9.0/3	0.45	20.2	27.41	25.52	29.625	22.3	0.13	51.04
8/8.1/9.0/4	0.45	16.1	27.26	26.5	26.5	11.8	0.19	38.72

5 Conclusions and Suggestions

The calculated erodibility coefficient was found to strongly depend on the test duration for given sediment and hydraulic conditions i.e. geotechnical properties of sediments influence erosion characteristics for given hydraulic conditions. A large variation in the values of k_d with respect to time required for the development of scour hole was found. A better method for estimating the critical shear stress and ultimately average erodibility coefficient from jet test results is likely required.

References

Allen PM, Arnold J, Jakubowski E (1997) Design and testing of a simple submerged-jet device for field determination of soil erodibility. Environ Eng Geosci 3(4):579–584

Annandale GW (2006) Scour technology: mechanics and practice. McGraw Hill, New York

Ansari SA (1999) Influence of cohesion on local scour. Ph.D. thesis, Dept of Civil Engg., IIT, Roorkee, India

Ansari SA (2017) Estimation of soil erodibility by jet erosion technique. IGS Kanpur chapter, 13–14 Oct 2017, IIT., Kanpur, India

Ansari SA (2018) Discussion of "using an improved jet-erosion test to study the influence of soil parameters on the erosion of a silty soil" by Nguyen V-N, Courivaud J-R, Pinettes P, Souli H, Fleureau J-M 143(8) 04017018(1–11) J Hydraul Eng ASCE, 2018, 144(11):07018013

Ansari SA, Kothyari UC, Ranga Raju KG (2002) Influence of cohesion on scour around bridge piers. J Hydraul Res 40(6):717–729

Ansari SA, Kothyari UC, Ranga Raju KG (2003) Influence of cohesion on scour under submerged circular vertical jets. J Hydraul Eng, A.S.C.E. 129(12):1014–1019

Ansari SA, Kothyari UC, Ranga Raju KG (2007) Incipient motion characteristics of cohesive sediments. ISH J Hydraul Eng 13(2):108–121

Arulanandan K, Loganathan P, Krone R (1975) Pore and eroding fluid influences on surface erosion of soil. J Geotech Div, ASCE 101(GT1):51–66

ASTM Standard D5852, 2000 (2007) Standard test method for erodibility determination of soil in the field or in the laboratory by the jet index method. ASTM International, West Conshohocken, Pennsylvania, USA

Beltaos S, Rajaratnam N (1974) Impinging circular turbulent jets. J Hydr Div, ASCE 100(10):1313–1328

Bhasin RN, Lovell CW, Toebes GR (1969) Erodibility of sand-clay mixtures as evaluated by a water jet. Technical Report No. 8, Purdue University Water Resources Research Center, Purdue University, Lafayette, Indiana

Blaisdell FW, Anderson CL, Hebaus GG (1981) Ultimate dimensions of local scour. J Hydraul Div, ASCE 107(HY3):327–337

Briaud JL, Ting FCK, Chen HC, Cao Y, Han W, Kwak KW (2001) Erosion function apparatus. J Geotech Geoenv Engr, ASCE, 127(2):105–113

Clark LA, Wynn TA (2007) Methods for determining streambank critical shear stress and soil erodibility: implications for erosion rate predictions. Trans ASABE 50(1):95–106

Daly ER, Fox GA, Al-Madhhachi AT, Miller RB A scour depth approach for deriving erodibility parameters from jet erosion test. Trans ASABE, 56(6):1343–1351

Hanson GJ (1990a) Surface erodibility of earthen channels at high stresses: part I. Trans ASAE 33(1):127–131

Hanson GJ (1990b) Surface erodibility of earthen channels at high stresses: part II. Trans ASAE 33(1):132–137

Hanson GJ (1991) Development of a jet index to characterize erosion resistance of soils in earthern spillways. Trans ASAE 34(5):2015–2020
Hanson GJ (1993) Effects of consolidation on soil erodibility. A.S.A.E. Paper 932091, St. Joseph, MI.A.S.A.E
Hanson GJ, Cook KR (1997) Development of excess shear stress parameters for circular jet testing. In: Proceedings, 1997 ASAE annual international meeting, Minneapolis, Minnesota, Paper 972227
Hanson GJ, Cook KR (2004) Apparatus, test procedures, and analytical methods to measure soil erodibility in-situ. Trans ASAE 20(4):455–462
Hanson GJ, Robinson KM, Temple DM (1990) Pressure and stress distributions due to a submerged impinging jet. In: Hydraulic engineering, proceedings 1990 national conference, ASCE, Reston, VA, pp 525–530
Hollick M (1976) Towards a routine assessment of the critical tractive forces of cohesive soils. Trans ASAE 19:1076–1081
Krishnappan BG (1993) Rotating circular flume. J Hydr Eng 119(6):758–767
Mazurek KA (2001) Scour of clay by jets. Ph.D. thesis, University of Alberta, Edmonton, Alberta, Canada
Mazurek KA (2010) Erodibility of a Cohesive Soil using a submerged circular turbulent jet tests. In: 2nd Joint Federal interagency conference, Las Vegas, NV, June 27–July 1, 2010
Mazurek KA, Rajaratnam N, Sego DC (2001) Scour of cohesive soil by submerged circular turbulent impinging jets'. J Hydr Eng 127(7):598–606
Moore WL, Masch FD Jr (1962) Experiments on the scour resistance of cohesive sediments. J Geophys Res 67(4):1437–1449
Partheniades E (1965) Erosion and deposition of cohesive soils. J Hydraul Div, ASCE 91(1):105–139
Shurgar D, Kostaschuk R, Ashmore P, Desloges J, Burge L (2007) In situ jet-testing of the erosion resistance of cohesive streambeds. Can J Civ Eng 34:1192–1195
Stein OR, Julien PY, Alonso CV (1993) Mechanics of jet scour downstream of a headcut. J Hydraul Res 31(6):723–738
Thoman RW, Niezgoda S (2008) Determining erodibility, critical shear stress, and allowable discharge estimates for cohesive channels: case Study in the Powder River basin of Wyoming. J Hydr Engr, ASCE, 134(12):1677–1687
Tolhurst TJ, Black KS, Shayler SA, Mather S, Black I, Baker K, Paterson DM (1999) Measuring the in-situ erosion shear stress of intertidal sediments with the cohesive strength meter (CSM). Estuar, Coast, Shelf Sci 49:281–294

Numerical Simulation of Desilting Chamber Using Flow 3D

M. Z. Qamar, M. K. Verma, A. P. Meshram, and Neena Isaac

1 Introduction

FLOW-3D is general-purpose CFD software. It employs specially developed numerical techniques to solve the equations of motion for fluids to obtain transient, three-dimensional solutions to multi-scale, multi-physics flow problems. Various components of desilting chamber may be modelled in this CFD program. The best possible alternative may then be tested on a physical model. The applicability of Flow3D in modeling of desilting chambers and flow simulation are discussed in this paper with the help of data and results of Mangdechhu H.E. Project, Bhutan for which physical model studies have already been carried out at CWPRS, Pune. Formulation of geometry, meshing, initial and boundary conditions for the simulation are described. Various velocity profiles and sediment movement profiles are also included. The number of particles escaping through silt flushing tunnel and head race tunnel are ascertained by providing baffles at these two locations. The results in terms of settling efficiency for 0.2 mm size particles would be obtained by sediment count through silt flushing tunnel and head race tunnel. The results obtained from CFD simulation and physical model studies will be analyzed to improve the design parameters for forthcoming studies.

2 Hydraulic Model Studies for Desilting Chamber

Hydraulic model studies, for individual projects are used at CWPRS, Pune as the principle tool for assessing the performance of desilting chamber in respect of settling as well as flushing. Several studies have been conducted on geometrically similar

M. Z. Qamar (✉) · M. K. Verma · A. P. Meshram · N. Isaac
Central Water & Power Research Station, Pune 411024, India
e-mail: ziaul_qamar@rediffmail.com

R. Jha et al. (eds.), *River and Coastal Engineering*, Water Science and Technology Library 117, https://doi.org/10.1007/978-3-031-05057-2_16

scale models at CWPRS for various types of desilting chambers for optimizing the design. The model scales are based on the availability of cost, space, head and discharge etc. The experience has been that bigger models yield better and more reliable results. Transparent Perspex sheets are used for convenience of fabrication and for visualization of the flow in the chamber. View of a typical model at CWPRS is shown in Photo 1.

Generally, model studies for desilting chamber are conducted for testing the adequacy / feasibility of the desilting chamber for 90% removal of suspended sediment coarser than 0.2 mm and efficacy of flushing tunnel below desilting chamber in transporting the settled sediment (Verma et al. 2015). During the experiments, a known quantity of low specific gravity material, the crushed and sieved walnut shell powder is injected at the inlet corresponding to designed sediment concentration. The view of prototype and its replica in model for Teesta H.E. Project, Stage V, Sikkim is shown in Photo 2.

Generally, suspended sediment is removed from desilting chambers by continuous flushing through silt flushing tunnel provided below. An extra discharge of about 20% of design discharge is drawn through power intake for continuous flushing of settled sediment to maintain the desired settling efficiency. The layout and size

Photo 1 Model of desilting chamber

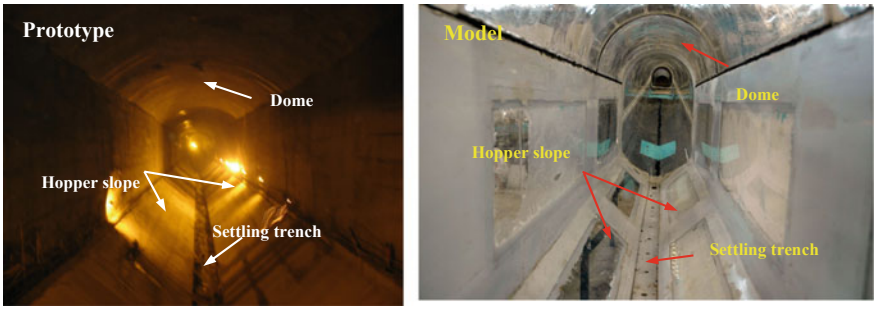

Photo 2 Inside view of chamber in prototype and model

of the flushing tunnels are so worked out that flushing velocity is maintained and total discharge did not exceed 20% of the design discharge. During the experiments, the inlet water level is maintained between MDDL and FRL. Design discharge is maintained at inlet, head race tunnel and silt flushing tunnel discharges are maintained at the outlet separately. During the experiments, if the performance of various parts of desilting chamber viz. inlet transition, outlet transition, settling trench etc. is not satisfactory, the modifications are done in consultation with project authorities and concerned model part is re-fabricated and tested to evolve optimum design. For design parameters, the scope of reduction of length of desilting chamber is especially worked out, which saves a huge amount of project cost as these are costly structures.

3 Numerical Modeling Through CFD

After the development of numerical methods for simulation of two dimensional flow patterns, better mathematical models such as Computational Fluid Dynamics (CFD) software are available which may be used for 3 D numerical model studies for the desilting chamber. In the settling chamber, flow is three dimensional especially in the inlet divergence and outlet convergence. At the inlet, there are structural arrangements for proper distribution of flow. Similarly, at the outlet the arrangements are made for smooth skimming off the flow layers containing less sediment in the suspension. Geometrical approximations are required to be made in two dimensional mathematical modeling which is not considered adequate in the mathematical modeling. All these add to the three dimensionality of the flow. The limitation of mathematical models is their ability to represent only two dimensional flows whereas; the flow in the prototype is three dimensional which is being nowadays taken care of by CFD.

Computational Fluid Dynamics (CFD) is the computer solution of the governing equations for fluid flows (the conservation of mass, momentum, and energy) for three dimensions. The equations are discrete and solved using the numerical methods (Flow 3D User's Manual). Using CFD software is in many ways similar to setting up a physical experiment. If in a physical model, experiment is not set up correctly to simulate a real-life situation, then the results will not reflect the real-life solution, similar is the case for numerical model. It is important to ensure that the problem being modeled represents the actual physical situation as closely as possible. Simple hand calculations (Bernoulli's equation, energy balance, wave speed propagation, boundary layer growth, etc.) help in selecting physics and parameters, and provide checks to compare with results.

To conduct CFD model studies, the first step is to make exact 3 D geometry of the desilting chamber. Then mesh is created to define the flow area, inlet and outlet boundary conditions are specified and model is run for simulation. Initially, desilting chamber model studies may be done using the CFD program before conducting physical model studies as it is comparatively difficult to make additions and alterations in a physical model. Various design parameters may be tested on this CFD program and

only the best possible alternative may be selected to conduct physical model studies to finalize the design. Thus, CFD can be used as a complementary tool for analysis of flow in desilting chambers.

4 Mathematical Formulation

The Flow-3D simultaneously solves the Reynolds-averaged Navier–Stokes (RANS) equations for fluid flow, the conservation of mass equation, and scalar transport equations (FLOW-3D user manual, ver. 10.1). Flow 3D numerically solves the continuity and momentum equations using finite volume approximation. The flow region is subdivided into a mesh of fixed rectangular cells. Various design parameters such as length of desilting chamber, length and bed slope of inlet transition, outlet transition, size of silt flushing tunnel, size and spacing of openings connecting main chamber with silt flushing tunnel etc. may be modelled in this CFD program. The best possible alternative may then be tested on a physical model.

4.1 Meshing and Geometry

The desilting chamber consists of inlet and outlet transition, main chamber, silt flushing tunnel (SFT) and several small openings connecting main chamber with silt flushing tunnel. It is not possible to capture the whole geometry using a single mesh; therefore, several mesh layers of different sizes are to be used at different locations. In spite of this, the mesh count becomes huge and difficult to run the simulation as shown in Photo 3. Smaller cell size reduces time step and increases the computational time.

To avoid this situation, the problem was simplified; since the total number of particles escaping through the openings is same as that through SFT, it was eliminated from the geometry as shown in Photo 4. The number of openings also reduced to

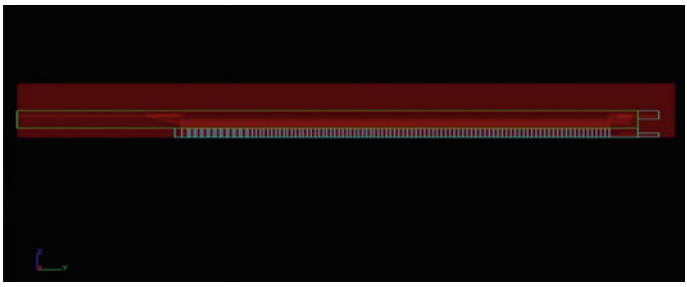

Photo 3 Meshing and geometry with SFT

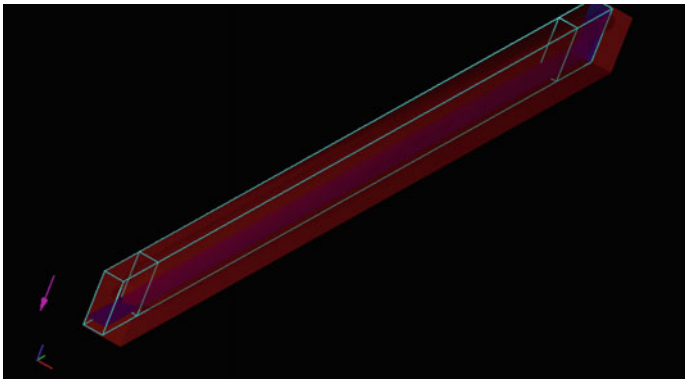

Photo 4 Meshing and geometry without SFT

18 (instead of 54) maintaining the same cross sectional area. Single mesh block was sufficient to model the entire domain. This reduced the number of mesh blocks by eradicating the adjacent and nested mesh blocks. Moreover, as the desilting chamber is symmetrical on both sides longitudinally, meshing is done on one half of the geometry only. This gave lesser mesh count and reduced computational time. To know the number of particles escaping through SFT and head race tunnel (HRT) two baffles were provided.

1. At bottom (Bot1) of desilting chamber to ascertain number of settled particles escaping to silt flushing tunnel through bottom openings and
2. Near the outlet (Out1) to ascertain number of particles escaping through outlet tunnel (HRT).

Following conditions were imposed on the model:

- Total number of particles at inlet: 10,00,000 @ 500/sec
- Particle Size = 0.2 mm
- Inlet Discharge Q = 33.925 m^3/s
- Outlet Discharge = 29.5 m^3/s; Flushing Discharge = 4.425 m^3/s
- Number of flushing holes: 18
- Models activated: (1) Gravity and non-inertial reference frame (2) Particles and (3) Viscosity and turbulence
- Simulation run time: 5400 s; Total Number of real cells = 8,00,000.

Following boundary conditions were employed. The forward flow direction is at Y axis.

- Xmin Symmetry; Xmax Symmetry
- Ymin Volume Flow Rate 33.925 m^3/s; Ymax Outflow
- Zmin Volume Flow Rate 4.425 m^3/s;Zmax Specified Pressure

5 Velocity Profiles

Velocity profiles inside desilting chamber at various time frames during simulation run are shown in Photos 5, 6, 7 and 8.

Photo 5 Velocity profile at T = 100 s

Photo 6 Velocity profile at T = 5400 s

Photo 7 Velocity profile near inlet; orthographic view at T = 5400 s

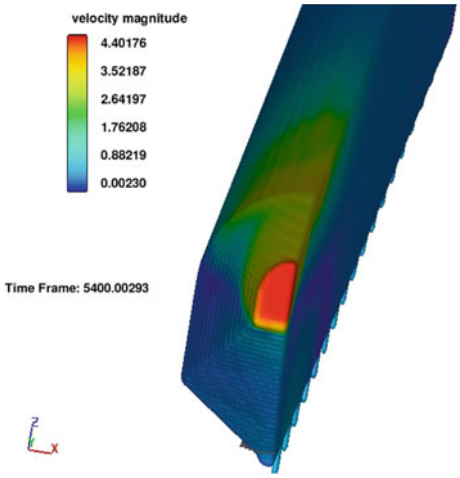

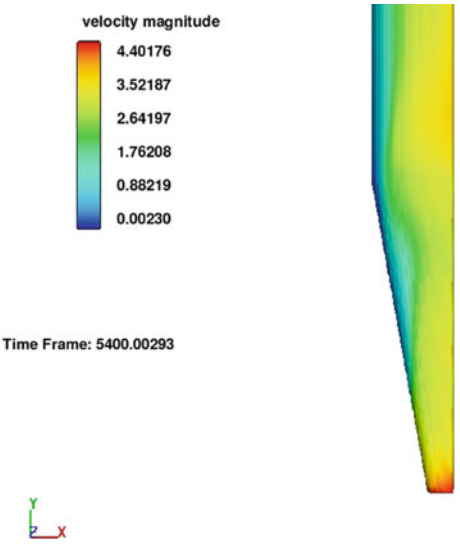

Photo 8 Velocity profile near inlet; top view at T = 5400 s

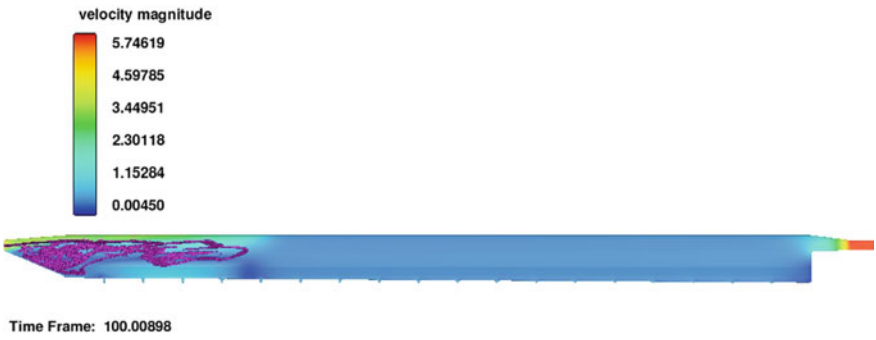

Photo 9 Sediment movement at T = 100 s

6 Sediment Movement Inside Desilting Chamber

Snapshots for sediment movement inside the desilting chamber at various time frames during simulation run are shown in Photos 9, 10 and 11.

7 Pressure Profiles

Pressure profiles inside the desilting chamber at time frame at end of the simulation i.e. 5400 s are shown in Photo 12.

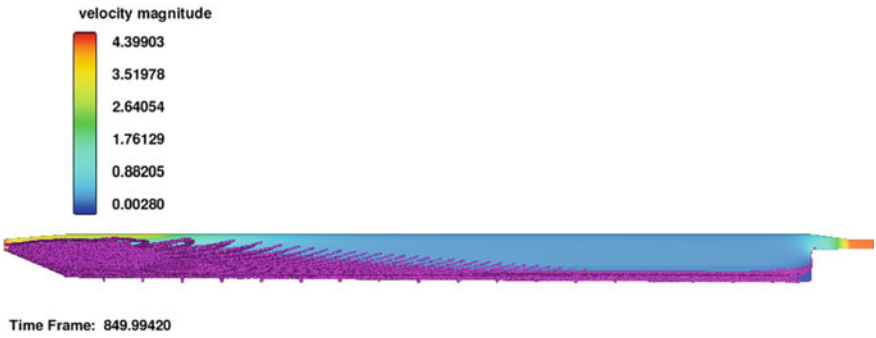

Photo 10 Sediment movement at T = 850 s

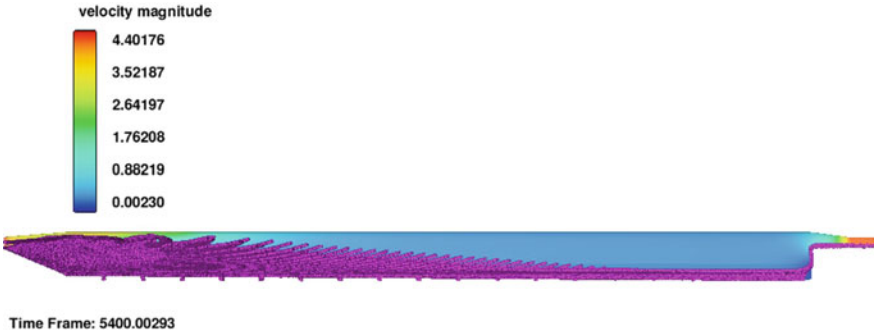

Photo 11 Sediment movement at T = 5400 s

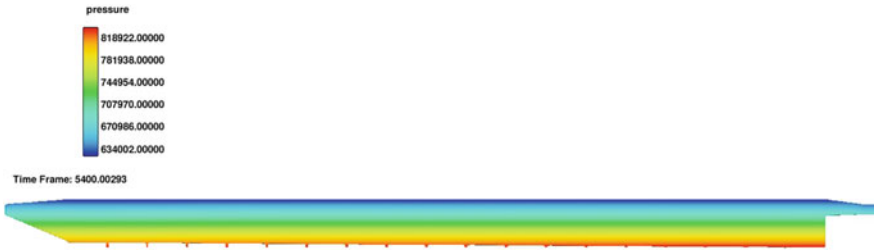

Photo 12 Pressure profile at T = 5400 s

8 Results

The number of particles escaping through SFT and HRT was ascertained by providing baffles at these two locations. The number of particles escaping through SFT and HRT at different time steps is represented in graphical form in Fig. 1.

The results are shown in Table 1, wherein; the number of particles escaping

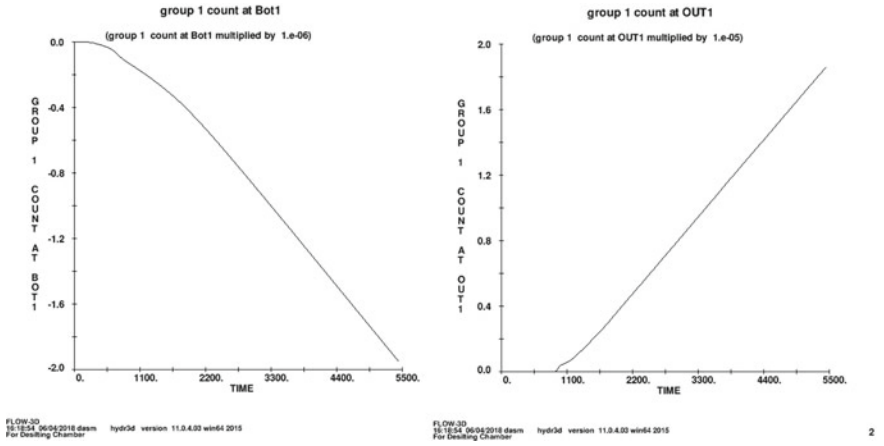

Fig. 1 The number of particles escaping through SFT and HRT at different time steps

Table 1 Efficiency of desilting chamber at different time steps

Time (s)	Number of particles through			Eff (%)	Time (s)	Number of particles through			Eff (%)
	SFT	HRT	Total			SFT	HRT	Total	
900	127,062	31	127,093	99.98	3200	958,157	90,113	1,048,270	91.40
1000	150,284	3957	154,241	97.43	3400	1,046,073	98,601	1,144,674	91.39
1200	200,088	7962	208,050	96.17	3600	1,133,908	107,214	1,241,122	91.36
1400	254,430	14,828	269,258	94.49	3800	1,222,705	115,927	1,338,632	91.34
1600	312,497	22,251	334,748	93.35	4000	1,311,364	124,439	1,435,803	91.33
1800	378,226	30,191	408,417	92.61	4200	1,400,400	132,978	1,533,378	91.33
2000	451,540	38,886	490,426	92.07	4400	1,489,318	141,307	1,630,625	91.33
2200	530,189	47,409	577,598	91.79	4600	1,577,922	149,882	1,727,804	91.33
2400	612,767	55,788	668,555	91.66	4800	1,667,163	158,445	1,825,608	91.32
2600	697,525	64,343	761,868	91.55	5000	1,755,994	166,996	1,922,990	91.32
2800	783,505	73,013	856,518	91.48	5200	1,844,778	175,516	2,020,294	91.31
3000	870,727	81,538	952,265	91.44	5400	1,933,411	183,944	2,117,355	91.31

through SFT and HRT is given based on which the settling efficiency of desilting chamber is ascertained at different time steps.

9 Conclusions

The settling efficiency of desilting chamber for 0.2 mm size particle using Flow 3D simulation as ascertained above is 91.3%. Whereas, the same obtained by physical

model studies works out to be 90% (CWPRS 2013). Therefore, it is seen that settling efficiency estimated using Flow 3D and physical model studies are in close agreement with each other. However, further refinements, simulation runs and validations are required to gain more confidence. In physical models, flushing efficiency is also ascertained in addition to settling efficiency. Currently, CFD modelling of sediment transport is done, similarly CFD modeling of sediment flushing can be done. It is worth noting that CFD will be handy tool to estimate sedimentation efficiency and provides insight into flow conditions inside desilting chamber.

Acknowledgements The authors sincerely thank Dr. (Mrs) V.V. Bhosekar, Director, CWPRS for constant encouragement, guidance and kind permission for publishing this paper. The authors are also thankful to project authorities for referring studies to CWPRS and making available the necessary data for conducting these studies.

References

CWPRS (2013) Technical Report No. 5121. Hydraulic model studies for desilting chamber for Mangdechhu HE Project, Bhutan

Flow Science. Flow 3D user's manual version 11.0.3, Flow Science Inc.

Verma MK, Qamar MZ, Neena Isaac Bhosekar VV (2015) Design optimization of desilting chamber by model studies. In: HYDRO 2015 International at IIT, Roorkee during 17–19 Dec 2015

Flood Management—An Overview

Mayuraksha Bardhan

1 Introduction

Flood is a natural calamity which causes colossal losses to human society. The Chamber's Dictionary defines flood as a great flow of water/an inundation/a deluge/a condition of abnormally great flow in a river/the rise of tide. Flood occurs often frequently in almost all the river basins, low lying areas and coastal areas of the world for variety of reasons. The causes of flood are rivers carrying water flows much in excess of their transporting capacities due to concentration of run off and heavy rains, synchronization of peak of floods of main rivers and tributaries, heavy rainfall with spill of rivers, inadequate and inefficient drainage of low lying and flat areas to carry water with desired quickness to the outfall, synchronization of upland flood and high tides, tidal waves, typhoons and cyclones and failure of dams. Notwithstanding the experiences gained over many years in studying the nature of flood and tremendous effort put forth for flood control, the damages caused due to flood have been steeply increasing due to the increase in flood plain occupancy for developmental activities, encroachments due to increase of population, deforestation and other environmental degradation. Flood is a natural phenomenon and total flood control is not possible. There is a possibility of a high flood exceeding the one for which the control facility has been designed. All that can be done is to adopt measures to minimise the damage caused by the flood. Therefore the term 'Flood Management' is used. Flood management includes structural and non-structural methods. Structural measures accomplish flood moderation by methods such as channel improvement, flood embankments, diversion, by passes, reservoirs, detention and retarding basins, pumping, land treatment, etc. The non-structural method includes flood defence education, flood plain management, flood forecasting and warning, environmental hazard reduction and drainage system, disaster preparedness and response planning, flood mapping

M. Bardhan (✉)
River Research Institute, Mohanpur, Nadia, West Bengal 741246, India
e-mail: mayur.bardhan@gmail.com

R. Jha et al. (eds.), *River and Coastal Engineering*, Water Science and Technology Library 117, https://doi.org/10.1007/978-3-031-05057-2_17

and damage assessment, flood insurance, etc. Computer–mediated communication systems, geographical information systems (GIS), remote sensing, digital elevation models (DEM), electronic decision support systems (DSS) and risk–analysis techniques have been developed substantially and show great promise for sustainable flood mitigation. Flood management is a time and area specific job. Detailed knowledge of impacts of flood is necessary for efficient planning and operation of flood management programme.

2 Literature Review

Johnson and William (1978) discussed regarding physical and economical feasibility of non-structural flood plain management measures. Jamil and Beg (1998) reported about flood control by non-structural strategies. Patel and Trivedi (2006) discussed about the devastating flood in Vadodara City in the state of Gujarat in the year 2005 and suggested some preventive measures against flood. Shah and Patel (2006) reported about evaluation of decision support system (DSS) for sustainable planning and management of flood disaster. Sharma and Patel (2007) reported about the disastrous flood in Surat city in the year 2006 and submitted their views for reducing the effects of flood. Mizanur Rahman et al. (2014) discussed about flood management in Bangladesh by structural and non-structural measures.

3 Impact of Flood

Complete assessment of the impacts of flood on the socio-economic condition and environment are not available. It is hardly possible to assess and repair the losses to human life, cattle and property and the set-back to the society due to stagnation of economic growth resulting from flood hazard. The impacts of flood on human society are manifold. Damages to roads and railway communication, flood control works, irrigation systems, water supply systems, ports, air fields, agricultural crops, loss of human lives and cattle, etc. are identified as physical losses. Impacts of some of the previous floods are given here to identify the areas from which guidance can be obtained and applied to prepare effective plans for mitigation of losses and miseries of the society to the possible extent. Table 1 depicts flood affected area and flood damages in India during the period 1953–2010.

Table 1 Flood affected area and flood damages in India (period 1953–2010)

S. No.	Item	Unit	Average annual flood damages	Maximum damage	
				Extent	Year
1	Area affected	M ha	7.57	17.50	1978
2	Population affected	Million	3.19	7.045	1978
3	Human lives lost	Nos	1,612	11,316	1977
4	Cattle lost	Nos	89,345	6,18,248	1979
5	Cropped area affected	M ha	3.679	15.18	2005
6	Value of damaged crops	Rs. Crores	693.866	4246.622	2000
7	Houses damaged	Million	1.22	3.51	1978
8	Value of damaged houses	Rs. Crores	275.481	1307.89	1995
9	Value of damages to Public Utilities	Rs. Crores	814.596	5604.46	2001
10	Total damages to Crops, Houses, Public Utilities, etc	Rs. Crores	1804.419	8864.54	2000

Source Report of Working Group on Flood Management and Region specific Issues for XII Plan

3.1 Impact of Flood in the State of West Bengal Within Last Fifty Years

In the state only five years could be identified as flood free years within last fifty years (1959–2009), when only less than 500 km^2 of area were inundated as depicted in Table 2. After last 1959 major flood, the state suffered consecutively in 1978, 1985, 1998, 1999 and 2000. In terms of loss of property and life, the 2000 flood was almost comparable to 1978 flood. It had another grim feature not recorded in our living memory. Seventy two hours of continuous and concentrated rainfall over the western river basin areas of Bhagirathi viz. from the Pagla-Bansloi to the Ajoy, generated so huge flood volume that all embankments on the eastern side of the Bhagirathi were almost washed away and the whole of Nadia and larger part of Murshidabad were flooded and remained under water for a long period. In this trans-basin transfer of flood, people were caught unaware and all sorts of speculative ideas were propagated. Table 3 depicts record of large floods in West Bengal. Flood prone areas of West Bengal are shown in Fig. 1.

Table 2 Analysis of area flooded against years of occurrence

Flood affected area (in sq. km)	Years during which the flood occurred	Total No. of years
Below 500	1985, 89, 92, 94 and 97	5
Between 500 and 2000	1962, 63, 64, 65, 66, 72, 75 and 96	8
2000–5000	1960, 61, 67, 69, 70, 74, 76, 80, 81 and 82	10
5000–10,000	1973, 77, 93, 95 and 98	5
10,000–15,000	1968, 79, 83, 90 and 99	5
15,000–20,000	1971, 86, 87 and 88	4
Above 20,000	1978, 84, 91 and 2000	4

Source Google Search

4 1968 North Bengal Flood, West Bengal

The total damages due to the devastating 1968 flood of North Bengal could not be assessed. The damages and losses were high and widespread. The communication between Assam and rest of India was disrupted due to damages of railway lines and roadways and approaches to railway and road bridges in number of places. Thousands of passengers were stranded at various wayside stations between Kisanganj in Bihar and Fakirgram in Assam. With the destruction of Anderson Bridge across river Teesta, Kalimpong and Sikkim main surface link with outside world was a major catastrophe. The hilly roads of Darjeeling district were in shambles due to landslides at numerous places trapping motorists at various points. The major part of protective embankment of Jalpaiguri was washed away. The water supply and power supply system of Jalpaiguri town was completely disrupted. There were wide spread damages to Diesel Power Station at Bigan Bari, Darjheeling, Kurseong and Siliguri due to onrush of flood water. Protective walls of Jaldhaka Hydel Power Station were washed away by sudden flood. The whole of the areas of North Bengal depending on this power station went without electricity. A huge transmission tower near sevoke was washed away by Teesta water. The turbulent Teesta damaged Oil India pipe line that brings crude oil from Naharkatia in Assam. Jalpaiguri town was inundated during night following the devastating flood in the river Teesta and Karala. Heavy loss of life and property was feared. After seven days of flood, the accumulated silt and carcasses could not be cleared. Many people left Jalpaiguri facing grave health hazards. Acute shortage of relief material and food was experienced. Reports of looting food grains at different places were received. No reports were available about the losses and

Table 3 Record of large floods in West Bengal

Period	Description
1978	Major flood
1986	Flooding due to heavy rains in some areas of Kolkata, Hooghly, Howrah, Parganas and Midnapore
1988	Monsoonal rains caused flooding in areas of Balurghat and Dinajpur lying under the purview of the Ganges and Churani rivers
1991	Flash floods caused damage 35,000 houses
1995	Flooding triggered by heavy rains caused erosion, severe agricultural damage and outbreak of diseases
1998	Monsoon rains caused flooding of the Ganges River
1999	Tropical cyclones caused destruction of an estimated number of 1500 villages. Floods due to brief torrential rains affected areas of Kolkata, Burdwan and Birbhum
2000	Besides flash floods triggered by incessant torrential rains, disaster is also accredited to the opening of sluice gates of dams. The fatalities counted to the tune of 1262, besides affecting millions of people
2002	Flooding in Jalpaiguri, Cooch Behar and Jalpaiguri in north Bengal due to monsoonal rains. Flash floods swamped ten villages, causing four deaths and 11,000 displacements
2003	Monsoonal rains caused floods affecting the regions of Darjeeling, Jalpaiguri, Malda and Murshidabad
2004	Heavy monsoonal rains affected several districts
2005	Heavy rains caused floods in many areas. About 3000 coastal villages were inundated and 60,000 huts and many roads washed away
2005	Heavy rains caused floods in many areas. About 3000 coastal villages were inundated and 60,000 huts and many roads washed away. Heavy monsoon rains triggered flash floods and landslides
2006	The regions of Birbhum, Burdwan and Murshidabad were affected mainly from continuous monsoonal downpour Monsoonal rains and tropical cyclone-driven storms in the Bay of Bengal hit India and Bangladesh. West Bengal recorded 50 deaths, 300 were injured and 30,000 mud houses destroyed. Heavy rains left large parts of Kolkata city under water; subsequently 2000 people were evacuated from the city
2007	Heavy rain from tropical depression in the Bay of Bengal caused flooding leading to 51 deaths, and affecting 3.2 million people
2013	Heavy rainfall & water release from various dams by DVC led to widespread flooding in the districts of Paschim & Purba Medinipur, Howrah, Hooghly, Bardhaman and Bankura Causing 17 deaths, 8790 villages affected, and affecting 2.1 million people

Source Google Search

damages of the villages. In fact, assessment of damages and losses was not possible and no factual report of damages of this flood is available. The major casuality of the landslides was the tea industry in the hill areas. This industry employed 60,000 workers and its earnings ran into several millions of Rupees annually. Hundreds of labour quarters were washed away. Factories, Powerhouse, Hospitals were damaged. It was estimated that the calamity wiped out a chunk of capital assets of the tea

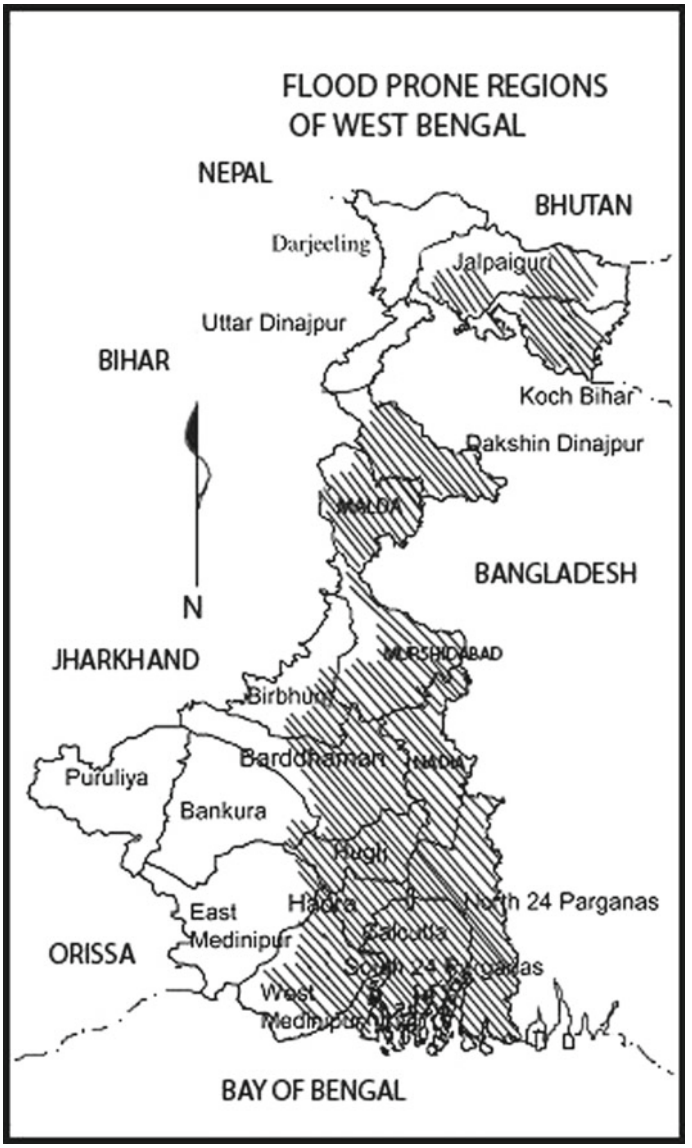

Fig. 1 Flood prone regions of West Bengal. *Source* Google Search

industry. There were major damages to forest and forest lands due to soil erosion and bank erosion of rivers at many places. There were also changes of river courses due to siltation and erosion and changes of the geomorphology of the area. As per unofficial sources, casuality figure was 6000. Losses to cattle heads and other properties could

Fig. 2 Flood in North Bengal during the year 1968. *Source* Google Search

not be assessed. The review of the hydraulic parameters of the design for the structures like flood embankments, bridges, protection works, drainage system, etc. was felt necessary considering the experience gained and accordingly structures/systems were remodelled. Figure 2 depicts flood situation in North Bengal during the year 1968.

5 1978 Flood in Midnapur and Other Districts, West Bengal

The flood of 1978 in the district of Murshidabad, Nadia, Burdwan, Howrah, Hooghly, Midnapur and 24-parganas including Kolkata city caused a widespread havoc inundating more than 30,000 km^2. Area. The Kangsabati Dam authorities played a successful role in reducing the peak flood from 3.4 lakhs cusecs to 1.6 lakhs cusecs at Mukutmonipur by storing a voluminous quantity of flood water. A peak flood discharge of more than eight lakh cusecs was moderated to about 3.5 lakhs cusecs at Maithon and Panchet Dams by DVC authorities. Had there been no dams, the intensity of flood would have been more than double in the Midnapur, Burdwan, Howrah and Hooghly Districts. Mayna Block, an island protected by flood embankment all round in Midnapur, was inundated, the depth of water being 1–3.5 m. All the inhabitants and the cattle took shelter on the embankment. Pilfering and looting of the houses caused a law and order problem. Drainage of the accumulated water within the saucer shaped island was the major problem at that time. Drainage was affected by cutting the embankment at a place though it caused submersion to another area which was unavoidable in such situations. Figure 3 depicts flood in the district of Midnapur in West Bengal during the year 1978.

Fig. 3 Flood in Midnapur district of West Bengal during the year 1978

6 Purulia Flood of 1992, West Bengal

Purulia is the only drought prone district in West Bengal. Surprisingly the district has experienced a devastating flood in 1992, with loss of lives of fifteen persons and damages to private and public property of value rupees ten crores. The properties within one kilometre on both banks of the river under spate washed away. The road bridge on National High way and railway bridge on Kangsabati river near Purulia town outflanked resulting in disruption of communication. Many other road bridges were damaged. Most of the structures constructed by local authorities other than Public Works Department were either washed away or heavily damaged, indicating designs insufficiency. The general experience is that the waterway provided for bridges, weirs, spillways was inadequate to cater to the flood discharges. Though no dams were overtopped/damaged, in several cases the free board was encroached during this flood, causing panic to the operational staff. In all these cases, either all the gates of the spillway of the dam were opened in time or the spillways were ungated. Agricultural lands were damaged and became unfit for cultivation due to sediment deposition. Kangsabati Dam is situated at about 1 km downstream of District boundary of Purulia and Bankura in the district of Bankura, the catchment area of Kangsabati Dam in two days was 540 M. Cum. (4,37,000 cusec) from this storm run off. The country slope being comparatively steeper in the district, the times of concentration is less. The flood water rushed through the channels and rivers causing damages during short duration flood. The benefit of storage of water in Dam constructed for irrigation purpose is once again proved after 1978 flood. The flood waters which cause damages in Purulia district have been utilised for boro-cultivation in the command area of the dam. This is the only plus-point of the impact of the flood in this case.

7 Flood of 2000 in West Bengal

The Deluge in 2000 happened mainly in the Bhagirathi–Hooghly basin and the basin area of Mathabhanga, Churni and Ichhamati. However, there was trans-basin flood spill that continued eastwards up to Bangladesh. The three most affected districts were Murshidabad, Nadia and North 24 Parganas. These are adjacent districts located in the eastern part of southern Bengal. Rainfall had been erratic in 2000. Towards the end of the monsoon there was incessant rainfall in the 3rd and 4th weeks of September 2000 not only in these districts but also in the upper catchment area of Bihar, Jharkhand and North Bengal. The accumulated water posed severe threats to reservoirs, dams and barrages in the region. From 18 to 23 September, Murshidabad alone received 1200 mm. of rain in addition to its annual quota of 1500 mm. The Mayurakshi catchment area upstream of Messanjore Dam received 1008 mm rainfall in 96 h from 18 to 22 September, which remains a record to this day. All the major rivers were flowing above their danger levels by 19th September 2000 and the low lying areas were already inundated. There was water-logging in most areas, rural and urban alike. Discharge of water from barrages under compelling circumstances was the last nail in the coffin. The water level of Bhagirathi-Jalangi at Swarupganj (Nadia) was 9.61 mtr on 20.9.2000 (Danger Level 9.05 m.) after the Tilpara Barrage released nearly 1.5 lakh cusec of water followed by another release of 1.2 lakh cusec. It has been estimated that a discharge of more than 4.5 lakh cusec passed through the Bhagirathi against its carrying capacity of 1.05 lakh cusec. Again, more than 1.5 lakh cusec of discharge entered into the Ichhamati-Churni system. The carrying capacity of Ichhamati is at the most 20,000 cusec. The consequences were obvious– the most devastating floods in the history of West Bengal.

8 Flood in Bankura and Jhargram Districts of West Bengal During the Year 2018

Several low lying areas in and around Bankura were inundated by the Gandheswari river following heavy rains. The Bankura district recorded 224 mm rainfall during last 24 h since 6 A.M. on 5.8.2018 resulting in swelling up of river Gandheswari and spilling the banks. Large areas in Bankura 2, Gangajalghati and Mejia blocks and a part of Bankura municipality were submerged. Two two-storied concrete houses at Junbedia village on the outskirts of Bankura town collapsed under the impact of surging water from a canal connected with Gandheswari river as shown in Fig. 4. The houses were vacated on a prior notice and no casualties were reported. Altogether 750 concrete and mud houses either collapsed or were damaged in three blocks of the district. Traffic on Durgapur-Bankura road was stopped as water started flowing over the Bridge at Satighat. Due to heavy rain and water logging, flood occurred in

Fig. 4 A two-storied house was washed away due to floods following heavy rainfall in Junbadia village in Bankura district of West Bengal as observed on 6.8.2018

Fig. 5 Photograph of Raghunath Block in Jhargram district of West Bengal as observed on 6.8.2018. *Source* Google Search

Jhargram district also. Figure 5 depicts flood in Raghunath block of Jhargram district as observed on 6.8.2018. Figure 6 depicts relief and rescue operations in Bankura district of West Bengal.

9 Flood Impact Assessment and Management

Full details of losses and distress of any flood hazard can not be presented as full information is neither available nor amenable for collection due to various limitations. Damages to crops, houses, individual property, factories, etc. causes destruction of the socio-economic condition of the individual as well as society and revival of the

Fig. 6 Rescue personnel evacuate local residents in Bankura on August 6, 2018

same takes a long time affecting the livelihood of many. Damages to public utility services like roads, railways, public buildings, irrigation and drainage system, water supply, power supply, ports, airfields, etc. cause set back to the national economy and funds available for developmental works are to be diverted for repairs to the damages. Health hazards are also attributed as one of the primary impact. After the flood water recede, the surviving population need drinking water, food, clothing and shelters. They are affected with diarrhoea, gastro-enteritis and starve to death for want of food. Similarly the casualty to cattle is also high.

The operation of the flood management works is vested on the District Magistrate/District Collector, who is responsible for establishing co-ordination among different departments at district level to fight against anticipated disaster in advance. Similar management bodies are formed at sub-divisional level as well as Block level. Apex body is at State level.

Flood Management includes both structural and non-structural methods. Structural measures accomplish flood moderation by methods such as channel improvement, flood embankments, diversion, by passes, reservoirs, detention and retarding basins, village raising, pumping, land treatment, etc. The non-structural method includes flood plain management, flood forecasting and warning and flood damage prevention. Flood plain management includes the legal and administrative control over the area prone to flood hazard through by flood plain zoning, land use planning, restriction on certain activities in flood prone areas. Serious thought should be given and required actions taken. Flood forecasting and warning systems have already been developed and will be further developed with advancement of space technology. Participation of people living in flood prone area should be encouraged. The flood damage prevention planning comprises advance preparedness for flood fighting, evacuation of flood affected people, guarding evacuee property, relief operations, medical assistance and allied operations. The co-ordinations among different departments of government and other organisations is the prime factor for success of

the flood management programmes. The action starts as soon as the flood signal is received. The action plan may be prepared considering type of storm coming, time available, area to be affected, population to be handled, etc.

10 Action Plan of Flood Management

There are control room to work round the clock, Police and local authorities to disseminate the flood warning and alert without causing panic, Transport system for evacuation and rescue on short notice, All staff, rescue parties and medical teams to be kept ready, Public buildings and shelter should be ready to receive flood victims, Police forces to be ready to maintain law and order. Other arrangements like flood fighting, medicine, food, drinking water, temporary shelter, relief, fire brigade, fodder, seeds, disinfectants, etc. and services of civil defence, military, Animal Husbandry, meteorology, Public Works Department, etc. The southern state Kerala experienced devastating flood during the month of August 2018. Figures 7 and 8 depict relief and rescue operations in the state of Kerala.

Post flood evaluation workshops may be arranged for exchange of ideas of different persons working at the field level with flood victims and the persons working

Fig. 7 A truck carries people past a flooded road in Thrissur, Kerala on August 18, 2018.Rescuers used helicopters and boats to evacuate thousands of people stranded on their rooftops following unprecedented flooding in the state of Kerala that killed hundreds

Fig. 8 A doctor checks a patient at a medical centre in a flood-relief camp in Kozhikode, about 385 km north of Trivandrum, in the south Indian state of Kerala, on August 17, 2018. *Source* Google Search

at the control room. The information recorded would help freshers who will perform the Flood Management job in future.

11 Application of New Technology

Computer-mediated communication systems, geographic information systems (GIS), remote sensing, digital elevation models (DEM), electronic decision support systems (DSS) and risk-analysis techniques have developed substantially and show great promise for supporting sustainable flood mitigation. For example, GIS models enable managers to consolidate information from a range of disciplines, including the natural and social sciences and engineering and to formulate plans accordingly. Remote sensing can be used to show changes over time, feed information to GIS models and gather information in the wake of floods. Flood extent study can be very much helpful in developing flood map with advanced geospatial technique for flood risk assessment analysis. Essential dataset for measuring and analyzing extent of flood in urban area includes the Highest Flood Level (H.F.L) of various urban regions, natural topography of such regions, soil conditions, pattern of urban growth, river carrying capacity, bank full stage and tidal situations in case of coastal areas. Close contour information is important in flood control for acquisition of very

high resolution data using Digital Camera (DC) and also high resolution elevation data using Airborne Laser Terrain Mapper (ALTM) from aerial platform. Web based applications have been developed in GIS environment for identification of suitable sites for flood shelters. Finally, decision support systems (DSS) can fill a gap in flood management by analyzing information from core databases. The systems can then be asked "what-if" questions about future losses to inform today's decision making. Such systems are now constrained by the lack of comprehensive local data, but they will become more important as the process of evaluating and managing risk grows in complexity.

12 Conclusions

Flood in India has become one of the biggest disasters which have killed thousands of the people in last few years. The recurrence and intensity has amplified over the time which damaged life and economy at a great extent. Government of India has taken up many measures to lessen the damage caused by flood and other disasters, but there is a long way to go. Workshops/Symposia may be arranged on different themes of flood management after the flood season is over. The results of preparedness and actual operation should be recorded and discussed. The success or failures/lapses of any operation and planning should be critically examined for future guidance on flood management. Use of science and technology, telecommunication and media for alarming and pre-disaster measures can be effective to reduce the devastations. To set up alarming system at the bank of rivers which can alert neighbouring dwellers about rising water level can also be an affective measure to minimise the damage. Along with it, awareness programmes and preparedness campaign at the flood affected areas can help in limiting losses. Rehabilitation of the neighbouring community to a safe and higher place before flood arrives can reduce the danger to life. Quick action in supply of goods and services like medicine, food and water supply helps in quick recovery and limited loss after the disaster. Analysis of flood trend and damage caused by it suggest that there is a need for effective pre-and post-disaster mechanism as the nature cannot be checked but disaster can be reduced.

References

C.W.C Report on 'Flood situation in the Country'

Jamil M, Beg M (1998) Flood control by non-structural strategies. In: National conference on geo-environment, M.N.R Engineering College, Allahabad

Johnson, William K (1978) Physical and economic feasibility of non-structural flood plain management measures, Hydrologic Engineering Center, Corps of Engineers, U.S.A

Patel AS, Trivedi AK (2006) Flood in Vadodara City. In: Proceedings of the national conference 'HYDRO-2006', BVDUCOE, Pune, Maharashtra, 8th to 9th December 2006, pp 149–157

Rahman MM, Hossain MA, Bhattacharya AK (2014) An analytical study of flood management in Bangladesh. J 'River Behav Control', 34:35–44, 2013–2014

Shah S, Patel JN (2006) An evaluation of DSS for sustainable planning and management of flood disaster. In: Proceedings of the national conference 'HYDRO-2006', BVDUCOE, Pune, Maharashtra, 8th to 9th December 2006, pp 116–123

Sharma ND, Patel JN (2007) An overview of decadal floods in Surat City. In: Proceedings of the national conference 'HYDRO-2007', BVDUCOE, SVNIT, Surat, pp 114–120

Grid Sensitivity Study of Modular Ocean Model in Capturing Regional-Scale Dynamics of Bay of Bengal Under Seasonal Wind Patterns

Mousumi Sarkar, Shweta Sharma, Siddhesh Tirodkar, Rajesh Chauhan, Sridhar Balasubramanian, and Manasa Ranjan Behera

1 Introduction

Ocean processes, ranging from submeso-scale to large scale, effect ocean properties which, in turn, effect the oceanic climate conditions. Small-scale regional processes are important components of the drivers that defines the regional scale weather and large scale climate conditions. Meso-scale and submeso-scale processes are considered to be as regional processes. The meso-scale processes range from 10 to 100 km in the spatial scale (e.g. waves, gyres, meso-eddies), while the submeso-scale processes (e.g. filaments, plumes, small-scale eddies & vortices) are in the order of 1 km (Thomas et al. 2007). Some of the regional dynamics such as upwelling, downwelling, mixed layer dynamics, sea surface temperature change, sea level rise, change in salinity etc. happen in response to several atmospheric forcing. The surface mixed layer is an important part of the upper ocean, where the ocean–atmosphere interaction happens. Varying intensities of wind forcing cause turbulence in the upper ocean, which leads to form a well-mixed layer with a small vertical gradient in temperature,

M. Sarkar (✉)
IDP in Climate Studies, IIT Bombay, Mumbai, India
e-mail: mousumi.sarkar@iitb.ac.in

S. Sharma
Department of Mechanical Engineering, IIT Bombay, Mumbai, India

S. Tirodkar
IDP in Climate Studies, IIT Bombay, Mumbai, India

R. Chauhan
IDP in Climate Studies, IIT Bombay, Mumbai, India

S. Balasubramanian
Department of Mechanical Engineering, IIT Bombay, Mumbai, India

M. R. Behera
Department of Civil Engineering, IIT Bombay, Mumbai, India

R. Jha et al. (eds.), *River and Coastal Engineering*, Water Science and Technology Library 117, https://doi.org/10.1007/978-3-031-05057-2_18

salinity, and density (Grant and Belcher 2011). The depth of this mixed layer is known as the *mixing layer depth* (MLD). Ocean MLD is primarily determined by the action of turbulent mixing of the water mass due to wind stress and heat exchange at the air-sea interface (Kara et al. 2003). The mixed layer depth helps define the climate and weather conditions by balancing the exchange of mass, momentum, energy, and heat between the atmosphere and the ocean (Kantha and Clayson 2000). The SST changes with seasons giving a feedback to the atmosphere are central to the regional weather patterns (Xie 2009). Large scale ocean–atmosphere coupled models can capture this feedback and reproduce the observed trends in averaged global temperature. Most of the existing studies simulate the global and basin scale climate conditions with horizontal resolution ranging from 0.25° to 3.75° and vertical resolution ranging from 5 to 50 m in the upper ocean which gradually increases with depth (Behara and Vinayachandran 2016; Chowdary et al. 2016; Paul et al. 2009; Thompson et al., 2006; Dewitt and Schineider 1999; Zhang et al. 1998). However, they do not resolve all the meso-scale and submeso-scale processes, which impacts the regional ocean circulations and mixing. Also, the subsurface mixing dynamics and the internal structure of the ocean has an impact on the surface temperature, salinity and hence, the MLD. So, it is important to run ocean as a stand-alone model, with inputs from atmosphere and understand its dynamics. To model and analyse the effect of meso-scale and submeso-scale processes, high resolution regional modelling approach should be adopted with appropriate boundary and initial conditions.

In this study, a regional domain is selected in the Indian Ocean located over Bay of Bengal (BoB). The domain faces seasonal winds with varying intensities and directions, current reversals, changes in precipitation patterns, and vertical stratification which makes this region interesting to study the impacts of regional scale processes on ocean dynamics. During June to September, the summer-monsoon wind flows eastward, while the winter-monsoon wind flows westward during December to February (Shankar et al. 2002; Shetye et al. 1996). The increased intensity of wind forcing during the summer-monsoon period leads to a greater ocean mixing and higher MLD formation. This regional domain is taken to consider the meso-scale and submeso-scale processes present there and to analyse their effects on the ocean dynamics.

2 Model Description

Numerical experiments with multiple horizontal and vertical grid-sizes were performed using Modular Ocean Model version 5.0 (MOM 5.0), developed by NOAA's Geophysical Fluid Dynamics Laboratory. The model uses fundamental mass, tracer conservation equations and momentum equation with Boussinesq approximation for three dimensional fluid. The tracer conservation equation takes the following form

$$\frac{\partial u}{\partial x} + \frac{\partial v}{\partial y} + \frac{\partial w}{\partial z} = 0 \tag{1}$$

where, u, v, w are the velocity components in x, y, z directions respectively. The momentum or Navier-Strokes equation for three dimensional fluid with Boussinesq approximation is

$$\frac{\mathrm{Du}}{\mathrm{Dt}} = -\frac{1}{\rho_0}\nabla \mathrm{p}' + \frac{\rho'}{\rho_0}\mathrm{g} + \upsilon \nabla^2 \mathrm{u} \tag{2}$$

where $\upsilon = \frac{\mu}{\rho_0}$, is the kinematic viscosity, ρ_0 is the reference density, ρ' is the density perturbation, p' is the pressure perturbation, **u** and **g** are the vectors for velocity and gravitational acceleration respectively. The model equations are discretized with generalized horizontal coordinates using Arakawa B-grid. It separates the evaluation of the two sets of quantities, e.g., one might evaluate velocities at the grid centre and masses at grid corners. Also, in vertical direction, depth based vertical coordinates are used to discretize the Boussinesq equations (Griffies 2012).

For this study, a regional domain is selected in BoB which spans from 82° east to 92° east and 7° north to 15° north. Horizontal grid resolutions in both the x and y directions are taken as 1/4° (0.25° i.e., coarser horizontal grid) and 1/8° (0.125° i.e., finer horizontal grid). For both the coarser and finer horizontal grids, multiple vertical resolutions are taken into account with 0.5, 1, 3, 5, and 10 m grid sizes near the surface region. Vertical grid sizes are non-uniform and increase downwards. Bottom bathymetry is taken as per the bathymetry available in two-minute gridded global relief data (ETOPO2). The northern, eastern, and western boundaries of the model domain are treated as solid walls and the southern boundary is taken as an open boundary, which is similar to the geographical structure of the BoB, surrounded by land with southern boundary open to the Indian Ocean. Sea surface temperature and sea surface salinity are restored for flux correction at the surface with a time scale of 30 days. The model is started from a state of rest, and annual average climatological temperature and salinity (Chatterjee et al. 2012) is given as initial conditions to run for a period of 10 years (Jan, 1970–Dec, 1979) using monthly climatological wind stress (Hellerman and Rosenstein 1983) as a forcing to the model. Figure 1 shows the vertical profiles of the initial temperature and salinity in the upper 1000 m at the middle of the domain. Figure 2 shows the seasonal wind stress intensities with directions. The model chosen for the present study is primarily to test regional scale modelling capability of MOM for Indian context. Hence, only wind stress forcing and climatology of an arbitrary year are chosen.

As a regional scale domain is used for the study, it is needed to implement *open boundary condition* (OBC) in order to allow exchange of mass, momentum and heat transport, and hence the ocean properties, in and out of the domain. OBC is applied for the variables like surface elevation, traces and velocities etc. Most of the OBCs available in MOM, are based on *Sommerfeld radiation conditions* with a different prescription for the phase speed (Chapman 1985; Herzfeld et al. 2011). Equation (3)

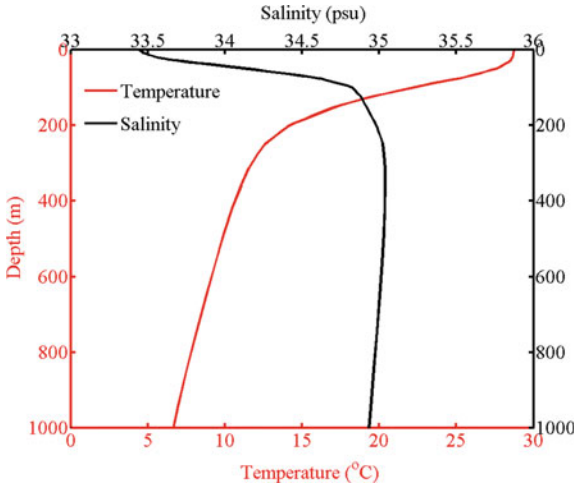

Fig. 1 Vertical profile of initial temperature and salinity in upper 1000 m

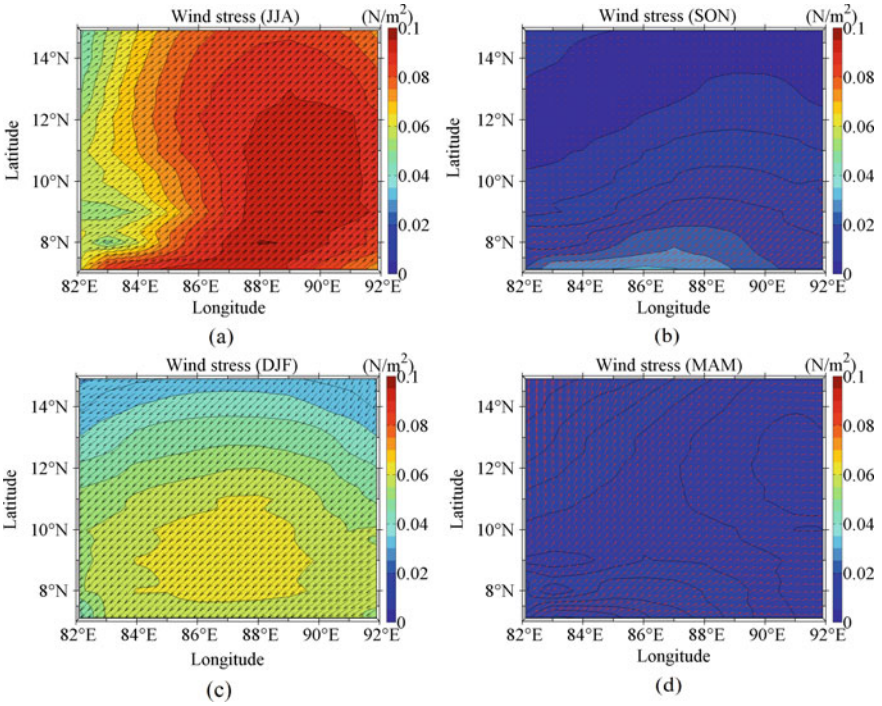

Fig. 2 Seasonal wind stress forcing with directions. **a** Summer-monsoon (Jun–Aug), **b** Autumn (Sep–Nov), **c** Winter-monsoon (Dec–Feb), **d** Spring (Mar–May)

describes the Sommerfeld radiation condition in general form.

$$\frac{\partial \eta}{\partial t} + c\frac{\partial \eta}{\partial x} = 0 \tag{3}$$

Here, η is the surface elevation and c is the phase speed (Sommerfeld 1949). MOM 5.0 has multiple OBC options to choose the right one from. It is important to select the right OBC scheme to implement in a particular case because OBC can change with different domains or forcing scenarios (Herzfeld et al. 2011). Open boundary conditions for a regional model is a complex problem. For realistic applications, the numerical solution near a boundary always turns out to be a superposition of outgoing and incoming waves which are non-separable. Application of radiation condition and relaxation of boundary values to this complex variables makes OBC a mathematically ill-posed problem and there exists no universally perfect scheme for OBC. So, it is difficult to find one suitable OBC for all kinds of regional models. Hence, MOM has implemented several schemes for boundary conditions and has given the provision to choose one scheme from them while designing the experiment (Griffies 2012). Chapman 1985, compared several OBC conditions for experiments with wind stress forcing and found out that Orlanski radiation condition (Orlanski 1976) gave the best performances. Since, in this study, results of the experiments with wind stress forcing are presented, the open boundary condition is implemented based on the technique proposed by Orlanski (1976). For vertical mixing scheme, constant background diffusivity is used and general biharmonic scheme is used for horizontal friction scheme (Griffies 2012). The main purpose of the study is to implement OBC and analyse the effect of changing grid resolution on the ocean dynamics present in the domain.

3 Results and Discussions

After five years of model spin-up, the last five years of simulated output data is considered for the analysis. Figures 3 and 4 depict the MLD evolution with time at the centre of the domain for various cases with different vertical resolutions (indicated in the legends of the figures) for the horizontal resolution of 0.25° and 0.125°, respectively. The model uses density based criteria for MLD calculation, i.e., it considers the MLD as depth up to which the density differs by 0.01–0.03 kg/m^3 from the surface density (Courtois et al. 2017). It is found that MLD is higher during the winter months (Dec–Jan–Feb) and the summer monsoon period (Jun–Jul–Aug–Sep) and lower during pre-monsoon (spring) and post-monsoon (autumn) seasons. The effect of wind stress forcing is presented for the analysis in all considered cases. The higher intensities of the wind stress cause the MLD to be higher on the above-mentioned periods. However, the cases with coarser vertical resolutions (3 m and above near the surface region) for both the finer and coarser horizontal

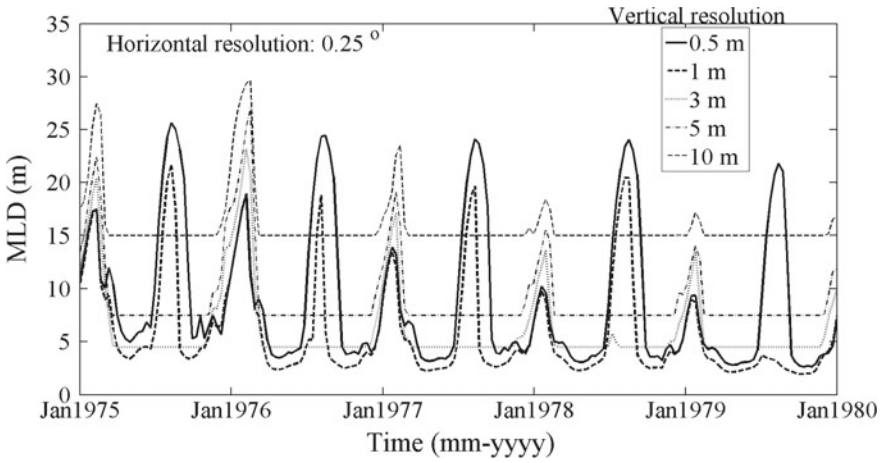

Fig. 3 Mixing layer depth (MLD) evolution over time: case with 0.25° horizontal resolution with different vertical resolutions (seen in the legends)

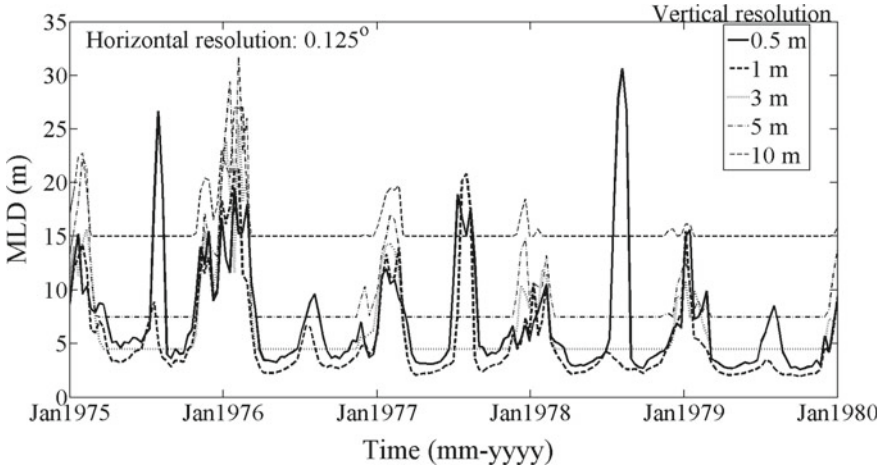

Fig. 4 Mixing layer depth (MLD) evolution over time: case with 0.125° horizontal resolution with different vertical resolutions (seen in the legends)

resolutions fail to capture the MLD variations during the summer-monsoon periods. Further, as the vertical grid size increases to 3, 5, and 10 m, the MLD trends show a shift toward the higher values. Cases with vertical grid sizes of 1 m and lower are able to capture the seasonal variations in MLD values. In Figs. 3 and 4, cases with 0.5 m vertical resolution show the best trends for MLD evolution over time, which capture the seasonal variability similar to the MLD observed in an operational ocean analysis/reanalysis system, ECMWF ORA-S3 (Balmaseda et al. 2008), as shown in Fig. 5. The results underestimate the MLD values compared to the observed values,

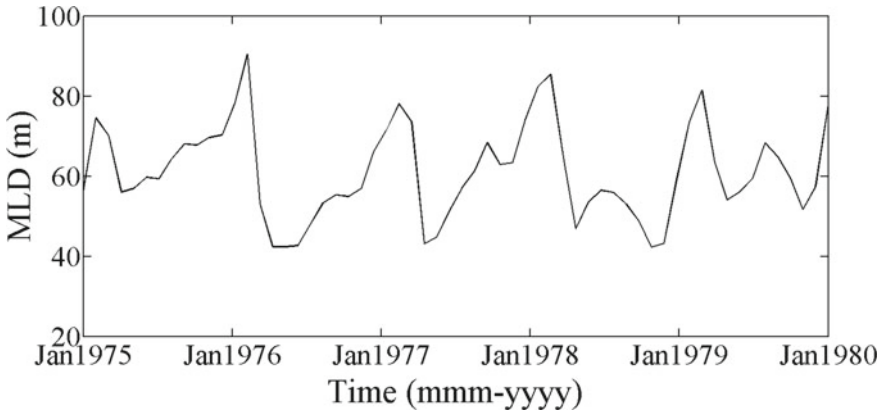

Fig. 5 Mixed layer evolution with time captured in an operational ocean analysis/reanalysis system, ECMWF ORA-S3

because in this study, only the effect of the wind stress is considered rather than the combined effect of wind, solar radiation, precipitation, evaporation, and river runoffs. Figure 6 shows the comparison between spatial variations of 5 years averaged MLD over the entire domain for the summer monsoon and winter monsoon seasons for both coarser (Fig. 6a, b) and finer (Fig. 6c, d) horizontal resolutions. These figures help us in understanding the effect of varying horizontal resolution on MLD. It is observed from the plots that the case with finer resolution (0.125°) underestimates the MLD values compared to the coarser resolution (0.25°) case near the boundaries. For both the cases with coarser and finer horizontal grids, though the SST values not differ much but SSS is ~0.2–0.3 psu higher in the case with finer horizontal resolution. Figure 7 depicts the SSS patterns over the domain in summer monsoon and winter monsoon seasons for both the cases. As SSS variation is qualitatively sensitive to small-scale processes, which are happening in regional domain and prominently captured in the finer grid resolution.

Regional scale modelling using MOM was successfully performed using seasonal winds as the forcing. This approach would allow one to perform high resolution simulation runs to better understand the small-scale process dynamics, which are not captured by basin scale simulations, and significantly affect the MLD. Although our simulation results presented here is far from real case, but it shows the effect of changing grid resolution on the ocean dynamics and the resulting MLD.

4 Concluding Remarks

The sensitivity of mixing layer depth formation to grid resolution is studied using Modular ocean model (MOM) version 5.0 for a regional domain in the Indian Ocean. A domain in Bay of Bengal is considered for the present study, wherein

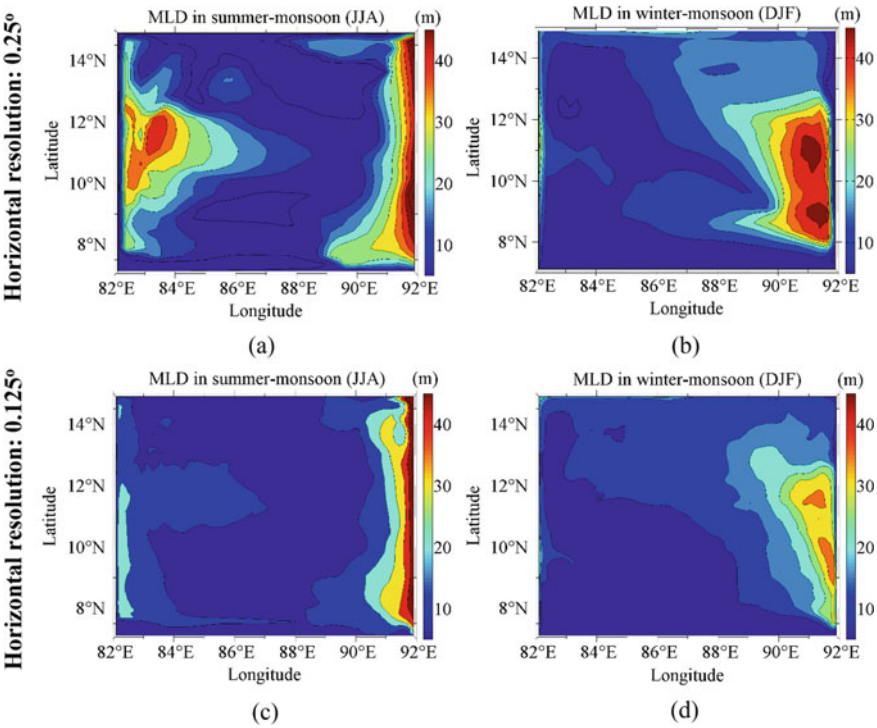

Fig. 6 Five years averaged mixing layer depth (MLD) during summer monsoon (JJA) and winter-monsoon (DJF) with horizontal grid resolution of 0.25° (upper panel) and 0.125° (lower panel)

a regional-scale modelling was done using open boundary conditions. It is found that MLD is highly sensitive to the grid resolutions, especially the vertical grid-sizes. The domain in consideration faces winds with higher intensities during winter and summer monsoon and lower intensities during wind reversals. This forms the pattern of the MLD evolution over time including higher values during the winter and summer monsoon periods, while lower values during pre- and post-monsoon seasons. The experiments with vertical resolution as 1 and 0.5 m near the surface region are able to capture the trend, while the cases with grid-size above 1 m fail to capture the seasonal variations in the values of MLD. Change in horizontal resolution does not show much difference in the MLD patterns. However, the case with finer resolution underestimates the MLD values compared to the coarser resolution case near the boundaries. For both the cases with coarser and finer horizontal grids, though the SST values do not differ much but SSS is ~0.2–0.3 psu higher in the case with finer horizontal resolution. It is important to note that in this study, we have only considered the wind stress as the input forcing, and hence, only the wind is acting behind the turbulence which leads to MLD formation. Thus, the results presented here underestimates the values compared to the observed data. In future studies, the

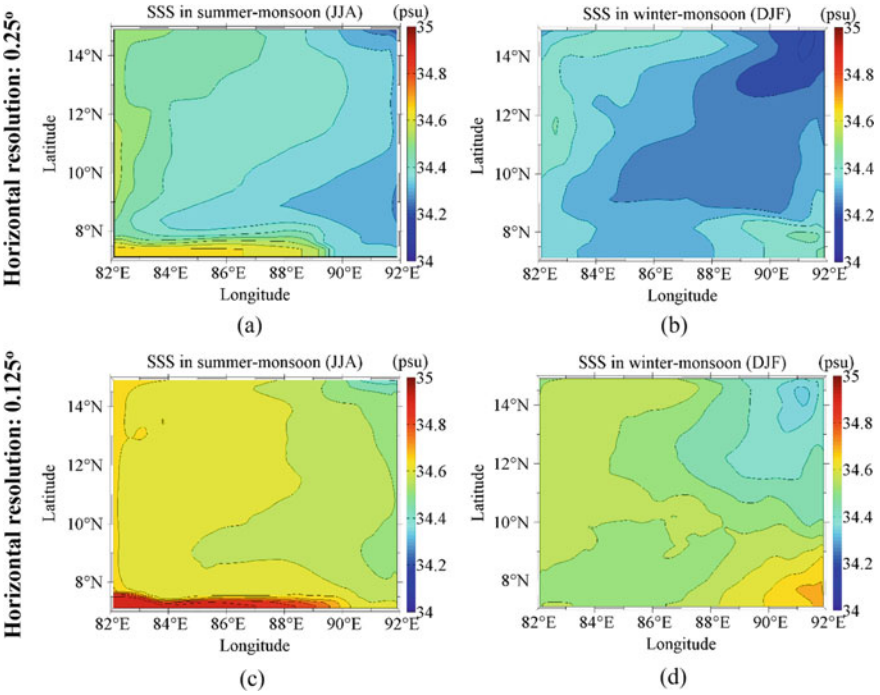

Fig. 7 Five years averaged sea surface salinity (SSS) during summer monsoon (JJA) and winter-monsoon (DJF) with horizontal grid resolution of 0.25° (upper panel) and 0.125° (lower panel)

combined effect of wind, solar radiation, river runoffs, precipitation and evaporation will be considered in the line of observed data.

References

Balmaseda MA, Vidard A, Anderson DL (2008) The ECMWF ocean analysis system: ORA-S3. Mon Weather Rev 136(8):3018–3034

Behara A, Vinayachandran PN (2016) An OGCM study of the impact of rain and river water forcing on the Bay of Bengal. J Geophys Res: Oceans 121(4):2425–2446

Chapman DC (1985) Numerical treatment of cross-shelf open boundaries in a barotropic coastal ocean model. J Phys Oceanogr 15:1060–1075

Chatterjee A, Shankar D, Shenoi SSC, Reddy GV, Michael GS, Ravichandran M, Gopalkrishna VV, Rao ER, Bhaskar TU, Sanjeevan VN (2012) A new atlas of temperature and salinity for the North Indian Ocean. J Earth Syst Sci 121(3):559–593

Chowdary JS, Srinivas G, Fousiya TS, Parekh A, Gnanaseelan C, Seo H, MacKinnon JA (2016) Representation of Bay of Bengal upper-ocean salinity in general circulation models. Oceanography 29(2):38–49. https://doi.org/10.5670/oceanog.2016.37

Courtois P, Hu X, Pennelly C, Spence P, Myers PG (2017) Mixed layer depth calculation in deep convection regions in ocean numerical models. Ocean Model 120:60–78

DeWitt DG, Schneider EK (1999) The processes determining the annual cycle of equatorial sea surface temperature: a coupled general circulation model perspective. Mon Weather Rev 127(3):381–395

Grant ALM, Belcher S (2011) Wind driven mixing below the oceanic mixed layer. J Phys Oceanogr 41(8):15561575. https://doi.org/10.1175/JPOD1005020.1. ISSN 00223670

Griffies SM (2012) Elements of the modular ocean model (MOM). GFDL Ocean Group Tech Rep 7:620

Hellerman S, Rosenstein M (1983) Normal monthly wind stress over the world ocean with error estimates. J Phys Oceanogr 13:1093–1104

Herzfeld M, Schmidt M, Griffies S, Liang Z (2011) Realistic test cases for limited area ocean modelling. Ocean Model 37:1–34

Kantha LH, Clayson CA (2000) Small scale processes in geophysical fluid flows, vol 67, International Geophysics Series, Academic Press, San Diego, CA, 883

Kara AB, Rochford PA, Hurlburt HE (2003) Mixed layer depth variability over the global ocean. J Geophys Res: Oceans 108(C3):3079. https://doi.org/10.1029/2000JC000736

Orlanski I (1976) A simple boundary condition for unbounded flows. J Comput Phys 21:251–269

Paul S, Chakraborty A, Pandey PC, Basu S, Satsangi SK, Ravichandran M (2009) Numerical simulation of Bay of Bengal circulation features from ocean general circulation model. Mar Geodesy 32(1):1–18. https://doi.org/10.1080/01490410802661930

Shankar D, Vinayachandran P, Unnikrishnan A (2002) The monsoon currents in the north Indian ocean. Prog Oceanogr 52:63–120

Shetye SR, Gouveia AD, Shankar D, Shenoi SSC, Vinayachandran PN, Sundar D, Michael GS, Nampoothiri G (1996) Hydrography and circulation in the western bay of Bengal during the northeast monsoon. J Geophys Res: Oceans 101:14011–14025

Sommerfeld A (1949) Partial differential equations in physics, vol 1. Academic press

Thomas LN, Tandon A, Mahadevan A (2007) Submesoscale processes and dynamics. Ocean Model Eddying Regime 177:17–38

Thompson B, Gnanaseelan C, Salvekar PS (2006) Variability in the Indian Ocean circulation and salinity and its impact on SST anomalies during dipole events. J Mar Res 64(6):853–880

Xie SP (2009) Ocean-atmosphere interaction and tropical climate. Trop Meteorol, pp 189–201

Zhang J, Schmitt RW, Huang RX (1998) Sensitivity of the GFDL modular ocean model to parameterization of double-diffusive processes. J Phys Oceanogr 28(4):589–605

Bathymetry Retrieval Using Remote Sensing Techniques for Inter-tidal Regions of Tapi Estuary

S. Shanmuga Priyaa, A. Aruna Kumar, and Basanta Kumar Jena

1 Introduction

Remote sensing techniques have been extensively used for bathymetry studies based on the principle of penetration of the solar radiation into the water at different wavelengths (Lyzenga 1981; Jupp 1988; Philpot 1989). The fundamental principle is that different wavelengths of light will penetrate water to varying degrees. Red light attenuates rapidly in water and therefore does not penetrate more than a meter or so. In contrast, blue light penetrates much further and in clear water the seabed can reflect enough light to be detected by a satellite sensor even when the depth of water approaches 30 m. The depth of penetration is dependent on water turbidity. Suspended sediment particles, phytoplankton, and dissolved organic compounds will all affect the depth of penetration because they scatter and absorb light.

Water turbidity is the most important factor affecting the accuracy of optically sensed bathymetry. Turbidity obstructs the path of electromagnetic radiation, and reflectance from suspended particles becomes confused with bottom reflectance. Waters of different turbidity levels scatter the incoming radiation differently. Both the form and accuracy of the empirical model are affected by water turbidity that exerts a varying impact on the accuracy and depth of remotely sensed bathymetry. The regression relationship also varies due to water clarity.

Bottom reflectance is the reflectance from the sea floor that is not indicative of water depth directly. It occurs in shallow waters or in relatively deep clear water when the solar radiation is able to penetrate the water column to reach the floor. The regression coefficients deteriorate with mixed bottom types because the variability in brightness values from a heterogeneous bottom has a deleterious effect on the correlation coefficient. A uniform type of bottom reduces this variability and leads to

S. Shanmuga Priyaa (✉) · A. Aruna Kumar · B. K. Jena
National Institute of Ocean Technology, Velachery-Tambaram Main Road, Pallikaranai, Chennai 600100, India
e-mail: sspriyaa@niot.res.in

R. Jha et al. (eds.), *River and Coastal Engineering*, Water Science and Technology Library 117, https://doi.org/10.1007/978-3-031-05057-2_19

Table 1 Previous studies on tide co-ordinated shoreline method

S. No.	Authors	Data	Tide data	Study area	Depth range
1	Ryu et al. (2002)	Landsat TM and EOS-Terrs ASTER	Field observations	Gomso Bay, Korea	Intertidal region
2	Zhao et al. (2008)	Landsat TM	Field observations	Yangtze Delta	Intertidal region
3	Mason et al. (2010)	SAR images	LiDAR data	Morecambe Bay, U.K	0–4 m
4	Yanyan et al. (2017)	HJ-1A/B CCD and Landsat TM/OLI	Water level data from 2D Hydrodynamic model	Radial Sand Ridges (RSR) along the Jiangsu Coast, China	0–30 m

a strong correlation between depth and brightness value, thus improving the accuracy of estimated depths. In this study, the highly dynamic region, Tapi estuary has been considered where the sedimentation forms tidal flats. This paper aims to bring out the efficient use of satellite images to extract the bathymetry from the highly dynamic turbid waters.

2 Existing Methods to Retrieve Bathymetry from Satellite Images

2.1 Tide Co-ordinated Shoreline Method

The delineation of land water boundary using the multispectral images can be done based on the wavelength dependent light penetration. Blue band penetrates the clear water upto 25 m deep; red penetrates upto 5 m whereas infrared region never penetrates the water. Infrared and shortwave infrared regions have been used to delineate the land water boundary. Infrared is preferably used when the tidal flats are completely covered with mangroves or grass, whereas SWIR is commonly used for the shoreline extraction (Guy 2015; Yamano et al. 2006) from the exposed tidal flats with fewer green cover. Table 1 lists the literature that follows tide co-ordinated shoreline method.

2.2 Band Ratio Method

Band ratio method works on the assumption that light attenuates exponentially with water depth by comparing the ratio of different attenuation rates between wavebands

to determine depth. Table 2 lists the literatures that followed various methods to derive bathymetry. As depth increases, the water leaving radiance of a band with higher absorption (green) will decrease proportionately faster than that of a band with lower absorption (blue) and the ratio of blue to green values will therefore increase (Stumpf et al. 2003). The basis of the ratio transfer equation (Eq. 1) is the linear relationship presented by Lyzenga (1981) that states:

$$z = m_1 \frac{\ln(nR_w(\lambda_i))}{\ln(nR_w(\lambda_j))} - m0 \tag{1}$$

Table 2 Previous studies on satellite bathymetry

S. No.	Author	Data	Algorithm	Study area	Depth range
1	Jagalingam et al. (2015)	Landsat 8	Ratio Transform Algorithm	New Mangalore Port Trust	1–20 m
2	Pacheco et al. (2014)	Landsat 8 and LiDAR	linear transform bathymetry algorithm originally developed by Lyzenga (1978, 1981)	Ria Formosa system in southern Portugal	0–12 m
3	Pattanaik et al. (2015)	IRS-1C/1D LISS-III satellite	Philpot method, Jupp method	eastern coastal area of Odisha region & wheeler island region	0–10 m
4	Stumpf et al. (2003)	IKONOS	Log ratio transform algorithm, Principal component algorithm, Non-linear inversion algorithm	northwest Hawaiian Islands	0–25 m
5	Philpot (1989)	Landsat TM	Multiband log linear algorithm	The Bahamas, Gulf of Mexico	0–20 m
6	Lyzenga (1978, 1981)	Airborne sensor with lidar and multispectral scanner	linear transform bathymetry algorithm	The Bahamas, Gulf of Mexico	0–25 m

where, m_1 is a tunable constant to scale the ratio to depth, n is a fixed constant for all areas to ensure the terms remain positive and m_0 is an offset for a reference depth of 0 m. The theoretical benefit of a ratio transform is a compensation for variable bottom reflectance. It is claimed a change in bottom albedo affects both bands similarly, but a change in depth affects the higher waveband more, so variable bottom types can be analyzed more accurately.

3 Study Area

Tapi estuary is one of the major estuaries of west coast river in India, marked by funnel shaped outline, tidal meanders and macro tidal estuary. The river drains into Gulf of Khambhat (GoK) which is an inlet of the Arabian Sea along the west coast of India, in the state of Gujarat (Fig. 1a). Hazira is located at the mouth of the Tapi estuary. Tapi river has basaltic and alluvium as a major lithologies with 282 mm/yr run off and 19 km^3/year discharge (Madhavan and Subramanian 2001). This region also has mineral placer deposits that contribute to the industrial development around this estuary. The sediments carried away by the stream get deposited at the mouth of the estuary forming mudflats.

Tapi estuary is fully mixed estuaries similar to Mahi and Sabarmati as they experience strong tidal currents and weak discharges of fresh water. Due to the horizontal variation of salinity in these regions, the nature of sediments on either side of the bank varies. Tapi is funnel shaped or trumpet shaped estuaries where width decreases drastically upstream. This morphology of the stream and the concentration of energy of the tidal wave lead to the deposition of sediments at the mouth (Langbein 1963). This sedimentation in the Tapi estuary poses a serious problem to navigation and port operations.

Intertidal slope includes three types of mudflats based on the nature of the source material. The Type I mudflat sometimes have either marsh or grass on it. At many places, between Narmada and Tapi estuaries, patches of alluvium are found within mudflats. Type I mudflat is mainly found between the Mahi and the Tapi estuaries (Baqer 2003). Tapi estuary have marshes and grass on their mudflats, hence it falls under Type I mudflats.

4 Datasets Used

4.1 Satellite Images

In this study, the satellite images of series of dates have been collected (listed in Table 3). Sensor specifications of both Landsat 8 OLI (Operational Land Imager) and Sentinel 2 MSI (MultiSpectral Instrument) have been provided in Table 4.

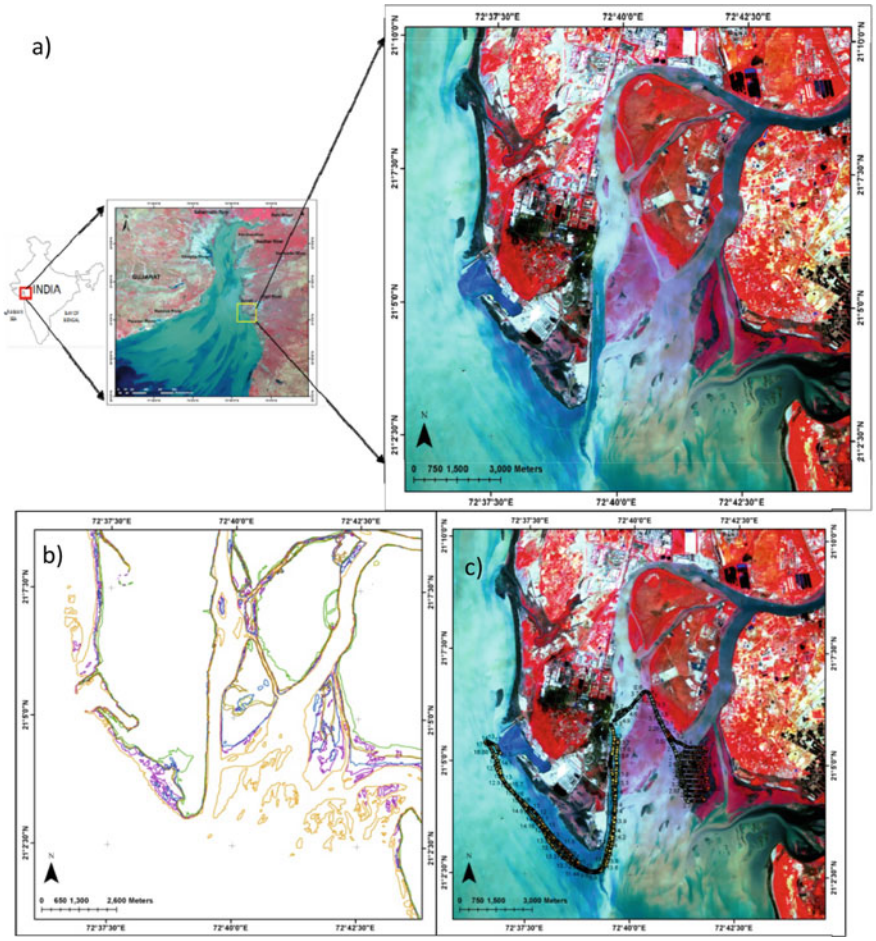

Fig. 1 **a** Map showing the extent of study area-Tapi estuary and **b** shoreline extracted from different date of satellite images **c** field collected bathymetry data

Table 3 Date & time of satellite data used with corresponding tide data

Sensor	Date & time	Tide (m) MSL
Landsat 8 OLI	17-04-2016 11:03	0.79
Landsat 8 OLI	29-02-2016 11:03	−0.92
Landsat 8 OLI	13-02-2016 11:03	−2.28
Landsat 8 OLI	12-01-2016 11:03	−3.35
Landsat 8 OLI	04-07-2016 11:03	−1.6
Landsat 8 OLI	01-04-2016 11:03	0.39
Landsat 8 OLI	03-05-2016 11:03	1.38
Sentinel 2A MSI	29-03-2016 11:11	−1.69

Table 4 Sensor Specifications

Parameters	Landsat 8 OLI	Sentinel 2 MSI
Spatial resolution (m)	15–30	10–60
Spectral resolution (nm)	10	15–180
Spectral range (nm)	440–2200	440–2190
No. of bands	11	13
Swath (km)	185	290

4.2 Bathymetry

The bathymetry data from the bathymetry surveys carried out by NIOT, in two phases during May & November 2016. Water depth has been measured using Ceeducer pro integrated with DGPS positioning system. Total line kilometre covered is around 305 kms and the area covered is about 9 km^2 during this survey. Hypack software (single beam editor tool) has been used for capture online raw data and for post processing.

4.3 Tide

Tide information along the shoreline has been extracted from the co-tidal model developed at CEE, NIOT using MATLAB® program. The Co-Tidal model is used to predict the tide level at any location inside the observations boundary. The Co-Tidal model predicts tide using tidal constituents from tidal observations. An open source code called "T_Tide" developed in Matlab was used as basis for Co-Tidal model to predict the tidal constituents from the observation by Harmonic analysis method. The Co-Tidal model reads all the constituents (amplitude and phase) from all the locations as a base parameter. The model calculates the constituents at any given location of interest by interpolating individual constituents from the tide observatory locations. These constituents were used to re- syntheses the tide level at required time. The tide information from this model has been collected for the various date and time of imaging (Table 3) the along the entire coastline.

5 Methodology

The methodology of this paper involves hybrid of two methods to derive the bathymetry data viz.: band ratio method and tide co-ordinated shoreline method as discussed in the Sect. 2. The methodology flowchart has been shown in Fig. 2. Band ratio method uses the single date imagery to derive the values which is then correlated with the existing bathymetry and the co-efficient values are derived to

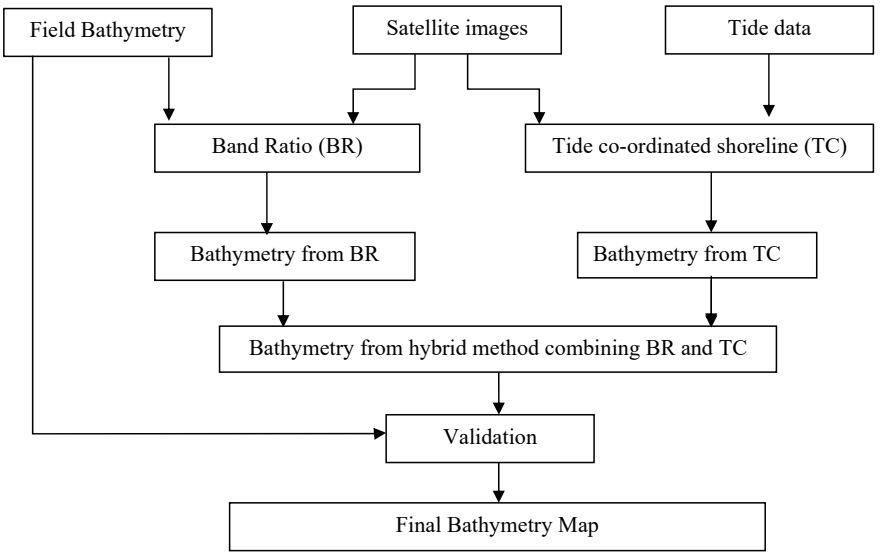

Fig. 2 Flowchart depicting the methodology of the study

map the depth. For tide co-ordinated shoreline method, a series of satellite image and the corresponding predicted tide data has been tagged to the coastline derived from the satellite image. A detailed explanation of the methods used is provided in the following sections.

5.1 Tide Co-ordinated Shoreline (TC) Method

In this method, the land–water boundary is demarcated using strong SWIR reflectance, which differentiates land and water at that instance. Using the date and time of acquisition of the image, the corresponding predicted tide data has been assigned. Thereby the exposed mudflats are also assigned with the tide values. From the predicted tide data along the coastline, the tide value varies from 0.01 to 0.03 m per km along the coast. This change in tide values has been considered in deriving bathymetry of the inter-tidal zones, thereby delineating the mudflats and the bottom topography. The predicted tide values and variation along the coastline for the satellite imagery has been used for analysis. Similarly the predicted tide values for different dates of images have been incorporated to derive the bathymetry of intertidal region. The shoreline extracted from different dates of images is provided in Fig. 1b.

5.2 Band Ratio (BR) Method

The automatic estimation of water depth using remotely sensed data uses the spectral reflectance of the sea floor at different wavelength based on their depth of penetration. The authors such as Lyzenga et al. (1978), Jupp (1988), and Philpot (1989) have used the remotely sensed multispectral data to estimate the bathymetry. Often a highly reflective (blue) and highly absorptive (NIR/SWIR) band is considered to derive the bathymetry from satellite images. Suspended sediments that include organic matter and algae have higher spectral reflectance. In this study the reflectance values have been correlated with the corresponding depth values measured from field.

With respect to depth, blue and other visible channel penetrates into the water, however the turbid nature of the water abstains from penetration and the scattering of the suspended particles contribute to the reflectance measured by the sensor. Hence, in this study band ratio combination has been attempted by correlating with the field measured depth values.

From Table 5, the correlations of combination of bands have been employed to bring out the depth values. The ratio of red to NIR and SWIR shows higher correlation regression (Eq. 2). Due to the turbid nature of water, SWIR band has to be used so that the contribution to the reflectance values can be reduced while deriving the depth. To incorporate a higher range of depth to the ratio values, a linear trend equation (Eq. 3) has been formed to derive the depth values. The slope and the intercept value has been derived using a correlation of the band ratio with the field collected depth values. The equations are as follows:

$$BR = \frac{Red}{(NIR + SWIR)} \tag{2}$$

$$\text{Depth} = 10.75 * \text{BR} - 8.9175 \tag{3}$$

Table 5 Regression co-efficient attempted for various combination of band ratio

S. No.	Band ratio	R^2 (N = 1933)
1	Blue/Green	0.4312
2	Blue/Red	0.4596
3	Blue/NIR	0.5539
4	Blue/NIR + SWIR	0.6665
5	Blue/Red + SWIR	0.2885
6	Green/Red	0.4237
7	Green/Red + SWIR	0.1190
8	**Red/NIR**	**0.7034**
9	Red/SWIR	0.5860
10	**Red/NIR + SWIR**	**0.7410**

5.3 Hybrid (TCBR) Method

To overcome the drawbacks of the two methods, hybrid method has been adopted. The hybrid method uses both the band ratio methods that work well in places except mudflats and tide co-ordinated shoreline method which work well at mudflats and can delineate them. Similarly band ratio method can extract depth upto 20 m and tide co-ordinated shoreline method has the restriction depending on the availability of image data at different dates/ different water levels. Using GIS and image processing techniques, the final bathymetry map has been prepared using clip and merge tools.

6 Results and Discussion

6.1 Result from Tide Co-ordinated Shoreline (TC) Method

The results (shown in Fig. 3a, b) from this TC method entail the tidal region between 0.39 m and −3.35 m from eight available dates of images over a period of seven months (January 2016 to July 2016). With the higher temporal resolution of the sensor, the images collected between high tide and low tide level will enable to mark more number of tide co-ordinated shorelines exposing the morphological features present beneath. However, the overall percentage error from this method is about 15.79% for 1005 samples. This is due to the fact that this region covers only the tidal region between 0.39 and −3.35 m. The efficiency of the method works within this region thereby leading to the error contribution of 15.79%. The regression (R2) value achieved by this method for the above said range is 0.7143 whereas when considered beyond the range, the R2 value drastically reduces to 0.3137. Hence this method can be used only for the regions of mudflats.

6.2 Result from Band Ratio (BR) Method

The result from this BR method (Fig. 3c, d) shows depth ranging upto 20 m. With single date imagery (preferably low tide), the depth has been estimated using band ratio of red, NIR and SWIR bands. As discussed in Sect. 3, the region falls under type I mudflat with grass and mangrove on it. Mangroves and the other chlorophyll containing organisms have higher reflective in NIR region. This region is used for mangrove species classification (Kamaruzaman and Kasawani 2007). Similarly the exposed mudflats are highly reflective in SWIR region. NIR reflectance is also influenced by the scattering contributed by the suspended sediments (Karabulut and Ceylan 2005). The overall percentage error derived from this method involves 12.42%

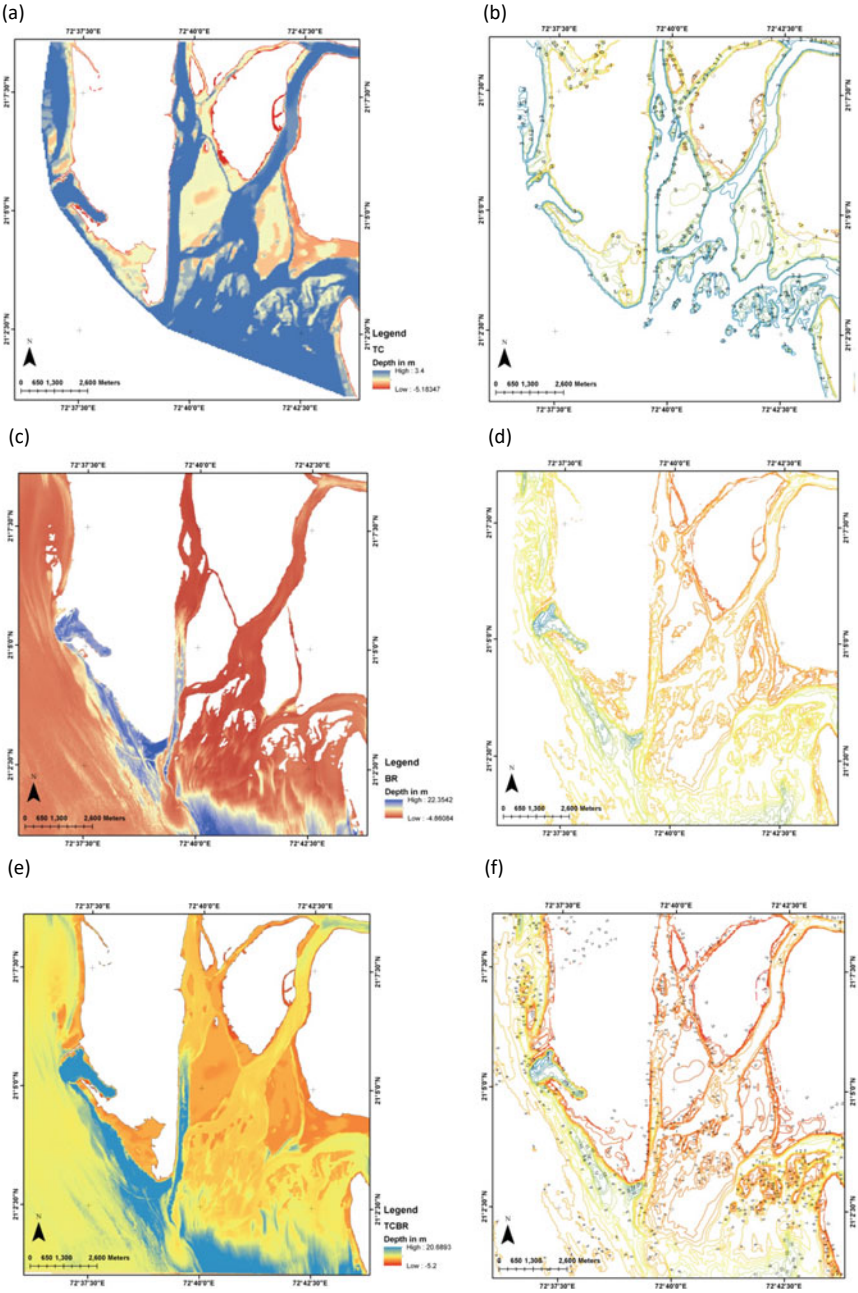

Fig. 3 **a** Bathymetry map showing the depth ranges. **b** Contour map at 1 m interval derived from Tide co-ordinated shoreline method. **c** Bathymetry map showing the depth ranges. **d** Contour map at 1 m interval derived from band ratio method. **e** Bathymetry map showing the depth ranges. **f** Contour map at 1 m interval derived from Hybrid method

(for 1005 samples) due to the factor of turbid nature of water and the reflectance of exposed and submerged tidal flats. The regression (R2) value achieved by this method is 0.3044 which includes mudflats region whereas the R2 value achieved greater than 2 m depth is 0.7395.

6.3 Result from Hybrid (TCBR) Method

As discussed in previous section, the regression values indicate the difference in their performance at different environment such as mudflats and deep channel. The data from the two methods that work well in different region has been masked and merged to form a hybrid result using GIS techniques. The bathymetry result and contour map from the hybrid method is provided in the Fig. 3e, f, it can be inferred that the map represents the gradients both at the channels and the mudflat regions. The efficiency of the hybrid method represented using profiles derived from the results has been presented in Fig. 4. By bringing the efficiency of two methods that works well in different conditions, the percentage error has been reduced to 1.3% for 1005 samples. The regression value achieved by the hybrid method is 0.765.

7 Validation

To validate the model, it is essential to assess the accuracy of the proposed method. Here, in this study, both RMSE (Root Mean Square Error) and correlation regression are estimated. The root mean square error of depth estimation is calculated using Eq. 4.

$$\mathrm{RMSE} = \left[\sum \left(\mathrm{Depth}_{\mathrm{measured}} - \mathrm{Depth}_{\mathrm{predicted}}\right)^2 / \mathrm{N}\right]^{0.5} \tag{4}$$

where, $\mathrm{Depth}_{\mathrm{measured}}$ is depth measured in field, $\mathrm{Depth}_{\mathrm{predicted}}$ is depth concentration predicted from the TCBR hybrid model and N represents the number of samples.

The best fitting model can be determined from the co-efficient (R^2) and RMSE. The Regression coefficient and their corresponding error results are listed in Table 6. It can be noticed that the lower depth range with higher regression co-efficient have less error. The error increases with the higher depth ranges.

The error increases with the depth, the results meets the standards of second order bathymetry as per IHO standards for hydrographic surveys. Though the turbid nature of water contributes to the error in bathymetry derived from satellite images apart from cloud cover, the bathymetry information can be retrieved using the hybrid method specified in this study. The result indicates that satellite image can be used for deriving bathymetry even for intertidal regions.

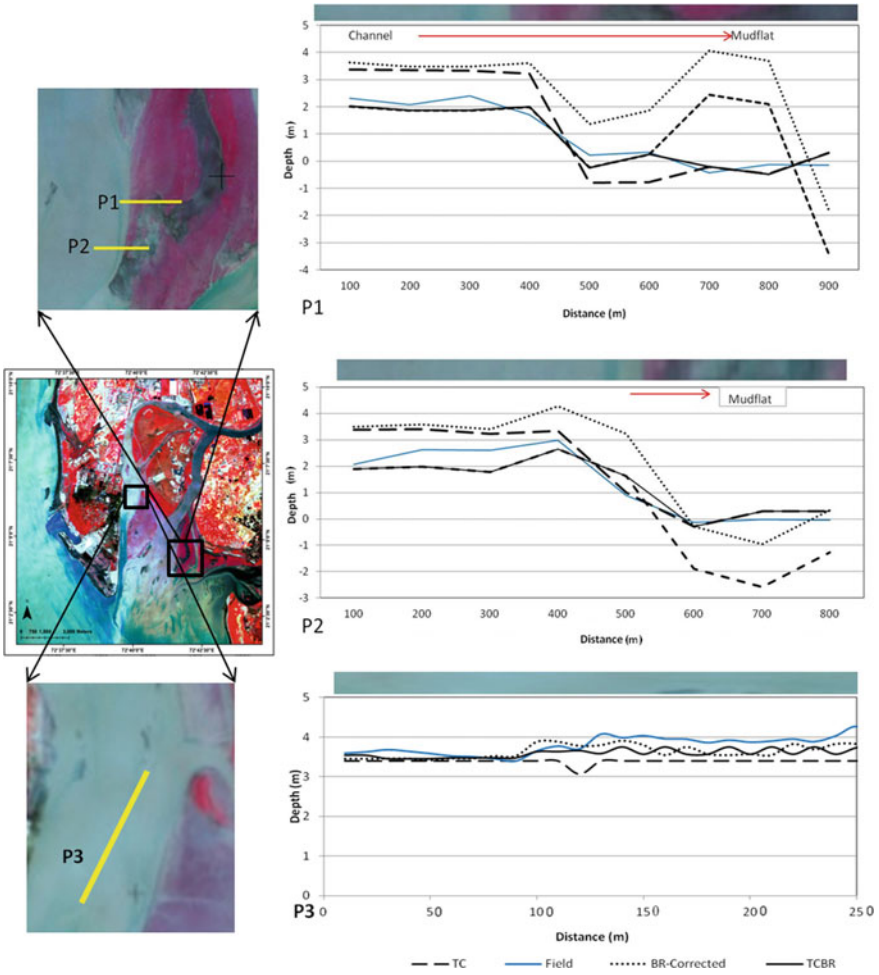

Fig. 4 Comparison of profiles derived from the different methods and field measured bathymetry

Table 6 Regression co-efficient, %Error and RMSE for varying depth and samples

N	Depth range	R^2	% Error	RMSE
74	<2	0.8469	12.61	0.3476
884	<5	0.8081	16.18	0.8095
971	<10	0.7794	19.39	0.9971
1477	<15	0.7752	26.68	2.42
2828	<20	0.765	28.8	3.53

8 Conclusions

This work attempts to combine both the existing method to derive the bathymetry. The percentage error of derived depth from tide co-ordinated shoreline is 15.79%, from band ratio method is of 12.42% and the hybrid method is 1.3% (1005 sample location). The regression co-efficient (R^2 value) achieved by the hybrid method is 0.765 including both the regions of mudflats and deep channels while the other two TC, BR methods could achieve only 0.3137 and 0.3044 respectively. The result indicates the robustness of satellite images that can be used for deriving bathymetry even for turbid waters.

Though the turbid nature of water contributes to the error in bathymetry derived from satellite images apart from cloud cover, the bathymetry information can be retrieved using the hybrid method followed in this study. Though the error increases with the depth, the results meet the standards of second order bathymetry as per IHO standards for hydrographic surveys.

Acknowledgements The authors wish to thank Dr. M.A. Atmanand, Director, National Institute of Ocean Technology (NIOT), Chennai and Dr. M.V. Ramanamurthy, Group Head, Coastal and Environmental Engineering Division, National Institute of Ocean Technology (NIOT), Chennai for their constant encouragement and other team members involved in data collection under shoreline management project funded by Ministry of Earth Sciences. The authors also thank the USGS for the Landsat 8 OLI image data and ESA for the Sentinel 2 MSI data.

References

Baqer D (2003) Ecology of selected critical environments of Gulf of Cambay using Indian remote sensing data. Thesis report from shodhganga http://hdl.handle.net/10603/51577

Guy KK (2015) Barrier island shorelines extracted from Landsat imagery: U.S. Geological Survey Open-File Report 2015–1179, 3 p, https://doi.org/10.3133/ofr20151179

Jagalingam P, Akshaya BJ, Arkal VH (2015) Bathymetry mapping using Landsat 8 Satellite imagery. Procedia Eng 116:560–566

Jupp DLB (1988) Background and extensions to depth of penetration (DOP) Mapping in Shallow Coastal Waters. In: Proceedings of the symposium on remote sensing of the coastal zone. Gold Coast. Quennsland., pp IV.2.1–IV.2.19

Kamaruzaman J, Kasawani I (2007) Imaging spectrometry on mangrove species identification and mapping in Malaysia. WSEAS Trans Biol Biomed 8, 4:118–126

Karabulut M, Ceylan N (2005) The spectral reflectance responses of water with different levels of suspended sediment in the presence of algae. Turkish J Eng Env Sci 29:351–360

Langbein WB (1963) The hydraulic geometry of a small tidal estuary. Bull Int Asso Sci Hydrol 8:84–94

Lyzenga DR (1978) Passive remote sensing techniques for mapping water depth and bottom features. Appl Opt 17(3):379. https://doi.org/10.1364/AO.17.000379

Lyzenga DR (1981) Remote sensing of bottom reflectance and water attenuation parameter in shallow water using aircraft and Landsat data. Int J Remote Sens 2:71–82

Madhavan N, Subramanian V (2001) Fluoride concentration in river waters of south Asia. Curr Sci 80:1312

Mason DC, Scott TR, Dance SL (2010) Remote sensing of intertidal morphological change in Morecambe Bay, U.K., between 1991 and 2007. Est Coastl Shelf Sci 87:487–496. https://doi.org/10.1016/j.ecss.2010.01.015

Pacheco A, Horta J, Loureiro C, Ferreira O (2014) Retrieval of nearshore bathymetry from Landsat 8 images: a tool for coastal monitoring in shallow waters. Remote Sens Environ. https://doi.org/10.1016/j.rse.2014.12.004

Pattanaik A, Sahu K, Bhutiyani MR (2015) Estimation of shallow water bathymetry using IRS-multispectral imagery of Odisha Coast, India. Aquat Proc 4:173–181

Philpot WD (1989) Bathymetric mapping with passive multispectral imagery. Appl Opt 1989(28):1569–1578

Ryu J, Won J, Min KD (2002) Waterline extraction from Landsat TM Data in a Tidal Flat: a case study in Gomso Bay, Korea. Remote Sens Environ 83(3):442–456. https://doi.org/10.1016/S0034-4257(02)00059-7

Stumpf RP, Holderied K, Sinclair M (2003) Determination of water depth with high-resolution satellite imagery over variable bottom types. Limnol Oceanogr 48:547–556

Yamano H, Shimazaki H, Matsunaga T, Ishoda A, McClennen C, Yokoki H, Fujita K, Osawa Y, Kayanne H (2006) Evaluation of various satellite sensors for waterline extraction in a coral reef environment: Majuro Atoll, Marshall Islands. Geomorphology 82:398–411

Yanyan K, Xianrong D, Fan X, Changkuan Z, Xiaoping G (2017) Topographic mapping on large-scale tidal flats with an iterative approach on the waterline method. Est. Coastal Shelf Sci. https://doi.org/10.1016/j.ecss.2017.03.024

Zhao B, Guo H, Yaner Y, Wang Q, Li B (2008) A simple waterline approach for tidelands using multi-temporal satellite images: a case study in the Yangtze Delta. Est Coastal Shelf Sci 77:134–142. https://doi.org/10.1016/j.ecss.2007.09.022

Numerical Model Studies to Assess Wave Transmission Through Array of Wave Energy Converters, with Different Configurations

K. H. Barve, K. S. Vighe, and L. R. Ranganath

1 Introduction

The need for pollution free power generation is the need of the day and has resulted in a renewal of renewable energy. One such form of energy is the energy that can be derived from ocean waves. Waves are generated because of the wind passing over the sea and not because of the lunar and solar attraction. Higher waves have more energy associated with it. Height of the wave is directly proportional to the fetch. Longer the fetch higher will be the wave. Hence, the energy is a concentrated in the form of waves. The research to make wave energy extraction viable is being carried out extensively. The research work is primarily in two directions firstly to assess wave energy potential of a coast and identify sites, to generate extensive accurate information of wave energy potential.

Various types of Wave Energy Converters (WEC) like Oscillating Wave Surge converter, Oscillating water column converter Point Absorber, Submerged Pressure differential converter have been explored. It is necessary to check the performance of these WECs from the point of view of energy absorption in the device. Other direction is to study various designs of wave energy converters (WEC) and to estimate their efficiency. For the estimation of the WEC efficiency, it is imperative to assess the actual wave energy which will be absorbed by the wave energy converter. To estimate wave energy absorption, the transmission through the Wave Energy Converter is observed. To observe the wave transmission through a WEC, physical wave flumes

K. H. Barve (✉)
Scientist B (retd), Central Water and Power Research Station, Pune 411038, India
e-mail: barvekh@gmail.com

K. S. Vighe
Assistant Research Officer, Central water and Power Research Station, Pune 411038, India

L. R. Ranganath
Retd Scientist' E', Central water and Power Research Station, Bengaluru, India

R. Jha et al. (eds.), *River and Coastal Engineering*, Water Science and Technology Library 117, https://doi.org/10.1007/978-3-031-05057-2_20

are used. The prototype wave and dimension conditions are considered with appropriate scaling. This process is time consuming and takes long time. However this method gives accurate results as well.

Numerical flume experiments are carried out in last few years. In this regard, since wave energy converters allow part of the waves to pass through the structure, they can be considered as permeable structures and the numerical studies can be carried out.

Beels et al. (2009) (Ref. 1) did the Numerical simulation of wake effects in the lee of a farm of Wave Dragon wave energy converters, using mild slope wave equation. Nørgaard (2010) (Ref. 2) conducted numerical model studies to obtain wave height reduction by means of wave energy converters. Norgaard and Andersen (2012) (Ref. 5) investigated Wave Transmission from a Floating Wave Dragon Wave Energy Converter. A numerical model was used to determine the wave transmission through the floating WD in varying wave conditions. Jha et al. (2017) (Ref. 4), these investigations showed very good match with the physical wave flume results. The numerical model method is verified.

In the present study three types of arrays of WECs are considered. The wave transmission through these at various locations with respect to the WEC array is observed. The parametric studies are described in this paper.

2 Methodology

2.1 Numerical Model

A WEC can be considered as a permeable structure. The permeability of the breakwater can be modeled in certain Boussinesq type mathematical models. The Boussinesq wave model is widely used for various studies in ports, harbours and coastal areas. This model is capable of reproducing the combined effect of all important wave phenomena such as diffraction, refraction, shoaling, non-linear wave wave interaction, bottom dissipation etc. It can handle partial reflection from the structure and wave transmission through the structure. In order to study the WEC array, the Boussinesq wave model MIKE 21 BW was used. The model has been successfully used to assess wave transmission through permeable structures. MIKE 21 BW can incorporate simulation of wave reflection and transmission through the permeable structure using porosity layer. The MIKE 21 BW model was used for studying simple arrays of WECs.

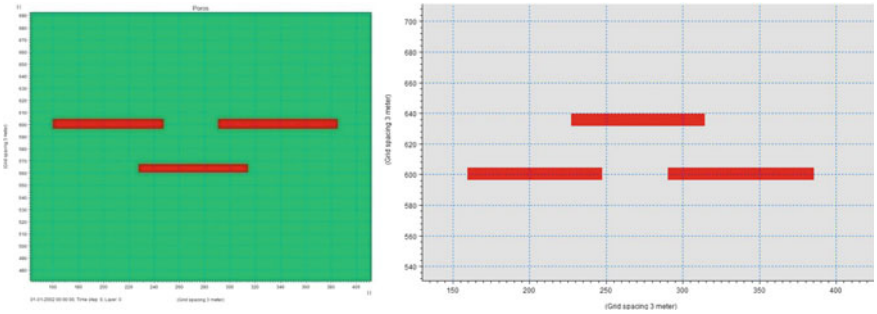

(A) Array 1 (B) Array 2

Fig. 1 Schematics diagram of Array 1

2.2 Numerical Wave Flume

A numerical wave flume 3000 m long and 1650 m wide was setup. The constant water depth of 8 m was considered. The area was discretised into 3 m × 3 m grid.

Three wave energy converters of length 260 m each and width 18 m were tested. These three WECs were arranged in two arrays. The wave transmission was numerically studied for these two arrays. The schematic picture of the array 1 is shown in Fig. 1.

In both the arrays the first structure obstructing the wave attack is 1500 m from the wave generating line. The distance between the first line and the second is 85 m and vertical separation is 150 m.

2.3 Experiments

The MIKE 21 BW model was run for Array 1 and Array2. Model was run for different incident wave heights 1, 1.5 and 2 m and wave periods 8, 9 and 10 s. The incident wave direction is normal to the structures. Thus total 9 simulations for each array were carried out.

The wave disturbance coefficient is calculated at different locations. Firstly the observations at locations M1, M2 are extracted in the middle of the horizontal distance. Care has been taken to avoid effect of both the reflection and diffraction by choosing the observation points, two wave lengths before and after the structure (Fig. 2).

A typical the wave disturbance coefficient plot for wave incident wave height of 1 m, wave period 9 s. and incident wave direction normal to the structures, is shown in Fig. 3. The figure shows the area near the structures.

The array is symmetric with respect to a vertical axis. It can be seen from the figure that the wave height distribution is symmetrical along the vertical axis. Hence

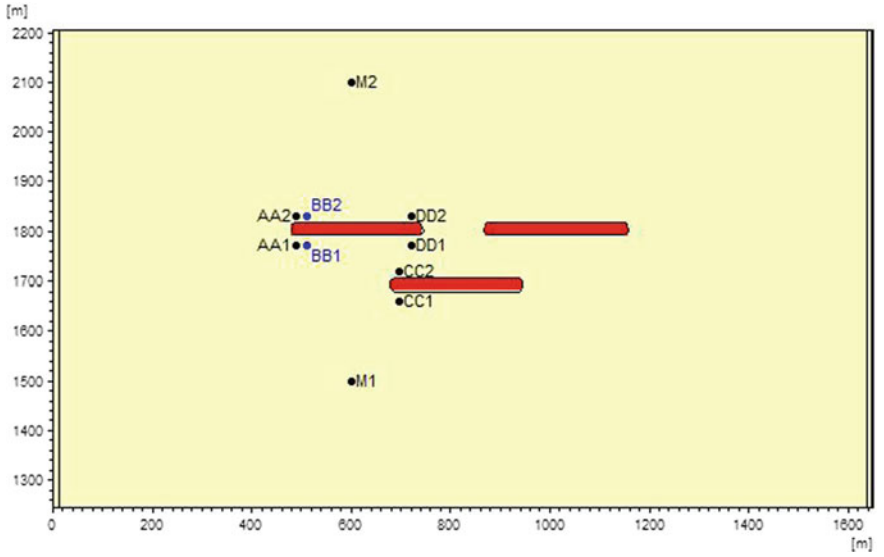

Fig. 2 Locations to extract the wave disturbance coefficient. (Array 1)

the observations are taken on the left side only. In the middle portion due to the effect of diffraction and wave transmission wave heights are higher.

The points AA1, AA2 are at the corner adjacent to the edge. Locations BB1 and BB2 are slightly away from the end, but nearer to the corner. A diffraction effect as well as effect of reflections will be seen here. CC1 and CC2 are similar points for the single structure. DD1 and DD2 are in the shadow region. At DD1 the diffracted waves from the single breakwater will also add.

3 Results and Discussion

The transmission coefficient is calculated by taking the ratio of wave disturbance at M2 to that of M1. The transmission coefficients are plotted as graph. The graphs for 8, 9 and 10 s are plotted for incident wave heights of 1, 1.5 and 2 m. It is observed that the transmission coefficient reduces as wave period increases (Fig. 4).

The locations where wave disturbance coefficients were extracted and transmission coefficients are calculated are shown in Fig. 5. The locations AA1, AA2 and CC1 and CC2 are between the overlap of the two structures. There will be diffracted waves at AA2 and between AA2 and the next structure. CC1 may indicate a certain increase in wave disturbance if the wave formation takes place in between the structures. The wave disturbance plot is given below which confirms these observations. The difference in the magnitude is not high but is significant. This implies that the corners of the single WEC will absorb more energy (Fig. 6).

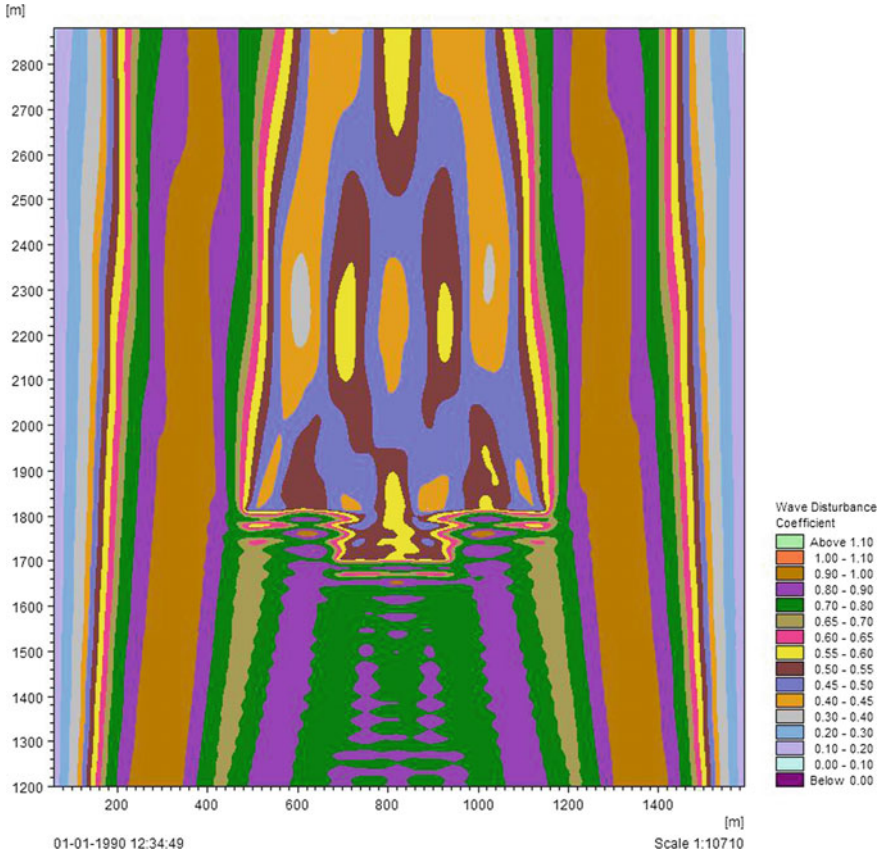

Fig. 3 Wave Disturbance coefficient plot for Array, 9 s

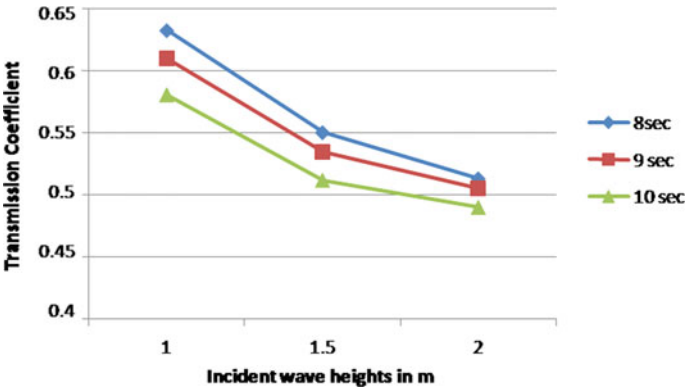

Fig. 4 Comparison of transmission coefficients for the middle points

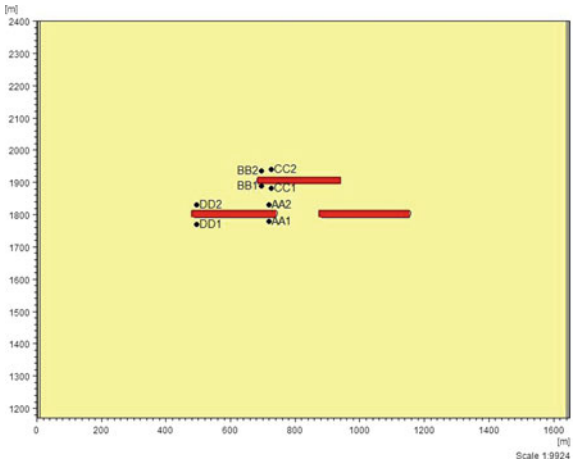

Fig. 5 Locations to extract the wave disturbance coefficient (Array 2)

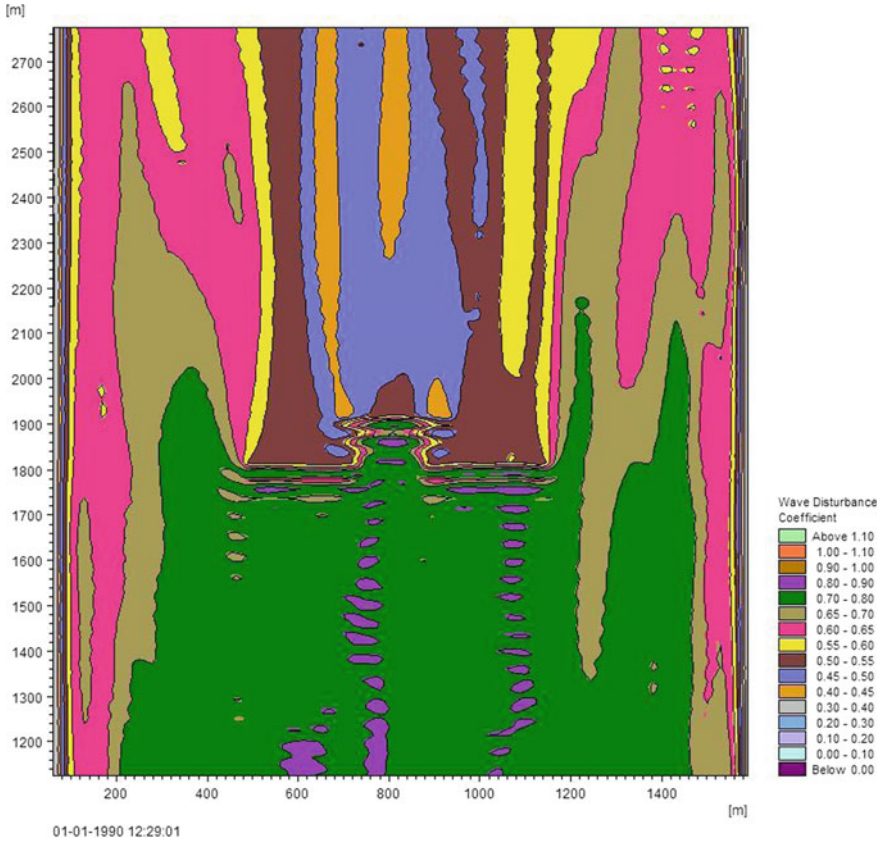

Fig. 6 Wave disturbance coefficient plot for Array 2 (9 s. wave period)

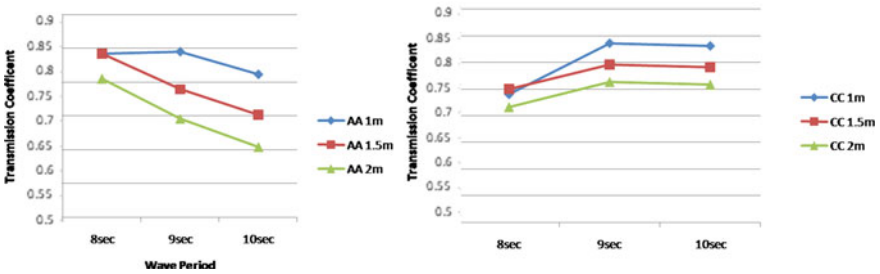

Fig. 7 The Comparison of transmission coefficient versus wave period at location AA and CC

3.1 Comparison of Transmission Coefficients

The AA1 and AA2: BB1 and BB2; CC1 and CC2; and DD1 and DD2 are on the opposite sides of the structures i.e. WEC. Thus the ratio of wave disturbance coefficient at AA2 to AA1 is the transmission coefficient at Location AA. Similarly transmission coefficients at BB, CC and DD are defined. The further analysis of wave transmission through the WEC array was carried out for different incident wave heights 1, 1.5, 2 m and wave periods 8, 9 and 10 s. The transmission coefficients at different locations for wave periods 8, 9 and 10 s are calculated and compared. Figure 7 shows the graphs of this comparison at the locations AA and CC. It is observed that for higher incident wave heights the transmission is less at the location AA, as well as CC. From 8 to 10 s the transmission coefficient has declined at the location AA, this trend is reversed at the location CC. The range of the transmission coefficients is smaller for CC. AA are the points at the first wave impact and at CC the diffracted waves are dominant.

For different wave periods the transmission coefficient for AA, BB, CC and DD locations for incident wave heights 1.0, 1.5 and 2.0 m model results are compared. The graphs are presented in Fig. 8. It is observed in all the three wave periods that the transmission is more at BB than that of at AA. Transmission coefficient at CC is more than that at BB. The transmission coefficients at CC and DD are almost the same. It is further seen that with the increase in the incident wave heights transmission coefficients decrease.

4 Conclusions

1. Boussinesq wave model MIKE21 BW can be used successfully. The different experiments in numerical flumes were done efficiently. This approach saves time and is flexible.

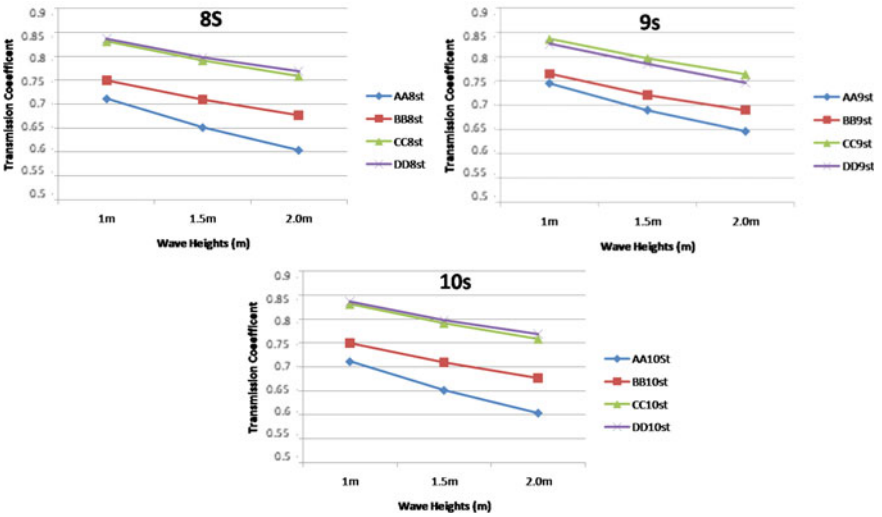

Fig. 8 The Comparison of transmission coefficient versus incident wave heights. For wave periods 8, 9, and 10 s

2. For efficient wave energy extraction array of Wave Energy Converters (WECs) are used.

   Considering the WEC as a permeable breakwater with known permeability, numerical study of WEC is carried out. To study the wave transmission through WEC, numerical modelling is the most feasible way. Boussinesq type model MIKE 21 BW was used successfully for studying two layouts of three WECs each.

3. In a numerical wave flume of 1650 m by 3000 m, wave was simulated. Two arrays of 3 WECs are tested. The simulation was done with three incident wave heights 1, 1.5 and 2 m for wave periods of 8, 9, 10 s. The experiments were carried out for array1 and 2.
4. The Transmission of the wave through the middle portion of the structure, the observations are taken so as to avoid the effect of reflections and diffraction. The transmission coefficient is in the range of 0.5–0.65. Transmission coefficients decreased with increase in the wave heights. For higher wave periods the transmission coefficient decreased. Observations at the locations in the corner of the structures, the transmission coefficient are greater. In the range of 0.7–0.85. This is due to the inclusion of reflection and diffraction effects. It is observed that for higher incident wave heights the transmission is less. From 8 to 10 s the transmission coefficient has declined at the location AA, this trend shows reversal at the location CC. AA are the points at the first wave impact and at CC the diffracted waves are dominant.

Acknowledgements The authors are thankful to Director, CWPRS Dr. (Mrs.) V. V. Bhosekar for her kind permission for the publication of this paper.

References

Jha A, Barve KH, Ranganath LR (2017) Numerical model studies to assess wave transmission through permeable structure. HYDRO 2017, Ahemadabad

Beels C, Troch P, Visch KD, Kofoed JP, Backer GD (2009) Application of the time-dependent mild-slope equations for the simulation of wake effects in the lee of a farm of Wave Dragon wave energy converters. Renew Energy 35:1644–1661

Nørgaard JH (2010) Wave height reduction by means of wave energy converters. Msc thesis in Civil Engineering, Sohngaardsholmsvej, Aalborg University, Denmark

Nørgaard JH, Andersen TL (2012) Investigation of wave transmission from a floating wave Dragon wave energy converter. In: Proceedings of the twenty-second international offshore and polar engineering conference, Aalborg University Denmark, pp 17–22

Physical and Numerical Modeling of Flow Pattern Near Upstream Guide Wall of Jigaon Dam Spillway, Maharashtra

Vaishali P. Gadhe, S. R. Patnaik, M. R. Bhajantri, and V. V. Bhosekar

1 Introduction

In earthen dam if geological site for the spillway is not suitable in river gorge, then a spillway is provided at a suitable site which may be away from the river gorge. In such situation, a separate appurtenant structures are required to connect the spillway and the earthen dam. Guide walls are provided to connect the spillway with earthen dam. Suitable design of the guide wall is a key factor so as to guide the flow smoothly from river gorge for acceptable approach flow conditions in front of spillway. If guide walls are not aligned properly, they lead to adverse approach flow conditions, which in turn cause intermixing of flow, due to abrupt change in the direction of flow near the guide wall and the formation of eddies resulting in reduced discharging capacity of spillway. Therefore, proper alignment of guide wall is very important for proper approach flow condition in front of spillway.

Jigaon Project is one of the major irrigation project under construction on River Purna of Maharashtra comprising of of 8.24 km long and 35.245 m high earthen dam. The spillway consists of 16 spans of size 15 m (W) $\times$ 12 m (H) with radial gates to pass the maximum outflow flood of 24,131 m^3/s. The equation for the ogee spillway is $y = 0.0708 \times 1.763$. The MWL, FRL and MDDL have been fixed at El. 240.561 m, 239.21 m and 233 m respectively. The energy dissipator is in the form of stilling basin of length 10 m at El. 211.6 m. Hydraulic model studies for the

V. P. Gadhe (✉) · S. R. Patnaik · M. R. Bhajantri · V. V. Bhosekar
Central Water & Power Research Station, Pune 411024, India
e-mail: vpgadhe@gmail.com

S. R. Patnaik
e-mail: patnaik.sangeeta@gmail.com

M. R. Bhajantri
e-mail: bhajan_mr@rediffmail.com

V. V. Bhosekar
e-mail: vvbhosekar@yahoo.co.in

R. Jha et al. (eds.), *River and Coastal Engineering*, Water Science and Technology Library 117, https://doi.org/10.1007/978-3-031-05057-2_21

original design of this project were conducted on 1:100 scale 3-D comprehensive model at CWPRS for evolving the optimum design of spillway with guide walls and to assess the performance of spillway in respect of discharging capacity, water & pressure profiles and performance of stilling basin provided as energy dissipator. Main objective of this paper is to simulate approach flow conditions in front of spillway with proper alignment of guide wall. Numerical studies carried out using Flow 3D software and results are compared with physical model studies.

1.1 Physical Model

Hydraulic model studies were conducted at CWPRS by constructing a 3-D comprehensive model of 1:100 geometrically similar scale. Upstream river reach of about 900 m and downstream reach of 3.5 km from dam axis has been reproduced in the model. For hydrostatic pressure measurement, piezometers along the centre of span and side of pier were provided on the spillway surface up to endsill. The model was equipped with suitable inlet and outlet arrangements to measure various discharges with corresponding reservoir water levels, tail water levels and velocities (CWPRS 2017a, b). Figures 1 and 2 show general layout plan and section of the spillway respectively.

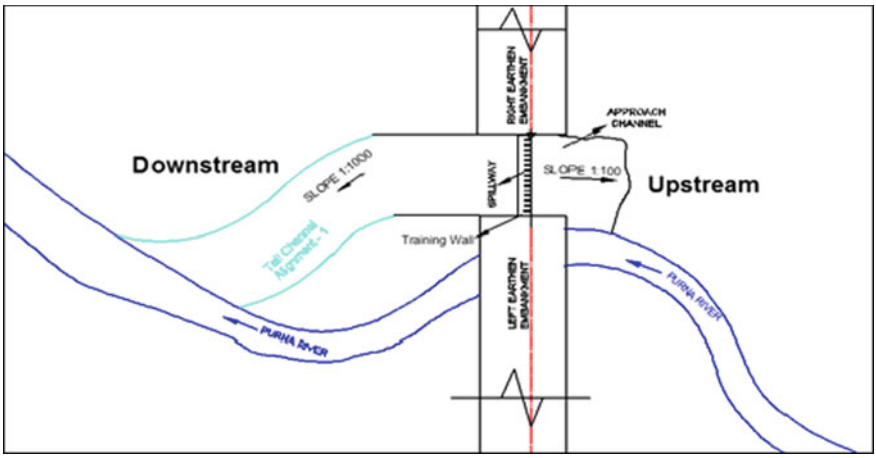

Fig. 1 General layout plan

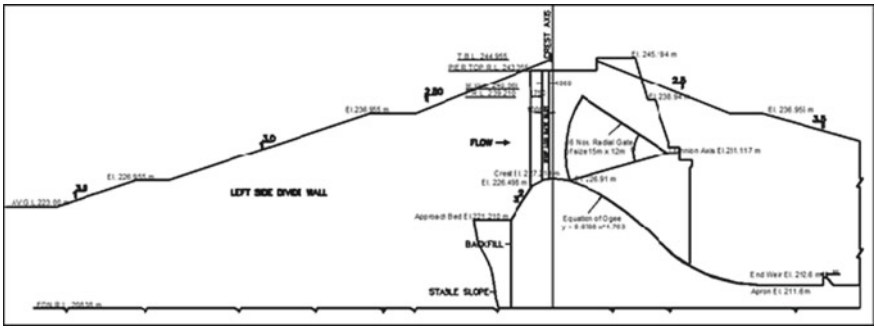

Fig. 2 Section of the spillway

2 Numerical Model

In the field of numerical simulation, the governing equations of the flow which are usually Navier–Stokes equations together with turbulence models are solved with powerful numerical methods such as finite volume and finite elements (Parsaie et al. 2015). Several turbulence models have been proposed for solving the turbulent flow. In this regard the K-epsilon, RNG K-epsilon and large eddy simulation (LES) are the advanced turbulence models that recently have been widely used in the hydraulic engineering (Versteeg and Malalasekera 2007). Several commercial software and open source codes have been proposed for comfortable use of the numerical modeling in the hydraulic engineering studies. In this regard, the commercial software Flow-3D, developed by Flow Science, is used for the numerical modeling of the flow. Numerical modeling of turbulent flow over hydraulic structures helps to define flow properties including velocity and pressure distribution through the structure. In addition to define hydraulic characteristics, numerical models have high ability to show the flow pattern which is also an important flow property. Physical model dimensions were used to generate the computational domain geometry. After the .stl file is imported into Flow 3D, the geometry of spillway is embedded in the computational grid by the pre-processor using the FAVOR concept (Hirt and Sicilian 1985). In Flow 3D, grid generation is the most important issue for accurate solution. If good quality of mesh is generated, one can obtain realistic results from the numerical model. Flow 3D uses a grid system of orthogonal meshes in the Cartesian or cylindrical coordinates. Cartesian coordinate system is selected for this investigation. The flow region is subdivided into a mesh of fixed rectangular cells. The grid generation does not depend on the geometry. That is, the geometry in the domain is represented in a simple and proper way without requiring a body fitted grid system so that the geometry and grid generation are independent of each other. A uniform mesh is used for the first simulation trial, as it took more computational time non-uniform mesh system was generated for other trials in order to provide more grid refinement close to the block of spillway. For non-uniform mesh system, there are some advices in

Flow 3D Users Manuel in order to generate an appropriate grid. The most significant issue is to avoid large differences in sizes between adjacent cells. The size ratio between adjacent cells should be as close to unity as possible, and not exceed 1.25 for efficient results. Hence In the upstream domain 16 lakh no. of cells were provided whereas in the spillway domain fine mesh with 32 lakh no. of cells were provided and in the downstream coarse mesh with 8 lakh of cells were provided to optimize the use of computational resources and time. In this paper, physical modeling data was used for numerical simulation for finding an optimal shape for the guide wall which removes the cross waves in the maximum flood design.

3-D Computational domain geometry was generated in AutoCAD software. Physical model dimensions were used to generate the computational domain geometry. Numerical simulations were carried out to study approach flow condition in front of spillway for the design discharge of 24,131 m^3/s at ungated operation of spillway. While conducting simulation, upstream boundary was set as a Volume Flow Rate for the design discharge of 24,131 m^3/s for ungated operation of spillway and downstream boundary as a pressure outlet. The extent of the mesh in the upstream X-direction was adjusted until any further increases had negligible effect on the discharge. Numbers of probes were provided at different locations for observing different parameters of the flow such as surface velocity and free surface elevation. Baffles were provided at the inlet and outlet boundary to observe the discharge passed through the spillway. The simulation was conducted upto 50 s which was found to be enough for flow stabilisation. Figure 3 shows numerical model setup in Flow -3D for Jigaon dam spillway for original design.

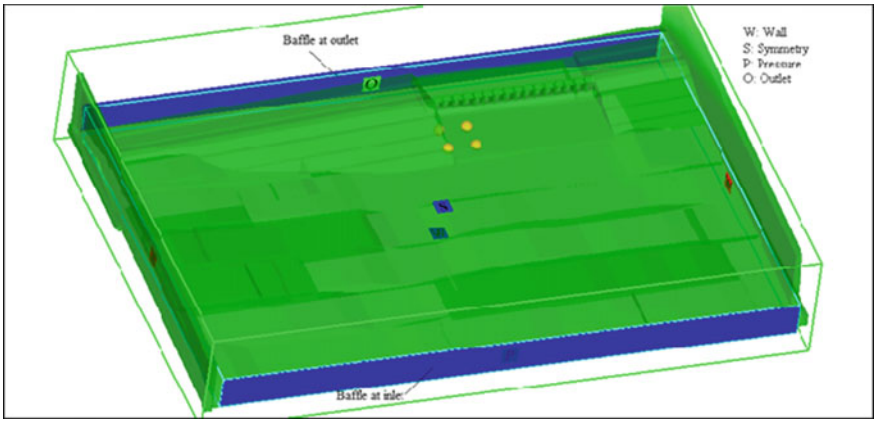

Fig. 3 Numerical model setup in flow-3D for Jigaon dam spillway for original design

2.1 Comparison of Numerical Model Results with Physical Model Results for Original Design of Spillway

Studies were conducted on both physical and numerical modeling on the original design and modified design of the spillway, for the condition of the design discharge of 24,131 m^3/s for ungated operation of spillway. The results obtained from the numerical simulation were compared with the physical model studies result for the conditions as given below.

2.2 Flow Conditions Over the Spillway for Fully Open Gate Operation

Studies were conducted for discharging capacity of spillway for entire range of discharges for ungated operation of spillway for all the spans. It was observed that a discharge of 24,131 m^3/s could be passed at RWL El. 240.49 m. Flow conditions at the upstream and downstream of spillway were observed for ungated operation of spillway for the design discharge of 24,131 m^3/s. The approach flow conditions upstream of spillway were found to be tranquil in front of all the spans except end spans. However, the flow in the reservoir entering the approach channel falls directly in front of 1st and the 16th span, thereby causing intermixing of flow due to sudden change in the direction of flow. This occasional touching of trunnion of 1st and the 16th span is due to unguided flow along the approach channel in the 1st and the 16th span for the entire range of discharges up to design outflow flood of 24,131 m^3/s. Therefore, it was suggested to provide curved guide walls to improve the approach flow conditions in front of end spans. Photos 1 and 2 show the upstream view of physical model, upstream flow condition of spillway for design discharge of 24,131 m^3/s for ungated operation of spillway respectively. Numerical studies were carried out for the discharge of 24,131 m^3/s at ungated condition. It shows close agreement of numerical simulation with the physical model studies. Photo 3 and Fig. 4 shows the upstream flow condition depicting the intermixing of flow due to abrupt change in the direction of flow for the discharge of 24,131 m^3/s for ungated operation of spillway at ungated condition in the physical model studies and numerical simulation respectively.

2.3 Velocity in the Upstream of the Spillway for Fully Open Gate Operation

The flow in the reservoir entering the approach channel falls directly over the upstream left and right training wall in front of 1st and the 16th span, resulting in intermixing of flow due to abrupt change in the direction of flow. Therefore the

Photo 1 Upstream view of physical model

velocities in the approach channel at which intermixing of flow observed were found to be very high specifically in front of 1st span of spillway at chainage 50 m in the upstream from dam axis. This velocity was observed in the range 11.3–12.3 m/s for ungated operation of spillway for design discharge of 24,131 m^3/s. In Numerical simulation velocities were find out with the help of probes. Positions of the Probes were kept at the same locations where intermixing of flow observed in the physical model. As compared the numerical results with the physical model results it shows the close agreement. Table 1 shows the comparison of surface velocities obtained from the physical model study and numerical model study in front of the spillway

Table 1 Surface velocities for ungated operation of spillway

Chainage	Gates fully open					
	Physical model results			Numerical simulation results		
	Q = 24,131 m^3/s			Q = 24,131 m^3/s		
	Velocity (In front of span no. 1) m/s	Velocity (In front of span no. 9) m/s	Velocity (In front of span no. 16) m/s	Velocity (In front of span no. 1) m/s	Velocity (In front of span no. 9) m/s	Velocity (In front of span no. 16) m/s
Upstream in the approach channel						
10	6.7	2.9	2.3	7.8	3	3.5
50	12.3	11.5	2.5	15.6	13.6	4
100	4.2	1.3	0.4	6	2	1.4
150	2.3	0.7	0.6	3.4	1.8	1
200	2.0	0.9	0.4	3	1.9	1.2

at which intermixing of flow observed for the design discharge of 24,131 m^3/s at ungated operation of spillway.

3 Revised Design of Spillway

Taking the due cognizance of the result of the model studies, 1:100 scale geometrically similar 3-D comprehensive model was modified incorporating revised length of stilling basin, curved guide walls, submersible divide walls, training walls and tail channel. This paper is focused on performance of guide wall for the design discharge of 24,131 m^3/s at ungated operation of the spillway with various alternatives for the alignment of guide walls suggested by CWPRS to optimise the design of guide walls as given below:

1. Sloping guide wall with straight length of 40 m from dam axis with top at El. 244.955 m and further providing curvature with a radius of 80.67 m which was sloping linearly with a slope of 1(V): 4 (H) was provided as shown in Photo 4a. it was observed that the flow in the reservoir entering the approach channel cause mild circulation in front of the spans 1–5 for the discharge above 15,642.59 m^3/s (Inglis flood) as shown in Photo 4b
2. As the performance sloping guide wall was not satisfactory guide wall was provided as curved guide wall with full curve height upto dam top El. 244.955 m as shown in Photo 5. It was observed that the flow in the reservoir entering the approach channel was tranquil and no circulations were observed as shown in Photo 6. Performance of the curved guide wall was also observed in the numerical simulation. In physical model studies all the modification regarding guide wall were done in left guide wall and similar modifications were consider for right guide wall. In numerical simulation left as well as right curved guide wall were reproduced. From the numerical simulation results the improvement in the approach flow condition were observed. As compared the numerical results with the physical model results it shows the close agreement. Figures 5 and 6 shows the geometry of the curved guide wall and flow conditions of the curved guide wall in numerical model respectively.

4 Conclusions

Model studies of the original design of spillway with guide walls indicated that flow conditions in front of the spillway are not satisfactory as the flow in the reservoir entering the approach channel falls directly over the upstream left and right training wall in front of 1st and the 16th span, resulting in intermixing of flow due to abrupt change in the direction of flow. To optimise the design of guide walls model studies with various alternatives for alignment of guide walls are carried at CWPRS. From the model studies it is observed that upstream curved guide wall for full curve height

Photo 2 Upstream flow condition of spillway for Q = 24,131 m^3/s for ungated operation of spillway

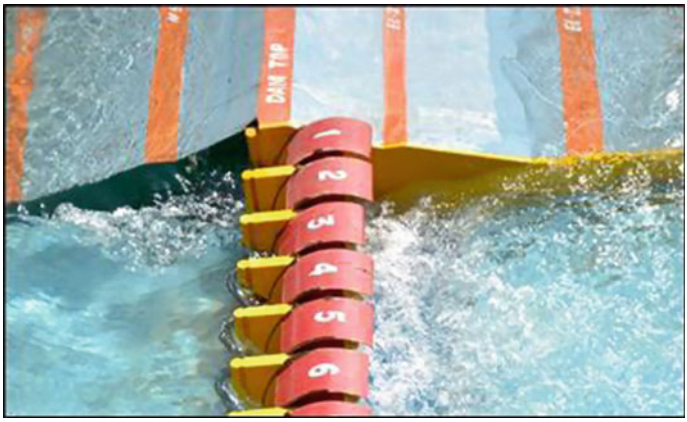

Photo 3 Intermixing of flow due to abrupt change in the direction of flow for Q = 24,131 m^3/s for ungated operation of spillway

upto dam top El. 244.955 m is acceptable as the flow in the reservoir entering the approach channel is tranquil and no circulations are observed. It is suggested from the project authorities that the provision of full curve height guide wall would be uneconomical and occurrence of the discharge above 15,642.59 m^3/s would be rare. Therefore, the upstream curve guide wall with slope of 1(V): 4 (H) would be acceptable. Thus, the model studies played an important role in enhancing the overall performance of spillway with guide wall and energy dissipator arrangement which will ultimately help the project in achieving a techno-economic design of spillway. With the physical model studies, numerical simulation is also used as a complementary tool for assessing the hydraulic performance of structures. Utmost expertise is necessary for analysis and interpretation of the results of numerical simulation.

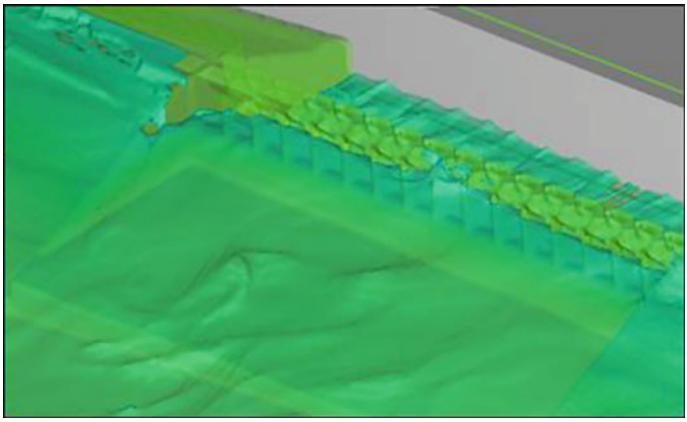

Fig. 4 Upstream flow conditions for fully open gate condition of spillway at Q = 24,131 m^3/s in numerical simulation

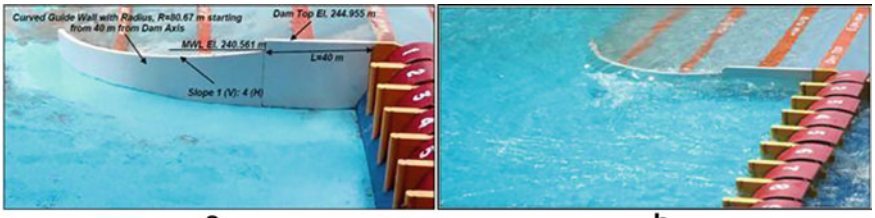

Photo 4 **a** View of the model for curved guide wall with slope 1(V): 4(H), **b** flow condition near the upstream curved guide walls

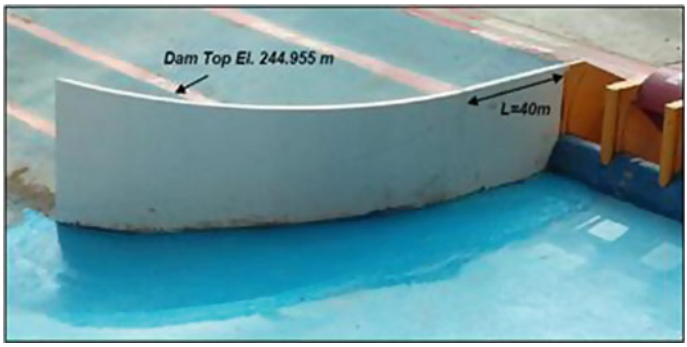

Photo 5 Modified upstream curved guide wall with full curve height upto dam Top El. 244.955 m

Photo 6 Flow conditions after modifying upstream curved guide wall with full curve height upto dam Top El. 244.955 m

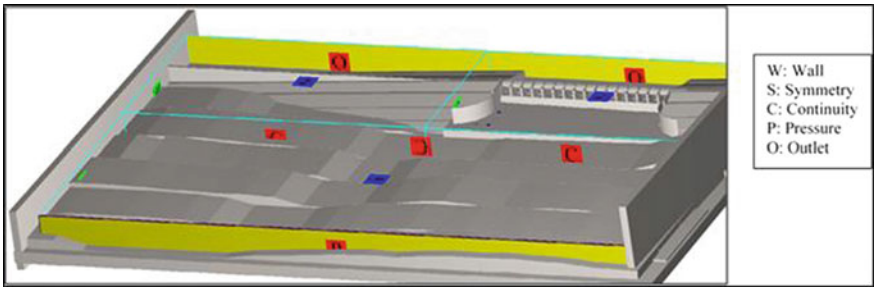

Fig. 5 Geometry of the modified upstream curved guide wall with full curve height upto dam top El. 244.955 m

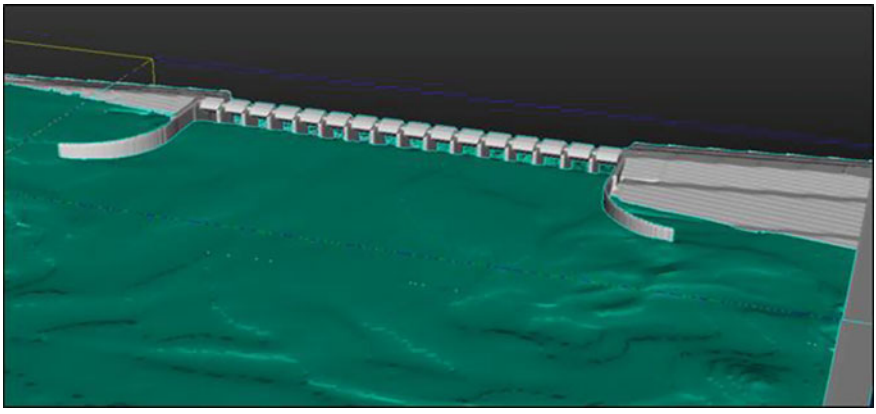

Fig. 6 Flow conditions of the curved guide wall in numerical model

Acknowledgements The authors are thankful to the project engineers from Jigaon Project Maharashtra and design engineers from CDO, Nashikfor constant interaction during the course of studies. The help of all the staff in conducting the studies and compiling the data is gratefully acknowledged.

References

Computational Fluid Dynamics Software—Flow 3D from Flow Science, CFD. www.flow3d.com

CWPRS Technical Report No. 5491 (2017a) Hydraulic model studies for Jigaon Dam Spillway, Maharashtra. 1:100 Scale 3-D comprehensive model

CWPRS Technical Report No. 5539 (2017b) Hydraulic model studies for the revised design of Jigaon Dam Spillway, Maharashtra. 1:100 Scale 3-D comprehensive model

Hirt CW, Sicilian JM (1985) A porosity technique for the definition of obstacles in rectangular cell meshes. In: Proceedings 4th international conference Ship Hydro, National Academy of Science, Washington, DC, September, pp 1–19 (1985)

Parsaie A, Haghiabi A, Moradinejad A (2015) CFD modeling of flow pattern in spillway's approach channel. Sustain Water Resour Manag 1(3):245–251

Rodi W (1993) Turbulence models and their application in hydraulics. Taylor & Francis

Versteeg HK, Malalasekera W (2007) An introduction to computational fluid dynamics: the finite volume method. Pearson Education Limited

Assessing the Impact of Ports on Tiruvallur Coast of Tamilnadu

S. Subburaj, R. S. Kankara, M. Umamaheswari, and S. Chenthamil Selvan

1 Introduction

Shoreline changes elicited by erosion and accretion are natural processes that happen over a range of time scales. They will occur in response to short-term events like storms, regular wave action, tides, and winds or in response to large-scale events like glaciations which alter sea levels and tectonic activities that cause coastal land subsidence or emergence (Fenster et al. 2001; Lee 2005). Human activities on the coast (land reclamation, port development, shrimp farming), inside watercourse catchments and watersheds (river damming and diversion), and offshore (dredging, sand mining) together with these natural processes usually exacerbate coastal erosion in several places (Moller 2006; Sundar and Sundaravadivelu 2005; Thieler et al. 2009). Development in coastal areas has inflated interest in erosion issues (Reddy et al. 2008); it has led to major efforts to manage the coastal erosion problem. In order to combat the erosion problem, proper measures need to be identified, the decision to suggest a proper solution for the problem should be based on a thorough analysis of the shoreline changes and developments in the past and estimated developments in the future. The best method to investigate the shoreline change is with the help of remote sensing and GIS techniques (Nayak 2002; Chandrasekar et al. 2013; Srinivasa Kumar et al. 2008; Charatkar 2004; Kaliraj et al. 2013; Kankara et al. 2015). This study investigates long-term coastal variation using multi spectral imageries with aid of the Digital Shoreline Analysis System. Mathematical modelling is a powerful and flexible engineering technique to understand and predict the changes due to the construction of coastal structures (Di Bona 2013; Sheela Nair et al. 2015; Ichikawa et al. 2010). CEDAS GENESIS Numerical response model is used to predict the response of various coastal structures. The objective of this research work is to

S. Subburaj (✉) · R. S. Kankara · M. Umamaheswari · S. Chenthamil Selvan
Ministry of Earth Sciences, National Centre for Coastal Research, Pallikaranai, Chennai, Tamil Nadu 600100, India
e-mail: subburaj@nccr.gov.in; subburajiom@gmail.com

R. Jha et al. (eds.), *River and Coastal Engineering*, Water Science and Technology Library 117, https://doi.org/10.1007/978-3-031-05057-2_22

understand the shoreline changes due to various developmental activities and identify the hotspots of erosion to find a better suitable long-term solution among various alternatives to armor the coast against the changes.

2 Study Area

Coastal stretches from Ennore creek to Pulicat of Tiruvallur district are being targeted in the study, this specific study space is chosen as a result of a lot of developmental activities that have taken place for the last two decades such as the construction of ports and thermal power plants. The selected stretch has unique significance due to the neighboring estuarine ecosystem. It is of a twenty-five-kilometer-long stretch of coastal regions bounded by two inlets—Pulicat Lake on the north and Ennore Creek on the south (Fig. 2.1). Ennore Port is found at a distance of 2.5 km north of Ennore creek and Kattupalli port is located at a distance of 6.5 km north of Ennore creek. The Ennore port was commissioned during 2001 for bringing in coal to nuclear energy stations and to help the proposed Industrial park north of it. All the industrial development of Chennai city is taking place on the southern facet of the Ennore Creek region of the study area. The south breakwater lies in an East–West direction for a length of 1.1 km and the north breakwater could be a length of 3 km in arcuate shape with an approach channel facing south and Adani Kattupalli Port private limited was incorporated on 14 August 2015 consist of the southern breakwater of 2.35-km length and northern breakwater of 2.75-km length. Since Pulicat Lake is the second—biggest brackish water lake in India with a 430 km^2 area, located on the north-western side of the study region, the study on this coastal stretch has prime importance.

3 Data Used

The long-term shoreline change assessment is studied for a period of 45 years from 1972–2017. This long period is elected to understand the changes that are induced before and after the construction of ports in the area. Shoreline change evaluations are based on comparing historical shorelines extracted from different satellite imageries. Multi-temporal satellite data of LANDSAT (MSS, TM & ETM+) were downloaded freely from the website www.landsat.org & http://glovis.usgs.gov for the period 1972, 1989, 1991, 2000, 2006, 2011, 2015 and 2017. The short-term assessment is done with a set of four historical recent shorelines for 2014, 2015, 2016, and 2017. Seasonal variation is studied with three sets of shorelines for 2017 to understand the yearly seasonal variation. Modelling requires several input data such as wave data, bathymetry data, and shoreline position data. The wave input data which were used for offshore boundary condition is collected from European Centre for Medium-range Weather Forecasts (ECMWF) datasets, bathymetry data were collected from

Fig. 1 Location of study area. *Source* Google earth

Generalized Bathymetric Charts of Ocean (GEBCO) in XYZ format and the shoreline position was taken by digitizing the satellite LANDSAT images based on the high water level (Figs. 1, 2 and 3).

4 Methodology

In this study shoreline change analysis is done using DSAS to find the long-term (Mageswaran et al. 2015), short-term (Armah et al. 2011), and seasonal variation of the coast, it helps us to know the past and present scenario of the coast. Based on the above results from DSAS the hot spots of erosion are identified. Then CEDAS GENESIS model is used for simulating the future scenario of the coast with and without various alternative measures to elect the best mitigating measure (Fig. 4).

Downloaded satellite images are projected to UTM projection with zone 44 North and WGS 84 datum. Initially, the image rectification technique is done using ERDAS IMAGINE 9.1 software. False Colour Composites (FCC) are generated using band

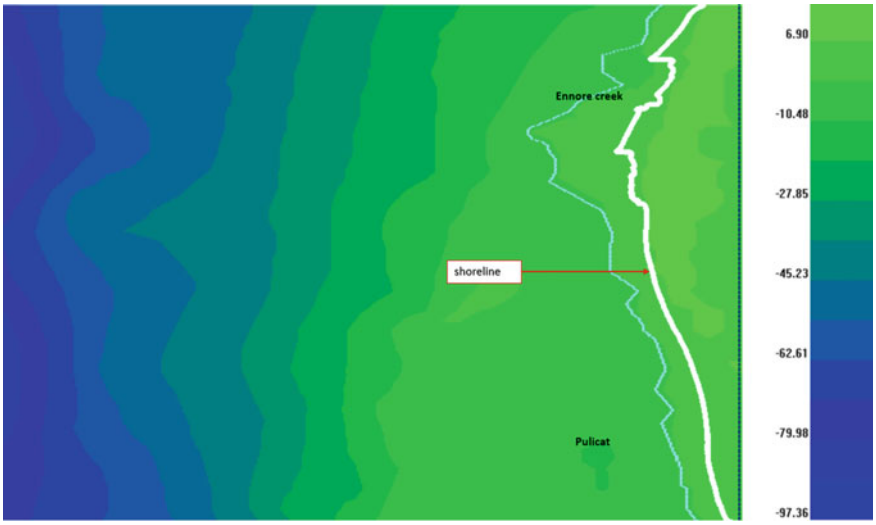

Fig. 2 Shows the bathymetric dataset contours with the shoreline

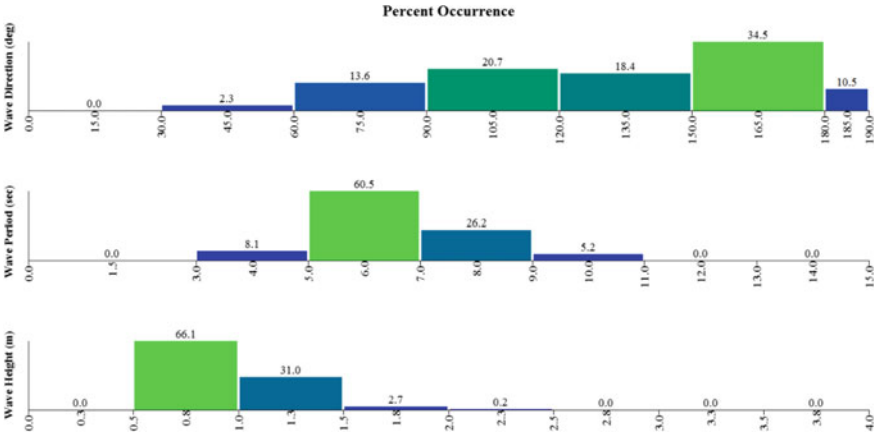

Fig. 3 Shows the statistical analysis result of input offshore wave dataset

combination for the satellite imageries which depicts water-land interface. Further, an image enhancement technique is carried out for satellite images for better visualization and delineation of the shoreline (Saranathan et al. 2011; Sathyanaryanan Sridhar et al. 2009). The shorelines were drawn through on-screen digitization using the visual interpretation technique in ArcGIS software. The multi-date shorelines were given as input in Digital Shoreline Analysis System (DSAS) to calculate the shoreline change rate (USGS 2005). Transects were generated using DSAS to 1 km

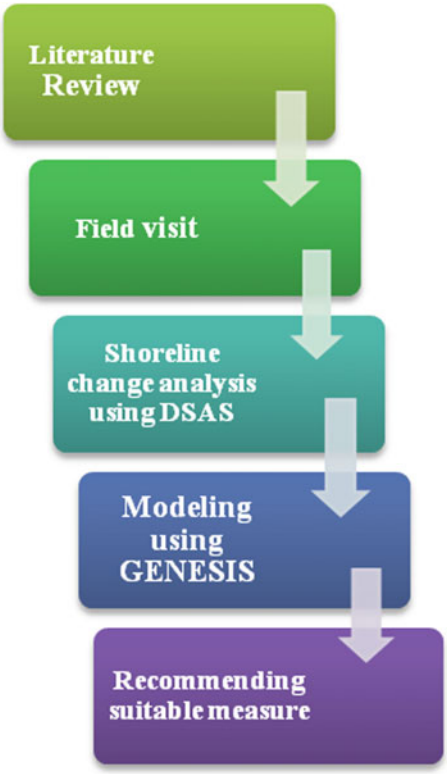

Fig. 4 Methodology flow chart

length with 50 m spacing to study the changes that occurred along the Tiruvallur coast.

In this study, the GENESIS model is implemented with a set of NEMOS codes. The partial differential equation governing shoreline change is given by

$$\partial y/\partial t + (\partial Q/\partial x + q)/DB + DC = 0$$

The y quantity represents the shoreline position (m), x is the longshore coordinate (m), t is the time (s), DB is the average berm height above the mean water level (m), DC is the depth of closure (m), Q is the longshore transport rate (m^3/s) and q represents the line sources/sinks along the coast ($m^3/s/m$ shoreline).

The empirical predictive formula for the longshore transport rate used in GENESIS is

$$Q = (H2Cg)b(a1\sin 2\theta bs - a2\cos\theta bs\partial H/\partial x)b$$

The Cg quantity represents wave group speed given by linear wave theory (m/s), the subscript b denotes wave breaking conditions, H (m) and θ (°) represent wave height and wave angle to the local shoreline direction at breaking.

The overall process flow is that it creates a spatial domain that defines the project area boundaries and bathymetric information; then wave model is prepared with the elaboration of the forcing wave climate; then all external input data are ready for the user to be operative within GENESIS and finally, a user configures GENESIS with the desired long-term simulations.

5 Result and Discussion

5.1 Long Term Analysis

The shoreline change analysis has been carried out for various years considering before and after the construction of Ennore and Kattupalli port. Tiruvallur district shoreline is about 25 km in length so a total of 520 transects were generated with a spacing of 50 m and the length of the transect was 500 m towards onshore. The long-term analysis was carried out for the year 1972–2017. It is found that before the construction of Ennore port more than 80% of the coast shows an accretion pattern while after the construction of the port more than 50% of the coast shows eroding pattern. During analysis of the year 1972–2000 (before port construction) maximum erosion of −5.12 m/yr was found to be near Ennore and maximum accretion of 11.97 m/yr was found near Pulicat creek mouth (shown in Fig. 5a). Analysis was carried for the years 2000–2010 to evaluate the changes due to the construction of Ennore port and initialization of Kattupalli port, it is found that maximum erosion was observed near Kattupalli Northern breakwater and Maximum accretion was observed near Ennore southern breakwater. During analysis of the year 2000–2017 (After both port construction) maximum erosion of 23.4 m/yr was observed near Kattupalli Northern breakwater and Maximum accretion of 26 m/yr was observed near Pulicat mouth (shown in Fig. 5a). Analyzing 2010–2017 (Present impact) it is found that maximum erosion was observed near Kattupalli northern breakwater at a rate—32.1 m/yr and maximum accretion was observed between the southern breakwater of Kattupalli port and northern breakwater of Ennore port at the rate of 27.6 m/yr (shown in Figs. 6a and 7).

5.2 Short Term Analysis

The short-term analysis was carried out for recent years to evaluate the exact changes that have been taken place over the recent years. It is found that in recent years erosion is dominating the various spots of the coast. During analysis of the year, 2014–2015

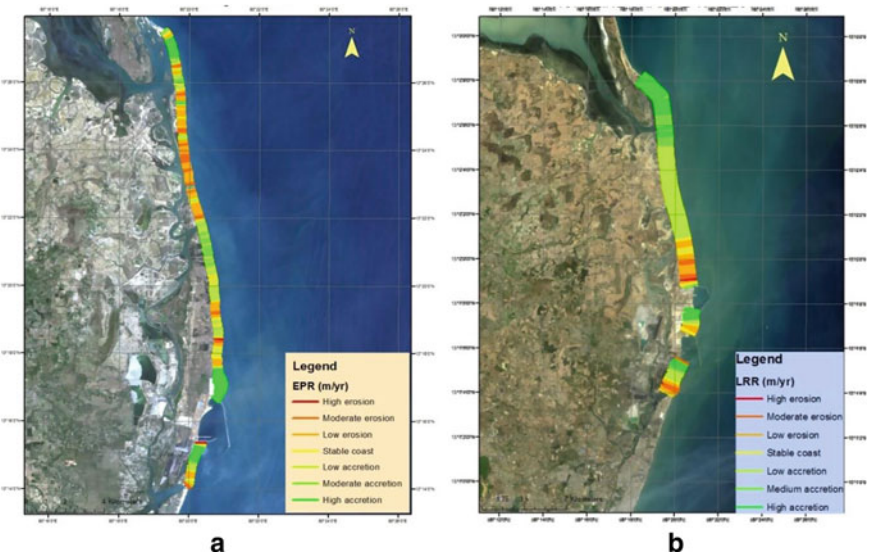

Fig. 5 Shoreline change map for **a** 1972–2000 **b** 2000–2010

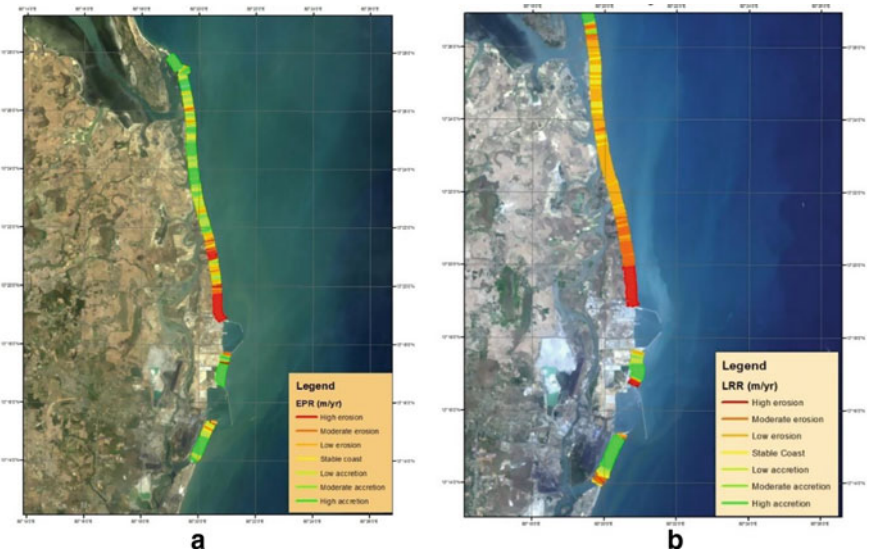

Fig. 6 Shoreline change map for **a** 2010–2017 **b** 1972–2017

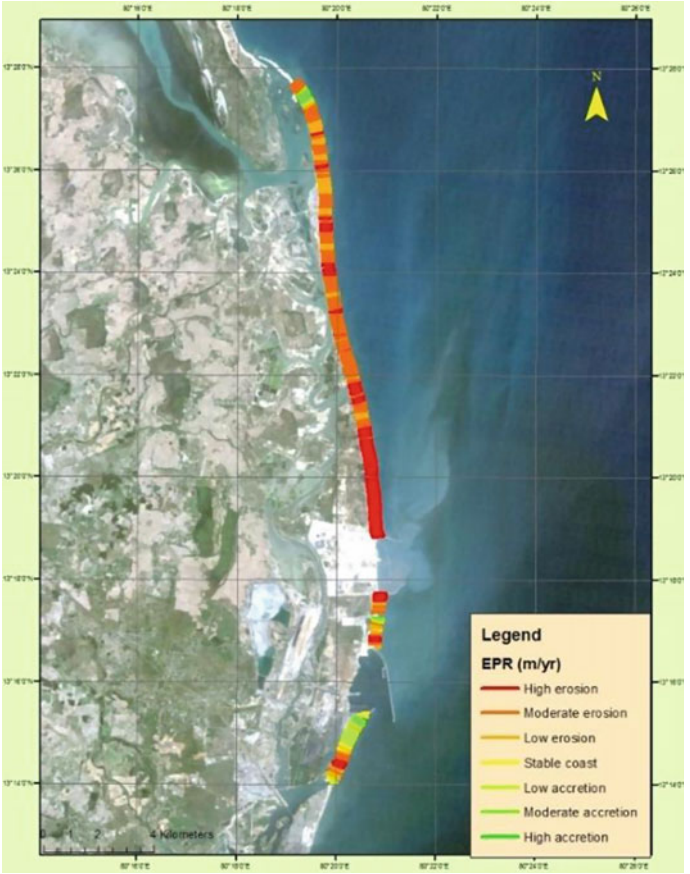

Fig. 7 Shoreline change map for 2000–2017

maximum erosion of −9.69 m/yr was found to be near Kattupalli northern breakwater and maximum accretion of 12.56 m/yr was observed near Kattupalli southern breakwater (shown in Fig. 8a). Analyzing 2015–2016, maximum erosion of −13.27 m/yr was found near Ennore mouth and maximum accretion was observed near the Southern breakwater of Ennore at a rate of 12.98 m/yr (shown in Fig. 8b).finally analysing 2016–2017, maximum erosion of −13.67 m/yr was found near Karungali village and maximum accretion was observed near Pulicat mouth at a rate of 16.42 m/yr (shown in Fig. 9a).

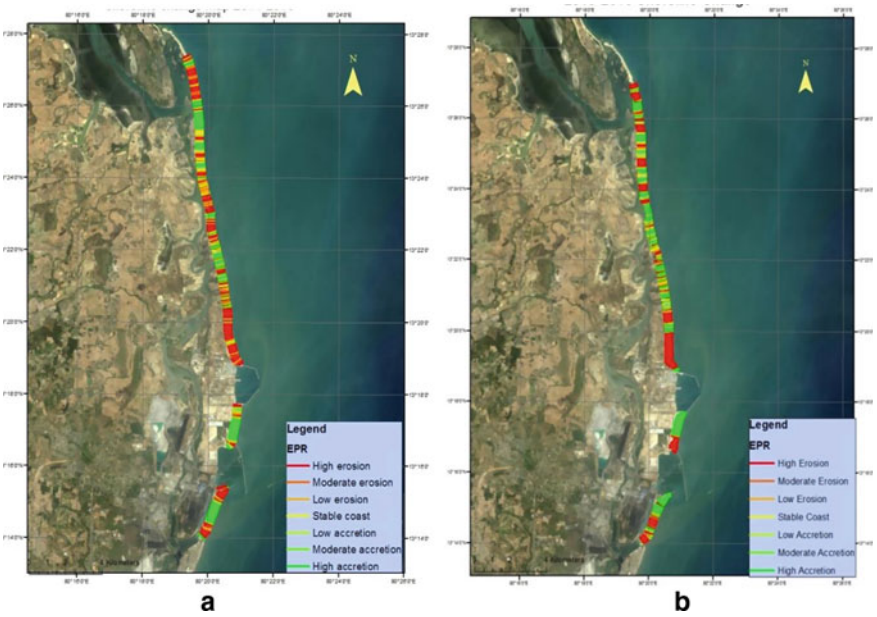

Fig. 8 Represents shoreline change map **a** 2014–2015 **b** 2015–2016

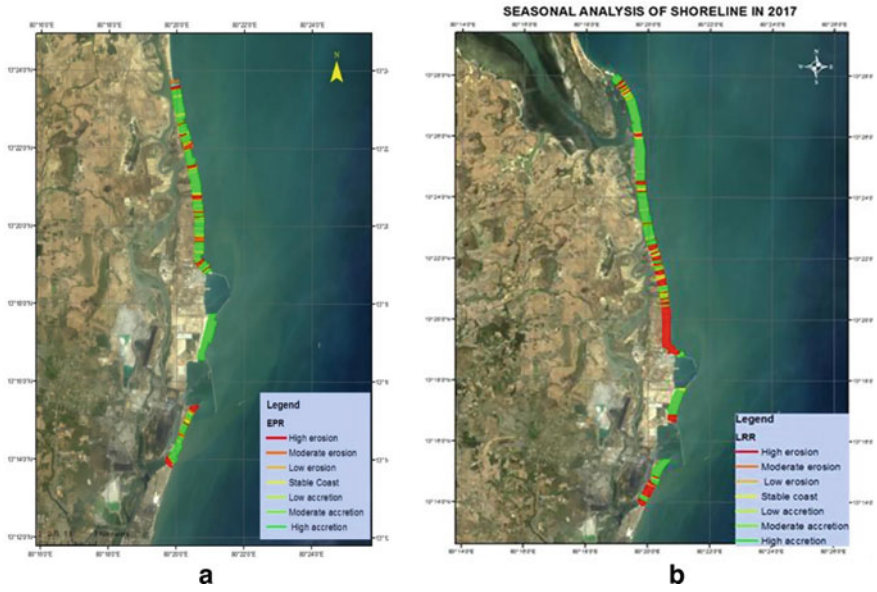

Fig. 9 Shoreline change map for **a** 2016–2017 **b** 2017 (seasonal changes)

5.3 Seasonal Analysis

The seasonal shoreline analysis was carried out for the year 2017. This is particularly carried out to analyze the changes that are taken over the various seasons for a year to understand the seasonal changes in the shoreline pattern. It revealed that maximum erosion was observed near the Northern breakwater of Ennore port at a rate of −48.1 m and maximum accretion was observed near Pulicat creek mouth at a rate of 39.4 m (shown in Fig. 9b).

5.4 Simulations of Shoreline Evaluation and Sediment Transport

GENESIS response model is used for simulating the present and future time scales scenario of our study area. The shoreline changes and sediment transport were predicted with 2016 shoreline for various years from 2016 onward, assuming that no interventions will be carried out in the coast. The purpose of this simulation is to find out the coastline evolution, the equilibrium shoreline position and the time needed to reach it. Model was validated with 2018 shoreline. The entire input wave series (from 2016 to 2018) was used to cover the longest simulation period. When the simulation period is longer than the input wave data the model runs the wave data in a loop way. Simulation is done from 2016 to 2030. The predicted results show that there is a continuous erosion pattern along the period of time. Based on the model calculation, the gross transport observed is 1.34×10^6 m^3/year and net annual transport in the direction of north is at a rate of 0.928×106 m^3/year for the study profile in 2016. Net Gross transport for 2030 it is $1.56 \times 10^6 m^3$/year and net annual transport in the direction of north is at a rate of 1.218×10^6 m^3/year. Based on the model the average volumetric change for 2016 to 2030 is -8.3×10^5 $m^{3.}$ The modelled shoreline change evolution and sediment transport is represented in the Fig. 10.

From simulation it is inferred that near Kattupalli northern breakwaters, Ennore port northern breakwaters, karungali, kalanji and near Ennore mouth will be serious hotspots of erosion in future and places near Kattupalli and Ennore port southern breakwaters, Gunangkuppam will shows a good accretion trend (Figs. 11, 12 and 13).

6 Conclusion

The hotspots of erosion obtained from DSAS results showed a very huge erosion pattern after the construction of ports, from simulating the future scenario of the coast it's obvious that the various pockets will face huge eroding problems in the

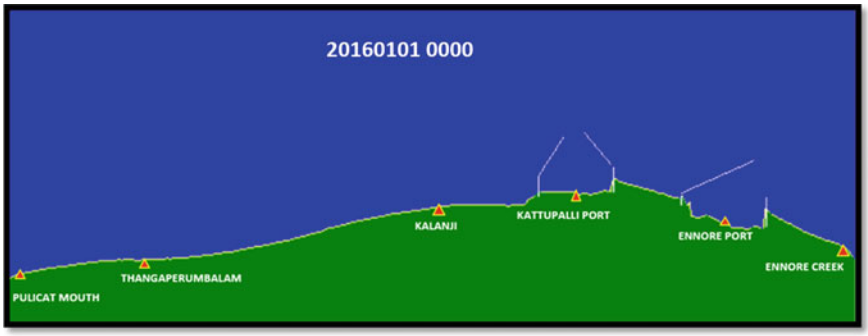

Fig. 10 Represents initial time step scenario of study area

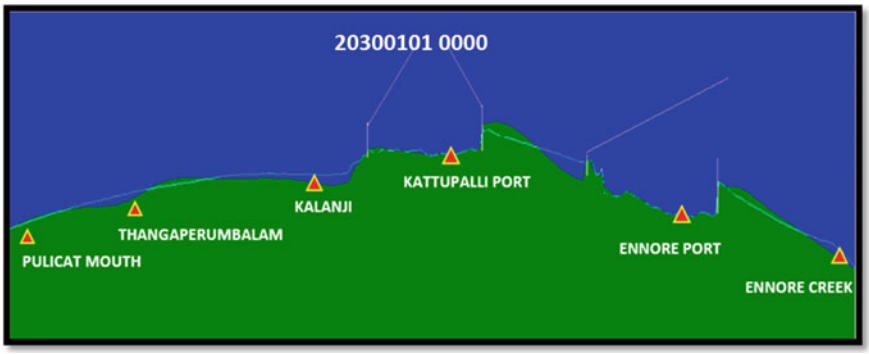

Fig. 11 Represents final time step scenario of study area

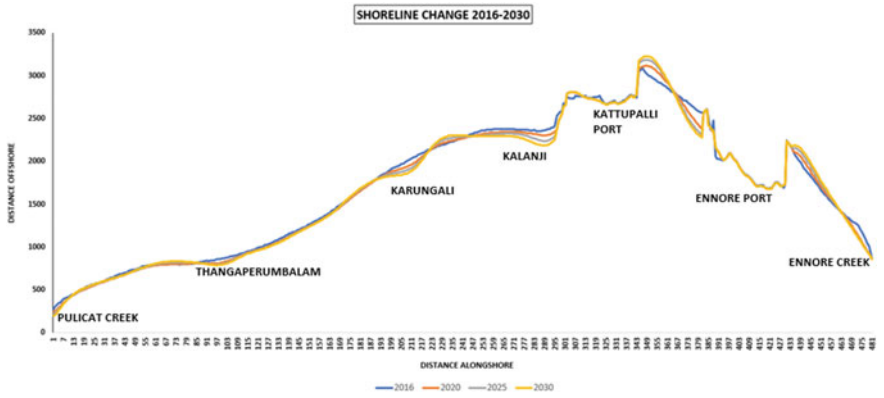

Fig. 12 Represents variation of shoreline positions for various years

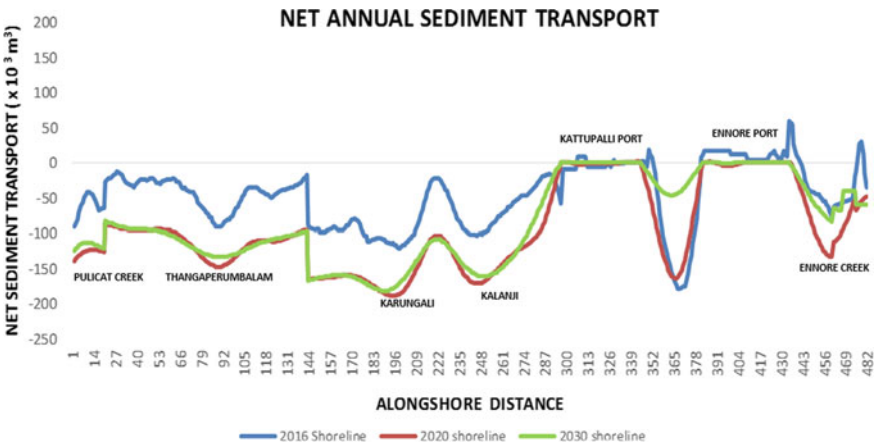

Fig. 13 Net annual sediment transport rate in the study area

future also. It is evident that the stretches are highly eroding and the impacts are huge after the port construction. The average rate of erosion in the study area is found to be 8 m/yr and around 13 km of 25 km stretch of coastline shows eroding pattern. If this continues then the coast will face adverse effects in the future, thus the problem statement is clearly identified. So, there is an unstinting need for a long-term protection measure and nurture the coast from future impacts (Mahalingaiaha et al. 2015). It is further recommended to study and analyze the various alternatives of various hard and soft measures to elect the best measure which holds good for the study area and it should be a stable long-term protection measure to protect the coast and save beaches.

Acknowledgements The author is thankful to Dr. R. S. Kankara for guiding throughout the project and Dr. M. V. Ramana Murthy and Dr. S. Srinivasalu for supporting it. I also express my sincere thanks to Secretary, Ministry of Earth Sciences and NCCR for their support and encouragement to carry out the research work.

References

Armah FA (2011) GIS-based assessment of short term shoreline changes in the coastal erosion sensitive zone of Accra, Ghana. Res J Environ Sci 5:643–654

Charatkar SL, Mitra D, Biradar RS, Radhakrishnan KV (2004) A study of erosion and accretion along Gulf of Khambat, Gujarat coast using remote sensing and GIS. AFITA/WCCA, Joint Congress on Agriculture, Bangkok, Thailand, pp 574–589

Chandrasekar N, Joevivek V, Saravanan S (2013) Coastal vulnerability and shoreline changes for southern tip of India-remote sensing and GIS approach. J Earth Sci Clim Change 4:144

Di Bona S (2013) Modeling of coastal evolution: long term simulation in the Vagueira Region. ICEA

Fenster M, Dolan R, Morton RA (2001) Coastal storms and shoreline change: signal or noise. J Coastal Res 17:714–720

Ichikawa M, Saitoh T, Miao G (2010) Theoretical analysis of wave and structure interaction around a composite type coastal structure-a case study of a seawall and detached breakwaters. J Hydrodyn 22(5):482–488

Kaliraj S, Chandrasekar N, Magesh NS, (2013) Impacts of wave energy and littoral currents on shoreline erosion/accretion along the south-west coast of Kanyakumari, Tamil Nadu using DSAS

Lee TM (2005) Monitoring the dynamics of coastal vegetation in South-western Taiwan. Environ Monit Assess 111:307–323

Mageswaran T, Ram Mohan V, Chenthamil SeIvan S, Arumugam T, Usha T, Kankara R-S (2015) Assessment of shoreline changes along Nagapattinam coast, using Geospatial techniques. Int J Geomatics Geosci c(4)

Mahalingaiaha AV, Tayade BR, Gokhale NV, Kudale MD (2015) Design of submertied offshore reefs for the coastal protection measures. In: CWPRS, Pune-411024, India

Kankara et al (2015) Estimation of long and short term shoreline changes along Andhra Pradesh coast using remote sensing and GIS techniques. Proc Eng 116(1):855–862

Moller I (2006) Quantifying salt marsh vegetation and its effect on wave height dissipation: results from a UK east coast salt marsh. Estuarine Coastal Shelf Sci 69:337–351

Nayak SR (2002) Use of satellite data in coastal mapping. Indian Cartographer 22:147–157

Sundar V, Sundaravadivelu R (2005) Protection measures For Tamil Nadu Coast. Final Report Submitted to Public Works Department Government of Tamil Nadu

Reddy CS, Babar S, Sudha K, Raju VS (2008) Vegetation cover mapping and landscape level disturbance gradient analysis in Warangal district, Andhra Pradesh, India using satellite remote sensing and GIS. Space Res J 1:29–38

Saranathan E, Chandrasekaran R, Soosal Manickaraj D, Kannan M (2011) Shoreline changes in Tharngampadi village, Nagapattinam district, Tamil Nadu, India-a case study. Indian Soc Remote Sens 39(1):107–115

Sathyanaryanan Sridhar R, Elangovan K, Suresh PK (2009) Long TermShoreline Oscillation and changes of Cauvery Delta Coastline Inferred from Satellite Imageries. Indian society of Remote sensing, March 2009

Sheela Nair L, Sundar V, Kurian NP (2015) Longshore sediment transport along the coast of Kerala in Southwest India, MoES, pp 40–46

Srinivasa Kumar T, Mahendra RS, Nayak S, Radhakrishnan K, Sahu KC (2008) Coastal vulnerability assessment for Orissa State, East coast of India. J Coastal Res 26(3):523–534

Thieler ER, Himmelstoss EA, Zichichi JL, Ayhan E, (2009) Digital Shoreline Analysis System (DSAS) version 4.0 An ArcGIS extension for calculating shoreline changes. U.S. Geological Survey Open-File Report 2008–1278

USGS (2005) U.S. Geological Survey Open-File Report 2005-1001

Observed Spatio Temporal Trends of Precipitation and Temperature Over Afghanistan

S. Rehana, P. Krishna Reddy, N. Sai Bhaskar Reddy, Abdul Raheem Daud, Shoaib Saboory, Shoaib Khaksari, S. K. Tomer, and U. Sowjanya

S. Rehana (✉) · U. Sowjanya
HydroClimatic Research Group, Lab for Spatial Informatics, International Institute of Information Technology, Gachibowli, Hyderabad 500032, India
e-mail: rehana.s@iiit.ac.in
URL: https://fac-webpages.iiit.ac.in/hrg/

U. Sowjanya
e-mail: sowjanyauppuluri878@gmail.com

P. Krishna Reddy
Data Sciences and Analytics Center, IT for Agricultural Research Centre, International Institute of Information Technology, Hyderabad, India
e-mail: pkreddy@iiit.ac.in

N. Sai Bhaskar Reddy
Climate Change Expert and Team Leader, MgtWell, Kabul, Afghanistan
e-mail: saibhaskarnakka@gmail.com

A. R. Daud
CCAP/CBARD, Ministry of Agriculture, Irrigation and Livestock, Kabul, Afghanistan
e-mail: daud.rahimi@mail.gov.af

S. Saboory
IT Specialist Agromet, Agrometeorological Unit, Ministry of Agriculture, Irrigation and Livestock, Kabul, Afghanistan
e-mail: shoaib.saboory@mail.gov.af

S. Khaksari
Climate Change Adaptation Project, Ministry of Agriculture, Irrigation and Livestock, Kabul, Afghanistan
e-mail: shoaib.khaksari@mail.gov.af

S. K. Tomer
Satyukt Analytics Private Limited, Bengaluru, Karnataka, India
e-mail: satkumartomer@gmail.com

R. Jha et al. (eds.), *River and Coastal Engineering*, Water Science and Technology Library 117, https://doi.org/10.1007/978-3-031-05057-2_23

1 Introduction

An increase in the number and magnitude of extreme climate events has been observed globally in recent years causing huge loss of lives, extensive damages to crops, properties and immeasurable misery to millions of people (Hartmann et al. 2013). The issue of management of risks of extreme events and disasters under climate change adaptation has been main focus by the Intergovernmental Panel on Climate Change (IPCC) in the Special Report on Extremes (SREX) (IPCC 2012). Globally, understanding past changes in the characteristics of extreme climate events became critical for reliable projections of future changes (Donat et al. 2013; Panda et al. 2017).Hence, the understanding the variability of precipitation and temperature extreme events in the historical data is essential. Moreover, the study of historical trends of climate extremes will serve as the basis for understanding the possible physical vulnerabilities and adaptive measures. To this end, the study of climate events has gained higher scientific and societal interest over the last few decades (e.g. Zhang et al. 2005; Donat et al. 2013; Curry et al. 2014; Razavi et al. 2016). The study of such climate trends may be critical for any arid to semiarid counties such as Afghanistan as it can directly impact the droughts, floods, heat waves etc. and can be more intense under climate change. Afghanistan is a landlocked semi-arid country and most vulnerable to precipitation extremes related hazards, including droughts, floods and heat waves that cause huge losses in life and property impacting the socio-economic development of the country. Currently, Afghanistan is among the countries with low levels of greenhouse gas (GHG) emissions. The Global Adaptation Index (2012) ranked Afghanistan as the most vulnerable countries in the world under climate change. There is a limitation over the climate extremes studies over Afghanistan due to limited weather data availability. More than three decades of war in Afghanistan that started in the late 1970s caused a huge interruption in water-resources data collection and destroying many of the older records of meteorological and hydrological data (Campbell 2015). Specifically, only a few (e.g. Aich et al. 2017) climate change assessment studies have been carried out in the literature. In this context, the present study tried to use the open source data sets to analyze the current trends in the precipitation and temperatures. We report the changes and trends in precipitation and temperature extremes in the recent years for seven agro-climatic zones of Afghanistan.

2 Case Study and Data

Afghanistan is a landlocked country and geographically highly heterogeneous with the glaciated peaks of the Hindukush and arid deserts of the South, located between 29–39° N and 60–75° E (Fig. 1). Entire Afghanistan is divided into seven agro-climatic zones following to climate classification scheme of Köppen-Geiger system (Köppen and Wladimir 1884), Beekeeping survey report (2014) and Ministry of

Fig. 1 Seven agro-climatic zones of Afghanistan with Provinces

Agriculture, Irrigation and Livestock (MAIL) as Central, Eastern, Northern, North-East, Southern, South-West, and Western agro-climatic zones (Fig. 1). The parts of Central, North, North-East and South agro-climatic zones have mid-latitude steppe climate, desert climate and Mediterranean climate. The parts of East and South-West agro-climatic zones have Mediterranean climate; and tropical and subtropical—steppe and desert climates. The parts of South-West and West agro-climatic zones have mid-latitude steppe, and desert climate; tropical and subtropical desert climate; and Mediterranean climate.

One of the major challenges in the initiation of the present study is the availability of long time series historical weather station meteorological data sets. Therefore, to understand the spatial variation of precipitation and temperature extremes, the study used a long time series fine scale gridded dataset, Asian Precipitation-Highly-Resolved Observational Data Integration towards Evaluation of Water Resources (APHRODITE) datasets for a 48-year period from 1951 to 2007 for analysing the spatial trends in the precipitation over Afghanistan. APHRODITE daily gridded precipitation is the long-term continental-scale datasets which considered a dense network of daily rain-gauge data (about 5000–12,000) with 14 quality control processes, such as controlling for erroneous values, repetition, homogeneity etc. (Hamada et al. 2011). The APHRODITE data is mainly developed for Asia including Himalayas, South and Southeast Asia and mountainous areas in the Middle East at 0.5 Degree resolution. The details of the data can be found at: https://climatedataguide.ucar.edu/climate-data/aphrodite-asian-precipitation-highly-resolved-observational-data-integration-towards. The APHRODITE data set is first extracted covering entire Afghanistan and further cropped to each agro-climatic zone to study the recent changes in the daily precipitation and temperature trends spatially.

3 Analysis Approach

The present study estimated the changes in each of the precipitation extreme statistics using linear and Mann–Kendall trend tests.

3.1 Linear Regression

One of the simplest methods to calculate the trend of the data is linear regression. The equation of linear regression line is given by:

$$Y = a + bX \tag{1}$$

where, X is the explanatory variable and Y is the dependent variable, b is the slope of the line and a is the intercept. The slope of the regression describes the trend, with positive as increasing and negative as decreasing trend. The observed trend study is conducted by considering the rainfall and temperatures as dependent variables and time as explanatory variable.

3.2 Mann–Kendall Trend Test

The Mann–Kendall (Mann 1945; Kendall 1975) trend test is a non-parametric trend test, which has been widely used for trend detection in hydrologic and climate data to assess if there is an upward (positive) or downward (negative) trend of a variable of interest over time. The test compares the relative magnitudes of sample data rather than the data values themselves (Gilbert 1987). The following procedure explains the Mann–Kendall trend test:

- The time series,x_i, of the variable, for which the trend test to be applied is considered as an ordered time series.
- Each of the data point, x_i, is compared with the all subsequent data values to estimate the Mann–Kendall statistic, S, as follows:

$$S_i = \sum_{i=2}^{n} \sum_{j=1}^{i-1} sign(x_i - x_j) \tag{2}$$

where

$$sign(x_i - x_j) = \begin{cases} 1 & if\ x_i > x_j \\ 0 & if\ x_i = x_j \\ -1 & if\ x_i < x_j \end{cases} \tag{3}$$

- A very high positive value of S is an indicator of an increasing trend, and a very low negative value indicates a decreasing trend.
- From the Mann–Kendall statistic, S, the normalized test statistics, Z, is computed as follows:

$$\text{if S} > 0,\ Z = \frac{S-1}{[VAR(S)]^{1/2}} \tag{4}$$

$$\text{if S} = 0,\ \text{Z} = 0 \tag{5}$$

$$\text{if S} < 0,\ Z = \frac{S+1}{[VAR(S)]^{1/2}} \tag{6}$$

where $VAR(S)$ is the variance of S. According to (Kendall 1975) $VAR(S)$ can be written as follows:

$$VAR(S) = \frac{1}{18}\left[n(n-1)(2n+5) - \sum_{p=1}^{g} t_p(t_p-1)(2t_p+5)\right] \tag{7}$$

where n is the number of data points, g is the number of tied groups (a tied group is a set of sample data having the same value), and t_p is the number of data points in the Pth group. The Z-value follows a standard normal distribution. For testing the decreasing or increasing trend a significance level α is used. The probability associated with the computed test statistics, Z-value is estimated. The trend is identified as decreasing if Z-value is negative and the computed probability is less than the level of significance and the trend is identified as increasing if the Z-value is positive and the computed probability is less than the level of significance. If the computed probability is greater than the level of significance, there is no trend.

The trend analysis is performed on APHRODITE daily data to test the increasing or decreasing rainfall trends using Mann–Kendall trend test for each zone spatially. To estimate the rainfall trends in terms of increasing or decreasing, the Mann–Kendall trend test is carried out at each grid point. Changes in the daily precipitation trends in recent years with reference to distant past are assessed by dividing the historical data into two-time slices as 1951–1990 and 1991–2007. The period of 1951–1990 is considered as base period as followed by several studies in the literature (Sharma and Mujumdar 2017), which often depend on the availability of the climate data. Further, the period 1961–1990 is likely to have larger anthropogenic trends embedded in the climate data (https://www.ipcc.ch/ipccreports/tar/wg1/483.htm). Throughout the manuscript, the study considered a trend as being significant if it is statistically significant at the 5% level (p-value <0.05).

4 Results and Discussion

The spatial average monthly precipitation from 1951 to 2007 for seven agro-climatic zones of Afghanistan is shown in Fig. 2. The maximum precipitation occurrence months are observed as January, February, March, April and May for all zones of Afghanistan. Whereas, June, July, August, September, October, November and December and generally considered as dry months. To study the precipitation trends at annual scale, the annual total precipitation for each zone is estimated for a period of 1951–2007 with APHRODITE data. Zone wise annual precipitation is calculated

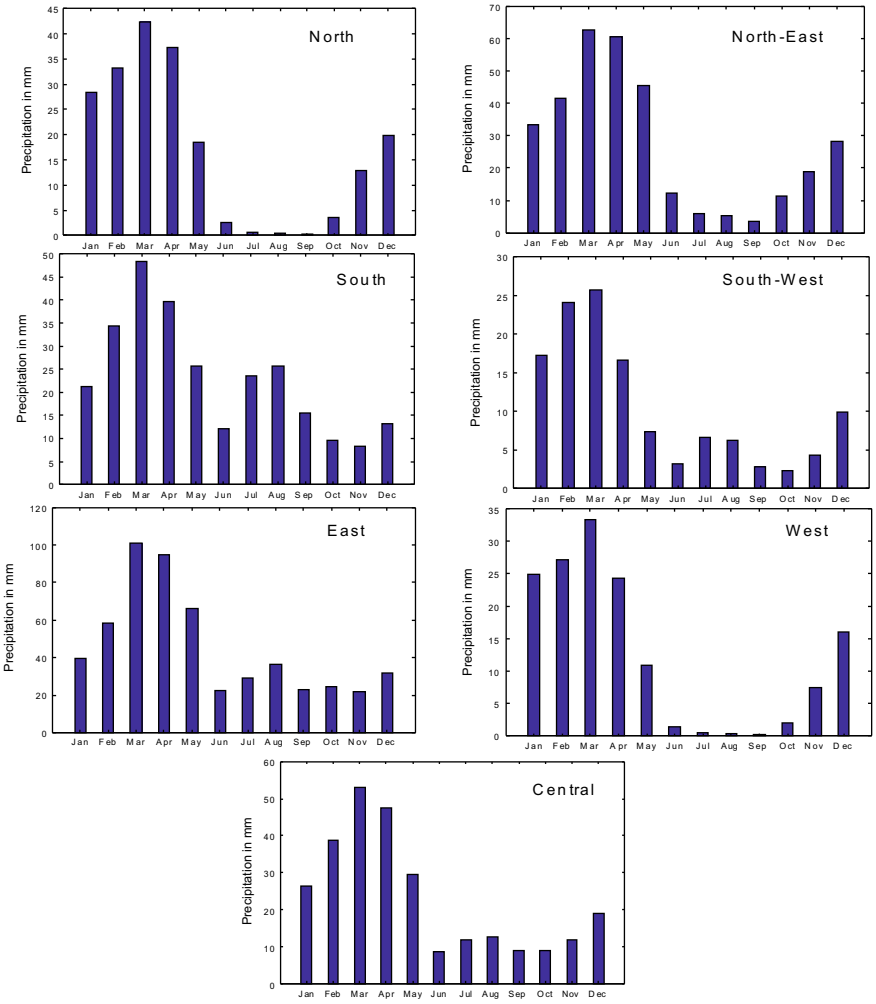

Fig. 2 The spatial average monthly precipitation from 1951 to 2007 for seven agro-climatic zones of Afghanistan

from the mean precipitation of all valid gridded points of APHRODITE data encompassing each zone. The annual total rainfall has decreased over North zone at a rate of 0.5 mm/decade, whereas for North-East zone as 17.3 mm/decade, the West zone at a rate of 6.3 mm/decade. However, the annual total rainfall over South zone has increased at a rate of 2.8 mm/decade, the South-West zone at a rate of 1.7 mm/decade, the East zone at a rate of 10.7 mm/decade, the Central zone at a rate of 6.3 mm/decade. Overall, the annual total rainfall has shown an increasing trend for the zones of South, South-West, East and Central, whereas, a decreasing trend has been observed for the zones of North, North-East and West zones based on linear regression trend test as shown in Fig. 3. Further, the trend analysis was performed on daily data to test the increasing or decreasing rainfall trends using Mann–Kendall trend test for each grid point for various zones of Afghanistan. The change in the rainfall variability in recent years with reference to distant past was assessed by dividing the historical data into two time slices as 1951–1990 and 1991–2007. Figure 4a–g show the trend analysis results with Mann–Kendall trend test at 5% significance level for each zone of Afghanistan for two time slices of 1951–1990 and 1991–2007. The Fig. 4a–g shows the spread of increasing (positive trend), decreasing (negative tend) and no trend at 5% significance level over North zone and most of the grid points shown a decreasing trend in rainfall in recent years over Afghanistan. The trend analysis of the rainfall with gridded data sets also reveals that for most part of the Afghanistan region the rainfall has been observed as decreasing.

The spatial average monthly temperature from 1961 to 2006 for seven agro-climatic zones of Afghanistan is shown in Fig. 5. The maximum temperature can be observed in the months of May, June, July and August, with hottest month as July for all seven zones of Afghanistan. The annual average temperatures from 1961 to 2006 are studied for the possible trend in the temperature with spatially averaged annual average temperature with APRODITE data (Fig. 6). Figure 6 shows the spatially averaged annual average temperature trends over seven agro-climatic zones of Afghanistan for the observed period of 1961–2006 with APRODITE data. The annual average air temperature has increased over the North zone at a rate of 0.4 °C/decade, the North-East zone at a rate of 0.3 °C/decade, the South zone at a rate of 0.02 °C/decade, the South-West zone at a rate of 0.4 °C/decade, the East zone at a rate of 0.1 °C/decade, the West zone at a rate of 0.4 °C/decade, the Central zone at a rate of 0.2 °C/decade. All seven agro-climatic zones of Afghanistan have shown an increasing trend of temperatures in recent years. The spatio-temporal trends of temperature for the time periods of 1961–1990 and 1991–2006 for each agro-climatic zone is shown in Fig. 7a–g.

5 Conclusions

The study has investigated the spatio-temporal analysis of precipitation and temperatures for seven agro-climatic zones of Afghanistan using gridded daily long time series datasets of APHRODITE from 1951 to 2007. The maximum precipitation

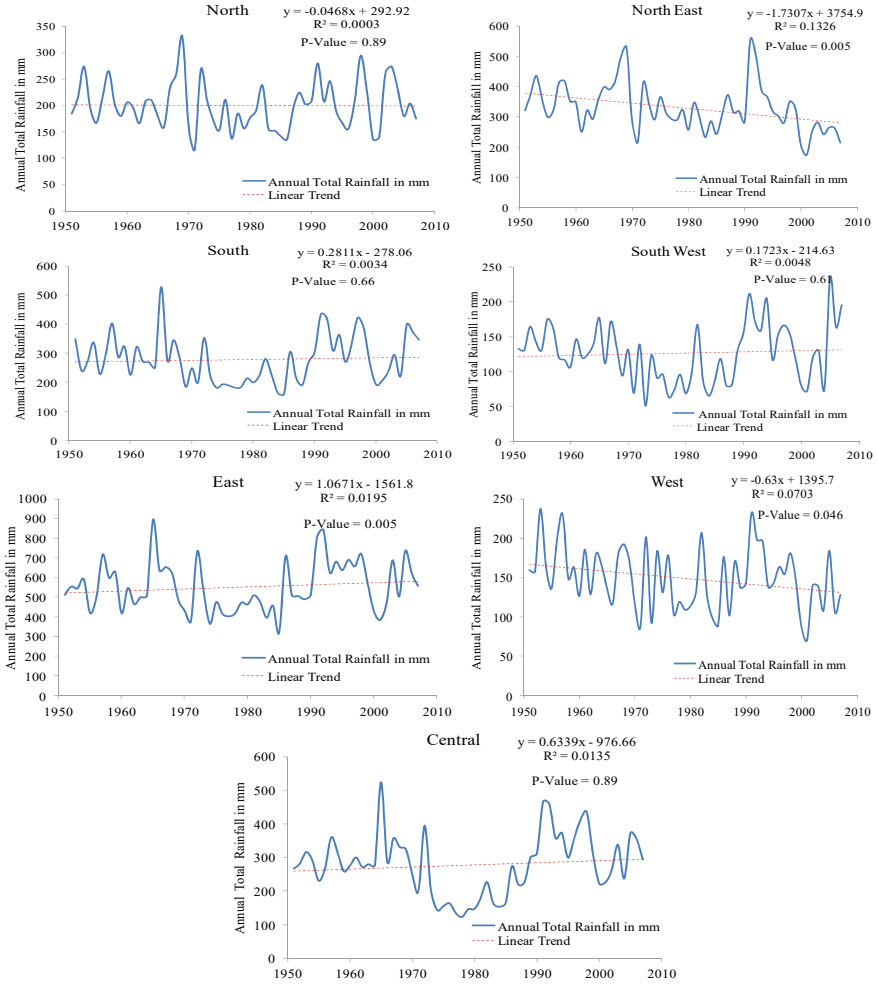

Fig. 3 The spatially averaged annual total rainfall trend over seven agro-climatic zones of Afghanistan for the observed period of 1951 to 2007 with APHRODITE data

occurrence months were observed as January, February, March, April and May for all zones of Afghanistan. Whereas, June, July, August, September, October, November and December and generally considered as dry months. The annual total precipitation has shown an increasing trend for the zones of South, South-West, East and Central, whereas, a decreasing trend has been observed for the zones of North, North-East and West zones. The changes in the magnitude of daily gridded precipitation in recent years (1991–2007) with reference to distant past (1951–1990) were analysed with significant decreasing trends (p-value < 0.05) for most parts of Afghanistan. The temperature was observed as maximum in the months of May, June, July and August, with hottest month as July for all seven zones of Afghanistan. The daily

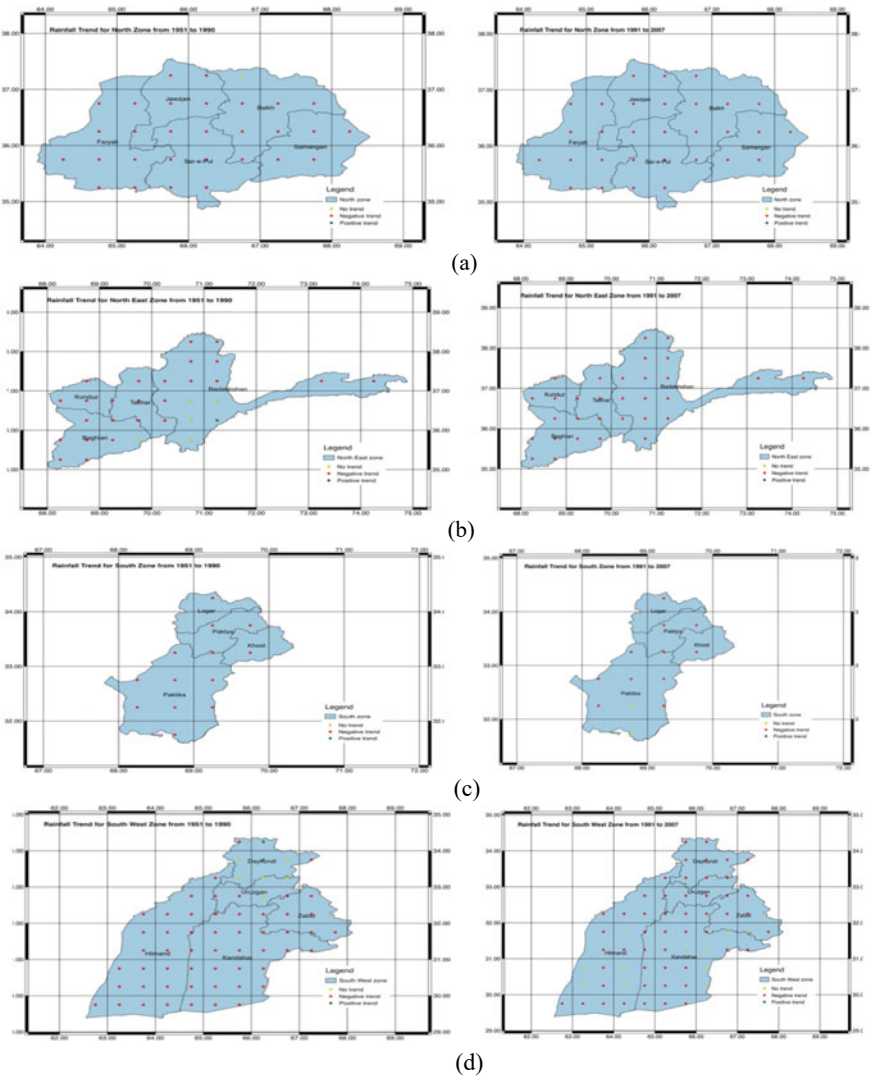

Fig. 4 Rainfall trend analysis for **a** North **b** North-East **c** South **d** South-West **e** East **f** West **g** Central zones with daily data of rainfall for two time slices of period of 1951–1990 and 1991–2007 with Mann–Kendall trend test. Positive Trend—Increasing rainfall trend; Negative Trend—Decreasing rainfall trend; No Trend—no trend at 5% significance level

temperature trend analysis has revealed positive trends of temperatures for two time periods of 1951–1990 and 1991–2007 with Mann–Kendall trend test at 5% significance level. Overall, the North, North-East and West zones of Afghanistan are more vulnerable with decreasing precipitation and increasing temperatures indicating more dry and warm periods indicating increasing drought conditions. Whereas, the South,

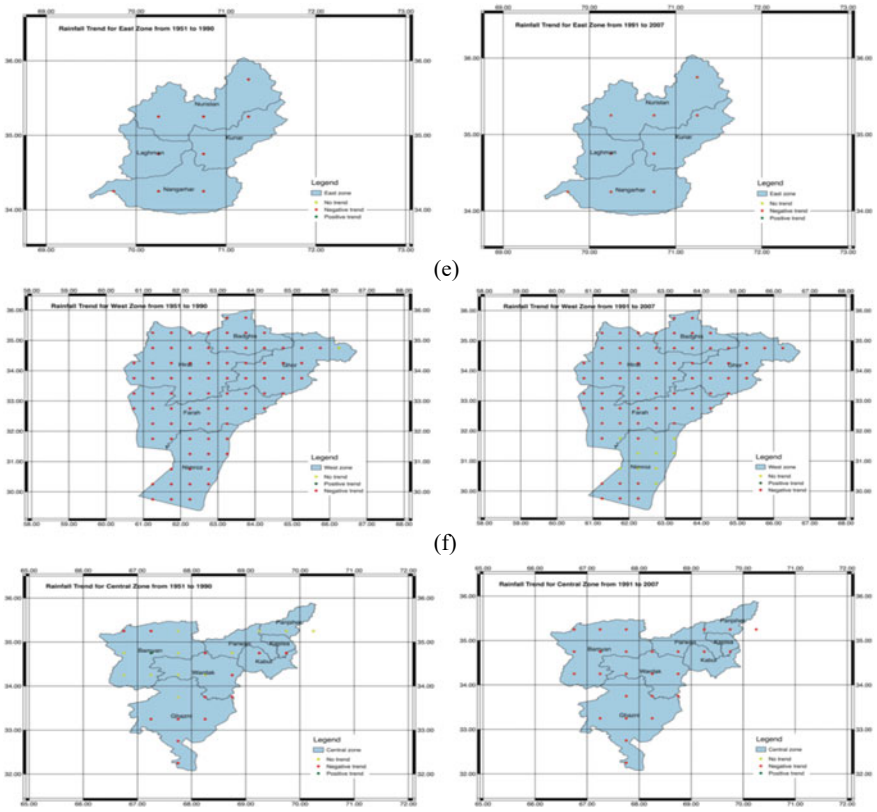

Fig. 4 (continued)

South-West, East, and Central zones are more vulnerable with increasing trends of both precipitation and temperatures indicating increase of more wet and warm climates. The zonal level climate analysis carried in the present study has a benefit to the stakeholders and farmers in the agricultural water availability and demands perspective.

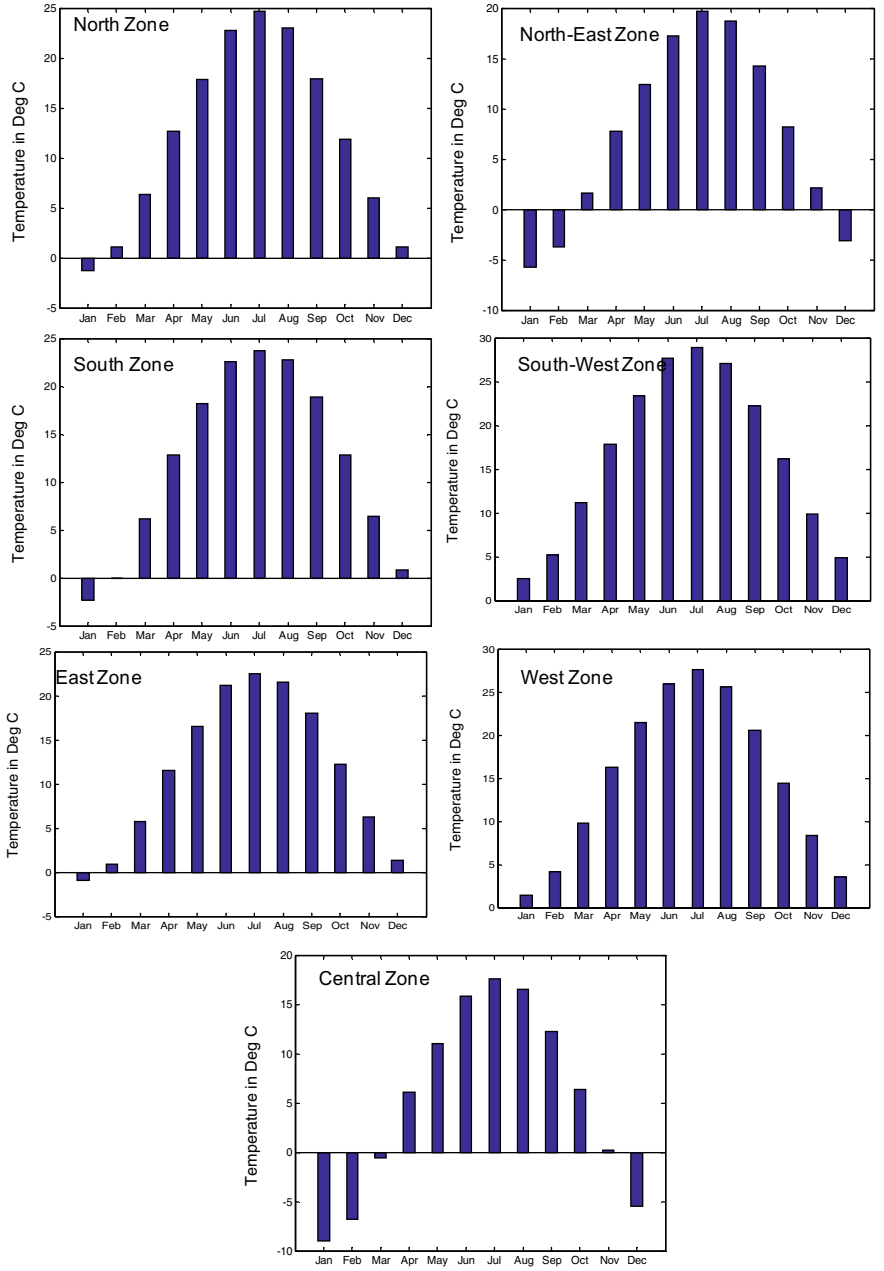

Fig. 5 The spatial average monthly temperature from 1961 to 2006 for seven agro-climatic zones of Afghanistan

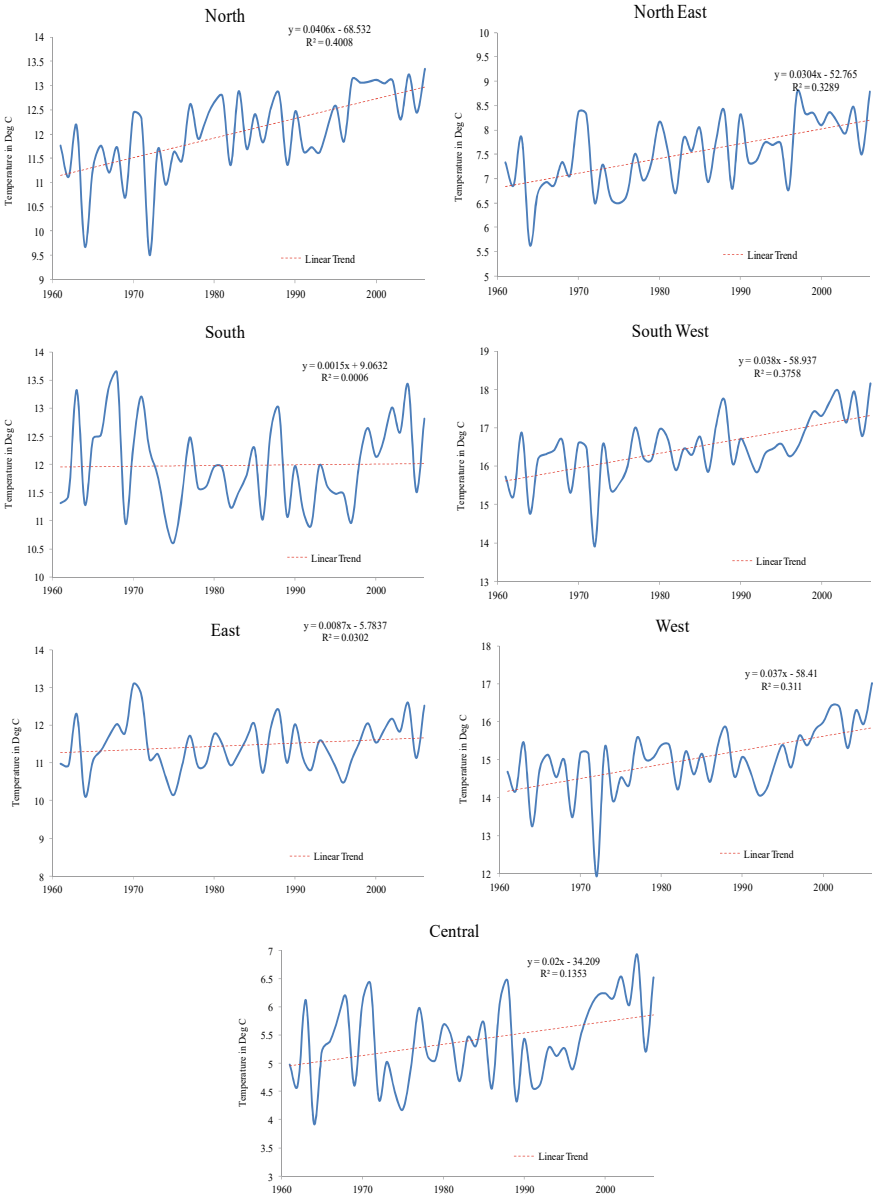

Fig. 6 The spatially averaged annual average temperature trend over seven agro-climatic zones of Afghanistan for the observed period of 1961 to 2006 with APHRODITE data

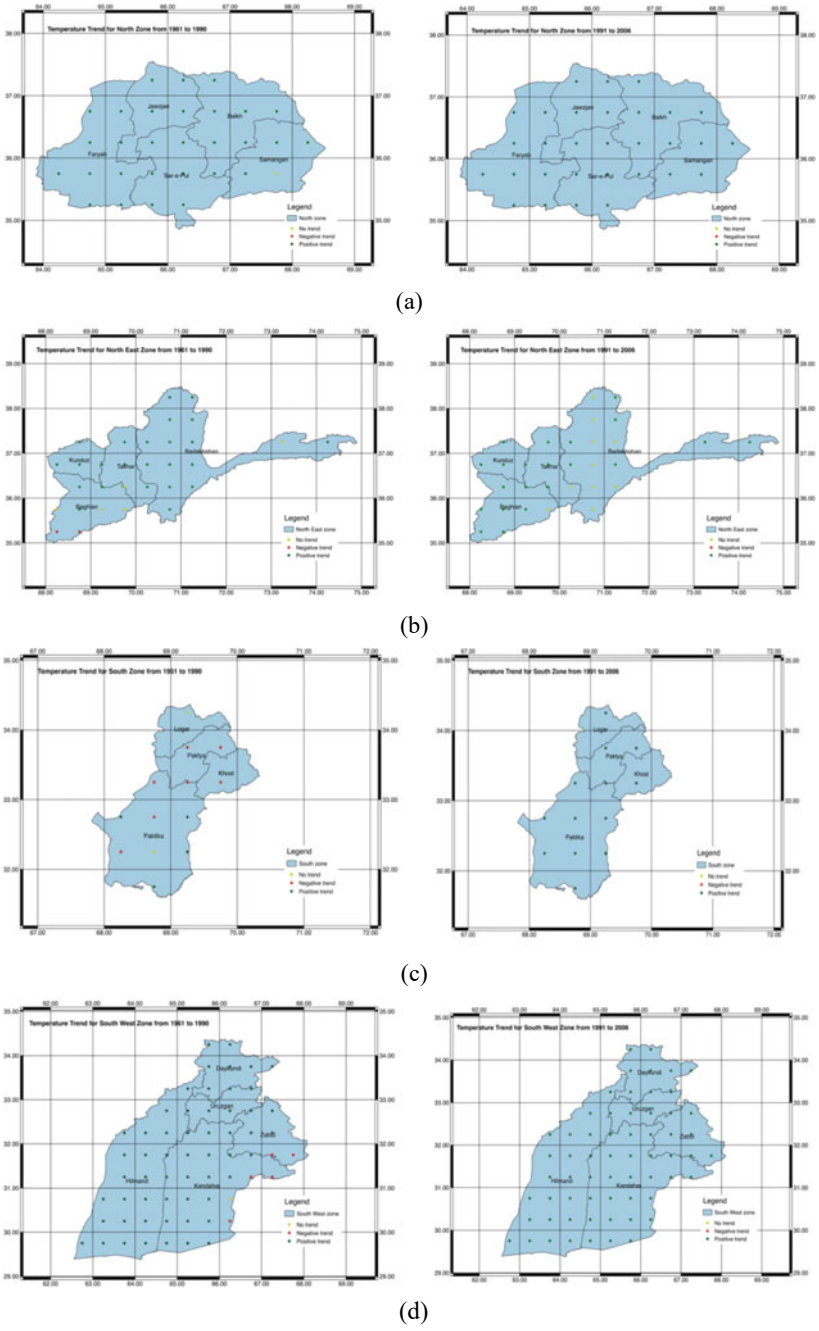

Fig. 7 Temperature trend analysis for **a** North **b** North-East **c** South **d** South-West **e** East **f** West **g** Central zones with daily data of rainfall for two time slices of period of 1951 to 1990 and 1991 to 2007 with Mann–Kendall trend test. Positive Trend—Increasing rainfall trend; Negative Trend—Decreasing rainfall trend; No Trend—no trend at 5% significance level

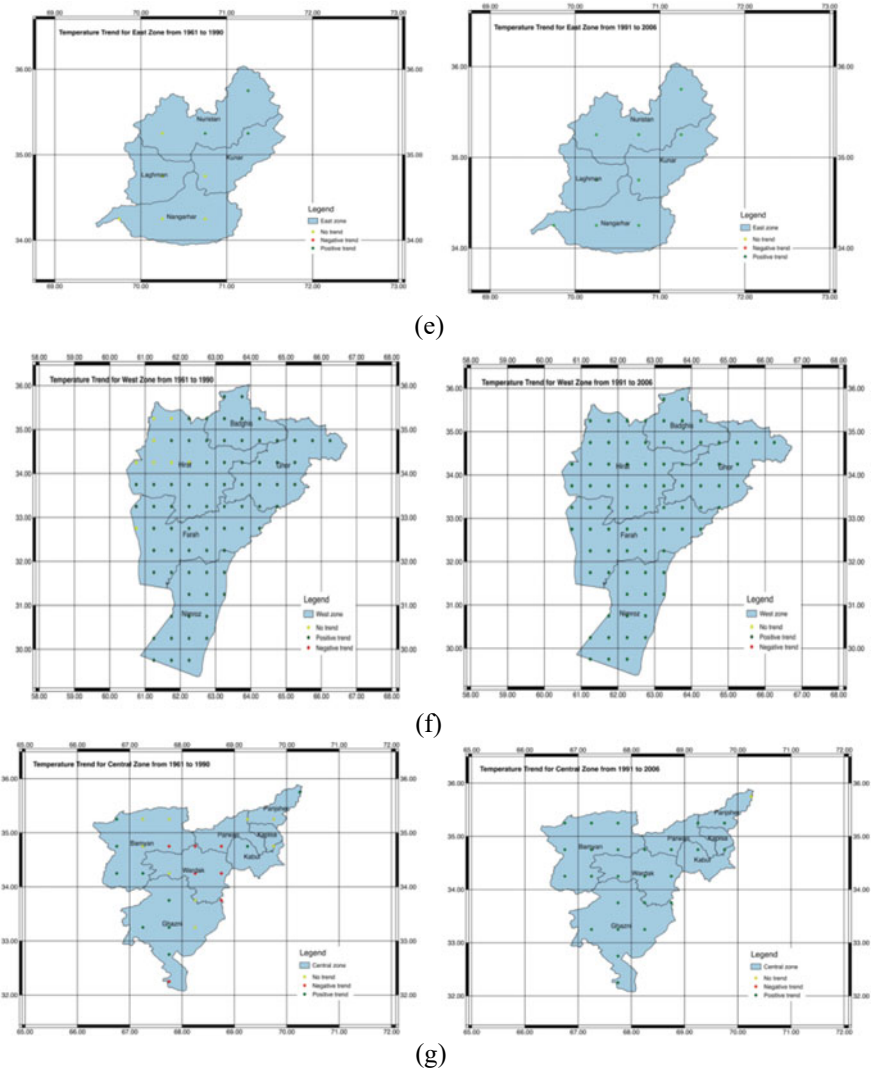

Fig. 7 (continued)

Acknowledgements The authors would like to thank the Ministry of Agriculture, Irrigation and Livestock (MAIL) and AGROMET, Afghanistan for the permission to use meteorological data. This publication is a part of the Climate Change Adaptation Project, MAIL, GoIRA by MgtWell Consulting Services through a project awarded ID no. 00087639 through the GEF/UNDP Grant No. 00076056 between the period of August 2016 and May 2017.

References

Afghanistan Statistical Organization (CSO), Ministry of Agriculture, Irrigation and Livestock, Agriculture data 2008–2016

Aich V, Akhundzadah NA, Knuerr A, Khoshbeen AJ, Hattermann F, Paeth H, Scanlon A, Paton EN (2017) Climate change in Afghanistan deduced from reanalysis and coordinated regional climate downscaling experiment (CORDEX)—South Asia simulations. Climate 5:38. https://doi.org/10.3390/cli5020038

"Beekeeping survey report", Beekeeping and Animal Husbandry Development Project (BAHDP) and Beekeeping Development Project (BDP), Ministry of Agriculture, Irrigation and Livestock (MAIL), Conducted from September–November 2014

Campbell J (2015) A dry and ravaged land: investigating water resources in Afghanistan. Earth 60(1&2):48–55. http:www.earthmagazine.org/article/dry-and-ravaged-land-investigating-water-resources-afghanistan

Climate Change Scenarios for Agriculture of Afghanistan, Climate change adaptation project, Ministry of Agriculture Irrigation and Livestock, The Islamic Republic of Afghanistan, Mgtwell consulting Services, Kabul. GEF/UNDP Grant No: 00076056

Curry CL, Sillmann J, Bronaugh D, Alterskjaer K, Cole JNS, Ji D, Kravitz B, Kristjánsson JE, Moore JC, Muri H, Niemeier U, Robock A, Tilmes S, Yang S (2014) A multimodel examination of climate extremes in an idealized geoengineering experiment. J Geophys Res Atmos 119:3900–3923. https://doi.org/10.1002/2013JD020648

Donat MG, Alexander LV, Yang H, Durre I, Vose R, Dunn RJH, Willett KM, Aguilar E, Brunet M, Caesar J, Hewitson B, Jack C, Klein Tank AMG, Kruger AC, Marengo J, Peterson TC, Renom M, Oria Rojas C, Rusticucci M, Salinger J, Elrayah AS, Sekele SS, Srivastava AK, Trewin B, Villarroel C, Vincent LA, Zhai P, Zhang X, Kitching S (2013) Updated analyses of temperature and precipitation extreme indices since the beginning of the twentieth century: the HadEX2 dataset. J Geophys Res Atmos 118:2098–2118. https://doi.org/10.1002/jgrd.50150

Gilbert RO (1987) Statistical methods for environmental pollution monitoring. John Wiley and Sons, New York

Hamada A, Arakawa O, Yatagai A (2011) An automated quality control method for daily rain-gauge data. Global Environ Res 15(2):183–192

Hartmann DL, Tank AMK, Rusticucci M, Alexander LV, Brönnimann S, Charabi YAR, Soden BJ (2013) Observations: atmosphere and surface. In: Climate change 2013 the physical science basis: working Group I contribution to the fifth assessment report of the intergovernmental panel on climate change

IPCC (2012) Managing the risks of extreme events and disasters to advance climate change adaptation. A Special Report of Working Groups I and II of the Intergovernmental Panel on Climate Change [Field CB, Barros V, Stocker TF, Qin D, Dokken DJ, Ebi KL, Mastrandrea MD, Mach KJ, Plattner G-K, Allen SK, Tignor M, Midgley PM (eds)]. Cambridge University Press, Cambridge, UK, and New York, NY, USA, 582 pp

Kendall MG (1975) Rank correlation method. Griffin, London, UK

Köppen and Wladimir (1884) Translated by Volken E, Brönnimann S. The thermal zones of the earth according to the duration of hot, moderate and cold periods and to the impact of heat on the organic world. Meteor Zeits 20(3):351–360 (June 2011)

Mann HB (1945) Nonparametric tests against trend. Econometrica: J Econometric Soc 245–259

Panda DK, Aghakouchak A, Ambast SK (2017) Increasing heat waves and warm spells in India, observed from a multiaspect framework. J Geophys Res Atmos 122:3837–3858. https://doi.org/10.1002/2016JD026292

Razavi T, Switzman H, Arain A, Coulibaly P (2016) Regional climate change trends and uncertainty analysis using extreme indices: a case study of Hamilton, Canada. Climate Risk Manag 13:43–63.https://doi.org/10.1016/j.crm.2016.06.002

Sharma S, Mujumdar P (2017) Increasing frequency and spatial extent of concurrent meteorological droughts and heatwaves in India. Sci Rep 7(1):15582. https://doi.org/10.1038/s41598-017-15896-3

Zhang X, Aguilar E, Sensoy S, Melkonyan H, Tagiyeva U, Ahmed N, Albert P (2005) Trends in Middle East climate extreme indices from 1950 to 2003. J Geophys Res: Atmos 110(D22)

Micro Hydro Power Generation in India-A Review

Aparna M. Deulkar, Vivek S. Chavhan, and Pankaj R. Modak

1 Introduction

Energy is very important for all human activity. Development of country is depending on available energy resources. Water is a natural source to generate the energy. In the past decades, there is a world-wide problem of fossil fuel depletion, climatic change, and increased electricity demand (Anandh and Vinoth 2018). There is a fast depletion of renewable sources that was used in the past for the generation of electricity and the difficulty in reachability of the grid supply to the remote villages was a big challenge faced. The best possible remedial measure in this scenario is to make use of some renewable energy source like hydro power, wind, biomass etc. so that it will be first step to reduce fossil fuel depletion. The aim of present work is to focus on micro hydro power generation in India as renewable energy source to full fill energy demand. Study of micro hydro power plant focuses on three main folds such as technical as well as economical feasibility studies, design of civil works and selection of electro mechanical components. There is a huge potential to develop a micro hydro power plant which would meet the energy demand of the tribal settlement in India and thereby improving their living condition.

By considering advantages of Micro hydro power plant like no air pollution, no waste product like nuclear power plant, water left from the dam or cannel can be reuse, it provide provision for flood and it is a clean source of energy. For rural development and employment, micro hydro power plant is the best solution. Since

A. M. Deulkar (✉) · V. S. Chavhan · P. R. Modak
Department of Civil Engineering, AISSMS COE, Kennedy Road, Near R.T.O. Office, Pune 411001, India
e-mail: aparna.deulkar2015@gmail.com

V. S. Chavhan
e-mail: vschavhan@aissmscoe.com

P. R. Modak
e-mail: prmodak@aissmscoe.com

R. Jha et al. (eds.), *River and Coastal Engineering*, Water Science and Technology Library 117, https://doi.org/10.1007/978-3-031-05057-2_24

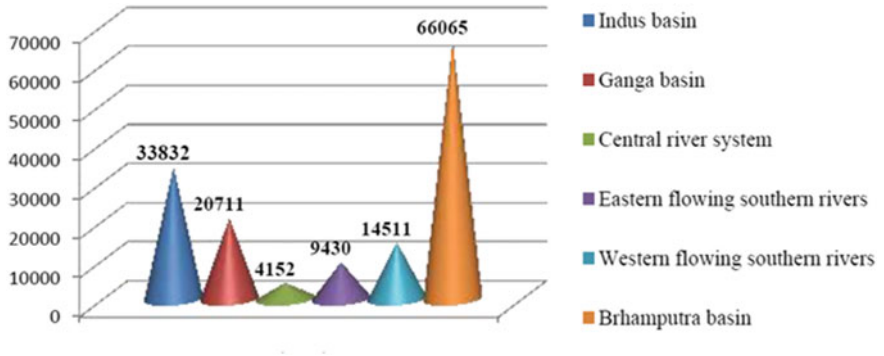

Fig. 1 Estimated hydro potential

small hydro power plants do not require long term planning, less expensive, for rural electrification over a complete lifetime they are cheapest technology available. It is noted every time that the development of large hydro power plant is resisted by local community, environmentalist and NGOs due to issues such as deforestation and resettlement of the community (Hoffken 2014). Another advantage of micro hydro power plant is they use available flow of river and no storage is required.

India is blessed with large number of river flowing over a country. All these rivers have great potential for hydro power which can be harnessed. Figure 1 shows the basin wise potential of Indian River system (Chauhan and Vig 2017).

India is ranked third biggest in the USA, with 5.5% global share in 2016 (Anandh and Vinoth 2018). Since India is largely dependent on fossil fuel imports to meet its energy demands, about 70% of India's electricity generation capacity is from fossil fuels (Anandh and Vinoth 2018). To meet the future energy demands, it is essential to tap all possible sources of small hydro energy using decentralized power generation (Anandh and Vinoth 2018). Micro-hydro power is the small-scale harnessing of energy from falling water which converts hydraulic energy to electric energy. It is cheapest solution for poor communities in rural areas with an affordable, easy to maintain and long-term solution to their energy needs. In India, the total hydro electrical potential is about 69% (including both large and small hydro projects and those installed/under installation) (Anandh and Vinoth 2018). According to the international energy agency (IEA), large-scale hydro-electric plants currently supply 16% of the world's electricity. However, such kind of projects requires tremendous amounts of land impoundment, dams and flood control, and often they produce environmental impacts (Singh 2009). Among the renewable energy source small hydro power contributes 13% of the total grid connected power generation, thereby constituting second largest grid-connected system after wind power, as per the report by Ministry of New and Renewable Energy (Michael and Jawahar 2017). Micro-hydro power is a type of Hydroelectric power that typically produced up to 5 to100 kW of electricity using the natural flow of water. This type of power plant can provide power to a small community.

Up to November 2016, the installed capacity of hydropower in India is 43133.43 MW. This installed capacity of hydropower is about 13.97% of the total installed capacity of the country. The current potential of hydropower in India is about 148,701 MW. This potential is 3.45 times the installed capacity (Chauhan and Vig 2017). Indian power is generally based on fossil fuel. To move toward renewable energy source and as 13.69% (Chauhan and Vig 2017) is the contribution by hydro power plant. To promote micro hydro power plant by considering advantage above mentioned it is necessary to take step toward micro hydro power plant. Hence, this paper gives a review of micro hydro power generation in India the water resources, current status, potential and future of hydro energy in India.

2 Literature Review

This part is compiled with a review of past research work in the field of micro-hydro in India. Purpose of this literature review is to find key for further research in this field.

Anandh and Vinoth (2018) studied current scenario and future potential of small hydropower plant India. Share of hydro power in our country is declining persistently, from 46% in the year 1960 to 16.33% in the year 2015. Small-scale hydropower is a concentrated energy source with a long-lasting and robust technology, and its systems' life can extend to up to 50 years or more without any major new investments.

Chauhan and Vig (2017) Present paper gives a complete review of the water resources, current status, potential and future of hydro energy in India. India ranks third after China and USA in the world in terms of numbers of dams. But large hydro power plant required many years for full construction and its commissioning of plant. Author suggest that besides the large hydro potential, small hydro power plant is the best solution to full fill rural energy demand by utilizing present hydro potential and it also provide employment to rural population.

During the study author observed that, Hydro generating unit sizes has been increased from 22 MW (from the independence) to 250 MW till today. Till august 2016 only 34.29% of the northern region of India potential and near about 2% of the north eastern region of India potential has been utilized. If the hydro power potential in these region is utilized completely then nation's dependence on thermal power plants can be reduced significantly.

Adamantia Zoi Vougioukli et al. (2017) studied about climate change with respect to growing demand of energy. Globally-averaged temperatures in 2016 were 0.99 °C (1.78 °F). By studying advantages of renewable energy i.e. micro hydro power plan authors provide a comprehensive assessment of the environmental impacts of small hydropower plants (SHPs) considered the problem of assessing the environmental cost of a Micro hydro power (MHP) by using the approach of external cost. The external cost was derived from the combination of Life Cycle Air pollutants emission factors for the three main construction components (concrete, steel, aggregates).The external cost was estimated to play a non-negligible part in the total investment cost

that can affect the feasibility of the scheme. Also, more applications of the method on renewable energy sources will better demonstrate its benefits and drawbacks through additional practice.

Michael and Jawahar (2017) studied energy scenario. According to study, at the end of the Aug 2014, the power generation reached around 20,000 Mw only by Small hydro power plant with more than 15,000 Mw potential remaining unexploited. Authors consider Kerala state of India for study. Which is having seasonal discharge but more discharge in rainy season. Tribal Village in Kerala state does not have access to electricity. They use kerosene for lighting purpose. To full fill energy demand of Tribal Village first energy requirement and energy potential is calculated. Available discharge is reduces by 80% to account for various losses. By considering losses electro mechanical equipment (like Turbine, Generator) is selected for power generation of 120 family. This study resulted with micro hydro power plant is found to be technically and economically viable as operation cost is 60 lakhs.

Manual (2015) gives brief idea, advantages and challenges associated to the micro hydropower. India is endowed with rich hydropower potential to the tune of 148 GW. India ranks fifth in the world in terms of usable hydro power potential. India has around 36 GW of installed hydropower capacity whereas an additional 13 GW is under construction.

Saxena (2013) studied potential of small hydro power plant in India. According to his study potential of small hydro (upto 25 MW station capacity) in India is of about 20,000 MW of which about 3632 MW has been exploited. In India, hydro projects up to 25 MW station capacity have been categorized as SHP projects and responsibility of small hydro development rests with Ministry of New and Renewable Energy (MNRE). India has a history of about 110 years of hydropower. The first small hydro project of 130 kW commissioned in the hills of Darjeeling in 1897 marks the development of hydropower in India. The total hydroelectric power potential in the country is assessed at about 150,000 MW, equivalent to 84,000 MW at 60 per cent load factor. The potential of SHP projects is estimated at about 20,000 MW. Of this, 6474 potential sites with an aggregate capacity of 19,749 MW have been identified. Today the SHP programme in India is essentially private investment driven. In fact 329 private sector SHP projects of about 1748 MW capacity have been setup. Private sector entrepreneurs are finding attractive business opportunities in small hydro and state governments also feel that the private participation may be necessary for tapping the full potential of rivers and canals for power generation. Author conclude that appropriate selection of sites and sizing of projects to give higher plant load factors are considered important to further improve economic viability of commercial SHP projects.

Bhoi and Ali (2014) studied Hydro power plant in India and its environment impact also studied HYDRO power plant projects in India. Hydro power can be classified as: large hydro power, medium hydro power, Small hydro power. These are classified according to the power generation capacity. Large hydro power: > 100 MW, Medium hydro power: 30–100 MW, Small hydro power: 1–30 MW. Very small scale hydro power plant classified as: Mini hydro power whose capacity is between 100 kW and 1 MW and Micro hydro ranging up to 100 kW. Authors studied component part of

hydro power plant along with turbine types according to head. Kaplan and Propeller $2 < H < 40$ Francis, $10 < H < 350$ Pelton, $50 < H < 1300$ (head in m). In environmental impact author explain advantages and problem associate with hydropower like plant require Suitable site, weather condition, local habitat, climatic condition, flow of water, head. A large part of the land area is required to install a hydro project so may create disturbance to the local habitat. Requirement of large area is meeting by the afforestation programmes which disturb the ecosystem. Sometime many aquatic animals are also affected by the construction of dam across water mass.

Saxena and Kumar (2010) studied Hydropower Development in India. In which they studied whole country is divided into five power regions and planning is done on a regional concept. At the time of independence in the year 1947 only 1362 MW of electricity was produced in India. After that installed capacity of power generation had grown to 164,509 MW of which Hydro is 37,086 MW (25%), Thermal is 106,433 MW (65%), Nuclear is 4560 MW (2.9%) and Renewable energy sources 16429 MW (7.7%) The share of small scale hydropower (SHP) is 2820 MW. The potential of small hydro power projects is estimated at about 15,384 MW with 5718 potential identified sites.

Baidya (2006) studied Indian Scenario of small hydro power and its advantages as a renewable resource. Author explain importance of Small hydro power (SHP) and how it is optimally and viably source of energy to improve economic condition of the people in the village area and overall development of the country. This in turn help in capacity addition to the hydro power generation and shortage of electricity can be avoided to some extent.

Vyas et al. (2015) studied Micro hydel Power system Design and its Implementation in Rajasthan. In this study authors observed that though India blessed with hydro potential, only marginal amount of power is so far tapped from the renewable source, because these potential sites are located in difficult terrains and remote access. Considering the design and the cost estimation it can be concluded that the small hydro projects are feasible in the arid and semi arid regions of Rajasthan. Author suggested that by considering important aspects like proper maintenance, providing silt excluders we can improved micro hydro potential as renewable source.

Choudhury and Ghosh (2013) focus on responsible hydro power development in India. As hydro power is important and renewable source of energy but this article is focus on "responsible" hydropower development. Means hydropower development should more stable and sustainable investment for medium-to-long term.

Souza and Donald (2015) studied need for hydropower in India. Hydro potential and Growth and share of hydroelectric Installed capacity and generation. Share of hydro power in India is 16.9% of the total installed capacity of 237,742.94 MW as on 28th Feb, 2015 and 4.4% global install capacity and ranked 6th in the list of global nations. The hydropower generation for 2012–12 and 2013–14 stood at 12.5% and 14% of the total energy generation. As against the power generation target of 122,263 MU for 2013–14, generation from hydroelectric power stations (above 25 MW Installed Capacity) was 134,847.52 MU, which was 10.29% more than the target.

3 Conclusion

During literature study it was observed that micro hydropower is the best solution to overcome growing energy demand. Some work has been carried out related to the same, but there is need to more focus on micro hydro power development in sustainable way in state of dependency on hydropower. It is observed that to improve livelihood of villagers and also remote villages' micro hydro power is the solution.

Hydro is a renewable resource that is replenished by the environment over a relatively short period of time. Water is neither depleted nor its composition altered during the generation cycle. A run of river plant stores water in the weir for a short duration and the water is returned to water cycle on each day. Small hydro projects (90%) efficient in utilization of the resource than solar (15–20%), wind (35%) and other renewable energy sources. In long term, small hydro schemes have the least impact amongst the environmental indicators like acidification, climate change, ozone layer depletion, photo chemical oxidation (smog) etc., Capital subsidy for small hydro power should be increased and better mechanism to deliver the subsidy should be devised. Incentive available to small hydro projects up to 25 MW may be extended to the hydro power projects up to 100 MW. Small hydro power plants have advantage of life span almost 50 years i.e. more than twice the life span of other renewable sources like wind, solar etc.

References

Adamantia ZV, Didaskalou E, Georgakellos D (2017) Article on financial appraisal of small hydropower considering the cradle-to-grave environmental cost: a case from Greece

Anandh T, Vinoth R (2018) A comprehensive assessment of small hydro power in India—current scenario and future potential. J Mech Prod Eng 8:413–424

Baidya G (2006) Development of small hydro. Himalayan Small Hydropower Summit, pp 34–43

Bhoi R, Dr Ali SM (2014) Potential of hydro power plant in India and its impact on environment. J Eng 10:114

Cai L, Cheng GH, Xu Z (2005) Capacity expansion and restructuring with intermittent wind and small hydro energy. Presented at the conference transmission and distribution

Chauhan D, Vig S (2017) A review of present status and potential of hydro power in India. Int J Modern Trends Eng 4. 2349-9745

Choudhury N, Ghosh A (2013) Responsible hydropower development in India. Manual by the Council on Energy, Environment and Water for the Independent Power (EEW)

Donaek PJ (2007) Update on small hydro technologies and distributed generation including run-of-river plants. IEEE Spectr 44(07):1–2

Höffken JI (2014) A closer look at small hydropower projects in India: social acceptability of two storage-based projects in Karnataka, pp 155–66

Michael PA, Jawahar CP (2017) Design of 15 kW micro hydro power plant for rural electrification at Valara. In: 1st International conference on power engineering, computing and control, PECCON, pp 163–171

Khan MA, Badshah S (2014) Design and analysis of cross flow turbine for micro hydro power application using sewerage water. Res J Appl Sci Eng Technol 8(7):821–828

Nasir BA (2013) Design of high efficiency cross-flow turbine for hydro-power plant. Int J Eng Adv Technol (IJEAT) 2(3). ISSN: 2249-8958
PWC Manual (2015) Hydro power in India key enables for a better tomorrow. www.pwc.in
Saxena P**,** Kumar A (2010) Hydropower development in India. Alternate Hydro Energy Centre, Indian Institute of Technology Roorkee
Saxena P (2013) Renewable energy. Akshay Urja, vol 6, p 24
Schumann K, Saili L, Taylor R, Abdel-Malek R (2013) Hydropower and sustainable development: a journey. World Energy Congress, p 392
Singh D (2009) Micro-hydro-power. Resource assessment handbook, an initiative of the Asian and Pacific Center for transfer of technology
Souza SMD, Donald J (2015) Green growth and hydropower in India. Draft by The Energy and Resources Institute (Teri)
Vyasa A, Gupta NK, Gupta, Pradeep Gautam SK, Jehoo AS (2015) Mini/micro hydel power system design and its implementation in Rajasthan. In: International conference on water resources, coastal and ocean engineering (ICWRCOE). Aquatic Procedia, vol 4, pp 1537–1544
Wakati R (2010) Development of cross-flow turbine for local manufacturing. M.Sc. Thesis, University of Dar Es Salaam

An Analysis of Operational Life Cycle of SHP Plant Components: A Study in Himalayan Region

Ravi Kumar and S. K. Singal

1 Introduction

To assess the overall development in innovation and economy, energy utilization and accessibility is the most vital source. Vitality has a more critical task to carry out in all the activity of economy and advancements and it's the request specifically complements with the advancement (Padhy and Saini 2008). The sustainable power source assets (solar, wind, hydropower, geothermal and biomass) are the most thorough answer to ecological and vitality situations issues (Naidu 2005; Nigam 2008). For future energy consumption renewable energy is the new rising assets. The sustainable power sources particularly, Small hydro power (SHP) control have an boundless potential and may help in easing the weight of non-renewable energy sources between the interest and the supply with conservative advantages to the nation. SHP is considered as a standout amongst the most encouraging accessible energy sources on the planet having many advantages and to be a promising option than other energy sources (Kumar and Singal 2015a, b).

In SHP plant, power is created, when water weight is changed over into mechanical energy by utilizing hydro turbine and used to derive an electric generator (Naidu 2005). The power accessible is corresponding to the result of head and discharge. The mechanical power P in watt, created at the turbine shaft can be calculated as given in Eq. 1.

R. Kumar (✉)
Department of Mechanical Engineering, Government Engineering College Bikaner, Bikaner, Rajasthan 334004, India
e-mail: er.ravi.49@gmail.com

S. K. Singal
Department of Hydro and Renewable Energy, Indian Institute of Technology Roorkee, Roorkee, Uttarakhand 247667, India
e-mail: sunil.singal@hre.iitr.ac.in

R. Jha et al. (eds.), *River and Coastal Engineering*, Water Science and Technology Library 117, https://doi.org/10.1007/978-3-031-05057-2_25

$$P = \eta \rho g Q H \quad (1)$$

where η is the efficiency of the turbine, ρ the density of water (kg/m^3), g the acceleration due to gravity (m/s^2), Q the discharge (m^3/s) and H is the head of water acting on the turbine (m) (Naidu 2005; Kumar and Singal 2015a, b).

2 Components of SHP Plants

The components of SHP plants are broadly categorized as (1) Civil works, (2) Hydro-mechanical works and (3) Electro-mechanical equipment (Alternate Hydro Energy Centre 2012a, b). In Himalayan region hydropower stations, the size of civil works and electromechanical equipment are smaller due to lower discharges. Most of the components are common in different plants; however, some may vary as per site conditions. A broad classification of high head/Himalayan region SHP scheme components consisting of various sub components is shown in Fig. 1.

The useful life of hydro power plants can be more than 100 years as many such plants constructed more than 100 years ago are still operational. The economic operating life of SHP is considered as 30–40 years, which includes time to time major repairs, replacement, rehabilitation and modernization of some of the components. Thus, the profitable operational life cycle of SHP plants has been considered 35 years (International Finance Corporation (IFC) World Bank Group 2015; Mishra et al. 2011).

In 9th Century, various hydropower plants came under rehabilitation or replacement of some components, which are operational even today. The components whose life was less than economical operational life were repaired/replaced many times.

A study was performed by Pascale et al. (2011) on Huai Kra Thing micro hydropower plant situated in rural Thailand for life cycle assessment of the different components, construction material and their adverse effect on the environment. Studies of Hanafi and Riman (2015) presented life cycle of inventory and their environmental effect with the help of Simapro software. With the help of LCA, Koj et al. (2015) compared environmental impacts of Primary Control Provision (PCP) by novelion large-scale Battery Energy Storage Systems (BESSs) to assess impact of PCP through Coal Power Plants (CPP) and found that BESS is a better strategy to reduce the harmful impact of PCP on environment. Study conducted by Goal et al. (2008) showed that life cycle energy payback period and GHG emissions of renewable sources are less as compared to non- renewable energy sources. Ribeiro and Silva (2010) found reservoir filling, steel life-cycle, cement life-cycle and the operation of civil works as the most important sources of environmental burdens. Nordgard et al. (2010) presented quantitative risk analysis model for energy distribution system by using life curve approach as an input for decision making. From literature study, it is found that the average life expectancy of components of SHP plant depends upon the site conditions like water quality, sedimentation, environment, operational approach and geological condition etc. as given in Table 1. The average useful life act as a

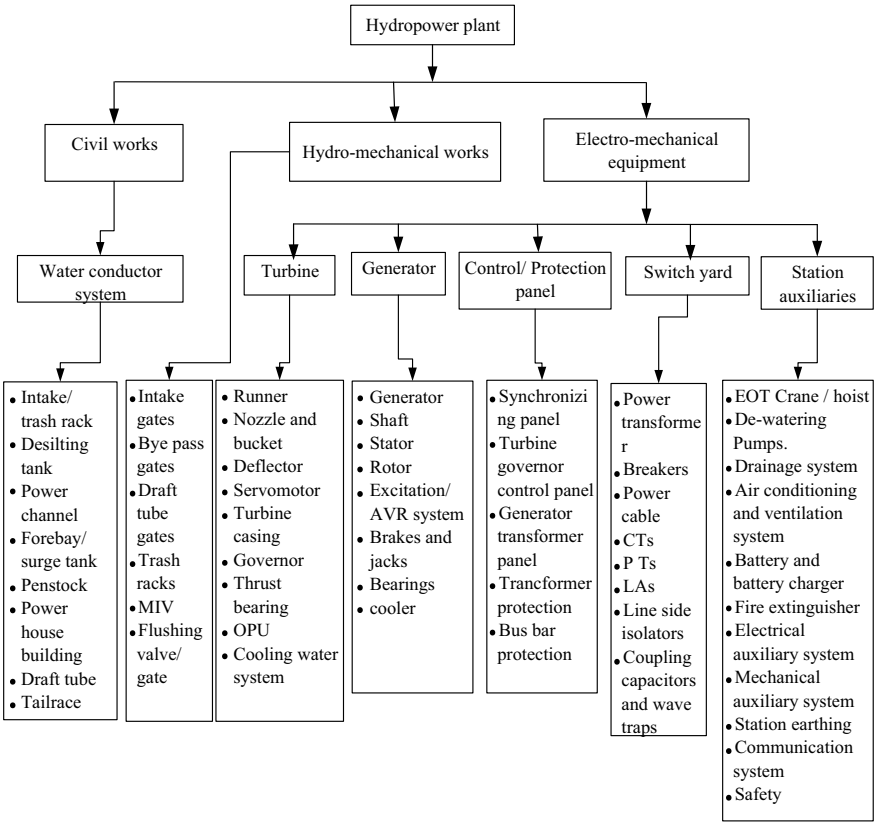

Fig. 1 A broad classification of components of high head SHP plants

mean to assess maintenance and larger rehabilitation works required to be done for all civil, hydro-mechanical, and electro-mechanical components (Alternate Hydro Energy Centre 2012a; International Finance Corporation (IFC) world bank group 2015;).

3 Study Area and Data Collection

In order to analyse operational life cycle of SHP plants in Himalayan region, Kangra district of Himachal Pradesh state of India was considered as study area. SHP plants having capacity up to 25 MW were selected for the study and data regarding the actual maintenance problems and replacement of different components were collected from 12 SHP plants. The detail of all the selected SHP plants is given in Table 2.

These plants were visited several times in different seasons and details related to main problems occurring in different components, major breakdowns, replacement

Table 1 Expected useful life for SHP plant components (International Finance Corporation (IFC) World Bank Group 2015)

Component	Expected useful life (years)
Civil work components	
Dam, power house building	100
Intake weirs, desilting tank, power channel, spillway, forebay, penstock	70
Hydro-mechanical components	
Gates, stoplogs, trash racks	70
Electro-mechanical components	
Transmission lines	70
Generator, motor, governor, excitation system, power transformer, main inlet valves, turbine equipment other than runners	40
Plant auxiliary mechanical and electrical equipment like drainage and dewatering pumps, cooling system, compressed air system, ventilation and air conditioning system, AC/DC power supply, emergency diesel generator, etc	30
Control and protection system, remote control, SCADA, communication, equipment, metering, switchyard equipment	20
Turbine runners, nozzle, bearing, breaks	10

Table 2 Detail of selected SHP plants

Plant name	Year of commissioning	No of generating Units	Installed capacity (MW)	Design Head (m)	Design discharge (Q) m^3/s
Binwa	1984	2	6	233.20	1.615
Baner	1996	3	12	330.10	4.0
Gaj	1996	3	10.5	212.90	6.30
Dehar	2004	2	5	290	2.01
Khauli	2007	2	12	475.73	2.94
Upper awa	2008	2	5	530.81	0.7
Baner-III	2009	2	5	305.0	1.19
Iku-II	2009	2	5	370.0	1.69
Luni-2	2009	2	5	340.45	0.88
Luni-3	2009	2	5	329.33	0.91
Drinidhar	2010	2	5	255.0	1.49
Upper Khauli	2010	2	5	440.50	0.834

time cycle of major components and repetition of major overhauling of the units were collected.

Based on the observation and discussion, a structured questionnaire was prepared for the data collection. The suggestions of other experts of SHP plants at Alternate Hydro Energy Centre (AHEC), Indian Institute of Technology (IIT) Roorkee were also included in the questionnaire. The questionnaire approach considered the problems occurring frequently in components, maintenance actions, major break downs, replacement cycle of components, major overhauling of units and maintenance cost.

4 Data Analysis

From the analysis of collected maintenance data of SHP plants, it has been found that the maintenance problems in civil works components are very few and maximum probability of damage of these components is mainly because of any natural calamity and heavy flood during rainy season. Their operational life cycle being more than the economic life of the plants, these components are not considered for further study.

From the data analysis, it has also been found that the electro-mechanical equipment face maximum problems and contribute maximum to the maintenance cost. The components facing more problems and requiring frequent maintenance/repair/replacements are found to be turbine and auxiliary components, cooling system, generator and auxiliary components, governor, control panel, switchyard components and station auxiliaries. These components are considered for further study to determine their useful life and proper maintenance strategy.

4.1 Details of Replacement of SHP Components

The replacement of components is required during annual/routine maintenance or whenever the component has crossed its useful operational life. Concerned component is partially replaced with spare parts or repaired when a fault occurs, until the complete replacement of the component is done. Therefore, hydropower facilities are considered as a repairable system. The replaced facilities are also included for obtaining equipment reliability. From the observations and collected data, it was found that many components were replaced number of times during their operational life cycle. The details in terms of commercial operational dates (in the years) when the components were replaced in each SHP plants are given in Table 3.

5 Life Cycle Analysis

Life cycle analysis (LCA) is carried out to evaluate the useful life of a system. LCA can help to study the various areas of power plant like estimating the useful life of

Table 3 Details of replacement of SHP plant components

Plant name	Turbine and auxiliary component					Cooling system	Generator and auxiliary component		Governor	Control panel	Switchyard component					Station auxiliaries	
	Commissioned year	Runner	Nozzle	Deflector	Servomotor		DE/NDE bearing	Brakes and jacks			Breakers	CT/PTs	Power cables	Light arrestors	Isolators	DC battery/chargers	Firefighting system
Binwa	1984	2000*, 2001#, 2014*, 2015#	1994*, 2002#, 2014*	1992a, 2000a, 2007a, 2015a	1992a, 2000a, 2007a, 2015a	2007*, 2008#	1992a, 2002a, 2007a, 2010a	1995a, 2004a, 2015a	2006a	2008a	2000, 2013	2000, 2015	2000, 2013	2000, 2013	2000, 2013	2000a, 2013a	2000a, 2015a
Baner	1996	2012*, 2014#, 2013+	2005*, 2005#, 2010+, 2015*, 2016#	2007a, 2015a	2007a, 2015a	2013*, 2014#, 2015+	2002a, 2009a, 2015a	2005a, 2015a	2012*#	2012a	2014	2014	2014	2014	2014	2005a	2014a
Gaj	1996	2012*, 2014#, 2015+	2006*, 2006#, 2015+, 2015*	2006a, 2015a	2006a, 2015a	2012*, 2013#, 2014+	2003a, 2009a, 2015a	2003a, 2014a	2013*, 2014#	2013a	2014	2014	2014	N	N	2005a, 2014a	2013a
Dehar	2004	2013*, 2015#	2013*, 2015#	2009*, 2010#, 2012*, 2014#, 2015*	2009a, 2012a, 2015a	N	2010*, 2011#, 2015*, 2016#	2010a	N	N	2012	N	N	N	N	N	N
Khauli	2007	N	2014#	2011*, 2012#, 2014*	2010a, 2014a	N	2013*, 2015#	N	N	N	2015	2013	N	N	N	2014a	N
Upper Awa	2008	N	2014*	2012*, 2014#	2012a, 2015a	N	2013*, 2014#,	N	N	N	2013	2013	N	N	N	N	N
Baner-III	2009	N	2015#	2013*,2015#	2013a	N	2015a	N	N	N	2014	2014	N	N	N	2012a, 2015a	N

(continued)

Table 3 (continued)

Plant name	Turbine and auxiliary component					Cooling system	Generator and auxiliary component		Governor	Control panel	Switchyard component					Station auxiliaries	
	Commissioned year	Runner	Nozzle	Deflector	Servomotor		DE/NDE bearing	Brakes and jacks			Breakers	CT/PTs	Power cables	Light arrestors	Isolators	DC battery/chargers	Firefighting system
Iku-II	2009	N	2015*	2014[a]	2014[a]	N	2014[a]	N	N	N		2015	N	N	N	2012[a], 2015[a]	N
Luni-2	2009	2014*	N	2013[a]	2012[a], 2015[a]	N	2013*, 2015#	N	N	N	2014	2013	N	N	N	N	N
Luni-3	2009	2014*	N	2013[a]	2012[a], 2015[a]	N	2013*, 2014#	N	N	N	N	N	N	N	N	N	N
Drinidhar	2010	N	2015*	2014[a]	2014[a]	N	2015[a]	N	N	N	2013	2014	N	N	N	2013[a], 2016[a]	N
Upper Khauli	2010	N	N	2015[a]	2015[a]	N	2014[a]	N	N	N	2015	2015	N	N	N	2013[a], 2016[a]	N

Notes

i. For turbine and auxiliary components, cooling system, generator and auxiliary components, governor, control panel and station auxiliaries, the symbol used with year shows the unit wise replacement of component i.e. *—unit 1, #—unit 2, +—unit 3, a—all unit and N—no replacement.

ii. In switchyard components, single year shows the replacement of component based on their operating condition and any major break down or fault occurring in it.

iii. Single year in the Table 3 represents one unit being replaced in the same year. In breaks and jacks, control panel, DC battery/chargers and fire-fighting system, one year represent the change of whole system or units in the plants.

component, their impact on environment, can serve as database, can act as input to quantitative risk analysis model, for decision making etc.

Based on the details given in the Table 3, analysis has been carried out to determine the useful life of SHP plant components. Components which were replaced number of times during the operation were found as runner, nozzle, deflector, servomotor, cooling system, DE/NDE bearing, breaks and jacks, governor, control panel, breakers, CT/PT's, power cable, Light Arrestors (LA's), isolators, DC battery/chargers and fire-fighting system.

To determine the actual useful life, the data regarding how many times the replacement of a particular component was done were analysed. Time gap between the number replacements was calculated and its average value was estimated. This average value was considered as operational life cycle of the component. The same methodology was used to find out the operational life cycle of all the components in SHP plants.

Figure 2 shows the operational life cycle of selected components in different SHP plants. Figure 2 clearly indicates that a component may have different operational life cycle in different SHP plants depending on operational, geological and environmental conditions.

Note: In Fig. 2, Horizontal axis represent the components i.e. (1) turbine runner, (2) nozzle, (3) deflector, (4) servomotor, (5) cooling system, (6) DE/NDE bearing, (7) breaks and jacks, (8) governor, (9) control panel, (10) breakers, (11) CT/PT's, (12) power cable, (13) LA's, (14) isolators, (15) DC battery/chargers and (16) fire-fighting system.

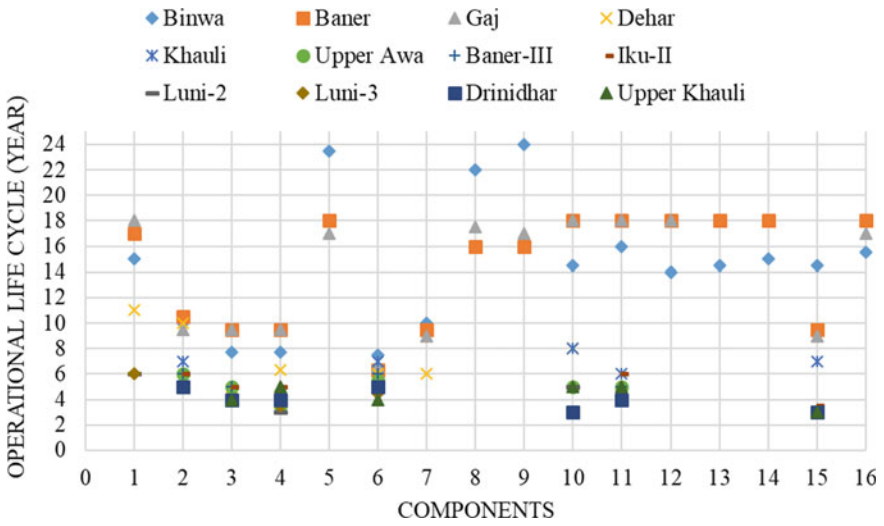

Fig. 2 Operational life cycle of SHP plant components

5.1 Average Operational Life of SHP Components

The details pertaining to the frequency of replacement of the components of each plant were analysed to determine the average operational life of each component. The analysed results of the average operational life of the SHP plant components are shown in Table 4 and Fig. 3. From Table 4, it has been found that the average operational life of Pelton turbine runner is 12.2 year. Similarly, average operational life of other components is also given in Table 4.

5.2 Validation of Results

In order to validate the life cycle of SHP components as obtained by analysis and given in Table 4 were compared with the expected useful life obtained from the literature as given in Table 1. The comparison is shown in Fig. 4. Figure 4, shows a very little variation in analysed and theoretical life cycle of most of the components. For some components, i.e. governor and DC battery system, the variation in analysed useful life is found large as compared to their theoretical life. This large variation is due to fast technology changes, which are more efficient, safer and user friendly. Also, these components were changed before their operational life as spare parts of previously installed components were not available due to change in technologies.

6 Conclusion

In this study, a detailed analysis has been carried out to determine the operational life cycle of the SHP components in Himalayan region based on the details like replacement of SHP plants components and results show that the operational life of most of the components is near to the theoretical useful life. However, some of the components have variations due to fast technology changes and unavailability of the spare parts of few components like governor, DC battery system etc. The operational life of the components can be increased by regular repair, maintenance and adaptation of technology changes.

Table 4 Average operational life of SHP plant components

Components	Runner	Nozzle	Deflector	Servomotor	Cooling system	DE/NDE bearing	Brakes and jacks	Governor	Control panel	Breakers	CT/PTs	Power cables	Light arrestors	Isolators	DC battery/chargers	Fire-fighting system
Average operational life (year)	12.2	7.8	5.5	5.4	19.5	5.7	8.6	18.5	19	9	8.7	16.7	16.3	16.5	5.9	16.8

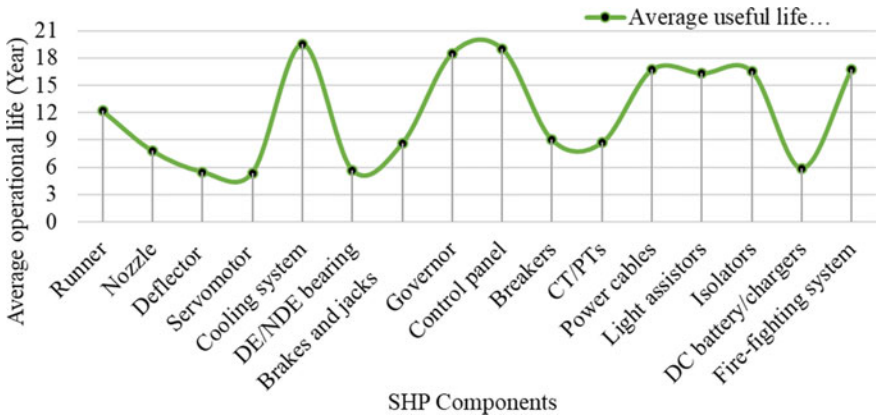

Fig. 3 Graphical representation of average life of SHP components

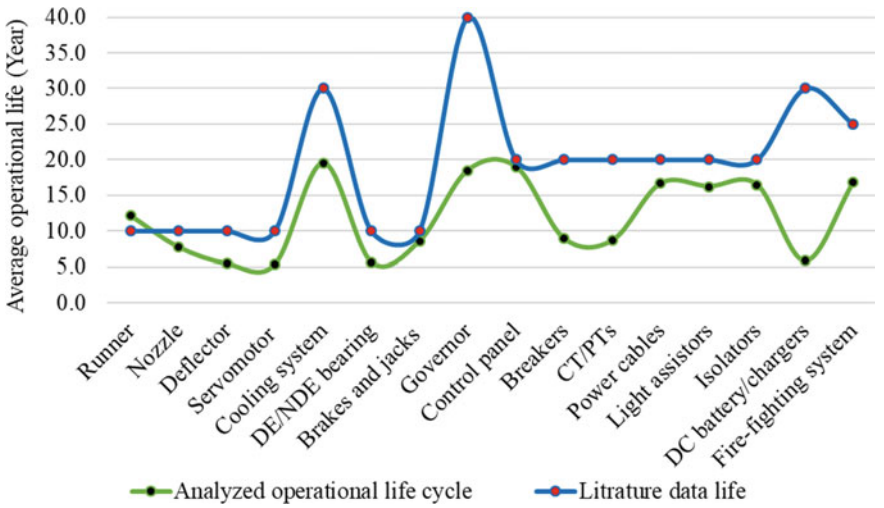

Fig. 4 Comparison of components operational life cycle analyses with literature data

Acknowledgements The author greatly acknowledge his supervisor and experts of SHP plants at Department of Hydro and Renewable energy, Indian Institute of Technology Roorkee, for their guidance and support to carry out this research work.

References

Alternate Hydro Energy Centre (2012a) Standards/Manuals/Guidelines for small hydro development. In: Electro-mechanical—Operation and maintenance, vol 3, issue 11, pp 1–95

Alternate Hydro Energy Centre (2012b) Standards/Manuals/Guidelines for small hydro development. Civil works—Maintenance of civil works (including hydro-mechanical), vol 2, issue 4, pp 1–24

Goal V, Bhat IK, Prakash R (2008) Life cycle analysis of run-of river small hydro power plants in India. Open Renew Energy J 1(1):11–16

Hanafi J, Riman A (2015) Life cycle assessment of a mini hydro power plant in Indonesia: a case study in Karai river. Procedia CIRP 29:444–449

International Finance Corporation (IFC) World Bank Group (2015) Hydroelectric power—A guide for developers and investors. Fichtner, Germany, pp 1–120

Koj JC, Stenzel P, Schreiber A, Hennings W, Zapp P, Wrede G, Hahndorf I (2015) Life cycle assessment of primary control provision by battery storage systems and fossil power plants. Energy Procedia 73:69–78

Kumar R, Singal SK (2015a) Operation and Maintenance problems in hydro turbine material in small hydro power plant. Mater Today: Proc 2(2015):2323–2331

Kumar R, Singal SK (2015b) Selection of best Operating site of SHP plant based on performance. Procedia Soc Behav Sci 189(2015):110–116

Mishra S, Singal SK, Khatod DK (2011) Optimal installation of small hydropower plant—A review. Renew Sustain Energy Rev 15(8):3862–3869

Naidu BSK (2005) Small hydro: highest-density, nonconventional, renewable-energy source, 1st edn. National Power Training Institute, New Delhi

Nigam PS (2008) Handbook of hydro electric engineering, 2nd edn. Nem Chand & Bros. Roorkee

Nordgard DE, Welte TM, Heggset J (2010) Using life curves as input to quantitative risk analysis in electricity distribution system asset management. Proc Inst Mech Eng Part o: J Risk Reliab 224(2):63–74

Padhy MK, Saini RP (2008) A review on silt erosion in hydro turbines. Renew Sustain Energy Rev 12(7):1974–1987

Pascale A, Urmee T, Moore A (2011) Life cycle assessment of a community hydroelectric power system in rural Thailand. Renew Energy 36(11):2799–2808

Ribeiro FM, Silva GA (2010) Life-cycle inventory for hydroelectric generation: a Brazilian case study. J Clean Prod 18(1):44–54

Spatio-temporal Variation and Trend Analysis of Groundwater Level in Bina and Khurai Blocks of Sagar District, Madhya Pradesh

Shashi Poonam Indwar, Ankit Kumar, and T. Thomas

1 Introduction

About 70% of the world's area is filled with water, but potable sweet water is only 3%, the remaining part is saline water. Only one percent of this sweet water can actually be used by us. This whole water, available on earth, revolves around specified water cycle. Generally 52% of fresh water is contained in lakes and ponds, 38% soil names, 8% vapor, 1% of rivers and 1% vegetation. The water cycle is deteriorating due to water pollution and water consumption due to economic development, industrialization and population explosion. Third world countries suffer more than this. It is true that the amount of water available in the world is still the same as it was 2000 years ago; the only difference is that at that time the population of Earth was only 3% compared to today.

Groundwater is a precious and most widely distributed resource of the earth and unlike any other natural resource, it gets annual replenishment from the precipitation and it is the major source for drinking and irrigation purpose in rural and urban areas of India. For sustainable development of groundwater resources it is necessary for trend analysis of groundwater from time to time in order to understand groundwater fluctuations (GWL) in context of recharge, abstraction from wells for various purposes etc. The trend analysis of hydrological series is of practical importance because of the effects of various changes in climate, land use, and demand patterns. Statistical procedures are used for the detection of the gradual trends over time (Thakur and Thomas 2011). Sustainable groundwater resources assessment and mitigation for future prospective can be estimated by time series analysis of historical datasets. Time series analysis and its inter-annual variability are dependent upon weather conditions and geographical features. The trend analysis can be utilized for detecting the trend in long-term observed historical time series of groundwater

S. P. Indwar (✉) · A. Kumar · T. Thomas
National Institute of Hydrology, Regional Centre, Walmi Campus Bhopal, Bhopal, India
e-mail: shashi.nihr@gov.in

R. Jha et al. (eds.), *River and Coastal Engineering*, Water Science and Technology Library 117, https://doi.org/10.1007/978-3-031-05057-2_26

level and its seasonal inter-variability over the specific duration (Kumar et al. 2018). The Mann–Kendall (MK) test is the most often used non parametric approach for analysing the trend in a time series (Mann 1945; Kendall 1975). This approach has been extensively used by researchers for a variety of hydrometeorological parameters (Sirois 1998; Gocic and Trajkovic 2012; Mondal and Mukhopadhyay 2012; Patle et al. 2013). In this study firstly the presence of a monotonic increasing or decreasing trend is tested with the nonparametric Mann–Kendall test and secondly the slope of a linear trend is estimated with the nonparametric Sen's method (Gilbert 1987). These methods are used in their basic forms; when the trend is assumed to be monotonic there is no seasonal or other cycle is present in the data in such cases Mann–Kendall test is suitable. Linear model is used to estimate the slope of the trend and the variance of the residuals should be constant in time, this defines the Sen's slope method. These methods offer many advantages that have made them useful in analysing groundwater trends. Groundwater trends estimation using non-parametric methods i.e Mann–Kendall, Modified Mann Kendall and Sen's Slope method were used (Kumar et al. 2018; Sumant et al. 2018).

2 Study Area

The study area entails Bina and Khurai blocks in Sagar district located at latitude of 24°02′37″ to 24°10′35″ N and longitude of 78°11′47″ E to 78°19′50″ and its comes under the 43N UTM zone (Fig. 1). Sagar district of Bundelkhand region is situated

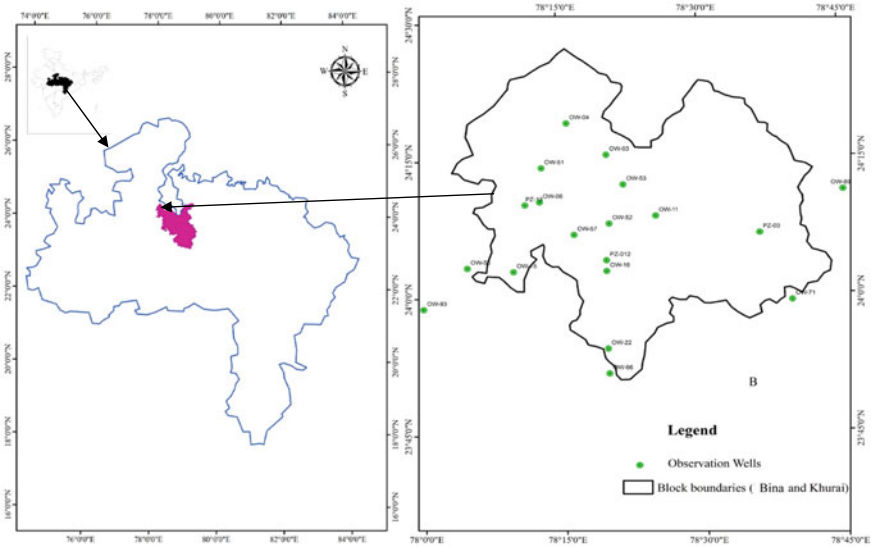

Fig. 1 Location map of the study area

in central India. The climate of this region is sub-tropical, with the coldest winter in January, the average minimum temperature of 11.5 °C, the hottest month in May and the average maximum temperature is 40.8 °C. Affected by Southwest Monsoon and average annual precipitation is about 1235/mm. Agricultural land is mainly black soil in both blocks. The Bina (river) is the main source of water for the Bina and Khurai blocks. In the Bundelkhand region of Madhya Pradesh, the Bina River is a major tributary of Betwa River. The Bina River starts from Begumganj block located in Raisen district, enters Sagar district to traverse through Khurai and Bina tehsil before confluence with river Betwa in Vidisha district.

3 Material and Methods

Man Kendal and Sen's slope test were used to determine groundwater level trends in 18 observation wells based on 17 years monthly data (2000–2017) for Bina and Khurai blocks in Sagar district (Table 1). Spatial and temporal variations has been analyzed for observation wells to predict groundwater flow direction and fluctuations in the respective wells. Mann- Kendall test using non-parametric method is the one of the best techniques for trend analysis.

3.1 Mann–Kendall Test

The Mann–Kendall test is applicable in cases when the data values *xi* of a time series can be.

assumed to obey the model

$$X_i = f(t_i) + \varepsilon_i \tag{1}$$

where $f(t)$ is a continuous monotonic increasing or decreasing function of time and the Residuals Ɛi can be assumed to be from the same distribution with zero mean. Therefore, it is assumed that the variance of the distribution is constant over time. Test the H_0 hypothesis, the null hypothesis signifying no trend. That is, the observations *xi* can be randomly assigned over time to the alternative hypothesis H_1, where the monotonic trend increases or decreases.

In calculating this statistical test, MAKESENS is used, which takes advantage of both the so-called S statistic and the normal approximation (Z statistic) given in Gilbert (1987). If the data points are less than 10 time series, the S test is used. (a) The number of data values is less than 10. The number of annual values in the survey data set is denoted by n. Missing values are allowed, so n can be less than the number of years in the time series under investigation. The S-statistic for the Mann–Kendall test was calculated using the following formula:

Table 1 Location and minimum, maximum and average Groundwater levels of wells

Wells	Location name	Latitude	Longitude	Minimum GWL m bgl	Maximum GWL m bgl	Average GWL
PZ-12	Khurai	24°03′54″	78°19′50″	1.80	27.60	17.90
PZ-13	Bina	24°10′06″	78°11′17″	3.1	23.25	13.39
PZ-03	Pali	24°06′41″	78°36′14″	0.20	27.00	4.85
OW-03	Niwari	24°15′27″	78°20′03″	0.42	7.85	3.83
OW-04	Bhangarh	24°18′57″	78°15′54″	0.65	7.10	4.06
OW-06	Bina	24°10′23″	78°12′50″	0.20	16.00	8.33
OW-11	Dugaha kalan	24°08′43″	78°25′12″	5.38	20.60	13.35
OW-15	Dhansara	24°02′50″	78°09′55″	0.70	10.75	6.03
OW-16	Khurai	24°02′45″	78°19′49″	0.20	12.75	8.50
OW-22	Nonagir	23°54′15″	78°19′48″	0.65	9.15	6.33
OW-51	Agasod	24°14′07″	78°13′05″	0.43	10.80	5.90
OW-52	Talapar	24°07′56″	78°20′13″	0.60	11.47	7.03
OW-53	Khimlasa	24°12′11″	78°21′50″	0.05	7.50	2.79
OW-56	Mandi bamora	24°03′17″	78°04′58″	0.80	16.30	7.97
OW-57	Kulwai	24°06′39″	78°16′27″	0.10	8.70	4.13
OW-93	Patauwa	23°58′51″	78°00′04″	0.45	11.30	6.07
OW-66	Jhila	23°51′32″	78°19′58″	1.00	10.80	6.29
OW-89	Dhamoni	24°11′16″	78°45′13″	0.10	6.50	3.18
OW-71	Mehar	23°59′17″	78°39′30″	0.26	9.30	4.73

$$S = \sum_{k=1}^{n-1} \sum_{j=k+1}^{n} sgn\left(x_j - x_k\right). \tag{2}$$

where xj and xk are the annual values in years j and k, $j > k$, respectively, and

$$\begin{aligned} &1\, if\, x_j - x_k > 0 \\ &sgn\left(x_j - x_k\right) = 0 if\, x_j - x_k = 0 \\ &-1\, if\, x_j - x_k < 0 \end{aligned} \tag{3}$$

The theoretical distribution of S derived by Mann and Kendall (Gilbert 1987) is compared directly to the absolute value of S if n is 9 or less. In MAKESENS the two-tailed test is used for four different significance levels α: 0.1, 0.05, 0.01 and 0.001. If the absolute value of S equals or exceeds a specified value $S_{\alpha/2,}$ H_0 is rejected in favour of H_1, when $S_{\alpha/2}$ is the smallest S which has the probability less than α/2 to appear in case of no trend. A positive (negative) value of S indicates an upward

(downward) trend. The minimum values of n with which these four significance levels can be reached are derived from the probability table for S as follows.

The significance level 0.001 means that there is a 0.1% probability that we make a mistake when rejecting H_0 of no trend and that the values *xi* are from a random distribution of no trend. Thus the significance level 0.001 means that the existence of a monotonic trend is very probable. Respectively the significance level 0.1 means that there is a 10% probability that we make a mistake when rejecting $H0$.

If n is at least 10 the normal approximation test is used, where the no: of data values is 10 or more. However when the number of data values is close to 10 and if there are several tied values (i.e. equal values) in the time series, it may reduce the validity of the normal approximation. First the variance of S is computed by the following equation which takes into account that ties may be present:

$$VAR(S) = \frac{1}{18}\left[n(n-1)(2n+5) - \sum_{p=1}^{q} t_p(t_p-1)(2t_p+5)\right]. \tag{4}$$

q no: of tied groups
t_p no: of data values in the pth group.

The values of S and VAR(S) are used to compute the test statistic Z as flows.

$$\begin{array}{ll} S - \frac{1}{\sqrt{VAR(S)}} & if\ S > 0 \\ Z = 0 & if\ S = 0 \\ S + \frac{1}{\sqrt{VAR(S)}} & if\ S < 0 \end{array}. \tag{5}$$

The presence of a statistically significant trend is evaluated using the Z value and it has normal distribution. A positive (negative) value of Z indicates an upward (downward) trend. To test for either an upward or downward monotone trend (a two-tailed test) at α level of significance, H_0 is rejected if the absolute value of Z is greater than $Z_{1-\alpha/2}$, where $Z_{1-\alpha/2}$ is obtained from the standard normal cumulative distribution tables. In MAKESENS the tested significance levels α are 0.001, 0.01, 0.05 and 0.1.

3.2 Sen's Method

Sen's nonparametric method is used to estimate the true slope of the current trend (annual change). The Sen Method can be used for linear trends (Xu et al. 2007). This means that f(t) in Eq. (1) is the same as:

$$f(t) = Qt + B \tag{6}$$

where Q is the slope and B is a constant.

To get an estimate of the slope Q in Eq. (6), first calculate the slope of all data-value pairs**.**

$$Q_i = x_j - x_k / j - k \tag{7}$$

where j ≫ k.

If there is a value of n, x_j in the time series, what is the estimated value of the slope *of* $N = n\ (n - 1)/2$ of Qi? The Sen slope estimate is the median of these N values of Qi. The N values for Qi are ordered from smallest to largest, and Sen's estimates are as follows:

$$Q = Q_{\left[\frac{(N+1)}{2}\right]} if\ N\ is\ odd. \tag{8}$$

$$Q = \frac{1}{2\left(Q_{\left[\frac{N}{2}\right]} + Q_{\left[\frac{(N+2)}{2}\right]}\right)} if\ N\ is\ even \tag{9}$$

Two sided 100(1−α)% confidence intervals for the slope estimated were obtained using a nonparametric method based on the normal distribution. This method works for n as small as 10 (Sen 1968) unless there are multiple constraints. The MAKESENS procedure calculates confidence intervals at two different confidence levels; α = 0.01 and α = 0.05, which gives two different confidence intervals. Firstly

$$C_\alpha = Z_{1-\alpha/2}\sqrt{VAR(S)} \tag{10}$$

here $VAR(S)$ is determined by Eq. (4) and $Z_{1-\alpha/2}$ is obtained with a standard normal distribution. This calculates $M_1 = (N-C\alpha)/2$ and $M_2 = (N-C\alpha)/2$. The lower and upper bounds of the confidence interval, Qmin and Qmax, are the M_1th largest and the (M_{2+1})th largest of the N ordered slope estimates Qi. If $M1$ is not a whole number the lower bound is interpolated. So, if M_2 is not a whole number the upper bound is interpolated. The n values of differences x_i – Qti are calculated to obtain an estimate of B in Eq. (6). The median of this provides an estimate of B (Sirois 1998). Row B estimates that are constant between the 99 and 95% confidence intervals are calculated using the same procedure.

4 Result and Discussion

The minimum depth to water (0.05 m bgl) has been observed in August, 2015 at Khimlasa whereas maximum value (27.60 m bgl) observed in June, 2015 at Khurai, based on 17 years GWL monthly data (Table 1). The pre and post monsoon groundwater contours maps (Fig. 2a, b) depict the spatial variation of average groundwater level. The average groundwater level in pre monsoon (month-may) varies from 4.96

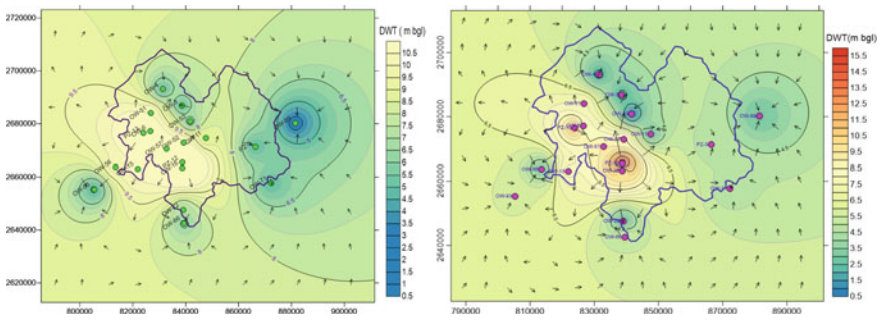

Fig. 2 Depth to water tables map for **a** Pre-monsoon, **b** Post-monsoon

to 24.22 m bgl (i.e., 431.14 m to 432.22 m above msl) whereas during post monsoon (month-November) groundwater level varies from 2.92 to 14.72 m bgl (i.e. 474.73 m to 442.38 m). GWL is shallower in northern, eastern and southern part of the city whereas deeper GWL can be observed in central and western part of the blocks boundary. Groundwater flow direction in the area helps us decide the location of abstraction wells and pollutant transport path. The directions of the groundwater flow are found similar for the pre- and post-monsoon period (Fig. 3). The direction of groundwater flow is towards Southwards and eastwards. The trend analysis was performed by using Mann Kendal at (95% confidence interval) & Sen's slope estimator method for monthly groundwater level (Tables 3 and 4). The Trend analysis summarised in Tables 3 and 4 for Pre-monsoon and Post-monsoon respectively. The negative S-statistics indicate a falling trend and positive indicates rising trend. A positive (negative) value of Z indicates an upward (downward) trend (Sumant et al 2018). The statistic Z has a normal distribution. In order to define if there is a trend or not at the selected level α of significance the absolute value of Z is compared to the standard normal cumulative distribution. The null hypothesis of no trend should be rejected when the test shows the smallest significance level α. The computed z-statistics less

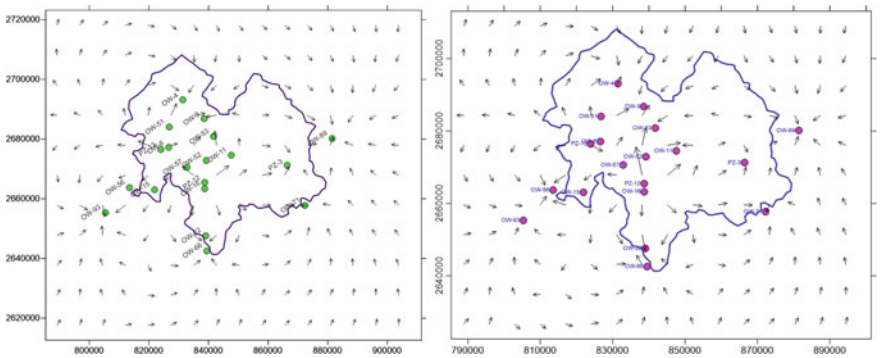

Fig. 3 Groundwater flow direction during Pre-Monsoon and Post-Monsoon period

Table 2 Probability table of S to showcase minimum value of n to derive significance level

Significance level α	Required n
0.1	≥4
0.05	≥5
0.01	≥6
0.001	≥7

than the z-value corresponding to 5% significance level (1.96) indicate no significant trend. It can be observed from Table 4 that groundwater level is showing falling and rising trend, which are not significant except few locations. These few locations are viz., Bina, Dhansara and Dugahakalan where groundwater level shows significant rising trend whereas Khurai, Kulwai showing significant falling trend (Table 4).

4.1 Results of Man Kendall Test

In the present study the results are shown in two scenario i.e. Pre-monsoon and Post Monsoon (Tables 3 and 4) respectively. Of the 15 observation wells (OW), 8 tend to increase and 7 tend to decrease over the pre-monsoon period (Table 3). At any rate, the magnitude of GWL varies from −0.055 m/yr (Kimlasa in Khurai block) to 0.480 m/yr at Bina in Bina block. After the monsoon, 8 of the 15 observation wells tend to decrease, 6 tend to increase, 1 remains unchanged and the magnitude of GWL varies from −0.041 m/yr (Kimlasa in Khurai block) to 0.370 m/yr at Bina in Bina block (Table 4). During the pre-monsoon period, the Z stats for 15 OW increased from −0.45 to 4.06. Of the 15 OWs before the monsoon, seven wells showing signs of decline were observed: PZ-12, OW-16(Khurai well) and OW-57 (Kulwai) i.e. −3.13, −3.21, −3.00 each (Table 3). However, among them, Khurai and Kulwai show a significant decreasing trend at significance level of 1 and 5%, and Bina, Dhansara, Dugahakalan show a significant increasing trend at significance level of 0.1%, 1% and 5%, respectively (Table 3). Of the 15 post-monsoon OWs, these 8 wells showed decline with not much significance, and all 6 wells tended to increase significantly at significance levels of 5% and 0.1% at Bina and Pali, respectively (Table 3).

The overall result of Man kendall and Sen's Slope are summarised in Tables 3 and 4 for Pre-monsoon and Post-monsoon respectively. Figures 4 and 5 show GWL time series charts showing a linear trend whose position indicates a significant upward or downward trend. The upward trend of some wells may be due to recharge from water bodies and less or no abstraction of groundwater from phreatic aquifer. Pre-monsoon and post-monsoon mean groundwater level fluctuations varied from 3.08 to 18.749 and 0.567 to 16.179, respectively. OW-53 site of Khurai block exhibits maximum groundwater extraction in pre and post monsoon periods. Thus, the seasons before and after the monsoon vary from 1.47 to 4.54 and from 0.05 to 3 (Tables 3 and 4).

Table 3 Summarized results of trend analyses for each observation wells for Pre-Monsoon

WELLS	Test Z	Trend	Significant	Slope (Q)	Intercept (B)
OW-51	0.34	**Rising**	Slope not significant	0.017	−5.02
OW-52	0.38	**Rising**	Slope not significant	0.050	−6.78
PZ-12	−0.49	***Falling***	Slope not significant	−0.163	−13.55
PZ-13	−0.91	***Falling***	Slope not significant	−0.122	−10.63
PZ-03	2.39	**Rising**	**(Significant)*	0.147	−4.65
OW-06	3.55	**Rising**	**(Significant)*	0.370	−10.84
OW-15	−0.04	***Falling***	Slope not significant	0.000	−4.20
OW-16	−1.06	***Falling***	Slope not significant	−0.115	−8.45
OW-57	−1.40	***Falling***	Slope not significant	−0.078	−3.29
OW-03	0.00	**No change**	Slope not significant	0.003	−3.34
OW-04	−1.10	***Falling***	Slope not significant	−0.050	−4.325
OW-11	−1.03	***Falling***	Slope not significant	−0.100	−4.7
OW-22	0.25	**Rising**	Slope not significant	0.026	−5.555
OW-53	−0.95	***Falling***	Slope not significant	−0.041	−0.859
OW-56	0.25	**Rising**	Slope not significant	0.019	−6.7

Table 4 Summarized results of trend analyses for each observation wells for Post-Monsoon

WELLS	Test Z	Trend	Significant	Slope (Q)	Intercept (B)
OW-51	1.15	**Rising**	Slope not significant	0.007	−10.44
OW-52	0.73	**Rising**	Slope not significant	0.000	−11.44
PZ-12	−3.13	***Falling***	***(Significant)*	−0.302	−21.27
PZ-13	−0.45	***Falling***	Slope not significant	–0.070	−16.66
PZ-03	1.14	**Rising**	Slope not significant	0.079	−7.49
OW-06	4.06	**Rising**	****(significant)*	0.480	−16.24
OW-15	2.92	**Rising**	***(significant)*	0.045	−10.55
OW-16	−3.21	***Falling***	***(significant)*	0.000	−12.75
OW-57	−3.00	***Falling***	***(significant)*	−0.125	−6.12
OW-03	−1.41	***Falling***	Slope not significant	0.000	−7.30
OW-04	−0.05	***Falling***	Slope not significant	0.000	−6.2
OW-11	2.15	**Rising**	**(significant)*	0.070	−12.44
OW-22	0.33	**Rising**	Slope not significant	0.000	−8.7
OW-53	−0.78	***Falling***	Slope not significant	−0.055	−4.4
OW-56	1.08	**Rising**	Slope not significant	0.033	−15.83

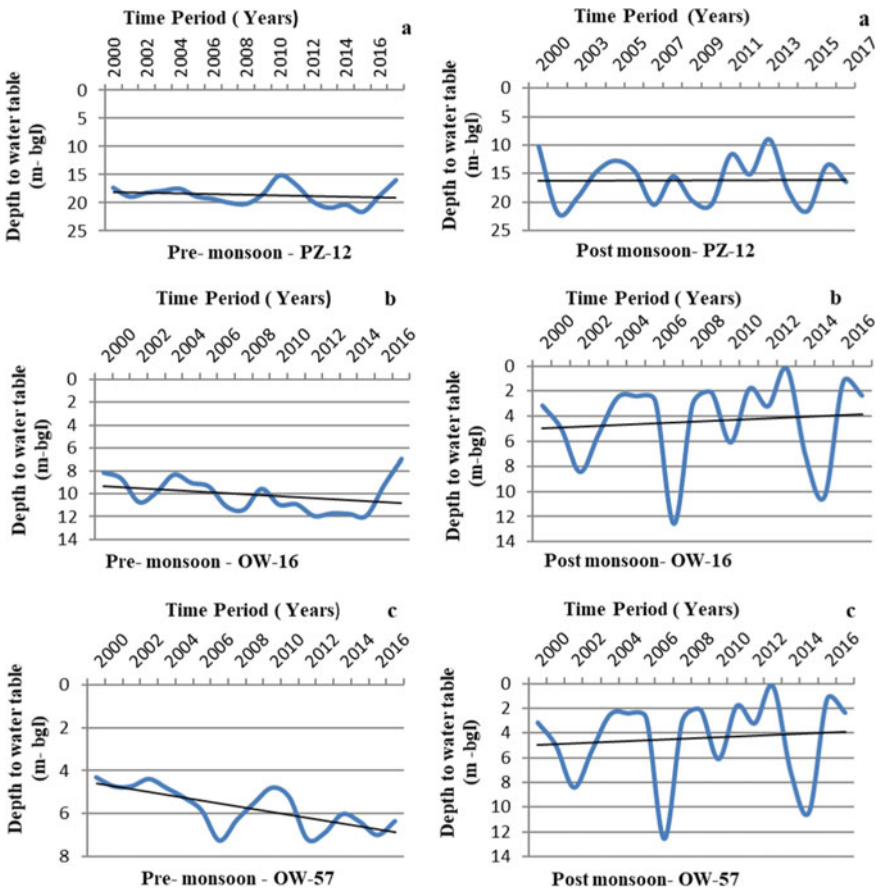

Fig. 4 Time series plot for depth to water for **a** Khurai showing falling trend, **b** Khurai (OW16) area showing falling trend, **c** Kulwai showing falling trend

5 Conclusion

Groundwater table trends and fluctuations can be used to estimate changes in aquifer retention due to the effects of groundwater capture and recharge, and are also useful in assessing the available water potential underground. This information can be used for groundwater management needs and for assessing conservation activities. Mann–Kendall test performed on time series data of pre-monsoon groundwater levels in two blocks Sagar district showed significantly declining trend (increasing depth of water level from ground surface) in pre -monsoon groundwater levels during 2000–2017 and post-monsoon ground water levels showed declining trend (increasing depth of water level from ground surface) in post- monsoon during 2000–2017 with insignificant slope. The extent of GWL varies from-0.055 m/yr (Kimlasa in Khurai

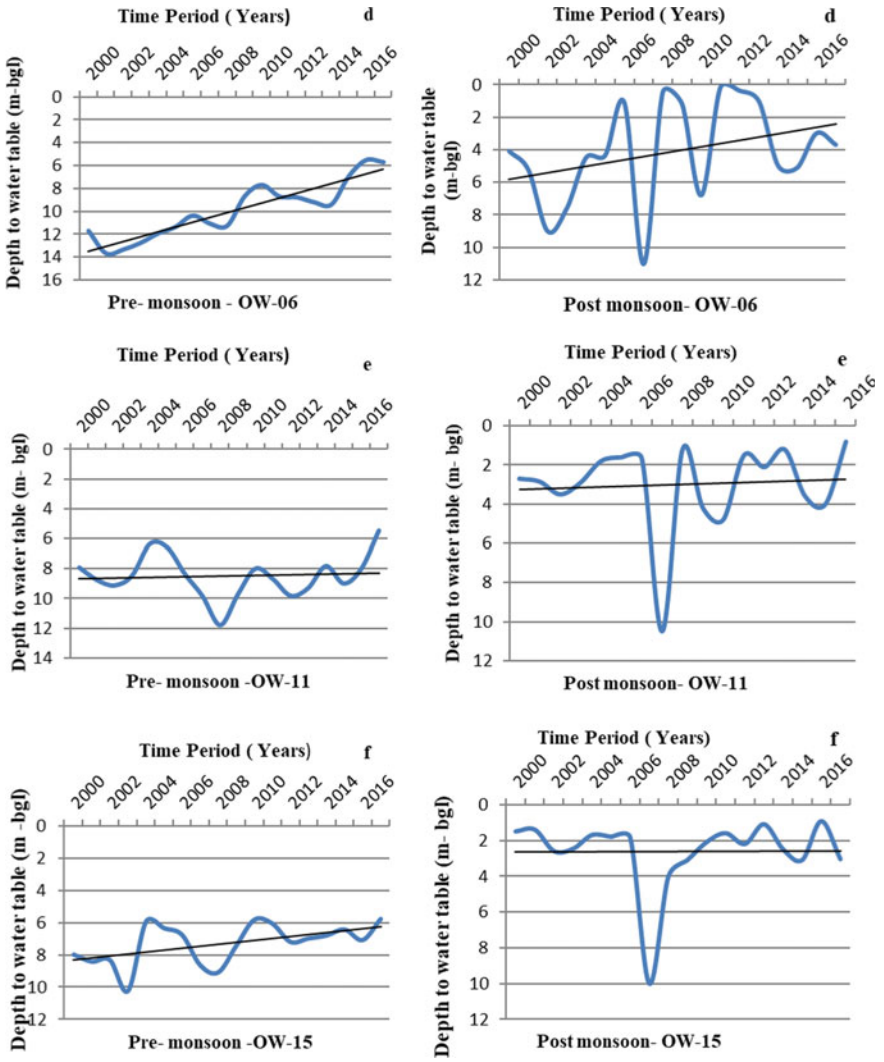

Fig. 5 Time series plot for depth to water for **d** Bina showing rising trend, **e** Dugahakalan area showing rising trend, **f** Dhansara showing rising trend

block) to 0.480 m/yr at Bina in Bina block, whereas in Post-Monsoon period the magnitude of GWL varies from −0.041 m/yr (Kimlasa in Khurai block) to 0.370 m/yr at Bina in Bina block. These few locations viz., Bina, Dhansara and Dugahakalan where groundwater level shows significant rising trend may be due to recharge from water bodies and less or no abstraction of groundwater from phreatic aquifer whereas Khurai, Kulwai showing significant falling trend are due to over extraction of ground water. It is to be mentioned here that there are no large surface water irrigation

schemes in these blocks during the period under study and as such the effect of return flow from field irrigation is minimal. (Thakur and Thomas 2011).In view of this it is imperative to arrest the rapidly falling groundwater levels at these locations for its sustainable use. Needful directives should be initiated towards identifying suitable artificial recharge zones in these blocks, so as to recharge the depleted aquifers and the exploitation should be limited within the dynamic recharge zone.

References

Gilbert RO (1987) Statistical methods of environmental pollution monitoring. Van Nostrand Reinhold, New York

Gocic M, Trajkovic S (2012) Analysis of changes in meteorological variables using Mann-Kendall and Sen's slope estimator statistical tests in Serbia. Glob Planet Change 100:172–182

Kendall MG (1975) Rank correlation methods, 4th edn. Charles Griffin, London, UK

Kumar P, Chandniha SK, Lohani AK, Nema AK (2018) Trend analysis of groundwater level using non-parametric tests in alluvial aquifers of Uttar Pradesh, India. Curr World Environ 13(1):44–54

Mann HB (1945) Non-parametric test against trend. Econometrica 13:245–259

Mondal K, Mukhopadhyay A (2012) Rainfall trend analysis by Mann-Kendall test: a case study of North-Eastern part of Cuttack District, Orissa. Int J Geol Earth Environ Sci 2(1):70–78

Patle GT, Singh DK, Sarangi A, Rai A, Khanna M, Sahoo RN (2013) Temporal variability of climatic parameters and potential evapotranspiration. Ind J Agric Sci 83(5):518–524

Sirois A (1998) A brief and biased overview of time series analysis or how to find that evasive trend. In WMO report No. 133: WMO/EMEP workshop on advanced statistical methods and their application to air quality datasets (Helsinki, 14–18 September 1998)

Sumant S, Kale G, Sonkusare MM, Chandniha SK (2018) Spatio-temporal variation and trend analysis of groundwater level in Raipur City, Chhattisgarh, vol 76. WSTL

Thakur GS, Thomas T (2011) Analysis of groundwater levels for detection of trend in Sagar District, M.P. J Geol Soc India 77:303–308

Xu ZX, Li JY, Liu CM (2007) Long-term trend analysis for major climate variables in the Yellow River basin. Hydrol Process

Challenges in Launching Unusual Structure at Off Shore

R. Suresh, K. Mullai Vendhan, K. Anbhazhagan, M. V. Ramanamurthy, and G. Vijaya Kumar

1 Introduction

The coastline of Puducherry has suffered due to severe natural coastal erosion and reorientation of coast due to port breakwaters. The sea walls and Groynes constructed onshore and offshore at various time to mitigate the problem, which has protected the coastline infrastructure but erosion has been shifted further to the North. The authorities and stake holders felt the need for an integrated long-term solution for protection and restoration of beach.

Puducherry government approached National Institute of Ocean Technology, an autonomous institute under Ministry of Earth Science to work out long term strategies for management of coast. NIOT has assessed the status of existing protection measures, studied long term shoreline changes using satellite data and carried out process based measurements during various seasons. Based on these studies a detailed shoreline management plan was prepared and submitted to Puducherry Government. Pilot nourishment was implemented by Puducherry government based on recommendation by NIOT which has resulted in formation of wide beach near New Pier. Based on the positive impact of pilot nourishment on the coast, the Puducherry government requested NIOT to restore the lost beach along Puducherry city.

Based on the learning from Pilot beach nourishment, process based measurements and numerical studies, construction of two reefs along with beach nourishment were proposed. Methodology and design for implementing beach nourishment were arrived and for which 0.45 million m^3 of sand were required immediately for

R. Suresh (✉) · G. Vijaya Kumar
Department of Civil Engineering, Pondicherry Engineering College, Pondicherry, India
e-mail: rsuresh.niot@gov.in

K. Mullai Vendhan · M. V. Ramanamurthy
OceanStructures, National Institute of Ocean Technology, Chennai, Tamilnadu, India

K. Anbhazhagan
M/s. Hi-Tech Civil Engineers Pvt. Ltd, Andhaman & Nicobar Islands, Portblair, India

R. Jha et al. (eds.), *River and Coastal Engineering*, Water Science and Technology Library 117, https://doi.org/10.1007/978-3-031-05057-2_27

beach nourishment. Studies on various configurations of offshore retaining structures were carried out to increase the life of the nourished beach and minimize the effect of erosion on the north side. Implementation of proposed hybrid solution (Beach Nourishment and construction of two Reefs) not only protects the coast but also, restores the beach. Based on this proposal the northern side reef was constructed by steel material and prepared a base on shore. A wedge shaped reef with a capacity of nearly 900 tonne was decided to launch at offshore using airbags by engaging contractor M/s Hitech Civil Engineers Pvt Ltd.

During the launching of the reef using airbags [1], following steps have been adopted:

1. Base Preparation
2. Air Bags Alignment
3. Placing additional airbags during launching
4. Winch Position
5. Securing with Ropes
6. Caisson Position.

1. Base Preparation

The suitable base must be prepared to have good flatness, inclination and proper compactness and consolidation. Many of the ship launching yards are with good concrete base for launching the ships, which is expensive. But, in the present site condition, it was ensured that the iron scraps, stones or boulder pieces were thoroughly removed before placing the airbags. Mechanical flat vibrators were used for soil compaction and watering layer by layer to improve bearing capacity of the soil (Fig. 1).

2. Air Bags Alignment

Ship launchers use standard methods calculating placement of airbags based on the size and load of vessels. But, the present structure is complex due to its unusual shape and hence the layout for alignment of airbags were derived using pre-checked the transferred load calculations of individual bags and also simultaneously concentrated on the revolving direction of airbags.

Fig. 1 Base preparation for placing airbags

For launching the quantity of rolling Air-bags was calculated as follows:

$$N = K1\frac{Q \cdot g}{Cb.R.Ld} + N1$$

where

N is the quantity of rolling Airbag, in pieces:

*K*1 is constant, K1 = 1.2–1.3.

Q is the weight of launching structure, t.

g is acceleration of gravity, m/s^2.

Cb is the block coefficient of launched ship.

R is the allowable bearing force per meter of airbag length, kN/m.

Ld is the contact length between ship bottom and airbag body at the mid-ship section, m.

N1 is the quantity of airbag replaced continuously, in pieces, normally it takes 2–4 pieces.

Details of Airbags

The main challenges faced during launching the air bags was that the bags could not be released as the bags were rolling forward even after reaching the floating draft area. An air bag of 2 m dia placed below the nose of the caisson to avoid immersion. The over all weight transferred to the nose point the air bag and hence showed deflected shape with nose [2]. All the air bags were recovered carefully and without any damage (Figs. 2, 3 and 4).

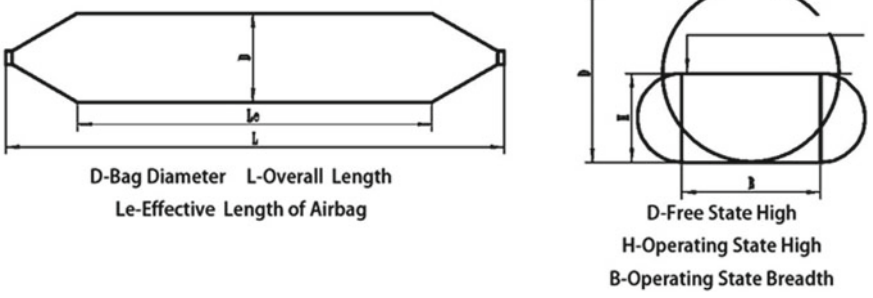

Fig. 2 Details of airbags

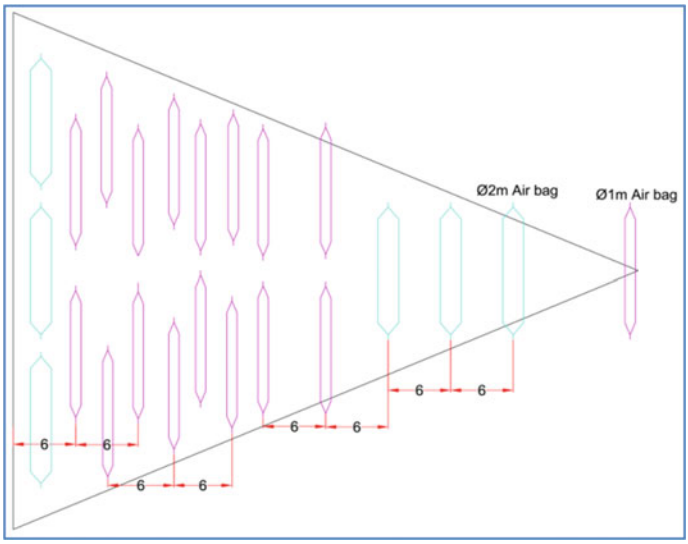

Fig. 3 Alignment of airbags

Fig. 4 Placement of airbags

3. Placing Additional Airbags During Launching:

The additional airbags with 6 mm thick poly propylene ropes were laid beneath across the caisson at different intervals. When the caisson was moved from one end to another, it was rolling to one side so airbags were inserted where ever required, filled the air and tied to the ropes [3]. This was very helpful in rolling the caisson successfully (Fig. 5).

4. Winch Positioning

All the air bags have to be connected to the winch by ropes so that the loads of the caisson shall be distributed equally. A suitable location for placement of winch

Fig. 5 Stages involved in installation of steel caisson through airbags

was arrived based on shape and load of the structure. The foundation of the winch made by concrete blocks and rocks for anchoring. The same method was adopted for fixing the pulley for the winch foundation, soil was excavated up to 3 m depth and foundation was made by 4 nos of 1 m × 1 m× 1 m size well cured the concrete cubes were interlinked with proper consolidation and compaction. All the winches and pulleys were controlled by experts (Fig. 6).

5. Securing with Ropes

The ropes were used for pulling the caisson based on the shape of the caisson by connecting at several points of hooks at multiple cross directions. The hooks were connected with high tension steel ropes and few places with poly propylene ropes. The caisson was moved straight direction. The forces of the winch and steel wire rope were calculated and assessed prior to launching (Fig. 7).

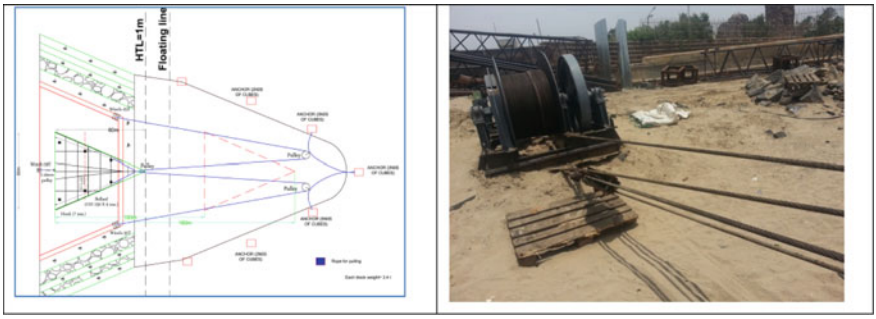

Fig. 6 Winch positioning layout

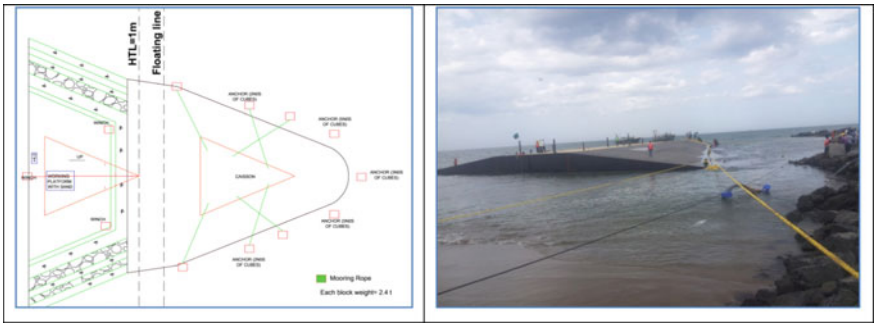

Fig. 7 Cassion positioning through Ropes

6. Caisson Position

Caisson is launched precisely as per determined coordinates, by monitoring its alignment and controlling with winches and ropes. The layout of positioning is shown in Fig. 8.

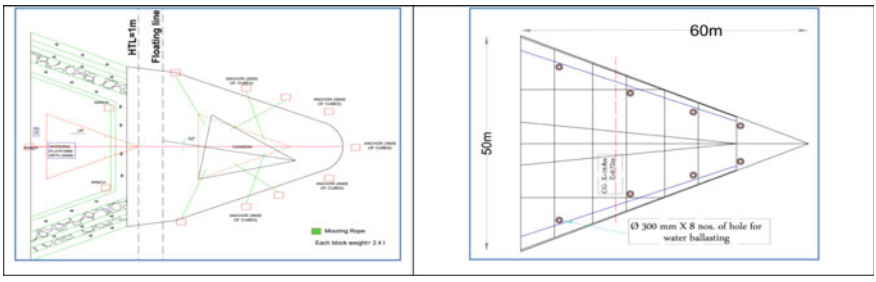

Fig. 8 Final positioning of Caisson

Material used for deployment			
S. No	Description	Capacity	Quantity
1	Winch	50 T	1
2	Winch	25 T	2
3	Poclain	20 T	2
4	Air bag/balloon (ø 1 m × 10 m long)	100 T	17
5	Air bag/balloon (ø 2 m × 10 m long)	100 T	6
6	Single sheave pulley		3
7	Double sheave pulley		2
8	Bow shackles		2
9	PP rope (ø 48 mm)		400 m
10	Steel rope (ø 32 mm)		600 m
11	30 ft boat		2
12	Generator	62 kVA	1
13	Generator	250 kVA	1

2 Conclusion

The launching of complex shape steel caisson using airbags was successfully demonstrated for installation of marine structure for beach restoration. The methodology adopted for launching using airbags, ropes, winches was successfully demonstrated at site for launching and positioning of 900 T steel caisson in Pondicherry which first of its kind.

References

International Standard-17682 first edition 2013-05-01. Ship and marine technology methodology for ship launching utilizing airbags

http://www.marineairbags.com/marineairbags/heavy-lifting-airbags.html

Launching procedure. Shandong Nanhai Airbag Engineering. Co. Ltd., Mingshui Economic Development Zone, Ji Nan, China

Air bags launching procedure. Trelleborg Marine System

http://evergreen-maritime.blogspot.com

Technical research of ship launching using airbags. Qingdao Evergreen Shipping Supplies Co. Ltd.

Comparison of Numerical Models for Wave Structure Interaction Studies

S. R. Shinde, V. V. Dabir, K. C. Khare, and S. N. Londhe

1 Introduction

Coastline erosion increases day by day due to impact of waves on unsupported coasts. To protect a coastline from erosion, it is essential to dissipate the wave energy. This can be achieved by construction of seawalls, breakwaters, and groins etc. which are constructed along a coastline. For designing of such structures, it is imperative to study the wave forces on the structure and response thereof. Such wave structure interaction studies are carried out using analytical, experimental and numerical investigations.

Analytical procedures involve the use of Morison's, Navier-Stoke and Lagrangian equation etc. to predict wave conditions and Vander Meere equation used for structural design response. For complicated cases, it becomes tedious to solve the equations considering the time constraints. Experimental investigations are scaled down studies. Such studies may compensate some of the properties of the prototype which cannot be scaled as per dimensional analysis. Hence numerical modeling tools are viable option which is ideal ways to simulate prototype conditions without compromising the scales.

S. R. Shinde (✉) · S. N. Londhe
Department of Civil Engineering, Vishwakarma Institute of Information Technology, Pune, India
e-mail: sapnarshinde94@gmail.com

S. N. Londhe
e-mail: shreenivas.londhe@viit.ac.in

V. V. Dabir · K. C. Khare
Department of Civil Engineering, Symbiosis Institute of Technology, Symbiosis International (Deemed University), Pune, India
e-mail: vaishnavi.dabir@sitpune.edu.in

K. C. Khare
e-mail: kanchan.khare@sitpune.edu.in

R. Jha et al. (eds.), *River and Coastal Engineering*, Water Science and Technology Library 117, https://doi.org/10.1007/978-3-031-05057-2_28

Various numerical tools are available for modeling waves. For checking structural response to impact of waves, coupling of two systems in a numerical tool is possible. Studies on tools like Nonlinear Shallow Water Equation (NSW), Smoothed Particle Hydrodynamics (SPH), Computational Fluid Dynamics (CFD), Reynolds Averaged Nervier Stokes (RANS), Finite Element Method (FEM) and Volume of Fluid (VOF) have shown effective modeling of such cases independently (Zijlema et al. 2011; Vanneste et al. 2014; Zabihi et al. 2015; Lara et al. 2013; Finnegan and Goggins 2012).

In this paper, the Volume of Fluid approach is used for modeling wave in a numerical tank and response of the seawall is obtained via coupling of VOF with FEM technic. Additionally highlights of various numerical tools based on NSW, SPH, CFD, RANS, FEM, and VOF are presented to compare with a coupled VOF and FEM modeling result.

2 Material

2.1 Nonlinear Shallow Water Equation

The flow under a surface of pressure in a fluid are defined as the shallow water equations are defined by a set of hyperbolic partial differential equations. Nonlinear shallow water equation is used for simulating non-hydrostatic, free-surface, and rotational flows in one and two horizontal dimensions. The execution of the same in the openly accessible SWASH (which is an abbreviation for Simulating WAves till SHore) is planned to be applied for predicting the change of surface waves and swiftly altered shallow water streams in beach front water. (Zijlema et al. 2011; Suzuki et al. 2017; Vanneste et al. 2014).

2.2 Smoothed-Particle Hydrodynamics (SPH)

Simulation of dynamics of continuum media, such as solid mechanics and fluid flows carried out using Smoothed-Particle Hydrodynamics (SPH).It is based on mesh-free Lagrangian method. SPH predicts a power spectrum that is far too steep and fails to resolve small-scale motions (Vanneste et al. 2014; Ni and Feng 2013).

2.3 Computational Fluid Dynamics (CFD)

The prime aim of this tool is to solve the flow and basic equations in approximation, which offer the movement and allied characteristics of the flow. However, it is difficult

for Multiphysics (Computational Fluid Dynamics) CFD to solve large simulations (Zabihi et al. 2015; Vanneste et al. 2014).

2.4 Reynolds-Averaged Navier–Stokes Equations (RANS)

The Reynolds-averaged Navier–Stokes equations (or RANS equations) are associated to time-averaged equations of fluid flow motion. Generally turbulent flows are described using RANS. k-eps and k-omega are not competent for the rotation and turbulence effect thereby giving bad results when there is swirl or streamline curvature (Lara et al. 2013; Hu et al. 2016; Chen et al. 2014).

2.5 Finite Element Method (FEM)

The most popular numerical method used to solve mathematical physics and engineering problems is Finite Element Method/Analysis (FEM/A). For solving a domain, it subdivides a larger domain into simpler and smaller parts termed as finite elements.

2.6 Volume of Fluid (VOF)

The volume of fluid (VOF) method is a numerical technique for tracking and locating the free surface (or fluid–fluid interface).

3 Method

Commercial tool Ansys is used for coupling the VOF technique with FEM. Wave tank and wave conditions of runs completed at Symbiosis Institute of Technology are used for simulation in the software. Waves criterion is setup in Ansys fluent (VOF domain) and structural properties of seawall is setup in Ansys structural (Transient structure). Ansys Fluent is based on fluid flow analysis system, fluent contains built in functions to generate waves, via the velocity inlet's open wave boundary condition. This function works on multiphase VOF by specifying a number of the wave characteristics, including the amplitude, wavelength, and phase. The wave should be such that it would reflect but not get overtopped. Finally the mesh could be designed to generate the waves.

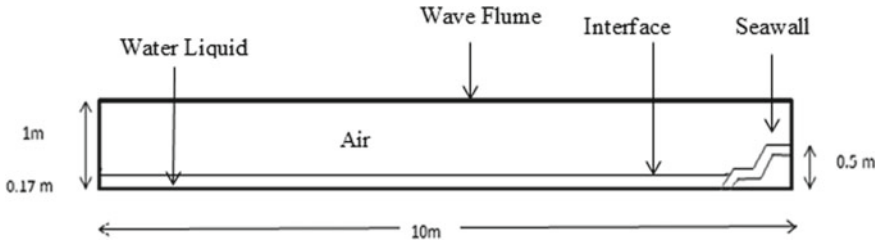

Fig. 1 Computational model scheme

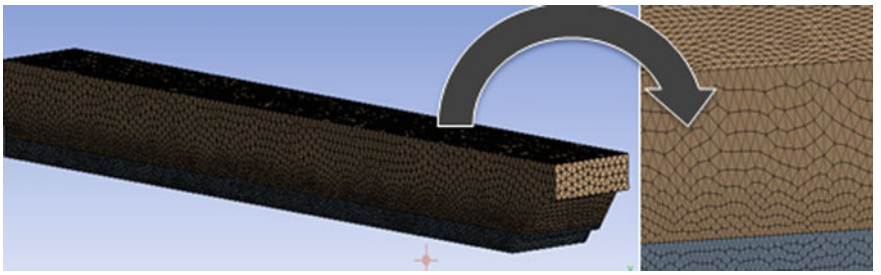

Fig. 2 Meshing scheme in VOF domain in Ansys fluent

3.1 Geometry and Meshing

The dimensions of numerical wave tank and seawalls were taken from experimental wave flume setup at Symbiosis Institute of Technology, Pune (Fig. 1).

Meshing is the process of dividing the whole component into smaller number of elements, such that after application of the load on the component, it gets distributed uniformly. Dynamic mesh function of fluent required tetrahedron mesh for bodies to move. Finer mesh having more nodes provides better results; however, calculation time will be more. To reduce calculation time fine meshing is adopted for region of interest and coarser mesh adapted to all remaining parts of geometry. Tetrahedron meshing was used having face size = 0.05, minimum size = 0.04 and maximum tet size = 0.08 as shown in Fig. 2. (Max tet size should be two times greater than face size).

3.2 Solver Settings

Fluent with numerous solver controls, have a large impact on the results.

3.2.1 Multiphase and Volume Fraction

Multiphase flow settings are modeled in the multiphase section of fluent. Volume of Fluid (VOF) model is required for generation of waves. VOF model is a surface tracking method that works very well for multiphase flows where a distinct interface is present. The free surface in the middle of air and water is provided with finer mesh for obtaining high accuracy of solution.

Implicit function asserts continuity equation with the momentum equation, solving for the volume fraction and flow field at the same time (Stoehr 2013).

3.2.2 Free Surface-VOF Model

For a particular phase, the main assumption in VOF approach is that the volume fraction is always between 0 and 1 that is there can be no empty regions and each control volume must be assigned with one or more present phases.

3.3 Governing Equations

The fluid is considered to be a continuum, the pressure field, velocity field involved are differentiable. Water is considered as a Newtonian fluid, and it is incompressible and its density will not change with time. The Navier–Stokes equation and continuity equation are used to describe the fluid motion.

3.3.1 Navier–Stokes Equation

The Navier–Stokes equation in vector form:

$$\rho\left(\frac{\partial v}{\partial t} + V.\nabla V\right) = -\nabla p + \mu\nabla^2 + f \tag{1}$$

3.3.2 Continuity Equation

The continuity equation in 2D Cartesian coordinates:

$$\frac{\partial u}{\partial x} + \frac{\partial v}{\partial y} = 0 \tag{2}$$

3.4 Boundary Conditions

Stated boundary condition such as wavelength set to 0.22 m, Height of wave assigned to 0.1 m and fifth order stokes wave theory is used and the Navier–Stokes, Continuity equations can be solved computationally. The velocity potential Φ, the boundary conditions are as follows for 2D case:

(a) Dynamic free-surface condition:

$$\frac{\partial \emptyset}{\partial x} = -gn - |\nabla \emptyset|^2 - \frac{\rho_0}{\rho} \tag{3}$$

where ρ_0 is the pressure on the free surface.

(b) Kinematic free-surface condition:

$$\frac{\partial n}{\partial t} = -\nabla \emptyset . \nabla n + \frac{\partial \emptyset}{\partial y} \tag{4}$$

In the numerical tank conditions, boundary condition (1) and (2) is satisfied by using the VOF scheme, and boundary condition (3) is satisfied by using wall condition (Du and Leung 2011).

3.5 FEM Modeling of Seawall

Material properties such as bulk modulus, density, young's modulus etc. are assigned to the geomechanical materials through engineering data and then in setup and model these materials are assigned to the structure. Highly porous sandstone used at upper part of seawall and soil used at the lower part of seawall. Waves get impacted mainly on the upper part of seawall and hence fine meshing used on the upper side as compared to lower part of the seawall. Type of meshing used for seawall is tetrahedron which is same as used in fluent (Fig. 3).

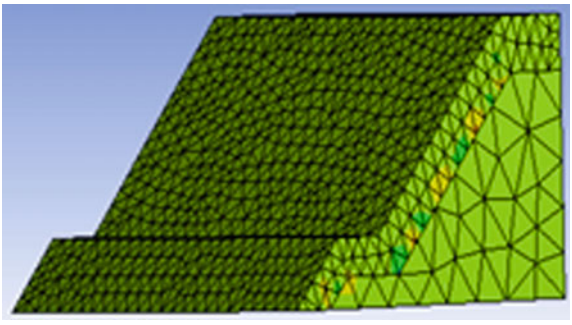

Fig. 3 Structural meshing

Fluid–solid interfaces specify the interfaces between solid element in transient structure and the fluid in the fluent system. During the execution of the simulation using the System Coupling component of workbench data get exchanged across these interfaces. System Coupling in Ansys is the tool allowing the mechanical application and fluent to send boundary condition results back and forth to one another (one or two way communication is possible).

4 Results and Discussion

Comparison of various numerical tools on the basis of literature is performed. Repetitive simulation can be done using NSWE which gives good results for wave transformation and overtopping but it takes longer time to run the calculation. The main advantage of SPH technique is that it can solve complex problems and provides physical data that can be difficult or even impossible to measure in real model but to solve small scale motions in SPH is terrible. CFD differs from other fluid dynamics software because it can give results for flowing fluid surfaces which are modeled with the VOF technique. The main con of this technique is that, to compute large simulations it required large computers and getting access to them could be difficult. RANS require less number of initial assumptions. Drawback of RANS model is the significant computational cost. Most sophisticated models for multiphase flows such as complicated viscous flow, turbulent flow can be solved by using FEM is one of the most leading advantage. NSWE overestimate the overtopping results by almost 10 times more than the other software's. While SPH model has averaged deviation of overtopping rate is about 6.8% which is also slightly more. In CFD results are not well synchronized and RAN's model has stiffness limit up to 0.033 whereas this limit in FEM is 0.1420.Only FEM technique can used for all types of numerical problems with well synchronized results of overtopping and complex time and spatial evaluation of flux.

In the present work, to obtain the precise results within less timespan, interface is added between two phases having very fine mesh size as compared to other phases. The maximum theoretical and numerical limits for wave stiffness obtained are 0.1420 and 0.1200 respectively. Maximum limit for Ursell number resulted as 25. The generated wave (Fig. 4) and results obtained agreed well with the experimental data.

The velocity profile (Fig. 5) converged well for the solution.

By coupling of numerical tools it is possible to obtain long term simulated results of existing experimental setup/prototype. Further work for structural response of wave using system coupling is in progress.

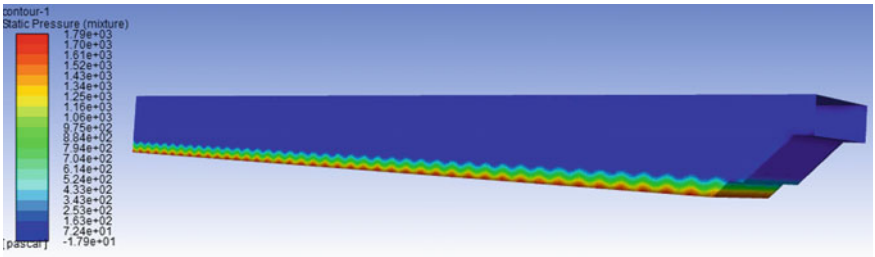

Fig. 4 Wave generated using VOF technique

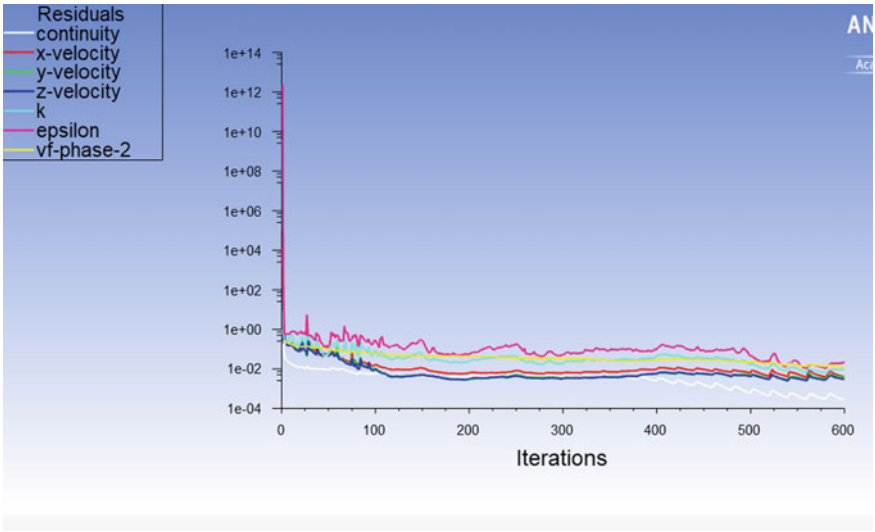

Fig. 5 Convergence of X, Y, Z velocities and volume fraction phase 2

5 Conclusion

In this paper various numerical tools such as NSW, SPH, CFD, RANS, FEM, and VOF are compared on the basis of literature, and a run is performed in Ansys Fluent. Various commercial codes available for the listed approaches possess varying performance capabilities and either of the tools can be selected as per solution needs of user. Computational time of VOF approach for wave generation can be reduced by providing a high resolution interface mesh at fluid air interface. VOF-FEM coupling can be a viable option for obtaining response of structure to incident waves. It is recommended to undergo further studies by coupling across available open source codes for further comparison of efficient tool for such studies.

References

Chen LF, Zang J, Hillis AJ, Morgan GCJ, Plummer AR (2014) Numerical investigation of wave-structure interaction using Open FOAM. Ocean Eng 88(1950):91–109. https://doi.org/10.1016/j.oceaneng.2014.06.003

Du Q, Leung DYC (2011) 2D Numerical simulation of ocean waves. Marine Ocean Technol 2183–2189. https://doi.org/10.3384/ecp110572183

Finnegan W, Goggins J (2012) Numerical simulation of linear water waves and wave-structure interaction. Ocean Eng 43:23–31. https://doi.org/10.1016/j.oceaneng.2012.01.002

Hu ZZ, Greaves D, Raby A (2016) Numerical wave tank study of extreme waves and wave-structure interaction using OpenFoam®. Ocean Eng 126:329–342. https://doi.org/10.1016/j.oceaneng.2016.09.017

Lara JL, Higuera P, Guanche R, Losada IJ (2013) Wave interaction with piled structures: application with IH-FOAM, vol 7: CFD and VIV, (August), V007T08A078. https://doi.org/10.1115/OMAE2013-11479

Ni XY, Feng WB (2013) Numerical simulation of wave overtopping based on DualSPHysics. Appl Mech Mater 405–408:1463–1471. https://doi.org/10.4028/www.scientific.net/AMM.405-408.1463

Stoehr LP (2013) Development of CFD models for the purposes of exploring free surface wave phenomena

Suzuki T, Altomare C, Veale W, Verwaest T, Trouw K, Troch P, Zijlema M (2017) Efficient and robust wave overtopping estimation for impermeable coastal structures in shallow foreshores using SWASH. Coast Eng 122:108–123. https://doi.org/10.1016/j.coastaleng.2017.01.009

Vanneste DFA, Altomare C, Suzuki T, Troch P, Verwaest T (2014) Comparison of numerical models for wave overtopping and impact on a sea wall. Coast Eng Proc 1(34):5. https://doi.org/10.9753/icce.v34.structures.5

Zabihi M, Mazaheri S, Mazyak AR (2015) Wave generation in a numerical wave tank. In: The 17th Marine industries conference (MIC2015) 22–25 December 2015. Kish Island, (2), 11. Retrieved from https://www.researchgate.net/publication/288280408

Zijlema M, Stelling G, Smit P (2011) SWASH: an operational public domain code for simulating wave fields and rapidly varied flows in coastal waters. Coast Eng 58(10):992–1012. https://doi.org/10.1016/j.coastaleng.2011.05.015

Recent Developments of Tidal Energy as Renewable Energy: An Overview

Md. Masood Ahmad, Amit Kumar, and Raushan Ranjan

1 Introduction

Marine energy also known as ocean energy is one of the main source of renewable energy as approximately 70% of the earth's surface is surrounded by it. It possess large amount of energies in the form of tidal energy, tidal currents, wave energy, temperature gradient and salinity gradient which are sufficient enough to meet the global energy demand. The tides and ocean waves consist of kinetic and potential energy which can drive the turbine to produce power. Similarly salinity gradient and temperature gradient within the bodies of ocean create dynamic forces that can also be exploited to generate electricity as well as to get fresh water.

Currently, a lot of research and studies are going on globally to identify the feasible areas, technologies needed to trap such energies, cost of generation and environmental impact assessment of such proposed technologies.

India is having advantageous position in respect of harnessing the ocean energy as it has a 7500 km long coastline and is surrounded by sea on three sides. Also it consists of 336 Islands in the Bay of Bengal and Arabian Sea (Afd 2014). Further being a tropical country, large temperature difference exists between surface and deep water which can also be utilized to produce electricity and fresh water. Government of India recognized these potentials and recently a lot of initiatives have been taken to extract such forms of energy. Govt. of India Ministry of New and Renewable Energy (MNRE) has proposed a plan to finance as much as 50% of the cost of projects working in these areas. Department of Ocean, IIT Madras and National Institute of Ocean Technology (NIOT) are doing a lot of research to access the potentials available and harnessing potentials, site selection, technology to be adopted, cost of generation and environmental impact analysis.

Md. Masood Ahmad (✉) · A. Kumar · R. Ranjan
Maulana Azad College of Engineering and Technology, Patna, Bihar, India
e-mail: masood.macet@gmail.com

R. Jha et al. (eds.), *River and Coastal Engineering*, Water Science and Technology Library 117, https://doi.org/10.1007/978-3-031-05057-2_29

2 Tidal Energy

Tidal energy is one of the most promising, predictable and reliable form of ocean energy which does not emit carbon dioxide or produce any waste. Tides in the ocean as shown in Fig. 1 are due to naturally occurring gravitational pull of the sun and moon which causes the cyclic rise and fall in the level of seas, usually every 12 h interval.

When the gravity of moon and earth is in the same line, the influence of gravitational pull becomes so strong that large quantity of seawater starts to flow towards the seashore, thus producing a condition known as high tide. During this, the water level reaches its highest level from the mean sea level. Similarly when the gravity of moon and earth is at 90° to each other, the influence of gravitational pull becomes so weak that the seawater starts to flow away from the seashore and moves towards other location of earth. This condition is known as low tide and water is at a lowest level.

The difference of elevation between high and low tides is called tidal range which depends upon the position, depth and shape of the coastline. This process happens twice a day. The number of tide per day is dependent on the declination of moon′s orbital plane relative to the axis of rotation of earth. In most part of oceans in the world, two tides occur in a day which is called as semi diurnal which is the most dominant pattern. There are 29 locations (Afd 2014) where only one tide occurs in a day which is known as diurnal. These types of tides occur in the Gulf of Mexico (along the northern shore)—Atlantic Ocean, Gulf of Tonkin—northern arm of South China Sea and Java Sea—Sunda Shelf of Java Island. Some tides combine the characteristics of both diurnal and semidiurnal tides, known as mixed tides. In this case tides are usually semidiurnal but occasionally the tides become diurnal and large inequality exists in high water height, low water height or both. It is more common along the Pacific coast of USA.

Depending upon the respective location of sun, moon and, earth; the amplitude of tides vary. When, these are aligned collinear during the full and new moon phase, the gravitational pulls are added up during each tidal cycle to produce highest and

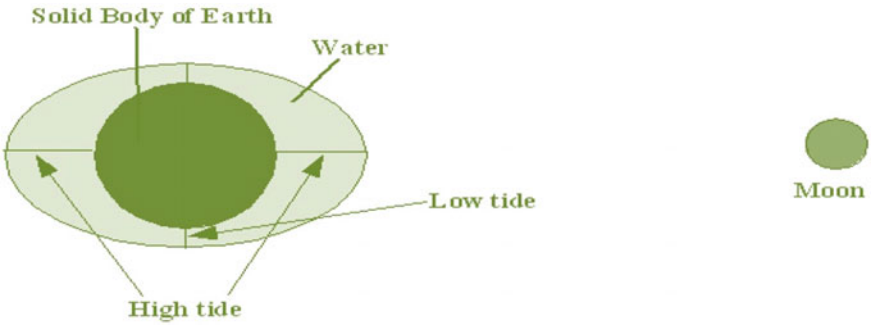

Fig. 1 High and low tide (Afd 2014)

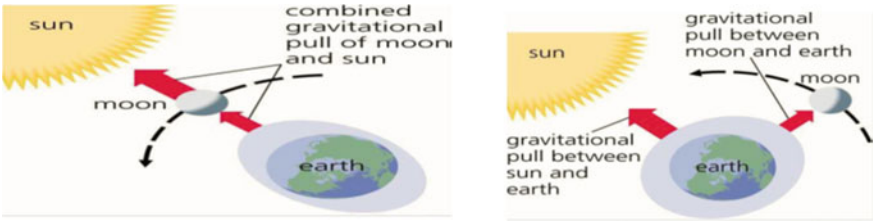

Fig. 2 Spring and neap tides (Afd 2014)

lowest tides. It is called as spring tides. Similarly when these are aligned at right angles during quarter moon phase, the tides are not so high or low. These weak tides are known as neap tides. Both these have been shown in Fig. 2.

Tidal range is the potential energy which can be harnessed to generate electricity. The exploitation of energy is very much depended upon the site as to get sufficient power, it is necessary that the tidal range should be more than 5 m. Approximately 20 locations (Adf 2014) are available on the earth′s surface which has more than 5 m tidal range. It also includes India. It is highly predictable and is hardly influenced by weather conditions and the energy can be harnessed throughout the day including night times. Maximum power is generated during spring tide while neap tide produces minimum power.

Further tidal currents which contains large amount of kinetic energy, can also be harnessed to generate power. The weather conditions affect it slightly but in the long run, the fluctuations are small. As the plants are under water, land infrastructure requirements are low and also in some cases, it may be integrated with the existing structures. For tidal stream plant, the depth of water should be more than 35 m and it requires flow velocity more than 3 m/s (Afd 2014).

2.1 Technology

There are two different ways by which tidal energy can be harnessed. One is to utilize the cyclic rise and fall of tides using barrage, known as tidal barrage method and other is to utilize the tidal currents due to movement of sea water which are similar to wind power, popularly known as marine current method. The details of these methods have been discussed below:

2.1.1 Tidal Barrage Method

This method utilizes the potential energy of tidal range by strategically positioning the dam. This system resembles the hydroelectric power generation through dam except that the dam is much bigger and spans across the full width of bay or estuary.

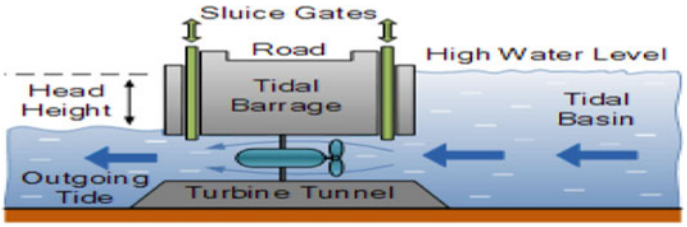

Fig. 3 Tidal barrage

As the water level of sea changes during tides, a difference of head is created across the barrage as shown in Fig. 3.

The flood tide i.e. allowing the reservoir to fill up with water through sluice gates; the ebb tide i.e. receding of water or both can be used to run the turbine which in turn produces electricity.

The potential energy P over a tidal cycle can be given as

$$P = \frac{1}{2}\rho g A(\Delta h)^2$$

where, ρ = sea water mass density in t/m^3, g = acceleration (due to gravity) in m/sec^2, A = enclosed horizontal area of the basin in Km^2 and Δh = basin mean tidal range in m.

A number of options are available for generation of power which has been discussed below:

(a) **Power Generation During Ebb Tide**

In this case, during flood tide, the reservoir is allowed to fill up with water through sluice gates and the same is closed as tides have reached its highest level. During ebb tides, water is released from the reservoir to drive the large turbines which generate power. Through this system, power can be generated only for 4 h per day.

Annapolis Royal Generation Plant located in Canada, is an ebb generation plant. It is producing 20 MW power. It was commissioned in 1984 by Nova Scotia Department of Energy Canada. It is the only tidal plant in North America. Annual generation of the plant is 50 GWh.

(b) **Power Generation During Flood Tide**

In this case, during flood tide, the sluice gates are closed and water from the sea is allowed to flow into reservoir through large turbines which generate power. This system has disadvantages that it has less capacity to generate power and also for longer period, the reservoir′s water level is kept at low level.

Sihwa Lake Tidal power station (South Korea) is a flood generation type plant. It is world′s largest tidal power station producing 254 MW and is operated by the Korea Water Resource Corporation. It was commissioned in 2011 and started to operate in

2012. The average tidal range at the station is around 5.6 m with a 7.8 m spring tidal range. The annual plant generation is of 552.7 GWh with capacity factor 24.8%.

(c) **Power Generation During both Flood and Ebb Tide**

In this case, both flood and ebb tides are utilized for generation of electricity through reversible turbines, operating both in and out direction. Through this system, power can be generated twice daily for 4 h.

Rance Tidal Power Station (located on the estuary of Rance River in Brittany, France), is a flood and ebb generation plant. It is the oldest and second largest plant in terms of installed capacity. It is operating since 1966 and generates 240 MW through 24 bulb type turbines of dia 5.4 m, rated at 10 MW and weighing 470 tonnes each. Currently, it is operated by Electrcite de France (EdF). The annual output of the plant is of approximately 600 GWh with capacity factor 28%. The average tidal range at the station is 8.2 m with maximum value of 13.2 m. The use of bulb type turbine allows the generation of power during both flood and ebb tide. Cathodic protection is used for all turbines, gates and locks. Hence, after 40 years of operation, none of the turbine blades have required any replacement.

Current Status

Currently tidal range plant capacity of 521 MW already exists and 1.7 GW is under progress and in construction phase. The various major projects which are at present operational, are given in Table 1.

Presently two large tidal plants are under construction, Incheon Tidal Power Plant of 1.3 GW and Saemangeum Reclamation Project of 0.4 GW, both located in South Korea on Yellow Sea. According to World Energy Council 2016 Report, approximately 13.7 GW project is under deployment and 0.7 GW has received consent in East China Sea, South Korea and Kenai Peninsula USA. Further, the status of other projects are: non-consented but in pipeline—10.7 GW, in planning stage—0.32 GW, early planning stage—2.8 GW and at conceptual stage—7.6 GW. All these are shown in Fig. 4.

Development in India

India has a huge potential of harnessing tidal energy as it has a 7500 km long coastline covering all along its three sides. The study of tide level at various locations along the coastline has been done by IIT Madras and National Institute of Oceanography. From the study, it has been observed that the most attractive locations in India are

Table 1 Tidal Power Plant in operation (Afd 2014)

Name of the project	Capacity (MW)
Sihwa Lake Tidal Plant (South Korea)	254
Rance Tidal Plant (France)	240
Annapolis Royal Tidal Plant (Canada)	20
The Jiangxia Tidal Plant (China)	3.2
The Kislaya Guba Tidal Plant (Russia)	0.4

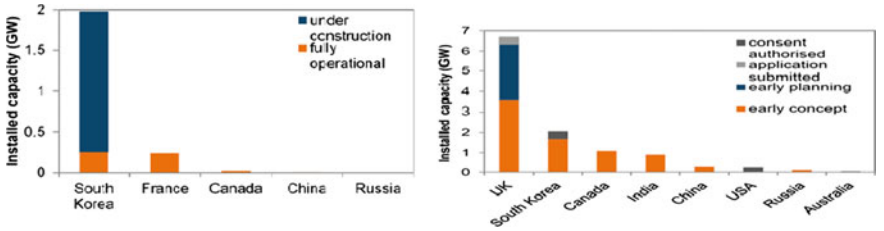

Fig. 4 Status of tidal range plant capacity in operation/under construction/progress

on the west coast—Gulf of Khambat and Gulf of Kutch and along the Sunderbans Ganges Delta areas of West Bengal. In the Table 2, the current estimate of gross potential of each site is given below.

The State-wise potential is also estimated which is given in Table 3.

Table 2 Potential assessment of tidal range power (Afd 2014)

Region	Site condition	Potential option	Current gross assessment (MW)
Gulf of Khambat	Depth—12–15 m Tidal Range—11 m	Barrage	7000
Palk Bay—Mannar Channel	Depth—60 m Tidal Range—1 m Four times a day	Barrage	230
Hoogly River	Depth—6 m Tidal Range—4–6 m	Barrage	900

Table 3 Potential of Tidal Range Power State-wise (Afd 2014)

State	Tidal range (m)	Technology	Tidal range power potential (MW)
Gujarat	5–11	Tidal Barrage	7000
Maharashtra	2–4	Tidal Barrage	200
Karnataka	1–1.5	Tidal Barrage	100
Kerala	1–1.5	Tidal Barrage	100
Tamil Nadu	0.8–1.0	Tidal Barrage	230
Andhra Pradesh	1–2	Tidal Barrage	100
West Bengal	4–6	Tidal Barrage	900
Orissa	2–4	Tidal Barrage	400

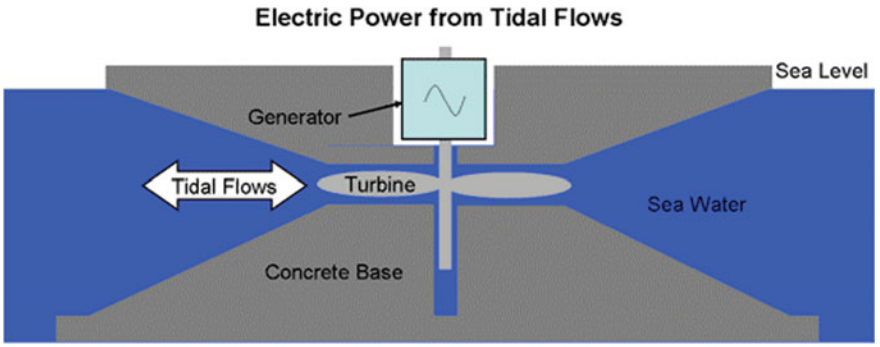

Fig. 5 Development of power through tidal currents

2.1.2 Marine Current or Tidal Current

The horizontal movement of water during tides which flows in and out of estuaries possesses enormous kinetic energy, generally known as tidal stream current. This kinetic energy can be harnessed to generate power which depends upon the velocity of flowing stream and the area intercepted. It generates power during both flood and ebb tides as shown in Fig. 5.

The power developed by this system can be expressed as:

$$P = C_P \frac{1}{2} \rho A V^3$$

where, P = power generated, C_P = coefficient of turbine power, ρ = sea water mass density, A = turbine swap area and V = flow velocity.

Tidal steam plants operate below the surface of sea or are mounted/fixed to sea bed. Various different types of devices exist which have been described below in detail:

(a) **Horizontal Axis Turbine**

In horizontal axis turbine, blades rotate about an axis parallel to the direction of water flow and sweeps through a circular area. It has 2–3 blades mounted on the rotor and lift type blades are usually employed to increase the power output. It requires specially shaped airfoil surface which creates pressure difference between the two sides of the blade. This develops a net force in the direction perpendicular to the water flow that drives the turbine. These are the most common and popular type of tidal plant developed. Approximately 76% of all tidal stream plants are horizontal axis turbine.

SeaGen device developed by Marine Current Turbines Ltd. UK which was undergoing full size prototype testing since April 2008 in Stangford Lough (Northern Ireland), is the first commercial scale device that started full power generation of 1.2 MW in December 2008. In July 2008, for the first time, it had fed 150 KW into

the grid. It has been designed for a life period of 20 years. Currently, it is the only device installed anywhere in the world at the commercial scale.

(b) **Vertical Axis Turbine**

In vertical axis turbine, the method of extraction of energy is same as that of horizontal one except here, the axis of rotation of the rotor is vertical to the water surface and also perpendicular to the incoming flow. It employs either lift type or drag type blade and also in some design using a combination of both. Approximately 12% tidal stream plants are of vertical axis turbine type.

The Kobold tidal turbine is a vertical axis turbine using the lift force to generate power. It is developed by Italian National Institute for Naval Architecture Studies and Testing (ISEAN), Italy and Ponte di Archimede International S.p.A. Messina, Italy. Its concept was started in 1995 and in 2001; a pilot plant was installed 150 m offshore near Messina. The current at the site was in between 1.5–2 m/s and at some location it was more than 3 m/s. The turbine was having 3 blades of 6 m diameter. When deployed, the turbine produced 25–30 KW. In 2005, it was connected to electric grid and a submarine cable was used to connect the turbine to the land based electrical grid.

(c) **Venturi type Device**

This type of device uses a shroud which increases the flow velocity through the turbine and it also aligns the current. Hence, for a given power output, a smaller diameter of the turbine is required. It can be placed both horizontally or vertically.

In 2002, Tidal Energy Pvt. Ltd, an Australian Company on the Gold Coast, Queensland; had undertaken the commercial trails of highly efficient shrouded turbines very successfully. It had also developed the shrouded turbine in the remote area of the Northern Australia where the current velocity was recorded as high as 11 m/s.

All the above three have been shown in Fig. 6.

(d) **Oscillating Hydrofoils**

This type of device consists of airplane wings shaped blades called hydrofoils placed at the end of a swinging arm as shown in Fig. 7. As the tidal stream flows on either side of blade, the hydrofoil moves up and down that generates lift perpendicular to the flow causing the liver to rise. These oscillating movements drive the water in a

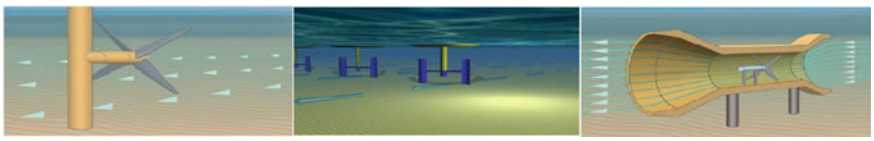

Fig. 6 Horizontal axis, vertical axis and Venturi type device

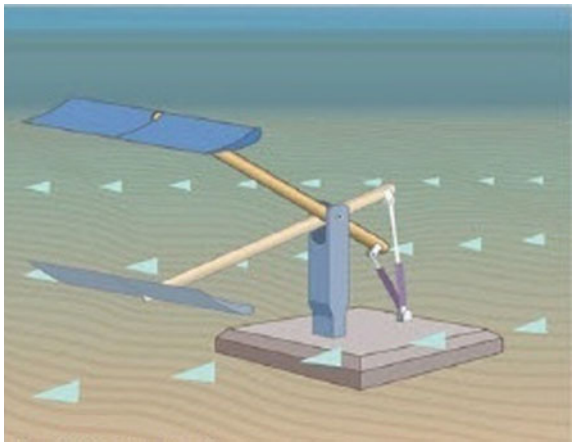

Fig. 7 Oscillating hydrofoils

hydraulic system to generate power. The advantage of this system is that the blade length is not restricted by the depth of water.

In 2014, Pulse has developed an oscillating hydrofoil tidal plant in the Humber Estuary in which tidal streams cause the horizontal blade to move up and down to drive the turbine. A 100 KW trail rig fed power in a chemical company situated on the bank of river. On successful demonstration of its technology, they are planning to develop a 1.2 MW plant for commercial deployment named as PS1200.

(e) **Tidal Kites**

Minesto′s Deep Green Concept has given a new technology to generate power in a stream which flows at a low speed between 1.2–2.4 m/s and depth of sea between 60 and 120 m. The basic principle on which this turbine operates is similar to flying kite along the sea beach. The hydrodynamic lift force on the wing is produced by the underwater flowing current which lifts the wing (kite) upwards into an eight shaped trajectory as shown in Fig. 8. The water flows through the turbine as the kite flies in the flowing current, which in turn produces power. The power plant consists of a wing which carries turbines directly coupled to generator.

Till date five prototypes based on this concept have been tested and first time electricity was produced in 2009. The first commercial scale plant of 0.5 MW has been installed in Holyhead Deep in Wales.

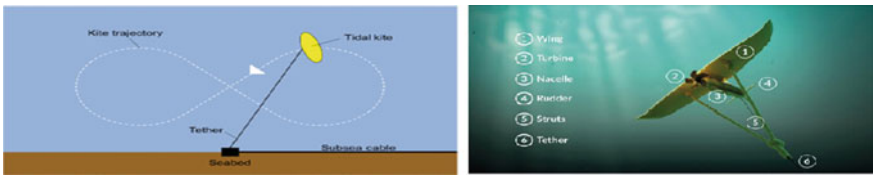

Fig. 8 Operation and components of tidal kite

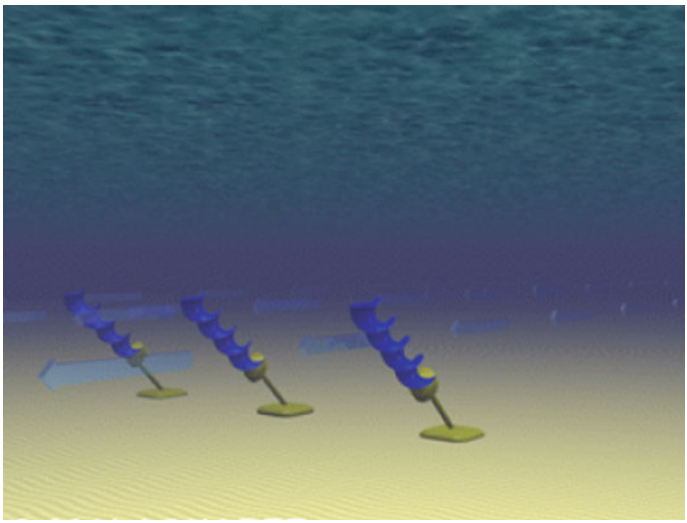

Fig. 9 Archimedes helical screw

(f) **Archimedes Tidal Screw**

It is a helical corkscrew shaped device consisting of a helical surface that surrounds a central cylindrical shaft. It extracts power from the tidal stream when the water moves up or through the spiral which in turn drives the turbine as shown in Fig. 9.

Current Status

The potential area of tidal current is located in the areas where there is a high tidal range. However, increased potential has been observed in areas where the flow of water is obstructed or constrained by local topography like headlands, narrow straits etc. and also where there is a relatively shallow water depth. It is very difficult to get the reliable estimation of global potential. However, it is widely agreed that this potential could exceed 120 GW but due to geographical, technical and other barriers and constraints; till now only a small percentage of it has been harnessed.

UK is having the greatest tidal power capacity of more than 10 GW. The Pentland Firth is considered one of the world′s best site for tidal power as the tides here shifts from the Atlantic into the North Sea and also the water is forced through a long narrow channel. The Bay of Fundy in Canada is having the potential to generate 30 MW of power. China has abundant tidal power resource with an estimated potential of 3.5 GW. Argentina, North America, France, Russia and South Korea are other countries which have significant potential.

The current commercial installed capacity of tidal stream plant is of 4.3 MW with two largest plants namely Uldomok Tidal Power Station (South Korea) and MCT′s SeaGen (Strangford Lough, North Ireland). Further three commercial plants of total capacity 10.5 MW are under construction. The largest is of 6 MW MeyGen in Scotland. The second one is of 4 MW Cape Sharp Project (Bay of Fundy, Canada)

and the third one are of 0.5 MW deployed by Sabella (Brittany, France). These have been shown in Fig. 10.

Development in India

The highest tidal currents in India have been found in the regions having large tidal range like Gulf of Khambat and Kutch and also in the Sunderbans areas. The various regions along the coastline have been categorized as given in Table 4:

The assessment of tidal stream potential in various regions is given in Table 5:

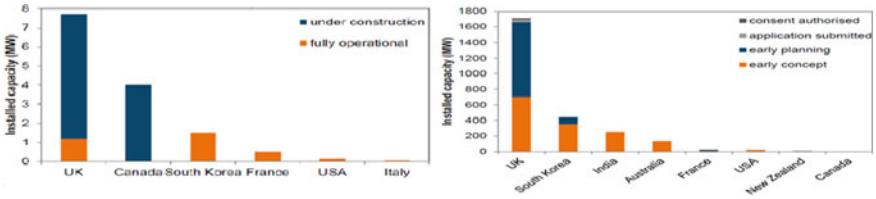

Fig. 10 Installed capacity of tidal stream in operation/under construction/conceptual/planning stage

Table 4 Categorization of coastal regions based on stream current (Afd 2014)

Coastal Regions	Tidal range (m)	Tidal stream current (m/s)	Classification
Gulf of Khambat	5–11	2.5	Class I Tidal Stream
Gulf of Kutch	4–9	3.0	Class I Tidal Stream
Sunderbans and Hoogly	4–7	2–3	Class I Tidal Stream
Maharashtra and South Gujarat Coast	2–4	1.5–2.5	Class II Tidal Stream
Orissa Coast	2–4	1.5	Class II Tidal Stream
Kerala and Karnataka Coast	1.0–1.5	1.0–1.5	Class III Tidal Stream
Andhra Coast	1–2	1.0	Class III Tidal Stream
Tamil Nadu Coast	1	0.8	Class IV Tidal Stream
Palk—Mannar Bay	1	0.6	Class IV Tidal Stream

Table 5 Tidal stream potential (Afd 2014)

Location	Site Conditions	Technology	Present Gross Assessment in MW
Gulf of Khambat	Depth—12.5 m Tidal Range—4 m Current—2.5 m/sec	Tidal stream turbine	950–1900
Gulf of Kutch	Depth—15 to 20 m Tidal Range—3.5 m Current—3.0 m/sec	Tidal stream turbine	2000

3 Barrier in the Development of Tidal Energy

There are four main barriers in the development of tidal energy:

- Technology Development
- Finance and Markets
- Environmental Issues
- Grid Issues.

The details have been discussed below:

3.1 Technology Development

For achieving global commercial success, two major bottlenecks—low turbine efficiencies and high equipment costs; need urgent and proper attention. At present, various technologies for harnessing already exist but great challenges arise due to lack of sufficient experience on materials to be used, its performance, placing the structures in a harsh and hostile sea environment, its life span, operation and maintenance of technologies and power plant. So, for the establishment and the growth of tidal market, it is absolutely necessary to develop a reliable technology as this issue also has impact on other barriers.

Hence in order to overcome this barrier; very effective, collaborative and focused efforts are required amongst the participating research Institutions, professional developers and concerned Governments agencies and policy makers. Further, more capital supports and incentives are to be provided for conducting research on new technologies, methodologies, materials to be used, model testing, functional prototype and pilot array development.

3.2 Finance and Markets

Globally, majority of the projects are funded by Government Agencies or by the professional technology developers themselves. At present; UK, South Korea, Ireland, France and Canada have well defined policies and framework to facilitate the research and for the technologies demonstration. Other potential countries have also started to frame active policy for harnessing marine energies. However, necessary financial framework conditions for sustaining on long term basis have not yet evolved. Hence, there is a need to develop new financial mechanism particularly for harnessing the tidal stream as full scale successful testing have already been done but for its commercial deployment, it requires a very serious market pull and support mechanisms. In this regard, some policy decisions are required to attract investors such as large capital grants, soft loans, project equity loans, tax exemption and other

incentives and support mechanism to deploy it into pilot arrays which will provide a clear picture to market. Now with practical experience and performance data, industry will be able to understand the real situations and issues and will be in a position to reduce risk and cost. These measures will stimulate the confidence of investors. Up to 2010, globally small entrepreneurial companies had dominated the Tidal Energy Projects but during last four-five years, large engineering and turbine manufacturers companies have entered the market. Prominent amongst them are Alstom, Siemens, GE, Hyundai Heavy Industries, Voith Hydro, Kawasaki Heavy Industries and Andritz Hydro. Recently, for some of the prototypes; electrical power systems are supplied by GE. Further, some demonstration projects are also run by big companies such as Bord Gais Energy, GDF Suez and Iberdola.

3.3 Environmental Issues

The tidal power projects may also have some adverse effect on environment. It may impact the existing marine ecosystems and other economic activities particularly fishing in the coastal areas. The fixing of turbine in the ocean may impact the wave patterns and may also disturb the natural aquatic environment due to increased noise level during its installations, operation and maintenance.

Hence, it is necessary to monitor the power plant project right from the stages of installation of pilot projects, so that the impact on marine life including fish could be analyzed in a better way. Latest monitoring equipment such as video cameras, telemetry, drift nets and other measuring equipment should be incorporated in both pilot and commercial projects. It will help a lot in designing the mitigation measures. Currently, these data are mandatory requirements for allowing the installation of projects in ocean. So, large incentives and investments are required to develop and implement the new technology and infrastructures on commercial scale and to know in a scientific way the impacts of project on marine life and also on the activities along the coastline.

3.4 Grid Issues

One of the major concerns of the tidal energy projects is to have the grid availability near the proposed site. Often, the site of tidal energy resource lacks grid infrastructure and requires either development of new network lines or existing network up gradations, the cost of which falls on the developers. European countries such as Portugal, Spain, France and Netherland have advantageous position as it has high voltage transmission lines closer to shore. For these sites, grid may not be the critical issues but majority of the sea test sites have not yet developed the grid array and connections.

Further, another important aspect is the grid integration issue. Concerted R&D efforts should be done to provide the multi-purpose platform to integrate both tidal energy and offshore wind in order to reduce the Levelised Cost of Energy (LCOE) and give stimulation in both sectors.

4 Conclusions

During recent year, technology and other infrastructures development of tidal energy have made tremendous progress. Large numbers of companies are taking keen interest and deploying the pilot projects. Initially, its cost is very high but with the development and research, its cost will reduce significantly. Currently 521 MW of tidal range plant capacity already exists globally and 1.7 GW is under construction. There is a huge potential to harness the tidal current which as per widely accepted estimate could exceed 120 GW but due to geographical, technical and other barriers and constraints, till now only a small percentage of it has been harnessed. UK is having the greatest tidal power capacity of more than 10 GW. As India has 7500 km long coastline surrounded from three sides with estuaries and gulfs, Govt. of India has recognized its potential to harness both form of tidal energy. As per the current estimate of the Govt. of India, Ministry of New and Renewable Energy (MNRE), the tidal energy gross potential of India is of approximately 8000 MW, out which the Gulf of Khambat (Gujarat) alone has approximately 7000 MW potential. In spite of huge potentials, still the technological development is in the early stage and also its commercial deployment has not progressed as expected. These developments face four major bottlenecks—appropriate technology development, financial and market supports, environmental impacts and grid connection issues. In order to overcome these barrier; very effective, collaborative and focused efforts are required amongst the participating research Institutions, professional developers and concerned Governments agencies and policy makers.

References

Afd (Agence Française De Développement) and IREDA (Indian Renewable Energy Development Agency Limited) (2014) Study on tidal & waves energy in India: survey on the potential & proposition of a roadmap final report

Bahaj AS (2011) Generating energy from the oceans. Renew Sustain Energy Rev 15(7):3399–3416

Bryden GI (2004) Tidal Energy. Encyclopedia of energy, vol 6. Elsevier, New York Brahmi, pp 132–150

Callaghan J, Boud R (2006) Future marine energy—results of the marine energy challenge: cost competitiveness and growth of wave and tidal stream energy. Carbon Trust, London

Denny E (2009) The economics of tidal energy. Energy Policy 35(5):1914–1924

EY-Ocean Energy (2013) Rising tide. Global trends in the emerging ocean energy market

GENI (Global Energy Network Institute) (2009) Ocean energy technologies for renewable energy generation

IPCC (Intergovernmental Panel on Climate Change) (2010) Report on ocean energy
IRENA (International Renewable Energy Agency) (2014) Ocean energy technology: innovation, patents, market status and trends
Magagna D, Uihlein A (2015a) 2014 JRC ocean energy status report: technology, market and economic aspects of ocean energy in Europe
Magagna D, Uihlein A (2015b) Ocean energy development in Europe: current status and future perspectives. Int J Marine Energy 11:84–104
O'Rourke F, Boyle F, Reynolds A (2010) Tidal energy update 2009. J Appl Energy 87(2):398–409
Pulse Tidal (2014) Our technology: overview
SI Ocean (Strategic Initiative for Ocean Energy) (2014) Wave and tidal energy strategic technology agenda
Sharma RC, Sharma N (2013) Energy from the ocean and scope of its utilization in India. Int J Environ Eng Manage 4(4):397–404. ISSN: 2231-1319
World Energy Resources (2016) Report on marine energy
https://www.alternative-energy-tutorials.com/category/tidalenergy
Wyre Energy Ltd. (2013) Comparisons of tidal power stations around the World. Wyre Energy Ltd
Yang H, Haas KA, Fritz HM (2012) Ocean current energy assessment for the Gulf stream. In: 4th Annual marine renewable energy technical conference, 30–31 October

River Cross Section Extraction from Elevation Models for Lower Ganga Basin

Ratnesh Kumar and Ramakar Jha

1 Introduction

Recently, the interest (due to rising stress on the rivers worldwide as a cause of growing population, industrialization and climate change) for hydraulic and hydrological models has increased (Mersel et al. 2013), carrying the need for improving model results (Domeneghetti 2016). In hydrological and hydraulic modelling, river geometry is a crucial input data. In flood modelling, information of the river geometrical characteristics is essential for reproducing past events, calibrate the model and make predictions that are used for flood management purposes. Whenever possible, river geometry is described by means of in situ surveys from which river bathymetry can be depicted. Geometry such as cross sections, floodplain and longitudinal profile acts as input in hydraulic models. However, in situ gauging stations, the principal method of measuring river gauging, fail to completely reflect spatial fluctuations and are inaccessible in many parts of the world (Perry et al. 1996; Sivapalan et al. 2003). Hydraulic and hydrological modelling are highly benefiting from the proliferation of satellite based information (e.g., water levels, topography and soil moisture) which is a great resource to relate to when there is a lack of data, especially in remote areas. As the global availability of gauging stations declines, these knowledge gaps are projected to worsen (Conway and Mahe 2009). Furthermore, political circumstances in many parts of the world require that certain existing gauge data not be made public (Conway and Hulme 1993). Given these challenges, alternative methods for estimating river flows are sought (Alsdorf et al. 2007). River remote sensing is a nascent sub discipline of hydrology that is pioneering novel techniques

R. Kumar (✉) · R. Jha
Department of Civil Engineering, National Institute of Technology (NIT), Patna, Patna, Bihar 800005, India
e-mail: ratnesh.ce17@nitp.ac.in

R. Jha
e-mail: rj@nitp.ac.in

R. Jha et al. (eds.), *River and Coastal Engineering*, Water Science and Technology Library 117, https://doi.org/10.1007/978-3-031-05057-2_30

to the study of fluvial systems (Alsdorf et al. 2007; Durand et al. 2010; Marcus and Fonstad 2010). DEM have been widely employed as a source of data to derive river cross sections throughout the past decade Pramanik et al. (2010), Tesfaye Haimanot Tarekegn et al. (2010), Gichamo et al. (2012) with varying levels of details. The influence of different resolutions of Digital Elevation Models (DEM) derived by satellite images in hydraulic modelling has been widely studied (Yan et al. 2013; Ali et al. 2015). However, DEM derived channel geometry often lack precision as the sensors cannot detect the submerged river parts. The extrapolated river cross sections from these DEMs are still uncertain and rough when it comes to the portion of the section below the water level.

The aim of the work made by these authors has been to try out and compare several DEM derived cross-sections using surveyed data and to reduce vertical bias through optimization routine in order to identify equivalent channel geometry.

2 Study Area

Lower Ganga basin located in the eastern part of India situated between Buxar and Azamabad in Bihar (25.57°–25.33° N, 83.97°–87.26° E) as shown in Fig. 1 is chosen for the study. The total length of the river between selected locations is 415 km. There are 4 gauging stations at Buxar, Patna, Hathidah and at Azamabad with a spacing of

Fig. 1 Study area map

Table 1 Yearly availability of cross-sections at different gauging stations of the Ganga River

Gauging site	Years	
	Calibration	Validation
Buxar	2009, 2010, 2011	2016, 2017
Patna	2009, 2014	2016, 2017, 2018
Azamabad	2009, 2010, 2012, 2013	2016, 2017

148 km, 97 km and 170 km between them respectively. Geomorphologically, river braiding and percentage of island area with scattered vegetation increases drastically downstream of the reach.

3 Data Sources

3.1 Measured Cross Section Data

For this study cross section of Ganga River at Buxar, Patna and Azamabad for 11-year time periods from 2005 to 2015 for pre-monsoon duration were used for calibration of synthetic (DEM extracted) cross sections and cross sections for period 2016 to 2018 for same season were used for validation purpose were provided by Central water commission (Bihar). However, for the above specified durations due to unavailability of observed cross sectional data, Hathidah gauging site was excluded from this study. The availability of cross-sectional data at specified location over the time period is shown in Table 1.

3.2 DEM Data

The network of interconnected channels that extends from Buxar down to Azamabad is extracted from 4 raster DEM of 30 m spatial resolution i.e., Shuttle Radar Topography Mission (SRTM), Advanced Spaceborne Thermal Emission and Reflection Radiometer Global DEM (ASTER GDEM), Advanced Land Observing Satellite World 3D (AW3D30), and Cartosat DEM (CartoDEM) Specifications of the elevation models is represented in Table 2.

4 Methodology

The tiles of four DEMs (SRTM, ASTER-GDEM, CARTOSAT and AW3D30) of resolution 30 m $\times$ 30 m were mosaicked in order to obtain the study area in a single

Table 2 Specifications of SRTM, ASTER GDEM, CartoDEM and AW3D30

Characteristics	SRTM	ASTER	Cartosat	AW3D30
Spatial resolution	1″ (30 m)	1″ (30 m)	1″ (30 m)	1″ (30 m)
Coverage	N 60°–S 56°	N 83°–S 83°	N 60°–S 83°	N 82°–S 82°
Vertical datum	EGM96	EGM96	WGS84	Above sea level
Horizontal datum	WGS84	WGS84	WGS84	WGS84

stretch. With the preprocessor tool of HEC-GeoRAS terrain data (TIN or Grid) were digitized into river centerline, banks, flow direction, and the start and end stations of a cross section. HEC-GeoRAS will read the elevation values at stations along a line defined as cross-section cut line. The automated extraction created issues since it frequently produced unrealistic cross-sections. This could be because the satellite imagery read the elevations of the water's surface.

Due to their inability in precisely reading the submerged portion of river (Vaze et al. 2010) the topographic outcomes from such global sources require correction (Hengl et al. 2010; Pramanik et al. 2010). To define the DEM's potential vertical bias, elevation value anomalies between DEM extracted cross-sections and their corresponding measured values which is available at the defined locations in the river stretch were computed. A simple vertical bias correction by adjusting the cross-sections for root mean square error (RMSE) of these points generated a significant increase in the model outputs. The following assumption were applied during the optimization process:

- Geolocation errors between DEMs are neglected;
- River width remains constant during study period;
- The modified cross-sections obtained after rectifying DEM-extracted cross-section using mean $\mathrm{RMSE_{DEM}}$ (Eq. 2) during the calibration period can be representative for the validation period also;
- No abrupt changes in the channel geometry is quantified;
- Inconsistency in availability of cross-section data can be removed through interpolation.

Root mean square error

$$\mathrm{RMSE} = \sqrt{\frac{\sum_{i=1}^{i=n} (\mathrm{Z_{GCP}} - \mathrm{Z_{DEM}})^2}{\mathrm{n}}} \tag{1}$$

Average root means square error

$$\text{Mean RMSE} = \frac{\mathrm{RMSE_1} + \mathrm{RMSE_2} + \mathrm{RMSE_3} + \ldots\ldots + \mathrm{RMSE_n}}{\mathrm{n}} \tag{2}$$

Here, subscript 1, 2, 3……. n represents the years for which the river cross-sections were used during the calibration process (at a particular station points) as

shown in Table 1. For a defined gauging site at a particular station points the RMSE values were computed throughout the calibration period, which was subscripted as 1,2,3 …… n. However, during calibration period the computed RMSE values at a station points were near about constant for different years unless there had been major changes observed in the channel geometry. Mean RMSE value at a particular station point during calibration period were computed (Eq. 2). Further, the vertical bias corrections were applied using mean RMSE value at each station points for all DEM extracted cross-sections.

5 Results

5.1 DEM Error Analysis

The Ganga River's braided channels and sand bar assembly is represented in Fig. 2. The active channel swings from one margin to other margin and shows prominent bedding sequences. The active channel at Patna and at Azamabad is 3.9 and 3.1 km wide in flood discharge respectively, braided with huge sandbars of around 1900 m at Patna and 1600 m wide at Azamabad. However, at Buxar no sand bars are observed. The elevations of the DEM derived cross sections were compared to their measured counterparts at pre-defined gauging stations for error analysis. The inaccuracies were calculated by deducting the elevation of the DEM heights from the values of the measured cross-sections.

Relation between the elevation points were plotted and shown in Fig. 2. The error analysis was bifurcated in two parts at Patna and Azamabad (error analysis for submerged portion of cross-section and for braided portion separately), in order to avoid any ambiguity. The deviation in elevation values between the DEM and spot heights was found to be greater with higher elevation values. One probable explanation for this gap is land cover, as elevation models are more likely to capture cover heights than bare soil elevations. The basic statistics of the errors are shown in Figs. 3 and 4. It is also noticed that the bulk of the error values are negative, indicating that the digital elevation models spot elevations are greater than the measured values. The overall analysis shows that a considerable portion of the error values are positive also. Figure 6 shows higher coefficient of correlation (R^2) for CARTOSAT and AW3D30 extracted cross-section at Buxar and Patna with slight better performance of CARTO-DEM at Buxar and AW3D30 at Patna. Meanwhile, at Azamabad SRTM extracted cross-sections were relatively better to its counterparts. However, overall performance of all 4 DEMs were unreliable at Azamabad in comparison to their outputs at Buxar and Patna. The performance of ASTER-GDEM were poor at all 3 gauging stations. As a result, adjustments to DEM-extracted cross-sections were made in order to make the geometries of the extracted cross-sections as near to the measured cross-sections as feasible.

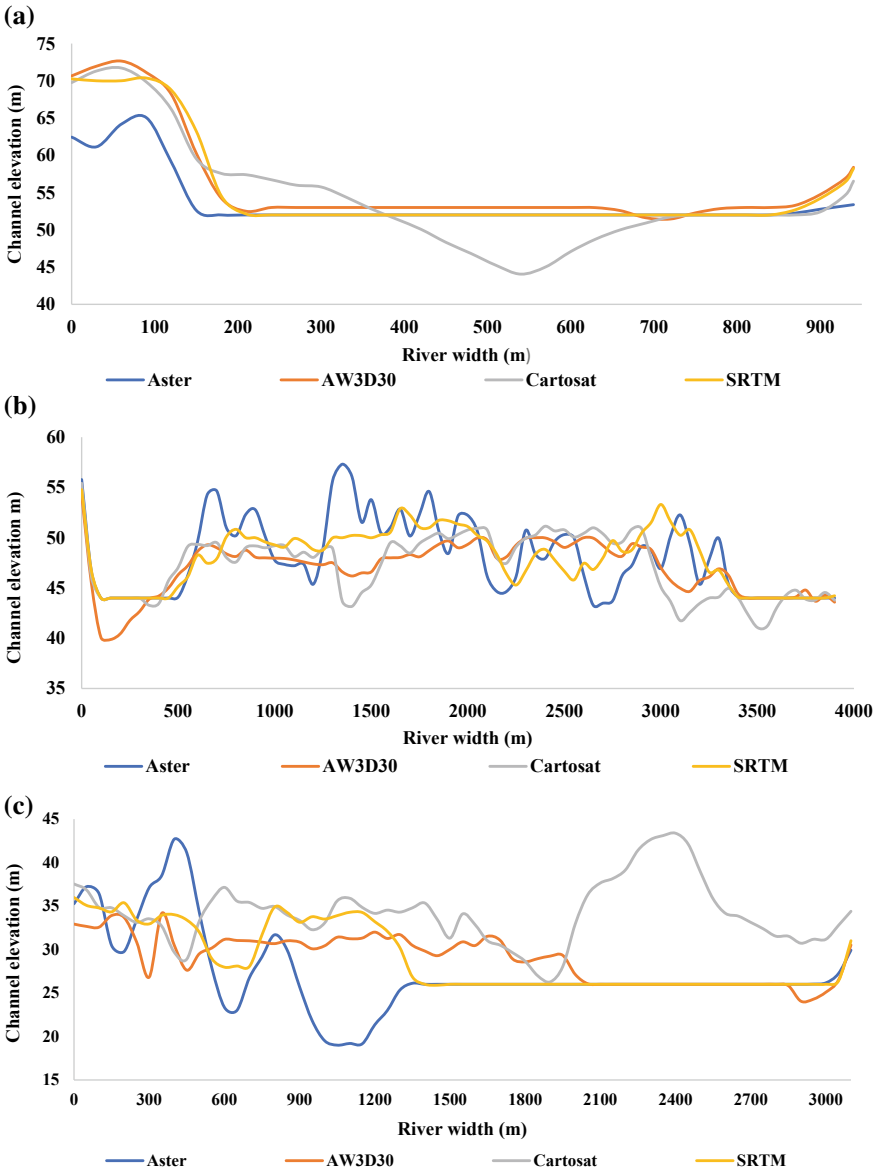

Fig. 2 DEM extracted cross sections **a** Buxar, **b** Patna and **c** Azamabad

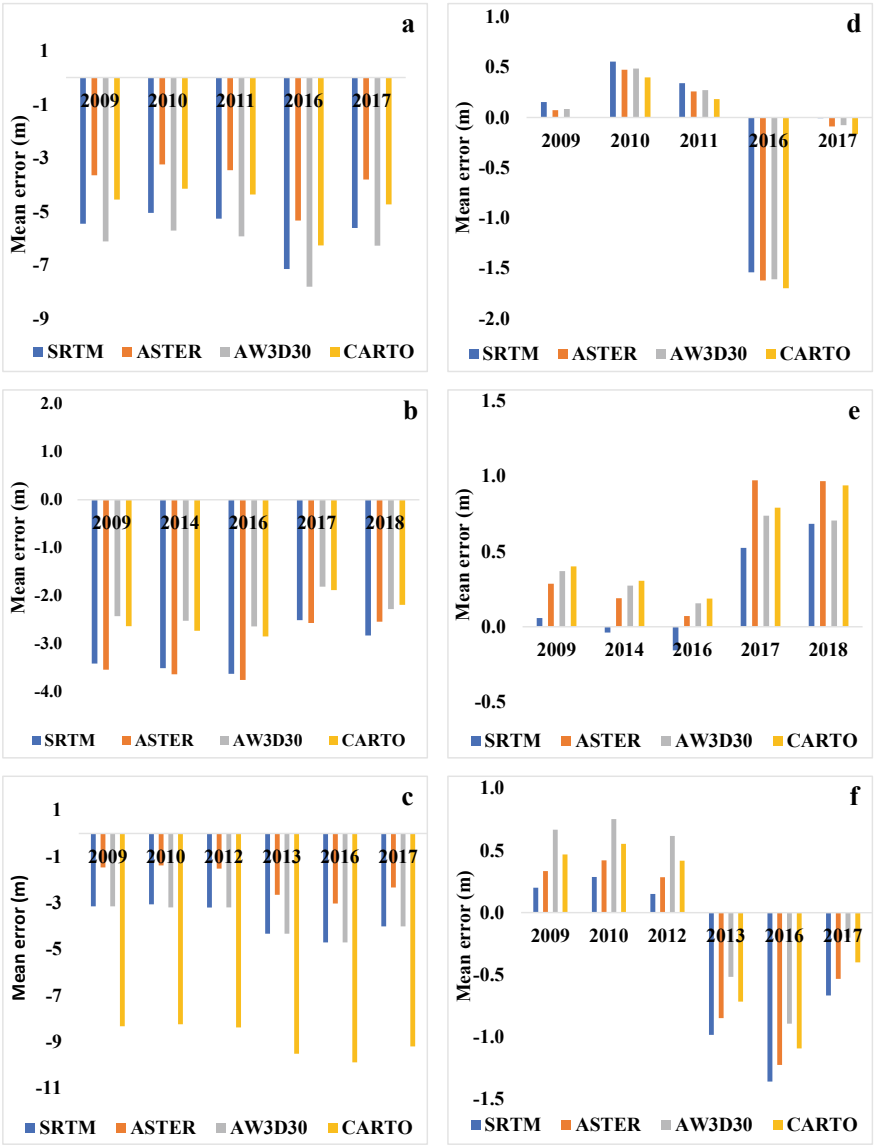

Fig. 3 Basic statistics of DEM errors representing mean errors for pre (**a** Buxar, **b** Patna and **c** Azamabad) and post modifications (**d** Buxar, **e** Patna and **f** Azamabad) for DEM-extracted cross-sections

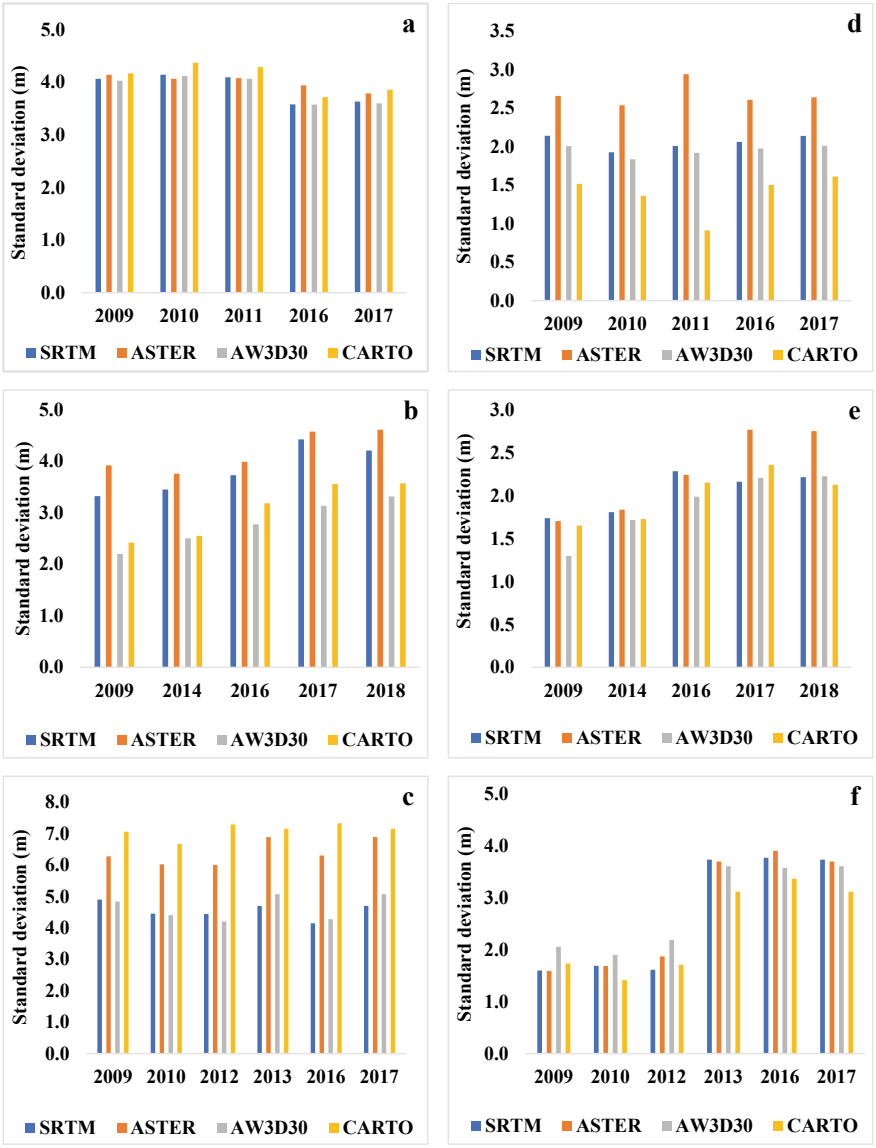

Fig. 4 Standard deviation of error for pre rectification (**a** Buxar, **b** Patna and **c** Azamabad) and post modifications (**d** Buxar, **e** Patna and **f** Azamabad) for DEM-extracted cross-sections

5.2 Modification of DEM-Extracted Cross-Sections

The multiple DEMs were acquired at different periods and had distinct vertical accuracies, therefore the elevation values in the overlapping areas of the river channel were not the same, as shown in Fig. 2. The unmodified DEM-extracted river cross-sections would result into an over prediction of flood hydrographs (both flow and stage) because of their higher elevation values. When compared to observed values, the DEM-extracted cross section would seem to be flat in the stream channels. This is due to the fact that the DEM data at 30 m intervals do not give enough information for accurate cross-section visualization. To smooth the elevation differences between the extracted values and their measured counterparts, the extracted cross-sections were modified using mean $RMSE_{DEM}$ (Eq. 2) as shown in Fig. 5. Rectification process was bifurcated into two segments for cross-sections at Patna and Azamabad i.e., correction for sand bars and another for river bed elevations, while at Buxar single channel corrections were applied. It was observed that the river cross-sections were better represented by Cartosat and AW3D30 in comparison to ASTER and SRTM. The ASTER GDEM and SRTM extracted cross-sections projected river bed as a planar surface which can be attributed to their inability to penetrate water and read bed elevation values. Both (ASTER GDEM and SRTM) read water surface as bed level, which can be observed by the narrower range of elevations representing cross-sections at all locations for which the corrections are to be applied. As, the surface elevation values represented by DEMs increases the mean RMSE corrections also increases. Generally, the corrections were negative, however at some locations positive corrections could be observed which represents the underestimation of surface elevation by DEMs. Mostly river bed surfaces were overestimated, hence negative correction are to be generally applied for elevation values projected as river bed by digital elevation models. Modifications to the DEM-extracted cross-sections using the mean RMSE values may not assure perfect geometry alignment. However, after the adjustment, the elevations of the river bed and banks grew closer to their observed values.

5.3 Validation of Assumptions

The modifications of DEM-extracted cross-sections using mean $RMSE_{DEM}$ obtained for the calibration period resulted into a refined cross-section at each pre-defined gauging stations (i.e., Buxar, Patna, and Azamabad). Because the Ganga river's cross-section geometry data is restricted, and inconsistent the final corrected channel geometry was compared with the available measured values throughout the study time period (i.e. the calibration as well as the validation period). The comparison between the simulated geometry and the measured values at Buxar, Patna and Azamabad is presented in Fig. 6. From the figures, it is observed that the simulated cross-sections are matching satisfactorily with the measured values.

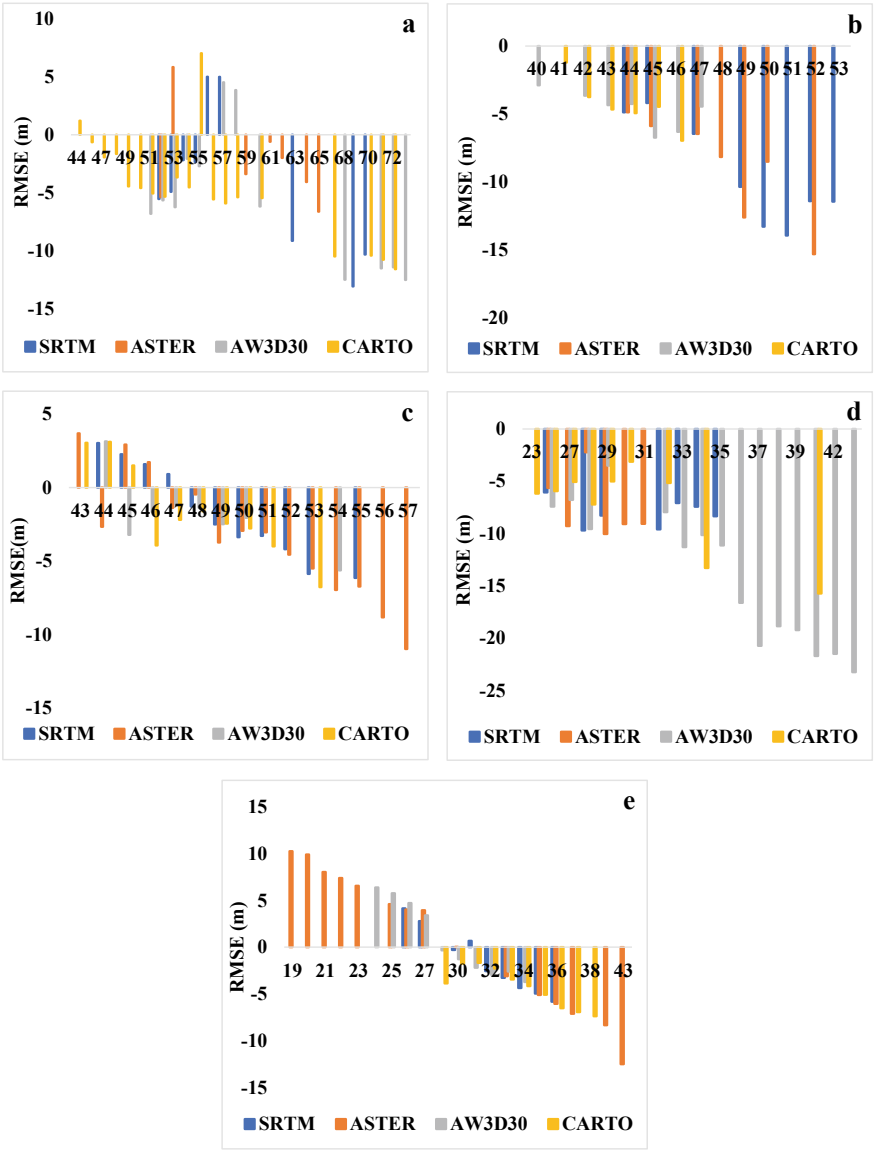

Fig. 5 Computed mean $RMSE_{DEM}$ for different elevations at **a** single channeled Buxar, **b** underwater surface at Patna, **c** sand bar at Patna, **d** underwater surface at Azamabad and **e** sand bars at Azamabad

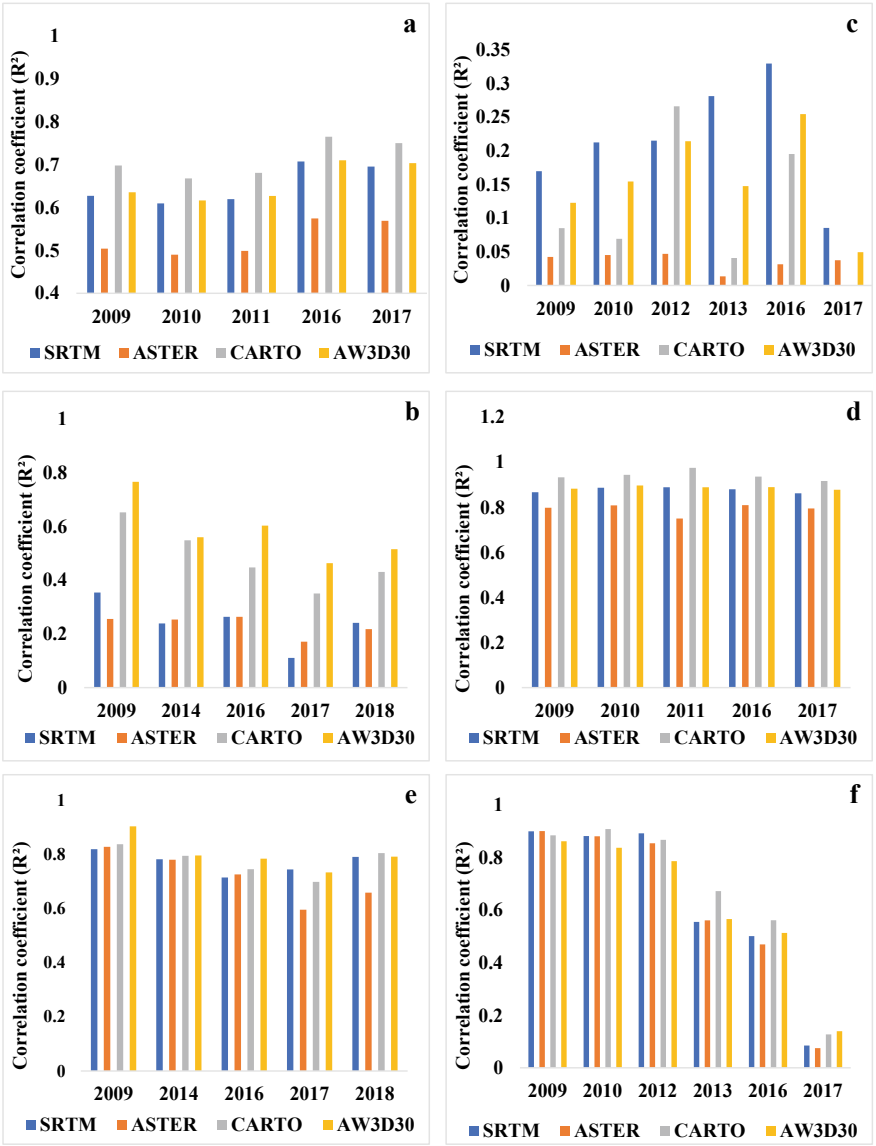

Fig. 6 Level of correlation among DEM-extracted cross-sections pre rectification (**a** Buxar, **b** Patna and **c** Azamabad) and post rectification (**d** Buxar, **e** Patna and **f** Azamabad) with measured values at respective gauging sites

However, at Azamabad assumptions failed drastically post 2016 (Fig. 6) as drastic variations in the measured cross-sections were observed (due to silting of the channel). In comparison to remaining DEM-extracted cross-sections ASTER GDEM gave relatively lower level of confidence in determining the river geometry. Moreover, Cartosat and AW3D30 were significantly better in representing channel geometry.

6 Conclusion

A method for obtaining river cross-sections using publically accessible satellite DEMs (SRTM, ASTER GDEM, AW3D30 DSM and CARTO-DEM) were discussed for Lower Ganga basin. When reliable river cross-sections and comprehensive flood-plain information from surveying or high-resolution aerial photographs are unavailable, the approach is beneficial. The cross-sections calculated from the 30 m DEMs were then adjusted for vertical bias using elevation error calculation between the DEM-extracted geometry and the observed river cross-sections. Even though elevation comparisons were only performed for three gauging stations for which measured values were available, vertical bias correction was a critical component of the approach used. According to the error analysis, the altitudes of DEM grids are greater than the corresponding recorded spot elevations.

The current method of modifying extracted river cross-sections based on mean $RMSE_{DEM}$ values at different elevations might be applied to other river basins with constrained data availability. The inaccuracy in the elevation values of the derived cross-sections might be reduced further by utilizing a DEM with a considerably better resolution. The methodology given has limitations, and it should not be used in place of correct topographical data when it is available; they can, however, be a useful tool for river flood routing in places with insufficient topographical and flow data.

References

Alsdorf DE, Bates P, Melack J, Wilson M, Dunne T (2007) Spatial and temporal complexity of the Amazon flood measured from space. Geophys Res Lett 34:L08402

Conway D, Hulme M (1993) Recent fluctuations in precipitation and runoff over the Nile sub-basins and their impact on main Nile discharge. Climatic Change 25(2):127–151

Conway D, Mahé G (2009) River flow modelling in two large river basins with non-stationary behaviour: the Paraná and the Niger. Hydrol Process: Int J 23(22):3186–3192

Domeneghetti A (2016) On the use of SRTM and altimetry data for flood modeling in datasparse regions. Water Resour Res 52:2901–2907

Durand M, Rodriguez E, Alsdorf DE, Trigg M (2010) Estimating river depth from remote sensing swath interferometry measurements of river height, slope, and width. IEEE J Sel Top Appl Earth Obs Remote Sens 3(1):20–31

Gichamo TZ, Popescu I, Jonoski A, Solomatine D (2012) River cross-section extraction from the ASTER global DEM for flood modeling. Environ Model Softw 31:37–46

Hengl T, Heuvelink GBM, Van Loon EE (2010) On the uncertainty of stream networks derived from elevation data: the error propagation approach. Hydrol Earth Syst Sci 14(7):1153–1165

Marcus WA, Fonstad MA (2010) Remote sensing of rivers: the emergence of a subdiscipline in the river sciences. Earth Surf Process Land 35(15):1867–1872

Md Ali A, Solomatine DP, Di Baldassarre G (2015) Assessing the impact of different sources of topographic data on 1-D hydraulic modelling of floods. Hydrol Earth Syst Sci 19(1):631–643

Mersel MK, Smith LC, Andreadis KM, Durand MT (2013) Estimation of river depth from remotely sensed hydraulic relationships. Water Resour Res 49(6):3165–3179

Pramanik N, Panda RK, Sen D (2010) One dimensional hydrodynamic modeling of river flow using DEM extracted river cross-sections. Water Res Manage 24(5):835–852

Perry GD, Duffy PB, Miller NL (1996) An extended data set of river discharges for validation of general circulation models. J Geophys Res: Atmos 101(D16):21339–21349

Sivapalan M (2003) Prediction in ungauged basins: a grand challenge for theoretical hydrology. Hydrol Process 17(15):3163–3170

Tarekegn TH, Haile AT, Rientjes T, Reggiani P, Alkema D (2010) Assessment of an ASTER-generated DEM for 2D hydrodynamic flood modeling. Int J Appl Earth Obs Geoinf 12(6):457–465

Vaze J, Teng J, Spencer G (2010) Impact of DEM accuracy and resolution on topographic indices. Environ Model Softw 25(10):1086–1098

Yan K, Di Baldassarre G, Solomatine DP (2013) Exploring the potential of SRTM topographic data for flood inundation modelling under uncertainty. J Hydroinformatics 15(3):849–861

Performance Study of Grid Connected Doubly Fed Induction Generator Designed for Small Hydropower Plant

Sundram Mishra, Sanjeev Kumar Gagrai, and Madhu Singh

1 Introduction

During the continuing epoch, electrical power is seeing as one of the basic requirements for all of us now, chiefly in inaccessible areas and it furthermore helps to advance the material comfort, fiscal enlargement and urbanization (Bhide and Monray 2011; Khan 2015a). As per data of the ministry of renewable energy [MNRE], the enduring 18,500 peculiar un-electrified villages in the country would be electrified in the subsequently 1000 days. In the current circumstances, India has 249.45 GW entirety installed power production capacity, even though, according to Government's reckon country would urgency pretty near 800 GW of inaugurated content still 2031–2032 (Mishra et al. 2015). To accomplish the upcoming mounting energy stipulate, India wishes each accessible resource of energy (Bhide and Monray 2011). In India, the renewable energy zone plays as a vital ingredient of the elucidation to meet the nation's energy desires. Renewable energy has been a noticeable impact in the Indian energy outcome during the past few years as India is on its manner to attaining the 175 GW mark for installed renewable energy till 2022. MNRE has engaged miscellaneous gaits for a clean energy future by captivating up the largest renewable capacity amplification involuntary in all over the world (Khan 2015b). For achieving the blot of 175 GW till 2022, the generation of electricity from the small hydroelectric plant is very obligation and for that reason, Small hydro power plant is using as an alternative source of energy to accomplish the electricity stipulate in India. In India thermal power plant is a chiefly widespread power plant since coal is used for generation of 60% of totality installed capability as publicized in the Fig. 1 (Government of India 2017). India is enlarged with hydropower potential and due

S. Mishra (✉) · S. K. Gagrai · M. Singh
Electrical and Electronics Engineering, NIT Jamshedpur, Jamshedpur, Jharkhand 831014, India
e-mail: 2017pgeepe01@nitjsr.ac.in

M. Singh
e-mail: madhu.ee@nitjsr.ac.in

R. Jha et al. (eds.), *River and Coastal Engineering*, Water Science and Technology Library 117, https://doi.org/10.1007/978-3-031-05057-2_31

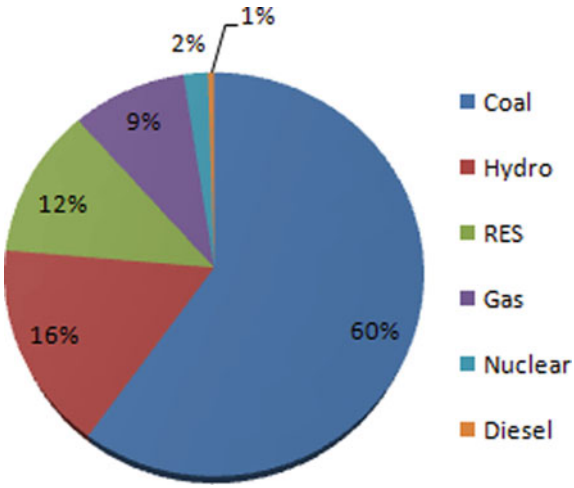

Fig. 1 Illustrative demonstration of diverse sources of energy

to this, attained 5th in the world. For countrified electrifying over the period of the system, small hydropower sector is the low-priced technology. Hydropower plant taking an inaugurated adequacy of 0.025 GW is deliberated as small hydropower plant (Mishra et al. 2015). Government of India and MNRE are providing pecuniary aid and subvention to widen the sectors of small hydropower plant. Small hydro power plant plays an energetic role in industrialization and sustainable development, (Nautiyan et al. 2011).

SHPP is valuable for two purposes; one is for surroundings and second for sustaining the fossil fuels (Mishra et al. 2015; Nautiyan et al. 2011). SHPP is unobstructed from relocation, deforestation, and edifice of dams as large hydropower plant is allied with these tribulations. SHPP is very much relatable for production of electricity in remote and sheltered areas as well as small hydropower plant have extensive convenient life and inflation liberated generation cost (Khan 2015a). Small hydropower plant is extra noticeable due to numerous pros which are specified in above.

2 Description of Hydro Energy Conversion System

Intended in favor of the production of electricity by using hydroelectric plant, rotation of the turbine is obligation which is completed by stored and capturing energy is used for a run the generator (Schmidt et al. 2011). Hydropower can be categorized into three focal mechanisms akin to as small hydropower, medium hydropower, and large hydropower. Hydropower plants are distinguishing with regard to the power generation capability (Kumar and Katoch 2014) (Fig. 2).

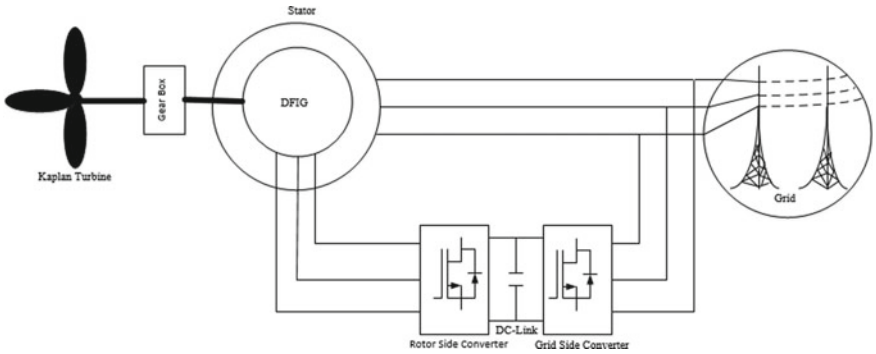

Fig. 2 The display of back to back converters with DFIG in SHPP system

- Large hydropower > 0.1 GW
- Medium hydropower > 0.03–0.1 GW
- Small hydropower > 0.002–0.025 GW.

3 Modeling of the Small Hydropower Plant

3.1 Kaplan Turbine Modeling

Intended for discharge that is high and head which is low power purpose, Kaplan turbine is preeminent apposite as well as the efficiency of Kaplan turbine is about to 90% or higher is recorded (Ansel et al. 2004) (Fig. 3).

$$P_{hydro} = \rho.\mathrm{g.Q.H} \tag{1}$$

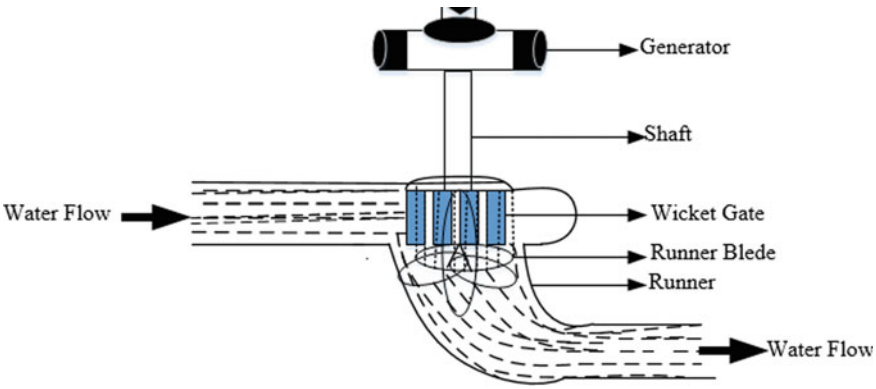

Fig. 3 Structural view of Kaplan turbine with axial water flow

$$P_{out} = P_m = \eta_t P_{hydro} \tag{2}$$

In favor of utmost of the cases the Kaplan turbine efficiency is proximate 90% so for easiness here we are assuming 90% efficiency. The water velocity in penstock is

$$U = K_u G\sqrt{H} \tag{3}$$

The flow in a pipe is given as:

$$Q = A.U \tag{4}$$

$$T_m = \frac{P_{out}}{\omega} = \frac{P_m}{\omega} \tag{5}$$

Now, switching the value of Pout in the "(5)".

$$T_m = \frac{\eta_t P_{hydro}}{\omega} \tag{6}$$

4 Modeling and Control Strategy of DFIG

4.1 Modeling of DFIG

DFIG dynamic model in (d, q) form is illustrated via "(7)" and "(8)", where R_s, R_r, L_s, L_r, and M indicates the constraints (Bendi et al. 1999).

$$\begin{bmatrix} v_{ds} \\ v_{qs} \end{bmatrix} = \begin{bmatrix} R_s & 0 \\ 0 & R_s \end{bmatrix} \begin{bmatrix} i_{ds} \\ i_{qs} \end{bmatrix} + \frac{d}{dt} \begin{bmatrix} \psi_{ds} \\ \psi_{qs} \end{bmatrix} + \begin{bmatrix} 0 & -\omega_e \\ \omega_e & 0 \end{bmatrix} \begin{bmatrix} \psi_{ds} \\ \psi_{qs} \end{bmatrix} \tag{7}$$

$$\begin{bmatrix} v_{dr} \\ v_{qr} \end{bmatrix} = \begin{bmatrix} R_r & 0 \\ 0 & R_r \end{bmatrix} \begin{bmatrix} i_{dr} \\ i_{qr} \end{bmatrix} + \frac{d}{dt} \begin{bmatrix} \psi_{dr} \\ \psi_{qr} \end{bmatrix} + \begin{bmatrix} 0 & -(\omega_e - P\omega_r) \\ (\omega_e - P\omega_r) & 0 \end{bmatrix} \begin{bmatrix} \psi_{dr} \\ \psi_{qr} \end{bmatrix} \tag{8}$$

The fluxes linkage equations are specified as in "(9)" and "(10)"

$$\begin{bmatrix} \psi_{ds} \\ \psi_{qs} \end{bmatrix} = \begin{bmatrix} L_s & 0 \\ 0 & L_s \end{bmatrix} \begin{bmatrix} i_{ds} \\ i_{qs} \end{bmatrix} + \begin{bmatrix} L_m & 0 \\ 0 & L_m \end{bmatrix} \begin{bmatrix} i_{dr} \\ i_{qr} \end{bmatrix} \tag{9}$$

$$\begin{bmatrix} \psi_{dr} \\ \psi_{qr} \end{bmatrix} = \begin{bmatrix} L_m & 0 \\ 0 & L_m \end{bmatrix} \begin{bmatrix} i_{ds} \\ i_{qs} \end{bmatrix} + \begin{bmatrix} L_r & 0 \\ 0 & L_r \end{bmatrix} \begin{bmatrix} i_{dr} \\ i_{qr} \end{bmatrix} \tag{10}$$

$$T_{em} = \frac{3}{2} P \begin{bmatrix} \psi_{ds} & \psi_{qs} \end{bmatrix} \begin{bmatrix} i_{qs} \\ -i_{ds} \end{bmatrix} \tag{11}$$

$$\begin{bmatrix} i_{qs} \\ i_{qr} \end{bmatrix} = \begin{bmatrix} \frac{1}{\sigma L_s} & -\frac{L_m}{\sigma L_s L_r} \\ -\frac{L_m}{\sigma L_s L_r} & \frac{1}{\sigma L_r} \end{bmatrix} \begin{bmatrix} \psi_{qs} \\ \psi_{qr} \end{bmatrix} \tag{12}$$

$$\begin{bmatrix} i_{ds} \\ i_{dr} \end{bmatrix} = \begin{bmatrix} \frac{1}{\sigma L_s} & -\frac{L_m}{\sigma L_s L_r} \\ -\frac{L_m}{\sigma L_s L_r} & \frac{1}{\sigma L_r} \end{bmatrix} \begin{bmatrix} \psi_{ds} \\ \psi_{dr} \end{bmatrix} \tag{13}$$

In the directly above specified matrix expression σ is illustrated as the leakage coefficient $\sigma = 1 - \frac{L_m^2}{L_r L_s}$.

The dynamics of the DFIG are delineated in the matrix configuration of state variables as:

$$\frac{d}{dt} \begin{bmatrix} \psi_{qs} \\ \psi_{ds} \\ \psi_{qr} \\ \psi_{dr} \end{bmatrix} = \begin{bmatrix} -c_1 & -\omega_e & c_2 & 0 \\ \omega_e & -c_1 & 0 & c_2 \\ c_3 & 0 & c_4 & (\omega_e - P\omega_r) \\ 0 & c_3 & (\omega_e - P\omega_r) & -c_4 \end{bmatrix} \begin{bmatrix} \psi_{qs} \\ \psi_{ds} \\ \psi_{qr} \\ \psi_{dr} \end{bmatrix} + \begin{bmatrix} 1 & 0 & 0 & 0 \\ 0 & 1 & 0 & 0 \\ 0 & 0 & 1 & 0 \\ 0 & 0 & 0 & 1 \end{bmatrix} \begin{bmatrix} v_{qs} \\ v_{ds} \\ v_{qr} \\ v_{dr} \end{bmatrix} \tag{14}$$

where $c_1 = \frac{R_s}{\sigma L_s}$, $c_2 = \frac{R_s L_m}{\sigma L_s L_r}$, $c_3 = \frac{R_r L_m}{\sigma L_s L_r}$ and $c_4 = \frac{R_r}{\sigma L_r}$.

5 PI Controller Design for Rotorside Converter of DFIG

The flux in the q-axis direction is considered as zero so the value of ψ_{qs} is equal to zero and the value of flux in d-axis ψ_{ds} is equal to ψ_s in the consideration. For the de-coupled governor of reactive power and active power as designated below (Zhao et al. 2007):

(Now we assume s = d/dt).

$$\begin{cases} s\psi_{qs} + c_1\psi_{qs} = v_{qs} + c_2\psi_{qr} - \omega_e\psi_{ds} \\ \sigma_{\psi qs} = v_{qs} + c_2\psi_{qr} - \omega_e\psi_{ds} \\ \psi_{ds}^* = \dfrac{1}{\omega_e}(v_{qs} + c_2\psi_{qr} - \sigma_{\psi qs}) \end{cases} \tag{15}$$

$$\begin{cases} s\psi_{ds} + c_1\psi_{ds} = v_{ds} + \omega_e\psi_{qs} + c_2\psi_{dr} \\ \sigma_{\psi ds} = v_{ds} + \omega_e\psi_{qs} + c_2\psi_{dr} \\ \psi_{qs}^* = \dfrac{1}{\omega_e}(\sigma_{\psi ds} - c_2\psi_{dr} - v_{ds}) \end{cases} \tag{16}$$

Equation (15) can be revised as:

$$\frac{2J}{P_r} s\omega_{rs} = (T_m - T_{em}) = \sigma_{wr} = K_{wr}(\omega^*_{rs} - \omega_{rs}) \tag{17}$$

where P_r is a nominal power of the hydraulic turbine and ω_r is the nominal speed of the hydraulic turbine.

$$K_{wr} = (K_{pwr} + \frac{K_{Iwr}}{s}) \tag{18}$$

Then "(17)" will be

$$\begin{cases} \dfrac{2J}{P_r} s\omega_{rs} = (K_{pwr} + \dfrac{K_{Iwr}}{s})\omega^*_{rs} - (K_{pwr} + \dfrac{K_{Iwr}}{s})\omega_{rs} \\ \dfrac{\omega_{rs}}{\omega^*_{rs}} = \dfrac{\frac{P_r}{2J}(sK_{pwr} + K_{Iwr})}{s^2 + s\frac{P_r K_{pwr}}{2J} + \frac{P_r K_{Iwr}}{2J}} \end{cases} \tag{19}$$

Now equating the denominator of "(19)" with standard second order equation $s^2 + 2\zeta\omega_n s + \omega_n^2$.

$$\omega_n^2 = \frac{P_r K_{I\omega r}}{2J} \text{ and } 2\zeta\omega_n = \frac{P_r K_{P\omega r}}{2J}.$$

Substitute $\psi_{qs} = 0$ in "(11)" and "(9)" results in "(20)"

$$\begin{cases} T_{em} = 1.5\psi_{ds} i_{qs} \\ i_{qs} = -\frac{L_m}{L_s} i_{qr} \end{cases} \tag{20}$$

Now, the real power by stator is specified as:

$$P_s = 1.5(v_{qs} i_{qs} + v_{ds} i_{ds}) = -1.5\frac{L_m}{L_s} v_{qs} i_{qr} \tag{21}$$

Now, the reactive power supplied stator by is specified as:

$$Q_s = 1.5(v_{qs} i_{ds} - v_{ds} i_{qs}) = 1.5 v_{qs} i_{ds} \tag{22}$$

Stator flux is assumed to be constant, neglecting the stator resistance and substituting i_{ds} from "(13)" gives

$$Q_s = (\psi_{ds}^2 - \frac{L_m}{L_r}\psi_{ds}\psi_{dr}) 1.5 \frac{\omega_e}{\sigma L_s} \tag{23}$$

Differentiating "(22)" w. r. t. time provides

$$sQ_s = -1.5\frac{\omega_e}{\sigma L_s}\frac{L_m}{L_r}\psi_{ds}s\psi_{dr} \tag{24}$$

$$\begin{cases} sQ_s = -1.5\dfrac{\omega_e}{\sigma L_s}\dfrac{L_m}{L_r}\psi_{ds}(v_{dr} + (\omega_e - \omega_r)\psi_{qr} - R_r i_{dr}) \\ sQ_s = -1.5\dfrac{\omega_e}{\sigma L_s}\dfrac{L_m}{L_r}\psi_{ds}(v_{dr} + (\omega_e - \omega_r)\sigma L_r i_{qr} - R_r\ i_{dr}) \\ \mu sQ_s = (Q_s^* - Q_s)K_{Qs} = \sigma_{Qs} \end{cases} \tag{25}$$

where μ is defined as $\mu = \frac{2L_r L_s \sigma}{3L_m \omega_e}$

$$K_{Qs} = \left(\frac{K_{IQs}}{s} + K_{PQs}\right)$$

Therefore "(25)" can be modified as given below:

$$\mu sQ_s = \left(\frac{K_{IQs}}{s} + K_{PQs}\right)Q_s^* - \left(\frac{K_{IQs}}{s} + K_{PQs}\right)Q_s \tag{26}$$

$$\frac{Q_s}{Q_s^*} = \frac{\frac{1}{\mu}\left(sK_{PQs} + K_{IQs}\right)}{s^2 + s\frac{K_{PQs}}{\mu} + \frac{K_{IQs}}{\mu}} \tag{27}$$

Now equate the denominator of "(27)" with standard second order equation $s^2 + 2\zeta\omega_n s + \omega_n^2$.

$$\omega_n^2 = \frac{K_{IQs}}{\mu} \text{ and } 2\zeta\omega_n = \frac{K_{PQs}}{\mu}.$$

From "(24)"and "(25)", following expression is specified as:

$$i_{dr}^* = \frac{1}{R_r}(v_{dr} + \frac{\sigma_{Qs}}{\psi_{ds}} + \sigma L_r i_{qr}(\omega_e - \omega_r)) \tag{28}$$

The common coupling term $\omega_{sl}\ \sigma i_{qr} L_r$ in "(28)" is very much lesser so its consequence is insignificant.

$$v_{qr} = R_r i_{qr} + \omega_{sl}\left(\frac{L_m}{L_s}\psi_{ds} + \sigma L_r i_{dr}\right) + \sigma L_r s i_{qr} \tag{29}$$

$$v_{dr} = R_r i_{dr} - \omega_{sl}\sigma L_r i_{qr} + \sigma L_r s i_{dr} \tag{30}$$

where ω_{sl} is defined as the slip speed $\omega_{sl} = (\omega_e - \omega_r)$

$$R_r i_{qr} + \sigma L_r s i_{qr} = v_{qr} - \omega_{sl}\left(\frac{L_m}{L_s}\psi_{ds} + \sigma L_r i_{dr}\right) \tag{31}$$

$$R_r i_{dr} + \sigma L_r s i_{dr} = v_{dr} + \omega_{sl}\left(\sigma L_r i_{qr}\right) \tag{32}$$

Then the currents can be structured by linear controllers, where

$$\sigma_{qr} = R_r i_{qr} + \sigma L_r s i_{qr} \tag{33}$$

$$\sigma_{dr} = R_r i_{dr} + \sigma L_r s i_{dr} \tag{34}$$

Then the voltages of d-axis and q-axis are designed as shown below.

$$v_{qr}^{*} = \sigma_{qr} + \omega_{sl}\left(\frac{L_m}{L_s}\psi_{ds} + \sigma L_r i_{dr}\right) \tag{35}$$

$$v_{dr}^{*} = \sigma_{dr} - \omega_{sl}\left(\sigma L_r i_{qr}\right) \tag{36}$$

So for finding rotor current in q-axis i_{qr} by means of current regulator loop from "(31)".

$$v_{qr}^{'} = R_r i_{qr} + \sigma L_r s i_{qr} = (R_r + s\sigma L_r) i_{qr} \tag{37}$$

$$v_{qr}^{'} = \left(K_{qp} + \frac{K_{qi}}{s}\right)\left(i_{qr}^{*} - i_{qr}\right) \tag{38}$$

$$(R_r + s\sigma L_r) i_{qr} = (K_{qp} + \frac{K_{qi}}{s}) i_{qr}^{*} - (K_{qp} + \frac{Ki}{s}) i_{qr} \tag{39}$$

Likewise, for finding i_{dr} by means of current regulator loop from "(32)",

$$v_{dr}^{'} = R_r i_{dr} + \sigma L_r s i_{dr} = (R_r + s\sigma L_r) i_{dr} \tag{40}$$

$$v_{dr}^{'} = (K_{qp} + \frac{K_{qi}}{s})(i_{dr}^{*} - i_{dr}) \tag{41}$$

$$(R_r + s\sigma L_r) i_{dr} = \left(K_{qp} + \frac{K_{qi}}{s}\right) i_{dr}^{*} - \left(K_{qp} + \frac{K_{qi}}{s}\right) i_{dr} \tag{42}$$

Now the transfer function from "(42)"amid the reference and authentic currents are rehabilitated as given below:

$$\frac{i_{qr}}{i_{qr}^{*}} = \frac{\frac{1}{\sigma L_r}(s K_{qp} + K_{qi})}{s^2 + s\frac{1}{\sigma L_r}(K_{qp} + R_r) + \frac{1}{\sigma L_r} K_{qi}} \tag{43}$$

Now equate the denominator of "(43)" with standard second order equation $s^2 + 2\zeta\omega_n s + \omega_n^2$.

$$\omega_n^2 = \frac{K_{qI}}{\sigma L_r} \text{ and } 2\zeta\omega_n = \frac{K_{qP} + R_r}{\sigma L_r}.$$

$$\frac{i_{dr}}{i_{dr}^*} = \frac{\frac{1}{\sigma L_r}(sK_{dp} + K_{di})}{s^2 + s\frac{1}{\sigma L_r}(R_r + K_{dp}) + \frac{1}{\sigma L_r}K_{di}} \tag{44}$$

Equating the denominator of "(44)" with basic second order equation $s^2 + 2\zeta\omega_n s + \omega_n^2$.

$$\omega_n^2 = \frac{K_{dI}}{\sigma L_r} \text{ and } 2\zeta\omega_n = \frac{K_{dP} + R_r}{\sigma L_r}.$$

The RSC control scheme is shown in Fig. 4.

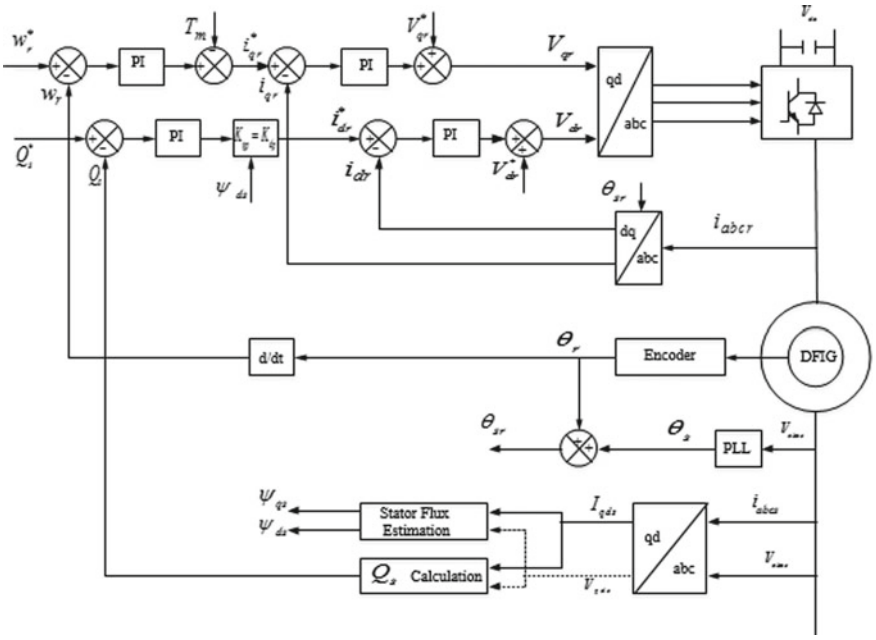

Fig. 4 Illustrative demonstration of rotor side controller (RSC) control scheme

6 PI Controller Design for the Grid Side Converter of DFIG

The dc bus voltage can be precise as (Devashish 2017):

$$Csv_{dc} = \frac{3}{4}(M_{qr}i_{qr} + M_{dr}i_{dr}) + \frac{3}{4}(M_{df}i_{df} + M_{qf}i_{qf}) \tag{45}$$

$$\begin{aligned} Csv_{dc} &= \frac{3}{4}(M_{qr}i_{qr} + M_{dr}i_{dr}) + \frac{3}{4}(M_{df}i_{df} + M_{qf}i_{qf}) \\ &= \sigma_{dc} \end{aligned} \tag{46}$$

Equation "(46)" can be revised as

$$C_{dc}sv_{dc} = \sigma_{dc} = K_{dc}(v_{dc}^{*} - v_{dc}) \tag{47}$$

$$K_{dc} = \left(\frac{K_{Idc}}{s} + K_{pdc}\right).$$

Then "(47)" will be presented as:

$$\frac{v_{dc}}{v_{dc}^{*}} = \frac{\frac{1}{C_{dc}}\left(sK_{pdc} + K_{Idc}\right)}{s^2 + s\frac{K_{pdc}}{C_{dc}} + \frac{K_{Idc}}{C_{dc}}} \tag{48}$$

Equating the denominator of "(48)" with standard second order polynomial, i.e. $s^2 + 2\zeta\omega_n s + \omega_n^2$, PI controller gains are acquired as:

$$\omega_n^2 = \frac{K_{Idc}}{C_{dc}} \text{ and } 2\zeta\omega_n = \frac{K_{Pdc}}{C_{dc}}.$$

From "(46)" following expression is provided as:

$$i_{qf}^{*} = \frac{4}{3}\frac{1}{M_{qf}}\left(\sigma_{dc} - \frac{3}{4}\left(M_{qr}i_{qr} + M_{dr}i_{dr}\right)\right) - \frac{M_{df}}{M_{qf}}i_{df} \tag{49}$$

By means of KVL across the RL, the filter provides

$$v_{qf} = R_f i_{qf} + L_f s i_{qf} + \omega_e L_f i_{df} + \frac{v_{qs}}{K_T} = M_{qf}\frac{v_{dc}}{2} \tag{50}$$

$$v_{df} = R_f i_{df} + L_f s i_{df} - \omega_e L_f i_{qf} = M_{df}\frac{v_{dc}}{2} \tag{51}$$

$$Q_f = \frac{1.5}{K_T} i_{df} v_s \tag{52}$$

In "(52)" K_T is deliberated as transformer turns ratio associated amid GSC and stator.

$$sQ_f = 1.5si_{df}\frac{v_s}{K_T} \tag{53}$$

Replacing "(51)"in "(52)"gives:

$$sQ_f = 1.5\frac{v_s}{K_T L_f}\left(v_{df} - R_f i_{df} + \omega_e L_f i_{qf}\right) \tag{54}$$

$$\lambda sQ_f = (v_{df} - R_f v_{df} + \omega_e L_f i_{qf}) = \sigma_{Qf} \tag{55}$$

where λ is well-defined as:

$$\lambda = \frac{2L_f K_T}{3v_s}$$

$$\sigma_{Qf} = \lambda sQ_f = (Q_f^* - Q_f)K_{Qf} \tag{56}$$

where K_{Qf} is the gain of PI controller for reactive power delivered by grid side converter specified as:

$$K_{Qf} = \frac{K_{IQf}}{s} + K_{PQf} \tag{57}$$

Again "(56)" will be modified as:

$$\lambda sQ_f = (K_{PQf} + \frac{K_{IQf}}{s})Q_f^* - (K_{PQf} + \frac{K_{IQf}}{s})Q_f \tag{58}$$

$$\frac{Q_f}{Q_f^*} = \frac{\frac{1}{\lambda}(sK_{PQf} + K_{IQf})}{s^2 + s\frac{K_{PQf}}{\lambda} + \frac{K_{IQf}}{\lambda}} \tag{59}$$

Equating denominator of "(59)" with standard second order polynomial, $s^2 + 2\zeta\omega_n s + \omega_n^2$, PI controller gains are acquired as:

$$\omega_n^2 = \frac{K_{IQf}}{\lambda} \text{ and } 2\zeta\omega_n = \frac{K_{PQf}}{\lambda}.$$

From "(55)"

$$i_{df}^* = \frac{1}{R_f}(v_{df} + \omega_e L_f i_{qf} - \sigma_{Qf}) \tag{60}$$

On the assumption that:

$$\sigma_{qf} = R_f i_{qf} + L_f s i_{qf} = K_{qf}(i^*_{qf} - i_{qf}) \tag{61}$$

$$\sigma_{df} = R_f i_{df} + L_f s i_{df} = K_{qf}(i^*_{df} - i_{df}) \tag{62}$$

$$K_{df} = K_{qf} = \frac{K_{I1}}{s} + K_{P1}$$

Then "(61)" can be re-written as

$$\frac{i_{qf}}{i^*_{qf}} = \frac{\frac{1}{L_f}(sK_{P1} + K_{I1})}{s^2 + s\frac{1}{L_f}(R_f + K_{P1}) + \frac{1}{L_f}K_{I1}} \tag{63}$$

Equating the denominator of "(63)" with the fundamental second order polynomial $s^2 + 2\zeta\omega_n + \omega_n^2$ contributes (Fig. 5):

$$\omega_n^2 = \frac{K_{I1}}{L_f} \text{ and } 2\zeta\omega_n = \frac{R_f + K_{p1}}{L_f}$$

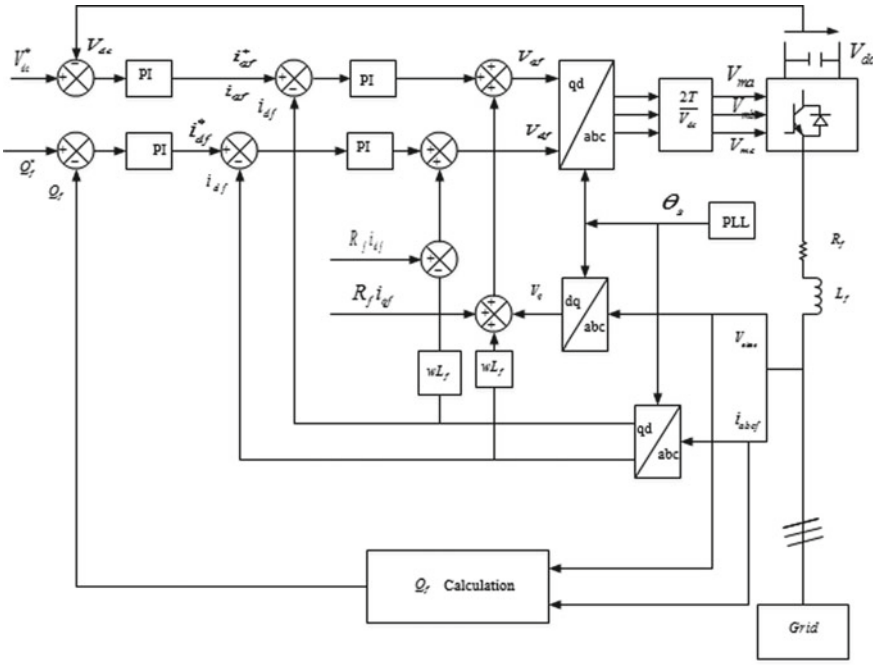

Fig. 5 Illustrative demonstration of grid side controller control scheme

Table 1 Estimation of the presentation of 2 MW SHPP associated with DFIG at diverse modes

ω_r (rad/sec)	I_{sf} (Hz)	I_{rf} (Hz)	P_{out} (MW)	Q_{out} (MVar)	V_{bus} (volt)	Q_{gr} (MVar)
141.3	50	10	−1.61	0	1150	0
157	50	0	−1.67	0	1150	0
172.7	50	−10	−1.73	0	1150	0

7 Results and Discussion

In the simulation results, the waveform acquired for a 2 MW SHPP associated with DFIG with PWM voltage source inverter and DFIG is working on the different speeds. For all modes of speed, the waveform for rotor speed, real and reactive powers are given in the simulation result. Intended for validation of process situation, currents of stator and rotor, voltage of the supply, and DC bus are publicized viva waveforms. All the outcomes are presented in Table 1 (Figs. 6, 7 and 8).

8 Conclusion

Owing to plentiful benefits as compared to an additional type of energy, grid connected small hydropower plant is being implemented in the obtainable situation. In this manuscript, a entire simulation model of a back to back converter fed DFIG for 2 MW SHPP is urbanized with PI controller schemes which manage the real and reactive power noticeably. To preserves, the supply frequency constant whenever the load increases and along with to minimize the losses and overheat, the regulatory of speed in small hydropower plant is very must. We used PI controller design in the rotor side as well as grid side also for finer recital. For existent time circumstances, we can use same given model in real time digital simulator (RT-LAB) and then the outcomes attained from real time digital simulator, as well as the outcomes attained from PI controller is very much analogous.

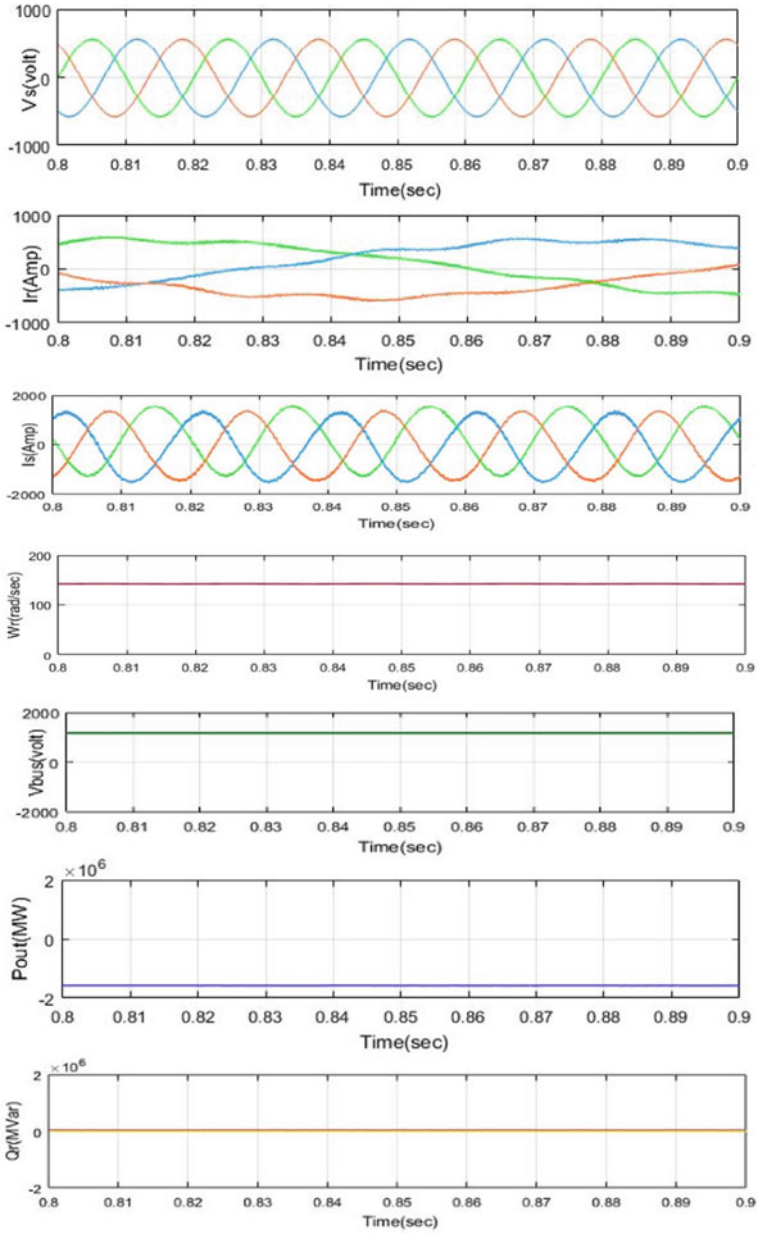

Fig. 6 Presentation of 2 Megawatt SHPP allied with DFIG at sub-synchronous speed (rotor speed = 141.3 rad/sec)

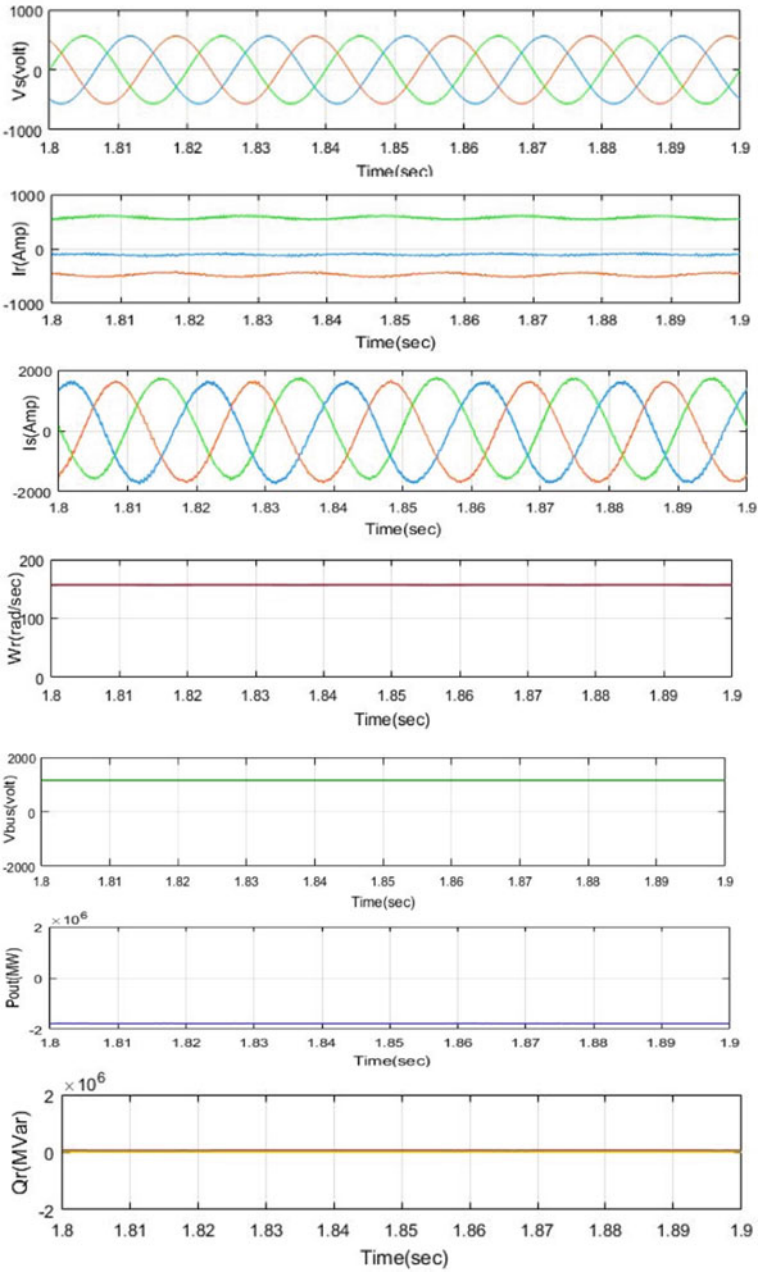

Fig. 7 Presentation of 2 Megawatt SHPP allied with DFIG at synchronous speed (rotor speed = 157 rad/sec)

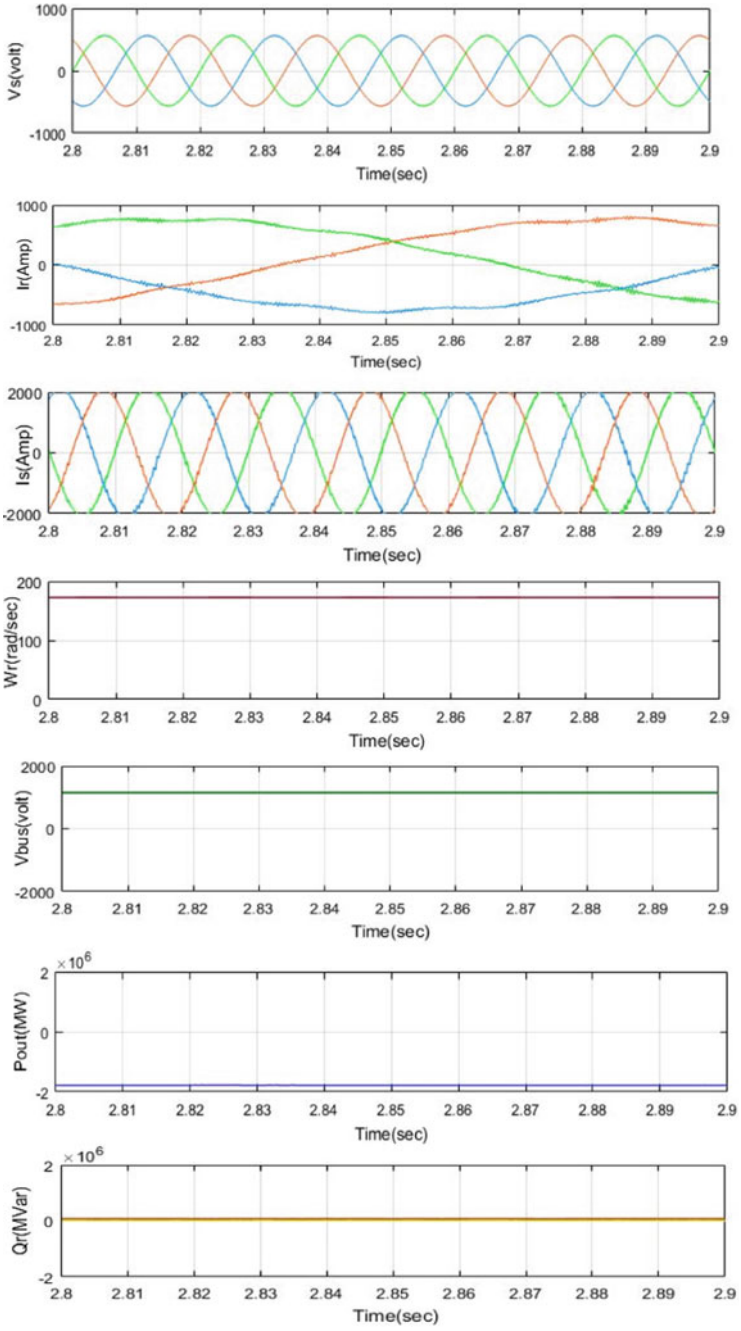

Fig. 8 Presentation of 2 Megawatt SHPP allied with DFIG at super-synchronous speed (rotor speed = 172.7 rad/sec)

References

Ansel A, Biet M, Robyns B (2004) Micro hydropower station based on a doubly fed induction generator excited by a PM synchronous machine. In: ICEM2004, Krakow, Poland, September 5–8, 2004, CD Rom

Bendi J, Chombt M, Schreier L (1999) Adjustable-speed operation of doubly fed induction machine in pumped storage power plants. In: Electrical machines and drives, ninth international conference on (Conf. Publ. No. 468), pp 223–227

Bhide A, Monray CR (2011) Energy poverty: a special focus on energy poverty in India and renewable energy technologies. Renew Sustain Energy Rev 15(2):1057–1066

Devashish AT (2017) A comprehensive review on wind energy system for electric power generation: current situation and improved technologies to realize future development. Int J Renew Energy Res 7(4):1786–1805

Government of India (2017) The National Electricity Plan. Ministry of New and Renewable Energy

Khan R (2015a) Towards realizing social sustainability in the small hydropower sector in India: opportunities for social innovations. Int J Innov Sustain Dev 9(1):48–62

Khan R (2015b) Small Hydro Power In India: is it a sustainable business? Appl Energy 152:207–216

Kumar D, Katoch SS (2014) Harnessing 'water tower' into 'power tower': a small hydropower development study from an India prefecture in Western Himalayas. Renew Sustain Energy Rev 39:87–101

Mishra MK, Khare N, Agrawal AB (2015) Small hydro power in India: current status and future perspectives. Renew Sustain Energy Rev 51:101–115

Nautiyan H, Singal SK, Sharma V (2011) Small hydropower for sustainable energy development in India. Renew Sustain Energy Rev 15(4):2021–2027

Schmidt E, Ertl J, Preiss A, Zensch R, Schurhuber R, Hell J (2011) Studies about the low voltage ride through capabilities of variable- speed motor generators of pumped storage hydro power plants. In: Universities power engineering conference (AUPEC), 21st Australasian, pp. 1–6, 25–28th Sept 2011

Zhao Y, Zou X, Huang D, Liu X, Cao F, Kang Y (2007) Research on excitation control of flexible power conditioner doubly fed induction machine. In: IEEE, Power electronics specialists conference, PESC2007, pp. 92–97, 17–21 June 2007

Study on Wave Transformation and Tranquillity Studies for the Development of Fish Landing Facility at Ajanur, Kasargod, Kerala

Amrita Jha, Biswakalyani Panda, and J. D. Agrawal

1 Introduction

Coastal engineering is the study of the processes ongoing at the shoreline and construction within the coastal zone. The field involves aspects of near shore oceanography, marine geology, and civil engineering, often directed at combating erosion of coasts or providing navigational access.

Coastal engineering can be divided in three groups:

- Understanding coastal processes.
- Coastal structures and their impacts on coastal processes.
- Tools available for solving the problems.

As seaways are the cheapest way of transportation, the development of ports and harbour contributes significantly to the development of country. India being the 3rd biggest exporter of fisheries, the construction of new fishing harbour and the maintenance of older fishing harbour and port also play an important role. In view of above, it is extremely needed to test the tranquillity of harbours by studying the wave conditions because waves are the most pre dominant phenomenon that affects the operation of berths and jetties. If the harbour is not tranquil then it will affect the loading and unloading of cargos (CWPRS Technical Report No 4645, 2009).

For this study, Ajanur village has been selected. Ajanur village is situated about 15 km south of Kasargod district at Latitude 12.330 and longitude 75.180 on the west coast of India in Kerala state Fig. 1.Wave tranquillity studies to assess wave disturbance in the harbour and the study of littoral movement and shoreline changes were done.

A. Jha (✉) · B. Panda · J. D. Agrawal
Department of Water Engineering & Management, Central University, Ranchi, Jharkhand, India
e-mail: amritajha.cuj@gmail.com

R. Jha et al. (eds.), *River and Coastal Engineering*, Water Science and Technology Library 117, https://doi.org/10.1007/978-3-031-05057-2_32

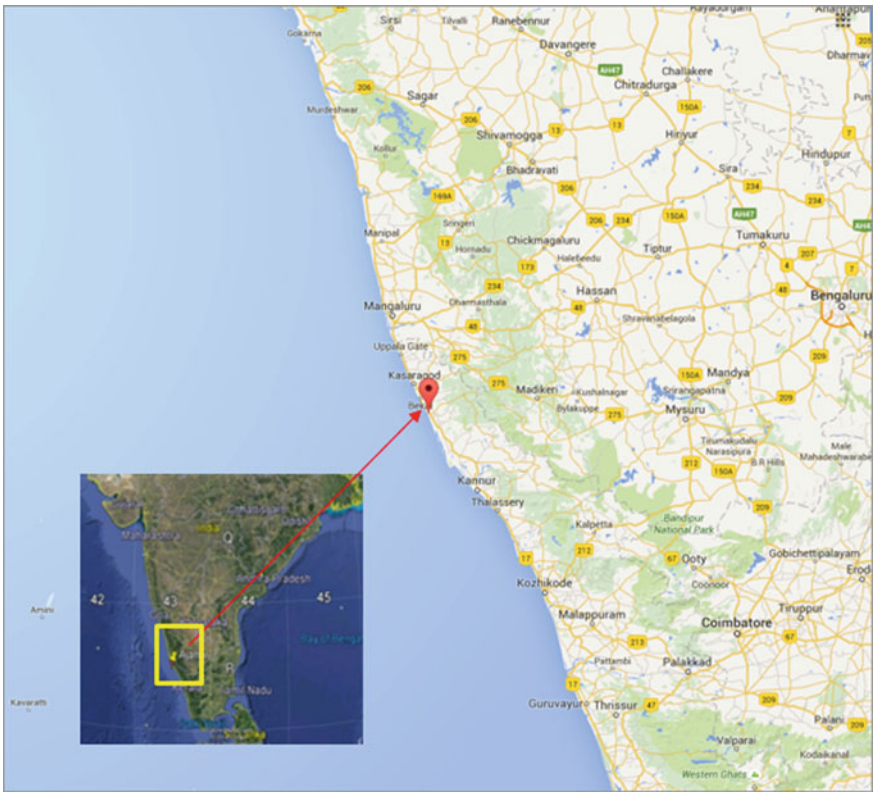

Fig. 1 Index map of Ajanur, Kasargod, Kerala

2 About MIKE Software

MIKE 21 is a computer program that simulates flows, waves, sediments and ecology in rivers, lakes, estuaries, bays, coastal areas and seas in two dimensions. It was developed by DHI.

MIKE 21 can be used for design data assessment for coastal and offshore structures, optimization of port layout and coastal protection measures, cooling water, desalination and recirculation analysis, environmental impact assessment of marine infrastructures, water forecast for safe marine operations and navigation, coastal flooding and storm surge warnings, inland flooding and overland flow modeling.

2.1 MIKE 21 SW (Phase Averaged Model)

It is a new generation spectral wind wave model based on unstructured mesh. The model stimulates growth, decay and transformation of wind-generated waves and swells in offshore and coastal areas. It is used in the design of offshore, coastal and port structure where accurate assessment of wave load is of utmost importance to the safe and economic design of these structures.

MIKE 21 SW can be used for the assessment of wave climates in offshore and coastal areas. A major application area is the design of offshore, coastal and port structures where accurate assessment of wave loads is of utmost important to the safe and economic design of these structures. Measured data is often not available during periods long enough to allow for the establishments of sufficiently accurate estimates of extreme sea states. In this case, the measured data can then be supplemented with hind-cast data through the simulation of wave conditions during historical storms using MIKE 21 SW. It is used to calculate wave conditions and associated radiation stresses (MIKE 21 SW Manual).

2.2 Mathematical Model MIKE 21 BW

The Boussinesq Wave model, MIKE 21 BW, is the state-of-the-art numerical model for calculation and analysis of short- and long-period waves in ports, harbors and coastal areas. MIKE 21 BW can also be used for detailed modeling of wave-induced current fields, surf zone dynamics and swash zone oscillations. The model is based on the numerical solution of the enhanced Boussinesq equations formulated by Madsen et al. (1991).

MIKE 21 BW is capable of reproducing the combined effects of all important wave phenomena of interest in port, harbor and coastal engineering (MIKE 21 BW Manual).

2.2.1 Basic Equations

The governing equation is the wave action balance equation. In horizontal Cartesian co-ordinates the conservation equation for wave action is

$$\frac{\partial N}{\partial t} + \nabla.(\vec{v}N) = \frac{S}{\sigma}$$

where $N(\vec{x}, \sigma, \theta, \mathrm{t})$ is the action density, t is the time, $\vec{x} = (\mathrm{x}, \mathrm{y})$ is the Cartesian co-ordinates, $\vec{v} = (\mathrm{Cx}, \mathrm{Cy}, \mathrm{C}\sigma, \mathrm{C}\theta)$ is the propagation velocity of a wave group in the four dimensional phase space $\vec{x}$, σ and θ. S is the source term for the energy balance

equation. ∇ is the four dimensional differential operator in the $\vec{x}$, σ and θ space. The equation is solved using cell–centered finite volume method (Berkhoff 1972).

3 Model Set-Up

3.1 Wave Data in Deep Sea

The offshore wave data reported by India Meteorological Department (IMD) as observed from ships plying in deep waters off AJANUR (Latitude 10° N to 15° N, Longitude 70° E to 75° E) were analyzed. The frequency distribution of wave heights from different directions during different seasons and entire year for the above offshore data is given in Tables 1, 2, 3 and 4. Corresponding wave rose diagrams are presented in Figs. 2 and 3. It may be noted that the wave height based on ship observed data closely corresponds to significant wave height, which represents average energy of the random wave train.

Table 1 Percentage occurrence of wave height and direction off Ajanur for South-West Monsoon (June–September)

Wave height (m)	0.5	1.0	1.5	2.0	2.5	3.0	3.5	4.0	4.5	Total
Direction								Calm %		0.56
22.50	0.09	0.00	0.18	0.00	0.00	0.00	0.00	0.00	0.00	0.27
45.00	0.00	0.00	0.12	0.00	0.00	0.00	0.00	0.00	0.00	0.12
67.50	0.00	0.00	0.12	0.00	0.13	0.00	0.00	0.00	0.00	0.25
90.00	0.00	0.09	0.07	0.00	0.08	0.07	0.00	0.00	0.00	0.31
112.50	0.00	0.00	0.17	0.15	0.00	0.12	0.00	0.00	0.00	0.44
135.00	0.14	0.11	0.18	0.37	0.29	0.34	0.00	0.23	0.00	1.67
157.50	0.22	0.25	0.42	0.05	0.19	0.21	0.00	0.23	0.03	1.60
180.00	0.06	0.27	0.40	0.66	0.13	0.15	0.06	0.41	0.18	2.32
202.50	0.30	0.15	0.51	0.34	0.24	0.20	0.21	0.23	0.00	2.17
225.00	0.51	1.08	1.49	1.59	1.11	0.93	0.71	0.33	0.21	7.97
247.50	0.58	2.02	2.09	3.72	1.63	1.72	0.82	1.17	0.71	14.46
270.00	1.43	5.03	4.48	5.58	4.80	6.08	3.15	4.19	2.91	37.66
292.50	0.84	2.47	3.89	4.11	3.01	2.94	1.15	1.27	1.65	21.33
315.00	0.14	0.88	1.16	2.09	1.07	0.72	0.04	0.21	0.48	6.77
337.50	0.18	0.60	0.33	0.36	0.08	0.08	0.00	0.00	0.00	1.63
360.00	0.30	0.07	0.00	0.09	0.00	0.00	0.00	0.00	0.00	0.46
	4.79	**13.02**	**15.62**	**19.11**	**12.77**	**13.58**	**6.14**	**8.25**	**6.16**	**100.00**

Table 2 Percentage occurrence of wave height and direction off Ajanur for North-East Monsoon Period (OCT-JAN)

Wave height (m)	0.5	1.0	1.5	2.0	2.5	3.0	3.5	4.0	4.5	Total
Direction								Calm %		0.86
22.50	1.95	2.41	0.95	1.06	0.28	0.16	0.00	0.10	0.00	6.91
45.00	2.22	2.60	1.90	1.81	0.04	0.24	0.00	0.10	0.11	9.03
67.50	1.88	2.71	1.94	0.75	0.33	0.22	0.14	0.00	0.00	7.96
90.00	2.69	3.23	1.71	0.84	0.19	0.43	0.07	0.00	0.00	9.17
112.50	1.55	2.00	0.98	0.80	0.08	0.35	0.10	0.00	0.00	5.87
135.00	0.56	1.45	0.61	0.48	0.03	0.44	0.10	0.00	0.00	3.67
157.50	0.52	0.78	0.99	0.51	0.09	0.22	0.10	0.03	0.00	3.26
180.00	1.19	1.70	1.17	0.97	0.38	0.07	0.00	0.17	0.00	5.65
202.50	0.97	0.50	1.03	0.92	0.25	0.21	0.08	0.00	0.00	3.97
225.00	0.50	1.17	0.77	0.65	0.46	0.04	0.13	0.00	0.10	3.82
247.50	0.90	1.82	1.57	0.83	0.69	0.75	0.10	0.00	0.00	6.67
270.00	0.65	1.82	1.31	1.50	0.17	0.41	0.00	0.00	0.00	5.87
292.50	1.21	1.48	1.63	0.67	0.13	0.19	0.00	0.10	0.00	5.41
315.00	1.15	2.04	0.99	0.47	0.34	0.00	0.00	0.00	0.00	4.98
337.50	1.96	2.77	1.61	0.80	0.11	0.10	0.00	0.00	0.00	7.35
360.00	2.51	3.58	1.73	1.37	0.12	0.22	0.00	0.00	0.00	9.53
	22.43	**32.05**	**20.91**	**14.44**	**3.70**	**4.05**	**0.83**	**0.51**	**0.21**	**100.00**

3.2 Wave Propagation and Surface Elevation Studies

While propagating the waves from 10 m to harbour area, the studies has been done for different layouts.

3.2.1 Studies with Layout 1

Layout 1 consists of north and south breakwaters. The north breakwater is of length 335 m. The southern breakwater consists of shore normal breakwater of length 270 m, which is extended along shore breakwater of length 340 m. The breakwaters extend up to 4–4.4 m depth (Fig. 4). Bathymetry, surface elevation plot of the wave propagation and contours of the wave height in the port for incident wave directions from SW, WSW and West are discussed in the result.

Table 3 Percentage occurrence of wave height and direction off Ajanur for non-monsoon period (Feb-May)

Wave height (m)	0.5	1.0	1.5	2.0	2.5	3.0	3.5	4.0	4.5	Total
Direction								Calm %		1.14
22.50	2.30	2.82	1.12	1.01	0.36	0.10	0.16	0.12	0.05	8.04
45.00	2.10	1.40	0.89	0.38	0.13	0.17	0.37	0.37	0.00	5.81
67.50	0.62	1.34	0.22	0.04	0.00	0.22	0.00	0.15	0.00	2.59
90.00	0.87	1.48	0.47	0.60	0.00	0.00	0.00	0.28	0.00	3.69
112.50	0.84	1.33	0.60	0.40	0.00	0.00	0.00	0.05	0.00	3.21
135.00	1.13	1.90	0.86	0.26	0.21	0.00	0.00	0.25	0.00	4.41
157.50	1.58	1.03	1.62	0.62	0.25	0.11	0.04	0.04	0.00	5.32
180.00	1.06	1.98	0.88	0.76	0.07	0.07	0.17	0.10	0.00	5.08
202.50	0.54	0.55	0.96	0.95	0.05	0.16	0.05	0.00	0.00	3.25
225.00	0.98	1.09	0.40	0.61	0.34	0.15	0.26	0.12	0.12	4.07
247.50	0.74	1.02	1.13	1.24	0.23	0.11	0.00	0.10	0.03	4.61
270.00	1.30	2.10	0.81	1.19	0.07	0.48	0.00	0.11	0.08	6.15
292.50	1.68	2.07	1.24	0.40	0.33	0.27	0.00	0.00	0.00	5.99
315.00	3.45	3.18	1.57	0.85	0.45	0.16	0.00	0.00	0.00	9.64
337.50	3.57	4.88	2.78	1.02	0.04	0.15	0.00	0.19	0.11	12.73
360.00	4.78	4.99	2.28	1.10	0.31	0.12	0.30	0.20	0.18	14.25
	27.54	**33.14**	**17.83**	**11.42**	**2.64**	**2.27**	**1.35**	**2.08**	**0.58**	**100.00**

3.2.2 Studies with Layout 2

Layout 2 consists of north and south breakwaters. The northern breakwater consists of shore normal breakwater of length 250 m which is extended along shore breakwater of length 315 m. The southern breakwater is 385 m long and shore normal. The breakwaters extend up to 4 m to 4.4 m depth as shown in Fig. 5

3.2.3 Studies with Layout 3

Layout 2 consists of a long north breakwater and a south breakwater. The northern breakwater consists of shore normal breakwater of length 260 m, which is extended along shore breakwater of length 700 m. The southern breakwater is 295 m long and shore normal. The breakwaters extend till 4 0.5 m depth as shown in Fig. 6.

Table 4 Percentage occurrence of wave height and direction off Ajanur for entire period (Jan–Dec)

Wave height (m)	0.5	1.0	1.5	2.0	2.5	3.0	3.5	4.0	4.5	Total
Direction								Calm %		6.34
22.50	1.30	1.61	0.71	0.62	0.19	0.08	0.05	0.07	0.01	4.64
45.00	1.29	1.26	0.90	0.67	0.05	0.12	0.11	0.13	0.03	4.57
67.50	0.75	1.26	0.71	0.26	0.14	0.13	0.04	0.04	0.00	3.35
90.00	1.06	1.50	0.75	0.48	0.10	0.15	0.02	0.08	0.00	4.15
112.50	0.72	1.04	0.57	0.43	0.04	0.14	0.03	0.14	0.00	2.98
135.00	0.56	1.07	0.56	0.37	0.12	0.24	0.03	0.14	0.00	3.08
157.50	0.70	0.68	0.96	0.42	0.19	0.18	0.05	0.09	0.01	3.28
180.00	0.69	1.22	0.78	0.76	0.20	0.10	0.07	0.20	0.06	4.08
202.50	0.54	0.40	0.78	0.68	0.18	0.18	0.10	0.07	0.00	2.93
225.00	0.60	1.03	0.86	0.90	0.60	0.36	0.33	0.15	0.13	4.97
247.50	0.66	1.51	1.52	1.86	0.86	0.84	0.31	0.41	0.23	8.21
270.00	1.02	2.73	2.15	2.76	1.73	2.26	1.01	1.37	0.91	15.94
292.50	1.12	1.88	2.14	1.74	1.17	1.12	0.40	0.46	0.50	10.52
315.00	1.42	1.91	1.23	1.13	0.61	0.29	0.02	0.07	0.14	6.83
337.50	1.70	2.58	1.50	0.71	0.09	0.10	0.00	0.05	0.03	6.77
360.00	2.24	2.65	1.26	0.78	0.14	0.10	0.09	0.06	0.05	7.37
	16.38	**24.32**	**17.39**	**14.56**	**6.39**	**6.41**	**2.67**	**3.42**	**2.10**	**100.00**

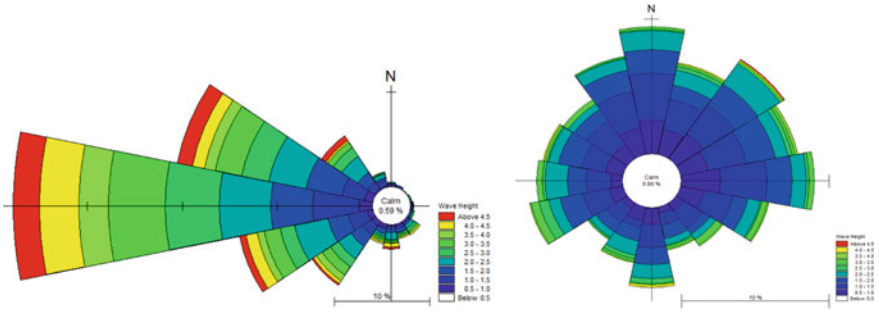

Fig. 2 Wave Rose diagram offshore of Ajanur for SW monsoon (Left) and NE monsoon (Right)

3.3 Spectral Wave Model Setup

From this setup, after simulation we can find the waves in the generation area are of variable heights and frequencies and propagate in all direction.

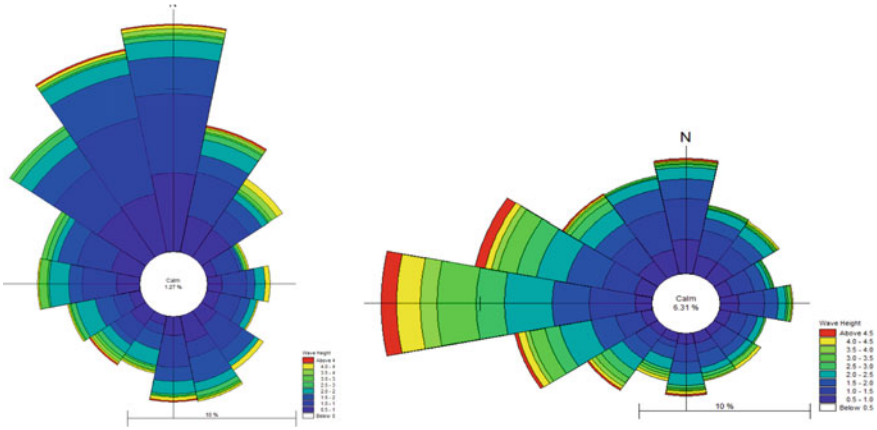

Fig. 3 Wave Rose diagram offshore of Ajanur for non-monsoon (Left) and entire year (Right)

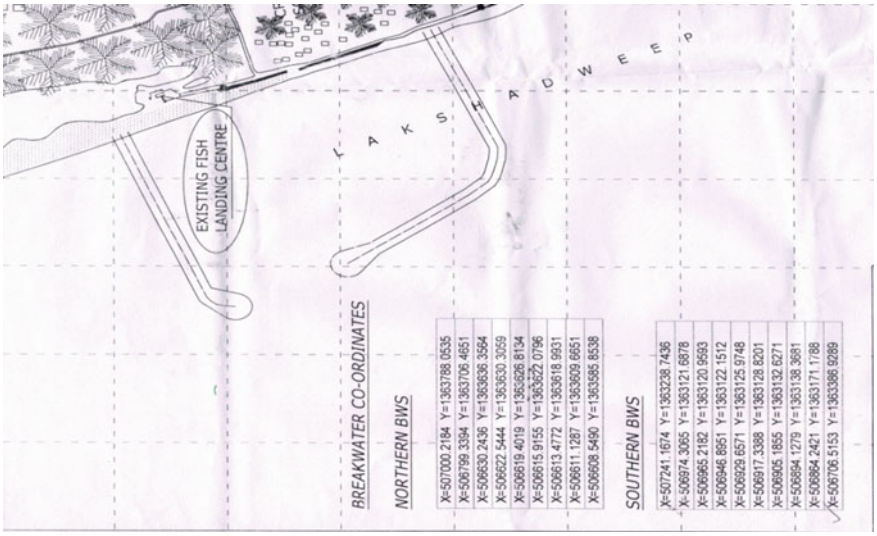

Fig. 4 Proposed layout 1

3.4 Boussinesq Wave Model Setup

This model solves the enhanced Boussinesq equations by an implicit finite difference techniques with variable defined on a space-staggered rectangular grid. This module is typically selected for calculation of short and long wave period, wave disturbance in ports and arbor.

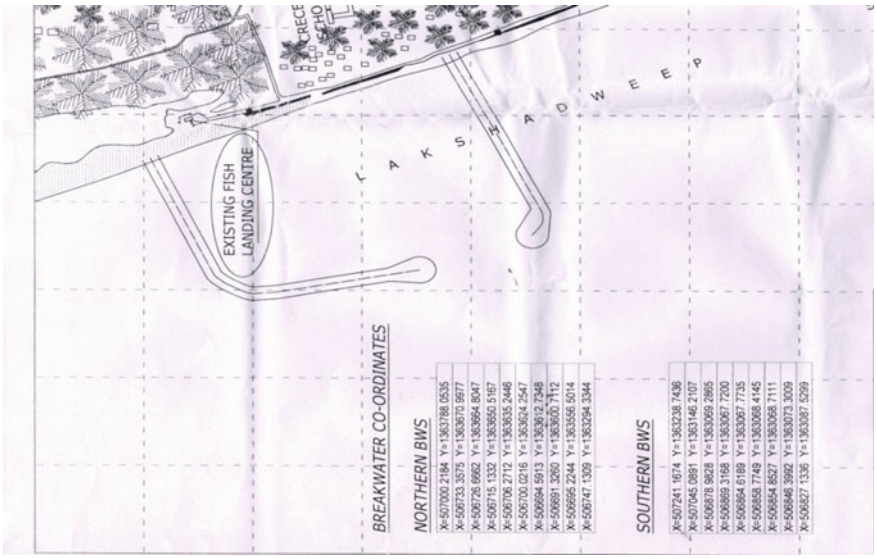

Fig. 5 Proposed layout 2

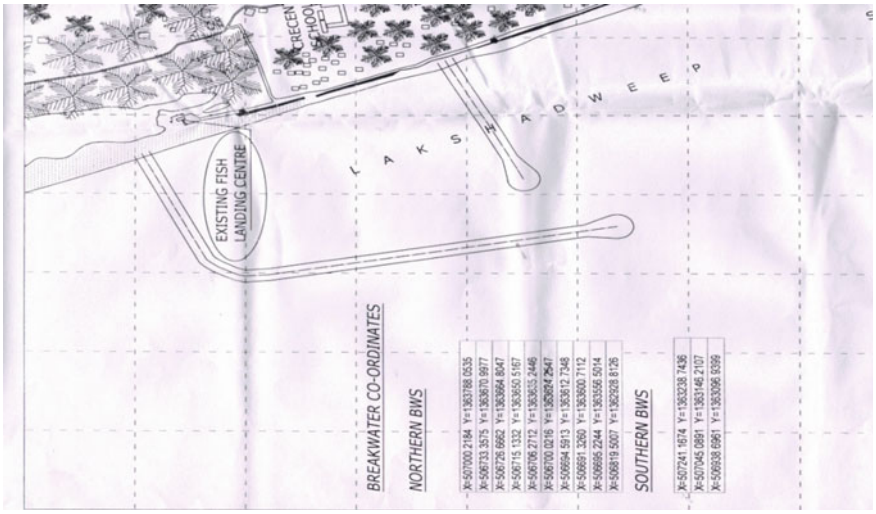

Fig. 6 Proposed layout 3

For BW model setup, basic focus is on generating 2–3 input parameters i.e. preparation and smoothing of bathymetry, creating wave generation line, porosity and sponge layer.

4 Results and Discussion

4.1 Result of SW

The results of the studies of wave transformation from deep water to 10 m depth near Ajanur are shown in rose diagrams (Figs. 7 and 8).

4.1.1 Concluding Remark

The input wave conditions for the wave tranquility studies with MIKE 21 BW model were shortlisted as given in Table 5.

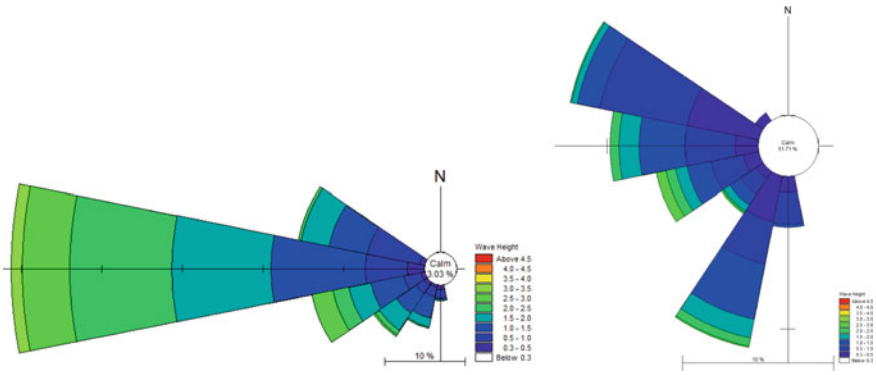

Fig. 7 Wave Rose diagram near Ajanur for SW monsoon (Left) and NE monsoon (Right)

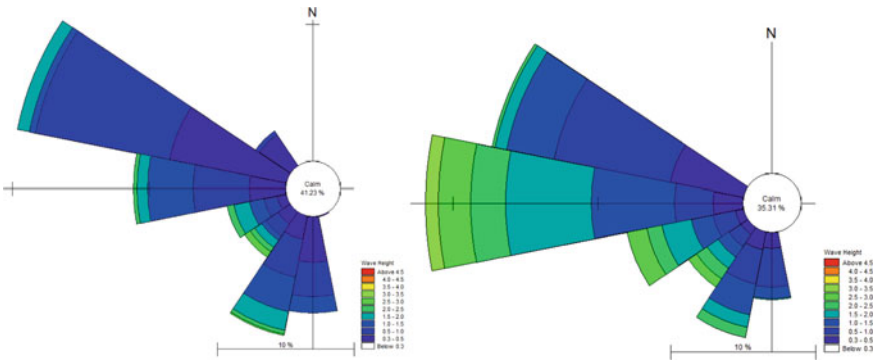

Fig. 8 Wave Rose diagram near Ajanur for non-monsoon (Left) and entire year (Right)

Table 5 Input wave conditions

Incident wave direction	Incident wave height (m)
SW	2.5
WSW	2.5
Wet	3.0

Table 6 Output from layouts

Wave height	Layout 1		Layout 2		Layout 3		Permissible limit
Incident wave direction	Range (m)	Avg (m)	Range (m)	Avg (m)	Range (m)	Avg (m)	
SW	0.10–0.38	0.22	0.09–0.30	0.19	0.027–0.036	0.03	0.3
WSW	0.13–0.26	0.18	0.23–0.42	0.23	0.028–0.039	0.03	0.3
West	0.16–0.4	0.30	0.19–0.40	0.30	0.018–0.025	0.02	0.3

Since the present development is for fish landing facility, a wave tranquility limit of 0.3 has been assumed for obbtaining the maximum number of operational days of fish landing facility.

4.2 Result of BW

With Layout 3, there is considerable improvement in the wave heights inside the harbour basin. The wave heights are always less than the wave tranquility limit of 0.3 m. With Layout 3, harbour will be operational throughout the year (Table 6).

5 Conclusion

The wave tranquility studies with Layout 1 and Layout 2 indicated that wave heights from west are greater than the wave tranquility criterion of 0.3 m. With the incident wave direction WSW and SW, the wave heights are less than wave tranquility limit of 0.3 m.

With Layout 3, there is considerable improvement in the wave heights inside the harbour basin. The wave heights are always less than the wave tranquility limit of 0.3 m. With Layout 3, the harbour may be operational throughout the year.

Acknowledgements The authors are thankful to CWPRS, Pune for providing the support to carry out studies.

References

Berkhoff JCW (1972) Computation of combined refraction and diffraction. Proceedings of the 13th International coastal engineering conference. ASCE, pp 471–490

CWPRS Technical Report No 4645 (2009) Mathematical model studies for wave tranquility for the proposed LNG terminal in the outer harbour at Cochin port, Kerala

Madsen PA, Murry R, Sorensen OR (1991) A new form of the Boussinesq equations with improved linear dispersion characteristics. Coast Eng 15:371–388

MIKE 21, SW and BW manual. DHI, Denmark

Comparison of Numerical and Data Driven Approaches for Rainfall-Runoff Modeling

Digvijay Saruk, Shreenivas Londhe, Pradnya Dixit, and Preeti Kulkarni

1 Introduction

Rainfall-runoff transformation over a catchment is a complicated phenomenon as the process is spatially distributed, non-linear and time varying. Rainfall runoff estimation from a catchment plays a very important role in water resources planning; flood forecasting related applications (Singh et al. 2014). In modeling, implicit and explicit factors such as Evaporation, transpiration, Precipitation distribution, abstraction, watershed topography and soil types are which affect rainfall-runoff process in modeling (Hafezparast et al. 2013). For modeling the rainfall-runoff process many hydrologic models are available and varying in nature and are difficult to understand. The broadly known rainfall-runoff (R-R) models are Green-Ampt method, rational method, soil conservation services (SCS) Curve number method (Galkate et al. 2014). Irrespective of above methods, Numerical method provides better runoff estimation which is continuously being researched and developed. Numerical models are mathematical models that use some sort of numerical time-stepping procedure to obtain the model behavior over time. These models are categorized into three categories: conceptual, black box and physics based models. Conceptual models are also known as grey box or parametric models. Rainfall, runoff, infiltration and evapotranspiration etc. are key factors used in conceptual modeling. In this model, the different model parameters are calculated using calibration approach which is based on time series of the rainfall and runoff. In these models, the catchment is considered as a homogenous single unit. MIKE 11 Nedbor-Afrstromnings Model (NAM) advanced by Danish Hydraulic Institute is a conceptual and lumped R-R model which is able to simulate surface flow, subsurface and base flow. There are many instances and case studies which detail out use and application of MIKE 11 in simulating R-R process in practical situations (Agrawal and Deshmukh 2016). However the exogenous data

D. Saruk · S. Londhe · P. Dixit · P. Kulkarni (✉)
Vishwakarma Institute of Information Technology, Pune, India
e-mail: preeti.kulkarni@viit.ac.in

R. Jha et al. (eds.), *River and Coastal Engineering*, Water Science and Technology Library 117, https://doi.org/10.1007/978-3-031-05057-2_33

requirement in the form of evaporation, evapotranspiration, land use, land cover, infiltration data sometimes become an impediment in the use of such models particularly in developing countries like India wherein such a data may not be available spatially and temporally. The data driven tools which can make use of available data rather than demanding data as per physics of the process can become handy in such situations. The recent approaches of Genetic Programming, Artificial Neural Network and Model Tree are prominent data driven techniques which have been used to develop R-R models by many research workers for last twenty years or so. A detail review of these applications can be located in The ASCE Task Committee (2000), Maier and Dandy (2000), Dawson and Wilby (2001), Londhe and Dixit (2012), Solomatine and Xue (2004). However practicing hydrologist and researchers are bit skeptical about use of data driven tools in actual practice perhaps owing to their 'Grey box' nature. The present work is a step in this direction wherein R-R model is developed for an experimental catchment area in UK with available data such as rainfall, discharge and evapotranspiration. The R-R models are developed using MIKE 11, ANN, GP and MT and their results are compared. In the second part of the study R-R models are developed without evapotranspiration as an input which ceases use of MIKE 11 while ANN, GP and MT models can still be developed. The results indicate that when all inputs are available MIKE 11 as well as data driven models perform equally good regarding accuracy of runoff prediction is considered. However in the absence of evaporation data results of ANN, GP and MT are reasonable and these models can be employed where numerical models like MIKE 11 can't be used.

2 Tools and Techniques

2.1 MIKE 11

Denmark based Danish Hydraulic Institute (DHI) developed a lumped and conceptual rainfall-runoff model named MIKE 11-NAM (Nedbor Afrstromnings Model) model (www.mikepoweredbydhi.com/products/mike-11). This model is based on the hydrological cycle for the quantitative simulation of water storage and flows in the watershed and its parameters represent an average value for the whole watershed. The structure of the model is divided in four different and mutually interrelated storages and their corresponding flows are shown in Fig. 1. Rainfall, evapotranspiration or potential evaporation and discharge are the input data required for this model and the catchment runoff is the output of the model. Inputs are provided to R-R parameters. Using auto-calibration, NAM parameters are set to build the R-R parameter. In auto-calibration, model fixes surface and root zone parameters and groundwater parameters automatically. The validation is done by taking R-R parameters as input for a given time period along with model inputs of rainfall, evapotranspiration which are not used in model calibration to simulate the runoff. For details of methodology,

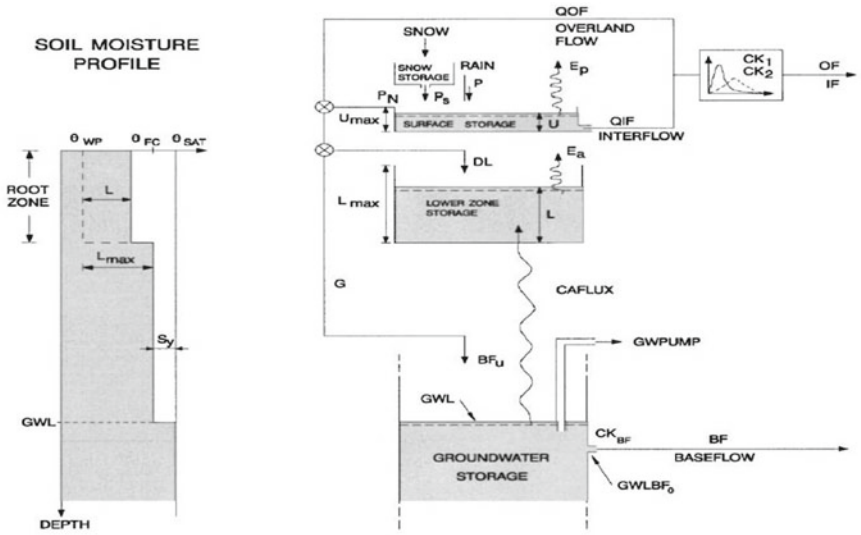

Fig. 1 NAM model's structure for rainfall-runoff simulation (Madsen 2000)

readers are referred to (DHI Manual 2009). In the present work, the inputs needed to the model were daily rainfall, daily evapotranspiration and daily discharge.

2.2 Artificial Neural Network (ANN)

A neural network is a massively parallel distributed processor that has a natural propensity for storing experiential knowledge and making it available for use (Haykin 1994). In brief, ANN's essentially involve an input layer and an output layer, which are used for supervised training. In between the input and output layers, one or more hidden layers connected by weights, biases, and transfer functions are often used. The input layer data are multiplied by initial trial weights and a bias is added to the product. This weighted sum is then transferred through either linear or sigmoid transfer functions to yield an output. This output then becomes the input for the following hidden layers and the procedure is continued until the output layer is reached. The difference between the network output and the target is used and transformed by an error function, and the resulting error is propagated back ("back propagation") to update the weights and the biases using an optimization technique like the gradient descent, which strives to minimize the error. The entire procedure is repeated for a number of epochs until the desired accuracy in the outputs or other specified conditions is achieved ("training"). Once the network is trained, it can be used to validate against unseen data using the trained weights and biases. Various algorithms namely Conjugate Gradient, Broyden-Fletcher-Goldfarb-Shanno (BFGS),

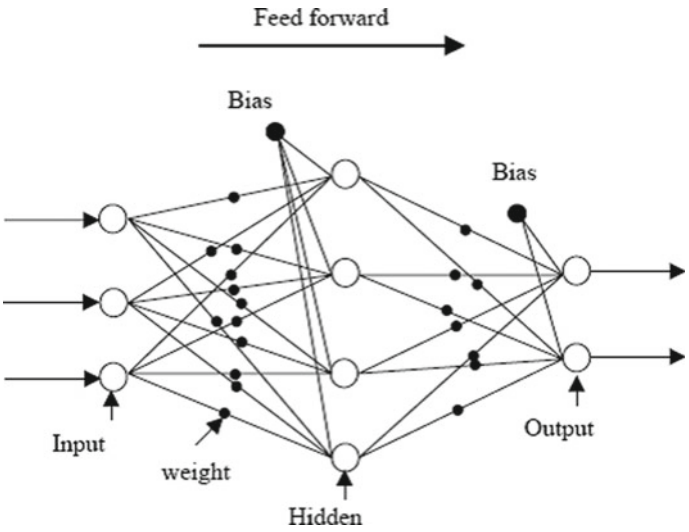

Fig. 2 Typical feed forward neural network

Levernberg-Marquardt (LM) can also be used for training the neural net. There are other classes of network also like Recurrent network (information flows both in forward and backward direction), Radial Basis Function Network, Generalized Regression Neural Network (GRNN) which are also used in predicting water flow variables. There are over 400 publications in international journals which describe use of ANN to model various hydrological processes, a review of which is beyond the scope of this work. However early details of application of Neural Networks can be located in The ASCE Task Committee (2000), Maier and Dandy (2000), Dawson and Wilby (2001), Bose and Liang (1998), Wasserman (1993). Figure 2 shows typical Feed Forward type of Neural Network.

2.3 Genetic Programming (GP)

Like genetic algorithm (GA) the concept of genetic programming follows the principle of 'survival of the fittest' borrowed from the process of evolution occurring in nature. But unlike GA its solution is a computer program or an equation as against a set of numbers in the GA and hence it is convenient to use the same as a regression tool rather than an optimization one like the GA. A good explanation of various concepts related to GP can be found in Koza (1992). In GP a random population of individuals (equations or computer programs) is created, the fitness of individuals is evaluated and then the 'parents' are selected out of these individuals. The parents are then made to yield 'offspring's' by following the process of reproduction, mutation and crossover. The creation of offspring's continues (in an iterative manner) till a

specified number of offspring's in a generation are produced and further till another specified number of generations are created. The resulting offspring at the end of all this process (an equation or a computer program) is the solution of the problem. The GP thus transforms one population of individuals into another one in an iterative manner by following the natural genetic operations like reproduction, mutation and cross-over. The GP has two versions namely Linear and Tree based out of which tree based GP is followed in the present work. Output of the tree based GP is a formula based upon the parameters used to develop the model. For further details of GP, readers are referred to Londhe and Dixit (2012). Applications of GP in modeling water flows are reviewed by Londhe and Dixit (2012).

2.4 Model Tree (MT)

The principle of recursive partitioning of input space using entropy-based measures, and finally assigning class labels to resulting subsets is used in the M5 Model Tree is a data driven method. M5 algorithm splits the parameter space into areas (subspaces) and builds in each of them a local specialized linear regression model as shown in Fig. 3. The splitting in MT follows the idea used in building a decision tree, but instead of the class labels it has linear regression functions at the leaves, which can predict continuous numeric attributes. Model trees generalize the concepts of regression trees which have constant values at their leaves. Therefore, they are similar to piecewise

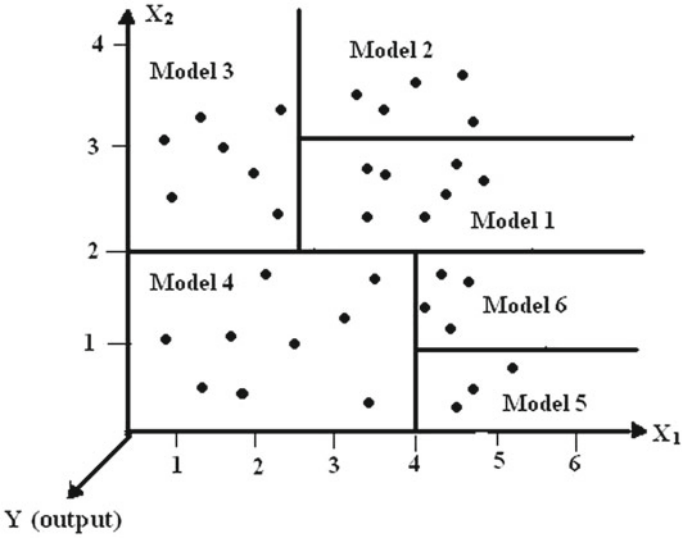

Fig. 3 Splitting the input space X1 × X2 by M5 model tree algorithm; each model is a linear regression model y = a0 + a1 × 1 + a2 × 2

linear functions called as non-linear. Model trees learn efficiently and can tackle tasks with very high dimensionality—up to hundreds of attributes. The main advantage of model trees over regression trees is that model trees are much smaller than regression trees, the decision strength is clear, and the regression functions do not normally involve many variables (Bhattacharya and Solomatine 2005). The M5 model tree algorithm is used for forming a model tree (Quinlan 1992) which works as given below.

Assume that a collection T of training examples is available. Each example is characterized by the values of a fixed set of (input) attributes and has an associated target (output) value. The goal is to construct a model that relates a target value of the training cases to the values of their input attributes. The quality of the model will be measured by the accuracy with which it predicts the target values of the unseen cases. A divide-and-conquer method is used to construct Tree-based models. The test is chosen that splits T into subsets corresponding to the test outcomes and the same process are applied repetitively to the subsets. The working principle of M5 Model tree algorithm is the splitting criterion which is based on treating the standard deviation of the class values that reach a node as a measure of the error at that node and calculating the expected reduction in this error as a result of testing each attribute at that node. The standard deviation reduction (SDR) formula is stated as:

$$SDR = SD(T) - \sum_i \frac{|T_i|}{|T|} sd(T_i) \tag{1}$$

where T represents a set of examples that reaches the node; Ti represents the subset of examples that have the ith outcome of the potential set and SD represents the standard deviation. After exploring all possible splits (i.e., the attributes and the possible split values), M5 chooses the one that maximizes the expected error reduction. Splitting in M5 stops when the class values of all the instances that reach a node vary just slightly or only a few instances remain. The relentless division frequently produces over complex structures that must be cut off, for instance by replacing a sub-tree with a leaf. The final stage is a smoothing process which is carried out to compensate for the sharp discontinuities that will inevitably occur between adjacent linear models at the leaves of the pruned tree, particularly for some models constructed from a smaller number of training examples. In smoothing, the adjacent linear equations are updated in such a way that the predicted outputs for the neighboring input vectors corresponding to the different equations are becoming close in value. For the details of the procedure, readers are referred to Quinlan (1992). Applications of MT in Hydrology are sparse and few like, Solomatine and Dulal (2003), Solomatine and Xue (2004), Solomatine and Siek (2004) Bhattacharya and Solomatine (2005), Londhe and Charhate (2010) to name a few.

3 Methodology

The data available for the current study was from 01/01/1993 to 31/12/2014 (total 7304 values) for Daily rainfall, daily evapotranspiration and daily discharge. For predicting the discharge in the Coalburn catchment area, two sets of models were developed. In set I discharge in m^3/s was predicted using the techniques: MIKE NAM model (MIKE11), Genetic programming (GP1), Artificial Neural Network (ANN1) and Model tree (MT1) and daily rainfall and daily evaporation as input parameters for each model. The data division in set I was decided as Training data from 01/01/1993 to 31/12/2011 and validation or testing data from 01/01/2014 to 31/12/2014. This is done to match the data division employed for MIKE 11 to compare the results.

In set II discharge in m^3/s was predicted using the techniques Genetic Programming (GP2), Artificial neural network (ANN2) and Model tree (MT2); and daily rainfall as input parameter for each model as MIKE 11 can't be used in evapotranspiration data is not available. The data were divided into 70% for training and 30% for testing as done usually for data driven models.

The model evaluation was done by calculating root mean squared error (RMSE), Coefficient of efficiency (CE) and correlation coefficient (r) between the observed and predicted values along with scatter plots and hydrographs. In Dawson and Wilby (2001), the formulae for the above error measures are mentioned.

4 Results and Discussions

As mentioned in Methodology 2 sets of models were prepared, one with rainfall and evapotranspiration as input (MIKE1, ANN1, GP1, MT1) and the other with rainfall as input with runoff as output of both models.

4.1 Set I

When results of set I models were compared (for validation data) it was observed that MIKE 11 is superior to all data driven techniques in that its accuracy of prediction was better than ANN1, GP1 and MT 1 models (refer Table 1). However it may be noted that without involving mechanism of the underlying process and working on the basis of data, the ANN 1, GP1 and MT 1 models are working reasonably well.

Figures 4 and 5 show scatter plots for MIKE 11 and ANN1 respectively which clearly indicate superiority of MIKE results over ANN model results.

Table 1 Results: SET I

Model	Error measures		
	r	RMSE m/s	CE
M1	0.848	0.0398	0.633
ANN1	0.719	0.0469	0.497
GP1	0.703	0.0536	0.337
MT1	0.707	0.0478	0.473

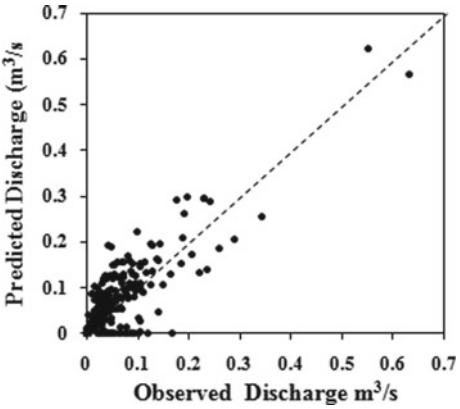

Fig. 4 Scatter plot for MIKE 11 model

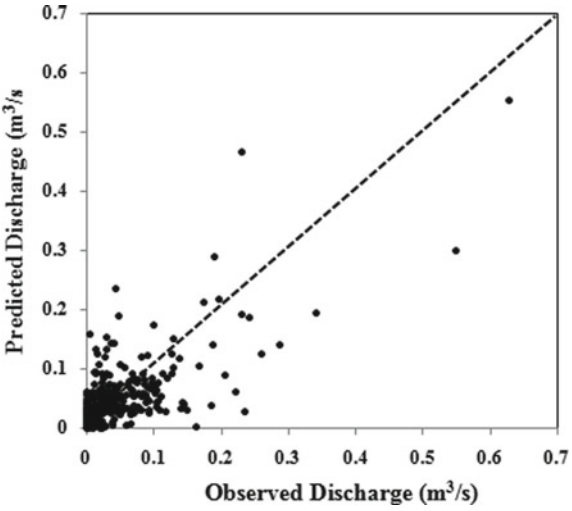

Fig. 5 Scatter plot for ANN1 model

Runoff predicted by all the models which also indicate that results of MIKE are better than all other data driven techniques are shown in Fig. 6. This is can be attributed to the inclusion of the underlying physical process MIKE while data driven

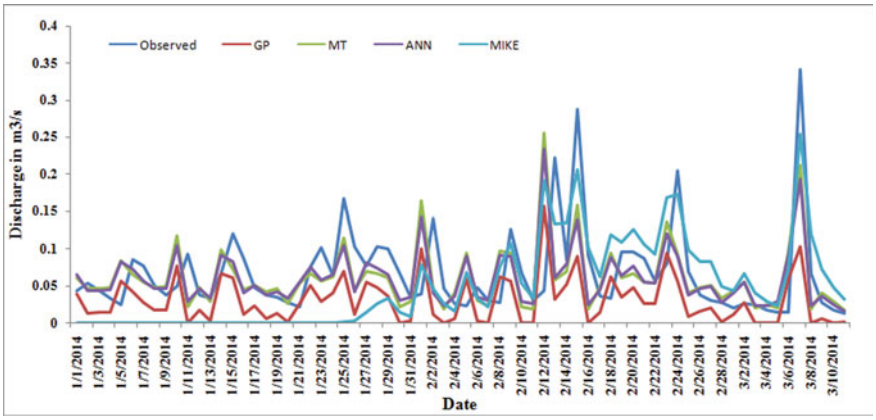

Fig. 6 Hydrograph of predicted discharge (Set I models)

tools solely depend upon the data and try to find the relationship of their own which entirely depends upon quality and quantity of data.

4.2 Set II

Models in set II were developed with input as rainfall with runoff as output. To develop models ANN2, GP2 and MT 2 models, three data driven techniques namely ANN, GP and MT were used. Results of models are shown in Table 2 which depict equal performance of GP, ANN and MT in predicting the discharge. All models perform reasonably as can been by the error measures. The scatter plots (Figs. 7 and 8) and hydrograph (Fig. 9) shown below endorse the above statement.

Thus it can be said that when all the exogenous inputs are available a numerical model like MIKE 11 is an obvious choice for rainfall –runoff modeling. In these circumstances the results of data driven techniques though not at par with MIKE 11 cannot be discarded either. However it should be accepted that the data driven techniques need further exploring if at all their results are to match (at least) with physics based numerical models. But non availability of any data other than rainfall and runoff, a data driven technique is very effective to model the rainfall runoff

Table 2 Results: SET II

Model	Error measures		
	r	RMSE m/s	CE
ANN2	0.724	0.057	0.511
GP2	0.727	0.059	0.472
MT2	0.726	0.057	0.521

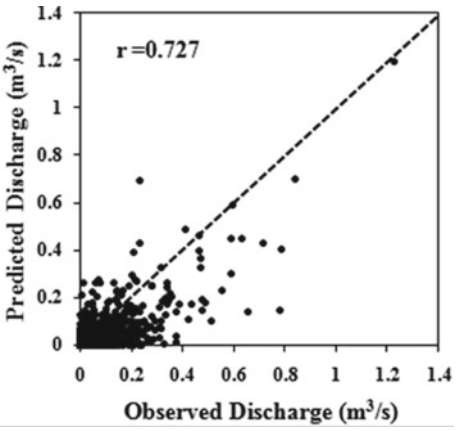

Fig. 7 Scatter plot for GP2 model

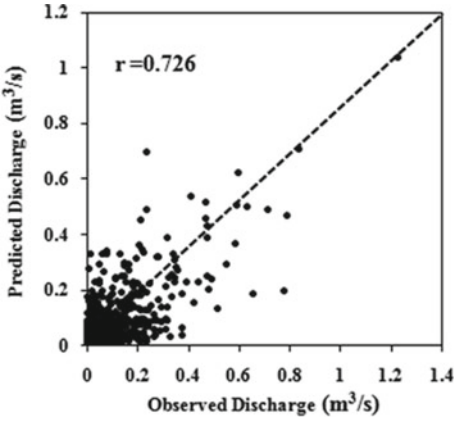

Fig. 8 Scatter plot for MT2 model

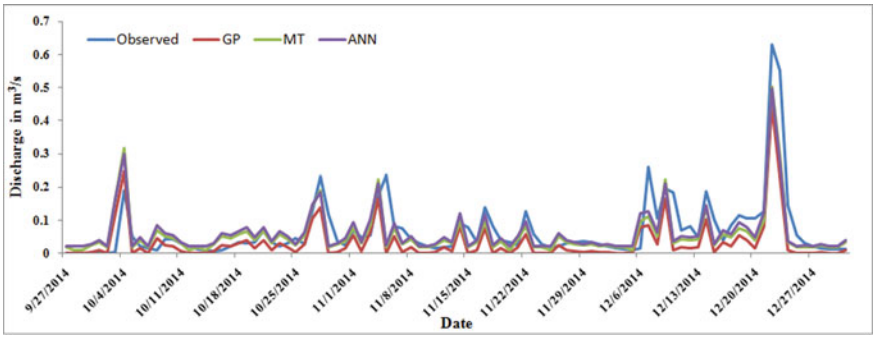

Fig. 9 Hydrograph of predicted discharge (Set II models)

process as it is the most important in managing the water resources. Another way can be coupling of these models with numerical models in that parameters like evapotranspiration can be predicted by ANN, GP or MT (Chaudhari et al. 2012) which can be used as an input in the numerical model. This will certainly enhance usability and adaptability of data driven tools.

5 Concluding Remarks

The rainfall-runoff models were developed separately with numerical model and data driven techniques. 2 sets of models of models were developed wherein for the first set three parameters namely rainfall, evapotranspiration and runoff were used to model the process. In this case results of numerical model were found to be better than all the three data driven techniques though they can't be discarded straight away. In the second set in absence of evapotranspiration data driven techniques were used, the performance of which was found to be of dame order of magnitude. Thus when the entire data required for using the physics based models is not available then the data driven techniques can certainly be useful. As introduced earlier these models can also coupled with numerical models which can be advantageous to both the techniques.

Annexure 1

Equation developed for GP1

$$\text{Discharge} = \left(\left(\text{RT} - \sqrt{(\text{ET}} \times \sqrt{\text{power(RT, 3)}}\right)\right) \times \text{power}(0.1956774,\ 3)$$

Equation developed for GP2

$$\text{Discharge} = \left(-3.2867\text{e-}0.002 \times (((\sqrt{(\text{RT} \times \text{RT})} + \sqrt{\text{RT}})) \times -3.7616\text{e-}0.002)\right)$$

Model for MT1

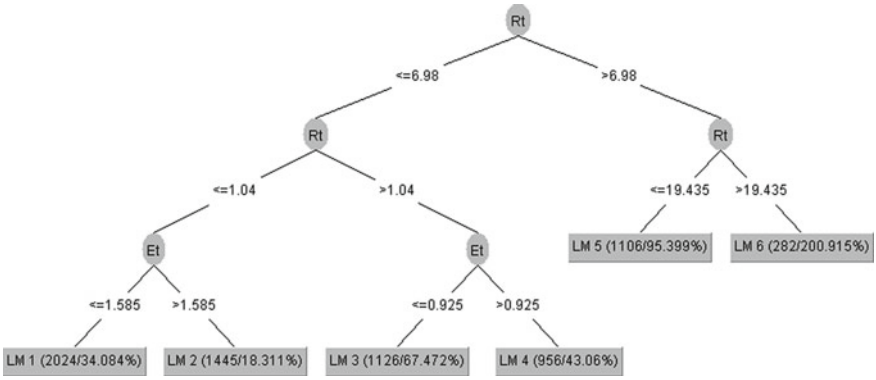

Model Tree for MT2

Rt = Daily rainfall Et = Daily evaporation

The first number is the number of samples in the subset sorted to this leave and the second one—root mean squared error (RMSE) of the corresponding linear model divided by the standard deviation of the samples subset for which it is built (expressed in percent).

References

Agrawal N, Deshmukh ST (2016) Rainfall runoff modeling using MIKE 11 NAM—a review. Int J Innov Sci Eng Technol 3(6):659–667

Bhattacharya B, Solomatine DP (2005) Neural networks and M5 model trees in modelling water level–discharge relationship. Neurocomputing 63:381–396

Bose NK, Liang P (1998) Neural network fundamentals with graphs, algorithms and applications. Tata McGraw-Hill, India

Chaudhari N, Londhe SN, Khare K (2012) Estimation of pan evaporation using soft computing tools. Int J Hydrol Sci Technol 2(4):373–390

Danish Hydraulic Institute (2009) MIKE 11: a modeling system for rivers and channels, reference manual, pp 278–325

Dawson DW, Wilby R (2001) Hydrological modeling using artificial neural networks. Prog Phys Geogr 25(1):80–108

Galkate RV, Jaiswal RK, Thomas T, Nayak TR (2014) Rainfall runoff modeling using conceptual NAM model. In: International conference on sustainability and management strategy, Nagpur

Hafezparast M, Araghinejad S, Fatemi SE, Bressers H (2013) A conceptual rainfall -runoff model using the auto calibrated NAM Models in the Sarisoo River. Hydrology 4(1):1–6

Haykin S (1994) Neural networks: a comprehensive foundation. MacMillan, New York

Koza J (1992) Genetic programming: on the programming of computers by means of natural selection. A Bradford Book. MIT Press

Londhe SN, Dixit PR (2012) Genetic programming: a novel computing approach in modeling water flows genetic programming—new approaches and successful applications. InTech. pp 200–224

Londhe SN, Charhate SB (2010) Comparison of data-driven modeling techniques for river flow forecasting. Hydrol Sci J 55(7):1163–1174

Madsen H (2000) Automatic calibration of a conceptual rainfall-runoff model using multiple objectives. J Hydrol 235:276–288
Maier HR, Dandy GC (2000) Neural networks for prediction and forecasting of water resources variables: a review of modelling issues and applications. Environ Model Softw 15:101–124
Quinlan JR (1992) Learning with continuous classes. In: Adams, Sterling (eds) Proceedings of 5th Australian joint conference on artificial intelligence. World Scientific, Singapore, pp 343–348
Singh A, Singh S, Nema AK, Singh G, Gangwar A (2014) Rainfall-runoff modeling using MIKE 11 NAM model for Vinayakpur intercepted catchment, Chhattisgarh. Indian J Dry Land Agric Res Dev 29(2):1–7
Solomatine DP, Siek MB (2004) Flexible and optimal M5 model trees with applications to flow predictions. In: Proceedings of the Sixth international conference on hydroinformatics, June 2004. World Scientific, Singapore
Solomatine DP, Dulal K (2003) Model tree as an alternative to neural network in rainfall-runoff modeling. Hydrol Sci J 48(3):399–441
Solomatine DP, Xue Y (2004) M5 model trees and neural networks: application to flood forecasting in the upper reach of the Huai River in China. J Hydrol Eng 9(6):491–501
The ASCE Task Committee (2000) Artificial neural networks in hydrology I: preliminary concepts. J Hydrol Eng 5(2):115–123
Wasserman PD (1993) Advanced methods in neural computing. Wiley, New York, NY, USA
www.mikepoweredbydhi.com/products/mike-11

Numerical Modelling of Tidal Hydrodynamics Along River Tapi, Gujarat

R. Balaji, J. Satheeshkumar, R. Cornelius, R. Naveen, G. Prasantha, and T. Prince

1 Introduction

The river is an important part of human civilization since it offers freshwater, inland transit, hydro energy, and assistance in leisure and tourism activities. However, various risk issues are associated with this due to the current rapid change in climate, which might result in flooding or drought. Climate change threatens coastal and riverine flood basins and the destruction of coastal ecosystems such as saltmarsh. These disasters have long-term consequences for coastal communities, socioeconomic activities, and the ecosystem. Cities near the river and coastal floodplain banks are more vulnerable to this hazard (Adhikari et al. 2010).

Furthermore, the situation has intensified as the combination of flooding and high tide conditions in this location raise the likelihood of a calamity. In today's world, numerical modelling is the most effective way for understanding this phenomenon (Cook and Merwade 2009; Gallegos et al. 2009; Mignot et al. 2006; Haider et al. 2003; Lindner and Miller 2012; Smith et al. 2005). As a result, in this study, the cutting-edge Delft3D modelling system was utilized to understand the hydrodynamics of the tidal river Tapi, which runs along the Gujarat coast. The following sections discuss the details of the modelling and the outcomes.

2 Study Area

The Tapi River is one of India's major rivers, starting 752 m above sea level in Madhya Pradesh's Satpura range. The river's overall length is roughly 724 km, and it flows through India's central region. The Tapi River passes through the states of

R. Balaji (✉) · J. Satheeshkumar · R. Cornelius · R. Naveen · G. Prasantha · T. Prince
Department of Civil Engineering, IIT Bombay, Mumbai 400076, India
e-mail: rbalaji@iitb.ac.in

R. Jha et al. (eds.), *River and Coastal Engineering*, Water Science and Technology Library 117, https://doi.org/10.1007/978-3-031-05057-2_34

Fig. 1 View of study area. *Source* Google Earth

Maharashtra, Gujarat, and Madhya Pradesh. Apart from the Narmada River, the Tapi River is the only one that runs westward and joins the Arabian Sea. With a total area of 65,145 square kilometers, the Tapi basin is India's second-largest. It flows through major cities and discharges into the Arabian Sea around 16 km from Surat (Fig. 1). As a result, Surat is frequently subjected to flooding due to the Tapi River, and its economy has suffered greatly from repeated floods over the last few decades. During the floods, a large percentage of the city is inundated, causing extensive damage to residential and industrial sectors. As a result, understanding the region's hydrodynamics is critical.

3 Data and Methods

3.1 Delft3D

In this research, the hydrodynamics along the Tapi River were simulated using the Delft3D modelling tool (WL| Delft Hydraulics 2006). It is comprised of multiple

modules that interact to simulate processes such as tidal hydrodynamics, wave transformation, water quality, sediment transport, and morphology. Delft3D-FLOW is a multi-dimensional (2D or 3D) hydrodynamic (and transport) modelling system that uses the finite-difference method to calculate non-steady flow and transport phenomena caused by tidal and meteorological forcing on a rectilinear or curvilinear boundary fitted grid with appropriate initial and open boundary conditions (Lesser et al. 2004). It solves the Navier Stokes equations for an incompressible fluid using the shallow water and Boussinesq assumptions, and it uses the continuity equation to determine vertical velocities for 3D models.

3.2 Hydrological Model Setup

The monsoon discharge of the Tapi River was calculated using a hydrological model built-in HEC-HMS. The river discharge was determined at a particular site near Surat's Magdala Bridge, at 21°8′47.25″N and 72°44′48.78″E. Until the Ukai Dam in Gujarat, drainage to the Arabian Sea was restricted. The model was constructed using ArcGIS 10.5 software and HEC-GeoHMS to extract basin parameters. As depicted in Fig. 2, the Tapi River's drainage lines and catchment area were determined using ArcGIS 10.5 and HEC-GeoHMS, followed by terrain pre-processing to yield watershed delineation. To combine relatively small sub-basins, HEC-Geo HMS basin processing was employed. The HEC-Geo HMS characteristic tool estimates the slope of a river, its length, the slope of a basin, the length of the longest flow channel, and the basin centroid. The basin's rainfall-runoff relationship was then estimated using monsoon rainfall data and the transfer and loss method with appropriate curve numbers.

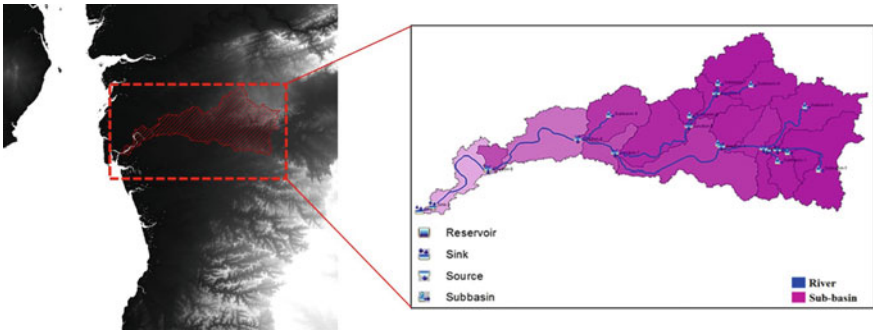

Fig. 2 View of river basin used for hydrologic model

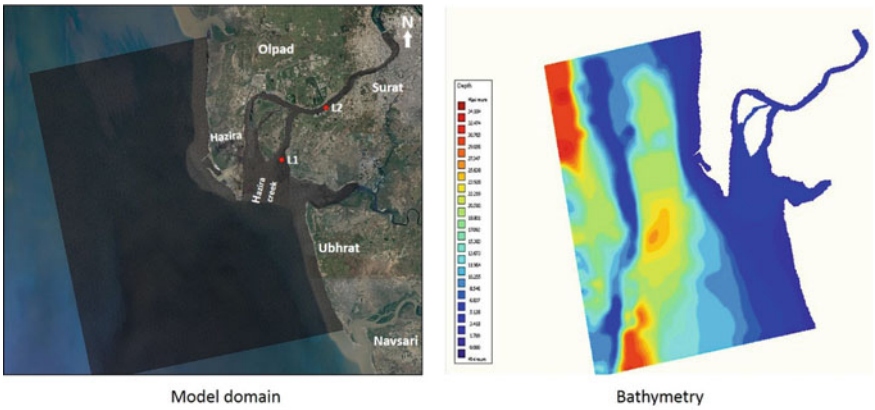

Fig. 3 View of study domain and bathymetry

3.3 Hydrodynamic Model Setup

As seen in Fig. 3, the Delft3D computational model grid encompasses the whole Tapi river basin. Admiralty charts (no. 1486 and 3460) were used to determine the bathymetry of the river and nearby coastal features such as inlets and estuaries. Throughout the domain, a rectilinear grid system with a spatial resolution of 100 m was used for simulation. The model's open boundary was set to 30 m of water depth and was forced with tidal astronomical elements extracted from a TPXO7.1 global tidal model (Egbert et al. 1994). River discharge values were estimated using the HEC-HMS model and then imposed on the upstream side of the boundary.

4 Results and Discussion

4.1 Hydrological Model Results

The rainfall data were obtained from GSDMA, Gujarat, for six days from 23 Jun 2017 to 28 Jun 2017, and it was observed that the peak discharge and the volume are 5.9 × 107 m^3/day and 1.4 × 105 mm at the specified discharge location. The estimated discharge was shown in Fig. 4.

4.2 Simulated Tidal Levels and Currents

The hydrodynamic model was simulated for ten days, from November 12 to November 22, 2017. The model-simulated results are validated in the following

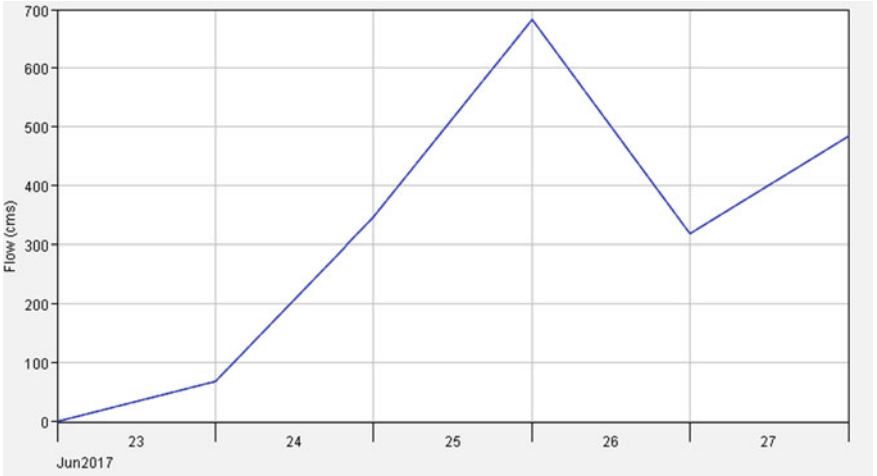

Fig. 4 Discharge hydrograph at Magdala Bridge, Tapi river

section using an in-situ field dataset collected on November 19, 2017 to assess the model's performance. Figure 5 illustrates the model's extracted water level and velocity. It is noticed that the overall model was capable of accurately simulating river hydrodynamics. Maximum water level and velocity were observed to be 2.2 m and 1.79 m/s, respectively. Contour plots of water level variation are depicted in Fig. 6.

4.3 Comparison of Measured versus Modeled Data

Field measurements were made on November 19, 2017, utilizing a total station and GPS Drifters to determine the water level and flow velocity. The measured water level and velocity ranges are compared to the model outputs to validate the model effectively. Figure 7 illustrates the time series comparison of measured and modelled water levels at River Tapi, while Table 1 shows the qualitative comparison. The measured and calculated drifting velocities are depicted in Figs. 8 and 9, and Table 2 gives a quantitative comparison.

5 Conclusion

The hydrodynamics of the Tapi River in Gujarat were studied using a two-dimensional shallow water-based finite difference model. According to the HEC-HMS hydrological modelling study, the estimated peak discharge and water volume

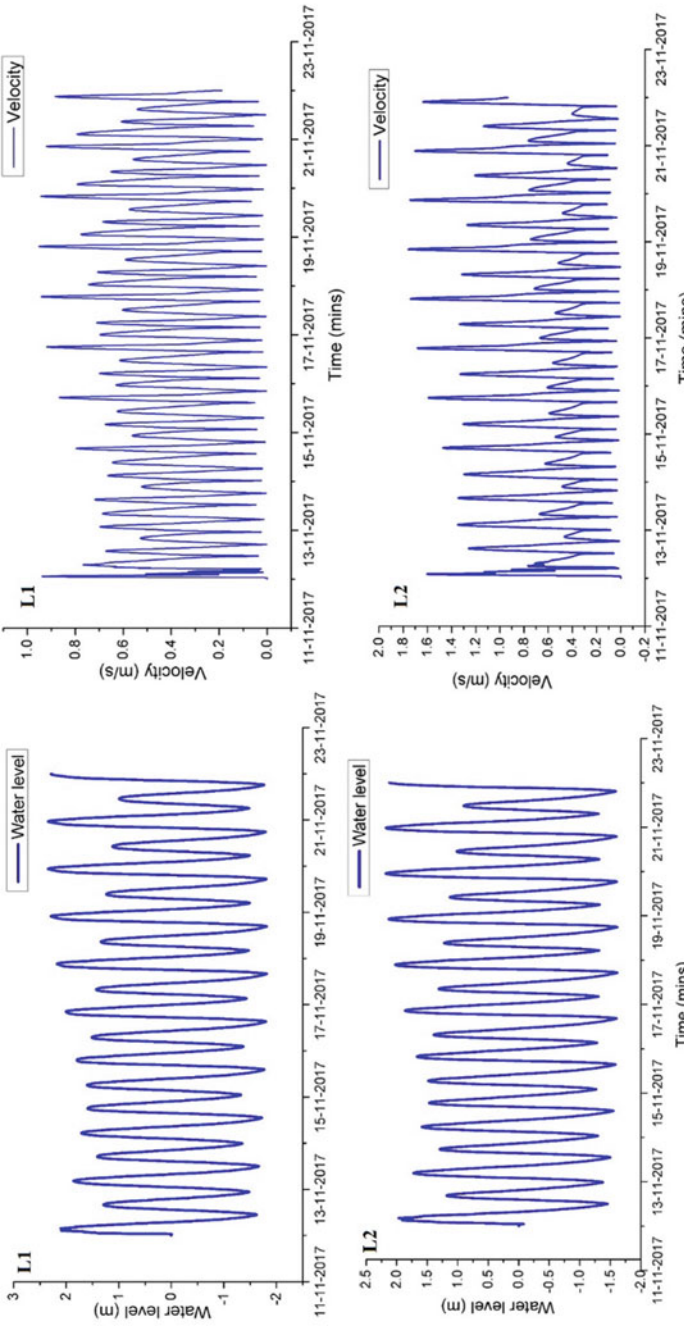

Fig. 5 Time series of simulated water level and velocity

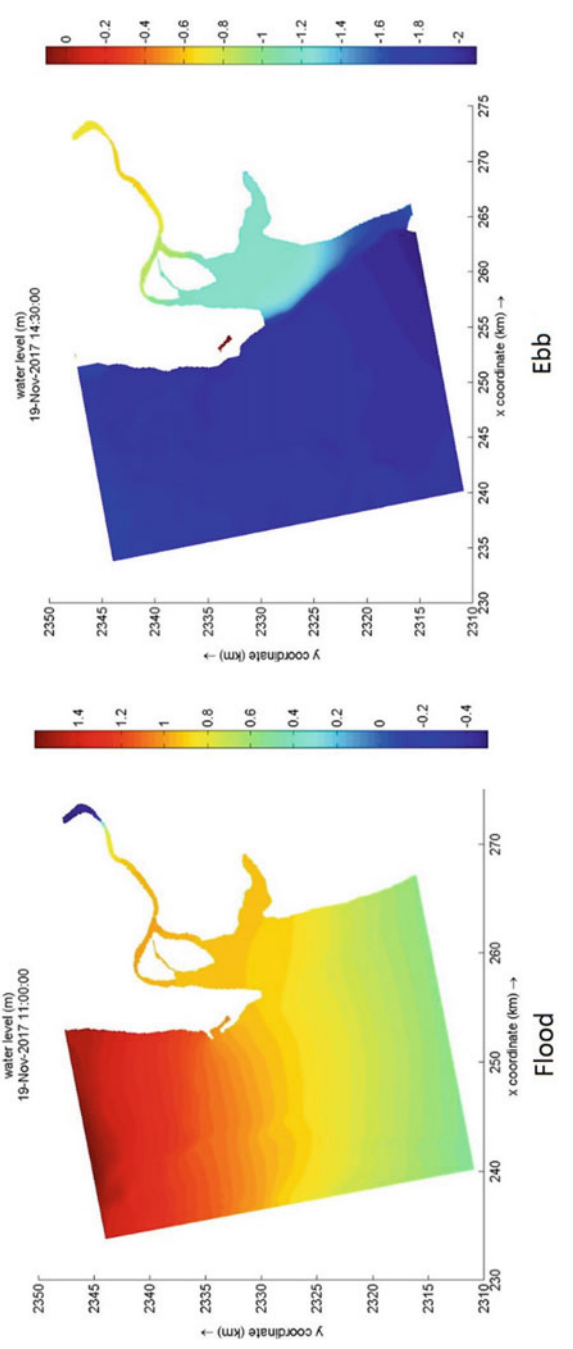

Fig. 6 Typical view of water level variation during flood and ebb

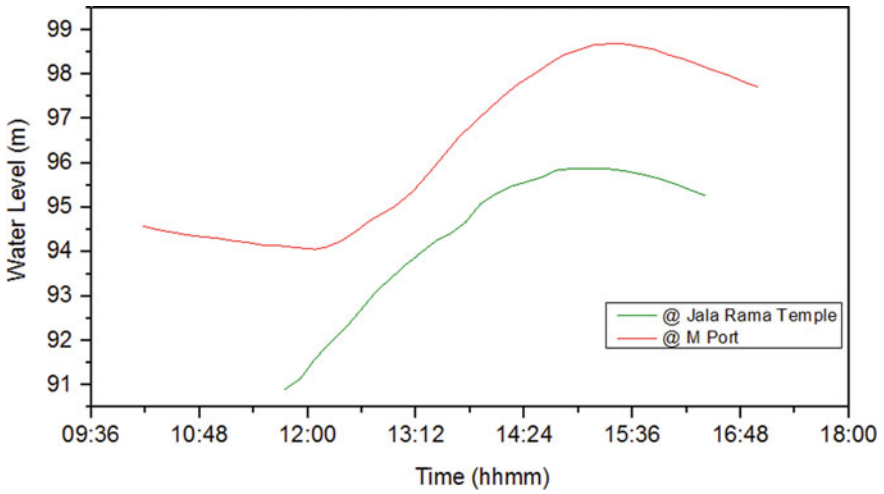

Fig. 7 Measured water level at two location in Tapi River

Table 1 Comparison of measured versus modeled water level values

Location	Measured range (m)	Modelled range (m)
L1-Joining	4.6	4.1
L2-At Site	4.5	3.5

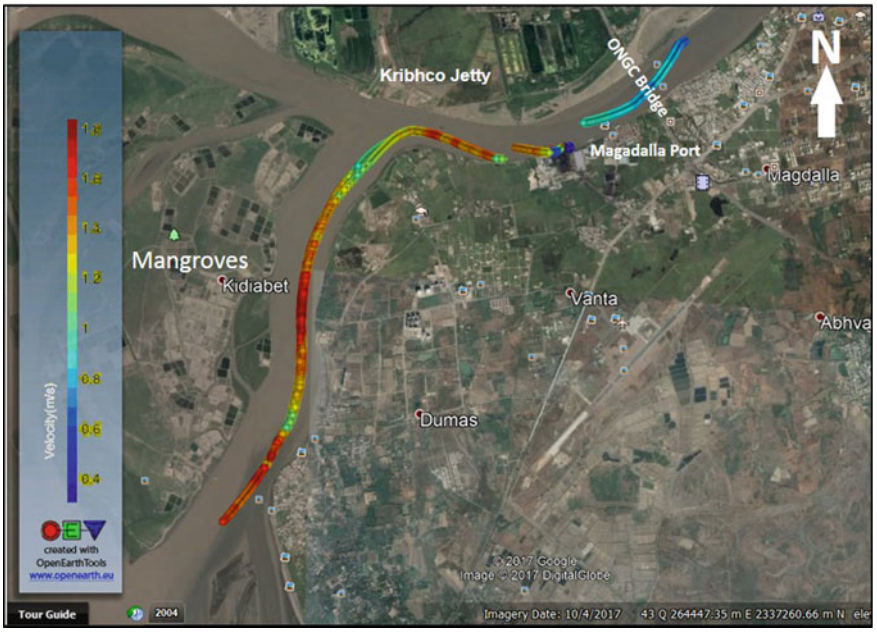

Fig. 8 Measured GPS drifter trajectories

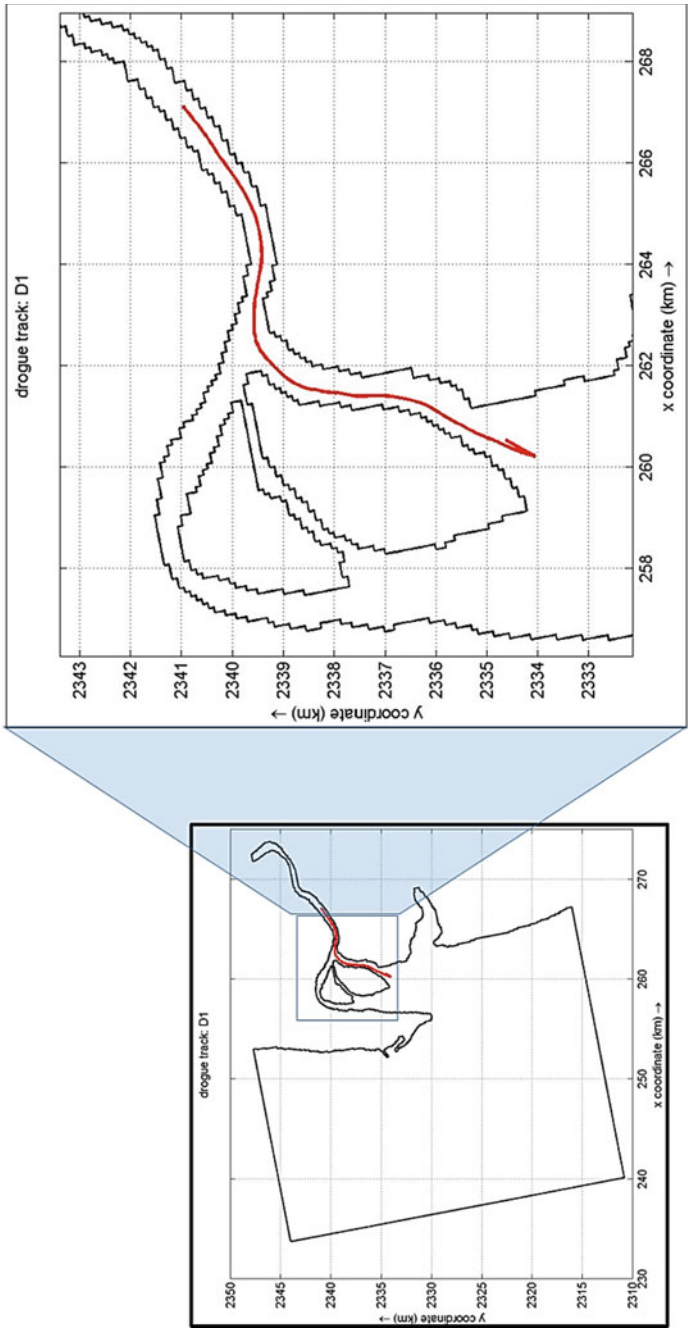

Fig. 9 View of model simulated trajectories

Table 2 Comparison of measured versus modeled drifter's surface velocity

Latitude	Longitude	Measured (m/s)	Modelled (m/s)
21.107458	72.702114	1.6	1.22
21.139184	72.711927	1.0	0.80
21.140485	72.724300	1.4	1.25

at the selected discharge location are 5.9×10^7 m^3/day and 1.4 × 105 mm. The tidal hydrodynamic model was forced with the predicted discharge values of several situations (monsoon and non-monsoon) to compute extreme water levels and flooding. The simulated results were successfully validated using the sparse field data that was available. It was also used to replicate the model's spatially variable hydrodynamic features, such as water level and current velocity. According to this study, the maximum water level and velocity in the combination of spring tide and extreme discharge scenarios reach up to 2.2 m and 1.79 m/s, respectively.

References

Adhikari Y, Osti R, Noro T (2010) Flood-related disaster vulnerability: an impending crisis of megacities in Asia. J Flood Risk Manage 3(3):185–191

Cook A, Merwade V (2009) Effect of topographic data, geometric configuration and modeling approach on flood inundation mapping. J Hydrol 377(1–2):131–142

Egbert GD, Bennett AF, Foreman MGG (1994) Topex/Poseidon tides estimated using global inverse model. J Geophys 99:24821–24852

Gallegos HA, Schubert JE, Sanders BF (2009) Two dimensional, high-resolution modeling of urban dam-break flooding: a case study of Baldwin Hills, California. Adv Water Resour 32(8):1323–1335

Haider S, Paquier A, Morel R, Champagne J-Y (2003) Urban flood modelling using computational fluid dynamics. Proc ICE, Water Marit Eng 156(2):129–135

Lesser GR, Roelvink JA, van Kester JATM, Stelling GS (2004) Development and validation of a three-dimensional morphological model. Coast Eng 51:883–915

Lindner GA, Miller AJ (2012) Numerical modeling of stage discharge relationship in urban streams. J Hydraul Eng 59:590–596

Mignot E, Paquier A, Haider S (2006) Modeling floods in a dense urban area using 2D shallow water equations. J Hydrol 327(1–2):186–199

Smith JA, Miller AJ, Baeck ML, Nelson PA, Fisher GT, Meierdiercks KL (2005) Extraordinary flood response of a small urban watershed to short-duration convective rainfall. J Hydrometeorol 6(5):599–617

WL | Delft Hydraulics (2006) Delft3D-FLOW User Manual